

Probing surface and interface morphology with Grazing Incidence Small Angle X-Ray Scattering

Gilles Renaud ^{a,*}, Rémi Lazzari ^b, Frédéric Leroy ^c

^a Commissariat à l'Energie Atomique, Institut Nanosciences et Cryogénie, Service de Physique des Matériaux et Microstructures, Nanostructures et Rayonnement Synchrotron, 17 Avenue des Martyrs, F-38054 Grenoble, Cedex 9, France

^b Institut des NanoSciences de Paris, Université Pierre et Marie Curie (Paris 6), CNRS UMR 7588, Campus Boucicaut, 140 Rue de Lourmel, 75015 Paris, France

^c Centre Interdisciplinaire de Nanoscience de Marseille, CNRS - UPR 3118, Campus de Luminy Case 913, 13288 Marseille Cedex 9, France

ARTICLE INFO

Article history:

Accepted 12 July 2009

editor: G. Thornton

Keywords:

X-ray scattering
Grazing incidence
Synchrotron X-rays
GISAXS
Grazing Incidence Small Angle X-Ray Scattering
Distorted Wave Born Approximation
DWBA
Local Monodispersed Approximation
Decoupling Approximation
Size-Spacing Correlation Approximation
Scaling Approximation
Theory of X-ray scattering
Form factor
Interference function
Assemblies of nanoparticles
In situ
Nano-particles
Nano-structures
Growth modes
Growth laws
Molecular beam epitaxy
Ultra-high-vacuum
Catalysis
Semi-conductors
Metal surfaces
Reconstructions
Self-organized growth
Patterned substrates
Polymers
Metal on oxide surfaces
Quantum dots

ABSTRACT

Nanoscience and nanotechnology are tremendously increasing fields of research that aim at producing, characterizing and understanding nanoobjects and assemblies of nanoobjects. Their new physical or chemical properties, which arise from confinement effects, intimately depend on their morphological properties, *i.e.* their shapes, their sizes and their spatial organization. This calls for dedicated morphological characterization tools, among which is the Grazing Incidence Small Angle X-Ray Scattering (GISAXS). This reciprocal space technique has emerged in the last two decades as a powerful tool that allows investigating in a non-destructive way the morphological properties from one to billions of nanoparticles, either on a surface, or embedded in a matrix, with sizes ranging from 1 nm to several microns. The advantages of the technique are that it is non-destructive; it yields statistical information averaged on a large number of nanoparticles; it allows probing both the surface or deep below it, by changing the incident angle of the X-ray beam; it can be used in very different sample environments, in particular *in situ* in the course of a given process such as growth, annealing, gas exposure; and it may be given chemical sensitivity by use of anomalous scattering.

This report presents a review of the GISAXS technique, from experimental issues to the theories underlying the data analysis, with a wealth of examples. The physical morphological information contained in GISAXS data and its analysis are presented in simple terms, introducing the notions of particle form factor and interference function, together with the different cases encountered according to the size/shape dispersion. The theoretical background of X-ray diffuse scattering under grazing incidence is presented in a general way, and then applied to the particular case of grazing incidence small angle X-ray scattering from assemblies of particles either on a substrate, or buried below it.

Most of the GISAXS measurements published to date are reported, covering the fields of *ex situ* studies of embedded metallic nanoparticles, granular multilayered systems, implanted systems, embedded or stacked or deposited semi-conductor nanostructures, porous materials and copolymer thin films. A special emphasis is brought on *in situ* experiments, performed either in ultra-high vacuum during nanoparticle growth by molecular beam epitaxy, or in gas-reactors during catalytic reactions. This covers a very broad field, from (i) the 3D island (Volmer–Weber) growth of metals on oxides surfaces to (ii) the organized growth of metals on surfaces that are nanopatterned either by surface reconstruction or by underlying dislocation networks or by deposit-induced nanofacetting, to (iii) the *in situ* investigation of the self-organized Stranski–Krastanow hetero-epitaxial growth of semi-conductor quantum dots on semi-conductor surfaces, or (iv) the *in situ* surface nanopatterning by ion bombardment. Many examples are discussed in detail, to illustrate the large diversity of systems and morphologies that can be addressed as well as the different analysis issues and the conclusions of the technique in terms of growth mode.

© 2009 Elsevier B.V. All rights reserved.

Contents

1. Introduction.....	258
2. X-ray techniques to probe density fluctuations near surfaces and buried interfaces	260

* Corresponding author. Tel.: +33 4 38 78 35 58; fax: +33 4 38 78 51 97.

E-mail addresses: grenaud@cea.fr (G. Renaud), lazzari@insp.jussieu.fr (R. Lazzari), leroy@cinam.univ-mrs.fr (F. Leroy).

URL: <http://grenaud@cea.fr> (G. Renaud).

2.1.	The basis of grazing incidence X-ray techniques on nanostructures	260
2.1.1.	The scattering geometry	260
2.1.2.	Reciprocal space of nanostructures on a surface	261
2.2.	The different geometries of surface X-ray scattering techniques at small angles	261
2.2.1.	Grazing Incidence Small Angle X-Ray Scattering (GISAXS)	261
2.2.2.	Specular X-ray reflectivity (XRR)	262
2.2.3.	Off-specular X-ray reflectivity	262
2.2.4.	Advantages and drawbacks of X-ray techniques	262
2.2.5.	Brief history of GISAXS applied to hard condensed matter	263
2.2.6.	<i>In situ</i> GISAXS and GIXS, in UHV, during growth	263
3.	Experimental considerations	263
3.1.	Background minimization	263
3.2.	First <i>in situ</i> GISAXS setup, on the ID32 ESRF beamline	263
3.3.	Second <i>in situ</i> GISAXS setup: Simultaneous analysis of morphology and structure by GISAXS and GIXS on the BM32 beamline	263
3.4.	Third <i>in situ</i> set up: <i>In operando</i> studies of model catalysts by GIXD and GISAXS	265
3.5.	Other <i>in situ</i> X-ray chambers	266
3.6.	Detectors	266
3.7.	Notations	267
4.	General trends of the analysis of 2D GISAXS data	267
4.1.	Introduction	267
4.2.	Form factor versus interference function	267
4.3.	Form factors of simple geometrical shapes	267
4.4.	The problem of the interference function	268
4.5.	Nanostructures spacing and maximum of the interference function	268
4.6.	Deducing nanostructure size and shape from a rapid data analysis	269
4.6.1.	The small polydispersity case	269
4.6.2.	The large polydispersity case: Nanostructure size distribution	269
4.6.3.	The large polydispersity case: Asymptotic behavior of the form factor	270
4.6.4.	Very fast data analysis of GISAXS patterns	270
4.7.	Nanostructure faceting	271
4.8.	Practical considerations	271
5.	Theoretical background of grazing incidence diffuse X-ray scattering	271
5.1.	Introduction	271
5.2.	Propagation of X-ray at interfaces	272
5.2.1.	Wave propagation in three dimensions	272
5.2.2.	Dielectric constant and index of refraction	272
5.2.3.	Propagation in stratified media and Helmholtz equation for X-rays	273
5.2.4.	The boundary conditions	273
5.2.5.	The analogy with Schrödinger propagation equation	274
5.2.6.	Snell–Descartes laws, Fresnel coefficients and penetration depth	274
5.2.7.	Reflection and transmission in layered materials: The matrix formalism	275
5.2.8.	Influence of roughness on the Fresnel coefficients: Nérot–Croce and Debye–Waller-like corrections	276
5.2.9.	Kinematic approximation of reflectivity and beyond	276
5.3.	The differential X-ray scattering cross section in Distorted Wave Born Approximation	278
5.3.1.	Introduction and historical overview	278
5.3.2.	The integral solution of the wave propagation and the Green function	278
5.3.3.	The scattering cross sections	280
5.3.4.	The Born approximation of first order (BA)	281
5.3.5.	The Distorted Wave Born Approximation (DWBA)	281
5.3.6.	The polarization effects: Toward a scalar wavefield scattering and an analogy with the Schrödinger equation	281
5.4.	Distorted Wave Born Approximation in action	282
5.4.1.	Reflectivity from a graded interface in the DWBA	282
5.4.2.	Single rough surface: DWBA versus BA	283
5.4.3.	Rough multilayers	285
5.4.4.	Buried density fluctuations	289
5.4.5.	Diffuse scattering from magnetic media	289
5.4.6.	Validity range of DWBA	290
5.4.7.	Improving DWBA accuracy?	290
6.	Grazing Incidence Small Angle X-Ray Scattering from assemblies of particles	291
6.1.	Introduction	291
6.2.	Dilute case: Form factor of an isolated particle in DWBA	292
6.2.1.	The particle form factor	292
6.2.2.	The supported nanoparticle	292
6.2.3.	The buried particle or the hole at the surface	293
6.2.4.	Particles or holes in a thin slab	293
6.2.5.	The core-shell particle	294
6.2.6.	The Fourier transform of particle shape	294
6.2.7.	Scattering from faceted particles	295
6.2.8.	Miscellaneous remarks	296
6.2.9.	Direct data inversion from coherent GISAXS?	296
6.3.	Concentrated case	297

6.3.1.	General formalism of the partial interference functions: Coherent versus incoherent scattering	297
6.3.2.	The decoupling approximation and the local monodisperse approximation.....	298
6.3.3.	Size and shape distributions and the asymptotic behaviors of the form factor	298
6.3.4.	The interference function.....	299
6.4.	Accounting for the particle-particle correlations: DA, LMA and beyond	301
6.4.1.	Decoupling Approximation.....	301
6.4.2.	Local Monodisperse Approximation.....	301
6.4.3.	Size-Spacing Correlation Approximation	302
6.4.4.	Scaling Approximation	304
6.5.	The graded interface model and the nanoparticle form factor	304
6.6.	Limitations of the quantitative analysis of GISAXS from nanoparticles.....	305
7.	Examples of extensive data analysis of GISAXS patterns	306
7.1.	First example: Pt/MgO(001).....	307
7.2.	Second example: Pd/MgO(001)	307
7.3.	Third example: Au/TiO ₂ (110)	308
7.4.	Diffuse scattering due to correlations	308
7.4.1.	Evidence of diffuse scattering in GISAXS	308
7.4.2.	Estimated diffuse scattering in GISAXS	308
7.4.3.	Size-position correlation deduced from GISAXS.....	309
8.	Non-UHV GISAXS experiments	310
8.1.	Embedded metallic nanoparticles	310
8.1.1.	Granular solids and multilayers of metallic clusters embedded into oxide matrices	310
8.1.2.	Encapsulated Ag, Fe, Pt and Au nanoparticles into carbon and boron nitride	311
8.1.3.	Embedded clusters into glass by ion implantation	315
8.2.	Porous materials	315
8.2.1.	Mesoporous silica thin films obtained by self-assembly: <i>ex situ</i> and <i>in situ</i> studies.....	315
8.2.2.	Low- <i>k</i> and ultralow- <i>k</i> nanoporous dielectric films	317
8.2.3.	Porosity in thin films prepared by chemical routes in solution	319
8.3.	Block copolymers thin films	320
8.3.1.	Ordering of block copolymers thin films	320
8.3.2.	Phase transition of block copolymer thin films	321
8.3.3.	Dewetting of polymer thin films	322
8.4.	Thermal stability and reactivity of supported clusters	323
8.5.	Ex situ GISAXS studies of semi-conductor nanostructures	324
8.5.1.	Introduction	324
8.5.2.	Self-assembled Si _{1-x} Ge _x islands	324
8.5.3.	Other self-assembled semi-conductor quantum dots	326
8.5.4.	GISAXS analysis of vertical stacking of semi-conductor quantum dots	327
8.5.5.	Characterization of defects induced by implantation in semi-conductors	330
8.5.6.	Porous materials	333
8.5.7.	GISAXS studies of semi-conductor nanocrystals	333
8.5.8.	Other GISAXS studies of semi-conductors	334
8.5.9.	The use of q_x and q_y in plane directions to distinguish long-range and short-range order: The case of bonded Si wafers	334
9.	<i>In situ</i> GISAXS measurements in ultra-high vacuum, during growth.....	336
9.1.	3D-island growth: The metal/oxide interfaces case	336
9.1.1.	Motivations	336
9.1.2.	Investigated systems	336
9.1.3.	Preparation of samples	337
9.1.4.	General trends during growth and coalescence of islands	337
9.1.5.	Evolution of morphological parameters with thickness: Nucleation, growth and coalescence	340
9.1.6.	Information on growth modes	342
9.1.7.	Equilibrium shape, Wulff-Kaischew construction and adhesion energy	343
9.2.	Looking by GISAXS at nanoparticles during a catalytic reaction	344
9.2.1.	Scientific background: Bridging the pressure gap in surface science	344
9.2.2.	<i>In operando</i> study of gold nanoparticles on TiO ₂ (110)	344
9.3.	Stranski-Krastanow growth in the Ge/Si(001) system	345
9.4.	Self-organized growth of nanostructures	350
9.4.1.	The ordered growth of Co on Au(111)	350
9.4.2.	The ordered growth of Co on a kinked vicinal surface of Au(111)	355
9.4.3.	Self-organized growth of Co on a misfit dislocation network Ag/MgO(001)	359
9.4.4.	Self-organized growth of Ni clusters on a cobalt-oxide thin film induced by a buried misfit dislocation network	362
9.5.	Surface nanofacetting: The case of Pt on W(111)	364
9.5.1.	Nucleation and growth of 3-fold symmetry nanopyramids	364
9.5.2.	Validity of the DWBA: GISAXS as function of the incident angle	366
9.5.3.	The growth of Co on a faceted Pt/W{211} surface	367
9.6.	Semi-conductor surfaces nanostructures induced by sputtering	368
9.7.	<i>In situ</i> studies of GaN surfaces	369
10.	Conclusion	369
	Acknowledgements	370
	Appendix. The analytical Fourier transforms of simple shapes	370
	References	372

1. Introduction

Nanomaterials are widely seen as having a huge potential to bring benefits to many areas of research and application, and are attracting rapidly increasing investments in many parts of the world. Nanomaterials are defined as having at least one dimension in the nanometer range (1–100 nm). Their properties differ significantly from those at a larger scale for two main reasons. First, quantum effects dominate the behavior of matter at the nanoscale affecting the structural, optical, electrical and magnetic properties of materials. Second, nanomaterials have a relatively larger surface area when compared to the same mass of macroscopic material. This can make them much more chemically reactive (in some cases materials that are inert in their larger form are reactive when produced in their nanoscale form), and affect their strength or electrical properties. Nanoscience and nanotechnologies are not new. For many decades, chemists have been making polymers made up of nanoscale subunits, and nanotechnologies have been used to create tiny features on computer chips for the past 20 years. However, advances in the characterization tools have allowed materials to be examined with great precision and enabled the expansion and development of this field. Nowadays, nanomaterials concern not only conventional domains such as physics and chemistry, but also earth and life sciences. Recent industrial developments are clearly targeted toward introducing nanostructures into everyday life [1]. For instance the ongoing trend of miniaturization in electronics is reaching the nanometer scale, where the performance such as tunneling, band structure or photon emission are determined by confinement effects (size, morphology, strain, atomic structure and composition). The past years have thus been marked by the elaboration and study of materials on nanometric scale, such as 2D layers or multilayers, and more recently 1D nanowires, or 0D nanoparticles, such as quantum dots, or buried aggregates. Indeed, the properties of interest can be tuned by confining phenomena in objects where at least one dimension is smaller than a typical bulk length scale (screening length, exciton radius, magnetic domain size etc...). For instance, (i) the reactivity and selectivity of catalysts made of supported metallic nanoparticles are driven by the nature of the exposed surfaces and by the particle electronic structure, which in turn depend on the particle size, shape and internal structure [2,3]; (ii) magnetic storage properties can be modulated and increased provided that controlled single domain magnetic nanoparticles can be elaborated [4,5]; (iii) in the field of semiconductors, the novel transport or opto-electronics properties in coherently strained semiconductor nanoparticles, the so-called “quantum dots” (QDs) [6,7], are tuned by playing on the particle size, strain and composition [1].

These few examples are illustrative of the need for characterizing and controlling the growth and morphology of nanoobjects. In particular, a better understanding of the growth mechanisms of nanoparticles is a prerequisite for their application on a large extent. This point is especially relevant in semiconductor devices. Their properties are highly dependent on the size, shape, strain, composition (interdiffusion), interface structure, roughness, defects and spatial organization on the substrate. Any change of these morphological parameters over the assembly of particles gives rise to a broadening of the distribution of properties. It is therefore essential to characterize these quantities precisely as a function of the growth parameters such as substrate quality, temperature and deposition rate. This points to the importance of controlling the growth of a large collection of nanoparticles by monitoring *in situ* and in real time the relevant parameters. From a more fundamental point of view, the growth mechanisms themselves must be investigated, in order to deduce the kinetic coefficients and energy barriers involved in the growth process [8].

In this context, the morphological and structural properties of nanomaterials are usually addressed by a wealth of techniques such as laboratory X-ray diffraction (XRD), Transmission Electron Microscopy (TEM), High resolution Scanning Electron Microscopy (SEM), Scanning Tunneling Microscopy (STM) or Atomic Force Microscopy (AFM), and synchrotron radiation based X-ray techniques. All these techniques have advantages and drawbacks and are thus complementary to each other. If, for particles on top of a surface, Near Field Microscopy (NFM) techniques most often provide the required morphological information, they also have some limitations, such as limited statistics, convolution with the tip shape, difficulty to use on bulk insulating substrates and to use *in situ* during growth because of shadowing effects and temperature drift. Therefore long acquisition times and interruption of the growth process are needed. For particles embedded in a matrix, below a surface, the NFM techniques are useless, and most other techniques are destructive.

Complementary information can be obtained in reciprocal space using X-ray scattering. For a long time, the small interaction of hard X-rays with matter hampered its straightforward use for surface or interface studies. However, since pioneering works in the 80th [9,10], the combined use of high brilliance synchrotron radiation and grazing incidence geometry allowed to reach surface sensitivity with a reasonable signal to noise ratio. Compared to microscopy, Grazing Incidence X-Ray Scattering or Diffraction (GIXS or GIXD) [11–15] and its small angle subset, Grazing Incidence Small-Angle X-Ray Scattering (GISAXS) [16] has several advantages:

- (i) The technique is fully non-destructive provided that the sample bears hard X-ray exposure;
- (ii) The measurement is averaged over all the sample surface, giving statistical information over several square millimeters at variance to microscopy;
- (iii) By varying the probed depth with the incident angle, X-rays offer the ability to probe from surface to buried interfaces as well as the bulk of the sample;
- (iv) The technique can be applied in various types of environment from ultra-high vacuum to gas atmospheres, even during chemical reactions, *in situ* and in quasi real-time when kinetic phenomena are involved like during growth or a catalytic reaction; the measurements themselves usually require no special sample environment or preparation;
- (v) The Grazing Incidence Small Angle Scattering (GISAXS) technique, which provides morphological information from the nanometer to micrometer length scales can be combined, on the same samples, with the grazing incidence wide angle X-ray scattering or diffraction (GIXS) technique which is sensitive to the atomic arrangement and strain state;
- (vi) The chemical contrast of a given element can be enhanced by performing anomalous scattering close to a specific absorption edge, thus yielding compositional information.

As with most techniques, X-ray scattering also has some drawbacks:

- (i) The use of synchrotron radiation is nearly mandatory because the collected signal scales with the amount of material, which can be rather small (of the order of the monolayer).
- (ii) The interesting information e.g. the morphology is obtained in reciprocal space, and thus has to be “translated” in the real world. As only scattered intensities can be measured, the phase information is lost, which means that some model assumptions are most often mandatory to fit the data. This problem can be overcome if the coherence of the synchrotron radiation is employed. The technique of coherent X-ray diffraction imaging is on the rise and allows for a model-free reconstruction of small crystals and nanostructures, mainly in diffraction configuration.

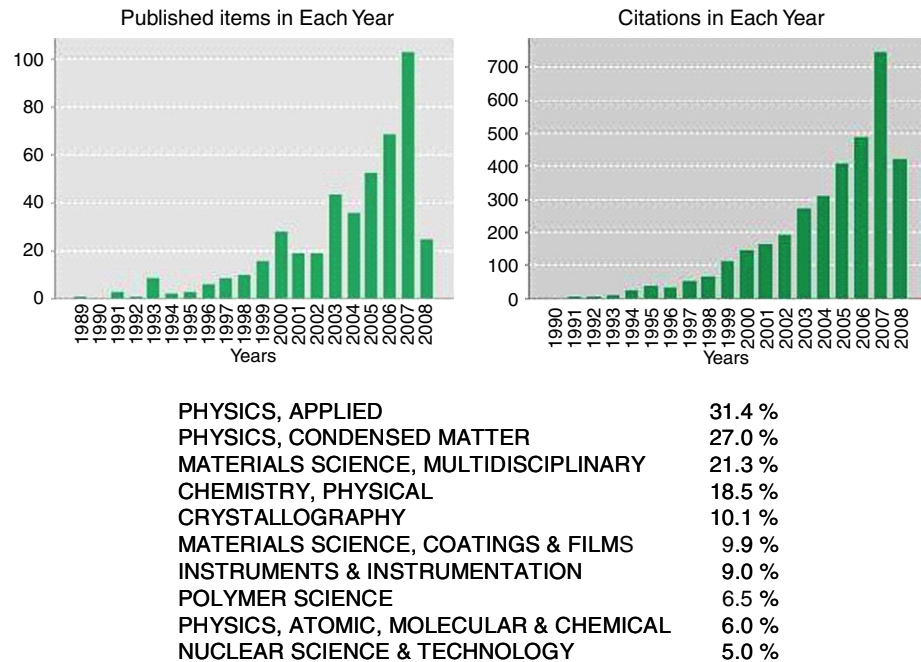


Fig. 1. Number of published and cited scientific papers with the keyword “GISAXS” per year. The dispatching on scientific fields is given below. From ISI Web of Knowledge.

(iii) It is difficult to characterize a single nanoobject because of the beam size, divergence, and limitations of X-ray optics (although this field, called coherent X-ray diffraction, is going to develop). The statistical average over the coherent domains can be seen as an advantage since the beam samples the growing particles in the same way as for the macroscopic properties of interest, and gives an image of the “mean island”.

Since the first experiments [16–18], the Grazing Incidence Small Angle X-Ray Scattering (GISAXS) technique has emerged in the last decade as a powerful tool to analyze the morphology and distribution of either islands on a substrate or buried particles, in parallel with the wide angle X-ray scattering techniques under grazing incidence, which provide unique average information on their atomic structure, strain and composition. The ability of GISAXS to characterize granular multilayered systems [19], implanted systems [20], as well as semiconductor quantum dots obtained by molecular beam epitaxy (MBE) or liquid phase epitaxy (LPE) is now well established [21–24]. Quite recently, new technical developments [25,26] allowed this technique to be applied to topics which are relevant for surface science, by performing it *in situ*, during particle growth. By combining an ultra-high vacuum environment and 2D-detection at small angles and by paying a special attention to the signal to noise ratio and measurement dynamics far away in reciprocal space, quantitative studies of various aspects of thin film growth, from sub-monolayer to percolation, or of surface nanostructuring became possible. High quality data and careful data analysis using the Distorted Wave Born Approximation with suitable programs [27,28] allow one to get in one experiment statically averaged information relevant to the growth process which, otherwise, would have implied lengthly *ex situ* measurements. For instance, it has been demonstrated that the technique is relevant to cope with issues such as the particle equilibrium shape for Pd/MgO(001) [2,13,25,29] or the self-organized growth of Co clusters on the herringbone reconstruction of the Au(111) surface [30,31,25,32]. Using the capability of X-rays to handle gas atmosphere, the technique starts now to be used to bridge the pressure gap for the study of catalytic nanoparticles at relevant pressure conditions [33,34]. In parallel with the measurements, the technique has benefited

from theoretical developments to handle scattering at grazing incidence [35–37].

GISAXS is nowadays becoming a very common technique to characterize nanoparticles, as evidenced by the exponentially growing number of publications (see Fig. 1). A clear trend toward *in situ* studies or routine characterization of samples clearly emerges in the literature in a broad range of fields ranging from physics and chemistry to material science and even biology. The present report gives an overview of the current state-of-the-art of the technique with an emphasis on hard condensed matter studies. The *in situ* and *ex situ* capabilities of the technique to analyze the morphology of nanostructures from the nanometer to micrometer scales is illustrated through a wealth of cases stressing on the knowledge brought to the surface scientist on processes at surfaces.

This report is organized as follows. Section 2 is devoted to a basic presentation of the reciprocal space of nanostructures and its exploration with the Grazing Incidence X-Ray Scattering techniques at wide and small angles, as well as by X-ray specular and off-specular X-ray reflectivity. Section 3 presents a few experimental considerations, especially to perform GISAXS measurements *in situ*, in ultra-high vacuum (UHV), during the elaboration of nanostructures or during catalytic reactions. Section 4 introduces the basic features of the GISAXS interpretation for nanoparticles, with a simplified presentation of the different problems in the description and analysis of GISAXS data. In Section 5, the theoretical bases of X-ray interaction and propagation at surfaces are given in a self consistent way. An emphasis is put on the refraction–reflection effects that are predominant when the beams are grazing with respect to the surface. Scattering processes are introduced in the framework of the classical Born Approximation and the popular Distorted Wave Born Approximation which allows to account for multiple scattering effects in grazing geometry. Several interface cases are explored as well as the limitations of the approximations. Section 6 is devoted to theoretical scattering from nanoparticles going from isolated objects to dense assemblies. An emphasis is put on the description of multiple scattering effects as well as the role of correlations. Examples of extensive GISAXS pattern analysis given in Section 7 illustrate the concepts developed in the two previous sections. Section 8 is a bibliographic review of *ex situ* GISAXS experiments stressing on hard condensed matter examples such

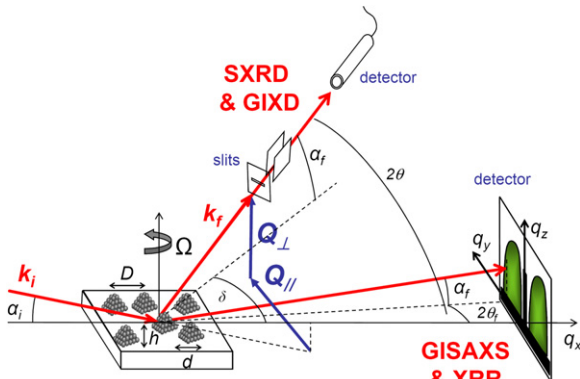


Fig. 2. Grazing incidence X-ray scattering geometry, at small angles (GISAXS and XRR), and large angles (GIWAXS or GIXD or GID and SXRD). The incident beam, of wavevector \mathbf{k}_i , makes a small incident angle α_i with respect to the sample surface. GISAXS and XRR probe the scattered intensity close to the specularly reflected beam. For GISAXS, a 2D detector is used, with a beam stop hiding the direct and specular beam, as well as the specular rod. The intensity is recorded as a function of the two angles, $2\theta_f$ and α_f , describing the in-plane and out-of-plane angles between the incident and scattered wavevectors, respectively. These angles are related to the wavevector transfer coordinates, q_x , q_y and q_z according to Eq. (1). The sample can be rotated by an angle ω around its surface normal. SXRD and GIXD correspond to large values of the scattering angle 2θ between \mathbf{k}_i and \mathbf{k}_f , and hence large values of the in-plane, $2\theta_f$, and out-of-plane, α_f , scattering angles. The direction of the exit wavevector \mathbf{k}_f is defined by slits parallel with and perpendicular to the surface, behind which lies the detector, which can be punctual or linear, or even two-dimensional.

as metallic nanoparticles and semiconductors nanostructures. Section 9 focuses on *in situ* GISAXS experiments during growth, mainly from the group of the authors. Works on metal/oxide interfaces, Ge/Si system, self-organized growth on Au reconstructions or patterned surfaces by buried dislocation networks and nanofacetting of W surface are presented. Finally, the review ends up with an outlook of the present and future capabilities and developments of the technique. A beginner in the field might first want to skip the theoretical chapters 5 and 6, which will be useful for those intending to understand the theory in depth, with the goal of a complete quantitative analysis of their data, as accurate as possible.

2. X-ray techniques to probe density fluctuations near surfaces and buried interfaces

2.1. The basis of grazing incidence X-ray techniques on nanostructures

2.1.1. The scattering geometry

X-ray scattering allows probing nanostructures by exploring the so-called reciprocal space, or the Fourier space. The principle of X-ray scattering from nanostructures is identical to traditional X-ray diffraction, except that, (i) synchrotron X-ray radiation is usually needed because the investigated volume of matter is small; and (ii) the incident X-ray wave vector \mathbf{k}_i is kept at a grazing angle with respect to the sample surface to minimize the unwanted background scattering (both elastic and inelastic) emanating from the bulk, and to enhance the near-surface scattering. Fig. 2 shows a schematic drawing of such measurements in grazing incident scattering geometry, for which the incident angle α_i is generally small and kept constant, most of the time close to the angle of total external reflection α_c . The scattered beam, of wave vector \mathbf{k}_f , makes the scattering angle 2θ with respect to the incident wave vector. It is detected at a direction defined by slits, and makes an angle α_f with respect to the sample surface and an in-plane angle $2\theta_f$ with respect to the transmitted beam. The wavevector transfer is defined as $\mathbf{q} = \mathbf{k}_f - \mathbf{k}_i$, and is often decomposed

into two components, \mathbf{q}_{\parallel} and \mathbf{q}_{\perp} , respectively parallel with and perpendicular to the surface. The absolute value of \mathbf{q}_{\perp} is a function of α_i and α_f : $|\mathbf{q}_{\perp}| = q_z = k_0[\sin(\alpha_f) + \sin(\alpha_i)]$, where $k_0 = |\mathbf{k}_f| = |\mathbf{k}_i| = 2\pi/\lambda$ is the elastically conserved wave vector modulus. λ is the X-ray wavelength. In GISAXS as well as in GIXS, the angular coordinates are related to the wavevector transfer coordinates according to:

$$\begin{aligned} q_x &= k_0[\cos(2\theta_f)\cos(\alpha_f) - \cos(\alpha_i)] \\ q_y &= k_0[\sin(2\theta_f)\cos(\alpha_f)] \\ q_z &= k_0[\sin(\alpha_f) + \sin(\alpha_i)] \\ k_0 &= 2\pi/\lambda. \end{aligned} \quad (1)$$

When all angles are small, the wavevector transfer is also small, typically between 0 and 1 nm^{-1} , and hence large dimensions are probed in real space. The corresponding techniques [38,14,15] are (i) X-Ray Reflectivity (XRR), in the specular geometry to probe the density profile perpendicular to the surface and in the off-specular geometry to probe large lateral electron density correlations (along q_x), and (ii) Grazing Incidence Small Angle X-Ray Scattering (GISAXS), which is used to probe the morphology parallel with the surface (along q_y) and perpendicular to it (along q_z), at intermediate length scales (typically between a few nm and a few hundreds of nm).

Wide angle scattering allows probing the order at the atomic scale, with two corresponding techniques: Grazing Incidence (Wide Angle) X-Ray Scattering (GIXS or GIWAXS), also often referred to GIXD or GIXRD or GID for Grazing Incidence X-ray Diffraction, which is the typical technique to probe the crystallographic lattice of nanostructures, and Surface X-Ray Diffraction (SXRD), which is basically the same, but applied to atomic structure determination (*i.e.* atomic positions) at surfaces and interfaces. When α_i and α_f are very small, $q \approx q_{\parallel}$, the scattering plane is nearly parallel with the surface, and diffracting lattice planes are perpendicular to it. The scattering geometry being defined by the incident beam and detector directions, one has only to rotate the sample around its surface normal to bring these lattice planes into diffraction condition. In that way, the long-range periodicity parallel with the surface is probed. It is often useful to measure the scattered intensity as a function of q_{\perp} , which is achieved by increasing α_f while keeping the grazing incidence.

Because the incident angle is small, it is necessary to consider the effects of refraction at the surface [39,35,36]. This point will be treated in depth in the theoretical section about propagation of X-rays at interfaces Section 5.2. However, it is worth recalling that the refractive index, n , of matter for X-rays is slightly less than unity: $n = 1 - \delta - i\beta$ with $\delta, \beta > 0$, so that, because of refraction, the transmitted beam bends toward the surface. When α_i is smaller than a critical value α_c , the beam is totally reflected, and only an evanescent wave, which decays over tens of angstroms, is present below the surface. When α_i is larger than the critical angle for total external reflection, the transmitted wave propagates into the bulk. Typical orders of magnitude are: $\delta \approx 10^{-5}$ and $\beta \approx 10^{-6}$, so that $\alpha_c \approx \sqrt{2\delta} \approx 0.1^\circ$ to 0.5° . Identical refractive effects occur as a function of the exit angle α_f .

The perpendicular components of the incident and emergent wave vectors are modified upon crossing the surface and become complex due to refraction and absorption. The scattering depth is thus strongly affected by refraction when α_i or α_f are close to α_c . Fig. 3 shows the variation of the scattering depth as function of α_i/α_c for different values of α_f/α_c . When $\alpha_i \ll \alpha_c$ and $\alpha_f \ll \alpha_c$, the scattering depth is of the order of a few nanometers. It rapidly increases to hundreds of nanometers when α_i and α_f are larger than α_c , through a transition region where $\Lambda \approx 10 \text{ nm}$. The incident and exit angles thus allow controlling the depth contributing to a given measurement, which can be varied from about 1 to 100 nm.

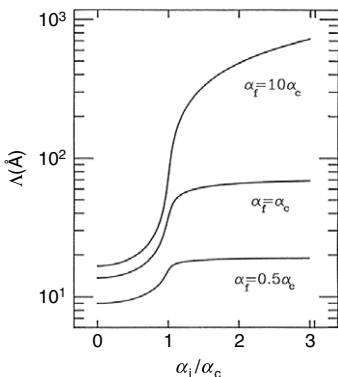


Fig. 3. Variation of the scattering depth as a function of the incident angle, for three exit angles, equal to half, one time and ten times the critical angle, for a Pt surface and 0.15 nm wavelength.

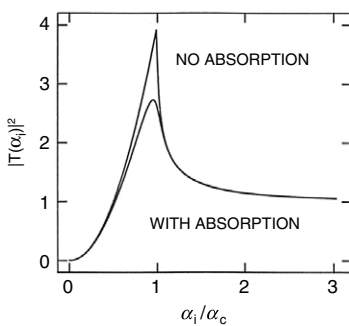


Fig. 4. Intensity transmission coefficient for a Pt surface as function of the incident angle over the critical angle. The wavelength is 0.15 nm, and the transmission is calculated with and without absorption.

The reflection R and transmission T coefficients for the intensity are also strongly affected by refraction. The variation of the transmission coefficient as function of $\alpha_{i,f}$ is reported in Fig. 4. Below α_c , $R_{i,f} = 1$ is the regime of total external reflection. At α_c , the intensity transmission coefficient T is maximum ($T = 4$). This property is sometimes used by fixing α_i and/or α_f at α_c , in order to enhance the surface scattering.

2.1.2. Reciprocal space of nanostructures on a surface

The intensity measured by X-ray scattering techniques depends on the angular coordinates α_i , α_f and $2\theta_f$. This allows building the intensity distribution in reciprocal space as depicted in Eq. (1). A schematic representation of a typical reciprocal space map (that of germanium nanostructures on top of a Si(001) surface) is shown in Fig. 5. The expressions of the intensity scattered by three-dimensional crystals, 2D crystals, surfaces of bulk crystals, and nanostructures deposited on a substrate can be found in standard text-books [40–42,38,15,14] or review articles [11,12,43,44,13,45,46]. The most important feature is that, since the interaction of hard X-rays with matter is weak (see Section 5.2.2), the kinematical approximation of single scattering, the so-called Born approximation (BA), or its application for grazing incidence geometry, the Distorted Wave Born Approximation (DWBA) (see Section 5.3), are valid in most cases, except for perfect crystals near Bragg scattering [41]. Fig. 5 qualitatively shows the intensity scattered by nanostructures (or an epilayer) on top of a substrate, as a function of the in-plane and out-of-plane wavevector transfers. The semi-infinite crystal yields CTRs [11,12], and the nanostructures yield wide Bragg reflections. They may be peaked at different \mathbf{q}_\perp (or \mathbf{q}_\parallel) values if the out-of-(in-) plane lattice vector differs from one to the other. This allows independent analysis of the out-of-plane and in-plane structural properties of the nanostructures, such as strain,

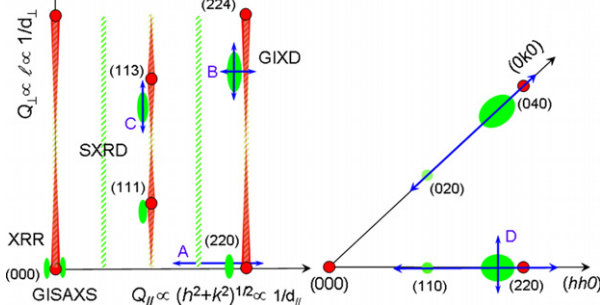


Fig. 5. (left side) Schematic representation of the reciprocal space of a three-dimensional crystal of the diamond (Si,Ge) structure, truncated by a (001) surface, giving rise to the crystal truncation rods (CTRs in red) with maximum intensity at the bulk Bragg positions (red disks) and quickly varying in between. In green the contribution from a strained two-dimensional, two-fold reconstructed epilayer is shown, yielding flat scattering rods (green shaded vertical rods) at the same position as bulk CTRs, since it is assumed that its lattice parameter parallel with the surface is fully strained to the one of the substrate. The scattering rod in half position is due to the (2 \times 1) surface reconstruction. In case of three-dimensional islands, diffraction peaks that are closer to the origin with respect to the substrate peaks are expected, as the overlayer is supposed to have a larger lattice parameter (note that the spacing between substrate and overlayer Bragg peaks has been enlarged for the purpose of representation). This reciprocal space pattern is typical for the Stranski-Krastanow growth of Ge islands on Si(001) for instance. Typical scans are represented by blue arrows. (right side) The corresponding intensity distribution in the (001) surface plane.

composition and shape, without interference with the substrate. The strain relaxation in the nanostructures parallel with and perpendicular to the surface can be analyzed separately by performing respectively \mathbf{q}_\parallel scans (such as scan A of Fig. 5) around in-plane Bragg peaks and \mathbf{q}_\perp scans (such as scans B or C of Fig. 5) around out-of-plane Bragg peaks. If the nanostructures are constrained to the substrate lattice parameter parallel with the interfacial plane, the nanostructures peaks appear at the same \mathbf{q}_\parallel position as the substrate CTRs and interferences occur between the waves scattered by the substrate and the nanostructures. Analysis of these interferences can provide information on the interface structure between the substrate and the nanostructures.

2.2. The different geometries of surface X-ray scattering techniques at small angles

2.2.1. Grazing Incidence Small Angle X-Ray Scattering (GISAXS)

GISAXS (Fig. 6) is a special case of GIXS, for which all angles considered are small, i.e. less than a few degrees. At these small angles, the curvature of the Ewald's sphere can be, most of the time, neglected ($q_x \simeq 0$) and the reciprocal space scales with the angular coordinates $q_y \simeq k_0 \sin(2\theta_f) \simeq k_0 2\theta_f$ and $q_z \simeq k_0 \alpha_f$, respectively parallel with and perpendicular to the surface. The intensity is measured very close to the origin of the reciprocal space, and hence $q_{y,z}$ span a small range, of a few nm^{-1} . If nanometer-size in-homogeneities of the electron density such as islands, roughness or electronic contrast variation are present on the surface, they scatter the incident, reflected and transmitted beams in a way that depends on their morphology and topography. The sample can be rotated around its surface normal by an angle ω , defining the orientation of the incident X-ray beam with respect to the in-plane crystallographic directions, which is necessary to investigate anisotropic islands. A T-shape beam-stop absorbs the direct and reflected beam before they hit the detector. Note that, as shown in Fig. 7, the origin of the out-of plane exit angle α_f is exactly between the direct and specularly reflected beams. Because these two beams are often hidden by a beamstop, determining the origin may not be trivial. Because of refraction and reflection effects [35,36] the maximum of the off-specular diffuse scattering

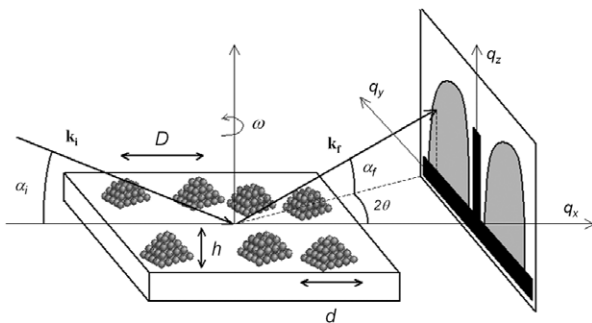


Fig. 6. Principle of GISAXS: \mathbf{k}_i and \mathbf{k}_f are the incident and scattered wavevectors, respectively, yielding the wavevector transfer (*i.e.* the reciprocal space vector) $\mathbf{q} = \mathbf{k}_f - \mathbf{k}_i$. The angles α_i , α_f and $2\theta_f$ are related to the components of the wavevector transfer either parallel with (q_x and q_y) or perpendicular (q_z) to the sample surface by $q_x = k_0[\cos(2\theta_f)\cos(\alpha_f) - \cos(\alpha_i)]$, $q_y = k_0[\sin(2\theta_f)\cos(\alpha_f)]$, $q_z = k_0[\sin(\alpha_f) + \sin(\alpha_i)]$ with $k_0 = 2\pi/\lambda$. Close to the origin in reciprocal space, since the in-plane and out-of-plane scattering angles, $2\theta_f$ and α_f , are small, they scale approximately with the components q_y and q_z of \mathbf{q} . The sample can be rotated around its surface normal by an angle ω , which defines the orientation of the incident X-ray beam with respect to the in-plane crystallographic directions. A beam stop protects the bidimensional detector from the direct and reflected beams.

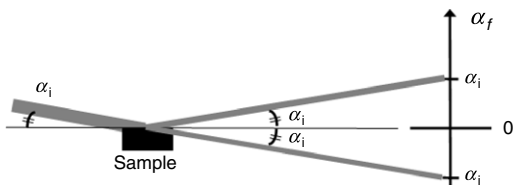


Fig. 7. Out-of-plane angles in GISAXS with definition of the zero of α_f : it bisects the direct and specularly reflected beams.

intensity, also called Yoneda peak, is located at the critical angle for total external reflection, noted α_c . In order to properly define the origin of reciprocal space, it might be wise to record an image of the direct and specularly reflected beams, without beamstop but for a strongly attenuated incident beam as several orders of magnitude in intensity separate the diffuse scattering from the transmitted and reflected beams.

2.2.2. Specular X-ray reflectivity (XRR)

Specular X-ray reflectivity [14,47,48] is also a special case in which the in-plane scattering angle $2\theta_f$ is null. Only the perpendicular wavevector transfer is changed, with the additional condition that the incident and exit angles with respect to the surface be kept equal: $\alpha_i = \alpha_f \equiv \theta$ (Fig. 8). The perpendicular wavevector transfer is then given by: $q_{\perp} = q_z = 2k_0 \sin(\theta)$. Only the intensity along the q_z direction is explored. Since $q_{\parallel} = 0$, XRR is insensitive to any lateral contrast in electron density: only the perpendicular electron density profile, averaged parallel with the surface, is probed. XRR is very useful to determine the average thickness of layers on substrates, continuous or in the form of nanoparticles. The interference between the waves scattered by the substrate/layer, layers/layers and layer/vacuum (or air) interfaces yield maxima and minima that are related to their average thickness; they are known as the Kiessig fringes [49]. XRR is also very useful to analyze the roughness and interdiffusion profiles at these interfaces as they strongly increase the decay of intensity above the critical angle as compared to flat interfaces [14] (see Section 5.2).

2.2.3. Off-specular X-ray reflectivity

Off-specular reflectivity measurements are performed in the so-called coplanar geometry [15,14] for which the incoming, the outgoing wavevectors and the surface normal belong to the same plane. Starting with the geometry of the specular reflectivity, *i.e.*

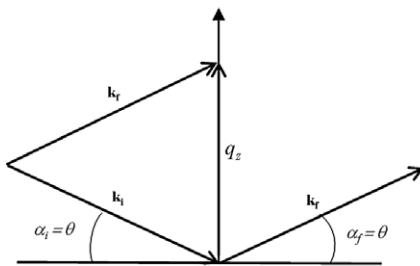


Fig. 8. Principle of specular XRR: the incident and exit angles are symmetrically raised, thus probing the reciprocal space perpendicular to the surface, along $q_z = q_{\perp}$.

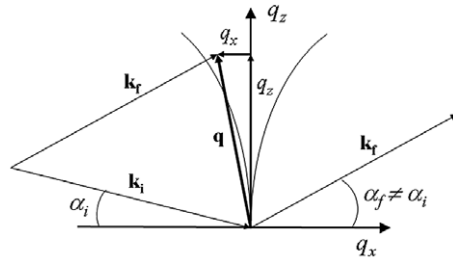


Fig. 9. Principle of off-specular reflectivity: the sum $\alpha_i + \alpha_f$ is kept constant, while the difference $\alpha_f - \alpha_i$ is scanned, thus probing the reciprocal space parallel to the surface, along the q_x direction. Only small values of q_x are probed, in comparison with the q_y values probed in GISAXS with similar angle values.

equal incident and exit angle, several scans are possible. Among others, the rocking scan consists in varying the incident angle (renamed θ as for reflectivity), while keeping constant the scattering angle $2\theta = \alpha_i + \alpha_f$, which is by definition the angle between \mathbf{k}_f and \mathbf{k}_i (Fig. 9). This scan is often performed by simply rocking the sample surface itself at constant beam and detector positions. In this way, to first order, the perpendicular wavevector transfer ($q_{\perp} \simeq k_0(\alpha_i + \alpha_f) = k_02\theta$) is kept constant, which selects a given amplitude of the surface or interface height-height correlation function, while the in-plane momentum transfer is varied according to $q_x = k_0[\cos(\alpha_f) - \cos(\alpha_i)]$ at $q_y = 0$. Off-specular reflectivity thus allows probing fluctuations of the electron density parallel with the surface, as does GISAXS. Although both probe similar fluctuations parallel with the surface, GISAXS and off-specular XRR are very complementary because in GISAXS, $q_{\parallel} = q_y$ is of first order with respect to the (small) angle $2\theta_f$, while in off-specular XRR, $q_{\parallel} = q_x$ is of second order with respect to the out-of-plane small angles. As a consequence, off-specular XRR is much better adapted to probe electron density fluctuations over long distances parallel with the surface (100 nm–1 μm), and GISAXS better adapted for smaller distances (1 nm–100 nm). At variance to GISAXS cut of intensity at constant incident α_i and α_f exit angles, the probed depth (see Section 5.2.6) is not kept constant in off-specular scans [50]. Moreover, the accessible range of reciprocal space is restricted by the sample horizon in the coplanar geometry [15,14].

2.2.4. Advantages and drawbacks of X-ray techniques

The most widely used techniques to study the fluctuations of electron density on or below surfaces are imaging techniques such as Transmission Electron Microscopy (TEM), Scanning Electron Microscopy (SEM), and near field microscopies like Scanning Tunneling Microscopy (STM) and Atomic Force Microscopy (AFM). However, if these techniques can provide some of the required information, real space observations often suffer from slowness, sampling limits, and artifacts, such as those due to the inevitable convolution with the tip in the cases of STM and AFM, or

the modifications induced by the necessary sample preparation (TEM, SEM). In addition, they are either difficult (AFM, STM, SEM) or impossible (TEM) to use *in situ*, e.g. in UHV during the growth of nanoparticles or on insulating substrates like oxides. These limitations can be overcome by techniques based on X-ray scattering. X-rays are adapted to any kind of materials without suffering from charging effects; they provide depth sensitivity, thus allowing to probe buried interfaces; they provide a statistical averaging over the whole sample area, thus sampling the same way as macroscopic characterization techniques; they can be used at any pressure or temperature, and in any kind of sample environment in particular in UHV, during growth and sometimes in real time. Chemical sensitivity can be achieved by tuning the X-ray wavelength across an absorption edge to vary the atomic structure factor of a chosen element. The main drawbacks of X-rays are the nearly unavoidable use of synchrotron radiation to get a reasonable counting time on nanostructures and data analysis that relies on modeling of reciprocal space measurements.

2.2.5. Brief history of GISAXS applied to hard condensed matter

Grazing incidence small angle X-ray scattering (GISAXS), has emerged as a powerful tool to analyze the morphology and distribution of either islands on a substrate or buried nanoparticles. In 1989, the first GISAXS experiments were performed with a rotating anode by J. Levine et al. on Au deposits on glass [16,17,51]. Naudon et al. developed also GISAXS at LURE (Laboratoire pour l'Utilisation du Rayonnement Electromagnétique, France) in order to study clustering near surfaces [52,18,53–56]. The first *in situ* experiments concerned the growth of metallic islands [57]. GISAXS allowed also studying the surface roughness [58,59], the lateral correlations, sizes and shapes of semiconductor dots [60–62,22,63], discontinuous multilayers [19], self-organized dot superlattices [62,64] or wires [65]. Recent developments consisted in GISAXS measurements performed in UHV, *in situ*, during MBE, and with no scattering element between the undulator synchrotron X-ray source and the detector, thus yielding a very high sensitivity and background-free data [25].

2.2.6. *In situ* GISAXS and GIXS, in UHV, during growth

In general, the structure and morphology of nanostructures (or an epilayer) on a substrate depend on many parameters, such as the initial structure of the substrate surface itself, the structure of the deposited material, the surface and interface energies, the lattice parameter misfit and the growth kinetics. The above GIXS technique (GIXS being taken as a generic name for GIXS, GIXD, GISAXS, XRR specular and off-specular, SXRD ...) is one of the very scarce tools that can be used *in situ*, for instance in UHV, to follow the evolution of the structure and morphology during growth, from sub-monolayer deposits to fairly thick films (up to μm in thickness). In principle, the factors influencing the overlayer growth, such as the defect density of the substrate, the temperature during growth and the incoming fluxes can be systematically varied. The structure of the substrate, either reconstructed or not, should be investigated first. Its average roughness can be deduced from analysis of the CTRs integrated intensities, and the surface domain size and average terrace width deduced from CTRs line-shape analysis. Systematic measurements during growth may then provide the evolution of the structure and morphology with the overlayer thickness; such as the interfacial distance between both materials in heteroepitaxy; the average in-plane and out-of-plane lattice parameters and strain distributions, the mosaic spread and the domain size parallel with and perpendicular to the interface. In the case of a three-dimensional growth, the domain size is directly related to the size of the nanostructures. The shape and size of these growing nanostructures can be measured *in situ* by grazing incidence small

angle X-ray scattering (GISAXS) experiments. GIXS can also be used to analyze different growth defects such as stacking faults, twins and dislocation nucleation. Indeed, stacking faults are planar defects, and thus yield rods of scattering perpendicular to the plane of the fault. Twinned crystals yield Bragg peaks that are related by mirror symmetry to those of the untwinned stacking. Finally, the nucleation of dislocations in the growing film leads to inhomogeneous deformations that may be detected through radial \mathbf{q} scans. These kinds of studies require the sample to be in Ultra High Vacuum (UHV), so that the necessary vacuum hardware has to be combined with an X-ray diffractometer. The main difficulty is to associate the necessary precise movements of the sample with a UHV environment. Several diffractometers devoted to performing *in-situ* GIXS have recently been built with these requirements in many synchrotron facilities around the world.

3. Experimental considerations

3.1. Background minimization

Because the signal is very close to the direct beam, a major constraint in GISAXS (like for any small angle X-ray scattering measurement) is to decrease as much as possible the background arising from the sample itself, from the beam divergence, from all the optical elements of the beamline, from beryllium windows placed in the beam path, and of course from air. This requires a bright beam with a very low divergence, high quality optical elements and several pairs of slits to define the beam and remove unwanted low-angle scattering. More importantly, when performing surface X-ray scattering in ultra-high vacuum (UHV) to study the growth by e.g. molecular beam epitaxy (MBE), a beryllium window is usually present to enter into and exit the UHV chamber. A Be window is also present at the end of the beamline and the X-ray beam passes through a small path of air between the beamline and the chamber. These Be windows and air-path generate large background scattering at small angles, which in addition varies very quickly with small, micrometric variations (which are inevitable on a synchrotron beamline) of the beam impact on the Be window. We have developed two different experimental setups to minimize these sources of background. We call them ID32 and BM32 from the names of the ESRF (European Synchrotron Radiation Facility, Grenoble-France) beamline on which they were developed. Before presenting the ID32 and BM32 setups, we first recall that the very first *in situ* GISAXS study during growth was performed at the Stanford Synchrotron Radiation Laboratory (SSRL) in the early 1990 [57]. A standard point detector was used, behind two pairs of slits placed on the detector arm in such a way to define an angular resolution of 0.2° parallel with the surface and to the detector scan, with an integration over 1° perpendicular to the surface.

3.2. First *in situ* GISAXS setup, on the ID32 ESRF beamline

This setup is described at depth in Ref. [26], and will thus be presented only briefly here. The main characteristics are that the UHV chamber was directly hooked to the beamline, and no beryllium window was present between the sample and the X-ray source [26]. The only Be window was at the end of the beam path, just before the 2D detector; it did not provide any additional background as the unwanted diffuse signal was hidden by the beam stop before it diverges.

3.3. Second *in situ* GISAXS setup: Simultaneous analysis of morphology and structure by GISAXS and GIXS on the BM32 beamline

The second experimental setup has been developed to allow simultaneously performing GISAXS, GIXS and X-ray Reflectivity

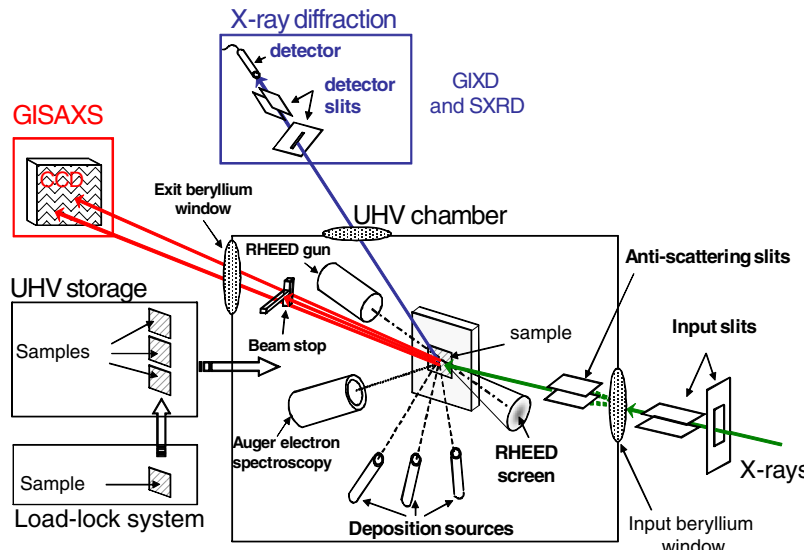


Fig. 10. Principle of the SUV/BM32 UHV chamber coupled to a diffractometer for GISAXS, GIXS and XRR measurements on the same sample, during growth. The doubly focused and monochromatic X-ray beam delivered by the beamline enters into the hutch from the right. Its size and divergence are further defined by slits working in vacuum. The beam hits the exit Be window of the beamline, then the entrance X-ray window of the UHV chamber. It is next scattered by the sample before exiting the UHV chamber, hitting again a Be window. The scattered beam can then be measured for GIXS or XRR measurements by a 1D (or 1D) detector placed after a pair of vertical and horizontal slits defining the direction of k_f , or at small angle by a 2D detector for GISAXS. In GISAXS, background is nearly suppressed thanks to input guard slits and a knife edge placed in UHV just after the entrance Be window, suppressing all the unwanted X-rays before the sample, and thanks to a beam-stop placed after the sample, just before the exit Be window, blocking the incident beam, and thus avoiding any scattering by the exit Be window. In addition, the UHV chamber is equipped with a RHEED set-up and an Auger spectrometer, and can be equipped with up to 6 depositions cells, all apparatus looking directly at the sample when in position for X-ray measurements. Sample introduction is performed through a load-lock and a storage/introduction UHV chamber.

measurements on the same sample, *in situ*, in UHV, at different growth stages. The sample position is kept fixed for all X-ray measurements, physical vapor deposition, as well as for sample preparation (ion bombardment and heating) and for characterization by Auger Electron Spectroscopy (AES) or Reflection High Energy Electron Diffraction (RHEED).

For that sake, the setup is made of a sophisticated UHV chamber coupled to a large diffractometer. Fig. 10 shows a schematic drawing and Fig. 11 a photograph of the UHV chamber dedicated to X-ray diffraction, while Fig. 12 shows a schematic drawing of the setup to perform GISAXS. The instrument is located at the end of an ESRF bending magnet beamline: BM32 (Collaborating Research Group/Interfaces) [66]. The white X-ray beam is first vertically collimated by a mirror coated with iridium; it is then monochromatized by a double crystal Si(111) monochromator, the second crystal focusing the beam in the horizontal direction; the beam is finally vertically focused at the sample location by a second mirror. The resulting beam size at the sample location is ≈ 0.25 mm (H) $\times \approx 0.15$ mm (V) (Full Width at Half Maximum (FWHM)), with a divergence of ≈ 0.5 mrad (H) $\times \approx 0.13$ mrad (V) (FWHM). It is further defined in the experimental hutch by two sets of vertical and horizontal entrance slits separated by 2 m (see Fig. 12). The first set defines the vertical beam size of typically 0.3 mm (V); the second set removes the unwanted scattering by the first slits. The incident beam then passes a filter box, and then a monitor based on two diodes measuring the scattering by a Kapton foil placed in the beam. It next enters the X-ray UHV chamber.

Because of many constraints, the UHV chamber could no longer be directly connected to the beamline: it had to be equipped with an entrance and an exit beryllium windows. These, together with the beamline slits and windows, generate a background at small angles. This background is eliminated by a series of slits and a beam-stop, in-vacuum and outside vacuum (Figs. 12, 10). The first is a vertical slit placed inside the chamber, in UHV, just after the entrance Be window, which lets only the incident beam hit the sample, and eliminates all the remaining unwanted X-rays, especially those scattered by the entrance Be window. Actually,

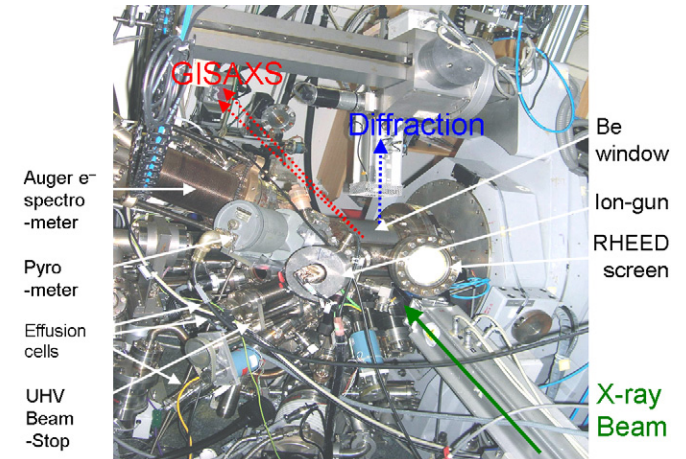


Fig. 11. Photograph of the core of the SUV/BM32 UHV diffractometer. The beam enters into the UHV chamber from the bottom right corner. The GISAXS 2D camera is at the top left corner; the slit/detector system for GIXD measurements is toward the top. UHV instrumentation and introduction are all around the UHV chamber. Parts are visible on the left and bottom sides of the photograph. On the right is the heavy-duty diffractometer holding the UHV chamber with all its pumps and instrumentation. A small part of the UHV chamber is visible at the center of the photograph, with the entrance and exit Be windows visible in gray. The sample, with a vertical surface, is held by a furnace allowing it to reach 2500 K.

a set of 3 tantalum slits with different fixed openings (0.25, 0.3 and 0.35 mm) can be used for this purpose. The horizontal size of the beam being much larger than the projected sample size, because of the very small incident angle, it is also mandatory to eliminate most of the beam which is not used in this direction. This is done by the molybdenum sample holder on the back side of the sample, and by a tungsten knife-edge mounted on a translation on the front side. This knife edge is located in UHV between the entrance Be window and the sample. The last UHV tool is a T-shape beamstop made of tungsten which is placed

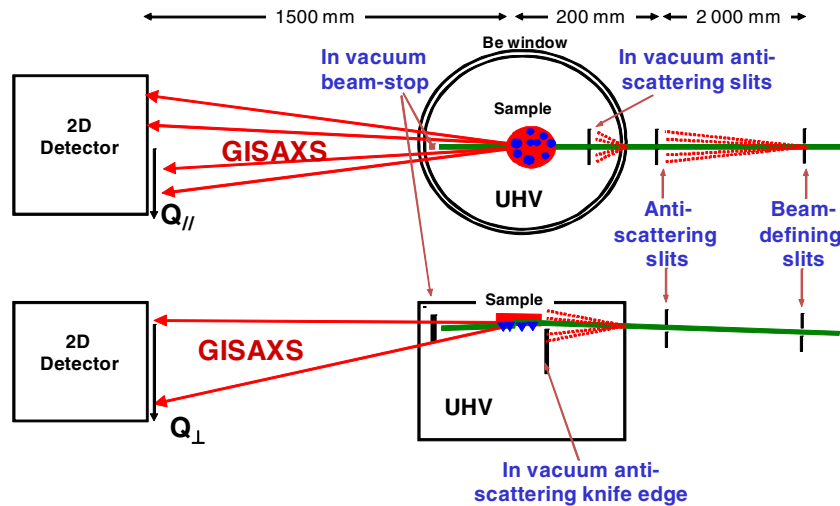


Fig. 12. Principle of the anti-scattering system for GISAXS measurements on the SUV/BM32 setup. The incident beam is schematized by a green line arising from the right. Slits and anti-scattering slits, knife edge and beam-stop are schematized in blue. The small angle X-ray scattering is schematized by red arrows.

inside the chamber, just before the exit window. Its role is to stop the incident and specularly reflected beams, while letting the small-angle scattering exit the chamber, thus avoiding unwanted scattering by the exit Be window. In principle, these three tools placed in UHV efficiently suppress the background scattering. If this is not the case, two additional T-shape tungsten beam-stops placed in air can be added: one just after the exit Be window, and one just before the 2D detector.

The 2D detector can be placed between 0.3 and 3 m downstream of the sample, thus allowing one to vary the measured fraction of reciprocal space over a wide range. A He-filled flight tube is usually inserted between the chamber and the detector to avoid absorption and scattering by air.

The UHV chamber can be equipped by as many as eight deposition sources; typically four effusion cells and four electron-bombardment cells. A large number of metals have been evaporated in this chamber, as well as semiconductors (Si and Ge). The chamber is equipped with a double-pass cylindrical mirror analyzer from STAIB for AES measurements, and with a 35 keV RHEED apparatus, also from STAIB. A quadrupolar residual gas analyzer is also available. The base vacuum is between 2×10^{-11} and 1×10^{-10} mbar according to preparation conditions.

The diffractometer, of “z-axis” [67] type, has been described elsewhere [68]. The reciprocal space can be explored at wide angles thanks to two detector rotations δ and β ($\equiv \alpha_f$), in addition to the two sample ones ω and α ($\equiv \alpha_i$). The detector acceptance can be fitted with different sets of slits (typical angular acceptance 3.5 mrad). For GIXD, the footprint is a lozenge of variable angle given by the in-plane scattering angle δ , and the lengths of the sides are 0.3 mm and the width of the vertical detection slits. For GISAXS, the beam footprint is a long, 0.3 mm wide stripe, of length equal to the sample diameter. As a result, the instrument can be used not only for GISAXS measurements, but also for XRR and GIXS ones, on the same sample, with no realignment.

3.4. Third *in situ* set up: *In operando* studies of model catalysts by GIXD and GISAXS

This *in situ* catalytic set-up was developed by the team of M.-C. Saint Lager [33,34] from Néel Institut (Grenoble) on the second end station GMT (Multi-Technique Goniometer) of the French BM32 beamline at ESRF. The catalytic batch reactor (Fig. 13) allows for simultaneous measurements of GIXD, GISAXS and chemical reactivity by mass spectrometry. The set-up is divided

into two chambers connected through a transfer rod: (i) an UHV one equipped with standard surface science tools for controlled preparation of model catalysts (ion beam sputtering, x, y, z, θ manipulator with electron bombardment furnace, four grids OMICRON LEED-Auger, evaporation cells, quartz microbalance); (ii) the reactor itself where the pressure ranges from UHV to atmospheric. The reactor is held on a “2 + 2” diffractometer and installed for each beam run. The detectors for GISAXS and GIXS as well as the typical beam sizes and divergences are the same as those of the SUV endstation, as described in the next paragraph. Vacuum guard slits and a blade similar to the SUV chamber (Fig. 14) are used to get rid of the unwanted background scattering from the entrance windows. The direct and reflected beams are suppressed thanks to a $x-y$ motorized beam stop just after the exit window (size 500 μm). At variance to the previously described set-up, there is no in vacuum beam stop because of space and reactivity constraints. The scattering background induced by the gas along the X-ray path in the reactor was found to be negligible at an energy of $E = 18$ keV and the overall mechanical stability was good up to pressure of $\simeq 100$ mbar. The reactor chamber is optimized to measure accurately chemical reactivity. Special care to the choice of materials has been taken to avoid spurious reactivity; in particular, a special coating of the heated sample holder is used (see Ref. [33] for details). The chamber is pumped down through a turbomolecular pump (8) that can be isolated from the chamber by a butterfly valve for gas feeding. The gas mixture is prepared in an ancillary stainless steel manifold which is carefully outgassed and fed with ultrapure gases. The mixture is introduced in the reactor through a stainless steel microvalve. A set of two capacitance diaphragm gauges and a cold cathode gauge (11–12) allows the measurement of pressure from UHV to atmospheric. The sample heating is ensured by a laser beam focused on the back of the sample holder, which is optimized for light absorption. Temperatures up to 1100 K in UHV and 800 K under gas atmosphere (when dissipation by convection starts to be efficient) can be reached. The temperature is recorded by optical pyrometry (15). The gas composition is monitored by a quadrupole mass spectrometer (13) fed by a leak valve and pumped by a small turbo pump station (14). Despite a reaction volume of $\simeq 6$ l, the detection sensitivity and the parasitic background (without sample) are such that submonolayer reactivity of supported gold nanoparticles during CO oxidation can be accurately obtained. For instance, for a turnover frequency of a few molecules/Au atom/s, 1 ML of gold (1.4×10^{15} atoms or 0.5 μg) catalyzes the oxidation of 25% of 0.1 mbar of CO in the reactor in 1 h [34].

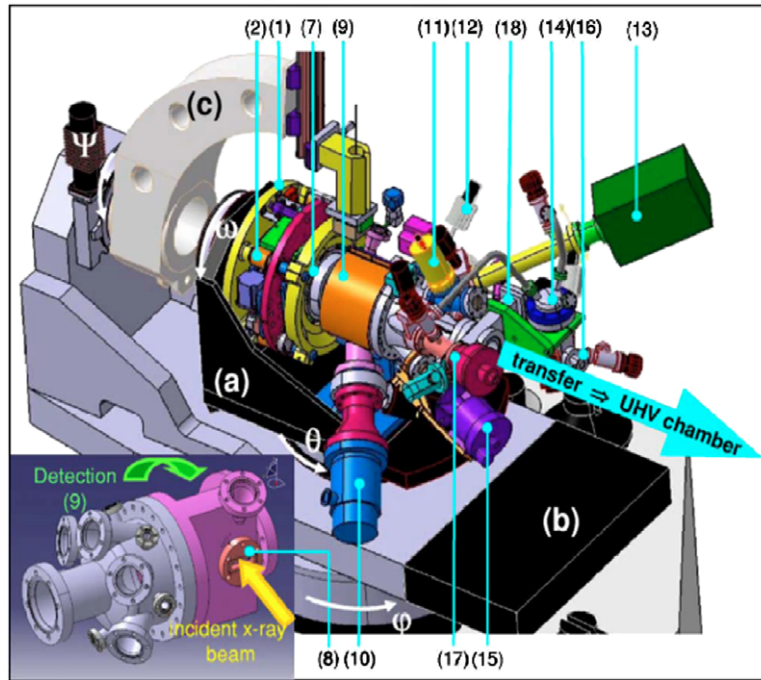


Fig. 13. Overview of the reactor mounted on the GMT end station of BM32. The reactor is mounted on a “2+2” diffractometer and connected to a UHV preparation chamber. The θ table (a) that holds the chamber allows defining the incident angle α_i . The sample azimuth can be oriented through the ω rotation; the transmission of the movement to the vacuum side is ensured through differential pumping. The normal of the sample surface is put parallel with the ω axis thanks to two rocker cradles ξ_1 , ξ_2 (amplitude $\pm 2^\circ$). A z-movement (amplitude ± 2 mm; precision $\approx 2 \mu\text{m}$) allows putting the sample surface inside the beam. The detector arm for GIXD (c) mounted on marble stone (b) rotates along the two axis ϕ (horizontal plane, aperture -1 to 40°) and ψ (vertical plane, aperture -1 to 95°). Its position defines the direction of the outgoing diffracted beam that goes through a large aperture beryllium window (9). The incident beam passes through beryllium windows mounted on a CF40 flange. From Ref. [34].

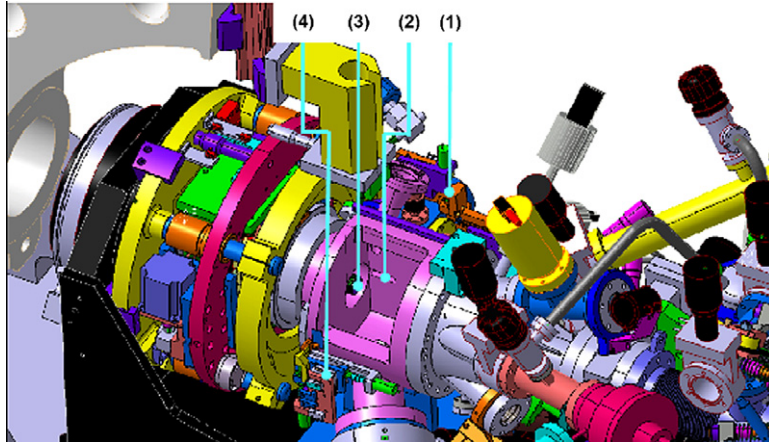


Fig. 14. Closer view of the reactor chamber showing the guard slits (1)(2), the sample (3) and the motorized Ta beam stop just after the output beryllium window (4). This latter have been removed from the drawing. Courtesy of M.C. Saint-Lager and P. Taunier.

3.5. Other *in situ* X-ray chambers

The capabilities to perform simultaneous GISAXS and GIXS/GIXD/SXRD *in situ*, in UHV, or *in operando*, during e.g. catalytic reactions, are being developed nowadays on several synchrotron beamlines, such as the ESRF ID03 beamline [69]. This latter comprises a UHV diffractometer setup devoted to GIXS and SXRD, which is being equipped for GISAXS measurements, as well as a very smart baby reactor chamber coupled also to a diffractometer, that allows UHV substrate preparation and deposition followed by X-ray measurements under gas flows, the chamber volume being then restricted to a few centiliters, to increase the active surface over chamber volume ratio.

3.6. Detectors

The detectors used for wide angle measurements are either standard scintillation detectors (NaI:Tl) with a typical energy resolution of 40% and a maximum count rate of 10^5 cts/s, or avalanche photodiodes with $\approx 10\%$ energy resolution and 10^6 cts/s maximum count rate, or a linear position sensitive detector (PSD). This last detector, provided by Vantec, is a gas detector using a wire as cathode, and a delay line to localize the pulses. Its resolution is $\approx 30 \mu\text{m}$, and maximum count rate $\approx 10^5$ counts/s.

The small angle scattering is typically collected on a high grade (1 MPP) 16-bit charge-coupled device (CCD) from Princeton Instruments. The detector has 1152×1242 pixels of $56.25 \times$

56.25 μm^2 size, with a rectangular acceptance of $65 \times 70 \text{ mm}^2$ and a threefold demagnification insured by a tapered assembly of optical fibers. The phosphor screen of $\text{Gd}_2\text{O}_2\text{S}$ is optimized for energies between 3 and 30 keV. The full well capacity is 3×10^5 electrons, with a readout noise of 7 electrons (for 100 kHz reading). The CCD is cooled down to -60°C by a four stage Peltier system, resulting in a very small dark current (<0.02 electron/pixel/s). The detector is under vacuum, and the X-rays enter through a 90 mm diameter 0.02 mm-thick Be window. It is mounted on three translations (vertical and horizontal, along the beam and perpendicular to it, respectively), at a variable distance between 0.3 and 3 m from the sample. Depending on this distance, the maximum 2θ angle typically ranges from 0.2° to 5° , and the maximum exit angle from 0.2° to 10° .

After acquisition, the data have to be corrected from the flat field, the dark counts, the CCD distortions. In addition, when needed, the reference signal from the bare substrate prior to deposition is subtracted.

3.7. Notations

As far as wide angle GIXS is concerned, through this paper, and otherwise specifically mentioned, the Miller indexes (hkl) are expressed in reciprocal lattice units (r.l.u.) of the substrate, by referring to its bulk parameter. In all cases, the ℓ index is related to the component of the wavevector transfer perpendicular to the surface.

For GISAXS the notations q_x (along the direction of the projection of the incident beam onto the sample surface), q_y (perpendicular to the incident beam, parallel with the sample surface) and q_z (perpendicular to the sample surface) are generally used. In some cases, they are replaced by the directions [hkl] in reciprocal space or by the parallel and perpendicular wavevector transfers: $q_{\parallel} = q_y$ and $q_{\perp} = q_z$, respectively.

4. General trends of the analysis of 2D GISAXS data

4.1. Introduction

In order to get accurate morphological characteristics of nanostructures from GISAXS data, it is extremely important to carry out a precise analysis. As a starter, the purpose of this section is to show how a two-dimensional (2D) GISAXS pattern can be precisely analyzed to deduce the average inter-nanostructures distance, nanostructures shape, size, and size distribution. The rigorous theoretical foundations are postponed to Section 6 after the introduction of the Distorted Wave Born Approximation in Section 5.3.

An important point to remember when analyzing the data, is that small angle scattering is made of a coherent scattering term, plus an incoherent one, which is present as soon as the size distribution of the nanostructures is not monodisperse. The coherent term is the product of the square modulus of the mean nanostructure form factor, $F(\mathbf{q})$, which is the Fourier transform (FT) of the nanostructure shape, with the interference function, $S(\mathbf{q}_{\parallel})$, i.e. the FT of the pair correlation function of the nanostructures position. The incoherent scattering is very difficult to evaluate analytically in the general case, and two limit cases are often used: (i) the Decoupling Approximation (DA), assuming no nanostructure correlations, and (ii) the Local Monodisperse Approximation (LMA), assuming full correlation between nanostructure sizes at a scale corresponding to the coherence length of the X-ray beam.

Furthermore, GISAXS is generally performed with an incident X-ray beam impinging on the surface at a grazing angle α_i

close to the critical angle for total external reflection α_c in order to minimize the bulk scattering and to increase surface sensitivity [70]. At these low angles, the surface acts as a mirror and multiple scattering effects come into play, leading to the inadequacy of the Born Approximation (BA). Instead, DWBA is more suitable; this is an extension of the single scattering formalism including the contribution of different single scattering processes arising from perturbations of the incident, reflected and refracted wavefields by the nanostructures [35–37] on the reflection-refraction of waves at interfaces. Hence, for nanostructures, a very different expression is obtained [37] in which the usual form factor $F(\mathbf{q})$ is replaced by the coherent sum $\mathcal{F}(\mathbf{q})$ of four terms, which represent different scattering events involving or not a reflection of either the incident or the scattered beam at the substrate surface. Each term includes the nanostructure form factor, evaluated at different values $\pm q_z = \pm(k_f - k_i)$ and $\pm p_z = \pm(k_f + k_i)$ and weighted by the Fresnel reflection coefficients $r(\alpha_i)$ and $r(\alpha_f)$ of the substrate (see Fig. 41). For substrates with an uncorrelated roughness, the Fresnel reflection coefficients may be modified by a decreasing exponential term depending on the Root Mean Square (rms) roughness, the z-component of the wave vector in vacuum and that of the wave vector in the substrate [38,14] (see Section 5.2.8). The form factor within the BA is recovered from the DWBA by setting $r(\alpha_i) = r(\alpha_f) = 0$. Hence, the BA is valid only when the reflection coefficients are negligible, i.e. when α_i and α_f are larger than $\simeq 3\alpha_c$ (see Section 5.2.6). At powerful synchrotron facilities, it could be thought relevant to carry out GISAXS at $\alpha_i \gg \alpha_c$ so that, as will be shown below, some quick analysis could be done in the BA but at the expense of a loss of scattered intensity. Moreover, in this case, some information is lost for small q_z values, which may affect the result if the nanostructures are very high.

For a matter of simplicity, in the following introduction section, the discussion is, most of the time, restricted to the BA, which is almost valid when considering only the scattered intensity parallel with the surface.

4.2. Form factor versus interference function

The most interesting specificity of GISAXS is to probe the nanostructure morphology, i.e., shape and size, which can be derived in principle from the form factor. However, the scattered intensity is the product of the form factor by an interference function as illustrated in Fig. 15. In the case of concentrated systems, these two terms are strongly correlated at small q_y values. Nevertheless, in disordered systems, the interference function tends to one as the wavevector transfer increases, and the GISAXS intensity is then entirely determined by the form factor. Hence, in order to discriminate between different shapes and accurately determine the nanostructure size and size distribution, the intensity must be measured (i) far from the origin of the reciprocal space and (ii) over several orders of magnitude. This requires a background as low as possible as the form factor decreases rapidly with increasing q_y values.

4.3. Form factors of simple geometrical shapes

We discuss below the behavior of the form factors $F(\mathbf{q})$ for several simple nanostructure shapes: cylinder, totally or partially emerging sphere, and complete or truncated four-fold pyramid. Information on the nanostructure shape can be gained from the symmetry properties that can be probed by rotating the sample around its surface normal. Possible facets on the sides of the nanostructures can also be put in evidence by the presence of characteristic scattering rods [71] (see Sections 6.2.6 and 6.2.7). Furthermore, the inspection of the intensity zeros or minima may be of great

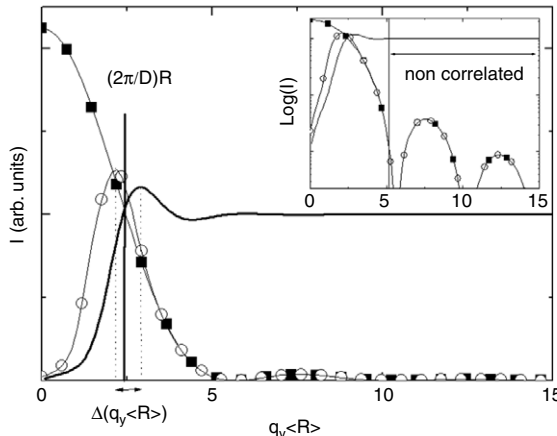


Fig. 15. Open circles: GISAXS intensity calculated within the BA as function of the parallel wavevector transfer $q_y \langle R \rangle$ and at $\alpha_f = 0$ for cylindrical nanostructures on a substrate in a disordered state. Filled squares: form factor of a cylinder. Continuous line: interference function with a distance between nanostructures of $D = 2.4 \langle R \rangle$. The difference between the maximum of the interference function and that of the GISAXS intensity is $\Delta q_y \langle R \rangle$. The inset shows the same evolution with the y-axis on a logarithmic scale. From Ref. [29].

help to determine the average size if the size distribution is sufficiently narrow. Nevertheless, the size polydispersity is usually large and the above criteria are not sufficient. Then, the asymptotic behavior at high \mathbf{q} may allow extracting the average shape (see Section 6.3.3).

The analytic expressions of the form factors of simple nanostructure shapes [27] are given in Appendix. For anisotropic nanostructures, the form factor depends on the orientation of the nanostructures with respect to the X-ray beam (see Section 6.2.6). Two important cases can be considered for faceted nanostructures: the X-ray beam aligned along a face or along an edge. Fig. 16 shows 2D maps of the form factor within the DWBA i.e. $|\mathcal{F}(\mathbf{q})|^2$ in the (q_y, q_z) space calculated within the DWBA for various nanostructure shapes and orientations, and for $\alpha_i = \alpha_c$. On these five maps, the intensity presents a maximum along the perpendicular direction at $\alpha_f = \alpha_c$, known as the Yoneda peak just above the horizon of the sample; it is due to the interference effects between the four scattered beams on the surface (see Section 6.2 and Figs. 41–42). For a cylinder, the pattern is composed of well separated lobes along both parallel and perpendicular directions (see Fig. 16a). For a complete sphere, one main zero order lobe is present, with a first order arc-shaped lobe (cf. Fig. 16b). The 2D map for a complete pyramid is characterized by a main lobe elongated along the perpendicular direction with a monotonous intensity decrease. For pyramid-like nanostructures of fcc material on a (001) surface, the main side facets are (111) that make an angle 54.7° with respect to the surface normal. If the incident X-ray beam is aligned along a face, pronounced scattering rods by facets appear at an angle of 54.7° with respect to the surface normal (cf. Fig. 16c). When the angle ω increases between 0° and 45° , these rods become less intense (cf. Fig. 16d and e).

Hence, a simple qualitative inspection of a 2D GISAXS pattern may allow a first guess of the average nanostructure shape, e.g., symmetry, facets However, this is not always possible and a detailed analysis of the intensity evolution as a function of q_y and q_z is then necessary to provide additional information on the nanostructure shape.

4.4. The problem of the interference function

Many theoretical or *ad hoc* interference functions (or equivalently pair correlation functions) can be used to analyze the GISAXS

data [27]. The most usual are the Debye hard core [40] interference function, the Gaussian pair correlation function [72], the Lennard-Jones pair correlation function [73], the gate pair correlation function, the Debye hard core with power-law decrease [40], the Zhu pair correlation function [74], the Venables pair correlation function [75], or the bidimensional hard core pair function [76]. Some other very useful interference functions are those deduced from 1D or 2D paracrystals [42,27]. If the relative positions of the nanostructures could result from an interaction pair potential, the pair correlation function could be deduced using a thermodynamics approach based on an interacting gas [77], if the system is at equilibrium and nearly monodisperse. However, the repartition of nanostructures grown on substrates is often the result of many competing phenomena that are dominated by the kinetic conditions and thermodynamic trends, so that the notion of “interaction potential” between nanostructures is meaningless.

In many cases, none of these functions allow to satisfactorily reproduce the exact shape of the first maximum of the GISAXS data parallel with the surface, as well as the intensity evolution close to the origin of reciprocal space. It might then be useful to resort to an *ad hoc* interference function deduced from other experimental investigations such as plane view transmission electron microscopy (TEM), scanning electron microscopy (SEM) or Atomic Force Microscopy (AFM) data. Such an analysis has been performed in the cases of Pd and Ag deposited on MgO(001) [29,78–80].

Revenant et al. [29] resorted to digitalized TEM plane views to define an *ad hoc* interference function. The nanostructure pair correlation function $g(r)$ was determined from the number of nanostructure centers of mass per unit of surface located at a distance between r and $r + dr$ from an origin nanostructure. Care had been taken to avoid image edge effects by excluding the borderline nanostructures. Large scale pictures with a few thousands of nanostructures allowed to derive the nanostructure pair correlation function, $g(r)$, and its Fourier transform, *i.e.* the interference function $S(q_{\parallel})$, the latter being fitted with a two parameter function D and σ (D inter-nanostructure distance and σ the disorder parameter) in order to introduce it in the fit procedure. Ultimately, this function, determined on the final deposits, was found much more appropriate than the model functions to fit the GISAXS data for all deposits.

4.5. Nanostructures spacing and maximum of the interference function

In many GISAXS studies [17,18,24], the average inter-nanostructure distance D is determined through the position of the GISAXS intensity maximum q_m by $D = 2\pi/q_m$. However, as the GISAXS intensity is the product of the interference function $S(q_y)$ by the square modulus of the form factor, the GISAXS peak position q_m is shifted from the $S(q_y)$ peak position noted q_p accordingly to the form factor slope. This behavior is illustrated in Fig. 15 within the typical context of metal/oxide studies [25,29] for cylindrical nanostructures of mean radius $\langle R \rangle = 7.5$ nm. The GISAXS intensity maximum is located at $q_m \langle R \rangle = 2.20$, corresponding to a distance of $2\pi/q_m = 21.5$ nm, whereas the maximum of the interference function (evaluated from TEM) is at $q_p \langle R \rangle = 2.92$, which corresponds to a distance of $2\pi/q_p = 16.2$ nm. There is a large discrepancy between these two distances. Nevertheless, the distance determination from the interference function by $2\pi/q_p$ is not exact either, as the exact mean inter-nanostructure distance from the TEM analysis is $D = 18.0$ nm. As a consequence, in order to get a precise determination of the mean inter-nanostructure distance, it is extremely important to fit the experimental scattered intensity with an adequate model for the interference function.

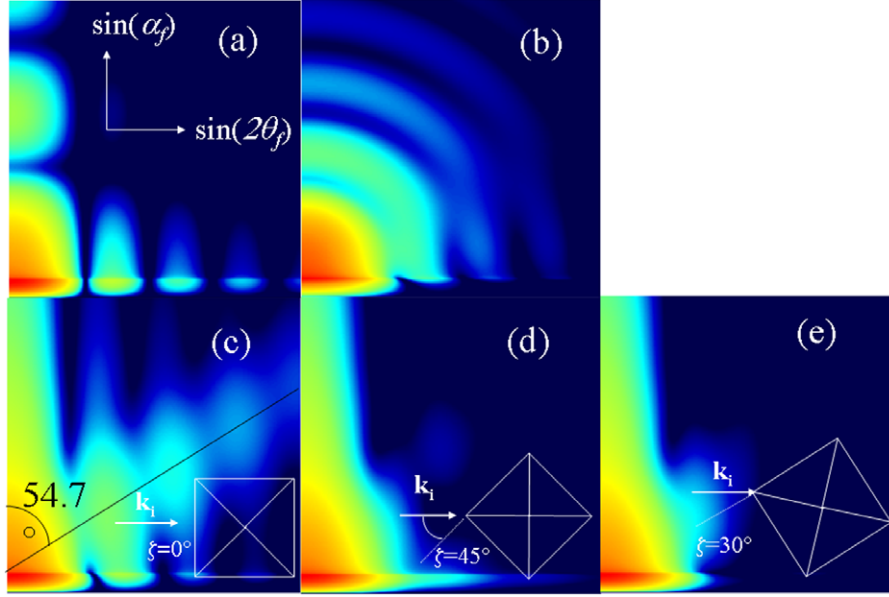


Fig. 16. The 2D $|F(\mathbf{q})|^2$ factor calculated within the DWBA of (a) a cylinder ($R = 5$ nm and $H/R = 1$), (b) a complete sphere ($R = 5$ nm), (c) a complete pyramid with $R = 5$ nm with the beam aligned along a face ($\xi = 0^\circ$), (d) same as (c) but with the beam aligned along an edge ($\xi = 45^\circ$), and (e) same as (c) but with $\xi = 30^\circ$. The intensity is represented on a logarithmic scale; $2\theta_f$ and α_f angles range from 0° to 3° . $\lambda = 0.1$ nm. From Ref. [29].

4.6. Deducing nanostructure size and shape from a rapid data analysis

In view of the complexity of a full quantitative analysis, using for instance the IsGISAXS program [27,28], it is very tempting to first deduce the nanostructure shape and if possible its average size from a first rapid data analysis. Different possibilities for such a rapid analysis are illustrated below.

4.6.1. The small polydispersity case

In the case of small polydispersity, *i.e.* when all nanostructures are close in size and shape, the position of the zeros of the form factor are indicative of the morphological parameters. This is illustrated in Fig. 17 which represents the square modulus of the form factor as a function of $q_y \langle R \rangle_h$, where $\langle R \rangle_h$ is the average of half parallel characteristic size R of the nanostructures over the coordinate h perpendicular to the interface. For isotropic nanostructures like cylinder and sphere based shapes, all the $|F(q_y \langle R \rangle_h)|^2$ functions are expressed with a Bessel function in the parallel plane and thus have their first zeros at $q_y \langle R \rangle_h \simeq 3.9$, as shown in Fig. 17a. For a pyramid based shape, for the beam aligned along a face, all the $|F(q_y \langle R \rangle_h)|^2$ functions are expressed with a linear combination of $\sin(x)/x$ functions and thus have their first zeros at $q_y \langle R \rangle_h \simeq 3.3$, as shown in Fig. 17b. For cylinder, sphere, and pyramid with the beam aligned along a face, the $|F(q_y \langle R \rangle_h)|^2$ function presents several well pronounced lobes. For the beam along an edge, the first zero or minimum is at $q_y \langle R \rangle_h \simeq 4.5$ for a heavily truncated pyramid (typically, $H/R \leq 0.5$) as shown in Fig. 17c. This value corresponds to the previous zero value (beam aligned along a face) times $\sqrt{2}$. On the contrary, the $|F(q_y \langle R \rangle_h)|^2$ function decreases in a monotonous way for a complete ($H/R = 1.4$) or slightly truncated pyramid (typically, $H/R \geq 0.9$).

4.6.2. The large polydispersity case: Nanostructure size distribution

Nanostructure shape and size distribution is a natural consequence of the growth-coalescence process. The exact size distribution law is a central information in numerous theoretical approaches of crystal growth. Nevertheless, depending on the growth stage (nucleation, growth or coalescence), the type of nucleation process

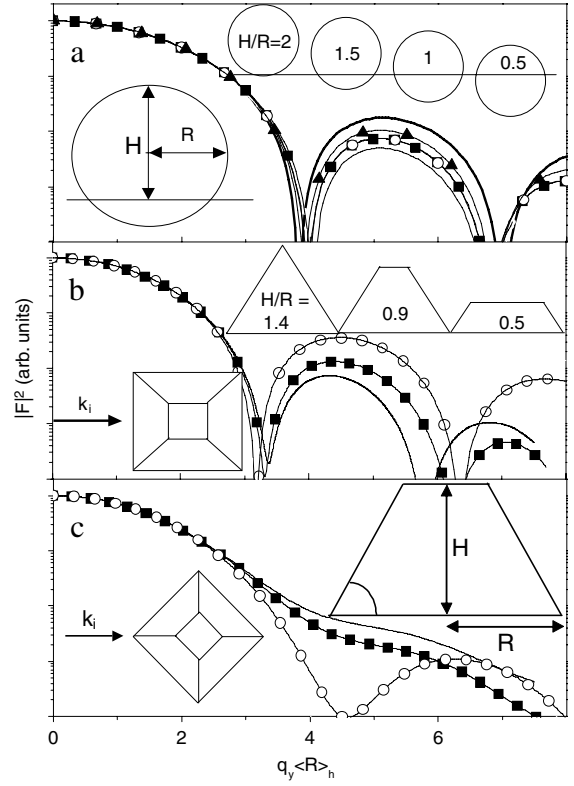


Fig. 17. Square modulus of the form factor calculated within the BA at $q_x = q_z = 0$ versus $q_y \langle R \rangle_h$. $\langle R \rangle_h$ is the average of the parallel nanostructure characteristic half size R over the coordinate h perpendicular to the surface/interface. (a) Isotropic nanostructures. Bold line: cylinder; filled triangles: sphere with $H/R = 1.5$; open circles: $H/R = 2$; filled squares: $H/R = 1$; line: $H/R = 0.5$. (b) Pyramid with the beam aligned along a face. Line: $H/R = 1.4$; filled squares: $H/R = 0.9$; open circles: $H/R = 0.5$. (c) Same as (b) but with the beam aligned along an edge. From Ref. [29].

(homogeneous or heterogeneous), the growth kinetics parameters (trapping energy, diffusion coefficient), the type of lattice mismatch relaxation, etc ..., it is difficult, if not impossible to predict it. Usually, the observed lateral size distribution is well

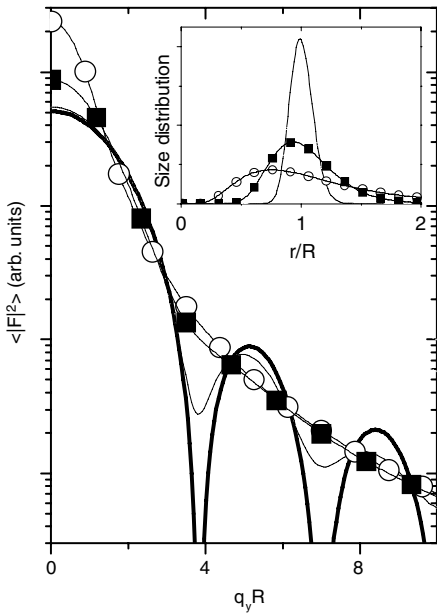


Fig. 18. The $\log\langle|F(q_yR)|^2\rangle$ function calculated within the BA for a cylinder at $q_x = q_z = 0$. Bold line: without any size distribution; thin line: with a lognormal distribution $\sigma = 1.1$; filled squares: $\sigma = 1.3$; open circles: $\sigma = 1.7$. The inset shows the corresponding lateral size distributions. From Ref. [29].

described by a lognormal probability distribution, which is asymmetric (Fig. 18). The obvious effect of the size distribution (see Fig. 18 and Section 6.3.3 with Fig. 49) is to smooth the scattering curve. Poorly known also is the height distribution and the cross correlation between lateral size and height distributions. From a practical point of view, they are either fitted independently or are supposed to be fully or partially correlated [81]. Fitting procedures used in SAXS [82] could be also applied to GISAXS to deduce the size distribution from the lineshape of the scattering but we are unaware of any GISAXS data analysis based on this approach, maybe because of limited counting dynamics.

4.6.3. The large polydispersity case: Asymptotic behavior of the form factor

In size distributed samples, further insight may be gained by studying the asymptotic behavior of the mean form factor, limit which is currently named the Porod approach in the field of small angle scattering on bulk samples (see Section 6.3.3 for the demonstration). Whatever the approximation is, for disordered systems, the intensity at large \mathbf{q} vectors is proportional to the average of the square modulus of the form factor. The curves $\log\langle|F|^2\rangle$ versus $\log(q_y)$ or $\log(q_z)$ shown in Fig. 19 for simple geometrical shapes demonstrate that, for sufficiently distributed sizes, the intensity varies as q^{-n} with an exponent n that depends on the sharpness of the nanostructure shape. For instance, $n = 3$ for a cylinder, 4 for a hemisphere or a pyramid in the parallel direction, whereas $n = 2.5$ for a cylinder, 3 for a hemisphere or a pyramid in the perpendicular direction in a range where $\log(q_yR)$ or $\log(q_zH)$ are comprised between 0.5 and 1. Hence, providing that measurements are performed sufficiently far away in the reciprocal space (typically q_yR or $q_zH > 3.5$) with a high dynamics, each considered nanostructure shape is fully characterized by a set of slopes in both directions. It is also worth noticing that the difference with the 3D-case where $n = 4$ for continuously curved interfaces is due to the reduced dimensionality and the absence of the orientation average as supposed in the 3D-Porod limit.

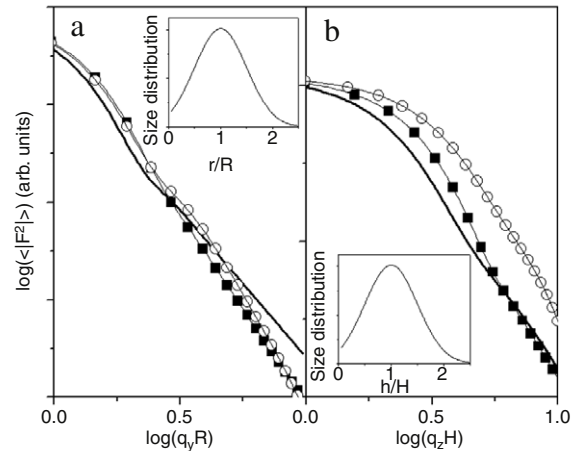


Fig. 19. Plots of $\log\langle|F|^2\rangle$ calculated within the BA (a) at the q_z position of total external reflection versus $\log(q_yR)$, and (b) at the q_y position of the interference maximum versus $\log(q_zH)$. Continuous line: cylinder $H/R = 1$; filled squares: hemisphere; open circles: pyramid $H/R = 0.9$, and $\zeta = 0^\circ$. The insets of (a) and (b) show, respectively, the lateral and vertical lognormal size distributions of $\sigma = 1.7$. Similar results are obtained within the DWBA. From Ref. [29].

4.6.4. Very fast data analysis of GISAXS patterns

The aim of this rapid analysis is to estimate easily and quickly the average morphological parameters of the nanostructures [80]: the inter-nanostructure distance D , the diameter (or in-plane size) d and the height H . In this analysis, the nanostructures are modeled by spheres or cylinders without size distribution whatever the real shape of the nanostructures. These crude approximations are made for the sake of simplicity and rapidity of the computations. In the direction parallel with the surface, the intensity is expressed as:

$$I(q_y) = A_{\parallel} |F(q_y)|^2 S(q_y), \quad (2)$$

where A_{\parallel} is a constant scale factor, $F(q_y)$ the form factor expression and $S(q_y)$ an *ad hoc* interference function given by:

$$S(q_y) = \left\{ 1 + e^{-|q_y - q_{y0}|D/\pi} \cos[q_y - q_{y0}]D \right\} E(q_y), \quad (3)$$

with

$$E(q_y) = 1 - \frac{1}{1 + e^{D/2(|q_y - q_{y0}| - 4\pi/D)}}, \quad (4)$$

where q_{y0} is the q_y coordinate of the maximum. In the perpendicular direction, the intensity is also calculated on the basis of an analytical form factor squared, multiplied by the intensity transmission factor expressed as a function of the incident and exit angles as if the particles were buried underneath the substrate. It is thus fitted with the following $I(q_z)$ function, calculated for a substrate of complex refractive index $n = 1 - \delta - i\beta$:

$$I(q_z) = A_{\perp} |F(q_z)|^2 T(q_z - q_{z0}), \quad (5)$$

with

$$T(q) = 4\lambda^2 \frac{q^2}{(\lambda q + a_+)^2 + a_-^2}, \quad (6)$$

and

$$a_{\pm} = \frac{1}{2} \sqrt{\sqrt{(\lambda^2 q^2 - 2\delta)^2 + 4\beta^2} + \lambda^2 q^2 \pm 2\delta}, \quad (7)$$

where A_{\perp} is a scale factor, q_{z0} is the coordinate of the maximum intensity, the parameters a_+ and a_- occur in the intensity ratio between the reflected beam and the incident one.

Fig. 20 shows a typical example of this rapid data analysis. If the intensity maxima parallel with the surface and the positions of

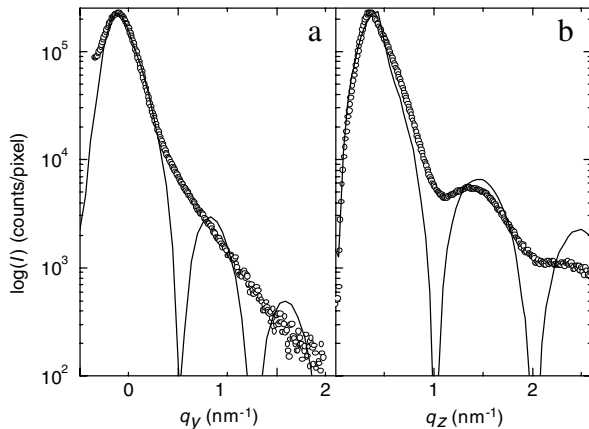


Fig. 20. GISAXS cut (a) parallel and (b) perpendicular to the surface for the 3.6 nm thick Ag deposit on MgO(001) at 300 K. Dots: cuts of the experimental GISAXS pattern; thin line: best fit of the experimental cut with the rapid data analysis. The intensity is represented on a logarithmic scale. From Ref. [80].

the maxima perpendicular to it are well reproduced, the absence of size distributions yields large intensity oscillations parallel to the surface that are obviously absent from the experimental data. A more sophisticated model should then be used if one is interested in the nanostructure shape and size distribution.

4.7. Nanostructure faceting

Another general feature is the signature of the nanostructure faceting on GISAXS patterns (see Section 6.2.7). We illustrate it for the Ag/MgO(001) system (Fig. 21). When the incident X-ray beam is along the [110] direction (Fig. 21b), an additional scattering rod at 54.7° with respect to the surface normal is observed. It is never found when the beam is along the [100] direction (Fig. 21a). This indicates that silver forms oriented faceted nanostructures with {111} side facets. Moreover, in the case of faceted nanostructures, the second and even sometimes third order scattering peaks perpendicular to the surface are indicative of a flat top (001) terrace and of a narrow height distribution. An additional feature can be deduced from a detailed comparison of Fig. 21a with b. Indeed, the intensity along the q_y direction, at the Yoneda peak position, is clearly larger when the X-ray beam is along [100] as compared to along [110]. This indicates that there is a scattering rod along the {010} direction. Hence, the Ag nanostructures also present {010} facets for Ag deposited thickness as small as 2 nm. These facets grow as the Ag deposition thickness increases from 2 to 7 nm. All these features point to a truncated cubo-octahedron like average shape with {001}, {111}, and {010} facets, which is represented in the inset of Fig. 21a.

4.8. Practical considerations

The above measurements were performed in UHV. As expected for vacuum measurements, the background is close to zero (less than ten counts for an acquisition time ranging from 400 ms to 25 s) [25,26]. The enhancement of intensity for $\alpha_f = \alpha_c$ in the perpendicular direction is usually referred to the Yoneda's peak [39]. Its origin will be explained in the framework of the DWBA scattering cross section in the theoretical part Section 6.2. The origin of reciprocal space is located (i) along $2\theta_f$, in the middle of the two lobes when the image is known to be symmetric, and (ii) along α_f , by setting the Yoneda's peak at the substrate α_c value at the early beginning of the growth, as given by the transmission function $T(\alpha_f)$ inside the substrate. The only discrepancy that was found between the theoretical $T(\alpha_f)$ function

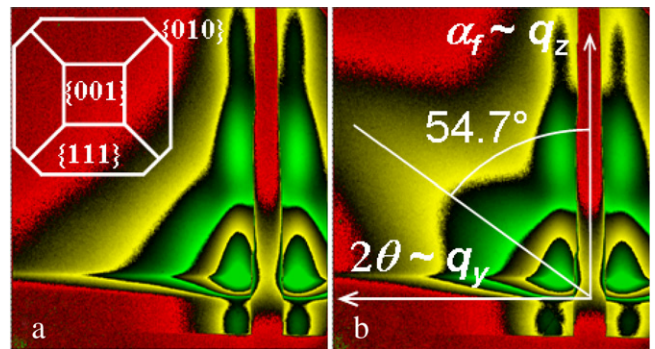


Fig. 21. GISAXS patterns of 2 nm of Ag deposited on a MgO(001) surface at 540 K, with the incident beam along the [100] (a) and the [110] (b) direction of the MgO(001) substrate. The intensity is represented on a logarithmic scale. Each black contour between two colors corresponds to an order of magnitude change in intensity. The q_y (respectively q_z) axis ranges from 0 to 2.7 nm⁻¹ (respectively 3 nm⁻¹). Inset: top view of the truncated cubo-octahedron nanostructures shape with the {001}, {111}, and {010} facets. From Ref. [79].

and the experimental intensity profile as a function of α_f is a wider experimental FWHM (factor 2) that gives an upper bound 0.05° for the instrument-induced broadening along α_f [81]. This corresponds to the horizontal convergence of the incident beam of the BM32 optics.

5. Theoretical background of grazing incidence diffuse X-ray scattering

5.1. Introduction

Despite the well known phase problem, one key advantage of X-ray scattering from bulk is the possibility to perform data analysis within the kinematic approximation [40,41] using suitable models. Indeed, contrary to more interacting particles like electrons or visible photons, X-ray photons interact weakly with matter and multiple scattering can be neglected except for highly perfect crystals. However, shallow scattering angles bring one more level of complexity. The standard Born approximation starts to fail and multiple scattering effects come into play. In other words, the dynamical effects of reflection and refraction at interfaces can no more be neglected in the scattering process. This section is devoted to the theoretical treatment of scattering under grazing angles using the most popular theoretical framework i.e. the Distorted Wave Born Approximation (DWBA). This section is aimed at giving a feeling of the underlying problems in a self consistent way but without any attempt at completeness. The interested reader can refer to the many standard text books [14,15,38] or reviews [43,12,83,44,84,13,85] that deal with the theoretical and experimental aspects of scattering from surfaces.

In a first part Section 5.2, the specificity of the propagation of X-ray at flat and abrupt interfaces are reminded after the definition of refraction index. The emphasis is put on the classical Fresnel coefficients, the concept of penetration depth and the phenomenon of total external reflection that is at the heart of the grazing incidence techniques (see Section 2). As a primer to diffuse scattering, it is necessary to present the matrix formalism for a graded interface as compared to the kinematic approximation of reflectivity to understand the notion of multiple scattering. Hand waving arguments are given to introduce the roughness Nérot–Croce damping factor in reflectivity.

The problem of scattering is introduced in Section 5.3 through the notion of integral equation of wave propagation and Green function. Perturbation treatments known as the Born and Distorted Wave Born Approximations are introduced and applied to a series

of relevant cases: the single rough surface, the multilayers, the buried density fluctuations, the magnetic scattering. The important case of nanoparticles is postponed to the next section Section 6.

5.2. Propagation of X-ray at interfaces

Two conventions are often used to define the monochromatic plane waves:

- (i) the crystallography one: $A \propto e^{i(\omega t - \mathbf{k} \cdot \mathbf{r})}$,
- (ii) the quantum mechanics or optics one: $A \propto e^{i(\mathbf{k} \cdot \mathbf{r} - \omega t)}$.

The difference comes into play in the sign of the imaginary part of the refraction index n or the atomic scattering form factor and the definition of the wavevector transfer \mathbf{q} . Even if the measurable quantities are given by squared modulii, it is important to keep consistently the same convention, particularly when using the DWBA formula. Contrary to many theoretical papers on the DWBA, the crystallography convention is used herein leading to $n = 1 - \delta - i\beta$ with $\delta, \beta > 0$; the wavevector transfer is given by $\mathbf{q} = \mathbf{k}_f - \mathbf{k}_i$ and the Fourier transform of any function $F(\mathbf{r})$ is defined by:

$$\mathcal{F}(\mathbf{q}) = \int_V F(\mathbf{r}) e^{i\mathbf{q} \cdot \mathbf{r}} d\mathbf{r}. \quad (8)$$

5.2.1. Wave propagation in three dimensions

The X-ray electromagnetic fields obey the classical Maxwell equations [86,87]:

$$\nabla \times \mathbf{E} = -\frac{\partial \mathbf{B}}{\partial t} \quad (9)$$

$$\nabla \times \mathbf{H} = \frac{\partial \mathbf{D}}{\partial t} \quad (10)$$

$$\nabla \cdot \mathbf{D} = 0 \quad (11)$$

$$\nabla \cdot \mathbf{B} = 0. \quad (12)$$

As usual, \mathbf{E} is the electric field, \mathbf{H} the magnetic field and \mathbf{D}, \mathbf{B} the associated displacement fields. These quantities depend on the spatial coordinate \mathbf{r} and on time t . These equations apply to charge free and current free media. For a non-magnetic medium characterized by its relative dielectric constant $\epsilon(\mathbf{r})$,

$$\mathbf{D} = \epsilon(\mathbf{r})\epsilon_0\mathbf{E}; \quad \mathbf{B} = \mu_0\mathbf{H}. \quad (13)$$

The time dependence of the dielectric constant is dropped as the propagation is supposed to be non-retarded. ϵ_0 and μ_0 are the dielectric and magnetic constants of vacuum. The case of scattering from magnetic media is beyond the scope of this review; we restrict the problem to scattering from variations of the dielectric constant. The problem of resonant scattering from structurally and magnetically rough interfaces and multilayers was recently tackled in the cases of specular reflectivity [88] and diffuse scattering [89] using the framework of DWBA (see Section 5.4.5 for further insights). Using the identities $\nabla \times \nabla \times \mathbf{A} = \nabla(\nabla \cdot \mathbf{A}) - \nabla^2 \mathbf{A}$ and $\nabla \cdot (\mathbf{f}\mathbf{A}) = f\nabla \cdot \mathbf{A} + \nabla f \times \mathbf{A}$ in Eqs. (9)–(10), one ends up with the propagation equations for the electric and magnetic fields:

$$\nabla^2 \mathbf{E} - \epsilon_0 \mu_0 \epsilon(\mathbf{r}) \frac{\partial^2 \mathbf{E}}{\partial^2 t} = -\nabla(\nabla \ln \epsilon(\mathbf{r}) \cdot \mathbf{E}) \quad (14)$$

$$\nabla^2 \mathbf{H} - \epsilon_0 \mu_0 \epsilon(\mathbf{r}) \frac{\partial^2 \mathbf{H}}{\partial^2 t} = -\nabla \ln \epsilon(\mathbf{r}) \times (\nabla \times \mathbf{H}). \quad (15)$$

For time harmonic waves with a $e^{i\omega t}$ dependence, Eqs. (14)–(15) becomes:

$$[\nabla^2 + \epsilon(\mathbf{r})k_0^2] \mathbf{E} = -\nabla(\nabla \ln \epsilon(\mathbf{r}) \cdot \mathbf{E}) \quad (16)$$

$$[\nabla^2 + \epsilon(\mathbf{r})k_0^2] \mathbf{H} = -\nabla \ln \epsilon(\mathbf{r}) \times (\nabla \times \mathbf{H}), \quad (17)$$

where the dispersion relationship for plane waves in vacuum, $k_0^2 = \epsilon_0 \mu_0 \omega^2$, has been introduced.

5.2.2. Dielectric constant and index of refraction

At variance to visible light [86,87], the description of X-ray radiation-matter interaction through a refractive index does not imply the spatial average of the microscopic Maxwell equations to hold but relies on the huge discrepancy between the wave frequency and the characteristic atomic transition frequency [38,14]. In this case, the indexes or the densities are determined at a local scale *i.e.* depending on the resolution of the experimental technique.

The dielectric constant $\epsilon(\mathbf{r})$ is related to the electric polarization density \mathbf{P} of the medium through:

$$\mathbf{D} = \epsilon_0 \epsilon(\mathbf{r}) \mathbf{E} = \epsilon_0 \mathbf{E} + \mathbf{P}. \quad (18)$$

With the classical model of the bound electron [87,40,38,84], the electron is submitted to three forces:

- (i) the electric force $\mathbf{F}_e = -e\mathbf{E}$ from the incident X-ray beam $\mathbf{E} = \mathbf{E}_0 e^{i\omega t}$,
- (ii) the restoring force $\mathbf{F}_r = -m\omega_0^2 \mathbf{r}$ due to the binding of the electron to the nucleus that is proportional to the shift of the electron position \mathbf{r} from its rest position,
- (iii) the damping force $\mathbf{F}_d = -\Gamma d\mathbf{r}/dt$ primarily due to the radiative loss of energy by the accelerated electron but also to photon absorption. Its expression can be found in Refs. [87,84].

The equation of motion of the electron reads:

$$\frac{d^2 \mathbf{r}}{dt^2} + \Gamma \frac{d\mathbf{r}}{dt} + \omega_0^2 \mathbf{r} = -e\mathbf{E}_0 e^{i\omega t}. \quad (19)$$

Seeking for time harmonic dependence $\mathbf{r} = \mathbf{r}_0 e^{i\omega t}$, the amplitude of the forced oscillator is:

$$\mathbf{r}_0 = -\frac{e\mathbf{E}_0}{m} \frac{1}{\omega_0^2 - \omega^2 - i\omega\Gamma}. \quad (20)$$

Far away from an adsorption edge, in the hard X-ray regime, the eigenfrequency $\omega_0 \simeq 10^{15} \text{ s}^{-1}$ of the bound electrons is much smaller than the driving frequency of X-ray $\omega \simeq 10^{19} \text{ s}^{-1}$. Therefore, the previous equation reduces to the classical Thomson expression $\mathbf{r}_0 \simeq e\mathbf{E}_0/m\omega^2$. The dipole density caused by the uncoupled electrons of density ρ_e is given by: $\mathbf{P} \simeq -e^2 \rho_e \mathbf{E}_0/m\omega^2$. Using Eq. (18), the dielectric constant follows:

$$\epsilon_r = 1 - \frac{r_e \rho_e \lambda^2}{4\pi}, \quad (21)$$

where the classical electron radius is given by: $r_e = e^2/4\pi\epsilon_0 mc^2 = 2.8 \cdot 10^{-15} \text{ m}$ and $\omega = 2\pi c/\lambda$. With $\lambda \simeq 1 \text{ \AA}$ and $\rho_e \simeq 1 \text{ e \AA}^{-3}$, the correction to 1 is in the range of $10^{-6} - 10^{-5}$. Thus, the refractive index is given by:

$$n = \sqrt{\epsilon_r} = 1 - \delta \quad \text{with } \delta = \frac{r_e \rho_e \lambda^2}{2\pi}. \quad (22)$$

An imaginary part $\beta \sim 10^{-6}$ due to absorption that is to say to the damping term Γ should be added to get the full complex refractive index $n = 1 - \delta - i\beta$. As the spatial dependence of a wave propagating in a medium is defined as $e^{i2\pi n/\lambda z}$, β is related to the linear absorption coefficient of intensity, μ , through $\beta = \lambda\mu/4\pi$. In fact, n is related to the atomic scattering form factor (*i.e.* the Fourier transform of the electronic cloud) $f(\mathbf{q}) = f^0(\mathbf{q}) + f' + if''$ (\mathbf{q} is the scattering wave vector) and to the atomic density ρ_a [38]:

$$n = 1 - \delta - i\beta; \quad \delta = \frac{r_e \rho_a (f^0(0) + f') \lambda^2}{2\pi}; \quad \beta = \frac{r_e \rho_a f'' \lambda^2}{2\pi}. \quad (23)$$

The anomalous dispersion correction $f' + if''$ applied on $f^0(\mathbf{q})$ is due to absorption edges and depends on the photon energy E ; $f(\mathbf{q})$ can be described on the basis of quantum mechanics. $f^0(0)$ is nothing

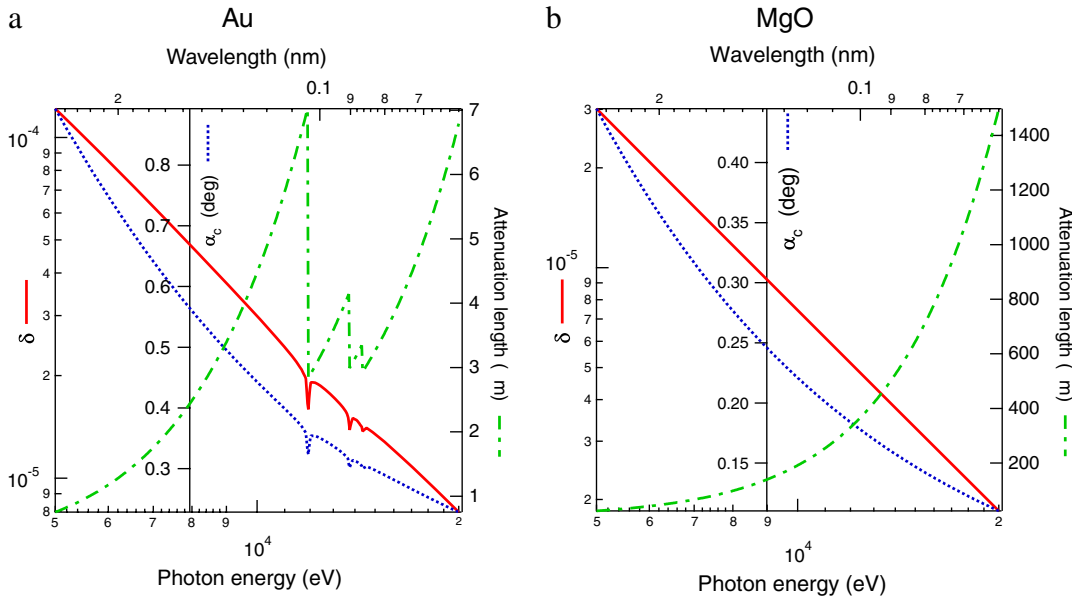


Fig. 22. Real part of refractive index δ , attenuation length $1/\mu$ and critical angle for total external reflection α_c versus photon energy for (a) a metal Au (density 19.32), (b) an oxide made of lighter elements MgO (density 3.58). Notice the absorption thresholds L_1 , L_2 , L_3 of gold leading to strong variations of δ , β , α_c , μ , f' , f'' . Data from Ref. [90].

else than the number of electrons per atom. A demonstration of the strong link between the refractive index n and the scattering length density in the forward direction $f^0(0)$ can be found in Refs. [87, 14, 38]. It relies on the weak interaction approximation that comes from the smallness of λ as compared to the extinction length $L_e = \lambda/(n-1)$. This link is a straightforward result of the Born scattering cross section (see Section 5.3.4).

A full data set of refraction indices δ , β , dispersion corrections f' , f'' and absorption coefficients can be found on the web [90]. The typical orders of magnitude are illustrated in Fig. 22.

5.2.3. Propagation in stratified media and Helmholtz equation for X-rays

The general discussion of Section 5.2.1 is now restricted to the case of the propagation in stratified media for which the dielectric constant depends only on the spatial coordinate z perpendicular to the stacking direction $\epsilon(\mathbf{r}) = \epsilon(z)$. As shown in Fig. 23, the wavefield can be conveniently divided into two parts:

- (i) a s -polarized wave with its electric field \mathbf{E} aligned along the y -direction perpendicular to the incident plane,
- (ii) a p -polarized wave with \mathbf{E} in the plane of incidence and its magnetic field \mathbf{H} aligned along y .

The matching of the boundary conditions at flat interfaces shows that both type of waves are not depolarized upon reflection or refraction [87] (see Section 5.2.6). Moreover, any type of waves can be decomposed in s or p components.

For a s -polarized wave, as the dielectric constant and the electric field E_y depend only on z , Eq. (16) reduces conveniently to a scalar one for the y component of \mathbf{E} :

$$\left[\frac{\partial^2}{\partial z^2} + \epsilon(z) k_0^2 \right] E_y = 0. \quad (24)$$

A similar equation can be inferred from Eq. (17) for the y -component of \mathbf{H} in the case of a p -polarized field:

$$\left[\frac{\partial^2}{\partial z^2} + \epsilon(z) k_0^2 \right] H_y = \frac{\partial \ln[\epsilon(z)]}{\partial z} \frac{\partial H_y}{\partial z}. \quad (25)$$

As previously shown in Section 5.2.2, the dielectric constant $\epsilon(z)$ and the refraction index $n(z) = \sqrt{\epsilon(z)}$ are very close to one in

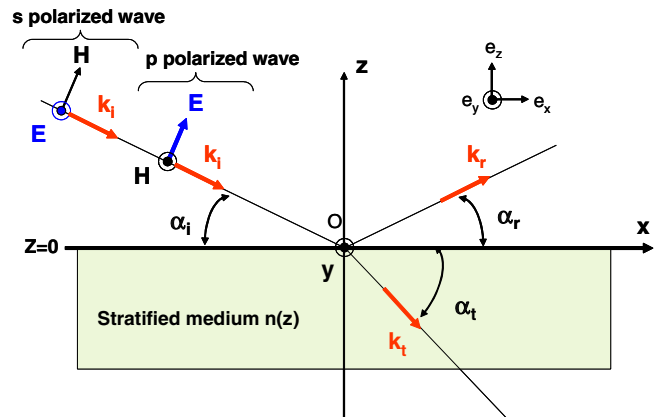


Fig. 23. An incident plane wave of wavevector \mathbf{k}_i is reflected along the \mathbf{k}_r direction and transmitted along the \mathbf{k}_t one by a stratified medium of index $n(z)$. The reflection plane (Oxz) contains \mathbf{k}_i , \mathbf{k}_r , \mathbf{k}_t . As usual with X-ray scattering, the incident α_i , the reflected α_r and the transmitted angles α_t are defined from the sample surface. The two polarization states s , p that are not modified upon reflection and transmission are represented. For a s -wave, the electric field E_x is parallel to the surface while for a p -wave, it is the magnetic one H_x .

the X-ray wavelength regime: $\epsilon(z) = 1 - 2\delta$ with δ in the range of $10^{-6} - 10^{-5}$. Therefore, for all practical purposes, the gradient of $\ln[\epsilon(z)]$ is of the same order of magnitude as δ and thus can be neglected with a great accuracy. Consequently, Eq. (25) reduces to:

$$\left[\frac{\partial^2}{\partial z^2} + \epsilon(z) k_0^2 \right] H_y = 0. \quad (26)$$

As a conclusion, both s and p -polarized X-ray waves obey a similar Helmholtz equation for either the electric or the magnetic field.

5.2.4. The boundary conditions

The boundary conditions on the electric and magnetic fields come from the Maxwell equations (Eqs. (9)–(10)). The path integral of \mathbf{E} or \mathbf{H} along a rectangular closed loop across the interface of normal \mathbf{n} that separates two media \pm is given by the flux integral of its rotational through the so defined area (see Fig. 24):

$$\oint_L \mathbf{E} \cdot d\mathbf{l} = \iint_A \nabla \times \mathbf{E} \cdot d\mathbf{s} = -\frac{\partial}{\partial t} \iint_S \mathbf{B} \cdot d\mathbf{s}$$

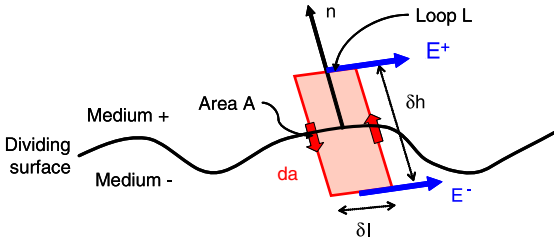


Fig. 24. The considered geometry for the derivation of the electromagnetic boundary conditions. A closed elementary rectangular loop of length L and area $A = \delta l \delta h$ intersects the surface of separation between two media \pm of local normal \mathbf{n} . The loop is oriented in such a way that $d\mathbf{a}$ is its elementary surface vector. Its height δh tends to zero while keeping the loop along the frontier between the media.

$$\oint_L \mathbf{H} \cdot d\mathbf{l} = \iint_A \nabla \times \mathbf{H} \cdot d\mathbf{s} = \frac{\partial}{\partial t} \iint_S \mathbf{D} \cdot d\mathbf{s}. \quad (27)$$

When the two sides of the rectangle perpendicular to the surface vanish $\delta h \rightarrow 0$, the surface integrals on left-hand side of Eq. (27) become zero and the only contributions of the path integrals come from both sides parallel with the interface. This yields the continuity of the tangential components of \mathbf{E} and \mathbf{H} across the interface:

$$\mathbf{n} \times (\mathbf{E}^+ - \mathbf{E}^-) = 0 \quad (28)$$

$$\mathbf{n} \times (\mathbf{H}^+ - \mathbf{H}^-) = 0. \quad (29)$$

For a s -polarized wave for which \mathbf{E} has only one component parallel with the interface, $E_y(z = 0^+) = E_y(z = 0^-)$. As the magnetic field is evaluated through the Maxwell equation (Eq. (9)):

$$H_x = \frac{1}{i\omega\mu_0} \frac{\partial E_y}{\partial z}, \quad (30)$$

it appears that the continuity of H_x gives rise to the continuity of the first derivative of the tangential component of the electric field:

$$\left(\frac{\partial E_y}{\partial z} \right) (z = 0^+) = \left(\frac{\partial E_y}{\partial z} \right) (z = 0^-). \quad (31)$$

For a p -polarized wave propagating in stratified media, the same reasoning leads to $H_y(z = 0^+) = H_y(z = 0^-)$. The continuity of E_x implies that:

$$\left(\frac{1}{\epsilon(z)} \frac{\partial H_y}{\partial z} \right) (z = 0^+) = \left(\frac{1}{\epsilon(z)} \frac{\partial H_y}{\partial z} \right) (z = 0^-), \quad (32)$$

since the Maxwell equation (Eq. (10)) links H_y to the tangential component of \mathbf{E} :

$$E_x = -\frac{1}{i\omega\epsilon_0\epsilon(z)} \frac{\partial H_y}{\partial z}. \quad (33)$$

The same argument that led to Eq. (26) i.e. the small difference between $\epsilon(z)$ and one for X-ray wavelength allows to write down the continuity of the normal derivative of H_y .

5.2.5. The analogy with Schrödinger propagation equation

In the two previous sections, it was demonstrated that for stratified media:

- (i) the propagation of the X-ray wavefields can be reduced to a scalar Helmholtz equation in the case of s (respectively p) polarized wave for the component of the electric E_y (respectively magnetic H_y) perpendicular to the incident plane,
- (ii) those components as well as their normal derivative are continuous across the interface.

Therefore, as a consequence of $n^2 \simeq \epsilon \simeq 1$ for X-rays, the vectorial character of the wavefield can be dropped and replaced by a scalar quantity $\Psi(z)$ that obeys:

$$[\nabla^2 + k_0^2 n(z)^2] \Psi(z) = 0; \quad \Psi(z = 0^+) = \Psi(z = 0^-); \quad (34)$$

$$\left(\frac{\partial \Psi}{\partial z} \right) (z = 0^+) = \left(\frac{\partial \Psi}{\partial z} \right) (z = 0^-). \quad (35)$$

For $n(z) = n$, the obvious solutions (Eq. (35)) are plane waves $e^{ik_0 nz}$. A complete analogy can be drawn with the Schrödinger equation [91,92]:

$$\left[-\frac{\hbar^2}{2m} \nabla^2 + V(z) \right] \Psi(z) = \varepsilon \Psi(z) \quad (36)$$

describing the propagation of the wave function of a particle of energy ε in a 1D potential $V(z) = -\hbar^2 k_0^2 n^2(z)/2m + \varepsilon$. The continuity of $\Psi(z)$ and its derivative result from the conservation of the flux of probability. Therefore, X-ray and neutron reflection from interfaces can be treated on the same footing [43,84] even for diffuse scattering at small angles (see Section 5.3.6 for demonstration).

5.2.6. Snell–Descartes laws, Fresnel coefficients and penetration depth

The Snell–Descartes laws and Fresnel coefficients of reflection and refraction are a simple consequence of the propagation equation and its boundary conditions. Even though the problem is treated in many standard textbooks of electromagnetism or optics [87], it is worth considering it in the case of X-rays [38, 14,83], not only because of the special convention of angles, but also because of the phenomenon of total external reflection and its implications.

Let us consider the simple sharp and abrupt dioptric between vacuum and a medium of refraction index n and a plane wave propagating in the (xOz) plane (see Fig. 23). In vacuum, the wavefield is made of an incident plane wave $A_i e^{-ik_i \cdot r}$ of wavevector \mathbf{k}_i and amplitude A_i superposed with a reflected one (wavevector \mathbf{k}_r , amplitude A_r) while a transmitted one (wavevector \mathbf{k}_t , amplitude A_t) appears inside the medium. As usual in X-ray reflectivity, the incident α_i , reflected α_r and refracted α_t angles are defined from the substrate surface and are related to the wavevector (see Fig. 23) through:

$$\mathbf{k}_i = k_0 [\cos(\alpha_i) \mathbf{e}_x - \sin(\alpha_i) \mathbf{e}_z] \quad (37)$$

$$\mathbf{k}_r = k_0 [\cos(\alpha_r) \mathbf{e}_x + \sin(\alpha_r) \mathbf{e}_z] \quad (38)$$

$$\mathbf{k}_t = nk_0 [\cos(\alpha_t) \mathbf{e}_x - \sin(\alpha_t) \mathbf{e}_z]. \quad (39)$$

If it is assumed that the transmitted wave is completely absorbed by a sufficiently thick substrate, the boundary conditions at $z = 0$ read:

$$A_i e^{-k_0 \cos(\alpha_i)x} + A_r e^{-k_0 \cos(\alpha_r)x} = A_t e^{-nk_0 \cos(\alpha_t)x} \quad (40)$$

$$A_i \sin(\alpha_i) e^{-k_0 \cos(\alpha_i)x} - A_r \sin(\alpha_r) e^{-k_0 \cos(\alpha_r)x} = A_t \sin(\alpha_t) e^{-nk_0 \cos(\alpha_t)x}. \quad (41)$$

The validity of Eq. (40) for any x leads to the well known Snell–Descartes laws:

$$\alpha_i = \alpha_r, \quad \cos(\alpha_i) = n \cos(\alpha_t). \quad (42)$$

In terms of wavevector, this equation means that the \mathbf{k} component parallel with the surface is conserved. This is a direct consequence of the translational invariance of the interface. The rewriting of the boundary conditions (Eqs. (40)–(41)) reads:

$$A_i + A_r = A_t \quad (43)$$

$$\sin(\alpha_i) A_i - \sin(\alpha_r) A_r = \sin(\alpha_t) A_t, \quad (44)$$

and allows one to evaluate the reflection coefficient in amplitude $r = A_r/A_i$ as well as the transmitted one $t = A_t/A_i$ (the so-called Fresnel coefficients):

$$r = \frac{\sin(\alpha_i) - n \sin(\alpha_t)}{\sin(\alpha_i) + n \sin(\alpha_t)} = \frac{k_{i,z} - k_{t,z}}{k_{i,z} + k_{t,z}};$$

$$t = \frac{2 \sin(\alpha_i)}{\sin(\alpha_i) + n \sin(\alpha_t)} = \frac{2k_{i,z}}{k_{i,z} + k_{t,z}}. \quad (45)$$

The corresponding reflectivity $R = |r|^2$ and transmittivity $T = |t|^2$ in intensity are simply given by the modulus square of r and t . The introduction of the Snell–Descartes laws (Eq. (42)) in Eq. (45) gives:

$$r = \frac{\sin(\alpha_i) - \sqrt{n^2 - \cos(\alpha_i)}}{\sin(\alpha_i) + \sqrt{n^2 - \cos(\alpha_i)}}; \quad t = \frac{2 \sin(\alpha_i)}{\sin(\alpha_i) - \sqrt{n^2 - \cos(\alpha_i)}}. \quad (46)$$

Upon combining a grazing angle hypothesis $\alpha_i \ll 1$ with $n^2 = 1 - 2\delta - 2i\beta = 1 - \alpha_c^2 - 2i\beta$ (Eq. (22)), one ends up with:

$$r = \frac{\alpha_i - \sqrt{\alpha_i^2 - \alpha_c^2 - 2i\beta}}{\alpha_i + \sqrt{\alpha_i^2 - \alpha_c^2 - 2i\beta}}; \quad t = \frac{2\alpha_i}{\alpha_i + \sqrt{\alpha_i^2 - \alpha_c^2 - 2i\beta}}. \quad (47)$$

$\alpha_c = \sqrt{2\delta}$ is the critical angle for total external reflection. As shown in Fig. 22, α_c is in the range of few tenth of degree. α_c scales with the square-root of the material electronic density (see Eq. (22)). Using the Snell–Descartes law (Eq. (42)), the amplitude of the wave propagating inside the medium behaves as:

$$\Psi_t \sim A_t e^{-k_0 n \cos(\alpha_t)x + k_0 n \sin(\alpha_t)z} = A_t e^{-k_0 \cos(\alpha_i)x} e^{ik_0 n \sin(\alpha_t)z}. \quad (48)$$

Writing $-2k_0 \text{Im}[n \sin(\alpha_t)] = 1/\Lambda(\alpha_i)$, it appears that the wave intensity $|\Psi_t|^2$ falls off exponentially with increasing depth inside the medium. $\Lambda(\alpha_i)$ is the penetration depth and is given by:

$$\frac{1}{\Lambda(\alpha_i)} = -2k_0 \text{Im} \left[\sqrt{\alpha_i^2 - \alpha_c^2 - 2i\beta} \right]. \quad (49)$$

Typical behaviors of the reflection, and transmission coefficients as well as the penetration depth as function of the normalized incident angle α_i/α_c are given in Fig. 25.

As the imaginary part of the refraction index is always small ($\beta \ll 1$), three different regimes can be distinguished as function of α_i :

- (i) $\alpha_i \ll \alpha_c$: as $r \simeq -1$, the reflected wave is in phase opposition with the incident one. Since α_t is almost imaginary, the transmitted wave is an evanescent one that propagates parallel with the surface on a penetration depth given by $\Lambda_c = 1/2k_0\alpha_c$. This is the phenomenon of total external reflection of X-rays.
- (ii) $\alpha_i = \alpha_c$: as $r \simeq 1$, the incident and the reflected waves are nearly in phase while the transmitted wave is close to twice that of the incident wave $t \simeq 2$. A steep decrease of reflected intensity is observed at $\alpha_i \geq \alpha_c$.
- (iii) $\alpha_i \gg \alpha_c$: the asymptotic behaviors of the Fresnel coefficients are $r \simeq \alpha_c^2/4\alpha_i^2, t \simeq 1$. There is almost complete transmission with a penetration depth that is only limited by the absorption β in the material. The reflected wave is in phase with the incident one.

Working with an incident angle α_i close or below the critical angle α_c appears as a convenient way to reduce the penetration depth of the X-ray beam [9,93] and thus to enhance any scattering signal coming from the surface in comparison with bulk signal. It is worth noticing that a value larger than one of the transmitted beam intensity does not violate the principle of energy conservation. Indeed, this latter should be written through the conservation of flux of intensity across a surface perpendicular to the beam *i.e.* $(1 - |r|^2) \sin(\alpha_i) = |t|^2 \sin(\alpha_t)$. Typical values of δ, β and α_c can be obtained from Ref. [90].

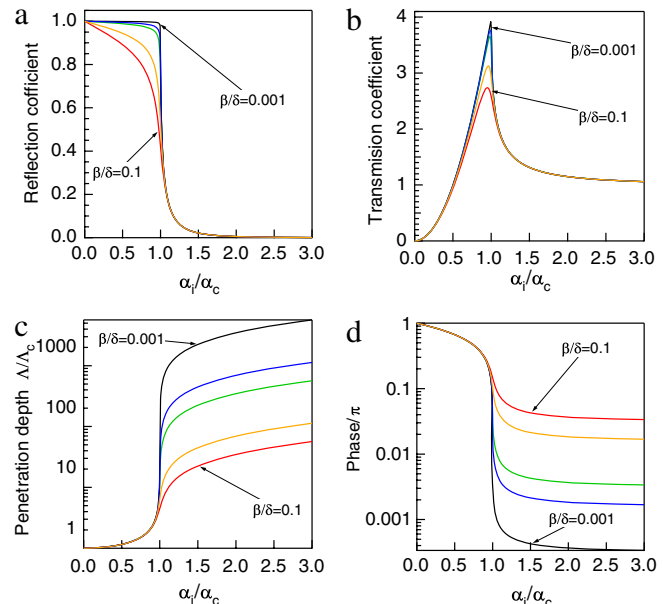


Fig. 25. The Fresnel quantities as function of the incident angle α_i normalized by the critical angle of the substrate $\alpha_c = \sqrt{2\delta}$ for absorption $\beta/\delta = 0.001, 0.005, 0.01, 0.05, 0.1$: (a) the reflection coefficient $R = |r|^2$, (b) the transmission coefficient $T = |t|^2$, (c) the penetration depth normalized to $\Lambda_c = 1/2k_0\alpha_c$, (d) the phase shift at reflection. (Adapted from Ref. [38].)

5.2.7. Reflection and transmission in layered materials: The matrix formalism

It is important to tackle the case of stacking layers with different thicknesses and electronic density not only because X-ray reflectivity turns out to be an invaluable technique [83,47] that provides parameters about these artificial structures but also because the case of graded interfaces (*i.e.* an interface with a index of refraction $n(z)$ that depends continuously on the perpendicular coordinate) can be treated using the same approach upon slicing. The involved matrix formalism is well known in X-ray optics [94,71,95,14,38] as well in electromagnetism where it is known as the Abelés formalism [96]. In the field of X-rays, the problem has been worked out originally by Parratt [97] in a recursive way and by Vidal and Vincent [98] with a matrix formalism.

Let us consider a stacking of N -layers labeled by an index j starting at the vacuum system interface ($j = 0, z = 0$) and ending at the substrate interface ($j = N, z = z_N$) (see Fig. 26).

Each layer located between z_j and z_{j+1} is characterized by its refraction index n_j and its thickness $z_j - z_{j+1}$. The wavefield Ψ_j is made in each layer j of a downward and an upward propagating wave of amplitudes A_j^+ and A_j^- respectively:

$$\Psi_j = [A_j^+ e^{ik_{z,j}z} + A_j^- e^{-ik_{z,j}z}] e^{-ik_x x}. \quad (50)$$

A_0^\pm and A_N^\pm are the amplitudes of the waves inside vacuum and in the substrate. The conservation of the parallel component of the wavevector k_x as well as the law of reflection have been implicitly used in the previous equation. The perpendicular component of the wavevector $k_{z,j}$ in each layer is given by the Snell–Descartes law:

$$k_{z,j} = -\sqrt{n_j^2 k_0^2 - k_x^2}. \quad (51)$$

Using the continuity equations (Eqs. (40)–(41)) at each interface and taking into account the propagation term in each layer, the calculation of all the amplitudes A_j^\pm is handled in terms of matrices

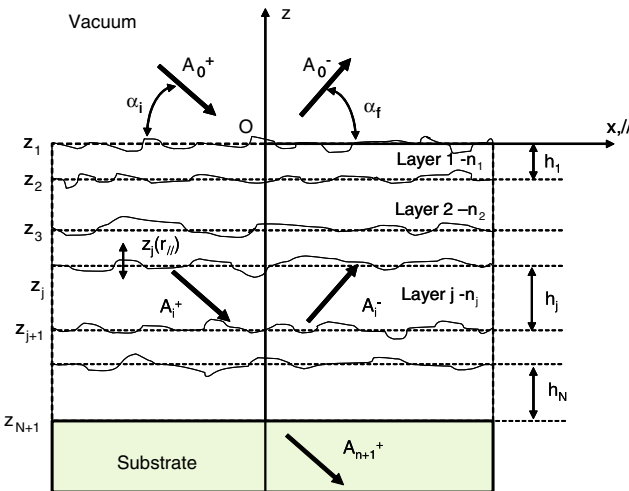


Fig. 26. Layout of the multilayer used in the matrix formalism of propagation. The stacking made of N -layers ends at the substrate surface. In each layer, the wavefield consists in an upwards and a downwards propagating wave of amplitude A_j^- and A_j^+ . The layer roughness $z_j(r_{\parallel})$ gives rise to non specular scattering (see Section 5.4.3).

that relate these quantities between adjacent layers:

$$\begin{bmatrix} A_j^+ \\ A_j^- \end{bmatrix} = \begin{bmatrix} p_{j,j+1} e^{i(k_{z,j+1}-k_{z,j})z_{j+1}} & m_{j,j+1} e^{-i(k_{z,j+1}+k_{z,j})z_{j+1}} \\ m_{j,j+1} e^{i(k_{z,j+1}+k_{z,j})z_{j+1}} & p_{j,j+1} e^{-i(k_{z,j+1}-k_{z,j})z_{j+1}} \end{bmatrix} \times \begin{bmatrix} A_{j+1}^+ \\ A_{j+1}^- \end{bmatrix} \quad (52)$$

where:

$$p_{j,j+1} = \frac{k_{z,j} + k_{z,j+1}}{2k_{z,j}}, \quad m_{j,j+1} = \frac{k_{z,j} - k_{z,j+1}}{2k_{z,j}}. \quad (53)$$

In fact, in the continuous limit, the above matrix formalism gives rise to a set of coupled differential equation for the reflection and transmission coefficients. The system of equation is closed by assuming that the substrate is infinitely thick i.e. there is no upward propagating wave inside the substrate $A_{N+1}^- = 0$. Writing:

$$\begin{bmatrix} A_0^+ \\ A_0^- \end{bmatrix} = \begin{bmatrix} M_{11} & M_{12} \\ M_{21} & M_{22} \end{bmatrix} \begin{bmatrix} A_{N+1}^+ \\ 0 \end{bmatrix}, \quad (54)$$

the stacking reflection coefficient r_s and its transmission coefficient t_s are obtained through:

$$r_s = \frac{A_0^+}{A_0^-} = \frac{M_{12}}{M_{22}}; \quad t_s = \frac{A_{N+1}^+}{A_0^-} = \frac{1}{M_{22}}. \quad (55)$$

This result is at the heart of all algorithms to fit reflectivity curves of layered materials. The best illustration is given by the propagation inside an homogeneous slab of thickness h on an infinite substrate:

$$r_s = \frac{r_{0,1} + r_{1,2} e^{2ik_{z,1}h}}{1 + r_{0,1} r_{1,2} e^{2ik_{z,1}h}}; \quad t_s = \frac{t_{0,1} t_{1,2} e^{ik_{z,1}h}}{1 + r_{0,1} r_{1,2} e^{2ik_{z,1}h}}, \quad (56)$$

where the reflection r_{ij} and transmission t_{ij} coefficients at each interface i, j read:

$$r_{ij} = \frac{k_{z,i} - k_{z,j}}{k_{z,i} + k_{z,j}}; \quad t_{ij} = \frac{2k_{z,i}}{k_{z,i} + k_{z,j}}. \quad (57)$$

Eq. (56) can be found from a Fabry–Perot like reasoning. In passing, the phase factor $e^{2ik_{z,1}h}$ is nothing else than the path difference between two reflected beams. The reflectivity curve displays oscillations known as the Kiessig fringes [49] due to the alternative in phase and out of phase interferences between waves reflected at the top and at the bottom of the film. Their spacing given by $2\pi/h$ in reciprocal wavevector is a direct measure of the film thickness.

5.2.8. Influence of roughness on the Fresnel coefficients: Nérot–Croce and Debye–Waller-like corrections

The roughness of the interfaces diminishes the reflection coefficient as a part of the intensity is scattered out of the specular direction. This long-standing question of scattering by rough surfaces [99] was first tackled for X-rays by Croce and Nérot [100,101] in an elegant way leading to a self consistent equation for the reflection coefficient of one interface. The reflection coefficient of a flat surface decreases at high wavevector transfer through a coefficient known as the Nérot–Croce factor. Later on, Vidal and Vincent [98] generalized this approach to multilayers.

Let us assume that the vertical position $Z_{j+1} + z_{j+1}(r_{\parallel})$ of the interface between layer j and $j + 1$ fluctuates by $z_{j+1}(r_{\parallel})$ rapidly at a length scale ξ_{\parallel} smaller than the projected coherence length L_{coh} of the X-ray beam (see Section 5.3.3 for definition). In other words, the expansion along upward and downward propagating waves is still valid but the phase relationships between two layers is only true on average (see Fig. 27a). In terms of transition matrix between layers (Eq. (52)), this is equivalent to take the average of the exponential phase terms over the fluctuating quantity $z_j(r_{\parallel})$. At the lowest order in $\langle z_{j+1}(r_{\parallel}) \rangle$ (which corresponds in passing to the range of validity of such an approximation), it is found that:

$$p_{j,j+1} = \frac{k_{z,j} + k_{z,j+1}}{2k_{z,j}} e^{-i(k_{z,j}+k_{z,j+1})\langle z_{j+1}(r_{\parallel}) \rangle}, \quad (58)$$

$$m_{j,j+1} = \frac{k_{z,j} - k_{z,j+1}}{2k_{z,j}} e^{-i(k_{z,j}-k_{z,j+1})\langle z_{j+1}(r_{\parallel}) \rangle}. \quad (59)$$

This leads to a decrease of the reflection and transmission coefficients by the well known Nérot–Croce factor [100,101,44,14]:

$$r_{j,j+1} = r_{j,j+1}^0 e^{-2k_{z,j}k_{z,j+1}\langle z_{j+1}^2(r_{\parallel}) \rangle}, \quad (60)$$

$$t_{j,j+1} = t_{j,j+1}^0 e^{(k_{z,j}-k_{z,j+1})\langle z_{j+1}^2(r_{\parallel}) \rangle/2}. \quad (61)$$

If absorption is neglected, there is no influence of roughness on the reflectivity in the angular range below the critical angle as $k_{z,j}$ becomes purely imaginary. Well above the critical angle of the layers, refraction starts to be negligible i.e. $k_{z,j} \simeq k_{z,j+1} \simeq q_z/2$ leading to a well known Debye–Waller like attenuation factor $e^{-2k_{z,j}^2\langle z_{j+1}^2(r_{\parallel}) \rangle}$ in the Born approximation. This latter can be obtained when the tangent plane approximation or Rayleigh approximation [103,99,104] holds (see Fig. 27b). Indeed, when $\xi_{\parallel} k_{z,j}^2/k_0 \gg 1$ (see Section 5.4.6), the field is assumed to be reflected at different heights along the surface leading to a precise phase relationship between the incident and reflected beams.

Justifications of the Nérot–Croce factor as well as its range of validity have been discussed on the basis of DWBA by Stearns [105], Pynn [106], Sears [107], de Boer [102,108–110] and Caticha [111]. However, an accurate description of the transition between both regimes implies to go beyond the DWBA of first order and to account for the in-plane structure of the roughness in the calculation of the reflection coefficient. A beginning of answer that interpolates between Nérot–Croce and Debye–Waller-like factors was proposed in Refs. [102,108–110].

5.2.9. Kinematic approximation of reflectivity and beyond

There is no need to stress the usefulness of the X-ray reflectivity technique in both fundamental and applied studies of surface and interfaces [83,47]. Even though the matrix formalism describes exactly all the dynamical effects of the reflection at a graded interface, an analytical expression with a more intuitive interpretation is obtained in the kinematic or single scattering approximation [94,38,14,48,83,47]. The range of validity is well

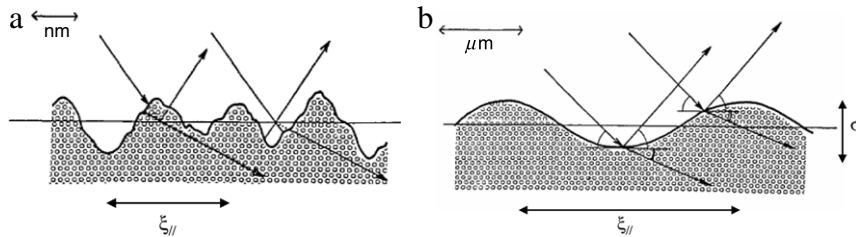


Fig. 27. The frameworks used to describe scattering from a rough surface as function of the in-plane correlation ξ_{\parallel} i.e. the typical spatial frequency of the roughness profile. (a) $\xi_{\parallel} k_z^2/k_0 \ll 1$. In DWBA, the roughness is treated as a perturbation of the reflection-refraction on the average interface. (b) $\xi_{\parallel} k_z^2/k_0 \gg 1$. In the Rayleigh approach, the local slope of the surface is sufficiently small to treat locally at each point of the surface the reflection-refraction of the wave. From Ref. [102].

above the critical angle $\alpha_i \gg \alpha_c$. The reflection coefficient is derived by neglecting (i) multiple reflections at interfaces and (ii) the effects of refraction on the propagation direction (see Fig. 28). For N -layers on a substrate (see Fig. 26), only the interference between reflected waves at each interface buried at a depth z_j is accounted for:

$$r_{KA} = \sum_{j=0}^N r_{j,j+1} e^{iq_z z_j} \quad (62)$$

$q_z = 2k_{0,z}$ is the perpendicular wavevector transfer independent of the depth according to the kinematic hypothesis. $r_{j,j+1}$ can be further simplified neglecting refraction in the denominator $k_{z,j} \simeq k_{z,j+1} = q_z/2$:

$$r_{j,j+1} = \frac{k_{z,j} - k_{z,j+1}}{k_{z,j} + k_{z,j+1}} = \frac{k_{z,j}^2 - k_{z,j+1}^2}{(k_{z,j} + k_{z,j+1})^2} \simeq k_0^2 \frac{n_j^2 - n_{j+1}^2}{q_z^2}. \quad (63)$$

By taking the infinitesimal limit for the layer thicknesses, the kinematic reflection coefficient reads:

$$r_{KA} = -\frac{k_0^2}{q_z^2} \int_{-\infty}^{+\infty} \frac{dn^2(z)}{dz} e^{iq_z z} dz. \quad (64)$$

Keeping in mind that $dn^2(z)/dz = d\delta(z)/dz = 4\pi r_e/k_0^2 d\rho_e(z)/dz$ (see Eq. (22)), the kinematic reflectivity can be recast as the Fourier transform of the derivative of the electronic density profile and compared to the Fresnel reflectivity $R_S(q_z)$ of the substrate with electronic density $\rho_{e,S}$:

$$R_{KA} = |r_{KA}|^2 = R_S(q_z) \left| \frac{1}{\rho_{e,S}} \int_{-\infty}^{+\infty} \frac{d\rho_e(z)}{dz} e^{iq_z z} dz \right|^2 \quad (65)$$

$$R_S(q_z) = \frac{(4\pi r_e \rho_{e,S})^2}{q_z^4} = \left(\frac{q_{c,s}}{2q_z} \right)^2. \quad (66)$$

The main conclusion is that only the variations of dielectric constant induce X-ray reflection. A similar result is achieved by applying the Born approximation as it will be shown later on in Section 5.4.1. To link Eq. (66) with the results of Sections 5.2.8 and 5.4.2 about scattering from a rough surface, it is worth considering the well known error function for the interface profile $z(\mathbf{r}_{\parallel})$. Its derivative is nothing other than a Gaussian function with $\sigma_z = \sqrt{\langle z(\mathbf{r}_{\parallel})^2 \rangle}$:

$$\frac{1}{\rho_{e,S}} \frac{d\rho_e(z)}{dz} = \frac{1}{\sigma_z \sqrt{2\pi}} e^{-z(\mathbf{r}_{\parallel})^2/2\sigma_z^2} \quad (67)$$

$$R_{KA} = R_S(q_z) e^{-q_z^2 \sigma_z^2}. \quad (68)$$

The previously introduced Debye–Waller-like factor is recovered. However, Feranchuk et al. [112] stressed that the natural limitation of the roughness amplitude leads to a breakdown of the exponential behavior and a change of the asymptotic behavior of

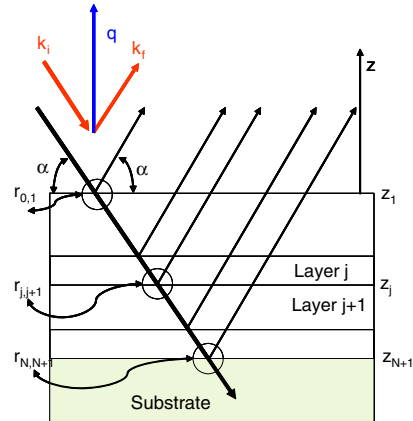


Fig. 28. The kinematic reflectivity of a layered interface is obtained by summing the reflection of the undeviated beam from each interface. A Fabry–Pérot phase $e^{iq_z z_j}$ due to propagation arises between each beam and the top reflected one.

the reflection coefficient at large incidence angles from a Gaussian to a power law.

For complex interface profiles, the fit is usually based on the exact matrix formalism of reflectivity to recover the interface electronic density from reflectivity measurements; however, such an approach may be hampered by multiple solutions and local minima. Some knowledge about the studied system is needed to overcome analysis uncertainties. Although relying on an approximation, the Born result (Eq. (66)) allows to have a better insight into the data inversion scheme by linking directly the electronic density profile and the reflectivity. In the inversion procedure of the density profile $n^2(z)$, the main drawback is of course the loss of phase. Various approaches have been developed to bypass the problem using several measurements across an absorption edge [113] like the heavy atoms method in crystallography or relying on physical constraints on the density profile [114,115]. Other approximations have been developed to handle the non-linear relationship between the reflectivity and the interface profile; the widest discussion of approximate methods has been given by Lekner [94,116]. Among others, can be quoted: the Distorted Wave Born Approximation (DWBA) [107,111,117] (see Section 5.4.1), the Kinematic Form Factor Approximation [118], the Small Curvature Approximation (SCA) [119], the Wentzel–Kramers–Brillouin Approximation (MWKB) [94,116,120], the Weighted Superposition Approximation (WSA) [121]. Their respective interests/drawbacks and links have been reviewed by Zhou in Refs. [117,84]. Recently, Feranchuk and coworkers [122,123] proposed a self consistent calculation of the Fresnel coefficients establishing an analytical though non-linear link with the graded interface profile through a suitable ansatz. The accuracy and convergence of the method was tested successfully against several profiles. In fact, the only case that can be handled analytically is the Epstein or tangent hyperbolic profile $\rho_e = \rho_0/(1 + e^{-2z/\sigma_z})$ [124,94,125–127,111,122]; therefore, it is a test bed for all these theories.

5.3. The differential X-ray scattering cross section in Distorted Wave Born Approximation

5.3.1. Introduction and historical overview

The theoretical treatment of scattering of a wave by rough surfaces or interfaces is a long standing question that can be traced back to the early work of Lord Rayleigh [103] on sound waves. For electromagnetic waves, most of the works were devoted to visible and radar waves for which the interaction with matter is strong and the multiple scattering effects are large. Several books across time summarized the developed approximations [99,128–130]. For these wavelength ranges, the tough problem is to find approximate solutions of the Maxwell equations accounting for the vectorial nature of the field which matches the boundary condition on a rough surface. For X-rays, the situation is somehow simpler as the interaction is weaker (see Section 5.2.2). For bulk scattering, under the assumption of the kinematic or Born approximation [14, 38] i.e. for coherent domains smaller than the extinction length $L_e = \lambda/2\pi|n - 1|$, multiple scattering can be neglected. The incident beam intensity is assumed to be unaffected by scattering. The incident beam actually polarizes the electronic clouds of atoms which re-emit spherical waves that no longer interact with the medium. The scattering cross-section is proportional to the square modulus of the Fourier transform of the electronic density or dielectric constant. However, such a picture is unable to describe the phenomena of reflection-refraction of X-rays at interfaces [38]. These are in fact by nature “dynamical”. For shallow incident angles, in particular below the critical angle, the reflected amplitude is close to one. This highlights the breakdown of the Born approximation already shown in Section 5.2.9. The dynamical theory of X-rays overcomes this deficiency at the expense of a light and easy treatment of the problem at hand [15]. To go beyond Born approximation while including reflection and transmission at interfaces and roughness scattering, pure dynamical calculations have gained by a lighter and versatile theory: the distorted wave Born approximation (DWBA). In DWBA, the roughness is viewed as a perturbation of a known reference state, most of the time taken as the Fresnel wavefield for flat interfaces (see Section 5.2.6). To first order in the Born expansion, the field that actually polarizes the dielectric contrast is taken as this eigenfield and the total scattered amplitude in the far field region (as measured experimentally) is the sum of spherical waves emitted by each point. DWBA can be thought as a semi-dynamical treatment where the multiple scattering due to interface boundaries is included in the reference state while the roughness leads to a single scattering event between reference states.

Actually, DWBA was originally developed in the framework of scattering theory in quantum mechanics [131,132]. In nuclear physics, collision cross-section between a probe particle and a target is one of the tools to get information about the interaction potential between elementary particles. Among standard textbooks, a full chapter of Schiff book [91] is devoted to the collision theory and gives a full account of the formal treatment of the scattering cross-section within DWBA. The analogy between the Schrödinger equation and the propagation equation of X-rays underlined in Section 5.2.3 is not restricted to stratified media in specular geometry. Indeed, it will be shown later on in Section 5.3.6 that, when the scattering angles are small, the vectorial propagation equation of the X-ray field can be reduced to a Helmholtz one as the polarization effects are negligible. This analogy is at the heart of the close similarity between DWBA and the formal treatment of elastic or inelastic scattering from surfaces of other particles: electrons [133, 134], neutrons [135,43], He atoms [136].

Despite some works on visible electromagnetic radiation scattering by rough surfaces [137,138], the actual application of DWBA to X-rays started with the work of Vineyard [139]; he revived the

DWBA in the context of the first grazing incidence X-ray diffraction experiments of Marra, Eisenberger and Cho [9,10] (see the review Ref. [12] for surface diffraction). Vineyard envisaged only the diffraction by crystal lattice planes of “the distorted wave” i.e. the transmitted wave at angles below the critical angle for total external reflection. A similar approach was followed by Mohanty and Rice [140] in the framework of diffuse scattering from a liquid vapor interface. Following the work on inelastic neutron scattering by magnet surfaces by Mazur and Mills [135], Dietrich and Wagner [141,93] generalized the result of Vineyard by including in the formula also the exit scattering angle α_f ; their idea was to demonstrate that under conditions of total external reflection of the incident or the scattered wave, diffraction from the restricted scattering depth would allow to probe critical phenomena at surfaces. Later on, in their seminal paper, Sinha and coworkers [35] tackled the topic of scattering by a rough surface at glancing angles using the quantum mechanics formalism of T -matrix [142, 91]. Coherent and incoherent scattering cross-section were linked in BA and DWBA (see Section 5.4.2) to the height-height correlation function. A clear explanation of the Yoneda wing or anomalous surface reflection [39,143,144] was brought on the basis of reciprocity principle through transmission prefactors in incidence as well as in emergence angles [141,35]. A somehow analog treatment of scattering by rough surfaces and multilayers was developed also by Andreev et al. [125]. Experimental confirmation for self-affine surfaces were given such as polished pyrex glass [35] and polycrystalline aluminum surfaces [145]. Pynn [106], Steyerl and coworkers [126] and Wu [146] in the context of neutron scattering as well as de Boer [102] confirmed those theoretical results, even going to second order in the perturbation expansion [147,102,108]. Daillant and Bélorgey [148,149] obtained similar results starting from the reciprocity theorem and using Green functions. Sears [107] and Caticha [111] focused their attention on the role of roughnesses on reflectivity calculation in DWBA (Section 5.4.1). Zhou (Refs. [84, 117] and references therein) tested DWBA accuracy against various other approximations which link reflectivity and interface profile. Crowley [118] developed a somehow modified DWBA description of the reflectivity of a given profile by singling out the discontinuity of the reflection coefficient at the critical angle in the perturbation expansion. The case of multilayers was treated by several authors (Section 5.4.3): Daillant and Bélorgey [148], Holý and coworker [58,59] and de Boer [109]. De Boer also carefully analyzed the range of validity of DWBA [108] (Section 5.4.6) and also the absorption of the waves in the context of grazing incidence X-ray fluorescence [147,109]. DWBA was extended to encompass magnetic scattering by Lee and coworkers [88,89] (Section 5.4.5). The similarity and discrepancy in terms of cross section for scattering from density fluctuations (Section 5.4.4) were highlighted by Rauscher et al. [36] in the context of small angle scattering from surfaces. The generalization to an isolated object form factor including reflection and transmission of waves at interfaces (Section 6) was obtained for buried nanoparticles [36,62], supported nanoparticles [37], a layer with holes [150,151] or embedded clusters or pores [152–154]. For dense collection of nanoparticles, Lazzari et al. [155,81] suggested to include in the particle form factor the particle coverage i.e. the actual profile of dielectric constant (Section 6.5).

5.3.2. The integral solution of the wave propagation and the Green function

Later on in this report, we have chosen to use the Green function formalism applied to electromagnetic waves instead of the fully equivalent but more used T -matrix approach [142,91].

The integral solution of the wave propagation equation. As for X-rays the dielectric constant differs from unity by only 1 part in $\sim 10^6$, the propagation equation (Eq. (16)) reduces to:

$$[\nabla^2 + n^2(\mathbf{r})k_0^2] \mathbf{E}(\mathbf{r}) = 0. \quad (69)$$

To work out a perturbation formalism, the dielectric constant $\epsilon(\mathbf{r}) = n^2(\mathbf{r})$ of the medium is split in two parts:

$$n^2(\mathbf{r}) = n_0^2(\mathbf{r}) + \delta n^2(\mathbf{r}), \quad (70)$$

where $n_0(\mathbf{r})$ is the index of refraction of a reference medium. In principle, the corresponding electromagnetic wavefield can be calculated easily. For a homogenous and in-plane invariant system, the value $n_0(z)$ averaged over the coherence length of the X-ray beam along the x - y directions is chosen since the wavefield is the analytical Fresnel one (see Sections 5.2.6–5.2.7). Obviously, the choice of the reference medium should minimize the contribution of the perturbation $\delta n^2(\mathbf{r})$ i.e. be as similar as possible to the actual system.

Eq. (69) can be rewritten as:

$$[\nabla^2 + n_0^2(\mathbf{r})k_0^2] \mathbf{E}(\mathbf{r}) = \delta n^2(\mathbf{r})k_0^2 \mathbf{E}. \quad (71)$$

Such an equation can be understood as the radiation of a fictitious dipole $\delta n^2(\mathbf{r})k_0^2 \mathbf{E}$ radiating in the reference medium. Owing to the linearity of the propagation equation, the total electric field \mathbf{E} is the sum of the reference field $\mathbf{E}_0(\mathbf{r})$, solution of the equation without right-hand side term, and the perturbation field $\delta \mathbf{E}(\mathbf{r})$ due to the fictitious dipole source.

$\delta \mathbf{E}(\mathbf{r})$ is inferred with the help of the Green tensor $\mathbf{G}(\mathbf{r}, \mathbf{r}')$ solution of the propagation equation with a point dipole source located at $\mathbf{r} = \mathbf{r}'$:

$$[\nabla^2 + n_0^2(\mathbf{r})k_0^2] \mathbf{G}(\mathbf{r}, \mathbf{r}') = \frac{k_0^2}{\epsilon_0} \delta(\mathbf{r} - \mathbf{r}'). \quad (72)$$

$\mathbf{G}(\mathbf{r}, \mathbf{r}')$ corresponds to an out-going wave. Eq. (71) can be recasted in an integral form, which is the starting point of the perturbation formalism:

$$\mathbf{E}(\mathbf{r}) = \mathbf{E}_0(\mathbf{r}) + \delta \mathbf{E}(\mathbf{r}) = \mathbf{E}_0(\mathbf{r}) + \epsilon_0 \int d\mathbf{r}' \mathbf{G}(\mathbf{r}, \mathbf{r}') \delta n^2(\mathbf{r}') \mathbf{E}(\mathbf{r}'). \quad (73)$$

To go on with the integral solution of the wave propagation (Eq. (73)), the Green function has to be obtained according to the chosen reference medium in the far field regime i.e. at an observer distance well above L_{coh}^2/λ , L_{coh} being the coherent domain size induced by the beam and the detector acceptance [14].

The integral solution of the wave propagation equation (73) can be inferred from the reciprocity theorem of light propagation (see review Ref. [156]). It states that if the two polarization fields $\mathcal{P}_0, \mathcal{P}_1$ induce the electric fields $\mathcal{E}_0, \mathcal{E}_1$ then,

$$\int d^3 \mathbf{r}' \mathcal{E}_0 \cdot \mathcal{P}_1 = \int d^3 \mathbf{r}' \mathcal{E}_1 \cdot \mathcal{P}_0. \quad (74)$$

The principle refers to the exchange of the source and field points. In the case of electromagnetic waves, the demonstration based on the Maxwell equations [86,87,14] relies only on the linearity of the media and the symmetry of dielectric tensors and not, as often assumed on the time-reversal invariance. It applies therefore to absorbing media. Eq. (73) is recovered if:

$$\mathcal{E}_0 = \delta \mathbf{E}(\mathbf{r}'), \quad \mathcal{P}_0 = \epsilon_0 \delta n^2(\mathbf{r}') \mathbf{E}(\mathbf{r}') \quad (75)$$

$$\mathcal{E}_1 = \mathbf{G}(\mathbf{r}, \mathbf{r}'), \quad \mathcal{P}_1 = \delta(\mathbf{r}' - \mathbf{r}) \mathbf{u}, \quad (76)$$

where \mathbf{u} is the direction of the dipole at \mathcal{P}_0 . The Green function $\mathbf{G}(\mathbf{r}, \mathbf{r}')$ appears as the field radiated by a point dipole placed at the detector position.

Dallant and Bélorgey [148] used the reciprocity principle as a starting point to demonstrate the similarity with the DWBA approach. However, its practical use needs the calculation of fields both in the near field and far field regimes leading to the account of emission and propagation of spherical waves in complex geometries. To overcome this problem, Caticha [157] developed an asymptotic form of the reciprocity theorem so that the relevant exchange involves a source point in the medium and a field at infinity. The tedious cases of specular reflection of polarized X-rays by rough surfaces and graded interface is easily handled; a key result is that within Nérot–Croce type approximations, the reflectivity is not affected by the polarization.

The Green function in vacuum. As found in standard textbooks on electrodynamics [86,87,95], the Green function in vacuum which corresponds to the electric field created by a dipole moment $\mathbf{p}(\mathbf{r}')$ located at \mathbf{r}' in vacuum (or in an homogeneous infinite medium) is given by an outgoing spherical wave:

$$\mathbf{G}(\mathbf{r}, \mathbf{r}') = k_0^2 [\mathbf{u} \times \mathbf{p}(\mathbf{r}')] \times \mathbf{p}(\mathbf{r}') \frac{e^{-ik_0|\mathbf{r}-\mathbf{r}'|}}{4\pi\epsilon_0 |\mathbf{r}-\mathbf{r}'|}. \quad (77)$$

\times is the vector product and \mathbf{u} is the unit vector along the direction $\mathbf{r} - \mathbf{r}'$ of observation or scattering. In the far field $r \gg r'$, $\mathbf{u} \simeq \mathbf{r}/r$ and

$$|\mathbf{r} - \mathbf{r}'| = |r\mathbf{u} - \mathbf{r}'| \simeq r - \mathbf{u} \cdot \mathbf{r}' \simeq r - \mathbf{k}_f \cdot \mathbf{r}'/k_0. \quad (78)$$

\mathbf{k}_f is the exit scattering wavevector, oriented along \mathbf{u} or \mathbf{r} . Thus the far field expansion leads to replace the dipole spherical wave by its tangent plane:

$$\mathbf{G}(\mathbf{r}, \mathbf{r}') = k_0^2 \frac{e^{-ik_0 r}}{4\pi\epsilon_0 r} e^{i\mathbf{k}_f \cdot \mathbf{r}'} \{\mathbf{p}(\mathbf{r}') - [\mathbf{p}(\mathbf{r}') \cdot \mathbf{u}] \mathbf{u}\}. \quad (79)$$

Only the component of the dipole \mathbf{p} perpendicular to the direction of observation \mathbf{u} has to be taken into account in the dipolar radiation. For a dipole normal to the scattering direction \mathbf{u} i.e. for a s or p polarization $\mathbf{e}_f^{s,p}$ (see Section 5.2.3), Eq. (78) yields:

$$\mathbf{G}(\mathbf{r}, \mathbf{r}') = k_0^2 \frac{e^{-ik_0 r}}{4\pi\epsilon_0 r} e^{i\mathbf{k}_f \cdot \mathbf{r}'} p \mathbf{e}_f^{s,p}. \quad (80)$$

The Green function for stratified media. For a planar stratified medium, Eq. (80) can be readily generalized as found in Refs. [142, 91, 158]. In the far field regime along the \mathbf{k}_f direction and for the two main states of polarization, a similar plane wave expansion of the Green function is obtained:

$$\mathbf{G}(\mathbf{r}, \mathbf{r}') = k_0^2 \frac{e^{-ik_0 r}}{4\pi\epsilon_0 r} E_0(\mathbf{r}', -\mathbf{k}_f) p \mathbf{e}^{s,p}, \quad (81)$$

where $E_0(\mathbf{r}', -\mathbf{k}_f)$ is the Fresnel solution of the wave propagation in the stratified media for an incoming $-\mathbf{k}_f$ incident wave. $E_0(\mathbf{r}', -\mathbf{k}_f)$ can be obtained through the standard method of matrix formalism in layered material. The interested reader can find a demonstration of Eq. (81) for a scalar field considering the Schrödinger equation in Ref. [91], Chap XIX.

The Born expansion. The integral solution of the wave propagation Eq. (73) is obviously self-consistent as the kernel of the integral acts on the electric field itself. After injecting Eq. (73) in itself, the essence of the Born expansion is to write it in terms of a power series of $\epsilon_0 \mathbf{G}(\mathbf{r}, \mathbf{r}') \delta n^2(\mathbf{r}')$:

$$\mathbf{E}(\mathbf{r}) = \mathbf{E}_0(\mathbf{r}) + \epsilon_0 \int d\mathbf{r}' \mathbf{G}(\mathbf{r}, \mathbf{r}') \delta n^2(\mathbf{r}') \mathbf{E}_0(\mathbf{r}') \quad (82)$$

$$+ \epsilon_0^2 \int d\mathbf{r}' \int d\mathbf{r}'' \mathbf{G}(\mathbf{r}, \mathbf{r}') \delta n^2(\mathbf{r}') \mathbf{G}(\mathbf{r}', \mathbf{r}'') \delta n^2(\mathbf{r}'') \mathbf{E}_0(\mathbf{r}'') \\ + \dots \quad (83)$$

Evaluating the convergence speed of such a series is not a trivial issue. For the first term of the expansion, the operator $\mathbf{G}(\mathbf{r}, \mathbf{r}')\delta n^2(\mathbf{r}')$ acts on the electric field $\mathbf{E}_0(\mathbf{r}')$ located at \mathbf{r}' to generate the reradiated field at \mathbf{r} . This can be understood as a simple scattering event of the incident field. When the operator comes into play twice, the corresponding term accounts for a double scattering event and so on. In the Born approximation of first order [142,91], the expansion (Eq. (83)) is restricted to the first term. This means that the medium is assumed to be polarized only by the incident field; therefore this latter is assumed to be undamped by the scattering. In passing, the Born approximation does not fulfill the requirement of energy conservation as checked from the optical theorem [86,87,95,14]. Indeed, to be consistent with the determination of the radiated power, one should expand the amplitude of the field to second order.

5.3.3. The scattering cross sections

Definition of the scattering cross-section. The integral solution of the propagation equation (Eq. (73)) allowed to isolate the amplitude of the scattered field $\mathbf{E}_f(\mathbf{r}) = \delta\mathbf{E}(\mathbf{r})$ i.e. the field radiated by the dipole $\epsilon_0\delta n^2(\mathbf{r}')\mathbf{E}(\mathbf{r}')$ induced in the sample by the incoming beam $\mathbf{E}_0(\mathbf{r})$. During an experiment, the measured quantity as function of the scattering angles is the differential scattering cross-section. This is the radiated power $d\sigma$ along a given direction \mathbf{r} far away from the sample in a given solid angle $d\Omega$ per incident energy E_0^2 . The relevant quantity is thus the flux of the Poynting vector $\mathbf{S}_f = \mathbf{B}_f \times \mathbf{E}_f/\mu_0$ through a surface $dS = d\Omega/r^2$.

For a Green function in vacuum equation (80), the scattered field reads:

$$\mathbf{E}_f(\mathbf{r}) = \frac{k_0^2 e^{-ik_0 r}}{4\pi} \int d\mathbf{r}' \delta n^2(\mathbf{r}') \mathbf{E}(\mathbf{r}') \cdot \mathbf{e}^{s.p} e^{ik_f \cdot \mathbf{r}'} \quad (84)$$

A similar results is obtained with the Green function of a stratified medium upon replacing the plane wave $e^{ik_f \cdot \mathbf{r}'}$ by the corresponding Fresnel wavefield $\mathbf{E}_0(\mathbf{r}', -\mathbf{k}_f)$. For a dipole far away from the source, the emitted spherical wave can locally be assumed as a monochromatic plane wave linearly polarized with a polarization normal to \mathbf{r} . Since the magnetic induction $\mathbf{B}_f(\mathbf{r})$ is orthogonal to the electric field $\mathbf{E}_f(\mathbf{r})$ with $E_f = cB_f$ as shown from the Maxwell equation (Eq. (9)), the Poynting vector reads:

$$\mathbf{S}_f = \frac{1}{2\mu_0 c} |\mathbf{E}_f(\mathbf{r})|^2 \mathbf{u}. \quad (85)$$

For an outgoing spherical wave, the flux of energy is indeed directed along the direction of observation. Therefore, the differential scattering cross section along \mathbf{k}_f or \mathbf{u} directions follows directly from the definition:

$$\frac{d\sigma}{d\Omega} = \frac{k_0^2}{16\pi^2 E_0^2} \left| \int d\mathbf{r}' \delta n^2(\mathbf{r}') \mathbf{E}(\mathbf{r}') \cdot \mathbf{e}^{s.p} e^{ik_f \cdot \mathbf{r}'} \right|^2. \quad (86)$$

Of course, for a stratified medium, the plane wave $e^{ik_f \cdot \mathbf{r}'}$ should be replaced by the Fresnel wavefield $\mathbf{E}_0(\mathbf{r}', -\mathbf{k}_f)$. Approximations about the electric field $\mathbf{E}(\mathbf{r}')$ that actually polarizes the medium are needed to go on.

Link between coherence length and coherent and incoherent scattering cross-sections. If a well-collimated X-ray beam impinges at glancing angle on a rough sample, coherent scattering gives rise to a specularly reflected beam and a single refracted-transmitted beam, whereas incoherent scattering causes diffusely reflected and transmitted radiations. A beginning of an answer about the influence of roughness on Fresnel coefficients was given in Section 5.2.8. Concerning the actually measured intensity, the question that arises now is twofold:

- (i) how to relate the scattered intensity to the statistical description of the sample although the sample morphology (roughnesses, fluctuations of density etc...) is by itself deterministic?
- (ii) how to take into account the experimental imperfections, in particular the finite angular and wavelength spreads of the incident beam and the angular aperture of the detector?

Up to now in the theoretical treatment of scattering, the incident and scattered beams are supposed to be perfectly collimated as they are treated as plane waves or Fresnel fields. In the case of a perfect point like detector and perfect incident beam, the whole sample of size L scatters coherently; the pattern recorded as function of scattering angles involves spiky behavior, the so-called “speckle”, with typical frequencies given by the inverse of the beam footprint on the sample. However, the experimental imperfections, in particular the wavelength spread $\Delta\lambda$, the beam divergences in-plane $\Delta\alpha_i$ and out-of-plane $\Delta 2\theta_i$ and the finite detector acceptance $\Delta\alpha_f$, $\Delta 2\theta_f$, make necessary the introduction of coherence length L_{coh} at the sample surface (see Fig. 29). Above this distance, the field emitted by two dipoles at the surface are no longer phase matched and interfere no more coherently in the far field (detector). Therefore, the collected intensity over the solid angle $\Delta\Omega = \Delta\alpha_f \Delta 2\theta_f$ is given apparently by an incoherent sum of intensity scattered by domains of size L_{coh} . The speckle behavior is replaced by a continuous average intensity if the illuminated area A_i or beam footprint contains a large number of coherent domains. The smearing of the speckles can be understood as the folding of the scattering with the instrumental resolution function [43,14]. Two major lengths define the volume of coherence of the incident beam [38]: the transverse coherence lengths $L_{T,\alpha_i} = \lambda/2\Delta\alpha_i$, $L_{T,2\theta_i} = \lambda/2\Delta 2\theta_i$ and the longitudinal one $L_L = \lambda^2/2\Delta\lambda$. Due to the grazing geometry, a projection effect increases L_{T,α_i} by a factor $1/\sin(\alpha_i)$. The detector spread gives rise to similar length definitions L_{T,α_f} , $L_{T,2\theta_f}$. Another important assumption is that the coherent domains are sufficiently large so that all domains have exactly the same statistical properties, provided that the sample is spatially homogeneous. To sum up, if the following inequalities are fulfilled $L \geq \sqrt{A_i} \gg L_{coh} \gg \xi_{\parallel}$ for a surface characterized by an in-plane correlation length ξ_{\parallel} , the scattering cross-section can be obtained by an ensemble average along the surface of the right-hand side of Eq. (86); the random roughness is thus called ergodic if the scattered intensity from one deterministic sample accounting for the measurement imperfections is equivalent to an average over many samples. Hereafter, this hypothesis is assumed to be fulfilled for GISAXS measurements. Indeed, the standard figures on a synchrotron beamline are:

- $\lambda/\Delta\lambda \sim 10^4$, $L_L \sim 0.5 \mu\text{m}$,
- $\Delta\alpha_i \sim 0.5 \text{ mrad}$, $L_{T,\alpha_i} \sim 0.1 \mu\text{m}$, $L_{T,\alpha_i}/\sin(\alpha_i) \sim 30 \mu\text{m}$
- $\Delta 2\theta_i \sim 0.1 \text{ mrad}$, $L_{T,2\theta_i} \sim 0.5 \mu\text{m}$
- $\Delta\alpha_f \sim \Delta 2\theta_f \sim 5 \text{ to } 10^{-5} \text{ mrad}$, $L_{T,\alpha_f} \sim L_{T,2\alpha_f} \sim 1 \mu\text{m}$
- $A_i \sim 300 \times 1000 \mu\text{m}^2$

for $\lambda \sim 0.1 \text{ nm}$, $\alpha_i \sim 0.2^\circ$ a 2D CCD detector pixel size of $50 \mu\text{m}$ and a sample-detector distance of 1 m. As a consequence, ξ_{\parallel} should be smaller than a few hundreds of nm.

A more rigorous treatment of the interplay between coherence and instrumental resolution function relies on the notion of mutual coherence function; the interested reader can refer to Refs. [159–162] and references therein. This theoretical problem was renewed during the last decade with the advent of scattering experiments with highly coherent beams (see Section 6.2.9).

The Born approximation of first order (see next section Section 5.3.4) leads to a cross-section that depends on the dielectric

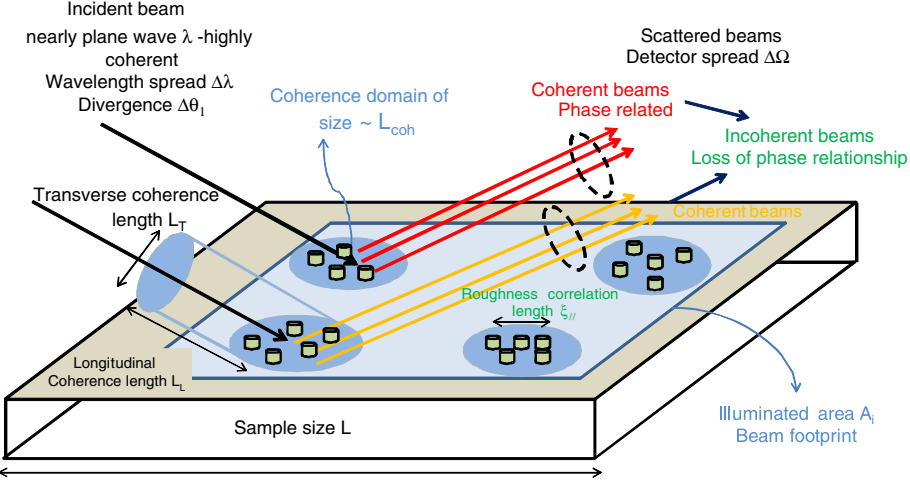


Fig. 29. Sketch of the interplay between coherence domains, statistical properties of the sample roughness and diffuse scattering.

contrast $\delta n^2(\mathbf{r})$. While taking the ensemble average, the average value $\langle \delta n^2(\mathbf{r}) \rangle$ in the integral equation (86) can be isolated:

$$\langle |\delta n^2(\mathbf{r})|^2 \rangle = |\langle \delta n^2(\mathbf{r}) \rangle|^2 + \langle |\Delta \delta n^2(\mathbf{r})|^2 \rangle \quad (87)$$

with $\delta n^2(\mathbf{r}) = \langle \delta n^2(\mathbf{r}) \rangle + \Delta \delta n^2(\mathbf{r})$. Two contributions appear in the total cross-section:

$$\begin{aligned} \left(\frac{d\sigma}{d\Omega} \right)_{tot} &= \left(\frac{d\sigma}{d\Omega} \right)_{coh} \left(|\langle \delta n^2(\mathbf{r}) \rangle|^2 \right) \\ &+ \left(\frac{d\sigma}{d\Omega} \right)_{incoh} \left(\langle |\Delta \delta n^2(\mathbf{r})|^2 \rangle \right). \end{aligned} \quad (88)$$

The first one is called the “coherent intensity” and the second one is known as “incoherent, diffuse or non-specular intensity”. The obvious interpretation of the previous equations is that the incoherent scattering is due to the shifts of dielectric index from the average one [163]. If the surface inhomogeneity or roughness is statistically homogeneous and random along the sample plane, $\langle \delta n^2(\mathbf{r}) \rangle = \delta n^2(z)$ is a function of only the z -coordinate; the coherent cross-section is thus a Dirac peak at $q_{||} = k_{f,||} - k_{i,||} = 0$ (see for instance, the Born cross-section (Eq. (90))). For this reason, it is also called specular intensity or specular rod. However, one has to bear in mind that because of all the resolution imperfections, both cross-sections mix up along the specular rod giving rise to a finite width of the rod inversely proportional to the coherence length L_{coh} . In other words, there is diffuse scattering along the specular direction.

5.3.4. The Born approximation of first order (BA)

Even though nothing is said in principle about the used Green function, the Born approximation in the field of surface scattering restricts $\mathbf{G}(\mathbf{r}, \mathbf{r}')$ to its expression in the vacuum equation (80). Therefore, all multiple reflections are neglected; e.g. the reflection-transmission of the incident and scattered waves at the interfaces. Obviously, to do so, the range of validity for the scattering angles is restricted well above the angle of total external reflection.

In the far field regime, substituting Eq. (80) in the first Eq. (83) yields, for a planar incident wave $\mathbf{E}_0(\mathbf{r}) = E_0 e^{-ik_i \cdot \mathbf{r}}$:

$$\mathbf{E}(\mathbf{r}) = \mathbf{E}_0(\mathbf{r}) + k_0^2 \frac{e^{-ik_0 r}}{4\pi r} (\mathbf{E}_0 \cdot \mathbf{e}_f^{s,p}) \mathbf{e}_f^{s,p} \int d\mathbf{r}' \delta n^2(\mathbf{r}') e^{i\mathbf{q} \cdot \mathbf{r}'} \quad (89)$$

The classical wave vector transfer $\mathbf{q} = \mathbf{k}_f - \mathbf{k}_i$ appears in the above formula. The total differential scattering cross-section defined in Section 5.3.3 reads:

$$\frac{d\sigma}{d\Omega} = \frac{k_0^4}{16\pi^2} (\mathbf{e}_f^{s,p} \cdot \mathbf{e}_i^{s,p})^2 \left| \int d\mathbf{r}' \delta n^2(\mathbf{r}') e^{i\mathbf{q} \cdot \mathbf{r}'} \right|^2 \quad (90)$$

where $\mathbf{e}_i^{s,p}$ and $\mathbf{e}_f^{s,p}$ are the polarization vector of the incident and scattered waves. As obtained in standard textbooks on scattering [40,41], the Born approximation cross-section is given simply by the square modulus of the Fourier transform of the dielectric index.

5.3.5. The Distorted Wave Born Approximation (DWBA)

A more often used and accurate approximation is the Distorted Wave Born Approximation (DWBA). The Green function (Eq. (81)) and the wavefield are those obtained from flat interfaces. DWBA is expected to better take into account the reflection-refraction of waves and to give more accurate results than the Born approximation for scattering angles close and below the critical angle of the substrate. Indeed, only the perturbation induced by roughness or dielectric contrast is included in $\delta n^2(\mathbf{r})$ and the electric field that is supposed to polarise the medium is the Fresnel wavefield $\mathbf{E}_0(\mathbf{r}', \mathbf{k}_i)$ due to the incident plane wave \mathbf{k}_i .

Merging Eq. (81) for the far field Green function, the Fresnel wavefield of the chosen reference medium $\mathbf{E}_0(\mathbf{r}', -\mathbf{k}_f)$ in the definition of the total cross-section (Eq. (86)) yields:

$$\begin{aligned} \frac{d\sigma}{d\Omega} &= \frac{k_0^4}{16\pi^2 E_0^2} (\mathbf{e}_f^{s,p} \cdot \mathbf{e}_i^{s,p})^2 \\ &\times \left| \int d\mathbf{r}' \mathbf{E}_0(\mathbf{r}', \mathbf{k}_i) \delta n^2(\mathbf{r}') \mathbf{E}_0(\mathbf{r}', -\mathbf{k}_f) \right|^2. \end{aligned} \quad (91)$$

5.3.6. The polarization effects: Toward a scalar wavefield scattering and an analogy with the Schrödinger equation

At shallow incident and scattering angles, the polarization vectors of the electric field in s (electric field perpendicular to the incident or scattering plane) or p orientations (electric field along the incident plane or scattering plane) are nearly equal. As function of the scattering angles, the scalar products that comes into play in the Born cross-section (Eq. (90)) are:

$$\mathbf{e}_i^s \cdot \mathbf{e}_f^s = \cos(2\theta_f), \quad (92)$$

$$\mathbf{e}_i^s \cdot \mathbf{e}_f^p = -\sin(\alpha_f) \sin(2\theta_f), \quad (93)$$

$$\mathbf{e}_i^p \cdot \mathbf{e}_f^s = -\sin(\alpha_i) \sin(2\theta_f), \quad (94)$$

$$\mathbf{e}_i^p \cdot \mathbf{e}_f^p = \cos(\alpha_i) \cos(\alpha_f) - \cos(2\theta_f) \sin(\alpha_i) \sin(\alpha_f). \quad (95)$$

With an accuracy to second order for grazing angles, polarization effects can be safely neglected and $\mathbf{e}_i^s \cdot \mathbf{e}_f^s \simeq \mathbf{e}_i^p \cdot \mathbf{e}_f^p \simeq 1$. Of course, for higher scattering angles ($\alpha_i \simeq \alpha_f > 10^\circ$) in the diffraction

regime, the angular dependence of this scalar product can no longer be neglected. In passing, in principle, the scattering cross-section should be summed over all the polarization states of the waves.

The role of the electric field polarization is more subtle than a simple prefactor when using the DWBA. Indeed, the Green function has to be developed according to the choice of the reference medium and its wavefield \mathbf{E}_0 . In a stacking of layers, the relative orientation of \mathbf{e}_i and \mathbf{e}_f in p -polarization will be different from layer to layer because of the refraction of the waves at each interface. Subtle effects are expected only in p -polarization around the Yoneda peak. In s -polarization, the problem reduces to a simpler in-plane prefactor $\cos^2(2\theta_f)$. As rule of thumb, the vectorial character of the electric field in BA and DWBA can be forgotten safely for small angle X-ray scattering. In parallel, in this range of scattering angles, the atomic structure can be safely neglected in the dielectric index $n^2(\mathbf{r})$; in other words, $n^2(\mathbf{r}) \simeq n^2V(\mathbf{r})$ where n is the index of refraction of the mean electronic density. This corresponds to the small- q expansion of the atomic form factor $f(\mathbf{q})$ (see Section 5.2.2).

Notwithstanding the simple treatment of the wave/matter interaction, this is one of the explanation of the success of DWBA in X-ray scattering at variance to visible light scattering. By neglecting the polarization effects, the propagation equation (Eq. (69)) used in the scattering theory can be reduced to a scalar one for the amplitude of the electric field:

$$[\nabla^2 + k_0^2 n^2(\mathbf{r})] \Psi(\mathbf{r}) = 0. \quad (96)$$

The $\Psi(\mathbf{r})$ notation is used on purpose to highlight the analogy with the Schrödinger equation for a particle of mass m , energy ϵ in a given potential $V(\mathbf{r})$:

$$\left[-\frac{\hbar^2}{2m} \nabla^2 + V(\mathbf{r}) \right] \Psi(\mathbf{r}) = \epsilon \Psi(\mathbf{r}). \quad (97)$$

For instance, the comparison can be drawn in terms of cross-section with neutron scattering for which $V(\mathbf{r}) = \sum_i b_i \left(\frac{2\pi \hbar^2}{2m} \right) \delta(\mathbf{r} - \mathbf{r}_i)$ is the Fermi pseudopotential, b_i being the diffusion length of each nucleus. By comparing Eqs. (96) and (97), the neutron optical index is defined by $n^2(\mathbf{r}) = 1 - V(\mathbf{r})/\epsilon$. Therefore, all the machinery of quantum mechanics treatment of scattering or collision theory can be applied to the X-ray field. This leads to the well known T -matrix approach [131]. A comprehensive treatment of DWBA can be found in several books of quantum mechanics [142,91]. Most of the theoretical papers of X-ray scattering dealing with DWBA use this language.

5.4. Distorted Wave Born Approximation in action

To go further on in the expression of the scattering cross-section, an explicit model of the dielectric contrast should be chosen. This section focuses on four main cases: reflectivity from a graded interface, a rough surface, a rough multilayer and density fluctuations. A great deal will be given in Section 6 to the case of particles that are at the heart of this report. As explained previously Section 5.3.6, the polarization factor will be dropped in the following of the report bearing in mind that we are dealing with small angle scattering.

5.4.1. Reflectivity from a graded interface in the DWBA

Using heuristic arguments, we gave in Section 5.2.8 a brief account for how the reflection and transmission coefficients of a planar interface are affected by the roughness. For short correlation lengths and grazing angles, the reflection coefficient is damped by the Nérot–Croce factor while in the Rayleigh limit (long wavelength) it is affected by the Debye–Waller-like factor. Looking only

to the specular reflectivity at $q_{\parallel} = 0$, the Nérot–Croce factor can be obtained using DWBA with a Gaussian roughness approximation [35,106,107,102,108,111] and generalized to a graded interface of arbitrary profile [138,118,107,111,120,84].

Focusing on the specular scattering only ($q_{\parallel} = 0$), the interface can be characterized by its perpendicular dielectric profile $n^2(z)$ obtained by in-plane averaging of an interface. $n^2(z)$ is appreciably different from the sharp interface in a limited region around $z = 0$. However, one has to keep in mind that for an actual interface, such an approximation ignores the influence of the in-plane roughness correlation function on the diffuse scattering at $q_{\parallel} = 0$ [102,108,164]. In the spirit of DWBA, let us split $n^2(z)$ in two parts: $n^2(z) = n_0^2(z) + \delta n^2(z)$, where $n_0^2(z) = 0$, n_1^2 if $z > z_0$, $z < z_0$ respectively. The choice of the dividing surface position z_0 is arbitrary and will be discussed later on. Forgetting useless parallel dependence as $q_{\parallel} = 0$, both the field amplitude, the propagation equation (Eq. (71)), its integral equivalent form (Eq. (73)) and the Green function depend only on the z -coordinate (see Section 5.2.3):

$$E(z) = E_0(z) + \delta E(z) = E_0(z) + \epsilon_0 \int dz' G(z, z') \delta n^2(z') E(z'). \quad (98)$$

The field due to scattering from a sharp interface of an unit incoming plane wave reads:

$$E_0(z, k_z) = E_0 \begin{cases} e^{-ik_{z,0}z} + r_{0,1} e^{ik_{z,0}z} e^{-2ik_{z,0}z_0} & \text{for } z > z_0 \\ t_{0,1} e^{-ik_{z,1}z} e^{i(k_{z,1}-k_{z,0})z_0} & \text{for } z < z_0. \end{cases} \quad (99)$$

The transmitted wavevector $k_{z,1}$ and the Fresnel coefficients are given by Eqs. (51) and (57). The main advantage of the reduction of all the propagation equations to 1D is that the Green function defined through the 1D equivalent of Eq. (72) can be inferred exactly through a Fourier transform of the propagation equation [165,95,137,126,107,111,84]:

$$G(z, z')$$

$$= \begin{cases} G_1(z, z') = \frac{i}{2k_{z,0}} \left\{ e^{ik_{z,0}|z-z'|} + r_{0,1} e^{-2ik_{z,0}z_0} e^{ik_{z,0}(z+z')} \right\} \\ \text{for } z, z' > z_0 \\ G_2(z, z') = \frac{i}{2k_{z,1}} \left\{ e^{ik_{z,1}|z-z'|} - r_{0,1} e^{2ik_{z,1}z_0} e^{-ik_{z,1}(z+z')} \right\} \\ \text{for } z, z' < z_0 \\ G_3(z, z') = \frac{i}{k_{z,0} + k_{z,1}} e^{i(k_{z,1}-k_{z,0})z_0} e^{ik_{z,0}z'-ik_{z,1}z} \\ \text{for } z < z_0 < z' \\ G_4(z, z') = \frac{i}{k_{z,0} + k_{z,1}} e^{i(k_{z,1}-k_{z,0})z_0} e^{ik_{z,0}z-ik_{z,1}z'} \\ \text{for } z' < z_0 < z. \end{cases} \quad (100)$$

In the Born approximation, the Green function is taken as the vacuum one $G_1(z, z')$ with $r_{0,1} = 0$. The field under the integral $E(z')$ as well as the field inside the medium in Eq. (98) are taken as plane waves. Straightforward algebra yields the reflection coefficient valid above the critical reflection region:

$$r = -\frac{k_0^2}{4k_{z,0}} \frac{\widetilde{(n^2)'}(2k_{z,0})}{n_1^2}$$

where:

$$\widetilde{(n^2)'}(Q) = \int_{-\infty}^{+\infty} \frac{dn^2(z)}{dz} e^{iqz} dz \quad (101)$$

is the Fourier transform of the derivative of $n^2(z)$. The Born reflectivity [94,38,14,48,83,47] is proportional to the Fourier transform of the gradient of dielectric constant as already demonstrated in Section 5.2.9. The goal is to use Eq. (98) to find in a self consistent way the reflection coefficient of the graded

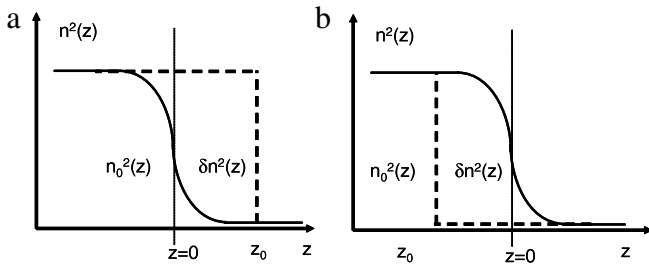


Fig. 30. The two choices of the position of the dividing surface z_0 used to define the perturbation part of the dielectric constant $\delta n^2(z)$ within the framework of DWBA for a graded interface: (a) $z_0 \gg 0$ (b) $z_0 \ll 0$. (From Ref. [111].)

interface. If $z_0 \gg 0$ is chosen well above the interface in vacuum such that most $\delta n^2(z)$ extends well above the interface (see Fig. 30), the field that appreciably polarizes the interface i.e. the field $E(z')$ in the right-hand side of Eq. (98) is the actual one in vacuum. By comparison with the flat surface, it can be approximated by: $E(z')/E_0 \simeq e^{-ik_{z,0}z'} + r(z_0 \gg 0)e^{ik_{z,0}z'}$; r is the required unknown reflection coefficient. It amounts to approximating the near field by its far field behavior, an assumption valid if the grading extension is small $k_z\sqrt{\langle z^2 \rangle} \ll 1$. For $z > z_0 \gg 0$, Eq. (98) gives access self-consistently to r :

$$r(z_0 \gg 0)e^{ik_{z,0}z} = r_{0,1}e^{-2ik_{z,0}z_0}e^{ik_{z,0}z} + \epsilon_0 k_0^2 \int_{-\infty}^{z_0} dz' G_4(z, z') \delta n^2(z') (e^{-ik_{z,0}z'} + r(z_0 \gg 0)e^{ik_{z,0}z'}). \quad (102)$$

The integral is computed from the $G_4(z, z')$ expression (Eq. (100)) and using the integration by parts of:

$$\int_{-\infty}^{z_0 \rightarrow +\infty} dz' \delta n^2(z') e^{iQz'} = \frac{n_1^2}{iQ} \left(e^{iQz_0} - \frac{\widetilde{(n^2)'}(Q)}{n_1^2} \right). \quad (103)$$

Finally, the position of the interface z_0 cancels out and it leaves:

$$r(z_0 \gg 0) = r_{0,1} \frac{\widetilde{(n^2)'}(k_{z,1} + k_{z,0})}{\widetilde{(n^2)'}(k_{z,1} - k_{z,0})}. \quad (104)$$

The same procedure leads also to the transmission coefficient $t(z_0 \gg 0)$ using Eq. (98) for $z \ll 0$:

$$t(z_0 \gg 0)e^{-ik_{z,1}z} = t_{0,1}e^{i(k_{z,1}-k_{z,0})z_0}e^{-ik_{z,1}z} + \epsilon_0 k_0^2 \int_{-\infty}^{z_0} dz' G_2(z, z') \delta n^2(z') (e^{-ik_{z,0}z'} + r(z_0 \gg 0)e^{ik_{z,0}z'}). \quad (105)$$

The final result is given in Ref. [111]. On the other hand, for the other choice of the dividing surface $z_0 \ll 0$, the polarizing field is essentially given by that transmitted through the graded interface into the bulk: $E(z') \simeq t(z_0 \ll 0)e^{-ik_{z,1}z'}$. In a similar way as in Eq. (102), the unknown transmission coefficient $t(z_0 \ll 0)$ is found self consistently using Eq. (98) for $z < z_0 \ll 0$. The found formula:

$$t(z_0 \ll 0) = t_{0,1} \frac{n_1^2}{\widetilde{(n^2)'}(k_{z,1} - k_{z,0})} \quad (106)$$

is next used to deduce the reflection coefficient $r(z_0 \ll 0)$. While $t(z_0 \ll 0) \neq t(z_0 \gg 0)$, the encouraging result in terms of reliability is that the reflection coefficient is independent of the choice of the dividing surface z_0 : $r(z_0 \ll 0) = r(z_0 \gg 0)$ [111]. For the special case of an error-function profile i.e. for Gaussian roughness of variance $\langle z^2 \rangle$, the Nérot–Croce factor [100,

101] $r = r_{0,1}e^{-k_{z,0}k_{z,1}\langle z^2 \rangle/2}$ is recovered while the two choices of the transmission coefficient agree if $k_{z,0}k_{z,1}\langle z^2 \rangle \ll 1$. Therefore, the accuracy of DWBA is restricted to the small roughness regime for which the extrapolation of the far field expression of $E(z')$ to the near field where the induced polarization takes place is valid.

Caticha [111] suggested to overcome the problem of the transmission coefficient by choosing the geometric mean $t_m = \sqrt{t(z_0 \ll 0)t(z_0 \gg 0)}$ starting from the finding that for a non absorbing medium, the expected energy conservation equation $|r|^2 + Re(k_{z,1})/k_{z,0}|t|^2 = 1$ is not satisfied while $|r|^2 + Re(k_{z,1}/k_{z,0})t(z_0 \ll 0)t(z_0 \gg 0) = 1$. To support that, he compared the exact result for these coefficients to those obtained analytically for the Epstein or tangent hyperbolic profile [124,94, 125–127,111,122] and Eq. (104) and t_m (Fig. 31).

Without absorption, the discrepancy is small on r, t for $\alpha_i = \alpha_f > \alpha_c$ while for $\alpha_i = \alpha_f < \alpha_c$, a better agreement is obtained for $t(z_0 \ll 0)$. The interesting feature is the enhancement due to the roughness of the transmission amplitude at the critical angle in comparison to the bare surface for which $|t|^2 = 4$ (see Fig. 25). While the phase mismatch at the interface is of no relevance for $|r|^2$ or $|t|^2$, this factor as well as the field discontinuities for a Gaussian interface (see Fig. 32) are detrimental for the accurate description of glancing-incidence X-ray fluorescence [108,109], which is more sensitive to the actual evanescent wave.

5.4.2. Single rough surface: DWBA versus BA

The case of diffuse scattering from a rough surface allows to clearly highlight the discrepancies between BA and DWBA. As the most ubiquitous example of surface disorder, roughness is the first example that was treated in depth with DWBA in the seminal paper of Sinha [35] and latter on confirmed by Pynn [106], de Boer [108] and Rauscher [36]. However, BA results were previously obtained by Wong and Bray [166].

The rough surface is characterized by its profile $z(\mathbf{r}_{\parallel})$. In the BA, the dielectric contrast with the substrate of index n which reads:

$$\delta n^2(\mathbf{r}) = (n_1^2 - 1) \begin{cases} 1 & \text{for } z \leq z(\mathbf{r}_{\parallel}) \\ 0 & \text{for } z > z(\mathbf{r}_{\parallel}) \end{cases} \quad (107)$$

can be put inside the corresponding total scattering cross-section (Eq. (90)):

$$\frac{d\sigma}{d\Omega} = \frac{k_0^4}{16\pi^2} |n_1^2 - 1|^2 \left| \int d\mathbf{r}_{\parallel} \int_{-\infty}^{z(\mathbf{r}_{\parallel})} dz e^{i\mathbf{q} \cdot \mathbf{r}} \right|^2. \quad (108)$$

The integration over the z -direction is readily made through integration by parts:

$$\frac{d\sigma}{d\Omega} = \frac{k_0^4}{16\pi^2 q_z^2} |n_1^2 - 1|^2 \times \left| \int d\mathbf{r}_{\parallel} \int d\mathbf{r}'_{\parallel} e^{iq_z \cdot (z(\mathbf{r}_{\parallel}) - z(\mathbf{r}'_{\parallel}))} e^{iq_{\parallel} \cdot (\mathbf{r}_{\parallel} - \mathbf{r}'_{\parallel})} \right|. \quad (109)$$

The modulus square has been split into the parallel and perpendicular components to allow for a change of variables along the surface $\mathbf{R}_{\parallel} = \mathbf{r}_{\parallel} - \mathbf{r}'_{\parallel}$. At that point, it is worth introducing the ensemble average due the coherence domains (see Section 5.3.3):

$$\frac{d\sigma}{d\Omega} = \frac{k_0^4 A_i}{16\pi^2 q_z^2} |n_1^2 - 1|^2 \int d\mathbf{R}_{\parallel} \langle e^{iq_z \cdot (z(\mathbf{R}_{\parallel}) - z(\mathbf{0}))} \rangle e^{iq_{\parallel} \cdot \mathbf{R}_{\parallel}}. \quad (110)$$

The integration over the remaining variable leads to the total illuminated area A_i . Another simplifying hypothesis is to assume that the fluctuations of heights follow a Gaussian statistics or to expand the exponential term only to second order if the surface roughness is small $q_z \langle (z(\mathbf{R}_{\parallel}) - z(\mathbf{0}))^2 \rangle \ll 1$:

$$\langle e^{iq_z \cdot (z(\mathbf{R}_{\parallel}) - z(\mathbf{0}))} \rangle = e^{-\frac{1}{2} q_z^2 \cdot \langle (z(\mathbf{R}_{\parallel}) - z(\mathbf{0}))^2 \rangle}. \quad (111)$$

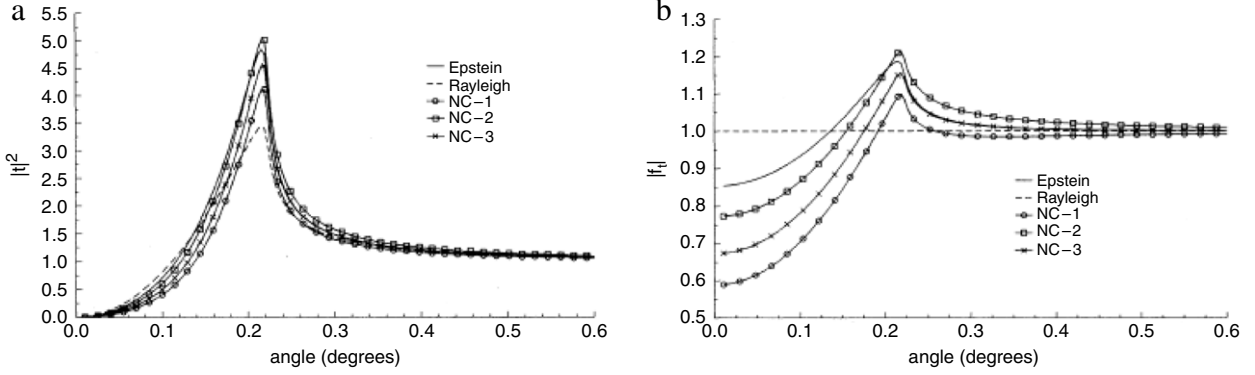


Fig. 31. Amplitude of a transmitted wave $|t|$ through a graded interface with an Epstein profile: exact calculation and Rayleigh or Nérot–Croce DWBA approximation $|t(z_0 \gg 0)|^2, |t(z_0 \gg 0)|^2, |\sqrt{t}(z_0 \gg 0)t(z_0 \ll 0)|^2$. (a) actual coefficient (b) after normalization by the Rayleigh one. From Ref. [111].

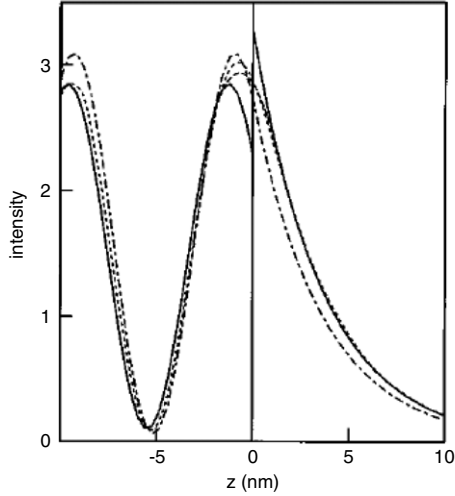


Fig. 32. X-ray intensity versus depth for an incident wave ($\text{Cu K}\alpha, k_z = 0.375 \text{ nm}^{-1}$) on a rough gold surface (error function profile, $\langle z^2 \rangle = 1.5 \text{ nm}$). Dash-dotted: no roughness; solid: calculation with the help of Croce–Nérot factors; short-dashed: exact calculation using the slicing method; long-dashed: interpolation. Note the discontinuity of the field with Croce–Nérot factors. From Ref. [109].

Finally, one ends up with:

$$\frac{d\sigma}{d\Omega} = \frac{k_0^4 A_i}{16\pi^2 q_z^2} |n_1^2 - 1|^2 e^{-q_z^2(z)^2} \int dR_{||} e^{q_z^2 \langle z(R_{||})z(0) \rangle} e^{iq_{||} \cdot R_{||}}. \quad (112)$$

For small perpendicular wavevector transfer, the exponential can be expanded into a series involving the Fourier transform of the height-height correlation function $\langle z(R_{||}) - z(0) \rangle$ i.e. the power spectrum of the roughness [35,167–169].

At large separation distances $R_{||} \rightarrow +\infty$ or small in-plane wavevector transfer $q_{||} \rightarrow 0$, the correlation between the heights of two points vanishes; therefore; the intensity (coherent intensity or specular component) includes a Dirac contribution $\delta(q_{||})$:

$$\left(\frac{d\sigma}{d\Omega} \right)_{coh} = \frac{k_0^4 A_i}{4q_z^2} |n_1^2 - 1|^2 e^{-q_z^2(z)^2} \delta(q_{||}). \quad (113)$$

Following Refs. [35,14,38], $\left(\frac{d\sigma}{d\Omega} \right)_{coh}$ can be linked with the square modulus of the reflectivity coefficient. The scattered intensity I_{sc} in the detector is related to the scattering cross section (see Section 5.3.3) through:

$$I_{sc} = \left(\frac{I_0}{A_0} \right) \int \left(\frac{d\sigma}{d\Omega} \right) \Delta\Omega \quad (114)$$

where I_0 is the intensity of the incident beam, A_0 its width and $\Delta\Omega$ the solid angle subtended by the detector. In the specular condition

of reflection,

$$\Delta\Omega = \frac{d\mathbf{q}_{||}}{k_0^2 \sin(\alpha_f)} = \frac{2d\mathbf{q}_{||}}{k_0 q_z}. \quad (115)$$

As the footprint of the beam is given by the projection of the beam section on the surface $A_0 = A_i \sin(\alpha_f)$, the reflectivity reads:

$$R = \frac{I_{sc}}{I_0} = |n_1^2 - 1|^2 \frac{k_0^4}{q_z^4} e^{-q_z^2(z)^2}. \quad (116)$$

The $1/q_z^4 \sim 1/\alpha_f^4$ power law decay expected for a perfectly flat surface (Section 5.2.6) is further damped by an exponential term due to roughness. This latter is nothing other than the Debye–Waller-like factor previously introduced in Section 5.2.8.

Eq. (112) encompasses both the coherent and incoherent cross section; the incoherent one is obtained by simple subtraction of Eq. (113) to Eq. (112).

As stated in Section 5.4.1, the DWBA cross-section expression for diffuse scattering depends on the choice of the position of the dividing surface $z = 0$ compared to the actual surface. Although for small roughness, all choices should be equivalent, better results should be expected for the average plane. In that case, the dielectric contrast reads:

$$\delta n^2(\mathbf{r}) = (n_1^2 - 1) \begin{cases} -1 & \text{for } 0 < z < z(r_{||}) \text{ if } z > 0 \\ 1 & \text{for } z(r_{||}) < z < 0 \text{ if } z < 0 \\ 0 & \text{elsewhere} \end{cases} \quad (117)$$

while the reference wavefield is given by the Fresnel expression

$$E_0(\mathbf{r}, \mathbf{k}) = E_0 e^{-ik_{||} \cdot \mathbf{r}_0} \begin{cases} e^{-ik_{z,0}z} + r_{0,1} e^{ik_{z,0}z} & \text{for } z > 0 \\ t_{0,1} e^{-ik_{z,1}z} & \text{for } z < 0. \end{cases} \quad (118)$$

The calculation of the scattered intensity is cumbersome [35], except if using an analytical continuation of the wavefield from above to below the surface i.e. by assuming that the expression of $E_0(\mathbf{r}, \mathbf{k})$ for $z < 0$ is still valid for $z > 0$. This approximation is reasonable for $q_z^2 \langle z^2 \rangle \ll 1$ since the fields and their derivatives are continuous at $z = 0$. Some authors [106,145] proposed instead to use the wavefield defined in terms of reflection-refraction on the rough surface leading to marginally different results. Using the analytical continuity at the interface, the calculation follows the BA one and yields:

$$\left(\frac{d\sigma}{d\Omega} \right)_{incoh} = \frac{k_0^4 A_i}{16\pi^2} |n_1^2 - 1|^2 |t_{0,1}^i|^2 |t_{0,1}^f|^2 \delta(q_{||}, q_z) \quad (119)$$

$$\delta(q_{||}, q_{z,1}) = \frac{e^{-\frac{1}{2}(q_{z,1}^2 + q_{z,1}^{*2})(z)^2}}{|q_{z,1}|^2} \times \int dR_{||} \left[e^{|q_{z,1}|^2 \langle z(R_{||})z(0) \rangle} - 1 \right] e^{iq_{||} \cdot R_{||}}. \quad (120)$$

The comparison between Eqs. (113) and (119) shows that the incoherent cross sections with BA and DWBA are the same except for:

- (i) the transmission factors $|t_{0,1}^i|^2 |t_{0,1}^f|^2$ in energy for the incident and exit waves;
- (ii) the use of the transmitted wavevector transfer $q_{z,1}$ in the substrate instead of that in vacuum q_z ; this is a consequence of the field continuity.

For large q_z , the DWBA cross section reduces to the BA one as $|t_{0,1}|^2 \simeq 1$ and $q_{z,1} \simeq q_z$. However, for incident α_i or emergent angle α_f close to the critical angle of the substrate, a maximum of 2 is reached for the transmission coefficient leading to what is known as the Yoneda peak [39,143] in GISAXS, or Yoneda wings in off specular reflectivity. In passing, note that Eq. (119) is symmetric with respect to \mathbf{k}_i and \mathbf{k}_f ; this is a manifestation of the reciprocity principle. An expression similar to Eq. (116) for the reflectivity is easily obtained but with the Debye–Waller-like factor $e^{-q_z^2(z)^2}$ replaced by the Nérot–Croce one $e^{-q_z q_{z,1}(z)^2}$.

Through suitable normalizations and extrapolations, a model independent inversion scheme [170] of Eq. (120) was proposed to get the height–height correlation function in a way similar to the one used to extract the pair correlation function of amorphous solids or liquids from the X-ray structure factor [171] (see Fig. 33). The back transformation can take benefit from the GISAXS scattering geometry [169]; at fixed α_i, α_f , the scattering depth $[1/\Lambda(\alpha_i) + 1/\Lambda(\alpha_f)]^{-1}$ (see Eq. (49)) is constant and the transmission functions (Eq. (119)) act only as prefactors while (z^2) results simply from measurements at two different out-of-plane angles α_f .

For an isotropic rough surface, $\langle z(R_{\parallel})z(0) \rangle$ is related to the mean square surface fluctuations $g(R_{\parallel})$ through:

$$g(R_{\parallel}) = \langle (z(R_{\parallel}) - z(0))^2 \rangle = 2 \langle z(R_{\parallel})^2 \rangle - 2 \langle z(R_{\parallel})z(0) \rangle. \quad (121)$$

Explicit models of the height–height correlation function or of $g(R_{\parallel})$ and their roughness spectrum, if available, are needed to go beyond Eq. (119). Several models have been proposed in the literature like Gaussian roughness, self-affine surfaces with spatial cut-off, liquid surfaces with capillary waves fluctuations [166, 35, 172, 106, 126, 169, 110, 14]. In the case of a self-affine surface (see Refs. [35, 173, 174, 169, 110] and references therein), the basic scaling hypothesis gives $g(R_{\parallel}) \propto R_{\parallel}^{2H}$, where $0 < H < 1$ is the roughness or Hurst exponent that describes the degree of jaggedness of the surface. H is related to the fractal dimension of the surface $D_s = 3 - H$. However, the fractal behavior of actual samples should saturate at sufficiently large horizontal length scales, at least because of finite size effects:

$$\begin{aligned} g(R_{\parallel}) &\propto R_{\parallel}^{2H}, \quad \text{if } R_{\parallel} \ll \xi_{\parallel} \\ g(R_{\parallel}) &= \langle z(R_{\parallel})^2 \rangle, \quad \text{if } R_{\parallel} \gg \xi_{\parallel}, \end{aligned} \quad (122)$$

where ξ_{\parallel} is the cut-off length between both regimes and is known as the correlation length. Various expressions for the interpolation between these two regimes have been proposed [35, 174, 169], in particular the exponential form of Sinha:

$$g(R_{\parallel}) = 2 \langle z(R_{\parallel})^2 \rangle \left(1 - e^{-(R_{\parallel}/\xi_{\parallel})^{2H}} \right). \quad (123)$$

Its main drawback is the lack of explicit expression for the power spectrum and of the expected logarithmic divergence at $H = 0$, leading to the introduction of other functional like the K-correlation function [173–175]. Many authors [173, 174, 176, 169] went to the conclusion that, whatever the choice of the height–height correlation function is, the roughness exponent H

should be accurately determined from the power law decay of the intensity far away in reciprocal space ($q_{\parallel} \geq 2\pi/\xi_{\parallel}$). Conversely, the cut-off or correlation length ξ_{\parallel} is very sensitive to the choice of the functional. A clear discussion of the best experimental conditions to achieve accurate measurements of those parameters is found in Ref. [169]. Nevertheless, the best data analysis [145, 168] were obtained with Eq. (123). An example extracted from Ref. [145] is given in Fig. 34 showing the previously introduced Yoneda wings around the specular rod. A craze [177, 178, 176] happened in the 90th for the capabilities of the X-ray technique to check kinetic roughening theory of non-equilibrium growth predicting self-affine behavior such as the Kardar–Parisi–Zhang equation [179].

5.4.3. Rough multilayers

X-ray reflectivity from multilayers is a fairly well established analytical tool in applied physics to characterize the average density profile of the layer stacking, in areas such as microelectronics, smart windows coatings, X-ray mirrors etc.... In this respect, the technique provides a measure of the layer thicknesses, mean electronic density and mean roughness (see review Ref. [50]). The reciprocal space of a perfect multilayer is made of equidistant points along the q_z axis, the so-called multilayer Bragg peaks. Their spacing $\Delta q_z = 2\pi/D$ is inversely proportional to the super-period D while their intensity is modulated by the content of the repeating unit cell leading to additional side maxima between Bragg peaks, known as Kiessig fringes. There are $N - 2$ maxima in between two Bragg peaks for N layers with q_z periodicity given by the layer thickness. However, it is well known that the specular reflectivity can be considerably influenced by imperfections of the interfaces leading to diffuse scattering. This latter brings information on the root-mean-square and the characteristic in-plane length scales of the roughness profiles as well as the cross-correlation or replication between layer roughnesses [180, 181] that are of paramount importance for the foreseen properties of the multilayers and also for its feedback on the growth process itself. A comprehensive review on this problem can be found in the book of Holý, Pietsch and Baumbach [15] about high resolution X-ray diffraction and scattering from thin films and multilayers. As compared to a single interface, multilayers bring several levels of complexity for the theoretical approach of scattering such as “dynamical” effects leading to Bragg interference peaks, cross correlation between layer thicknesses etc...

Following the approach of Eastman [182], Payne and Clemens [163], the reflection of a rough multilayer has been investigated using a technique of (i) phase perturbation of the wave traveling through the stack, and of (ii) Taylor expansion of the reflectivity to first order in the individual layer reflectivity. Under approximations of large correlation length scales (i.e. the Rayleigh one), they ended up with a generalization of the Debye–Waller-like factors for various models of roughnesses: correlated, uncorrelated, partially correlated and cumulative. The limit of the method is inherent to the used approximations (see Section 5.4.2) i.e. mainly neglecting the dynamical effects. Their most important result was the demonstration of the paramount role of the replication and correlation between layers.

Stearns [105, 167, 183] tackled the problem of diffuse scattering from multilayers in connection with the development of soft X-ray mirrors. He developed a so-called “specular field approximation” for which the specular field within the multilayer is treated dynamically and the non-specular field kinematically by adding the contribution of each interface with a simple phase factor due to propagation of the scattered waves up to the surface. In his approximation, the specular field in each layer is determined from a full dynamical treatment ignoring the energy removal due to the non specular component or accounting for it through

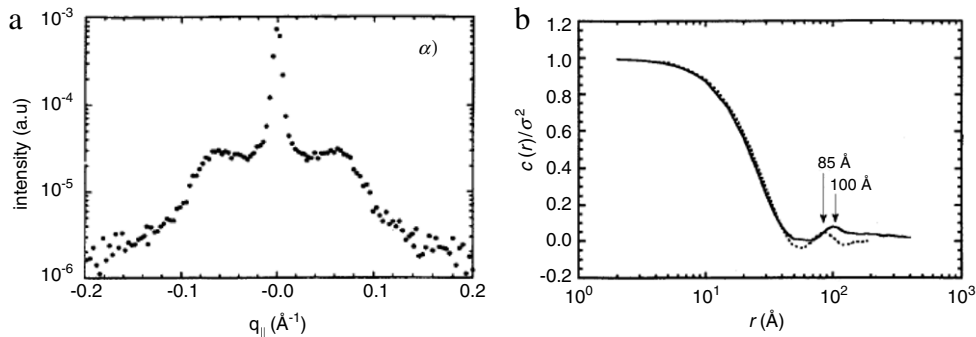


Fig. 33. (a) Diffuse scattering from a rough 400 Å thick Zr₃₅Co₆₅ film. The measurement is made in the GISAXS geometry at $\alpha_i = 0.25^\circ$, $\alpha_f = 0.9^\circ$ just below the Co-K edge. (b) Height-height correlation function $\langle z(R_{\parallel}) - z(0) \rangle / \langle z(R_{\parallel}) \rangle^2$ obtained from inversion of Eq. (120) (solid line) or from Scanning Tunneling Microscopy (dotted line). The hump at ~ 100 Å shows an enhanced correlation at a length scale of the diameter of the granular structure observed by STM. From Ref. [170].

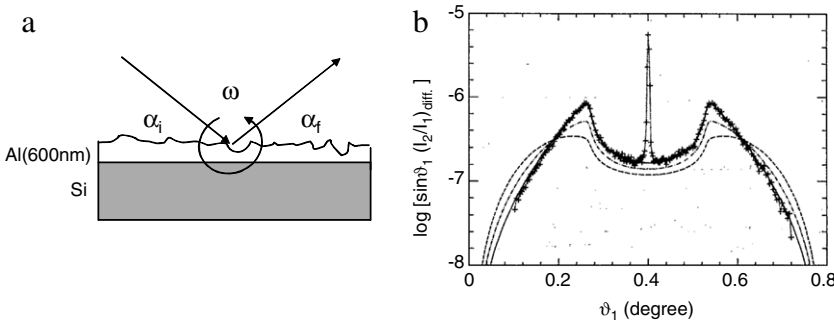


Fig. 34. Diffuse scattering from a rough aluminum film grown on silicon. (a) The measurement (b) is made by rocking the sample at a fixed angle $\alpha_i + \alpha_f = 0.8^\circ$ between incident beam and detector ($E = 7$ keV). The data points have been fitted (full line) through Eq. (120) with a Gaussian height-height correlation function (Eq. (123)) with $\sqrt{\langle z(R_{\parallel})^2 \rangle} = 17 \pm 2$ Å, $\xi_{\parallel} = 1100 \pm 50$ Å, $H = 0.7 \pm 0.1$. A Nérot–Croce correction (Eq. (61)) was applied on the transmission coefficients in order to achieve a good agreement (see Section 5.4.7). A comparison is made without this correction (dash dotted line) and with the Debye–Waller-like corrected transmission (dashed line). From Ref. [145].

a Debye–Waller-like factor (see Section 5.2.8). Therefore, the roughness is assumed to be small i.e. $q_z^2 \langle z^2 \rangle \ll 1$. However, the approximation breaks down either at grazing angles or when the non-specular grazing angle satisfies the multilayer Bragg condition, such that the multiple scattering of non-specular fields exhibits constructive interference. This approximation reverts to the DWBA limit at large scattering angles i.e. away from grazing angles and is equivalent to the work of Vineyard for a single interface [139]. A careful analysis of the problem of replication of interface roughnesses [167,183] leads to an explanation of the resonant diffuse scattering observed in correlated multilayers; these latter are due to the spreading into diffuse sheets of the Bragg lattice points of the multilayer located at multiple of $2\pi/D$, D being the period of the stack.

The first full DWBA treatment of scattering from stratified media was given by Daillant and Bélorgey [148] starting from the reciprocity theorem (see Section 5.3.2) and using Green function formalism. They studied the more restricted problem of scattering from two interfaces of a thin film; they applied their modeling to the scattering from a black-soap film [149]. In particular, they focused their interest on the ability of off-specular scans to obtain directly the height–height correlation functions of the two interfaces of the soap film (Eqs. (126)–(127)) so demonstrating a strong coupling between them. The generalization to a stratified media with an arbitrary number of layers was given in appendix of Ref. [148]. Pynn [106] ended up with a similar result for a rough thin film in the context of neutron scattering.

Readily after, Holý and coworkers [58,59] proposed a full DWBA treatment of specular and diffuse scattering from rough multilayers. They treated both the coherent and incoherent scattering and the case of uncorrelated and correlated roughnesses

between layers. The importance of conformality of the layers was stressed by Sinha and coworkers [168] in the framework of the Born approximation for stepped surfaces. These DWBA results were confirmed by Kopecky [184] using a Parratt like formalism to compute the unperturbed wavefield applied to the case of diffuse scattering from multilayer X-ray mirrors. In an earlier attempt [185], the transmission coefficients appearing in the scattering cross-section for one interface Eqs. (119)–(120) [35] were replaced by those obtained through the Parratt formalism; however, as compared to the full DWBA calculation Eq. (126); several scattering processes are missing. Later on, de Boer [186] generalized the DWBA formula for specular reflection up to second order perturbation and calculated the electric field inside the multilayer that is needed to obtain glancing incidence X-ray fluorescence intensities [147].

X-ray reflection from rough multilayer gratings was tackled by Mikulík and Baumbach [187] in the framework of kinematic (Born approximation) and semidynamical theories. The grating periodicity is supposed to be perfect with an infinite size. In the dynamical theory, the wave equation is transformed into an eigenvalue problem for the Fourier components of the diffracted waves. The problem was solved through a matrix formalism where the Fresnel reflection and transmission coefficients were generalized to each grating truncation rod; the roughness effects of the layers and the side walls were accounted for through a generalized Debye–Waller-like factor.

The influence of multilayer interface roughnesses on the diffuse scattering around Bragg diffraction peaks at wide angle can be treated within DWBA similarly as around the origin, either starting from kinematic [188] or dynamic [189] diffraction by lattice planes. However, both morphological and structural imperfections superimpose in the diffuse signal.

Let us consider a stacking of N layers (Fig. 26) starting from the vacuum interface $n = 1$ and ending at the substrate interface $n = N + 1$. While basically the demonstrations of the coherent and incoherent cross-sections follow the same steps as for a single interface [35] (see Refs. [58,59,184,109,15,14] and Section 5.4.2), the final result is lengthy. The unperturbed electromagnetic field involves the multiple reflection and transmission at each interface and is made of upward and downward propagating waves in layer n Eq. (50).

$$E_n(\mathbf{r}, \mathbf{k}) = E_0 [\tilde{A}_n^+(k_z)e^{ik_z n z} + \tilde{A}_n^-(k_z)e^{-ik_z n z}] e^{-i\mathbf{k}_{||}\cdot\mathbf{r}_{||}}. \quad (124)$$

Of course, the perpendicular component of the wavevector Eq. (51) is obtained through parallel component conservation in case of flat interfaces. The amplitudes \tilde{A}_j^\pm are calculated either through a Parratt or a matrix formalism (see Section 5.2.7). The roughness of each layer contributes to the perturbation in an analogous way to Eq. (117):

$$\delta n_n^2(\mathbf{r}) = (n_n^2 - n_{n-1}^2) \begin{cases} -1 & \text{for } 0 < z < z_n(r_{||}) \text{ if } z_n > 0 \\ 1 & \text{for } z_n(r_{||}) < z < 0 \text{ if } z_n < 0 \\ 0 & \text{elsewhere.} \end{cases} \quad (125)$$

The formulation of the problem is simpler in the case of a *s*-polarized wave as the same polarization factor is found for each interface. As in the case of a single interface, the analytical continuity of the field from below to above the interface yields a “more compact” expression involving a double sum over the layers of 16 terms:

$$\left(\frac{d\sigma}{d\Omega} \right)_{incoh} = \frac{k_0^4 A_i}{16\pi^2} \sum_{m,n=1}^N \sum_{\pm} \sum_{\pm} \sum_{\pm} \sum_{\pm} (n_m^2 - n_{m-1}^2) \times (n_n^2 - n_{n-1}^2)^* \tilde{A}_m^\pm(k_{iz}) \tilde{A}_m^\pm(k_{fz}) \tilde{A}_n^{\pm,*}(k_{iz}) \tilde{A}_n^{\pm,*}(k_{fz}) \times \delta_{mn}(q_{||}, \pm k_{iz,m} \pm k_{fz,m}, \pm k_{iz,n} \pm k_{fz,n}) \quad (126)$$

$$\delta_{mn}(q_{||}, q_z, p_z) = \frac{e^{-\frac{1}{2}(q_z^2(z_m)^2 + p_z^2(z_n)^2)}}{q_z p_z^*} \times \int d\mathbf{R}_{||} \left[e^{q_z p_z^*(z_n(\mathbf{R}_{||}) z_m(0))} - 1 \right] e^{i\mathbf{q}_{||}\cdot\mathbf{R}_{||}}. \quad (127)$$

The asterisk * denotes the complex conjugate. The coherent counterpart expression can be found in Ref. [58]. The diffuse intensity involves a generalization of the structure factor $\delta_{mn}(q_{||}, \pm k_{iz,m} \pm k_{fz,m}, \pm k_{iz,n} \pm k_{fz,n})$ involving the correlation functions $\langle z_m(\mathbf{R}_{||}) z_n(0) \rangle$ between the roughness profiles of interfaces m and n . The physical interpretation of terms $\pm k_{z,m}, \pm k_{z,n}$ is a scattering process from downwards/upwards to downwards/upwards propagating waves with a weight proportional to the corresponding products of amplitudes $\tilde{A}_n^\pm(k_z)$ and the generalized structure factors $\delta_{mn}(q_{||}, \pm k_{iz,m} \pm k_{fz,m}, \pm k_{iz,n} \pm k_{fz,n})$. This is known in the field of dynamical diffraction as *Umweganregung* [59,188,15], meaning the excitation of a scattering process (diffuse scattering) through another one (reflection, transmission).

Two components in the roughness width of each layer $\langle z_m^2 \rangle$ are often distinguished: an intrinsic one often assumed to be random and a extrinsic one due replication from layer to layer. As function of the degree of replication of thickness fluctuations from layer to layer, limiting cases with specific scattering behaviors can be pinpointed:

- (i) no replication i.e. fully uncorrelated roughnesses
- (ii) perfect replication without intrinsic roughness i.e. identical interfaces
- (iii) partially conformal layers.

Several models of cross-correlation or replication between layer roughnesses have been treated in the literature starting from a Edwards Wilkinson Langevin [179] equation of diffusion-like

propagation of roughness [167,190,183] or with an exponential form [191,59,192,15,14], both depending on a perpendicular correlation length ξ_\perp . The growth of multilayers on a stepped substrate leads to the special case of roughness replication tilted with respect to the growth direction [193,194].

The main characteristic of scattering from multilayers is threefold [59,15,14]:

- (i) the position of the multilayer Bragg peak are shifted in q_z as compared to a pure kinematic calculation because of refraction at the interfaces [196];
- (ii) the resonant diffuse scattering.

For uncorrelated layers, the diffuse scattering is the incoherent sum of the scattering from individual layers given by Eq. (120) (as $S_{mn} = 0$ for $m \neq n$) plus the specular rod. The intensity is therefore spread more or less uniformly in reciprocal space according to the roughness correlation function. In the case of a partial replication of the roughness from layer to layer, a partial phase coherence exists between the waves diffusely scattered on each layer for a given parallel wavevector. This leads to a spreading of the Bragg points into diffuse sheets of intensity along the $q_{||}$ direction [180, 196, 190, 181, 190, 197]. Because of beam refraction [59], these sheets are curved in the $q_{||}, q_z$ plane giving rise to the name of “bananas”. Their $q_{||}$ -length is governed by the in-plane correlation length of the layers $\xi_{||}$ [196]. The q_z -width at a given $q_{||}$ characterizes the decay length of the cross correlation between interfaces for a given spatial wavelength. More precisely, their q_z spread is related to the degree of roughness replication *i.e.* to the inverse of the cross correlation length ξ_\perp [167,190,197,50]. Similar sheets are found not only around the origin of reciprocal space but also as satellites around the diffraction peaks at wide angles of crystallized layers [188,189, 15]. In some cases of conformal and very rough layers, the intensity of the Bragg peaks is sometimes vanishingly small as compared to the diffuse scattering. A method of integration of the scattered intensity over $q_{||}$ has been proposed in the limit of the Born approximation [36] to recover the actual local reflectivity of the sample and therefore the actual profile of density. At the opposite limit, for strongly correlated interfaces, the shift between the Kiessig fringes in reflectivity and those in diffuse scattering allows to distinguish between conformal and anticonformal curvature morphologies at large length scales [198].

- (iii) The Yoneda wings and the Bragg-like peaks.

At variance to the resonant diffuse sheets that are of kinematic nature *i.e.* also reproduced by BA, Yoneda wings and Bragg-like peaks are caused by multiple scattering processes so that they are of pure dynamical nature [59,184,15]. The Yoneda peak is found when the incident α_i or emergent α_f angles are below the critical angle of the average layers (see Eq. (119)). In case of a single layer (see for instance Section 6.2.4), a wave guide effect in the amplitude of the transmitted-reflected waves (Eq. (138)) is observed when the incident or/and emergent transmitted wave vector fulfill the interference condition of Fabry–Perot. This concept of scattering enhanced by standing waves is readily generalized to the case of multilayers; enhancement of the intensity is expected along Bragg-like resonance lines when the incident or emergent angle fulfills the Bragg law corrected from refraction:

$$\sqrt{\langle n \rangle - \cos^2(\alpha_{i,f})} = \frac{p_{i,f} \lambda}{2D} \quad (128)$$

where $\langle n \rangle$ is the average refractive index, D the multilayer period and $p_{i,f}$ integers. These lines are a basic generalization of the Yoneda peak that corresponds to the zero order

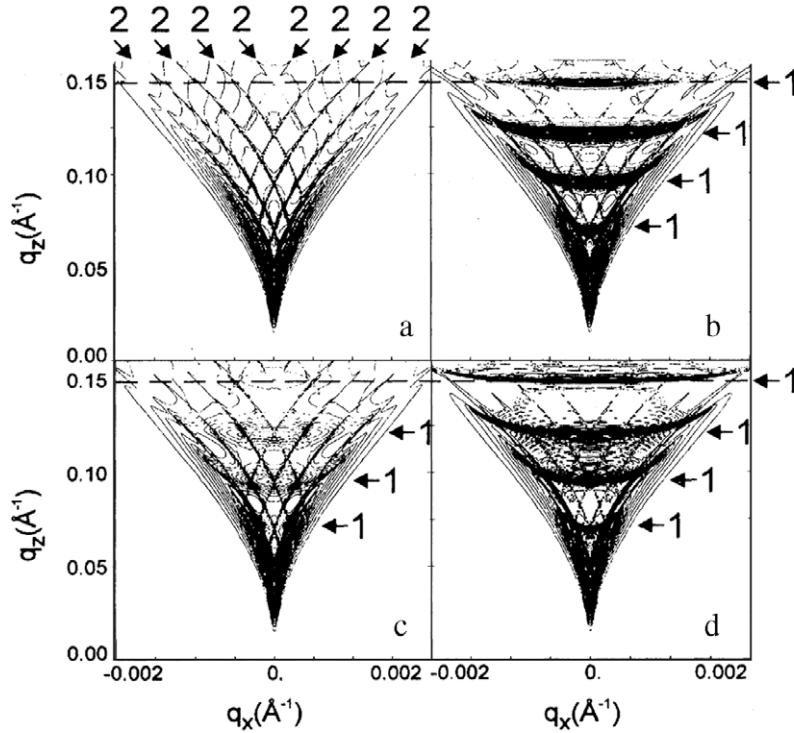


Fig. 35. Calculated diffuse scattering from a multilayer (20 periods) of GaAs(95 Å)/AlAs(125 Å) on a GaAs substrate ($\lambda = 1.5 \text{ \AA}$) using Eqs. (126)–(127). The height–height autocorrelation function is described by Eq. (123) with $\sqrt{\langle z^2 \rangle} = 8.6 \text{ \AA}$, $H = 1$, $\xi_{\parallel} = 2000 \text{ \AA}$. The interface profile replication is exponentially damped from layer to layer [191] with an increasing characteristic length (a) $\xi_{\perp} = 0 \text{ \AA}$, (b) $\xi_{\perp} = 200 \text{ \AA}$, (c) $\xi_{\perp} = 1000 \text{ \AA}$, (d) $\xi_{\perp} \rightarrow +\infty$. The intensity is plotted in the $q_x - q_z$ plane with the restriction on the availability of reciprocal space due to coplanar geometry (see Section 2.2). Arrow 2 show the pseudo-Bragg lines and arrow 1 the Bragg sheets. From Ref. [195].

effect. Of course, when both incident or emergent lines intersect, a Bragg-like peak appears with indexes p_i, p_f . The peak existence is of dynamic nature but its intensity is modulated by the roughness. A semi-analytical description of this modulation [195] showed that, when interfaces are uncorrelated, Bragg-like peaks follow the intensity of the X-ray standing wave pattern but minor correlations between interfaces can invert the contrast. One of the first experimental observations can be found in Refs. [180,196] and latter on in Ref. [192].

These various effects are exemplified in the simulation of Fig. 35 for progressively correlated layers. For completely uncorrelated layers, the scattering map is dominated by the Bragg-like resonance lines (arrow 2–Fig-a) and their intersection. Upon increasing the degree of replication, the intensity concentrates in the curved Bragg sheets while the intensity of the Bragg-like resonance peak can be sensitively modulated (see broken line of Fig. 36).

Fig. 37 shows one of the first experimental GISAXS study of multilayers [197,175,50,199] exhibiting the same features: Bragg sheets (Roman letters) and resonance lines (arrows). The increasing width of the Bragg sheets with $2\theta_f$ reflects the damping of the layer-to-layer cross-correlation for in-plane roughnesses of smaller wavelength. This latter as well as the logarithmic in-plane correlation were assigned to a mechanism of kinetic roughening [197,50,199] of the growing surface in the framework of Edwards–Wilkinson Langevin equation [179].

Many tests to assess the DWBA reliability to describe actual scattering data from multilayers can be found in the literature [15]. The first stringent tests on Si/Ge layers [200] and on CoSi₂/Si/CoSi₂/Si(111) [192] validated the theory by fitting simultaneously the reflectivity as well as several off-specular scans (detector scan, longitudinal scan, rocking scan) with the

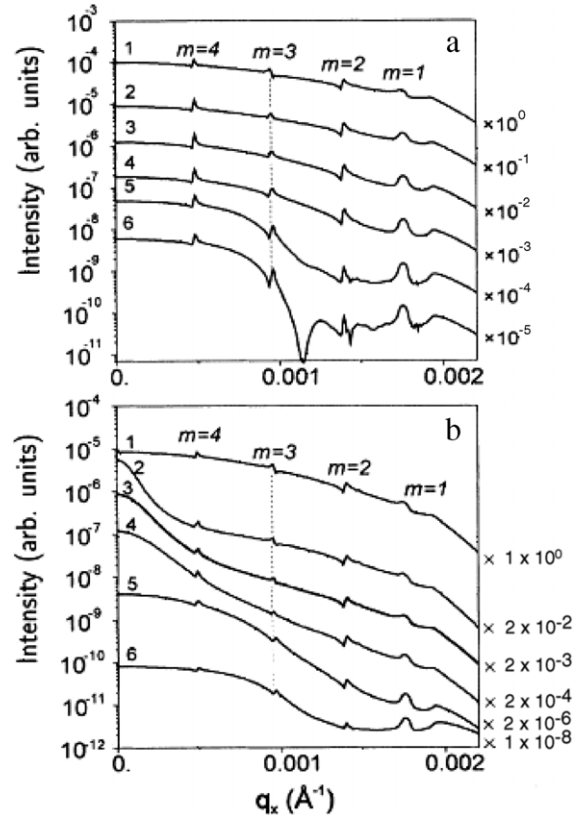


Fig. 36. Evolution of the intensity of the 5th Bragg sheet with increasing vertical correlation length. Line 1–6 correspond to $\xi_{\perp} = 0, 200, 500, 1000, 10000, +\infty \text{ \AA}$. Panels a,b correspond to accumulated and non accumulated roughnesses. Same parameters as in Fig. 35. From Ref. [195].

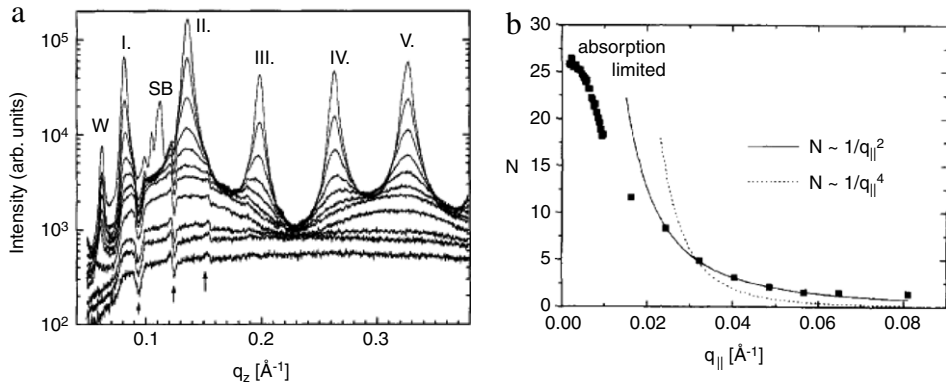


Fig. 37. (a) Scattering in GISAXS configuration from a 60 Si(68.5 Å)/W(28.5 Å) bilayers. From top to bottom, the in-plane angle increases from $2\theta_f = 0.2^\circ$, 0.3° , 0.4° , 0.5° , 0.6° , 0.7° , 0.8° , 1.0° , 1.5° , 2.0° , 3.0° , 5.0° while $\alpha_i = 0.7^\circ$ and $\lambda = 1.35 \text{ \AA}$. The Bragg sheets are labeled with Roman letters. (b) Number N of correlated layers as obtained from the inverse of the q_{\parallel} -width of the second Bragg sheet II. For small angles, $N \simeq 25$ is limited by the absorption while at higher angles, the $1/q_{\parallel}$ is indicative of a diffusion limited growth. From Ref. [50,199].

same set of parameters [201,202]; all the experimental features were accounted for and accurate values of the rms roughnesses, the in-plane coherence lengths, the Hurst exponents, the cross-correlations between layers were obtained. The tour de force in Ref. [192] was to fit up to 30 parameters on 18 different scans! Several softwares are now freely available to simulate reflectivity and diffuse scattering from imperfect multilayers [203].

5.4.4. Buried density fluctuations

Scattering from density fluctuations buried under a rough surface was evoked by Sinha [168] and fully treated by Rauscher et al. [36] under the assumption of the lack of cross-correlation with the surface roughness. In that case, the scattering from the rough surface and from the density fluctuations add up incoherently, except along the specular rod. Special cases of δ -like layer at the surface, columnar structures, isotropic density fluctuations and layered structures were chosen as basic examples. Multilayers of density inhomogeneities and density fluctuations at a liquid surface were treated in Ref. [14]. Later on, the scattering cross section was obtained for free standing nanostructures [37, 62], for pores in mesoporous thin films [152,153,204,154], for holes in a substrate [150]. Special attention is paid to those cases of “nanoparticles” in Section 6 for which the scattering cross section can be defined through an effective particle form factor involving several scattering paths.

The formal treatment is somehow identical to the rough surface case. Let us consider buried density fluctuations $\delta n^2(\mathbf{r})$ under a flat surface of a substrate with index n_1 . The useful part of the Fresnel wavefield (Eq. (118)) used as the eigenstate of the perturbation formalism is the transmitted wave only i.e. $t_{0,1} e^{-ik_{z,1}z}$ as $\delta n^2(\mathbf{r}) \neq 0$ only if $z < 0$. Following Eq. (91), for an homogeneous system, the incoherent cross-section for $q_{\parallel} \neq 0$ can be written in the form:

$$\left(\frac{d\sigma}{d\Omega} \right)_{incoh} = \frac{k_0^4 A_i}{16\pi^2} |t_{0,1}^i|^2 |t_{0,1}^f|^2 C(q_{\parallel}, q_z) \quad (129)$$

$$C(q_{\parallel}, q_z) = \int d\mathbf{R}_{\parallel} e^{i\mathbf{q}_{\parallel} \cdot \mathbf{R}_{\parallel}} \int_{-\infty}^0 dz \int_{-\infty}^0 dz' e^{iq_{z,1}z} e^{-iq_{z,1}z'} \times \langle \delta n^2(0, z) \delta n^{2*}(\mathbf{R}_{\parallel}, z') \rangle, \quad (130)$$

where $q_{z,1} = k_{fz,1} - k_{iz,1}$ is the wavevector transfer inside the substrate. The intensity is a kind of Fourier transform of the autocorrelation function of the dielectric contrast $\langle \delta n^2(0, z) \delta n^{2*}(\mathbf{R}_{\parallel}, z') \rangle$. However, at variance to the Born approximation, apart the transmission function prefactors, it is the wavevector transfer of the transmitted waves that comes into play in the formula. Only density fluctuations inside the scattering depth $1/\text{Im}(q_{z,1})$ actually

contribute to the cross-section. Compared to the definition of the penetration depth (Eq. (49)), it includes also the role of the exit evanescent wave. For scattering angles α_i, α_f above the critical angle of the substrate, only a slight shift of the scattering pattern as compared to BA is observed as $q_{z,1} \simeq q_z$ and $t_{0,1}^i, t_{0,1}^f \simeq 1$. On the contrary, below the critical angle, the scattering involves an evanescent wave; either $k_{fz,1}$ or $k_{iz,1}$ become imaginary leading to an enhanced surface sensitivity of the measurement as compared to classical transmission geometry. Concerning the coherent cross-section, the DWBA reflectivity can be computed from the averaged dielectric profile $n_0(z)$ using the results of Section 5.4.1.

5.4.5. Diffuse scattering from magnetic media

Information about magnetic structure of surfaces and thin films can be obtained with X-rays in an element-specific way by tuning the photon energy across an absorption edge (mainly L edge for transition or rare earth metals or an M edge for actinides) leading to a magnetic signal sufficient to be compared to charge scattering [205,206]. The real part of the atomic form factor gives rise to magnetic scattering while the imaginary part i.e. absorption to X-ray magnetic circular dichroism. A detailed description of the interaction of X-rays with magnetically polarized atoms can be found in the literature [207,14]. Although the technique was initially developed to describe Bragg peak intensities, the increasing interest in magnetic layers has pushed toward measurements and theories of specular and off-specular scattering to get information about disorder of magnetization at the length scale of the magnetic domains. The theoretical formulation of magnetic scattering from rough surfaces and multilayers was developed in the framework of BA and DWBA by Lee and coworkers for both specular reflectivity [88,208] and diffuse scattering [89]. In their treatment, the deviations from a smooth magnetic interface can be distinct from the structural ones (i.e. separated by a magnetic dead layer) but possibly strongly correlated through their roughness parameters and height-height correlation functions. Components of the magnetization at the interface which are disordered on much shorter length scales are ignored in this treatment, as they will scatter at much larger q -values than those of interest. Also, scattering from magnetic domains are equivalent to scattering from buried fluctuations of density and can be incorporated in the theory. The main difficulty leading to a quite complex formulation is that the scattering length, contrary to the Thomson one, is a tensor and not a scalar; in other words, the X-ray refractive index is anisotropic leading to two transmitted and two reflected waves at each interface depending upon the polarization state (*s*, *p* or circular polarization). The

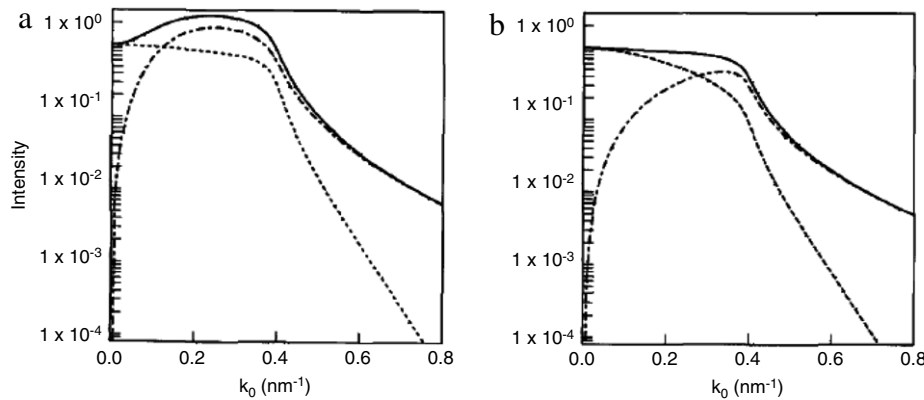


Fig. 38. Reflectivity versus k_z (denoted k_0 on figure) of a rough platinum surface with large correlation length ξ_{\parallel} (Cu K α wavelength, $\sqrt{\langle z^2 \rangle} = 1.5$ nm). (a) DWBA calculation of the specular reflectivity using Nérot–Croce factor Eq. (61) (dashed-line), total diffusely reflected intensity relative to incident intensity after integration of Eq. (119) (dot dashed line), sum of the specular and diffuse reflection (continuous line). (b) Same as (a) but using the Rayleigh approach. Note the lack of energy conservation of DWBA when $\xi_{\parallel} k_{iz}^2/k_0 > 1$. From Ref. [110].

reader interested by the actual formulation of the problem as well as by recent literature about this topic should refer to Refs. [208, 88,89].

5.4.6. Validity range of DWBA

Many subtle questions regarding the range of accuracy have been glossed over when introducing the DWBA in Section 5.3 and applying it to several cases in Section 5.4. For a single rough surface, what are the limitations of the DWBA in terms of the root mean square roughness $\sqrt{\langle z^2 \rangle}$ and the in-plane correlation length ξ_{\parallel} ? At some point, for very long wavelength components but still smaller than the coherence length of the beam L_{coh} , a rough surface may be seen as a set of flat surfaces making different inclinations when the issue of roughness merges into a flatness issue. At such length scale, the DWBA is expected to break down and the crossover can be understood simply from the diffraction principle. For an incoming beam \mathbf{k}_i , diffracted beams \mathbf{k}_f from a grating of period D are observed at a parallel wavevector that fulfills $k_f \parallel = k_i \parallel \pm 2n\pi/D$. As $k_f \parallel < k_0$ no diffraction happens if $k_0 - k_i \parallel < 2\pi/D$. A rough surface may be seen as the superposition of many grating periods with relative weights given by the roughness power spectrum; the “diffracted” peaks merge into diffuse scattering. As ξ_{\parallel} can be viewed as the largest active period of the roughness, the diffuse scattering is negligible as compared to the reflected beam if diffraction from ξ_{\parallel} is impossible: $k_0 - k_i \parallel = k_0[1 - \cos(\alpha_i)] \simeq k_0\alpha_i^2/2 \simeq k_{iz}^2/k_0/2 \ll 2\pi/\xi_{\parallel}$ i.e. $\xi_{\parallel} k_{iz}^2/k_0 \ll 1$; otherwise, it will be intense and will occur close to the specular beam. Moreover, as already discussed in Sections 5.2.8 and 5.4.1, the DWBA is restricted to small amplitudes $k_{iz}\sqrt{\langle z^2 \rangle} \ll 1$.

De Boer in a series of papers Refs. [102,108–110] critically reviewed the range of validity of DWBA as function of the two crossovers $\xi_{\parallel} k_{iz}^2/k_0$ and $k_{iz}\sqrt{\langle z^2 \rangle}$. He stressed that the Nérot–Croce factors obtained through various ways: (i) phase averaging [100] (see Section 5.2.8) (ii) self-consistent equation based on DWBA and Green function [35,107,106,102,111] (Section 5.4.1) relies explicitly or implicitly on the assumption of small correlation length $\xi_{\parallel} k_{iz}^2/k_0 \ll 1$ and on the use of an analytical continuation of the unperturbed field from one side of the interface to the other side, an assumption valid for small roughness up to order $k_{iz}^2\langle z^2 \rangle$. However, even for small correlation length, energy conservation within DWBA is strictly fulfilled only up to order $|q_z|^4\langle z^2 \rangle^2$ [147, 108]. The situation is even worse when increasing the correlation length; the total scattered intensity computed from Eq. (119) can

exceed the incident intensity (Fig. 38). At the other extreme limit, for large correlation length, the Rayleigh method [104,102,209] is more suitable. As ξ_{\parallel} is large, the local slope of the surface profile is so small that only the specular component of the Fourier series of the field are accounted for in the boundary conditions (see Fig. 27). It leads to an incoherent cross section similar to Eq. (119) (see Ref. [108]-Appendix D or Ref. [104] for details) but with the structure factor $\delta(q_{\parallel}, q_{z,0})$ identical to the one obtained in the BA (Eq. (112)). Contrary to DWBA, the intensity conservation is fulfilled in the Rayleigh method (Fig. 38).

By pursuing the DWBA expansion up to second order in $k_{iz}^2\langle z^2 \rangle$, de Boer [102] showed that the reflection and transmission coefficients actually depend on the power spectral density of the roughness and not only on the roughness amplitude as suggested by Eq. (61). He proposed, at least for the coherent cross section, formulas that interpolate smoothly as function of ξ_{\parallel} between the DWBA and the Rayleigh limit for $k_{iz}\sqrt{\langle z^2 \rangle} \ll 1$.

5.4.7. Improving DWBA accuracy?

In the X-ray scattering field, mainly two ways have been explored in the literature to go beyond the first order DWBA results, either through a better choice of the reference state or by iterating further on the Born expansion (Eq. (83)).

A first semiphenomenological try is to correct *a posteriori* the Fresnel coefficients from flat interfaces by the corresponding Nérot–Croce coefficients [100,101,14] due to roughness in order to cure the lack of energy conservation of first order DWBA [108]. Weber and Lengeler [145] argued that this resulted in better fits of their experimental data on X-ray grazing incidence scattering from rough surfaces. A similar approach was followed by Kopecky [184] for multilayers while Wormington [210] and coworkers argued that it is also necessary to include the effect of density gradient to accurately reproduce data from polished ceramics. Pynn [106] suggested to replace the Fresnel eigenstates by the actual one from the rough surface without giving any hint how to calculate them. Moreover, this leads to expressions that do not fulfill the reciprocity principle [109]. Fanchenko and Nefedov [211] tried to justify the use of a modified eigen-wavefield through a variational principle of the T-scattering matrix approach. However, the degree of accuracy of their approach in terms of roughness is difficult to assess. De Boer [109–111] highlighted the drawbacks of using such modified fields in the interfacial region as an input in the Green propagation equation (Eq. (73)) for the actual field that polarizes the matter. The field obtained with the aid of the Nérot–Croce factors shows a discontinuity at the interface between the incident

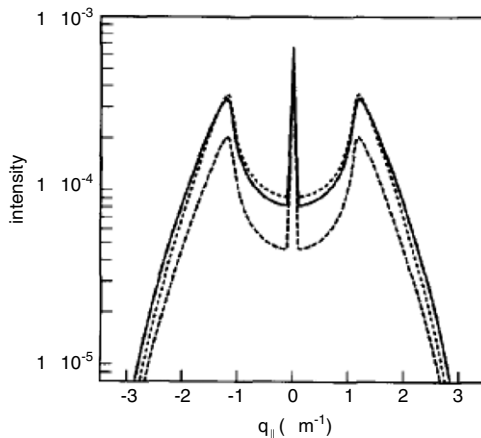


Fig. 39. Scattering versus q_{\parallel} at a given $q_z = 0.5 \text{ nm}^{-1}$ (rocking scan) on a silicon sample ($k_0 = 45 \text{ nm}^{-1}$, $\sqrt{\langle z^2 \rangle} = 4 \text{ nm}$) with a self-affine rough surface $H = 1$ Eq. (123). Solid line $\xi_{\parallel} = 400 \text{ nm}$ from Eq. (119); dashed line $\xi_{\parallel} = 400 \text{ nm}$ using field matched at the interface (see Fig. 32); dotted $\xi_{\parallel} = 800 \text{ nm}$ from Eq. (119). From Ref. [110].

wave and the evanescent wave below the critical angle of the surface (see Fig. 32). Interpolated fields using the average of the refractive index between media give better results for grazing incidence X-ray fluorescence and diffuse scattering [147,109,110] although the derivative is not continuous (see Fig. 39).

In the case of an in-plane homogeneous random rough surface, better results of diffuse scattering is expected in the framework of DWBA if the reference medium is the average interface or, in other words, the dielectric index is the one averaged along the direction parallel with the interface $\tilde{n}_0^2(z) = 1/A \int n^2(\mathbf{r}_{\parallel}, z) d\mathbf{r}_{\parallel}$ [109, 212, 164, 155, 81]. This method is in line with the calculation of scattering from multilayers (see Section 5.4.3). The main drawback is that no straightforward expression of the Fresnel wavefield $E_0(z, k_z)$ can be obtained except for special cases [124, 94, 44]; one needs to calculate the upward and downward waves amplitudes using the matrix formalism of Abelés [96] (see Section 5.2.7) in stratified media or the solution of differential equations. Moreover, the expression of the scattering cross-sections are cumbersome as the perturbation $\delta n^2(\mathbf{r}_{\parallel})$ is positive as well as negative. Despite that, a better accuracy is expected since:

- the perturbation is null on average along the interface $\langle \delta n^2(\mathbf{r}_{\parallel}) \rangle = 0$;
- the attenuation and the refraction of the incident and scattered waves by the graded interface and consequently the shape and position of the Yoneda peak are better described, in particular for angles close and below the critical angle;
- the method intrinsically accounts for the Nérot–Croce factors;
- once scattered, because of the intrinsic small X-ray scattering cross-section, a wave may be scattered again mainly in the forward direction and all the more than the angles are shallow.

A practical example will be given in Section 6.5 in the case of supported nanoparticles [155,81]. In the context of scattering of visible light from a 1D rough surface, the approach called Mean Field Theory [212,164] was further improved starting from a field that includes all doubly correlated multiple scattering processes or in other words, the role of the correlation length in the domain over which $n^2(\mathbf{r}_{\parallel}, z)$ is averaged.

In principle, multiple scattering effects are encompassed in the full Born series Eq. (83). However, beyond first order, the summation is cumbersome and nothing guarantees a small radius of convergence of the expansion. De Boer [102,110] has shown that corrective terms including not only the root-mean-square roughness $\langle z^2 \rangle$ but also the in-plane correlation function of the

roughness appears in the X-ray reflectivity when going up to second order. This result is counterintuitive as it is often assumed that lateral correlation cause non-specular scattering with a non-conserved parallel wavevector. The reason lies in the existence of two step scattering via intermediate scattering with opposite in-plane wave vector transfer. He proposed a generalization of this result valid for arbitrary roughness $k_z \langle z^2 \rangle$ for the reflection as well as transmission coefficients of a rough surface; the formula interpolates between Nérot–Croce and Debye–Waller-like regimes that is to say between the high $\xi_{\parallel} \ll k_0/k_z^2$ and low spatial frequencies $\xi_{\parallel} \gg k_0/k_z^2$.

Recently, Feranchuk and coworkers [122,123] have developed a self-consistent approach for specular X-ray reflection from interfaces with a continuous transition layer. An ansatz [122] for the wavefield for a given profile $\Lambda^{(0)}(z)$ has been proposed; it reproduces accurately both the amplitudes and the phases of the reflection and transmission coefficients. The key idea, to go beyond DWBA, is not to fix the profile of the layer $\Lambda^{(0)}(z)$ but to assume it as a variational function changing with the order of the DWBA expansion and depending on the perpendicular wavevector $\Lambda(z, k_z)$. The additional degree of freedom due to the dependence on k_z is used to get rid off of all the terms of DWBA expansion in the differential scattering cross-section except the zero order one. This gives a self consistent equation that defines the profile. This methodology that is equivalent to partial summation of the infinite DWBA series goes beyond the classical Nérot–Croce factor. However, the method was only applied to the analysis of specular reflectivity and not to diffuse scattering.

6. Grazing Incidence Small Angle X-Ray Scattering from assemblies of particles

6.1. Introduction

Handling the case of X-scattering from nanoparticles at surfaces or slightly buried is of great importance in the light of the amount of scientific papers on nanoparticles and the expected technological applications. In the context of morphological characterization of nanoobjects, the GISAXS technique offers the opportunity to probe as a whole an assembly of nanoparticles and to define an “averaged particle”. Not only the sizes and the particle density are available but others quantities like the particle shape, the width of the size distribution or higher order correlation parameters are hidden in the scattering profile. This section aims at highlighting the key ingredients for the experimentalist in order to answer the following questions:

- what are the differences and the similarities between bulk and surface sensitive small angle scattering? What is the impact of grazing incidence and exit angles?
- how does the particle shape come into play in the scattering pattern?
- how to get the mean size and the spacing between particles?
- what are the effects of size and spatial disorders in the scattering pattern?
- what does the particle density modify in the scattering pattern?

The term “particle” used hereafter stands for a size limited density inhomogeneity that scatters the X-ray beam. Fig. 40 summarizes the morphologies of interest that have been encountered experimentally in the literature:

- island on a substrate
- inclusions in a substrate or holes in a substrate surface
- inclusions or holes in a slab.

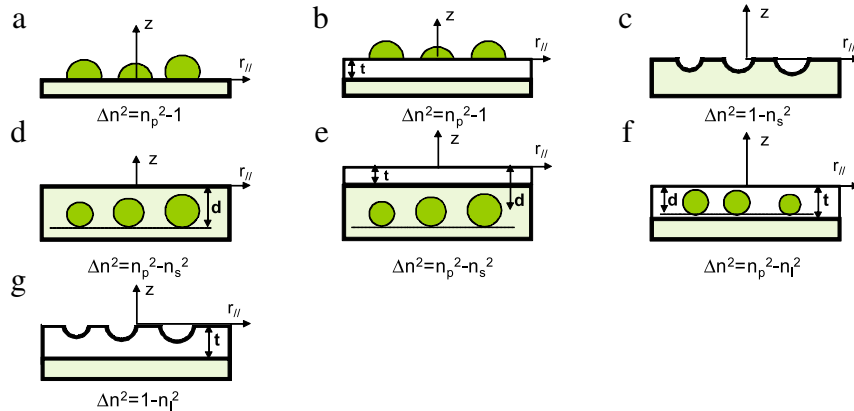


Fig. 40. Overview of all the described morphologies: (a) Nanoparticles on a substrate; (b) Nanoparticles on a thin layer; (c) Holes in a surface; (d) Inclusions in a substrate; (e) Inclusions in a substrate below a layer; (f) Inclusions in a layer; (g) Holes in a layer. t is the thickness of the layer and d the burying depth. The contrast of dielectric constant Δn^2 has been added; n_p , n_s , n_l , 1 are respectively the refraction index of the particles, the substrate, the layer and vacuum.

In each case, flat interfaces give rise to different scattering paths and cross-sections. The problem will be restricted to a plane of particles, ordered or not, to put the emphasis on the surface sensitivity of the GISAXS technique.

The problem will be tackled with an increasing complexity, first dealing with isolated particles and the scattering characteristics (Section 6.2), secondly introducing the interference between scatterers and the role of correlations (Section 6.3) and finally treating the influence of packing on the calculation of the form factor itself (Section 6.5). All the useful concepts of bulk small angle scattering such as asymptotic limits of the form factor or scattering from faceted objects are reminded in the context of surfaces. Software IsGISAXS [27] was developed to simulate and fit GISAXS patterns from nanoparticles; it includes all the theoretical background developed in this section. It is freely available from: <http://www.insp.jussieu.fr/axe2/Oxydes/IsGISAXS/isgisaxs.htm>. Several experimental examples will illustrate all these notions in the next section Section 7.

6.2. Dilute case: Form factor of an isolated particle in DWBA

6.2.1. The particle form factor

Let us consider a particle of shape $S(\mathbf{r})$ ($S(\mathbf{r}) = 1$ inside it; $S(\mathbf{r}) = 0$ outside) and an index of refraction n_p , embedded in a medium of index n_m . As shown in the general treatment of DWBA Section 5.3, the dielectric constant in the Helmholtz propagation equation (Eq. (96)) for $n_0(z)$ alone. Both Δn^2 and $E_0(\mathbf{k}, \mathbf{r})$ depend on the considered geometry:

$$n^2(\mathbf{r}) = n_0^2(z) + \delta n^2(\mathbf{r}) = n_0^2(z) + \Delta n^2 S(\mathbf{r}). \quad (131)$$

$\Delta n^2 = n_p^2 - n_m^2$ ¹ is the dielectric constant contrast between the particle and its embedding medium while $n_0(z)$ is the vertical profile of refraction index of the system. The DWBA perturbation treatment requires the Fresnel solution $E_0(\mathbf{k}, \mathbf{r})$ of the scalar wave equation (Eq. (96)) for $n_0(z)$ alone. Both Δn^2 and $E_0(\mathbf{k}, \mathbf{r})$ depend on the considered geometry.

6.2.2. The supported nanoparticle

In the case of a nanoparticle on a substrate (Fig. 40a), $n_0(z) = 1$ for $z > 0$ and $n_0(z) = n_s$ for $z < 0$; the dielectric contrast is: $\Delta n^2 = n_p^2 - 1$ where n_p is the index of refraction of the nanoparticle and 1 is that of vacuum. As demonstrated in Section 5.2.6 and using the notations of Section 5.2.7, the unperturbed wavefield reads:

$$E_0(\mathbf{r}, \mathbf{k}) = E_0 e^{-ik_{\parallel} \cdot \mathbf{r}_{\parallel}} \begin{cases} e^{-ik_{z,0}} + r_{0,1} e^{ik_{z,0} z} & \text{for } z > 0 \\ t_{0,1} e^{-ik_{z,1} z} & \text{for } z < 0 \end{cases} \quad (132)$$

¹ Note that the atomic structure is implicitly neglected because of the smallness of the scattering angles.

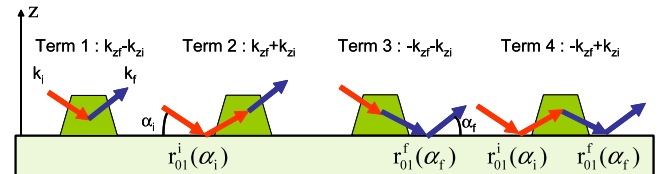


Fig. 41. “Diagrammatic” representation of the island scattering cross section in DWBA. Interpreted from Ref. [37].

\mathbf{k}_{\parallel} is the component of the wavevector \mathbf{k} parallel to the surface while the Fresnel coefficients $r_{0,1}$ and $t_{0,1}$ Eq. (57) are evaluated in terms of the perpendicular components of \mathbf{k} in a vacuum $k_{z,0}$ or in the substrate $k_{z,1} = -\sqrt{n_s^2 k_0^2 - k_{\parallel}^2}$. Following Eq. (91), the scattering cross-section [37,27,29] from \mathbf{k}_i to \mathbf{k}_f can be cast in the following form:

$$\frac{d\sigma}{d\Omega} = \frac{k_0^4}{16\pi^2} |n_p^2 - 1|^2 |\mathcal{F}(\mathbf{q}_{\parallel}, k_{iz,0}, k_{fz,0})|^2, \quad (133)$$

where the DWBA form factor of the nanoparticle is:

$$\mathcal{F}(\mathbf{q}_{\parallel}, k_{iz,0}, k_{fz,0}) = F(\mathbf{q}_{\parallel}, k_{fz,0} - k_{iz,0}) + r_{0,1}^f F(\mathbf{q}_{\parallel}, -k_{fz,0} - k_{iz,0}) + r_{0,1}^i F(\mathbf{q}_{\parallel}, k_{fz,0} + k_{iz,0}) + r_{0,1}^i r_{0,1}^f F(\mathbf{q}_{\parallel}, -k_{fz,0} + k_{iz,0}). \quad (134)$$

$\mathbf{q} = \mathbf{k}_f - \mathbf{k}_i$ is the wavevector transfer. $\mathcal{F}(\mathbf{q}_{\parallel}, k_{iz,0}, k_{fz,0})$ is given in terms of the Fourier transform of the particle shape:

$$F(\mathbf{q}) = \int_{S(\mathbf{r})} e^{i\mathbf{q} \cdot \mathbf{r}} d\mathbf{r}. \quad (135)$$

Note in passing that the superscript f in the reflection coefficients means that they are evaluated for the time inverted scattering wave vector $-k_{fz,0}$. A simple interpretation² of each term of Eq. (134) is given in Fig. 41 as the interference between elementary scattering paths. The first term is nothing other than the Born one i.e. the direct scattering by the particle as if it was isolated in vacuum (see Section 5.3.4). The other ones involve a reflection of either the incident or the scattered beams on the substrate surface; the actual perpendicular wavevector transfer should be used and the corresponding form factor should be weighted by the corresponding reflection coefficient. As an obvious consequence, at variance to scattering in vacuum, \mathbf{q} alone is not sufficient to describe the scattering.

An enhancement of the intensity at $\alpha_f = \alpha_c$ appears in the typical plot of $|\mathcal{F}(\mathbf{q}_{\parallel}, k_{iz,0}, k_{fz,0})|^2$ of Fig. 42. This feature, known

² Fig. 41 is, what is called in quantum mechanics, a diagram of interactions. In no way, it should be interpreted as geometrical X-ray paths.

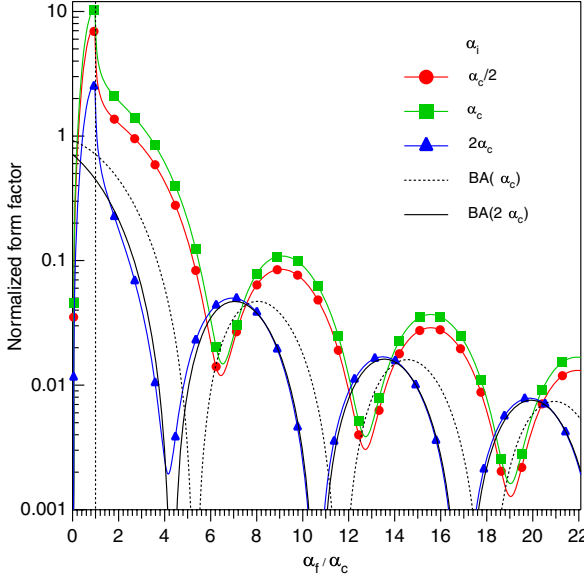


Fig. 42. DWBA form factor (Eq. (134)) of a cylindrical nanoparticle as function of the emergence angle α_f/α_c and for several incidence angles. The intensity was normalized by the particle volume squared. As a matter of comparison, the Born form factor (Eq. (135)) is also plotted. Interpreted from Refs. [27,29].

as the Yoneda peak [39], is due to the interplay between (i) the sharp variation of the amplitude and the phase of the reflection coefficients $r_{0,1}^{i,f}$ close to the critical angle α_c (see Fig. 25a) and (ii) the involved Fourier transforms $\mathcal{F}(\mathbf{q}_{||}, \pm k_{iz,0}, \pm k_{fz,0})$. As shown in Fig. 43, except close and below α_c , two contributions are dominating the scattering for $\alpha_f > \alpha_c$: the Born one and that involving the reflection of the incident wave before scattering. The wavevector shift of $2k_{iz,0}$ between both combined with the behavior of $r_{0,1}^i$ induce a blurring of the sharp interference fringes of the Born form factor; the zeros of $F(\mathbf{q}_z)$ Eq. (223) become minima which positions depend on the incident angle α_i . To conclude, as a general rule, when $\alpha_i, \alpha_f \gg \alpha_c$, the Born approximation is valid. The case of a nanoparticle on a thin layer on an infinite substrate (see Fig. 40b) is handled in a similar way; the only difference is the use of Eq. (56) instead of Eq. (45) or Eq. (57) for the reflection coefficients. This gives rise to (i) a coupling between the Kiessig fringes of the film and the oscillations of the form factor and (ii) a standing wave pattern below the critical angles of the substrate and the layer [213].

6.2.3. The buried particle or the hole at the surface

The treatment of X-ray scattering from density fluctuations below the substrate surface (particle buried at a depth d ; see Fig. 40d) and from a supported nanoparticle are exactly similar in terms of profile of refraction index $n_0(z)$ and of wavefield Eq. (132).

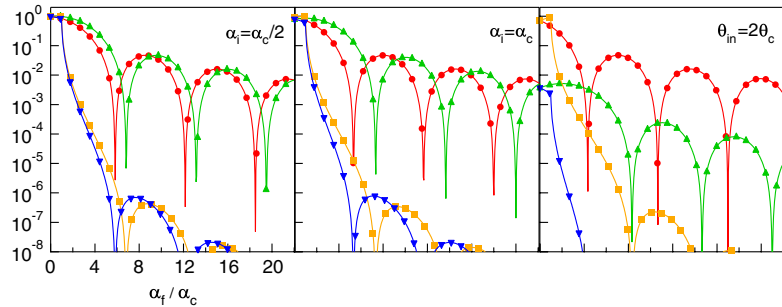


Fig. 43. Decomposition of the DWBA island form factor (Eq. (134)) along the four scattering components shown in Fig. 41. The symbols (o, \triangle , ∇ , \square) correspond to the four scattering events of Fig. 41 from left to right. Interpreted from Refs. [27,29].

The only difference is the perturbation term $\delta n^2(\mathbf{r}) = (n_p^2 - n_s^2)S(\mathbf{r})$ that acts only for $z < 0$. Therefore, only the transmitted waves are involved in the cross-section (Eq. (91)) leading to:

$$\frac{d\sigma}{d\Omega} = \frac{k_0^4}{16\pi^2} |n_p^2 - n_s^2|^2 |\mathcal{F}(\mathbf{q}_{||}, k_{iz,0}, k_{fz,0})|^2, \quad (136)$$

$$\mathcal{F}(\mathbf{q}_{||}, k_{iz,0}, k_{fz,0}) = t_{0,1}^i t_{0,1}^f F(\mathbf{q}_{||}, k_{fz,1} - k_{iz,1}) e^{id(k_{fz,1} - k_{iz,1})}. \quad (136)$$

The form factor is similar to the Born one but it is evaluated for the wavevector transfer inside the substrate i.e. $(\mathbf{q}_{||}, k_{fz,1} - k_{iz,1})$ and multiplied by a phase term that accounts for the wave propagations inside the substrate. At variance with the supported nanoparticle case, the DWBA form factor of an isolated buried particle still exhibits zeros. The signature of the DWBA is the symmetric presence of the transmission coefficients in incidence $t_{0,1}^i$ and in emergence $t_{0,1}^f$; this is a consequence of source-observer reciprocity theorem. The emergence transmission coefficient $t_{0,1}^f$, as shown in Fig. 25, gives rise to the Yoneda peak [39].

A capping layer (Fig. 40e) only slightly increases the complexity of the problem; in Eq. (136), $k_{z,2}$ is replaced by $k_{z,1}$ and $t_{0,1}$ by t_s from Eq. (56).

Holes (Fig. 40c) are treated on the same footing but $\Delta n^2 = n_s^2 - 1$, $d = 0$ and, if the convention of axis used in Section 6.2.6 is used, $F(q_x, q_y, q_z)$ in Eq. (136) is replaced by $F(q_x, -q_y, -q_z)$. Owing to the Babinet principle of optics, nothing in the scattering allows to distinguish between holes or inclusions, except the contrast of dielectric constant.

6.2.4. Particles or holes in a thin slab

For this case of a layer of thickness t on top of a substrate, the profile of refraction index is:

$$n_0(z) = \begin{cases} 1 & \text{if } z > 0 \\ n_l & \text{if } -t < z < 0 \\ n_s & \text{if } z < -t \end{cases} \quad (137)$$

while the Fresnel wavefield is given by sets of upward and downward propagating waves (Section 5.2.7)

$$E_0(\mathbf{r}, \mathbf{k})$$

$$= E_0 e^{-ik_{||}\cdot\mathbf{r}_{||}} \begin{cases} A_0^+ e^{ik_{z,0}z} + A_0^- e^{-ik_{z,0}z} & \text{for } z > 0 \\ A_1^+ e^{ik_{z,1}z} + A_1^- e^{-ik_{z,1}z} & \text{for } -t < z < 0 \\ A_2^+ e^{ik_{z,2}z} & \text{for } z < -t \end{cases} \quad (138)$$

As the particle is located inside the layer, the coefficients of interest are A_1^\pm ; they are evaluated using the matrix formalism of Section 5.2.7:

$$\frac{A_1^-}{A_0^-} = \tilde{A}_1^- = \frac{t_{0,1}}{1 + r_{0,1} r_{1,2} e^{2ik_{z,1}t}}, \quad (139)$$

$$\frac{A_1^+}{A_0^+} = \tilde{A}_1^+ = \frac{t_{0,1} r_{1,2} e^{2ik_{z,1}t}}{1 + r_{0,1} r_{1,2} e^{2ik_{z,1}t}}. \quad (140)$$

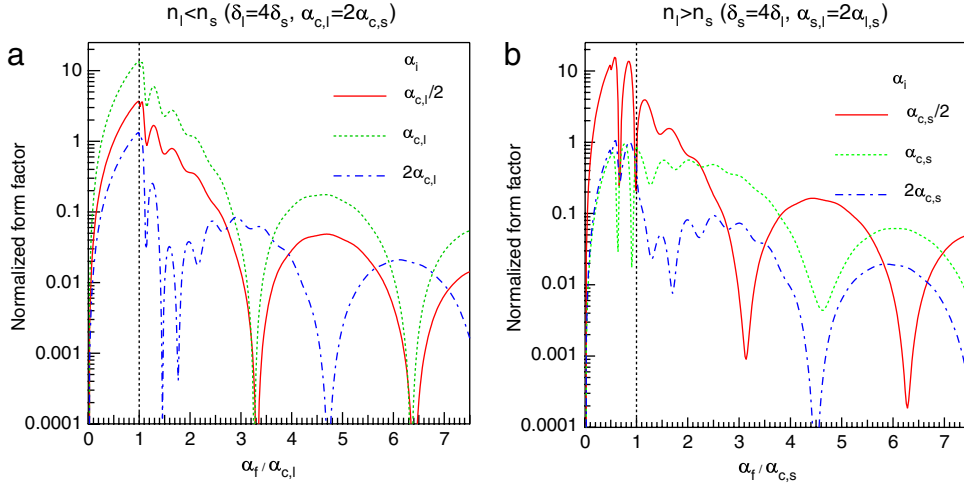


Fig. 44. Form factor of cylindrical holes of height H at the surface of a layer of thickness $t = 3.4H$. The layer is (a) less refringent ($\delta_l = 4\delta_s$) and (b) more refringent ($\delta_s = 4\delta_l$) than the substrate. The curves are plotted against the exit angle normalized by the highest critical angle $\text{Max}(\alpha_c, l, \alpha_c, s)$ for the same incident angle α_i . The form factor has been normalized by the hole volume squared.

The integration in Eq. (91) leads to the following cross-section:

$$\frac{d\sigma}{d\Omega} = \frac{k_0^4}{16\pi^2} |n_p^2 - n_l^2|^2 |\mathcal{F}(\mathbf{q}_{||}, k_{iz}, k_{fz})|^2. \quad (141)$$

where the form factor is given by:

$$\begin{aligned} \mathcal{F}(\mathbf{q}_{||}, k_{iz,0}, k_{fz,0}) \\ = & \tilde{A}_1^-(k_{iz,1})\tilde{A}_1^+(-k_{fz,1})e^{i(+k_{fz,1}-k_{iz,1})d}F(\mathbf{q}_{||}, +k_{fz,1}-k_{iz,1}) \\ & + \tilde{A}_1^+(k_{iz,1})\tilde{A}_1^-(-k_{fz,1})e^{i(+k_{fz,1}+k_{iz,1})d}F(\mathbf{q}_{||}, +k_{fz,1}+k_{iz,1}) \\ & + \tilde{A}_1^-(k_{iz,1})\tilde{A}_1^+(-k_{fz,1})e^{i(-k_{fz,1}-k_{iz,1})d}F(\mathbf{q}_{||}, -k_{fz,1}-k_{iz,1}) \\ & + \tilde{A}_1^+(k_{iz,1})\tilde{A}_1^+(-k_{fz,1})e^{i(-k_{fz,1}+k_{iz,1})d}F(\mathbf{q}_{||}, -k_{fz,1}+k_{iz,1}). \end{aligned} \quad (142)$$

The form factor (Eq. (142)) can be understood as the coherent superposition of four scattering events, involving or not a reflection of the incident beam and the scattered beam at the slab/substrate interface. A Fabry-Pérot type interference effect arises from the denominator of \tilde{A}_1^\pm . The phase factor accounts for the wave propagation up to the particle location.

The case of holes (Fig. 40g) is left to the sagacity of the reader. An illustration is given on Fig. 44 for a cylindrical hole in a layer that is less or more refringent than the substrate. The dynamical effects of scattering are more complex than for a simple hole in a substrate; two beating frequencies are observed, due to the hole depth H and to the layer thickness t . It is worth noticing that, for a layer more refringent than the substrate ($\delta_s > \delta_l$), a double Yoneda peak is observed because of the progressive penetration inside the media of the time inverted scattered wave $-\mathbf{k}_f$ as function of α_f . This phenomenon can be rationalized in terms of a standing wave pattern [213].

6.2.5. The core-shell particle

Using the same approach as in the previous section, the dielectric perturbation term induced by a core-shell particle (Fig. 45) can be written as:

$$\delta n^2(\mathbf{r}) = \delta n_{co}^2 S_{co}(\mathbf{r}) + \delta n_{sh}^2 [S_{sh}(\mathbf{r}) - S_{co}(\mathbf{r})], \quad (143)$$

where:

- $\delta n_{co}^2 = n_{co}^2 - 1$, $\delta n_{sh}^2 = n_{sh}^2 - 1$ for islands;
- $\delta n_{co}^2 = n_{co}^2 - n_s^2$, $\delta n_{sh}^2 = n_{sh}^2 - n_s^2$ for inclusions in a substrate;
- $\delta n_{co}^2 = 1 - n_s^2$, $\delta n_{sh}^2 = n_{sh}^2 - n_s^2$ for holes in a substrate surface;
- $\delta n_{co}^2 = n_{co}^2 - n_l^2$, $\delta n_{sh}^2 = n_{sh}^2 - n_l^2$ for inclusions in a layer;

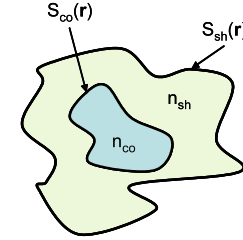


Fig. 45. The core-shell particle is made of a core of index of refraction n_{co} and of shape $S_{co}(\mathbf{r})$ and of a capping shell of index n_{sh} and of shape $S_{sh}(\mathbf{r})$. Note that, by convention, $S_{sh}(\mathbf{r})$ is the shape function of the whole particle and not only the capping shell (dotted area on figure).

- $\delta n_{co}^2 = 1 - n_l^2$, $\delta n_{sh}^2 = n_{sh}^2 - n_l^2$ for holes in a layer.

The core-shell particle form factor follows immediately from Eq. (143):

$$\begin{aligned} \mathcal{F}(\mathbf{q}_{||}, k_{iz}, k_{fz}) = & \mathcal{F}_{co}(\mathbf{q}_{||}, k_{iz}, k_{fz}) \\ & + \tau [\mathcal{F}_{sh}(\mathbf{q}_{||}, k_{iz}, k_{fz}) - \mathcal{F}_{co}(\mathbf{q}_{||}, k_{iz}, k_{fz})]. \end{aligned} \quad (144)$$

$\tau = \delta n_{sh}^2 / \delta n_{co}^2$ is the relative contrast between the core and the shell.

6.2.6. The Fourier transform of particle shape

As shown in the earlier work of Von Laue [214,71], the 3D integral over the volume V in the particle form factor Eq. (135):

$$F(\mathbf{q}) = \int_V e^{i\mathbf{q} \cdot \mathbf{r}} d^3\mathbf{r} = -\frac{1}{q^2} \int_V \nabla^2 [e^{i\mathbf{q} \cdot \mathbf{r}}] d^3\mathbf{r}, \quad (145)$$

can be transformed by means of the Green's theorem into a surface integral S :

$$F(\mathbf{q}) = -\frac{1}{q^2} \int_S \frac{\partial e^{i\mathbf{q} \cdot \mathbf{r}}}{\partial n} d^2\mathbf{r}, \quad (146)$$

in which $\frac{\partial}{\partial n}$ is the differentiation along the normal \mathbf{n} (oriented outwards of the particle) of the surface element $d^2\mathbf{r}$. \mathbf{q}_n is the component of \mathbf{q} along \mathbf{n} ,

$$F(\mathbf{q}) = -\frac{i}{q^2} \int_{S(\mathbf{r})} \mathbf{q}_n e^{i\mathbf{q} \cdot \mathbf{r}} d^2\mathbf{r}. \quad (147)$$

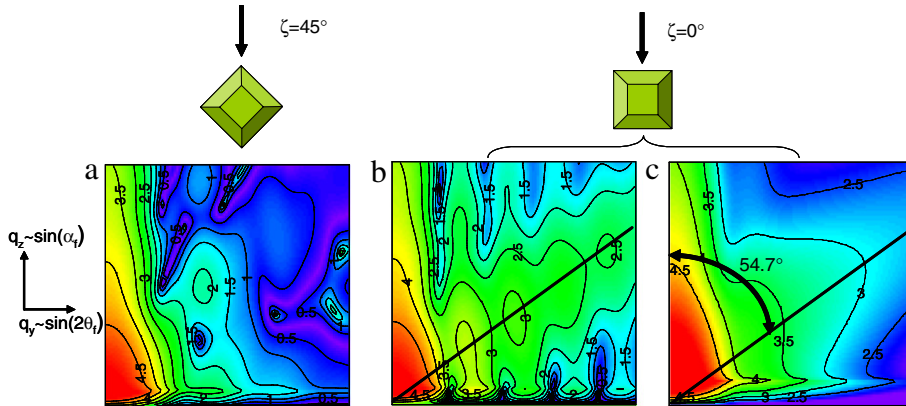


Fig. 46. Simulated GISAXS pattern of an square basis pyramidal island for two orientations ζ of the incoming beam with respect to the base edge: (a) $\zeta = 0^\circ$, (b) (c) $\zeta = 45^\circ$. Patterns a, b corresponds to an isolated particle while in pattern-c a size distribution was accounted for (see Section 6.3.3). The angle between the lateral facet and the substrate surface is that between (111) and (001) planes in fcc lattice i.e. 54.7° . The scattering angles range between $0 < 2\theta_f < 3^\circ$ while $\alpha_i = \alpha_c$. The numerical parameters are $\lambda = 0.1$ nm, $R = H = 5$ nm. (Interpreted from Ref. [27]).

The calculation can be further simplified if the crystal is bounded by a plane \mathcal{P} for which \mathbf{q}_n is constant; the contribution of this surface is:

$$F_{\mathcal{P}}(\mathbf{q}) = -\frac{i\mathbf{q}_n}{q^2} e^{i\mathbf{q}\cdot\mathbf{r}_n} \int_{\mathcal{P}} e^{i\mathbf{q}\cdot\mathbf{r}'} d^2\mathbf{r}' \quad (148)$$

For a scattering vector oriented along the normal to the surface, the integral in the previous equation reduces to the area $S_{\mathcal{P}}$ of the plane \mathcal{P} and $|F_{\mathcal{P}}(\mathbf{q})| = S_{\mathcal{P}}/q$ falls off inversely as q . Moving away from the surface normal at constant q , $F_{\mathcal{P}}(\mathbf{q})$ diminishes rapidly. The spines as Von Laue termed them which extend along \mathbf{q}_n and its opposite direction because of the Friedel rule $|F(-\mathbf{q})| = |F(\mathbf{q})|$ are known as facet truncation rods (see Section 6.2.7). In an exactly analogous way, the surface integral in Eq. (148) can be cast into a line integral over the contour of the plane \mathcal{P} and further simplified into the contribution of straight edges if any. Symmetry related faces or edges for polyhedrons can be paired and lead to pronounced interferences effects; intensity distribution have subsidiary spines in the direction perpendicular to well-defined edges. This reminds the notions of crystal truncation rod [11,12] in surface X-ray crystallography or of terrace truncation rod and step truncation rod for vicinal surfaces [215]. A clear experimental illustration of such phenomena in GISAXS was given by Vartanyants and coworkers [216] for Ge/Si quantum dots grown by liquid phase epitaxy.

A non-exhaustive library of $F(\mathbf{q})$ for basic shapes (Fig. 175) is given in Appendix. If the particle displays special symmetries, the expression of $F(\mathbf{q})$ reduces to a 1D integral or is even fully analytical. Each particle is characterized by a set of characteristic zeros of the interference fringes as well as by a given Porod exponent [29] (see Section 6.3.3 for definition and discussion). Of course, any azimuthal disorientation ζ of the particle axis z with respect to the incoming beam frame comes into play in the $F(\mathbf{q})$ formula through a rotation matrix of the wavevector transfer \mathbf{q} . For a rotation along z , this reads:

$$\mathcal{R}(\zeta)\mathbf{q} = \begin{pmatrix} \cos(\zeta) & \sin(\zeta) & 0 \\ -\sin(\zeta) & \cos(\zeta) & 0 \\ 0 & 0 & 1 \end{pmatrix} \begin{pmatrix} q_x \\ q_y \\ q_z \end{pmatrix} \quad (149)$$

6.2.7. Scattering from faceted particles

In reciprocal space, the facet gives rise to a scattering rod along the facet normal which width is inversely proportional to the lateral size of the facet. These rods anticipated by von Laue [214] are known as Crystal Truncation Rods (CTR) in the field of surface X-ray diffraction [12]. They can be clearly revealed when one

component of the wavevector transfer is perpendicular to the facet normal. In the scattering geometry of GISAXS (Fig. 46), this is easily achieved when the X-ray incident beam direction q_x is perpendicular to the facet normal. As the DWBA form factor of the particle $\mathcal{F}(\mathbf{q}_{||}, k_{iz}, k_{fx})$ can be written as a weighted sum of several $F(\mathbf{q})$, it also displays these scattering rods. Fig. 46 shows the scattering pattern of a square basis pyramidal particle which is typically encountered during the epitaxy of fcc metals on MgO(001) (see Section 4.7). The particle is limited by (111) and (001) planes that make an angle of 54.7° . A scattering rod tilted by 54.7° from the surface normal shows up when the beam is aligned along the particle edge (Fig. 46b). This anisotropic scattering feature disappears progressively upon rotation (Fig. 46a) and broadening of the size distribution. If the base angle is increased up to 90° and the particle shape reaches that of a parallelepiped, this scattering rod becomes parallel with the $q_y \sim 2\theta_f$ axis.

Through a combined experimental and theoretical work, Rauscher and coworkers [37] have highlighted the multiple scattering effects due to the grazing geometry in the case of nanoparticles. They have recorded the scattering pattern from faceted Ge quantum dots grown on boron terminated Si(111) for various incident angles and sample azimuths ω . On average, the particles have a tetrahedron shape exposing (113) facets and are oriented along the $(\bar{1}\bar{1}0)$ direction of the substrate. From the AFM microscopy (Fig. 47a), the particles have a size of 250 nm and a height of 30–50 nm. The particles are sufficiently large and separated to consider them as isolated; in other words, the interference effects lead to a correlation peak hidden by the specular rod. Fig. 47b shows the scattering curve at fixed α_f and α_i for several orientations ω with respect to the incoming beam. The scattering is not centro-symmetric with respect to $q_y \sim 2\theta_f$ because the particles are of three fold symmetry. The peaks on the left or right of the specular rod result from the cross-sections of the scattering rods of the tetrahedron as shown on the pattern Fig. 47c. This rod appears when the sides of the tetrahedrons are aligned with the X-ray beam ($\omega = 0, 60^\circ$). If present, the two bumps of Fig. 47b are due to the two dominating scattering terms in Eq. (134) and shown on Fig. 43: the Born one with a perpendicular wavevector transfer $k_{fx} - k_{iz}$ and the one involving the reflection of the incident wave on the substrate $k_{fx} + k_{iz}$ (Fig. 41). The others are negligible in the recorded angular range. In passing, a clear discussion about the symmetry of the particle and the Friedel rule in GISAXS can be found in this reference. Several similar experimental examples of scattering rods by faceted particles can be found in Section 7.

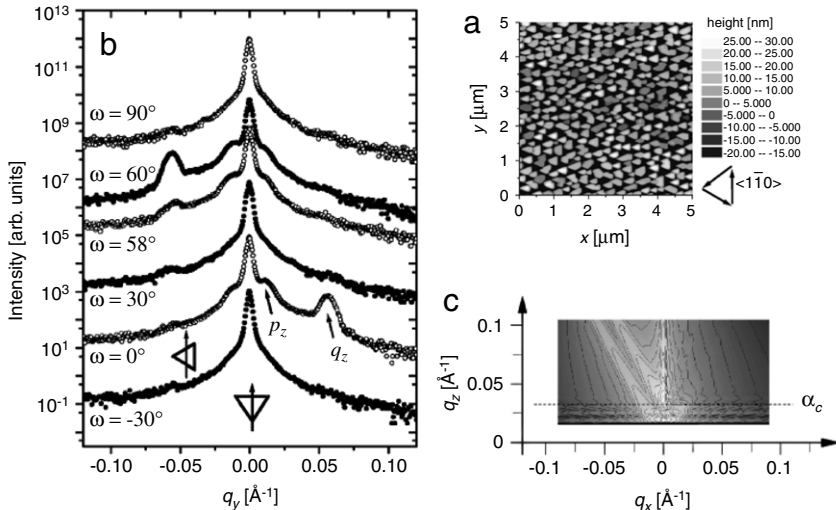


Fig. 47. GISAXS from Ge quantum dots grown on Si(111). (a) Atomic force microscopy of the Ge islands. The particles display a tetrahedron shape with their edges aligned along the $\langle 1\bar{1}0 \rangle$ direction of the substrate. (b) GISAXS cross-sections at $\alpha_i = 0.44^\circ$, $\alpha_f = 0.7^\circ$ for several in-plane azimuthal orientations ω . (c) Mapping in the $q_y - q_z$ plane of the scattering for $\alpha_i = \alpha_c = 0.177^\circ$. The lateral (113) facet gives rise to a scattering rod that is split because of multiple scattering effects. (From Ref. [37]).

6.2.8. Miscellaneous remarks

Several common features of the scattering cross-section of nanoparticles Eqs. (133), (136), (141) and (144) can be highlighted:

- as expected from classical small angle scattering [73,217], the intensity is proportional to the contrast of dielectric constants between that of the embedding medium and that of the nanoparticles;
- at high scattering angles *i.e.* for $\alpha_i, \alpha_f \gg \alpha_c$, the particle form factor reduces to the Born one Eq. (135) as the Fresnel coefficients go to zero (see Fig. 25). The analysis is simplified but at the expense of a reduced scattered intensity (see Fig. 42) and of an increase of the bulk background due to a higher scattering depth.
- at the opposite limit, for very shallow angles $\alpha_i, \alpha_f \ll \alpha_c$, the smallness of $k_{iz}, k_{fz} \simeq 0$ allows the following factorization for the island form factor Eq. (134):

$$\begin{aligned} \mathcal{F}(\mathbf{q}_{||}, k_{iz}, k_{fz}) &\simeq F(\mathbf{q}_{||}, 0)(1 + r_{0,1}^i + r_{0,1}^f + r_{0,1}^i r_{0,1}^f) \\ &= F(\mathbf{q}_{||}, 0)(1 + r_{0,1}^i)(1 + r_{0,1}^f) = F(\mathbf{q}_{||}, 0)t_{0,1}^i t_{0,1}^f. \end{aligned} \quad (150)$$

The formula for inclusions or holes Eq. (136) is recovered. A similar result is obtained for particles embedded in a layer. This scattering configuration corresponds nearly to transmission.

6.2.9. Direct data inversion from coherent GISAXS?

In the hard X-ray regime, coherent diffraction is a new and fast developing imaging technique of micrometer size particles giving access to the shape, strain and defects with $\simeq 20$ nm spatial resolution (see recent works Refs. [218–222] and all references therein). The method can afford imaging crystalline as well as non-crystalline materials, and is free of the inherent ensemble averaging of a classical scattering experiment (Section 5.3.3). The technique relies on iterative algorithms of phase retrieval of scattering patterns; in principle, it is aberration free, three dimensional and with a high spatial resolution. Contrary to holographic technique for which an interference between a reference wave of known phase and a diffracted wave is used to retrieve the missing phase,³ the method is based on the oversampling of the diffraction pattern of an object that is illuminated coherently; if the sampling

³ This idea is used in direct method of electron density recovery from surface diffraction measurements; the reference wave is the bulk scattering while the unknown one is the surface contribution (see Ref. [223]).

is at least twice the frequency required by the Shannon principle, the real space image can be in principle recovered uniquely in a model independent way using back and forth Fourier transforms between real and reciprocal space starting from random phases and using physical constraints and tricks to avoid stagnation. This technique is obviously advantageous for non-periodic samples or for internal structure characterization [221,222] if the beam coherence volume (around a few μm^3 at that time on third generation sources) is sufficiently large. The experiments are preferentially performed around a lattice Bragg peak to avoid background scattering and direct beam signal removal and to achieve sensitivity to crystalline defects. Experimentally, a coherent beam on a third generation synchrotron is prepared from a partially coherent one by cutting it with an aperture (micrometer size pinhole) smaller than the lateral coherence of the X-ray source; a 2D detector (or a 1D with pinhole aperture) is used as detector.

The first observations of coherent scattering from surface roughness [224–227] were performed in the reflectivity geometry. Due to this arrangement, the footprint of the beam on the sample is highly elongated such that its speckle pattern becomes one dimensional. The reconstruction of the 1D profile of the topography was achieved successfully with the above described algorithm [228] and used to describe the kinetics of silicon oxidation [227]. In the GISAXS geometry, test samples made of arrays of SiGe quantum dots grown on a patterned surface [229] have been inverted successfully; the size of the particles were in the $\simeq 100$ nm range. Speckle modulations from grain boundaries in a thin film [230] have also been explored as function of the scattering depth. In the present state of art, the imaging of one individual nanoparticle is impossible because of the experimental difficulties to single out a nanometer-sized object even with micro-focused beams and because of the too small scattering signal. In the near future, the availability of the 4th generation synchrotron in the form of Free Electron Laser opens the way for interesting perspectives of imaging with coherent X-ray diffraction of one isolated nanoobject.

Vartanyants and coworkers [231] have tested theoretically the influence of multiple scattering in the image formation and reconstruction of individual particles of nanometer size in the framework of coherent GISAXS. The algorithm of phase retrieval used by these authors relies on two constraints: the modulus of the scattered amplitude is replaced by the “experimental” one $\sqrt{I_{\text{exp}}(\mathbf{q})}$ and the average electronic density is assumed to be real

and positive. The result of the reconstruction of the calculated scattering from a square basis pyramid shown in Fig. 48 is easily explained starting from Eq. (134). When accounting only for two scattering channels for $\alpha_f \gg \alpha_c$ i.e. $r_{0,1}^f \ll 1$, this equation can be recast in the following form:

$$\begin{aligned}\mathcal{F}(\mathbf{q}_{\parallel}, k_{iz,0}, k_{fz,0}) &= \int S(\mathbf{r}) [r_{0,1}^i + e^{2ik_{iz,0}}] e^{i\mathbf{q}_{\parallel} \cdot \mathbf{r}_{\parallel}} e^{i(k_{fz,0}+k_{iz,0})z} d^3\mathbf{r} \\ &= \int \tilde{S}(\mathbf{r}) e^{i\mathbf{q}_{\parallel} \cdot \mathbf{r}_{\parallel}} e^{i(k_{fz,0}+k_{iz,0})z} d^3\mathbf{r}. \quad (151)\end{aligned}$$

The form factor appears as the Fourier transform of the complex function $\tilde{S}(\mathbf{r}) = S(\mathbf{r})(r_{0,1}^i + e^{2ik_{iz,0}})$. Because of the constraints on the electronic density introduced in the inversion scheme (symmetrisation of the whole scattering pattern along the z-axis), the final reconstruction is sensitive only to the modulus of the real part of $\tilde{S}(\mathbf{r})$:

$$|\text{Re}(\tilde{S}(\mathbf{r}))| = S(\mathbf{r}) [|r_{0,1}^i| \cos \phi(\alpha_i) + \cos(2k_{iz,0}z)], \quad (152)$$

where $\phi(\alpha_i)$ is the phase of the reflection coefficient $r_{0,1}^i$. For $\alpha_i = \alpha_c$, $\phi(\alpha_i) = 0$, $r_{0,1}^i = 1$, one gets:

$$|\text{Re}(\tilde{S}(\mathbf{r}))| \simeq S(\mathbf{r}) [1 + \cos(2k_{iz,0}z)]. \quad (153)$$

The original shape function is modulated by a function of period $\pi/k_{iz,0}$ as seen from the stripes appearing in Fig. 48c. For $\alpha_i \leq \alpha_c$, the situation is more complex as all the scattering channels of Fig. 41 contribute in particular for $\alpha_f \leq \alpha_c$ (see Fig. 42). For $\alpha_i, \alpha_f \gg \alpha_c$ the kinematic channel dominates ($r_{0,1}^i, r_{0,1}^f \ll 1$) and the reconstruction procedure sees:

$$|\text{Re}(\tilde{S}(\mathbf{r}))| \simeq S(\mathbf{r}) [\cos(2k_{iz,0}z)]. \quad (154)$$

The shape function is modulated by a fast oscillations that cannot be resolved during reconstruction (see Fig. 48d). In conclusion, multiple scattering hampers a direct reconstruction of the particle shape in the GISAXS geometry; however, the best conditions are found for $\alpha_i = \alpha_c$.

6.3. Concentrated case

When the particle concentration increases, two phenomena have to be taken into account:

- (i) the waves scattered by different particles can interfere in a way that depends on their spatial organization, their size and shape distribution and on the coupling between both;
- (ii) for shallow angles, a scattered wave may be scattered again by an other particle.

Once included multiple scattering effects at interfaces in the DWBA form factor, the formal treatment of point (i) can be found in many references of the literature dealing with X-ray scattering or diffraction from crystals [40,73,41,71], amorphous materials [171] or nanoparticles in bulk [73,217]. Because the scattering from surfaces is at the heart of this review, the particles will be assumed to lie in a plane; particular attention will be paid on the analysis in terms of partial interference functions. The case of oriented particles in 3D will be dropped on purpose. Some comments about the diffraction from thin films made of 3D self-assembled nanostructures can be found in Refs. [154].

Point (ii) is a consequence of the grazing incidence geometry, e.g. the layer of particles itself influences the propagation of the incident and scattered waves. The model of the graded interface will cure this point still keeping the notion of particle form factor.

6.3.1. General formalism of the partial interference functions: Coherent versus incoherent scattering

In the case of $N \gg 1$ particles of shape $S_i(\mathbf{r})$ located at $\mathbf{r}_{\parallel,i}$, the scattering potential is:

$$\delta n^2(\mathbf{r}) = \Delta n^2 \sum_{i=1}^N S_i(\mathbf{r}) \otimes \delta(\mathbf{r} - \mathbf{r}_{\parallel,i}), \quad (155)$$

\otimes stands for the folding product; the dielectric contrast Δn^2 varies from one type of morphology to another (Fig. 40). To go further on, one takes benefit of the decoupling between the parallel and perpendicular directions in the DWBA scattering cross-sections. Indeed, the parallel dependence of the wavefields (see Eqs. (132) and (138) for instance) of Eq. (91) introduces a simple Fourier transform (no DWBA effect) whereas the perpendicular dependence acts only on the particles shape $S_i(\mathbf{r})$ but DWBA effects come into play. Using the expression of the form factor suitable for each geometry, the scattering cross-section reads:

$$\begin{aligned}\left(\frac{d\sigma}{d\Omega} \right)_{\text{tot}} &= \frac{k_0^4}{16\pi^2} |\Delta n^2|^2 N \left(\frac{d\sigma}{d\Omega} \right)_{\text{part}}, \\ \left(\frac{d\sigma}{d\Omega} \right)_{\text{part}} &= \frac{1}{N} \left| \sum_{i=1}^N \mathcal{F}_i(\mathbf{q}_{\parallel}, k_{iz}, k_{fz}) e^{i\mathbf{q}_{\parallel} \cdot \mathbf{r}_{\parallel,i}} \right|^2. \quad (156)\end{aligned}$$

As explained in Section 5.3.3, a real measurement is sensitive only to an ensemble average $\langle \dots \rangle$ of the cross-section per particle over the “coherent domains”. The size of the coherent domains A_{coh} is limited by the coherence of the incident beam (wavelength spread and angular divergence) and by the angular resolution of the detector. If A_{coh} is sufficiently large (but still smaller than the footprint of the incident beam) and if the sample is homogeneous, it is possible to use statistical quantities that are representative of all the sample. The particles can be sorted out by class of size and shape α with a density of probability p_α while their relative positions can be described through the reduced⁴ partial pair correlation functions $g_{\alpha\beta}(\mathbf{r}_{\parallel})$. If n_s is the number of particles per surface unit, $n_s p_\beta g_{\alpha\beta}(\mathbf{r}_{\parallel}) d\mathbf{r}_{\parallel}$ is the number of particles of kind β at a position \mathbf{r}_{\parallel} from a central one of kind α . $g_{\alpha\beta}(\mathbf{r}_{\parallel}) = g_{\beta\alpha}(\mathbf{r}_{\parallel})$ and $g_{\alpha\beta}(\mathbf{r}_{\parallel} \rightarrow \infty) \simeq 1$ for disordered systems. The ensemble average of Eq. (156) can be written in the form [73,217,27]:

$$\begin{aligned}\left(\frac{d\sigma}{d\Omega} \right)_{\text{part}} &= N \left| \langle \mathcal{F}(\mathbf{q}_{\parallel} = 0, k_{iz}, k_{fz}) \rangle \right|^2 \delta(\mathbf{q}_{\parallel}) + \Phi_0(\mathbf{q}_{\parallel}, k_{iz}, k_{fz}) \\ &+ \sum_{\alpha, \beta} p_\alpha p_\beta \mathcal{F}_\alpha(\mathbf{q}_{\parallel}, k_{iz}, k_{fz}) \mathcal{F}_\beta^*(\mathbf{q}_{\parallel}, k_{iz}, k_{fz}) S_{\alpha\beta}(\mathbf{q}_{\parallel}), \quad (157)\end{aligned}$$

$$\Phi_0(\mathbf{q}_{\parallel}, k_{iz}, k_{fz}) = \left\langle \left| \mathcal{F}(\mathbf{q}_{\parallel}, k_{iz}, k_{fz}) \right|^2 \right\rangle - \left| \langle \mathcal{F}(\mathbf{q}_{\parallel}, k_{iz}, k_{fz}) \rangle \right|^2, \quad (158)$$

$$S_{\alpha\beta}(\mathbf{q}_{\parallel}) = 1 + n_s \int_A (g_{\alpha\beta}(\mathbf{r}_{\parallel}) - 1) e^{i\mathbf{q}_{\parallel} \cdot \mathbf{r}_{\parallel}} d\mathbf{r}_{\parallel}. \quad (159)$$

$\langle \dots \rangle$ is the average over the size-shape distribution p_α . The star symbol corresponds to the complex conjugate. The partial interference function $S_{\alpha\beta}(\mathbf{q}_{\parallel}) - 1$ appears as the Fourier transform of $g_{\alpha\beta}(\mathbf{r}_{\parallel}) - 1$. The -1 -term in Eq. (159) singles out the oscillatory behavior of $g_{\alpha\beta}(\mathbf{r}_{\parallel})$ around its asymptotic value. Other definitions of $g_{\alpha\beta}(\mathbf{r}_{\parallel})$ and $S_{\alpha\beta}(\mathbf{q}_{\parallel})$ are available in the literature; their links and their properties are detailed in Ref. [171]. Those used herein are known as the Faber-Ziman ones [232].

⁴ The term “reduced” or “normalized” means that the pair correlation function is suitably normalized by the particle concentration. This terminology will be dropped out in the following.

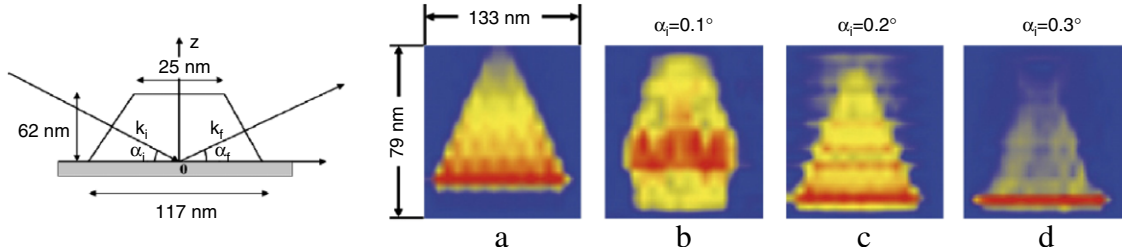


Fig. 48. (Left) Shape and size of the island used in the inversion of the coherent GISAXS patterns. (Right) Reconstructed shape from kinematic scattering equation (135) or multiple scattering equation (134) for several incident angles α_i ($\alpha_c = 0.2^\circ$ in that case). From Ref. [231].

Three terms appear in the cross-section Eq. (157):

- a “specular rod” at $q_{\parallel} \simeq 0$. This term is proportional to the number of particles in the “coherent domain” ($n_s \int_{A_{coh}} e^{i\mathbf{q}_{\parallel} \cdot \mathbf{r}_{\parallel}} d\mathbf{r}_{\parallel} \rightarrow N\delta(q_{\parallel})$ when $A_{coh} \rightarrow \infty$) and is modulated by the particle form factor at $q_{\parallel} = 0$. The specularly reflected beam adds up on this rod at $\alpha_f = \alpha_i$. The shape of this rod is given by all sources of coherence loss. Scarcely measured in GISAXS geometry as it is hidden by the beam stop, the specular rod intensity can be integrated through offset scans in reflectivity.
- an incoherent term $\Phi_0(\mathbf{q}_{\parallel}, k_{iz}, k_{fz})$ due to the fluctuations of sizes and shapes of particles. An analogy can be drawn with the incoherent neutron scattering length due to isotopic effects or the Debye–Waller-like uncorrelated thermal background [40,41,38].
- a coherent term that includes the interferences between waves scattered by different particles.

6.3.2. The decoupling approximation and the local monodisperse approximation

The practical use of Eq. (157) for data analysis is hampered by the lack of knowledge of all the partial pair correlation functions. Modeling $g_{\alpha\beta}(\mathbf{r}_{\parallel})$ would require a deep knowledge of the correlations of location between particles of different sizes or shapes and is beyond the scope of a simple analysis of experimental GISAXS patterns. Approximations are required. Further details will be given in Section 6.4.

Decoupling Approximation. The Decoupling Approximation (DA) [40] consists of neglecting all the correlations between the kind of scatterers and their relative location. With this approximation of completely uncorrelated spatial disorder, all the partial pair correlation functions $g_{\alpha\beta}(\mathbf{r}_{\parallel})$ are replaced by a common function $g(\mathbf{r}_{\parallel})$ obtained for a suitable monodisperse system [233]:

$$\left(\frac{d\sigma}{d\Omega} \right)_{\text{part}} = \Phi_0(\mathbf{q}_{\parallel}) + |\langle \mathcal{F}(\mathbf{q}_{\parallel}, k_{iz}, k_{fz}) \rangle|^2 S(\mathbf{q}_{\parallel}), \quad (160)$$

$$S(\mathbf{q}_{\parallel}) = 1 + n_s \int_A (g(\mathbf{r}_{\parallel}) - 1) e^{i\mathbf{q}_{\parallel} \cdot \mathbf{r}_{\parallel}} d\mathbf{r}_{\parallel}. \quad (161)$$

$S(\mathbf{q}_{\parallel})$ is known as the total interference function irrespective of the particles type. It is the Fourier transform of the total reduced pair correlation function (see Section 6.3.4).

Local Monodisperse Approximation. The Local Monodisperse Approximation introduced by Pedersen [234] assumes that the particle collection is made of monodisperse domains which size are larger than the coherence length of the X-ray beam. At variance to the DA, a nearly perfect correlation between the size and shape of neighboring particles is assumed [235]. As the monodisperse domains interfere incoherently, the LMA cross-section reads:

$$\left(\frac{d\sigma}{d\Omega} \right)_{\text{part}} = \left\langle |\mathcal{F}_D(\mathbf{q}_{\parallel}, k_{iz}, k_{fz})|^2 S_D(\mathbf{q}_{\parallel}) \right\rangle_D. \quad (162)$$

$\langle \dots \rangle_D$ is the average over the domain D in which the local interference function $S_D(\mathbf{q}_{\parallel})$ can depend on the particle size.

6.3.3. Size and shape distributions and the asymptotic behaviors of the form factor

Once known the statistical distributions of the morphological quantities that characterize all the particles, the averaged form factor of Eq. (157) is easily computed. Fig. 49 summarizes the main effects of the broadening of the particle size distribution in the Born approximation. Sharp fringes of interference are observed for monodisperse particles; the fringe minima positions are linked to the zeros of the particle form factor and do depend on the particles size and shape (Sine cardinal $\sin(x)/x$ function for a box, Bessel cardinal function $J_1(x)/x$ for a cylinder; see Appendix). Upon broadening of the size distribution, these fringes are washed out in $\langle |\mathcal{F}(\mathbf{q}_{\parallel}, k_{iz}, k_{fz})|^2 \rangle$. However, the behaviors of $\langle |\mathcal{F}(\mathbf{q}_{\parallel}, k_{iz}, k_{fz})|^2 \rangle$ and $\langle |\mathcal{F}(\mathbf{q}_{\parallel}, k_{iz}, k_{fz})| \rangle^2$ are pretty different as the first one involves an incoherent average of the scattering and the second one still keeps a phase factor between particles of different sizes. This difference gives rise to a peaked behavior of the incoherent scattering term $\Phi_0(\mathbf{q}_{\parallel}, k_{iz}, k_{fz})$ (Eq. (158)) at $\mathbf{q}_{\parallel} = 0$.

Porod limit. For particle systems with lack of long range order, all the partial pair correlations and interference functions tend asymptotically toward one at high scattering angles or high wavevector transfers. As a consequence, in this uncorrelated regime, the scattering cross-section per particle $(\frac{d\sigma}{d\Omega})_{\text{part}}$ is

dominated only by the particle form factor $\langle |\mathcal{F}(\mathbf{q}_{\parallel}, k_{iz}, k_{fz})|^2 \rangle$ which tends toward its Born value $\langle |\mathcal{F}(\mathbf{q})|^2 \rangle$ as shown in Section 6.2. $\langle |\mathcal{F}(\mathbf{q})|^2 \rangle$ presents an asymptotic power law decrease as q_{\parallel}^{-n} and q_z^{-n} . The exponents depend precisely on the particle shape. This behavior was already underlined in the general comments about the Fourier transform of a particle shape (see Section 6.2.6). The case of a cylinder is straightforward:

$$F_{cy}(\mathbf{q}, R, H) = F_{cy}^{\parallel}(\mathbf{q}_{\parallel}, R) F_{cy}^z(q_z, H),$$

$$F_{cy}^{\parallel}(\mathbf{q}_{\parallel}, R) = \pi R^2 \frac{J_1(q_{\parallel}R)}{q_{\parallel}R}; \quad F_{cy}^z(q_z, H) = H \sin_c(q_z H/2). \quad (163)$$

Using $J_1(x) \xrightarrow{x \rightarrow +\infty} \sqrt{\frac{2}{\pi x}} \cos(x - \frac{3\pi}{4})$ [165], the asymptotic behavior is:

$$\begin{aligned} \langle |F_{cy}(\mathbf{q}_{\parallel}, R)|^2 \rangle &\stackrel{q_{\parallel} \rightarrow +\infty}{\simeq} \frac{2}{\pi q_{\parallel}^3} \langle R \cos^2(q_{\parallel}R - 3\pi/4) \rangle \\ &= \frac{1}{\pi q_{\parallel}^3} (\langle R \rangle - \langle R \sin(2q_{\parallel}R) \rangle), \end{aligned} \quad (164)$$

$$\langle |F_{cy}(q_z, H)|^2 \rangle = \frac{4}{q_z^2} \langle \sin^2(q_z H/2) \rangle = \frac{2}{q_z^2} (1 - \langle \cos(q_z H) \rangle). \quad (165)$$

The asymptotic value at high q of Eqs. (164)–(165) is zero as the size distributions are bounded functions. The inferred exponents

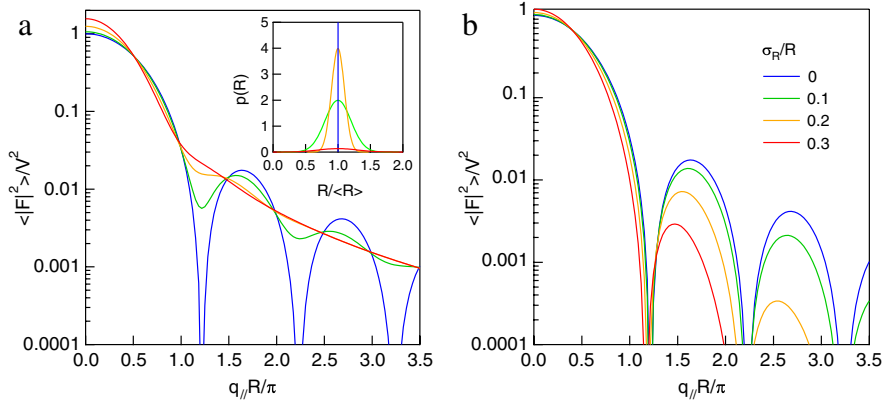


Fig. 49. Mean form factors of a cylinder and size distribution. (a) $\langle |F(q_{\parallel} R)|^2 \rangle$, (b) $\langle |F(q_{\parallel} R)|^2 \rangle / V$. The inset shows the used Gaussian size distribution with a variance σ_R/R ranging from 0, 0.1, 0.2, 0.3. The Born form factor has been normalized by the corresponding averaged volume.

are $n = 3$ and $m = 2$. As a general rule, this asymptotic behavior is reached if $q_{\parallel} \sigma_R \gg 1$ or $q_z \sigma_H \gg 1$ where $\sigma_{R,H}$ are a measure of the size distribution width. Also $n = m = 4$ for a full sphere, $n = m = 2$ for a parallelepiped. Even if the particle shape can be guessed from the asymptotic behavior, it should be kept in mind that exponent determination is often limited by signal/noise ratio, orientational averages⁵ or cross coupling between the parallel and perpendicular directions. To our knowledge, no determination of Porod dimensions [217] from scattering invariants (*i.e.* integrals of intensity over reciprocal space) was ever applied to GISAXS analysis contrary to bulk small angle scattering because of the inherent anisotropy between the parallel and perpendicular directions and the multiple scattering effects that invalidate the underlying approximations.

Guinier limit. For completely uncorrelated particles or in other words for very diluted systems, $S_{\alpha\beta}(\mathbf{q}_{\parallel}) = 1$ (Eq. (157)) and the scattering is driven only by the average particle form factor $\langle |\mathcal{F}(\mathbf{q}_{\parallel}, k_{iz}, k_{fz})|^2 \rangle$ as each particle scatter independently. The Guinier limit deals with the asymptotic behavior of the form factor close to the origin of reciprocal space. In the Born approximation, if the wavevector transfer \mathbf{q} tends toward zero along a direction \mathbf{n} , the Born form factor recasts in the following way [73,217]:

$$|F(\mathbf{q})|^2 \stackrel{q_n \rightarrow 0}{\simeq} V^2 (1 - q_n^2 R_g^2) \simeq V^2 e^{-q_n^2 R_g^2}, \quad (166)$$

R_g^2 , known as the gyration radius, is the inertial momentum of the particle with respect to the plane Π perpendicular to \mathbf{n} and going through the center of gravity of the particle:

$$R_g^2 = \frac{1}{V} \int_V d^2[\mathbf{M}(\mathbf{r}), \Pi] d\mathbf{r}. \quad (167)$$

Such an expansion is valid in the $q_n R_g \ll 1$ range. For size distributed or more or less randomly oriented particles, an average gyration radius $\langle R_g^2 \rangle$ is assessed from the slope of the logarithmic plot of the scattered intensity versus q_n^2 .

However, if measurements on truly uncorrelated particles are available, such a gyration radius analysis is questionable in GISAXS because the form factor is not simply the Fourier transform of the particle shape but involves multiple scattering effects along the perpendicular direction. For buried particle, a transmission function $t_{01}^f \stackrel{\alpha_f \rightarrow 0}{\simeq} \alpha_f / (\alpha_f + i\alpha_c)$ inside the substrate comes into play as well as a shift on the q_z component due to refraction of the incident beam. Along the parallel direction,

⁵ For instance, randomly in-plane oriented parallelepipeds give rise to a $n = 3$ exponent as for cylinder.

the Guinier approximation is justified if the form factor can be decomposed into two independent components along both directions $\mathcal{F}(\mathbf{q}_{\parallel}, k_{iz}, k_{fz}) = F_{\parallel}(\mathbf{q}_{\parallel}) \mathcal{F}_{\perp}(k_{iz}, k_{fz})$ (cylinder for instance). However, one has to bear in mind that in this case, the gyration radius obtained from $F_{\parallel}(\mathbf{q}_{\parallel})$ results from a surface and not from a volume integral as in Eq. (167).

6.3.4. The interference function

As usual in X-ray crystallography [40], two kinds of disorder can be distinguished in the collection of nanoparticles. They lead to different interference function behaviors:

- Disorder of the first kind keeps the long range order in the system and gives rise only to a decrease of the Bragg peaks intensity at high angles;
- Disorder of the second kind is characterized by a broadening of the peaks at high angles due to a progressive loss of correlation between particle positions.

Pair correlation function in disordered systems. Disordered systems characterized by the loss of long range order are defined by their reduced total pair correlation function $g(\mathbf{r}_{\parallel})$. For a homogeneous system, it depends only on the relative position of the scatterers irrespective of their size or shape. The autocorrelation of the particle position $z(\mathbf{r}_{\parallel})$ is related to $g(\mathbf{r}_{\parallel})$ through:

$$z(\mathbf{r}_{\parallel}) = \frac{1}{N} \left\langle \sum_{i,j} \delta(\mathbf{r}_{\parallel} - \mathbf{r}_{\parallel,i} + \mathbf{r}_{\parallel,j}) \right\rangle = \delta(\mathbf{r}_{\parallel}) + n_S g(\mathbf{r}_{\parallel}). \quad (168)$$

as $n_S g(\mathbf{r}_{\parallel})$ counts the number of particles per surface unit located at \mathbf{r}_{\parallel} from a central one. The average value n_S is often singled out to enhance the oscillatory part of $g(\mathbf{r}_{\parallel})$ around its mean value: $z(\mathbf{r}_{\parallel}) = \delta(\mathbf{r}_{\parallel}) + n_S + n_S(g(\mathbf{r}_{\parallel}) - 1)$. By a Fourier transform of the last equation, the total interference function $S(\mathbf{q}_{\parallel})$ shows up:

$$S(\mathbf{q}_{\parallel}) = 1 + N \delta(\mathbf{q}_{\parallel}) + n_S \int_A [g(\mathbf{r}_{\parallel}) - 1] e^{i\mathbf{q}_{\parallel} \cdot \mathbf{r}_{\parallel}} d\mathbf{r}_{\parallel}. \quad (169)$$

Once broadened by limited instrumental resolution, the $N \delta(\mathbf{q}_{\parallel})$ term is nothing other than the specular rod which is often dropped in the interference function as it is hidden by the beam stop. For 2D isotropic samples, $g(r_{\parallel})$ and $S(q_{\parallel})$ depend only on the moduli r_{\parallel} and q_{\parallel} and are related through a Hankel transform:

$$S(q_{\parallel}) = 1 + N \delta(q_{\parallel}) + n_S \int_A [g(r_{\parallel}) - 1] J_0(q_{\parallel} r_{\parallel}) r_{\parallel} dr_{\parallel}. \quad (170)$$

In a general way, $g(r_{\parallel})$ (respectively $S(q_{\parallel})$) shows broader and broader peaks upon increasing r_{\parallel} (respectively q_{\parallel}) which spacings

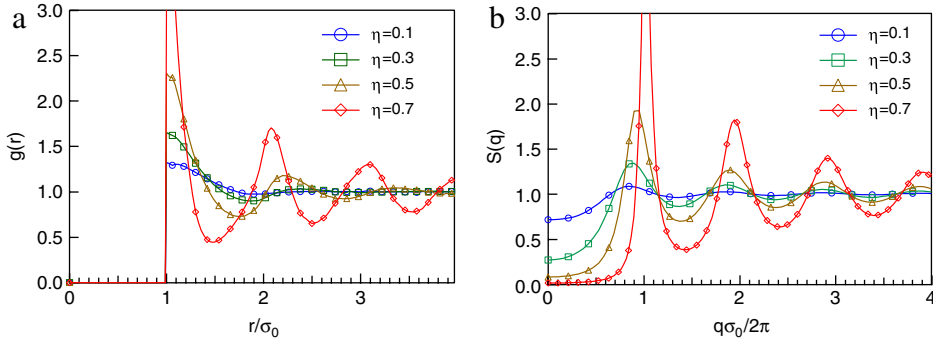


Fig. 50. (a) Pair correlation function $g(r_{\parallel})$ and (b) interference function $S(q_{\parallel})$ of hard core interacting disks of diameter σ_0 as function of the surface coverage η .

are related to the mean distance between particles D (its inverse $2\pi/D$) while $g(r_{\parallel}), S(q_{\parallel}) \rightarrow 1$ when $r_{\parallel}, q_{\parallel} \rightarrow +\infty$. Practical modeling of $g(r_{\parallel})$ function relies on the interaction between particles. Theoretical models like the Percus-Yevick or the hyper-netted chain approximations were developed in the field of fluids thermodynamics [77] to compute $g(r_{\parallel})$ from the pair potential interaction between molecules. The most simple case is that of particles interacting through a hard core potential. It is analytical in 3D while only approximate solution are known in 2D [76]. From Fig. 50, a preferential ordering at a distance equal to the diameter is observed. However, depending on the system studied and the elaboration method, particles (in particular in hard condensed matter) do not interact through a well defined potential and the correlations between particles (size and spacing) are dominated by kinetic effects (e.g. random nucleation process).

Scattering by ordered systems. As in conventional crystallography, scattering or more precisely diffraction by an ordered lattice of particles gives rise to Bragg peaks at the nodes of the reciprocal lattice defined with two basis vectors:

$$\mathbf{a}^* = 2\pi \frac{\mathbf{b} \wedge \mathbf{n}}{\mathbf{a} \cdot [\mathbf{b} \wedge \mathbf{n}]}, \quad \mathbf{b}^* = 2\pi \frac{\mathbf{n} \wedge \mathbf{a}}{\mathbf{b} \cdot [\mathbf{n} \wedge \mathbf{a}]}, \quad (171)$$

a, b are the two direct space basis vectors in the surface plane and **n** is the surface normal. The total interference function is made of sharp Bragg rods extending perpendicular to the surface:

$$S(\mathbf{q}_{\parallel}) = \sum_n \sum_m \delta(\mathbf{q}_{\parallel} - n\mathbf{a}^* - m\mathbf{b}^*). \quad (172)$$

For perfectly organized particles, the in-plane rod shape δ is a Dirac peak; in practice, those rods are broadened by defects, by finite size effects and by limited coherence of the beam. Their shape depends on the prevailing disorders [27] and the inverse of their width is a direct measure of the coherence length of the lattice. In the case of diffraction by a super lattice of particles, the curvature of the Ewald sphere is no longer negligible contrary to disordered systems for which the approximation $q_{\parallel} \simeq q_y$ is appropriate. Some experimental illustrations are given for patterned silicon substrates (Section 8.5.9) or for the self-organized growth of Co/Au(111) (see Section 9.4.1).

Paracrystalline domains. The paracrystalline description of scattering [40,41,236] belongs to the second kind of disorder. The paracrystal model was popularized in the 50th by Hosemann and coworkers [42,237,238]. The paracrystal lattice of nodes is basically a one-dimensional Markov chain where the loss of long range order is introduced in a cumulative way from point to point through the knowledge of the distance probability $p(x)$ between two neighboring nodes.

The node-node autocorrelation function $g_+(x)$ for positive values $x \geq 0$ reads:

$$g_+(x) = p(x) + (p \otimes p)(x) + (p \otimes p \otimes p)(x) + \dots \quad (173)$$

Each term corresponds to the distance probability of the n th neighbors to the origin. For instance between the origin and the second neighbor, the probability of having a distance x is the product of the probability of having a distance y up to the first neighbor $p(y)$ and a distance $x-y$ (i.e. $p(x-y)$) between the first and second neighbor integrated over all the intermediate distances y . This is nothing other than the folding product of $p(x)$ by itself ($p \otimes p$)(x). Once added the contribution of the origin $\delta(x)$ and of $x < 0$ i.e. $g_-(x) = g_+(-x)$, the interference function is obtained by Fourier transform of the total pair correlation function $g(x) = \delta(x) + g_+(x) + g_-(x)$:

$$S(q) = 1 + \mathcal{P}(q) + \mathcal{P}(q) \cdot \mathcal{P}(q) + \mathcal{P}(q) \cdot \mathcal{P}(q) \cdot \mathcal{P}(q) + \dots + c.c. + \dots \quad (174)$$

where $\mathcal{P}(q)$ is the characteristic function of the probability law $p(x)$ i.e. its Fourier transform. The geometric sum of Eq. (174) is convergent as $|\mathcal{P}(q)| \leq \int p(x)dx = 1$:

$$S(q) = \text{Re} \left[\frac{1 + \mathcal{P}(q)}{1 - \mathcal{P}(q)} \right]. \quad (175)$$

Finite size effects can be easily accounted for by restricting the sum to a given number of nodes [239,240,42,241,242]. For normally distributed distances,

$$p(x) = \frac{1}{\sigma_D \sqrt{2\pi}} e^{-\frac{(x-D)^2}{2\sigma_D^2}}, \quad \mathcal{P}(q) = e^{\pi q^2 \sigma_D^2} e^{iqD}. \quad (176)$$

the interference function is known as the Hosemann one:

$$S(q) = \frac{1 - \phi(q)^2}{1 + \phi(q)^2 - 2\phi(q) \cos(qD)}, \quad \phi(q) = \exp[\pi q^2 \sigma_D^2]. \quad (177)$$

As shown in Fig. 51, the reflections get broader and broader upon increasing the width of the distance distribution σ . The generalization to higher dimensions [42,243,244] is possible only in the framework of the perfect paracrystal for which the unit cells are parallelograms. The inherent restriction is the uncoupling of the distance distributions along all directions of space. This leads to an unphysical divergence of the scattering close to the origin and to scattering patterns that do not fulfill the symmetry of the mean unit cell. Those drawbacks can be cured by finite size effects [42,241] and symmetrization procedure [245]. Averaging over orientations allows to define a radial pair correlation function in dimension higher than one [27,239,240] (Section 6.3.4).

Among others, several applications of the paracrystal modeling to GISAXS data analysis can be found in Refs. [246,150,247,155,81,248] (see Sections 7 and 9.4). Scattering from stepped surfaces (Ref. [215] and references therein, see Section 9.4.2) is a special application of such paracrystal modeling for which the distances between neighboring terraces is exactly related to their sizes.

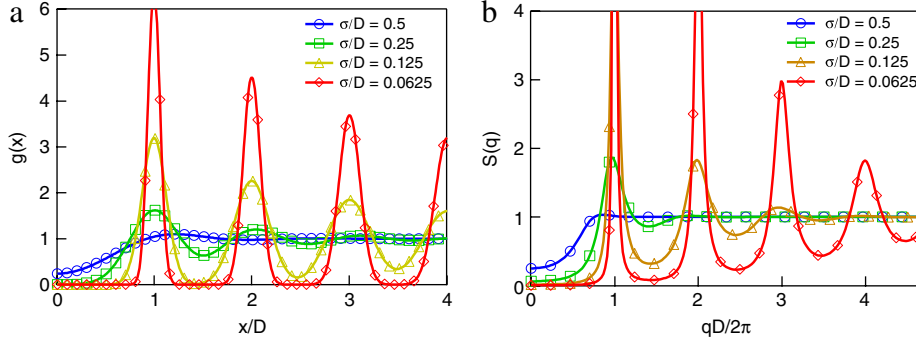


Fig. 51. (a) Pair correlation function $\bar{g}(x)$ and (b) interference function $S(q)$ of a paracrystal with Gaussian statistics. σ and D are respectively the square-root of the variance and the mean value of the distance probability. The curves are plotted against normalized units. From Ref. [27].

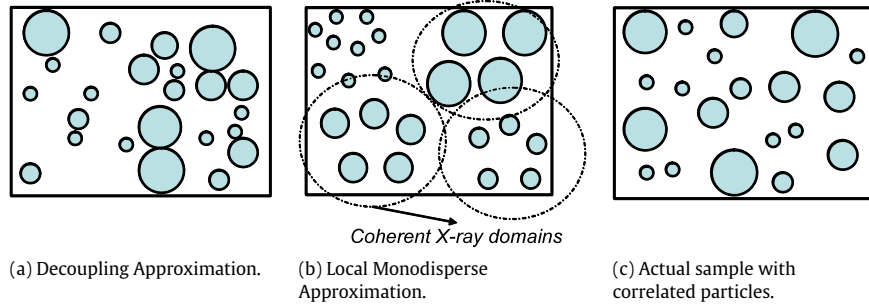


Fig. 52. Sketch of the morphology that would correspond to various approximations used to treat scattering from an ensemble of nanoparticles.

6.4. Accounting for the particle-particle correlations: DA, LMA and beyond

Analytical results about small angle scattering by systems of interacting polydispersed particles have been obtained only for hard spheres in 3D. The equations developed by Vrij [249–251] rely on the Percus-Yevick approximation. The use of fluid thermodynamics theory applied to mixtures of different components with arbitrary interaction potential is restricted only to very few components because of the cumbersome resolution of coupled integro-differential equations based on the Ornstein-Zernike equations [252,77]. Clearly, such an approach is intractable for actual SAXS data analysis all the more than, in many cases, interaction potentials between particles are unknown if they are relevant. For instance, the spreading of islands grown on a substrate results from a subtle interplay between random nucleation process, growth and coalescence kinetics, strain effect etc ...that can not be traced back to a “potential”. This is one of the reason of the use of approximations such as introduced in Section 6.3.2 to handle the problem of partial pair correlation functions. To go further the size and spatial correlations between neighboring particles must be precisely known. For instance MBE growth of nanostructures leads usually to a depleted zone (capture area) around each particle [8,253,254] which scales with the particle size. By GISAXS, Revenant et al. [29] demonstrated this effect by comparing experimental GISAXS with the expected diffuse scattering calculated from large scale in-plane electron microscopy images (see Section 7.4.3).

6.4.1. Decoupling Approximation

As sketched in Fig. 52, DA offers no restriction about particle overlap as a consequence of the underlying unrestricted disorder. DA is known in the theory of liquid mixture as the Random Mixture Approximation. The first successful numerical applications of DA

to colloid fluid were made by Kotlarchy and Chen [255]. The authors already noticed that the applicability of the modeling was restricted to low concentration or low size polydispersity. In fact, DA overestimates the diffuse scattering [29] close to the specular rod because of the too intense incoherent contribution $\Phi_0(q_{||})$ Eq. (158) (see Fig. 53).

6.4.2. Local Monodisperse Approximation

This approximation introduced by Pedersen [234,256–258] is widely used to analyze scattering from correlated systems. According to the original presentation, the actual system of interacting particles (kind α) is approximated by a set of non-interacting pure monodisperse sub-systems. The intensity in LMA, given by Eq. (162), is obtained as the incoherent sum of scattering by each domain weighted according to the actual size-shape distribution p_α . As the interference function of each sub-system $S_D(\mathbf{q}_{||})$ can be scaled on the particle size, LMA is, in practice, an efficient way to reintroduce partial correlation between particles, in particular the excluded volume effect. Pedersen [234] suggested to use for $S_D(\mathbf{q}_{||})$ the hard core interacting one (see Section 6.3.4) with an excluded volume that scales linearly with the actual particle size. This mimics the expected behavior of the capture area of each particle during growth.

The LMA cross section (Eq. (162)) can be recovered from the most general expression (Eq. (157)) by assuming no correlation between particles of different kinds i.e. $g_{\alpha\beta}(\mathbf{r}_{||}) = 0$ if $\alpha \neq \beta$ which reverts to:

$$S_{\alpha\beta}(\mathbf{q}_{||}) = 1 - n_s \int_A e^{i\mathbf{q}_{||} \cdot \mathbf{r}} d\mathbf{r}_{||} = 1 - N\delta(\mathbf{q}_{||}), \quad \alpha \neq \beta. \quad (178)$$

Straightforward algebra applied to Eq. (157) leads to:

$$\left(\frac{d\sigma}{d\Omega} \right)_{\text{part}} = \sum_{\alpha} p_{\alpha} |F_{\alpha}(\mathbf{q}_{||}, k_{iz}, k_{fz})|^2 S_{\alpha}^{\text{mono}}(\mathbf{q}_{||}), \quad (179)$$

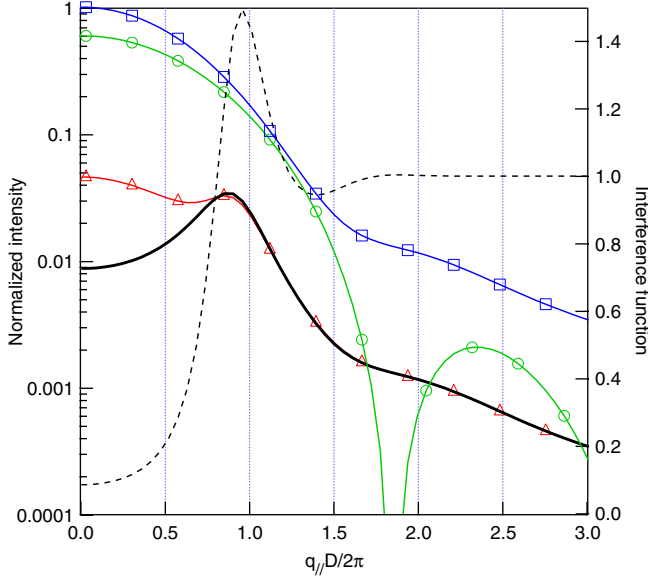


Fig. 53. Born scattering at $q_z = 0$ from a paracrystal of polydisperse cylinders calculated in LMA (thick line; Eq. (162)) or DA (thin line with triangles; Eq. (160)). The radii distribution and the paracrystal (Eq. (177)) distance distribution are Gaussian: $\langle R \rangle / D = \sigma_D / D = \sigma_R / \langle R \rangle = 0.3$; $H/R = 1$. The mean form factor $\langle |F(q_{\parallel})|^2 \rangle$ (line with square), the incoherent contribution $\Phi_0(q_{\parallel}) = \langle |F(q_{\parallel})|^2 \rangle - \langle |F(q_{\parallel})| \rangle^2$ (line with circle) and the interference function $S(q_{\parallel})$ (dotted line-right scale) are also displayed. All the curves have been normalized by $\langle |F(q_{\parallel} = 0)|^2 \rangle = \langle V^2 \rangle$. The scattered intensity has been shifted down by one decade for clarity and the specular rod is not shown.

$$\begin{aligned} S_{\alpha}^{\text{mono}}(q_{\parallel}) &= 1 + p_{\alpha}(S_{\alpha\alpha}(q_{\parallel}) - 1) \\ &= 1 + p_{\alpha}n_S \int_A (g_{\alpha\alpha}(\mathbf{r}_{\parallel}) - 1) e^{i\mathbf{q}_{\parallel} \cdot \mathbf{r}_{\parallel}}. \end{aligned}$$

Eq. (162) is recovered under the assumption that $S_{\alpha}^{\text{mono}}(q_{\parallel})$ can be replaced by the interference function $S_{\alpha}(q_{\parallel})$ of a truly monodisperse system of density $n_S p_{\alpha}$. In other words, $g_{\alpha\alpha}(\mathbf{r}_{\parallel})$ is assumed to be the pair correlation function of a monodisperse domain although by definition, it includes the existence of the other kinds of particles. Pedersen justified this approximation on the ground of a physical picture of slow variation of the size of the particles at a length scale lower than the coherence length. This means that each particle is surrounded by neighbors of the same size and shape. A smooth transition between DA and LMA is obtained by gradually increasing the size correlation between neighbors. Leroy et al. [235] illustrated this result in the framework of particles aligned along one dimension (see Fig. 54). The accuracy of LMA in 3D was tested against scattering from computer generated polydisperse systems [259,258] as well as the solvable Vrij scattering from hard core interacting spheres [233]. The failure of DA even at very low polydispersity was evident not only at small q but also from the shape of the correlation peak. LMA gives better agreement but without reproducing exactly the first peak shape.

6.4.3. Size-Spacing Correlation Approximation

The Size-Spacing Correlation approximation (SSCA) [235,155,81] is a one-dimensional analytical modeling of scattering from correlated particles. It gives a fairly good illustration of the problem at hand although its applicability to actual measurements of SAXS [81] is questionable owing to its 1D character. SSCA is derived from the paracrystal (see Section 6.3.4) by filling nodes along a line with polydispersed particles and by accounting for a coupling between the sizes of two neighbors and their spacing on a statistical point of view.

The starting point is to build-up the autocorrelation function of the electronic density along the chain $Z_+(r_{\parallel} \geq 0)$. For the sake of simplicity, the perpendicular direction is ignored here. Let us $p(R)$ be the size distribution of the particles along the chain and $S(r_{\parallel}, R)$ the shape function of a particle of size R . The size R_0 of the particle at origin is chosen according to $p(R)$. The size of its first neighbor R_1 is chosen independently of R_0 but the particle is put at a distance r from its previous neighbor following the probability $P(r_{\parallel}/[R_0, R_1])$ that depends on the sizes of the two particles R_0, R_1 . The following neighbors R_n are put using the same rule but starting from the previous particle R_{n-1} . In terms of $Z_+(r_{\parallel} \geq 0)$, this reads:

$$\begin{aligned} Z_+(r_{\parallel} \geq 0) &= z_0(r_{\parallel}) + z_+(r_{\parallel}) \\ z_0(r_{\parallel}) &= \int p(R_0) \{ \delta(-r'_{\parallel}, R_0) \otimes \delta(r'_{\parallel}, R_0) \otimes \delta(r'_{\parallel}) \} (r'_{\parallel}) dR_0 \\ z_+(r_{\parallel}) &= \iint p(R_0)p(R_1) \{ \delta(-r'_{\parallel}, R_0) \otimes \delta(r'_{\parallel}, R_1) \\ &\quad \otimes P(r'_{\parallel}/[R_0, R_1]) \} (r'_{\parallel}) dR_0 dR_1 \\ &+ \iiint p(R_0)p(R_1)p(R_2) \{ \delta(-r'_{\parallel}, R_0) \otimes \delta(-r'_{\parallel}, R_2) \\ &\quad \otimes P(r'_{\parallel}/[R_0, R_1]) \otimes P(r'_{\parallel}/[R_1, R_2]) \} \\ &\quad \times (r'_{\parallel}) dR_0 dR_1 dR_2 + \dots \end{aligned} \quad (180)$$

\otimes is the folding product along r_{\parallel} . The particle at the origin leads to $z_0(r_{\parallel})$, the first neighbor to the first term and so on. Like with the paracrystal, the probability of having a distance r_{\parallel} with the second neighbor is the product of the probability of having a distance r'_{\parallel} between the origin and the first neighbor and a distance $r_{\parallel} - r'_{\parallel}$ between the first and the second; this probability should be summed over all possible particle sizes and intermediate distances r' ; this is nothing other than the folding product of $P(r_{\parallel}/[R_0, R_1]) \otimes P(r_{\parallel}/[R_1, R_2])$. The idea can be generalized to the n th neighbor. As convolution products lead to simple products in Fourier space, the intensity proceeds from $z(r_{\parallel}) = z_0(r_{\parallel}) + z_+(r_{\parallel}) + z_-(r_{\parallel})$ with $z_-(r_{\parallel}) = z + (-r_{\parallel})$:

$$\begin{aligned} \left(\frac{d\sigma}{d\Omega} \right)_{\text{part}} &= V\delta(q) + \int p(R_0) |\mathcal{F}(R_0, q_{\parallel})|^2 dR_0 \\ &+ 2\text{Real} \left\{ \iint p(R_0)p(R_1)\mathcal{F}_0^*(q_{\parallel}, R_0)\mathcal{F}(q_{\parallel}, R_1) \right. \\ &\quad \times \mathcal{P}(q_{\parallel}/[R_0, R_1]) dR_0 dR_1 + \iiint p(R_0)p(R_1)p(R_2)\mathcal{F}^*(q_{\parallel}, R_0) \\ &\quad \times \mathcal{F}(q_{\parallel}, R_2)\mathcal{P}(q_{\parallel}/[R_0, R_1])\mathcal{P}(q_{\parallel}/[R_1, R_2]) dR_0 dR_1 dR_2 + \dots \end{aligned} \quad (181)$$

$\mathcal{F}(R_0, q_{\parallel})$ is the particle form factor and $\mathcal{P}(q_{\parallel}/[R_n, R_{n+1}])$ is the Fourier transform of $P(r_{\parallel}/[R_n, R_{n+1}])$. The Dirac term gives rise to the specular rod of Eq. (157). To go on, an excluded volume effect between neighbors is introduced by assuming a linear link between the average neighbor spacing and their sizes:

$$\int_{-\infty}^{+\infty} rP(r_{\parallel}/[R_n, R_{n+1}]) dr = D + \kappa [R_n + R_{n+1} - 2\langle R \rangle], \quad (182)$$

D and $\langle R \rangle$ are the average distance and radius of the particles all along the chain. A positive value of the correlation parameter κ is expected for hard core interacting objects. This linear relationship is changed into a product in Fourier space. The characteristic function $\mathcal{P}(q_{\parallel}/[R_n, R_{n+1}])$ reads:

$$\mathcal{P}(q_{\parallel}/[R_n, R_{n+1}]) = \phi(q_{\parallel}) e^{iq_{\parallel}D} e^{i\kappa q_{\parallel}[R_n + R_{n+1} - 2\langle R \rangle]}. \quad (183)$$

$\phi(q_{\parallel})e^{iq_{\parallel}D}$ is the characteristic function of the underlying paracrystal ($\kappa = 0$). Two additive contributions in the particle spacing can be distinguished: (i) an intrinsic one due to the paracrystal σ_D^2 Eq.

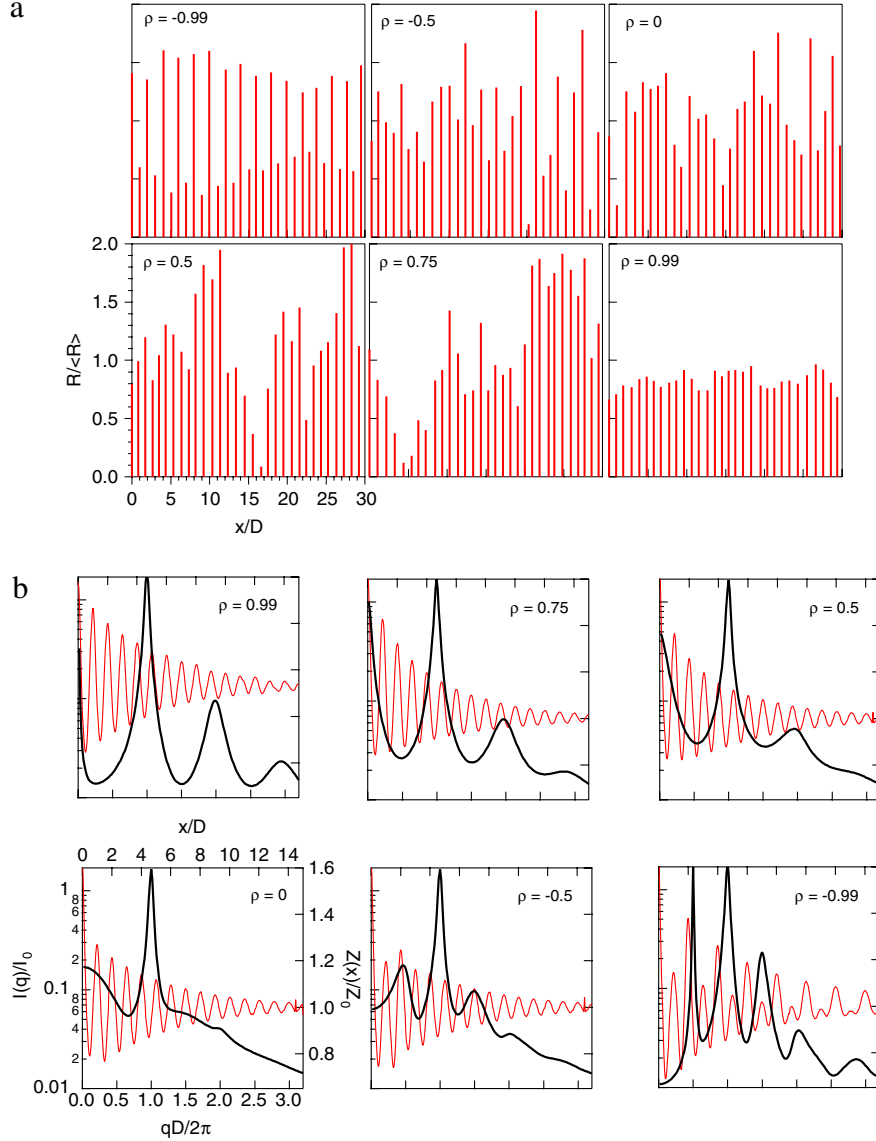


Fig. 54. Influence of size-size correlation between neighboring particles aligned along 1D. The correlation from site to site is normal with a correlation coefficient ρ and $\sigma_R/\langle R \rangle = 0.4$. (a) Representation of the chain for several ρ values. $\rho = 0$ means uncorrelated particles (DA) while $\rho = \pm 1$ means perfect correlation or anti-correlation. (b) Scattered intensity (thick line) and density autocorrelation function (thin line) for stick particles aligned along the chain. The particles are put according to the rule of a 1D paracrystal. The DA ($\rho = 0$) diffuse scattering close to $q_{\parallel} = 0$ is absent in LMA ($\rho = 1$). Notice the splitting of the diffraction peaks for $\rho = -1$ because of the alternate of small and large particles. From Ref. [235].

(176) and (ii) an extrinsic one due to the fluctuations of sizes $2\kappa^2\sigma_R^2$ ($\sigma_R^2 = \langle (R - \langle R \rangle)^2 \rangle$ is the variance of the size distribution). Using the hypothesis of Eq. (183), the sum in Eq. (181) reduces to a simple geometric sum. The final calculation of the cross section is therefore easily handled:

$$\left(\frac{d\sigma}{d\Omega} \right)_{\text{part}} = V^2 \delta(q_{\parallel}) + |\langle \mathcal{F}(q_{\parallel}) \rangle|^2 + 2 \text{Real} \left\{ \widetilde{\mathcal{F}}_{\kappa}(q_{\parallel}) \widetilde{\mathcal{F}}_{\kappa}^*(q_{\parallel}) \frac{\Omega_{\kappa}(q_{\parallel})}{\widetilde{p}_{2\kappa}(q_{\parallel}) [1 - \Omega_{\kappa}(q_{\parallel})]} \right\}, \quad (184)$$

$$\Omega_{\kappa}(q_{\parallel}) = \widetilde{p}_{2\kappa}(q_{\parallel}) \phi(q_{\parallel}) e^{iq_{\parallel} D}. \quad (185)$$

$\widetilde{p}_{\kappa}(q_{\parallel})$ is the characteristic function of the centered particle size distribution:

$$\widetilde{p}_{\kappa}(q_{\parallel}) = \int p(R) e^{ikq_{\parallel}(R - \langle R \rangle)} dR. \quad (186)$$

A new average form factor defined through:

$$\widetilde{\mathcal{F}}_{\kappa}(q_{\parallel}) = \int p(R) \mathcal{F}(q_{\parallel}, R) e^{ikq_{\parallel}(R - \langle R \rangle)} dR \quad (187)$$

appears in the cross-section. Eq. (184) shows no clear separation between coherent and incoherent scattering as in DA. By setting the particle form factor to one in the previous formula, one ends up with the total interference function:

$$S(q_{\parallel}) = 1 + 2 \text{Real} \left\{ \frac{\widetilde{p}_{\kappa}^2(q_{\parallel}) \Omega_{\kappa}(q_{\parallel})}{\widetilde{p}_{2\kappa}(q_{\parallel}) [1 - \Omega_{\kappa}(q_{\parallel})]} \right\}. \quad (188)$$

$\kappa = 0$ allows one to recover the DA cross-section or the Hosemann function for $S(q_{\parallel})$ Eq. (177) as $\widetilde{\mathcal{F}}_{\kappa}(q_{\parallel}) = \langle \mathcal{F}(q_{\parallel}, R) \rangle$ and $\widetilde{p}_{2\kappa}(q_{\parallel}) = 1$. Through an expansion around $q_{\parallel} = 0$ (and ignoring the specular term), one can demonstrate that the diffuse scattering is minimum around the special value $\kappa = \kappa_0$:

$$\kappa_0 = \frac{1}{2} \frac{D}{\sigma_R^2} \frac{\langle \mathcal{F}(q_{\parallel} = 0)(R - \langle R \rangle) \rangle}{\langle \mathcal{F}(q_{\parallel} = 0) \rangle}. \quad (189)$$

Scattering from 3D particles aligned in 1D can be described by the SSCA if the form factor of the particle is evaluated in 3D (*i.e.* $\mathcal{F}(q_{\parallel}, R_{\parallel}, \mathbf{q}_{\perp}, H_{\perp})$) and if one realizes that all previous formulae apply only for the alignment direction $q_{\parallel}, R_{\parallel}$. Finite-size effects along the chain can also be included [155,239,240,234,241,242].

The contribution of correlations in SSCA [235,155] is illustrated in Fig. 55 for several values of κ . Of course, whatever the approximation, the scattering at high wavevector transfer ($q_{\parallel} \gg 2\pi/D$) is only given by the mean form factor. As compared to DA or LMA for which $I(\mathbf{q}) \sim \langle |F(\mathbf{q})|^2 \rangle S(\mathbf{q})$, the introduction of correlations in disordered systems lead to a strong modification of the shape of the correlation peak. Its smearing as compared to the paracrystal interference function lies in the contribution of all the partial interference functions [235] while its position is no longer simply related to the mean particle spacing D . Despite the constant mean spacing D , it shifts toward low q_{\parallel} value upon increasing κ until merging with the specular rod. In GISAXS, an interesting cross-coupling between the parallel $2\theta_f$ and perpendicular α_f directions shows up on Fig. 55b for 3D particles of fixed aspect ratio. The scattering lobes along α_f are tilted toward the origin although the particle shape is a cylinder. The explanation is as follows. The biggest and thus the highest particles are farther apart and scatter closer to the specular rod and also closer to the sample horizon. The reverse happens for the smallest particles giving rise to this tilt. The tilt angle can be used as a measure of the coupling parameter between size and distance of particles if the particle aspect ratio is constant as when the thermodynamic equilibrium shape is reached [79] (see Section 7.4.3). A comparison between SSCA and LMA including correlations through a linear link between the inter-particle distance and the size in each monodisperse domain was undertaken in Ref. [155,81]. The main conclusion was that D between LMA and SSCA differs by 10%–30% while the discrepancies on the other parameters κ and σ_D are much higher. The interesting finding was that LMA and SSCA agree nearly perfectly on the estimate of the total fluctuations of particle spacing but not the exact ratio of the intrinsic and extrinsic components. Remember that this includes two contributions: paracrystal plus size distribution.

Strictly speaking, SSCA cannot be used to analyze actual data. However, experimentally in the case of gold islands on $\text{TiO}_2(110)$ [81] (see Section 7.3), SSCA and LMA were compared assuming interference functions given by the 1D paracrystal or by a 2D function deduced from hard core interacting disks model [76] (Fig. 50) with a hard core radius that scales linearly with the actual radius [234]. The introduction of correlations was mandatory to reproduce fairly well the shape of the correlation peak [29]. If the uncorrelated q_{\parallel} range *i.e.* the average particle form factor is suitably fitted, LMA and SSCA agree within the error bars on the most important parameters $\langle R \rangle, \sigma_R, D$ giving confidence in their evolution. The discrepancies comes only from the disorder description κ, σ_D . Both LMA and SSCA end up with a Voronoï cell size which is fully determined by the radius of the central particle. This finding is in line with what is expected from the growth theory of supported nanoparticles and with the overall self similar behavior that is observed for this peculiar system [260].

6.4.4. Scaling Approximation

The Scaling Approximation (SA) [233,261] assumes a conformality of all the partial pair correlation functions according to $g_{\alpha\beta}(r) \simeq g_{\text{mono}}(r^* \lambda_{\alpha\beta})$; g_{mono} is the pair correlation function of a monodisperse system which is assumed to depend only on a reduced distance r^* . Each $g_{\alpha\beta}$ is obtained by evaluating g_{mono} at a scaled pair distance $r^* \lambda_{\alpha\beta}$. For particles interacting through a given pair potential, SA is a further step after the hypothesis of conformal mixtures for which it is the interaction potential itself

$u_{\alpha\beta}(r)$ that is conformal to that of a monodisperse reference system. This conformality hypothesis is well suited to particles interacting through an hard core potential for which $u_{\alpha\beta}(r) = 0$ if $r < \sigma_{\alpha\beta}$ and $r^* = r/\sigma_{\text{mono}}$. Gazzillo and coworkers proposed the following scaling: $\lambda_{\alpha\beta} = \langle \sigma^2 \rangle^{1/2} / \sigma_{\alpha\beta}$ and $\sigma_{\text{mono}} = \sqrt{\langle \sigma_{\alpha\beta}^2 \rangle}$ leading to $g_{\alpha\beta}(r) \simeq g_{\text{mono}}(r \langle \sigma^2 \rangle^{1/2} / \sigma_{\alpha\beta})$. The choice of this scaling ensures that g_{mono} has to be evaluated at the same coverage $\eta = n_s \langle \sigma_{\alpha\beta}^2 \rangle = n_s \sigma_{\text{mono}}^2$ of the whole mixture. At variance to DA or LMA, SA takes better into account the excluded volume effect although SA incorrectly assumes that pair correlation functions have the same value at contact $g_{\alpha\beta}(\sigma_{\alpha\beta}) \simeq g_{\text{mono}}(\sigma_{\text{mono}})$. In terms of the involved partial interference function, SA reads:

$$S_{\alpha\beta}(q_{\parallel}) = 1 + \langle \sigma^2 \rangle^{1/2} / \sigma_{\alpha\beta} \left[S_{\text{mono}} \left(q_{\parallel} \sigma_{\alpha\beta} / \langle \sigma^2 \rangle^{1/2} \right) - 1 \right]. \quad (190)$$

SA [233,261] was compared in 3D systems to either the analytical solution of Vrij for polydisperse hard spheres [249,250] or to molecular dynamics simulations considering a Lennard-Jones interaction potential. The accuracy of SA is surprisingly good whatever the packing or the degree of polydispersity. The shape as well as the height of the correlation peak is very well reproduced. The only discrepancy comes from the low q behavior of the total interference function. SA is unable to reproduce the exact fluctuations of the particle density [40] but, in the total cross-section, this drawback is balanced by the product with the particle form factor. One of the drawback of SA scattering cross-section is that, instead of DA, LMA or SSCA, it involves a double sum over the size-shape distribution (see Eq. (157)). Even though very appealing in terms of accuracy, to our knowledge, SA was never applied to actual data analysis.

6.5. The graded interface model and the nanoparticle form factor

Up to now, the nanoparticles have been treated as independent or isolated perturbations of the wavefields obtained on flat interfaces. The linearity of the wave propagation equation Eq. (96) allows to decouple the parallel and perpendicular directions and to introduce the notion of a parallel interference function. However, increasing the particle packing leads to an enhanced absorption and refraction of both the incident and the scattered beams inside the particle layer itself. This is all the more true than the angles α_i, α_f are close to the critical angle and the beam paths in the particle layer is large. More accurate results are expected if the reference medium is taken as the graded interface that includes the particles themselves.

The method has been applied to the case of nanostructures (Refs. [155,81]) randomly distributed on a surface. The reference medium is defined through the average dielectric index perpendicular to the surface:

$$\tilde{n}_0^2(z) = \begin{cases} 1 & \text{if } z > t \\ \tilde{n}_l^2(z) = \frac{n_i^2}{A} \int_A \sum_i \delta_i(\mathbf{r}_{\parallel} - \mathbf{r}_{\parallel,i}, z) d\mathbf{r}_{\parallel} & \text{if } 0 < z < t \\ n_s^2 & \text{if } z < 0 \end{cases} \quad (191)$$

where $\delta_i(\mathbf{r}_{\parallel} - \mathbf{r}_{\parallel,i}, z)$ is the shape function of the particle located at $\mathbf{r}_{\parallel,i}$ and t is the boundary with vacuum. The corresponding reference field is made of upward and downward propagating waves $\tilde{A}_1^+(z)$ at each height z of the interface. Their amplitudes can be inferred through the matrix propagation formalism of Section 5.2.7:

$$\Psi(\mathbf{k}_{\perp,0}, z) = \begin{cases} \tilde{A}_0^+ e^{ik_z z} + e^{-ik_z z} & \text{for } z > t \\ \tilde{A}_1^+(z) e^{ik_{z,1}(z)z} + \tilde{A}_1^-(z) e^{-ik_{z,1}(z)z} & \text{for } 0 < z < t \\ \tilde{A}_2^- e^{-ik_z z} & \text{for } z < 0. \end{cases} \quad (192)$$

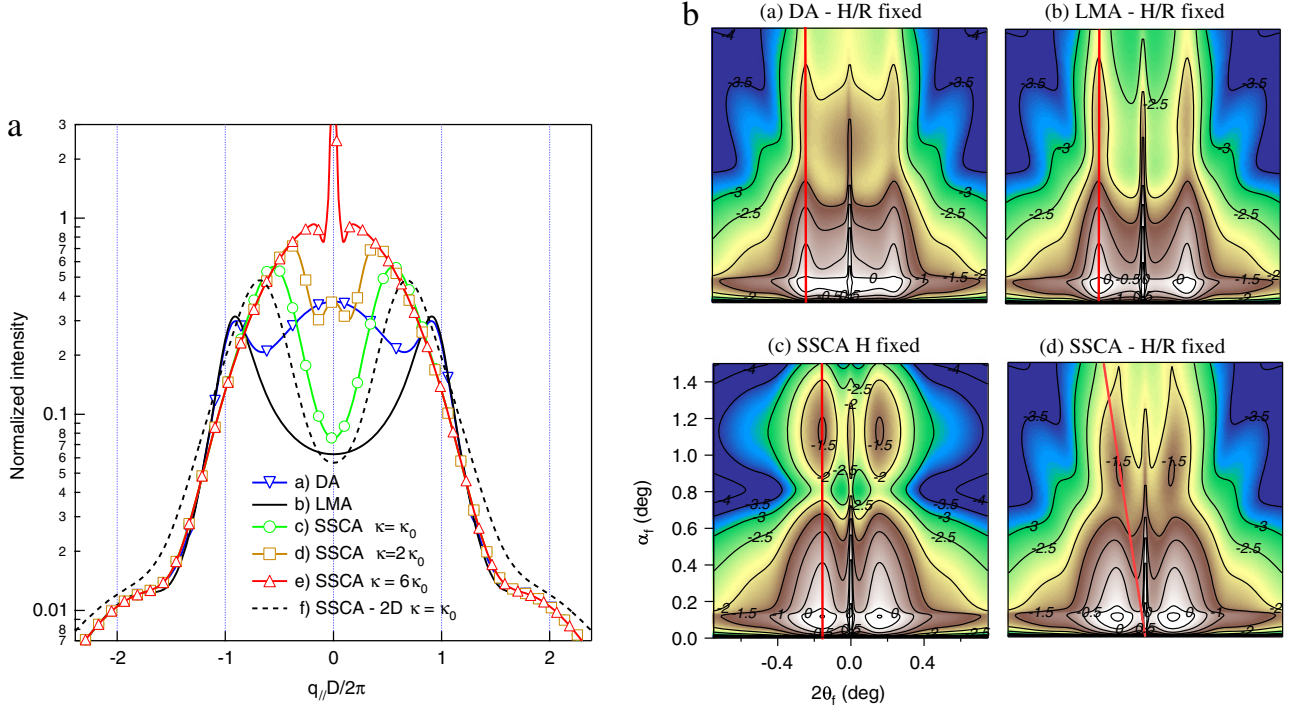


Fig. 55. Scattering from a line of size distributed cylinders. The size distribution and intrinsic fluctuations of distances are normal with $\sigma_R/R = \sigma_D/D = 0.25$ and $D = 3$ (R). Either the particle aspect ratio is constant $H/R = 1$ or its height $H/\langle R \rangle = 1$ i.e. that the particle volume scales with R^3 or R^2 . modeling has been performed in DA, LMA or SSCA using the same underlying paracrystal. κ_0 is the correlation parameter given by Eq. (189). The intensity is normalized by $\langle V^2 \rangle$. (a) 1D cut of intensity at $q_{\perp} = 0$ for different κ values. (b) Simulated GISAXS patterns for supported gold particles on $\text{TiO}_2(110)$. From Ref. [155].

The perpendicular wavevector is given by the conservation of the parallel component $k_{z,j}(z) = -\sqrt{\tilde{n}_j^2(z)k_0^2 - k_{\parallel}^2}$. The perturbation to $\tilde{n}_0^2(z)$ is brought by the particles as well as by the vacuum holes in between. As the shape of these latter is nothing else than the inverse of the fingerprint of the particles, the useful scattering potential is:

$$\delta n^2(\mathbf{r}_{\parallel}, z) = [n_i^2 - 1] \sum_i \delta_i(\mathbf{r}_{\parallel} - \mathbf{r}_{\parallel,i}, z) + [1 - \tilde{n}_i^2(z)][\Theta(z) - \Theta(z - t)]. \quad (193)$$

where $\Theta(z)$ is the step function. If only the contribution of the incoherent cross-section at $q_{\parallel} \neq 0$ is under concern as with GISAXS, the second term can be dropped out since it involves only a z -dependence. After a bit of calculation using the DWBA cross-section Eq. (91), it can be shown that the concept of DWBA particle form factor still applies but with an expression more complex than in Eq. (134) [37]:

$$\begin{aligned} \mathcal{F}(\mathbf{q}_{\parallel}, k_{iz}, k_{ fz}) &= \int d\mathbf{r}_{\parallel} e^{i\mathbf{q}_{\parallel} \cdot \mathbf{r}_{\parallel}} \int dz \delta(\mathbf{r}_{\parallel}, z) \\ &\times \left\{ \tilde{A}_1^{-}[k_{iz,1}(z)]\tilde{A}_1^{-}[-k_{ fz,1}(z)]e^{i[-k_{ fz,1}(z)-k_{iz,1}(z)]z} \right. \\ &+ \tilde{A}_1^{+}[k_{iz,1}(z)]\tilde{A}_1^{-}[-k_{ fz,1}(z)]e^{i[-k_{ fz,1}(z)+k_{iz,1}(z)]z} \\ &+ \tilde{A}_1^{-}[k_{iz,1}(z)]\tilde{A}_1^{+}[-k_{ fz,1}(z)]e^{i[-k_{ fz,1}(z)-k_{iz,1}(z)]z} \\ &\left. + \tilde{A}_1^{+}[k_{iz,1}(z)]\tilde{A}_1^{+}[-k_{ fz,1}(z)]e^{i[-k_{ fz,1}(z)+k_{iz,1}(z)]z} \right\}. \end{aligned} \quad (194)$$

The particle form is neither the Fourier transform of the particle shape as in the BA nor the sum of four Fourier transform weighted according to the reflection coefficients. Instead, it involves a continuous integration in each slice of the particle layer of the wave propagation equation, the scattering and the interference between upward and downward propagating waves (Fig. 56). The

cross-section of Section 6.2 is recovered in the dilute regime as $\tilde{n}_0(z) \rightarrow n_0(z)$, $k_{z,0} \rightarrow k_{z,1}$, $\tilde{A}_1^{+} \rightarrow \tilde{A}_0^{+}$ and $\tilde{A}_1^{-} \rightarrow \tilde{A}_0^{-} \simeq r_{01}$.

The effect of a large density of particles can be dramatic as shown in Fig. 57 for monodispersed supported full spheres. In that case, the shape of the profile of dielectric index is parabolic. The zero-coverage case should be understood as isolated particles. Fig. 57 demonstrates that the diffuse scattering is highly dependent on the coverage even for monodispersed particles in particular for angles close and below the critical angle. Both the Yoneda peak shape and the location of the interference fringes are modified because of the propagation and attenuation of the waves inside the layer of particles. The discrepancies between the two models, namely DWBA on the flat substrate and graded interface appear on the experimental results of Fig. 58. The cut of intensity from Au islands grown on $\text{TiO}_2(110)$ have been fitted with the graded interface model using a truncated sphere shape. The obtained morphology allowed to deduce the profile of refraction index (inset of Fig. 58) and to simulate the expected curve accounting only for the substrate. The Yoneda peak intensity is overestimated as the damping of the evanescent wave below the critical angle of the layer itself is forgotten. The same behavior is observed at higher angle because of the Croce-Nérot factor.

6.6. Limitations of the quantitative analysis of GISAXS from nanoparticles

The quantitative analysis of GISAXS patterns starts by the acquisition of good data with the widest dynamical range ! This obvious prerequisite includes background minimization [26] or subtraction (a promising procedure being the use of anomalous scattering [262]), detector correction and normalization, account for the resolution function (beam divergence, wavelength spread, detector acceptance, sample curvature and homogeneity) and measurements far away in reciprocal space to be sensitive to the

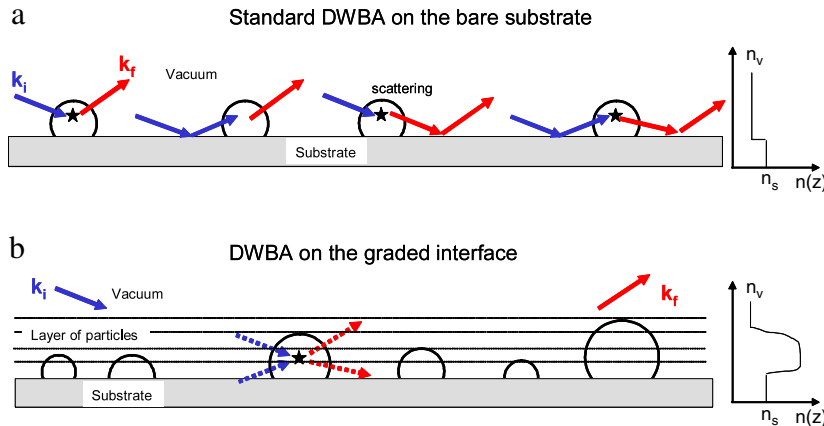


Fig. 56. Sketch of the involved scattering events for two approximations: (a) The DWBA formalism starts with a flat interface, which leads to four scattering events that involves reflection of the incident or scattered waves on the substrate; (b) The DWBA starts with the graded interface model taking into account the scattering of the upwards and downwards propagating waves inside each slice of the particle layer.

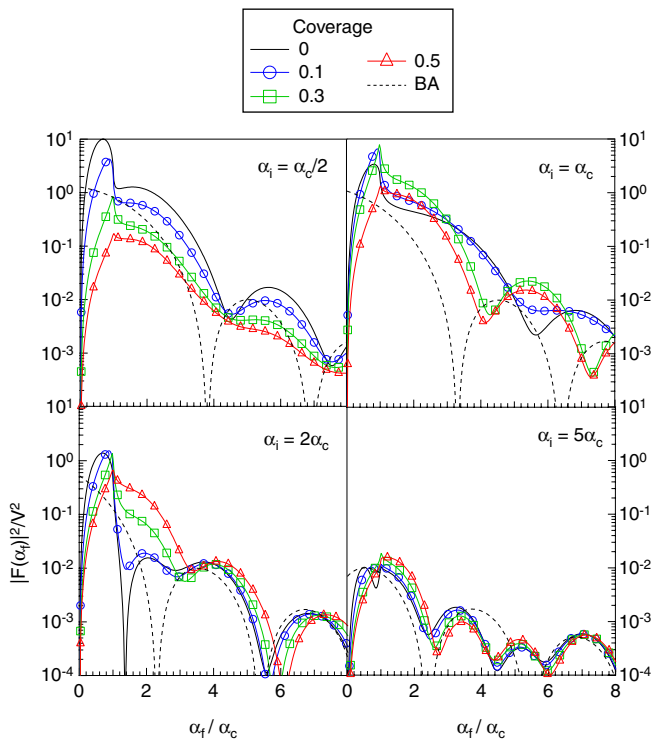


Fig. 57. Form factor $F(\mathbf{q}_{||} = 0, k_{iz}, k_{fz})$ (see Eq. (194)) of a full sphere of Au on $\text{TiO}_2(110)$ calculated in the framework of the graded interface as function of the particle coverage η and the incident angle α_i . The case of a dilute system (Eq. (134)) corresponds to a null coverage $\eta = 0$. The chosen dielectric contrast is strong enough to see the influence of the refraction index profile. From Ref. [155].

particle form factor only. The analysis of GISAXS data relies on direct modeling using non-linear χ^2 minimization [263] for fits. One has to be aware of all the pitfalls of such a procedure in terms of global minimum finding, accuracy and reliability [82]. As a rule of thumb, for a random distribution of nanoparticles, accurate measurements can be obtained for the mean values (in-plane and out-of-plane size, distance between particles) while larger error bars are obtained for the width (and therefore the shape) of the size distribution or the fluctuations of distances. The systematic error introduced by the used approximation to treat partial correlation (DA, LMA, SSCA, SA) should be balanced by a careful fit of the high q range even at the expense of the correlation peak. For long range ordered collection of particles, the form factor is sampled only at

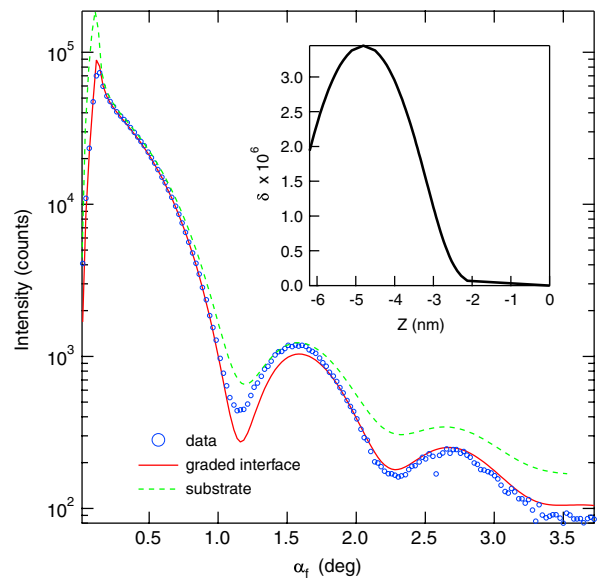


Fig. 58. Experimental cut of intensity from GISAXS of Au nanoparticles on $\text{TiO}_2(110)$. The full line corresponds to the fit assuming size distributed truncated spheres and using the graded interface model (Eq. (194)) (see Ref. [155] for further details). The dotted line is the calculated scattered intensity starting from the substrate only i.e. by assuming isolated particles. The profile of index of refraction $n = 1 - \delta - i\beta$ is displayed in the inset.

discrete values of the reciprocal space by the interference function. This hampers the accuracy of the shape and size determination. Actual examples and analysis methodology are presented in the next sections (Section 7).

7. Examples of extensive data analysis of GISAXS patterns

Beyond the rapid data analyses mentioned in 4.6, extracting precise morphological parameters such as average lateral size, height and separation distance needs the use of an appropriate model, that accounts for the exact shape of the islands, the distribution of sizes, an appropriate island-island pair correlation function, as well as refraction effects when the incident or exit angles are close to the critical angle for total external reflection. The method to perform an extensive, quantitative analysis of GISAXS patterns is described in detail in several papers [37,27,29] as well as in the above theoretical Section 6. The IsGISAXS software [27],

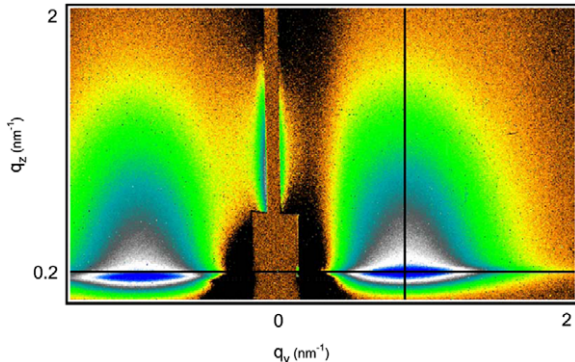


Fig. 59. A typical experimental GISAXS pattern of Pt deposited on MgO(001), with two scattering lobes in the (q_y, q_z) plane. The two characteristic line cuts used in the fit procedure are shown as bold line. From Ref. [247].

[28] allows such a quantitative analysis through a simultaneously fitting of several cuts of the 2D GISAXS data, performed in any direction before simulating the complete 2D picture. In general, the fitting procedure starts with one cut parallel with the surface at the q_z position of maximum intensity, and another one perpendicular to it at the q_y position of the interference maximum. Several examples of such a quantitative analysis are gathered below, in the case of the growth of metals on oxide surfaces.

Qualitatively, the experimental GISAXS data look similar in all the cases encountered (Ag [78], Pd [29], Pt/MgO(001) [247], Au/TiO₂(110) [81], Co/NiO(111) [264], Ag/ZnO(0001) [150,151]...). The two-dimensional GISAXS patterns (see for instance Fig. 59) present two large scattering lobes visible along the parallel direction, separated by the specular rod, which is partly hidden by the beam stop. The extent of the intensity parallel (resp. perpendicular) with the surface is inversely proportional to the average lateral size (resp. height) of the island. The separation between the two main lobes is inversely proportional to the average separation between neighboring islands.

7.1. First example: Pt/MgO(001)

The first example concerns the growth of Pt/MgO(001) [247] (Fig. 59). The analysis used the DWBA [37] and LMA [234,256] formalisms. The one-dimensional paracrystal [42] with Gaussian statistic was chosen as the theoretical model to account for the interference between scatterers. The size distributions parallel with and perpendicular to the substrate were modeled by coupled or uncoupled log-normal or Gaussian laws. Two cross-sections (Fig. 60) along q_y and q_z at the maximum of scattered intensity *i.e.* at the positions of the correlation and Yoneda's peaks, respectively, are first simultaneously fitted using a Levenberg–Marquadt χ^2 -minimization. To improve statistics, additional profiles collected farther away in the reciprocal space are also often fitted. Different island shapes of increasing complexity are in general considered to analyze the data. Scattering patterns from Pt/MgO(001) films deposited at 600 K, 800 K and 1000 K were analyzed at several thicknesses. Films grown at 600 K (Fig. 60) and 800 K were simply fitted by means of truncated sphere shapes. Indeed, the GISAXS intensity maps did not show any anisotropy upon rotating the sample, nor any scattering rod characteristic of oriented facets, and the behavior of the intensity at high wavevector transfer [29] (“Porod’s regime”) was characteristic of such a shape. The quality of the model was judged by the way it reproduced the intensity profiles (Fig. 60c and d) and the 2D-GISAXS pattern (Fig. 60b). However, models based on cylindrical and spherical particle shapes failed in the case of films deposited at 1000 K. Good fits were instead obtained only by representing clusters by a

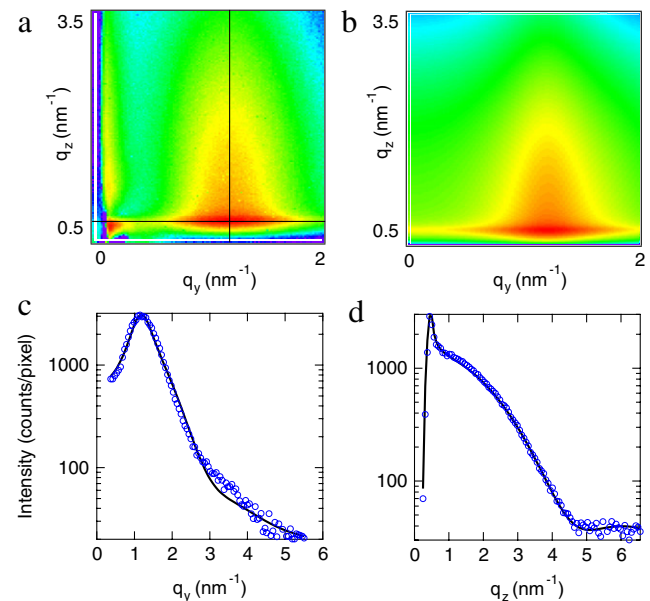


Fig. 60. 2D GISAXS patterns for a 0.3 nm thick Pt deposit on MgO(001) at 600 K. (a) Experimental 2D pattern and (b) GISAXS pattern simulated with the parameters obtained from the fits made along the (c) parallel and (d) perpendicular linear cuts through the intensity maximum (shown in a-map). In (c) and (d), the continuous lines correspond to the best fits and the dots to data points. Images are plotted on a logarithmic color scale. From Ref. [247].

truncated pyramid with a square-basis. The fitted angle of the side facets corresponds to islands that display (111) planes in cube-on-cube (001)_{MgO} || (001)_{Pt} epitaxy. Consistently, diffuse scattering rods [25] inclined by 54.7° were observed on some GISAXS images.

7.2. Second example: Pd/MgO(001)

The second example concerns the growth of Pd/MgO(001) at different temperatures [29] (550, 650 and 740 K), and for different thicknesses (0.1, 0.9, 1.0, and 3.0 nm). The general GISAXS formalism detailed in Section 6 has been used, within the DWBA and the LMA, to analyze the experimental data. It has been checked that the GISAXS simulation was not affected by the low roughness of the MgO(001) substrate even at large q . Hence, the substrate roughness was neglected in the Fresnel reflectivity for the GISAXS calculation. For a 0.1 nm thick Pd/MgO(001) deposit at 650 K, the mean island shape used to fit the GISAXS, a truncated pyramid with a square base was deduced from microscopy works for similar temperature and island size conditions [265]. A very good agreement was obtained between simulated and experimental data, with only a very small size distribution.

For a 1 nm thick Pd/MgO(001) deposit at 650 K, Fig. 61 displays the 2D GISAXS experimental patterns and the corresponding analysis with the incident beam along the MgO[110] (*resp.* MgO[100]) direction. The 2D GISAXS patterns present a scattering rod at 54.7° with respect to the surface normal in the <110> direction but not in the <100> direction. This indicates that palladium forms oriented faceted islands with {100} and {111} facets on the MgO(001) surface. Moreover, in case of faceted islands, the second and even sometimes third order scattering peaks perpendicular to the surface are indicative of flat (001) terraces and of narrow height distribution. All these features point to a truncated octahedron-like average shape as seen from TEM plane views. The simulated GISAXS patterns well reproduce the general features of the experimental ones, especially the scattering rod along the (111) direction visible in Fig. 61a. As an example,

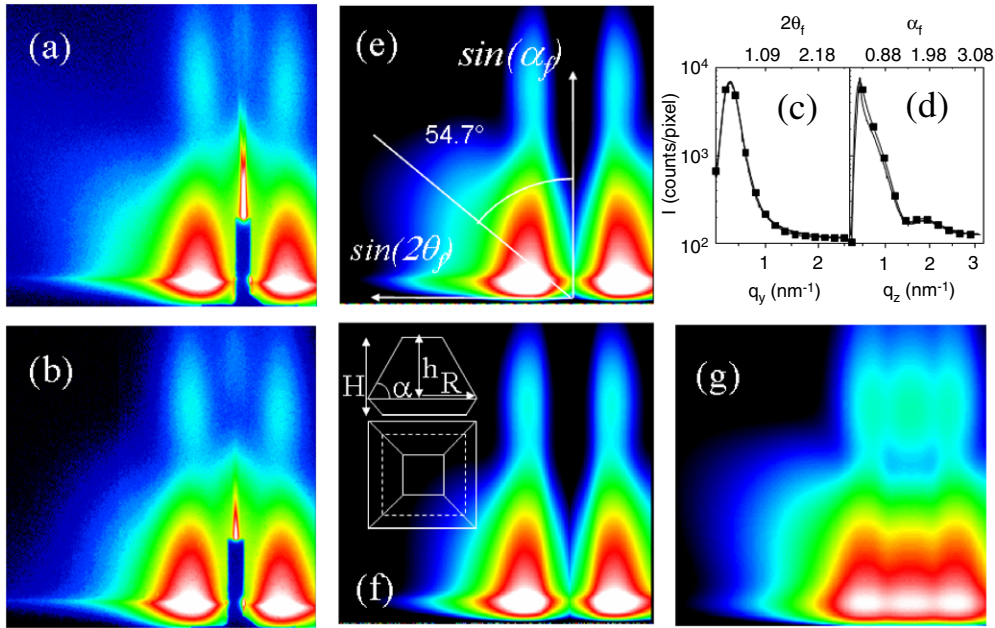


Fig. 61. 2D GISAXS intensity for a 1.0 nm thick Pd/MgO(001) deposit at 650 K: (a) Experimental patterns with the incident beam along the MgO[110] direction and (b) same as (a) but with the incident beam along the MgO[100] direction. Black lines show the positions of the two cuts used to fit the data, parallel with and perpendicular to the surface. For sake of clarity, are only shown (c) parallel and (d) perpendicular cuts for the 2D GISAXS pattern taken with the beam along the island edge (b). Continuous line: experimental cuts; filled squares: best fit of experimental cut. (e) and (f) Simulated 2D GISAXS patterns of (a) and (b) respectively obtained after fitting the above experimental cuts and using an island shape of a truncated octahedron with a square base schematically drawn. (g) Same as (e) but within DA. The intensity is represented with a logarithmic scale, the $2\theta_f$ (resp. α_f) axis ranges from 0 to 2.9° (resp. 3.3°). From Ref. [29].

one experimental GISAXS map (that with a scattering rod at 54.7° with respect to the surface normal in the (110) direction) has been simulated within the DA (cf. Fig. 61g). Notice that neither the DWBA-LMA, nor the DWBA-DA correctly reproduces the experimental diffuse scattering close to the beam stop, which will be discussed later.

7.3. Third example: Au/TiO₂(110)

The case of the analysis of GISAXS during the growth of Au on TiO₂(110) [155,81] will be discussed in more detail later (Section 9.1). We just compare here (Fig. 62) the experimental and simulated 2D GISAXS patterns for a 1.6 nm-thick deposit at room temperature. A good agreement between experimental and simulated image is achieved except near the specular rod. The simulated lobe displays a diffuse tail due to (i) the interplay between the size-spacing coupling and (ii) the strong correlation between the island radius and height [81]. The discrepancy with the experimental image could result from the beam stop shadowing. The above examples, for which the experimental 2D GISAXS maps are very well reproduced by the simulations, demonstrate on many different cases that the theoretical treatment presented above is well adapted to analyse 2D GISAXS data, at least when the islands are not ordered. The cases of ordered island repartition on the substrate will be treated in Section 9.4.

7.4. Diffuse scattering due to correlations

7.4.1. Evidence of diffuse scattering in GISAXS

Any fluctuation from a perfect system, such as a distribution of island sizes or correlations between sizes, positions or both, induces some diffuse (incoherent) scattering. A detailed analysis [29,235,155,81] of the induced diffuse scattering was given in the theoretical part Section 6.3 which introduces various approximations DA, LMA, SSCA, SA (Section 6.4). This diffuse

scattering is well evidenced by comparing the DA and LMA approximations (cf. Fig. 63). In the DA, in the parallel direction, incoherent scattering dominates over coherent scattering for small ($q_y R < 1$) and large ($q_y R > 3$) q_y values. Close to the position of the interference function maximum ($q_y R \approx 1.5$), the situation is reversed and the incoherent scattering is only equal to 10% of $S(q_y R) \times \langle |F(qyR)|^2 \rangle$. In the LMA, this small angle scattering is absent, which points to the fact that a long range size-position or size-size coupling exists. Notice that at high q_y values the two approximations give essentially the same results since the scattering is given only by the mean form factor for disordered systems.

7.4.2. Estimated diffuse scattering in GISAXS

The influence of such correlations on the scattered intensity was directly evaluated in the Pd/MgO(001) case [29] from the positions and sizes of the islands deduced from TEM plane views. Clearly, there was no size-size correlation, at variance to LMA hypothesis, but a strong coupling between the particle size and the distance to its nearest neighbors. This latter is easily understood in terms of depleted zone around each particle [8,253, 254]. The expected scattering was calculated from real space TEM images by assimilating each island scattering by that of a disk of equivalent surface (cf. Fig. 64). The analysis followed the treatment of scattering from correlated particles developed in the book of Guinier [40]. The intensity is decomposed accordingly to:

$$I(q_y) = \langle |F(q_y)|^2 \rangle S(q_y) + \sum_m I_{dm} \quad (195)$$

$$I_{dm} = \langle [F_n(q_y) - \langle F(q_y) \rangle] [F_{n+m}(q_y) - \langle F(q_y) \rangle] \rangle$$

where $\langle \dots \rangle$ is the average over the particles n and the index m runs over the closest neighbors shells. The scattering I_{d0} corresponds to the $\Phi_0(q_y) = \langle |F(q_y)|^2 \rangle - \langle |F(q_y)| \rangle^2$ term of Eq. (159), I_{d1} is the diffuse scattering obtained by considering the nearest neighbor (NN) shell around each island and I_{d2} is the diffuse scattering

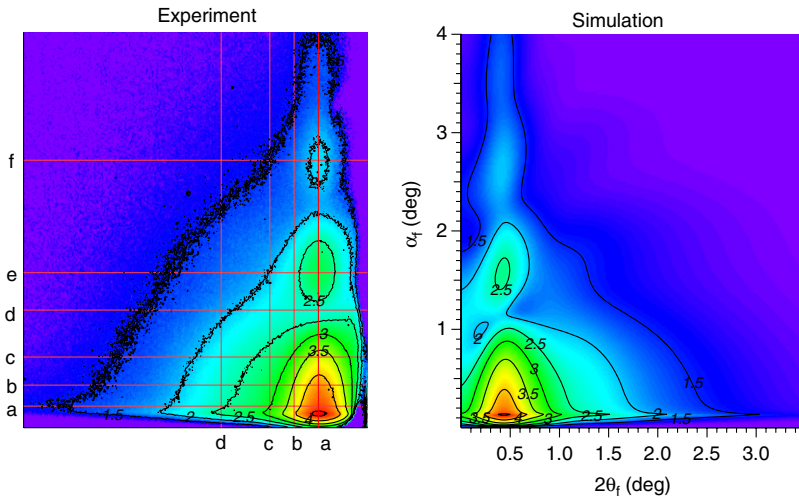


Fig. 62. Experimental (left) and simulated (right) GISAXS patterns of a 1.6 nm thick RT Au deposit on TiO₂(110). The color scale is logarithmic as given by the contour lines. From Ref. [81].

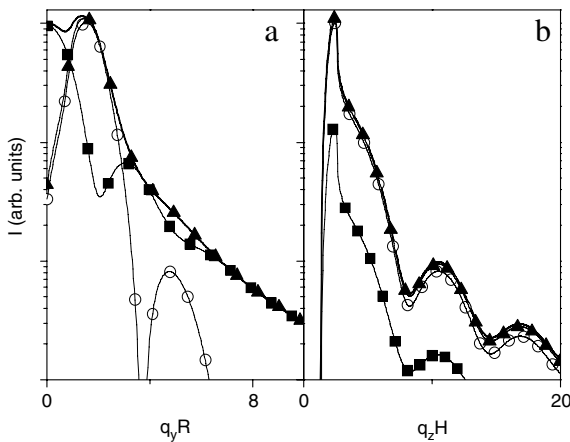


Fig. 63. (a) Intensity versus $q_y R$ for a cylinder within the DWBA. Open circles: $I_1 = S(q_y R) \times \langle |F(q_y R)|^2 \rangle$; filled squares: $I_2 = \langle |F(q_y R)|^2 \rangle - \langle |F(q_y R)| \rangle^2$; bold line: $I_1 + I_2$, i.e., the GISAXS intensity within the DA; triangle: GISAXS intensity within the LMA. (b) Same as (a) but versus $q_z H$. The parallel (resp. perpendicular) direction is taken at the maximum intensity in the perpendicular (resp. parallel) direction. The numerical values used for the simulation are those of 0.9 nm Pd/MgO(001) at 550 K. From Ref. [29].

obtained up to the second shell. For larger cutoff, the obtained curves were noisy due to poor statistics. For Pd/MgO(001) at 550 K (cf. Fig. 64a), the incoherent diffuse scattering intensity is nearly independent of the size of the neighbor shell used for the calculation. On the contrary, for the deposit at 650 K (cf. Fig. 64b) and 740 K (cf. Fig. 64c), the I_{d3} peak is larger and narrower than the I_{d0} one at small $q_y R$. This example shows that high order correlation between scattering objects can strongly influence the diffuse scattering particularly close to the origin of the reciprocal space in the parallel direction and reduce the intensity as compared to the expected one in DA.

7.4.3. Size-position correlation deduced from GISAXS

In all cases shown up to now, either the DA (no correlations between sizes or sizes and separations of nearest neighbors [73, 42]) or the LMA (full correlation between shape and sizes of neighboring islands over the coherent area of the X-ray beam [234, 256]) were assumed, while in many physical cases, strong correlations exist either between the sizes of nearest neighbors (e.g. during the organized growth of nanoparticles on a lattice of

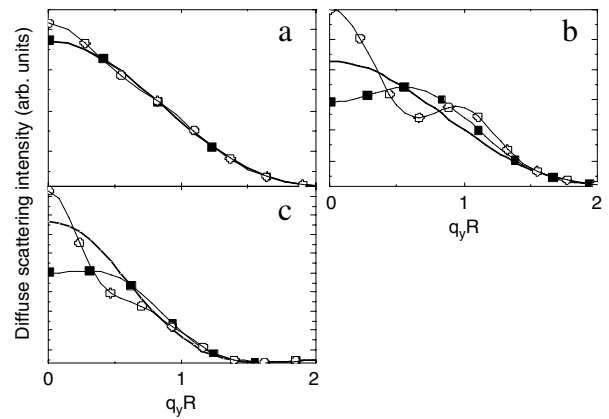


Fig. 64. Diffuse scattering calculated with a cylinder shape versus $q_y R$ for Pd at (a) 550 K (0.9 nm thick Pd), (b) 650 K (3.0 nm thick Pd), and (c) 740 K (3.0 nm thick Pd) deduced from the TEM plane views. Continuous line: I_{d0} ; filled squares: I_{d1} ; open circles: I_{d2} . From Ref. [29].

nucleation-growth sites) or between the sizes and the separation between nearest neighbors (which is the general case of growth on surfaces, where the size of the Voronoi cell of an island scales with the island size). It has been shown theoretically by Leroy et al. [235] using a purely one-dimensional model that the GISAXS intensity at small q_y depends on such size-size or size-spacing correlations.

A close examination of GISAXS data from the Ag/MgO(001) system [79] (see e.g. Fig. 21a and b) shows that the second and third order maxima are often slightly tilted with respect to the q_z axis, with a positive slope $\tan(\epsilon) = \delta q_y / \delta q_z$. This tilt is a signature of a size-position correlation. In first approximation, $D = 2\pi / q_{y,p}$, where $q_{y,p}$ is the q_y coordinate of maximum intensity. By derivation, $\delta q_y / \delta q_{y,p} = \delta D / D$. If the island is modeled by a simple geometric shape like a parallelepiped or a cylinder, in first approximation (i.e. neglecting the refraction effects): $H \approx 2\pi / q_{z,0}$, where $q_{z,0}$ is the smaller q_z position of minimum intensity. In a similar way, $\delta q_z / \delta q_{z,0} = \delta H / H D$. If there is a self-similar relationship between H and d , $\delta H / H = \delta d / d$ and thus $\delta D / \delta d = \tan(\epsilon) D^2 / H d$. For the 2-nm thick Ag/MgO sample at 540 K (see Fig. 21a and b), $\tan(\epsilon) = 6.3 \times 10^{-2}$ and hence $\delta D / \delta d = 0.279$. This was found to be in a very good agreement with an analysis of plane view TEM data [78,79]. As a conclusion, this tilt slope is a direct measure of coupling between the size and the spacing of the islands as shown for many other ones (Pd/MgO(001) [29] and Au/TiO₂(001) [81]; see Fig. 55).

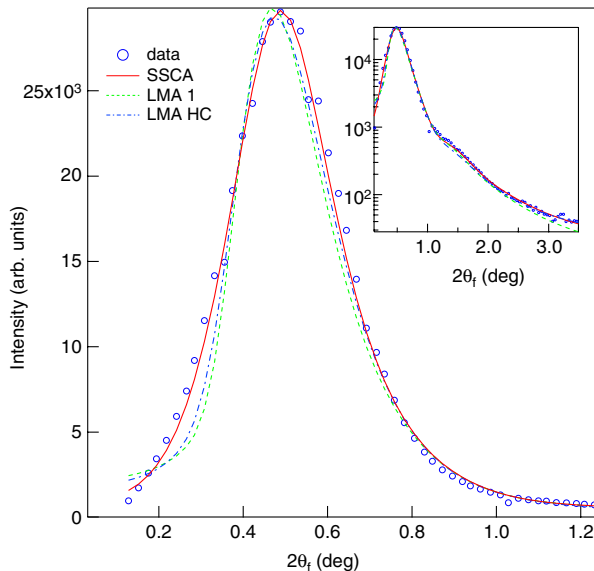


Fig. 65. Comparison of the various approximations used to fit the correlation peak of a 1.6 nm thick gold deposit on $\text{TiO}_2(110)$. Experimental data (points); SSCA (full red line); LMA 1 (green dotted line); LMA with a 1D paracrystal interference function with a linear link between size and distance; LMA HC (blue dash dotted line); same as LMA 1 but for 2D hard core interacting particles. See Ref. [81] for details. (For interpretation of the references to colour in this figure legend, the reader is referred to the web version of this article.)

On a theoretical point of view, those correlations can be partially taken into account either (i) in 1D in the framework of 1D paracrystal with the SSCA [235,155,81] (see Section 6.4.3) or (ii) in LMA by linking spacing on size. A satisfying agreement with the experimental lineshape of the correlation peak (Fig. 65) is obtained even though the underlying hypothesis are somehow drastic.

8. Non-UHV GISAXS experiments

8.1. Embedded metallic nanoparticles

The fabrication of nanometer size clusters embedded in a matrix may be very promising for future applications taking advantage of the new properties of these materials (see for instance Ref. [266]). For instance magnetic clusters inside an insulating matrix may induce Tunnel Magneto-Resistance effects (TMR) [267, 55,19] with potential applications for spin dependent electronic devices, or can be the building blocks for high density storage of information [268]. Metallic clusters can be also efficient absorbers of radiations in the visible and near-infrared regions [269] or can be inserted inside coatings for their mechanical and bio-compatibility properties [56]. However the controlled fabrication of these materials needs the development of appropriate characterization tools in the nanometer range. For that sake GISAXS has proved to be very helpful for analyzing the size distribution and spatial organization of buried clusters. Tuning the angle of incidence around the critical angle of total external reflection [270,271] it is possible to adjust the penetration depth of the beam and to extract a depth profile of the clusters size/shape. The quantitative analysis of the GISAXS patterns must take into account the refractions effects the X-ray beam at the interfaces. The appropriate theory for the X-ray scattering process in grazing angles conditions is the DWBA [35,58,59,36,37].

8.1.1. Granular solids and multilayers of metallic clusters embedded into oxide matrices

- In view of the fabrication of new materials with spin-dependent magneto-resistance or Coulomb blockade effects, it has been

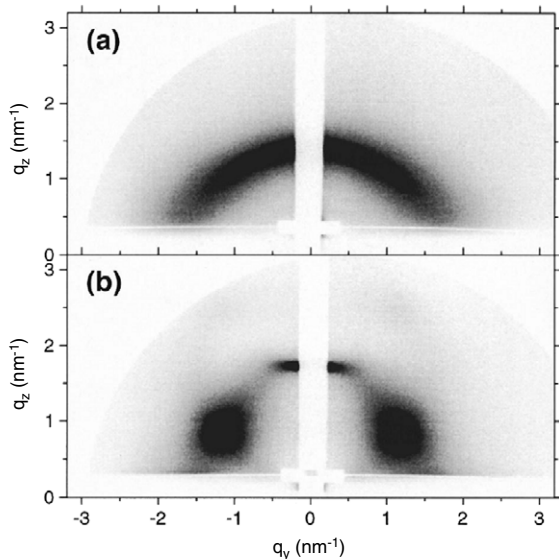


Fig. 66. GISAXS patterns of (a) a Fe 35% Al_2O_3 granular solid and (b) a $[\text{Co}(0.7 \text{ nm})/\text{Al}_2\text{O}_3(3 \text{ nm})]_{30}$ granular multilayer (from Ref. [55]).

proposed to grow metallic (and ferromagnetic) aggregates of nanometer size embedded in an insulating matrix [272,273]. In that purpose Naudon and coworkers [267,55] have grown granular solids and granular multilayers. Granular solids, such as Fe clusters embedded in an alumina matrix, are obtained by cosputtering of both materials. To achieve a better control of the size and ordering of the clusters granular multilayers are grown by sequential deposition. This approach has been applied to the growth of Co clusters in Al_2O_3 . The spacing and size of the Co clusters is tuned by choosing the thickness of the Co layer and the temperature while alumina serves as a spacer between layers. The deposition has been made at RT on Si(001) substrates by RF sputtering with a base pressure of 5×10^{-8} Torr and an Argon pressure during deposition of 4 mTorr. The characterization of the granular solid/multilayers has been performed *ex situ* by TEM and GISAXS at LURE (D22) [274]. Fig. 66a and b show two GISAXS images of a Fe- Al_2O_3 granular solid and a Co- Al_2O_3 granular multilayer. In the case of Fe- Al_2O_3 , the scattering pattern exhibits an elliptical halo revealing a dense distribution of Fe clusters with a slight anisotropy parallel with and perpendicular to the surface plane. Analysis shows that the Fe clusters are slightly elongated along the film growth direction ($D_\perp = 3.3 \pm 0.2 \text{ nm}$ and $D_\parallel = 2.5 \pm 0.2 \text{ nm}$). On the contrary the GISAXS pattern of the granular Co- Al_2O_3 multilayer shows much more characteristic features of ordering. The first Bragg peak from the multilayer periodicity appears at $q_z = 1.745 \text{ nm}^{-1}$ and is partially hidden by the beamstop. The second characteristic feature is the presence of two symmetric lobes arising from the Co clusters network. From their positions an in-plane and an out-of-plane ordering of the Co clusters induced by the vertical stacking of the layers is clearly evidenced. In combination with TEM measurements, the authors have proposed a fcc stacking model of the Co clusters network.

- Similarly, Thiaudiere and coworkers [19] have grown and characterized discontinuous Co/ SiO_2 multilayers. The samples were prepared at RT by sequential deposition of Co and SiO_2 (DC sputtering for Co and RF sputtering for the oxide). The thickness of the Co layer varies from 0.6 to 2 nm whereas the SiO_2 layer thickness is kept constant (4.3 nm) over the 60 Co/ SiO_2 bilayers. The sample was annealed under vacuum (10^{-5} Torr) during 10 min at 200 °C and 400 °C. The typical GISAXS (ESRF, ID1)

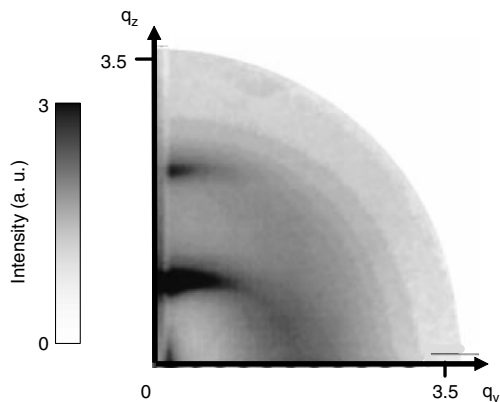


Fig. 67. Half GISAXS pattern of a $[Co_{(0.6\text{ nm})}/SiO_2(4.3\text{ nm})]_{60}$ discontinuous multilayer (adapted from Ref. [19]).

pattern shown in Fig. 67 displays characteristic Bragg peaks of the period of the bilayer (4.9 nm) along the specular rod ($q_y = 0$). The presence of scattering arcs show that the Co clusters are short range correlated but no clear anisotropy is put in evidence. The GISAXS data were fitted in the framework of the DWBA for buried clusters and assuming a spherical shape. It is clearly shown that the spacing between the Co clusters increases as function of the Co layer thickness indicating a coalescence process. Moreover from scaling theories of coalescence [275, 276], it was concluded that the nucleation mode of the Co clusters is heterogeneous.

- Studies on magnetic clusters with a high magnetic anisotropy are also stimulated by the demand for the fabrication of devices with a large storage density [4,277]. For that sake it has been shown that alloys of Pt and a transition metal (Co, Fe or Ni) exhibit a large magnetic anisotropy thanks to a large magnetocrystalline anisotropy and a hybridization between Pt and the transition metal. However, the magnetic properties of these clusters are strongly dependent on their size, morphology and crystalline phase. Recently, mixed CoPt clusters have been synthesized under UHV by laser vaporization and inert gas condensation [268]. The cluster deposition process (collimated supersonic beam) is simultaneously performed with the evaporation of a matrix to produce diluted clusters, either supported on a carbon-coated copper grid with a thin amorphous Si layer on top or embedded clusters inside a MgO or Si matrix. The morphology of the clusters has been characterized by GISAXS (ESRF, D2AM) for embedded clusters and TEM for supported ones. Fig. 68 shows a GISAXS pattern of clusters embedded in MgO. No correlation peak is visible in agreement with the presence of dilute clusters. The isotropic shape of the GISAXS pattern indicates that the clusters are roughly spherical. A quantitative analysis has been performed considering a log-normal size distribution of spheres and applying the DWBA for buried clusters [36]. Simulations of 1D GISAXS cuts based on TEM measurements are in a qualitative good agreement with the experimental GISAXS data (mean diameter: 2.1 nm; and FWHM: 0.35 nm). Moreover no change is detected between GISAXS images of clusters embedded in a Si matrix and a MgO matrix. Accordingly, the matrix does not play a role in the clusters' shape and size. Interestingly, the authors compared the determination of the size by GISAXS and wide angle X-ray scattering measurements. Contrary to GISAXS, this technique is only sensitive to crystallized regions. From the position and width of the Bragg peaks, the CoPt clusters are disordered fcc alloys, and the mean diameter is 1.3 nm. This value is smaller than the one deduced by GISAXS because the core of the clusters is well crystallized but the shell is

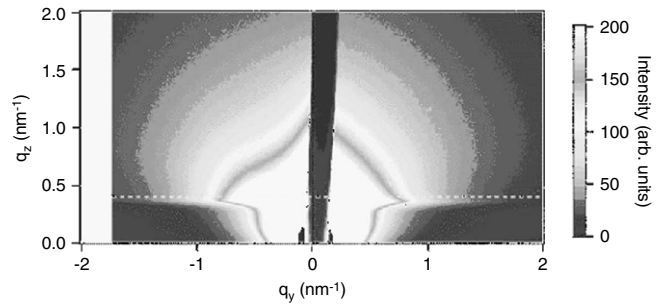


Fig. 68. GISAXS pattern of $Co_{58}Pt_{42}$ clusters embedded in a MgO matrix (from Ref. [268]).

amorphous due to the surrounding matrix. Complementary magnetic measurements by SQUID (Superconducting Quantum Interference Device) and XMCD (X-ray magnetic circular dichroism) have revealed that the blocking temperature is determined by the ferromagnetic core of the clusters and not the surrounding matrix.

- Confined metallic nanoparticles into an insulating matrix have also a considerable interest as absorber of radiation and could be used in the future as smart coatings for windows or as non-linear optic devices. The plasmon absorptions on which those systems rely depend strongly on the particle aspect ratio and density. The GISAXS technique has been used in combination with X-ray Reflectivity and TEM in the case of Pt nanoparticles inside an Al₂O₃ matrix [269]. The thin film is prepared by cosputtering of Pt and alumina onto a wafer of Si(100) held at 300 °C. The X-ray experiments were carried out at LURE (France) at the beamline D22. A typical GISAXS image is shown in Fig. 69. A ring is clearly visible related to an isotropic preferential distance between the Pt particles. Interestingly, this distance is also observed by X-ray Reflectivity: the reflectivity curve exhibits a very intense oscillation at the same q which can be attributed to a layering of the Pt clusters. To analyze the reflectivity curve and the GISAXS pattern, the authors assumed that the thin film is made of ordered regions with a layering of the Pt clusters which is responsible for the reflectivity curve and disordered regions giving rise to the scattering ring observed by GISAXS. This hypothesis is clearly confirmed by TEM. The Pt layers are more and more disordered as function of the distance from the substrate. This shows the complementarity of real space imaging techniques and scattering techniques to validate a structural model.

8.1.2. Encapsulated Ag, Fe, Pt and Au nanoparticles into carbon and boron nitride

Metal nanoparticles encapsulated in a cage of carbon or boron nitride are protected against outside degradation or coalescence by stopping the diffusion processes [278]. In case of magnetic nanoparticles, the matrix is also useful to reduce the particle-particle exchange coupling. These nanoparticles are prepared by co-sputtering (Kaufman Ar⁺ ion source at 1.2 keV) and deposited on a substrate providing directly thin films for magnetic, electronic or mechanical applications. Due to the limited solubility of metals in the matrix, a unmixing process occurs (for Fe into C the solubility is about 5% at 1100 K). It has been shown that a relative control of the size of the metal nanoparticles could be achieved by this method. In order to characterize encapsulated metal nanoparticles, *ex situ* GISAXS and TEM measurements have been performed completed in some cases with EXAFS and Mössbauer Spectroscopy.

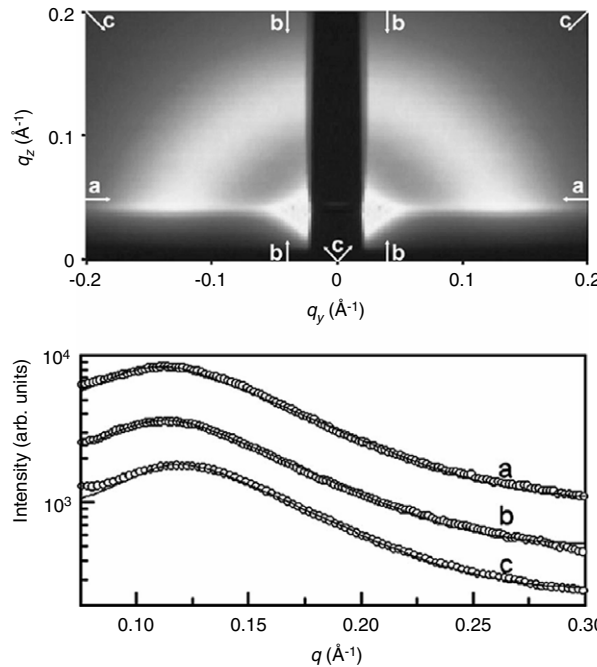


Fig. 69. GISAXS pattern of Pt-Al₂O₃ nanocermet thin film. Cross sections (open circle) and calculated profile (solid line) below (from Ref. [269]).

- Ag nanoparticles encapsulated in a cage of C [270,271].

Fig. 70 shows 3 GISAXS patterns of a C-Ag_{33%} (293 K) thin layer (210 nm) deposited on a Si wafer measured for different grazing angles. Changing the angle of incidence, the X-ray beam penetrates more or less into the bulk of the sample. It is a means to distinguish between nanoparticles close to the surface and deeply buried. For the largest incident angle (Fig. 70c), an elliptical halo indicates the presence of short range correlations between the Ag nanoparticles in the bulk of the sample. The in-depth average distance is slightly larger than the in-plane average distance (respectively 6.5 nm and 4.0 nm) and the in-plane and in-depth diameters are respectively 2.2 nm and 5.1 nm as deduced from the radius of gyration. Decreasing the angle of incidence (see Fig. 70a and b for $\alpha_i = \alpha_c$ and $\alpha_i = \alpha_c + 0.05^\circ$) two intense spots appear on both sides of the beamstop close to $q_z = 0$. This reveals that large Ag nanostructures are also present nearby the surface. The GISAXS data are accurately fitted considering spherical Ag nanoparticles of 10 nm diameter and a first neighbor mean distance of 23.3 nm as confirmed by AFM. To understand the formation of these two types of Ag clusters, in the bulk and at the surface, the authors made two additional experiments: (i) a similar C-Ag_{33%} (293 K) thin layer has been synthesized with an additional pure carbon layer (20 nm) on top just after the co-deposition process and still in vacuum, called C/C-Ag. (ii) a thin layer of Ag (0.8 nm thick) has been grown on top of a sublayer of carbon (20 nm), called Ag/C. The GISAXS characterization of the C/C-Ag sample shows only an elliptic halo due to small buried Ag clusters elongated perpendicular to the surface. However no intensity scattered by Ag clusters close to the surface is found. On the contrary, in the case of the Ag/C layer, GISAXS measurements reveal the presence of large spherical Ag clusters at the surface similar to the C-Ag_{33%} sample. It is concluded that, in the case of C-Ag_{33%} thin films, the carbon layer is a barrier of diffusion for Ag preventing the formation of large Ag clusters in the bulk whereas at the film surface, large Ag clusters grow by surface diffusion.

- Au nanoparticles on an amorphous C surface [53].

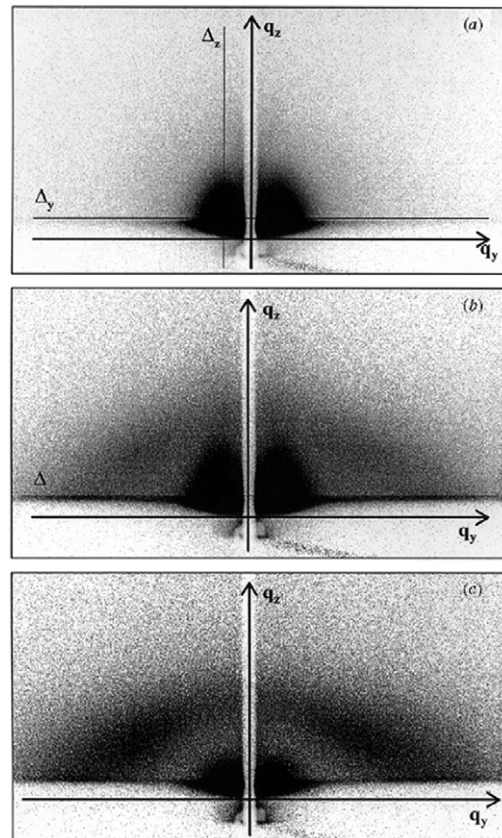


Fig. 70. GISAXS patterns of a co-sputtered C-Ag thin film (210 nm) measured at different grazing angles: (a) $\alpha_i = \alpha_c$, (b) $\alpha_i = \alpha_c + 0.05^\circ$, (c) $\alpha_i = \alpha_c + 0.1^\circ$ (from Ref. [271]).

Similarly to Ag, Au nanoparticles have been grown on an amorphous C surface [53]. In Fig. 71 is shown a GISAXS pattern of 1.7 nm of Au deposited on a thin film of amorphous carbon (25 nm) pre-deposited on a Si substrate. It exhibits two characteristic correlation peaks on both sides of the beamstop. The signal arises from in-plane short range ordered Au nanoparticles. This pattern is typical from 3D nanoparticles in agreement with the Volmer–Weber growth mode of Au on C. The authors have analyzed the GISAXS pattern in the framework of the DWBA but considering the calculation for buried clusters, *i.e.* taking into account the refraction effects at the air/C interface. A better approach should take into account the DWBA for supported clusters [35,37]. Supposing that the Au clusters are cylinders, the authors have deduced that the mean diameter and height are respectively 5.9 ± 0.5 nm and 4.5 ± 0.4 nm. The peak of the interference function gives a mean distance of 10.2 ± 0.5 nm.

- Pt nanoparticles encapsulated in a cage of C [53].

Pt nanoparticles embedded into a carbon matrix have been produced by the same physical process (co-deposition) at RT with an additional irradiation (Ar^+ , 120 keV) during growth [53]. Thanks to the phase separation of both elements, Pt aggregates into clusters. The corresponding GISAXS pattern shows the presence of a half ring indicating an isotropic spatial distribution of the nanoparticles. The intensity versus q can be analyzed considering a polar integration centered at the origin of the reciprocal space. The mean diameter (1.6 ± 0.2 nm) and the mean distance between the Pt clusters (3.4 ± 0.2 nm) are extracted, and found to be in good agreement with TEM data.

- Fe nanoparticles encapsulated in a cage of C [279].

Very similar results have been obtained by Babonneau et al. for Fe nanoparticles encapsulated into a C cage grown

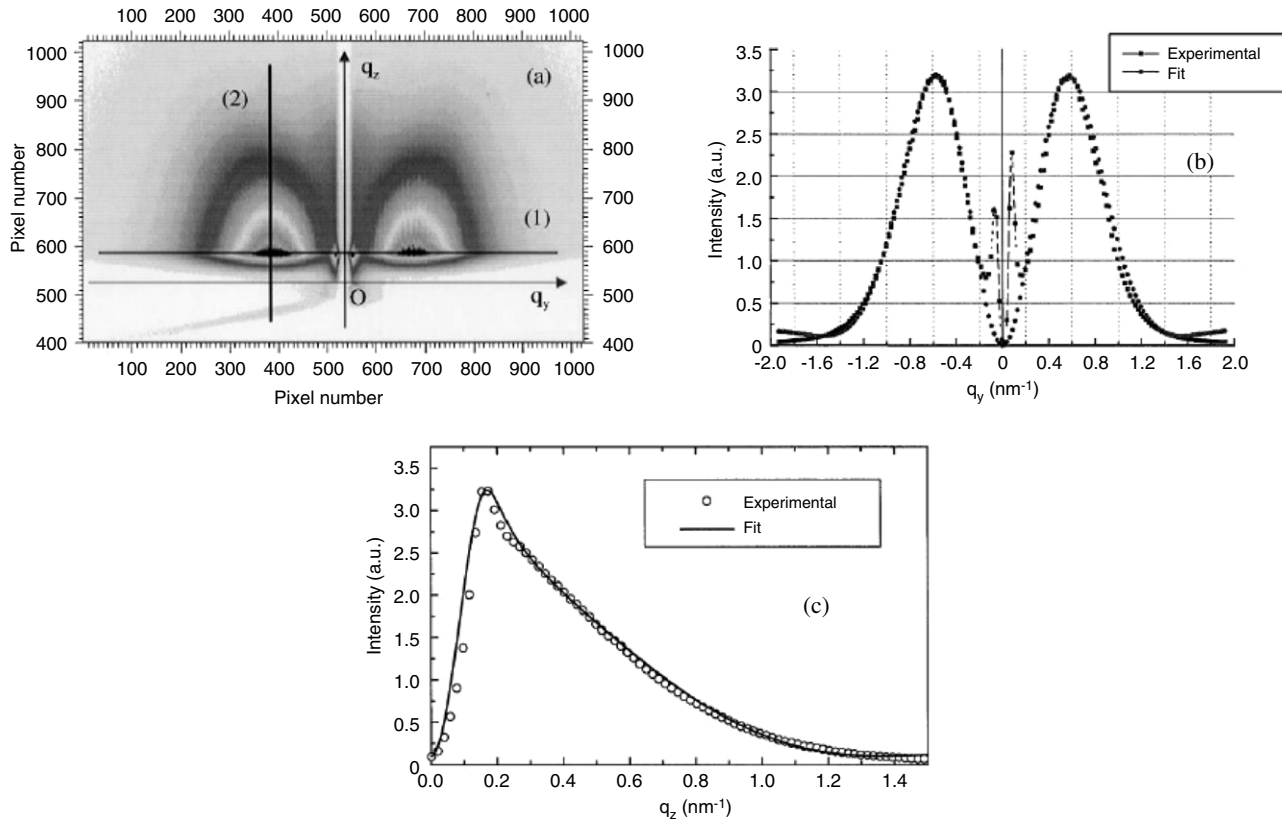


Fig. 71. Gold-deposited sample: 1.7 nm Au/25 nm a-C/Si: (a) Scattering pattern for $\alpha = \alpha_c$. Pixel sizes: 100 pixels corresponds to 0.36 nm^{-1} and 0.403 nm^{-1} vertical and horizontal respectively. Horizontal and vertical cross-sections made from the scattering pattern are labeled (1) and (2), respectively. (b) Horizontal cross-section. (c) Vertical cross-section (from Ref. [53]).

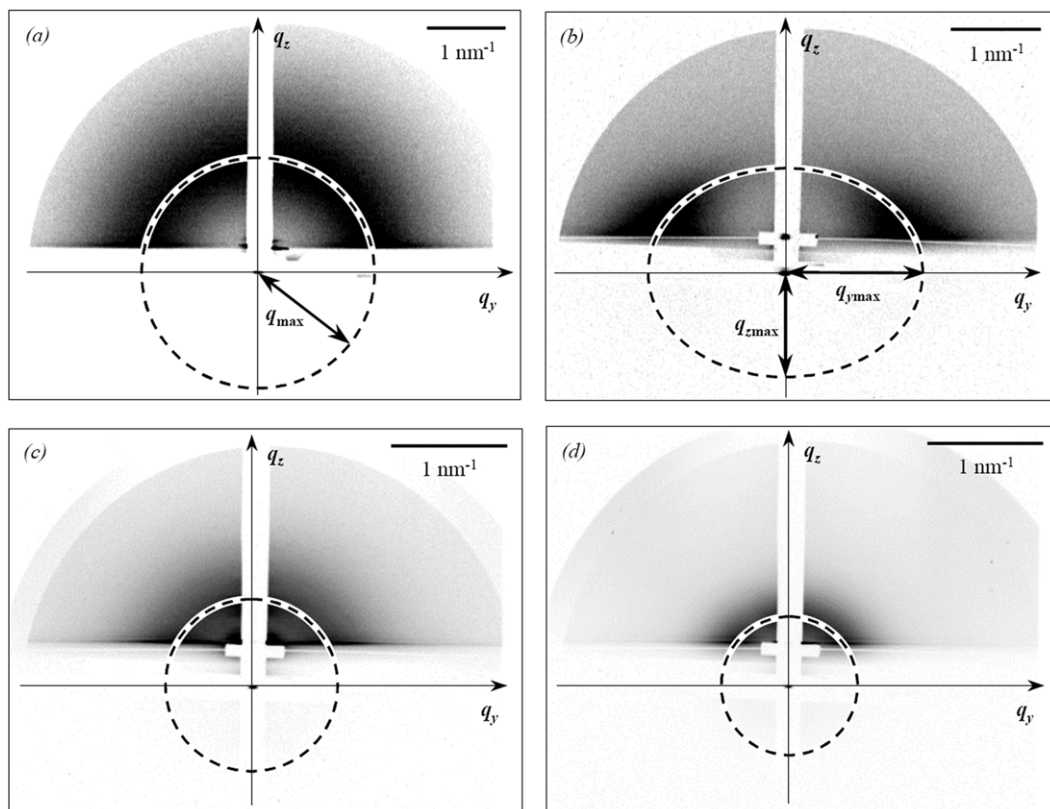


Fig. 72. GISAXS patterns of C-Fe thin films prepared by different procedures depicted in the text: (a) Fe^+ implantation into C, (b) C-Fe co-sputtering, (c) Ar^+ implantation during C-Fe co-sputtering and (d) Ar^+ implantation after C-Fe co-sputtering (from Ref. [280]).

by the same method. Fig. 72b shows a GISAXS pattern of the as-deposited C-Fe thin film (co-deposition ion-beam sputtering method at 573 K). The presence of an elliptical halo indicates the presence of correlations between particles which depend on the directions perpendicular to and parallel with the surface plane. The method of preparation of these Fe nanoparticles has been compared with other approaches (i) Fe^+ implantation into C, (ii) He^+ implantation during C-Fe co-sputtering, (iii) Ar^+ implantation during C-Fe co-sputtering and (iv) Ar^+ implantation after C-Fe co-sputtering. In case of (i) Fe^+ implantation into a C matrix, the GISAXS pattern (see Fig. 72a) is a perfect half-circle corresponding to correlated spherical nanoparticles without anisotropy. The influence of ion beam assistance during the co-sputtering process is different in the case of He^+ and Ar^+ implantation. For (ii) He^+ implantation, no change has been detected whereas for (iii and iv) Ar^+ implantation (Fig. 72c and d), the intensity scattered by the Fe clusters shows no spatial correlation (diluted clusters). Depending on the growth conditions very different Fe nanoparticles can be obtained.

- Embedded Au clusters in amorphous hydrogenated carbon thin films (*a*-C:H) [56].

Metal nanoparticles in an amorphous hydrogenated carbon thin film is promising in view of the fabrication of biocompatible coatings for medical implants (see for instance Ref. [281]) or coatings with selective optical solar absorber properties. Among them Au nanoparticles embedded in an amorphous hydrogenated carbon thin film is a model system due to the low reactivity of Au and C. Thin films were fabricated by magnetron sputtering with a Au target combined with Plasma-Assisted Chemical Vapor Deposition (PACVD) of a carbon monomer. The thickness of the films were about 80 nm and the gold content 6.6 at.% and 8.2 at.%. To characterize the size and spacing of Au nanoparticles GISAXS measurements have been performed at the beamline D22 (LURE, France). Fig. 73 shows a typical 2D GISAXS pattern of the *a*-C:H/Au 8.2 at.% film. It can be described as a quasi-isotropic half ring arising from a preferential distance between neighboring Au clusters. Azimuthal scans did not reveal any anisotropy and the Au clusters are probably not far from a sphere as also deduced from optical measurements. To extract more quantitative information concerning the anisotropy of the thin films, the authors analyzed 1D GISAXS cuts as functions of the polar angle ϕ in the range $30^\circ \leq \phi \leq 70^\circ$. The analysis is based on the DWBA theory for buried nanoparticles [36] combined with a traditional Guinier plot for monodisperse elliptic particles. An elongation of the Au nanoparticles perpendicular to the surface is found in contradiction with optical measurements. The Guinier plot is however erroneous because of the interference peak and because of the polydispersity of the nanoparticles. The authors proposed to solve both drawbacks considering a model based on the Local Monodisperse Approximation with an interference function based on the Perkus-Yevick approximation for hard spheres [282]. The fit of the GISAXS data show clearly that the Au nanoparticles are indeed spherical in average.

- Assisted growth of Fe nanocolumns in a Boron Nitride matrix [283,284]

Similar to encapsulated metallic particles in a C-cage, it has been proposed to encapsulate metallic particles into Boron Nitride (BN). BN provides not only corrosion and wear resistance as graphite but also electrical insulating which may be a great advantage for the sake of controlling the spin-dependent tunneling between adjacent nanoparticles. Babonneau et al. (see Ref. [283]) have prepared Fe-BN nanocomposite films on Si(100) wafers at 200 °C with an ion-beam codeposition process from a single target composed of

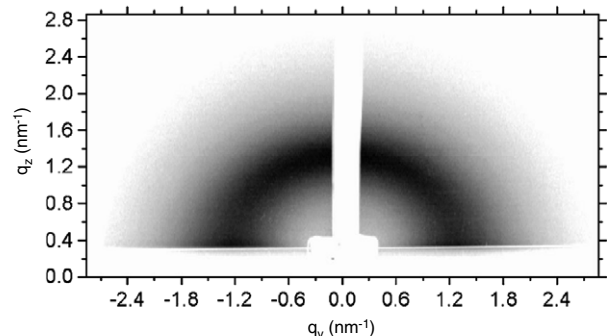


Fig. 73. GISAXS pattern of the *a*-C:H/Au 8.2 at.% thin film. The interference function is quasi-isotropic (half ring). From Ref. [56].

a pure BN disk and a high purity Fe platelet. The sputtering was carried out at 2×10^{-4} Torr of Ar^+ . An additional secondary ion beam was used to vary the growth conditions using either a reactive gas (N) or an inert one (Ne, Ar, Kr). A characterization of the samples has been performed *ex situ* by GISAXS (LURE, DW31B beamline, France) and HRTEM for the morphology of the Fe clusters; the chemical ordering has been studied by EXAFS and Mössbauer Spectroscopy. Fig. 74 shows the evolution of the GISAXS patterns as function of the preparation conditions. Qualitatively, the GISAXS patterns show different characteristic features. The unassisted and N-assisted films show an elliptic halo arising from correlated Fe-rich particles in all directions (the anisotropy is larger for the N-assisted sample). In the case of Ne, Ar or Kr assisted thin films, a clear in-plane organization is put in evidence but no ordering perpendicular to the surface. This anisotropy can be assigned to a columnar shape of the Fe-rich clusters. This result is consistent with microscopy images. The data fit has been performed in the framework of the DWBA assuming buried nanostructures [36]. The description of the system is based on the Local Monodisperse Approximation considering the Perkus-Yevick approximation (hard sphere approximation) for the interference function and different shapes for the clusters [282]: cylinder, oblate spheroid, capsule (cylinder ending with hemispheres on both sides). The values deduced from the fit shows that in the case of unassisted growth, the Fe-rich clusters are quasispherical nanoparticles, whereas oblate spheroids are found for the N-assisted growth. In the case of assisted growth by inert gases, the most appropriate cluster shape is an elongated vertical capsule. Therefore huge morphological changes occur as function of the assistance conditions. This result is confirmed by cross-sections images by HRTEM and a plane view by TEM. From the fit, it is shown that the Fe columns have a larger diameter than the spheroidal clusters and the in-plane ordering is improved in the case of Ar and Ne assisted films. The morphology change of the Fe clusters can be attributed to the enhancement of the surface diffusion induced by the ion beam (also responsible for the increase of diameter). However in the case of N, this effect is strongly reduced because N reacts with Fe or B to form nitride compounds. The complementary use of EXAFS and Mössbauer Spectroscopy provides details on the local chemical order of the Fe-rich nanoparticles showing that they contain a large amount of B. Growth of clusters inside BN has also been performed with Ag and then extended to multilayers [284]. Similarly the assistance of an ion beam in the encapsulation process plays a key role in the morphology of the clusters.

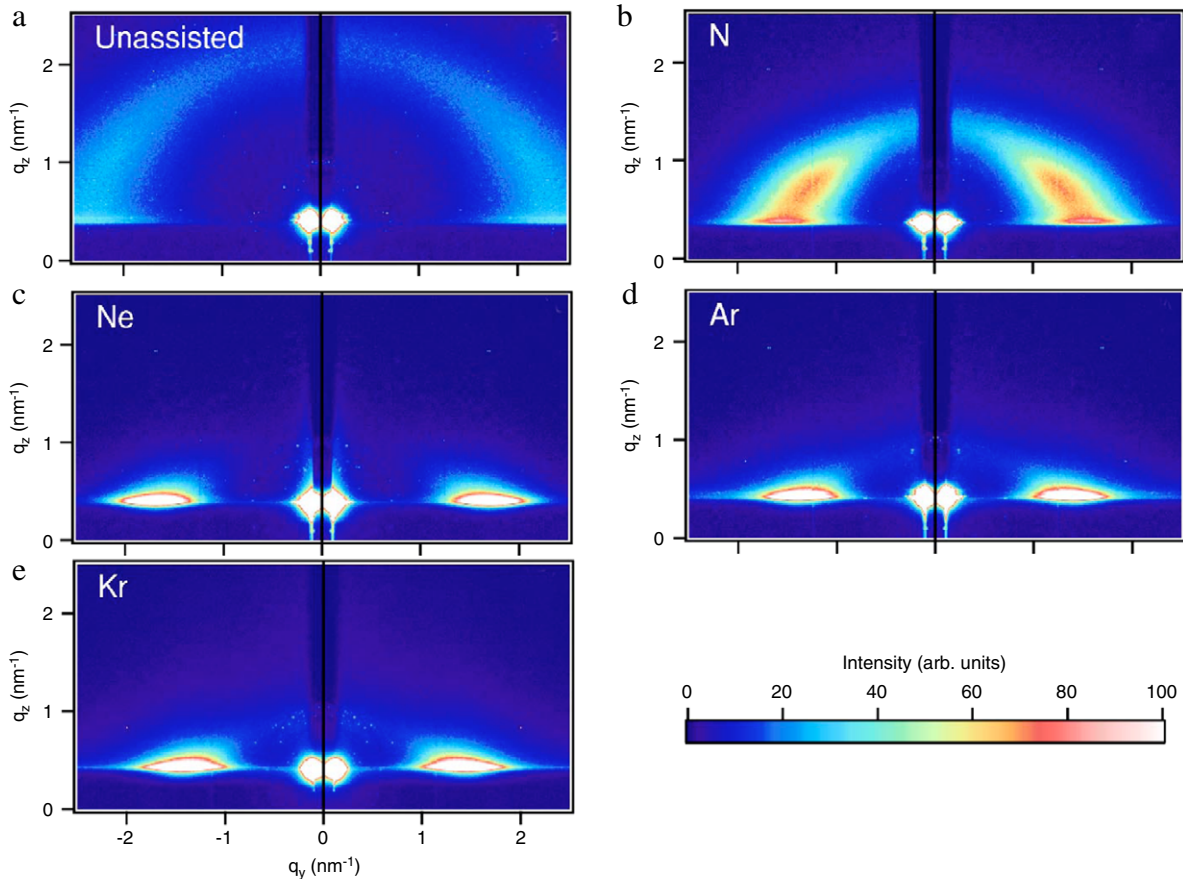


Fig. 74. GISAXS patterns of Fe–BN nanocomposite films: (a) unassisted, (b) N assisted, (c) Ne assisted, (d) Ar assisted and (e) Kr assisted (from Ref. [283]).

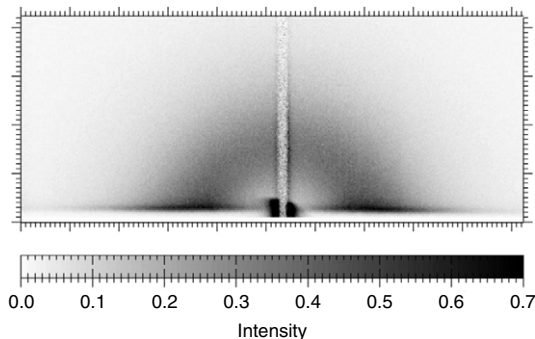


Fig. 75. GISAXS pattern of CuNi sample. The ϕ angle (see text) is measured from the vertical (from Ref. [285]).

8.1.3. Embedded clusters into glass by ion implantation

Nanoparticles into a matrix can be obtained also by ion implantation. This method provides far from equilibrium systems and in that way it is possible to avoid solubility and diffusion limitations. It has been applied in the case of the sequential implantation of Cu (90 keV) and/or Ni ions (100 keV) into silicates at RT. The embedded clusters have been studied by *ex situ* GISAXS at the ESRF (beamline ID1, France) combined with Rutherford Backscattering Spectrometry (RBS) and TEM [285]. A GISAXS pattern is shown in Fig. 75. The half-ring is a clear indication of spatially correlated particles without anisotropy as shown by radial scans at different polar angles. To extract information on the ordering and size of the clusters (assumed spherical), a complete quantitative analysis has been performed in the framework of the Local Monodisperse Approximation (LMA) and the Decoupling Approximation (DA) but in the Born Approximation. Both approximations give satisfactory

fits. However the values of the parameters are significantly different. For instance the mean radius of the particles deduced from the LMA is 1.86 nm whereas it is equal to 2.26 nm in case of the DA. Comparing the deduced density of particles with the metal concentration measured by RBS, the LMA seems to be the most reliable approximation. Similar isotropic GISAXS images have been obtained on Au + Cu implanted silica [286]. However in the case of Cu + Co implanted silica the presence of preferential in-plane correlations [286] have been observed.

8.2. Porous materials

8.2.1. Mesoporous silica thin films obtained by self-assembly: *ex situ* and *in situ* studies

Mesoporous thin films are potentially useful for a wide range of applications such as sensors [287], catalysts due to the large specific surface area, as well as waveguides [288], or nanofluidic systems [289]. It has been shown recently that well-defined mesoporous silica thin films could be obtained by controlling the evaporation of a silica/surfactant/solvent solution to obtain self-assembly of inorganic and organic constituents at the nanometer scale [290–293]. The technique relies on the use of the complex phase diagram of the surfactant/solvent system to orient the final morphology through a template effect. A subsequent high temperature thermal treatment allows one to condense the silica precursor and remove the organic part. A better understanding of the ordering mechanism during the evaporation-induced self-assembly is a critical need to achieve reproducible samples. For that sake, time resolved *in situ* GISAXS studies have been undertaken at X22C, NSLS. They were combined with gravimetric analysis to study the self-assembly process under controlled

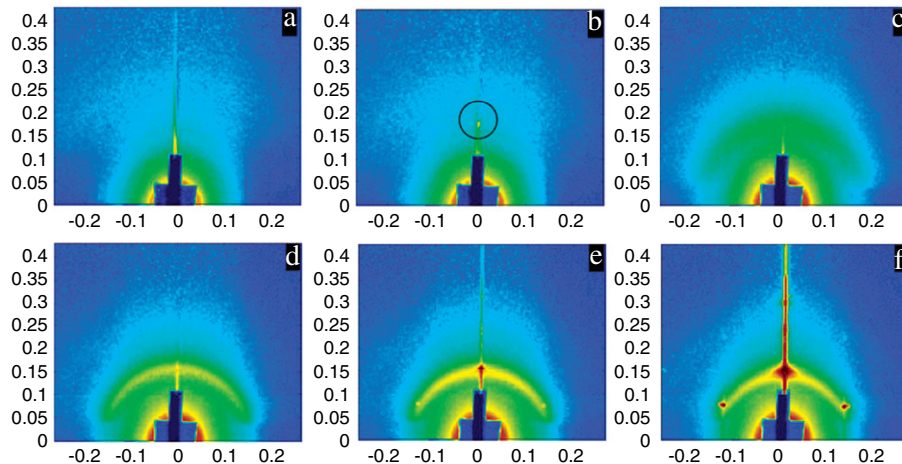


Fig. 76. GISAXS patterns measured at different times during the evaporation process. (a) isotropic phase, (b) lamellar phase, (c) and (d) correlated micellar phase, (e) and (f) hexagonal phase (from Ref. [294]).

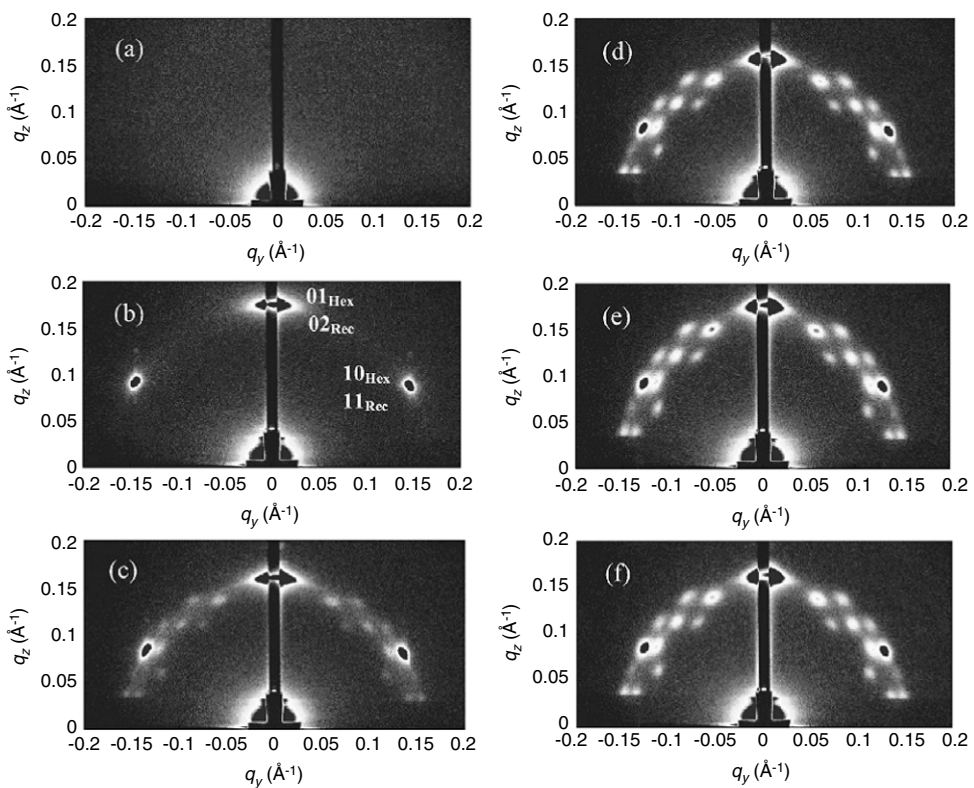


Fig. 77. Chronological measurement by GISAXS of the phase transformation of a diluted liquid film into a structured mesophase. (a) Liquid phase. (b) Hexagonal phase ($\text{RH} = 0.4$). (c) 2D hexagonal phase and onset of the cubic phase. (d) Coexistence of the 2D hexagonal phase and the cubic phase at high humidity ($\text{RH} = 0.8$). (e) Distorted 2D hexagonal phase and cubic phase at low humidity ($\text{RH} = 0.3$). (f) Distorted 2D hexagonal phase and cubic phase at high humidity ($\text{RH} = 0.8$) (from Ref. [295]).

environmental conditions [294]. Although true *situ* studies, we have kept them in the present section to separate them from *in situ* studies in UHV, during growth, which are gathered later. Fig. 76 shows a series of GISAXS patterns measured as function of evaporation time t . At time $t < 396 \text{ s}$ (Fig. 76a) no characteristic features are observed in agreement with an isotropic micellar phase. At $t = 396 \text{ s}$ (Fig. 76b) a Bragg spot appears on the specular rod at $q_z = 1.78 \text{ nm}^{-1}$ corresponding to an out-of-plane ordering (lamellar structure). At $t = 441 \text{ s}$ (Fig. 76c and d) the Bragg spot disappears and at the same time a broad halo appears corresponding to correlated micelles (either spherical or cylindrical). The halo is more and more intense resulting

from enhanced spatial correlations between the micelles. In the meantime the mean radial position of the halo increases due to an increasing number density. At last ($t = 531 \text{ s}$, Fig. 76e), 3 well defined Bragg spots at 0° and $\pm 60^\circ$ with respect to the q_z axis appear at the boundary of the halo. They are characteristic features of a hexagonal phase (p6 mm) with cylindrical micelles oriented parallel with the surface plane in an AB stacking configuration. Complementary X-ray Reflectivity measurements on a solidified sample have proved that a disordered phase coexists with two ordered hexagonal phases located at the solid/liquid and liquid/vapor interfaces. These results provide clear evidence for

a first order disorder/order phase transition and for the key role played by the interfaces in the ordering.

From the above example, it is expected that relative humidity strongly influences the structure of a dip-coated thin film under evaporation. In order to study its role in the self-assembly process of amphiphilic molecules, a solution containing surfactant, silica precursor, ethanol and hydrochloric acid was dispensed on Si(100) monitoring the relative humidity (RH) flowing either dry or humid nitrogen on the thin film [295]. To characterize the internal structure at the nanometer scale, *in situ* GISAXS measurements were carried out on the liquid spectrometer of the X22B beamline at NSLS (Stanford, USA).

Fig. 77 shows different GISAXS patterns collected at successive stages of the process, *i.e.* either under high or low relative humidity. The first pattern (**Fig. 77a**) is measured at the very beginning of evaporation and corresponds to the liquid state since no local order is detected. **Fig. 77b** is obtained after complete evaporation of ethanol (1 min). It reveals a 2D hexagonal network as already observed. This stage is known as the Modulable Steady State [290, 291] because the silica network is far from being completely condensed ($\text{RH} = 0.4$). Therefore the lattice is flexible. Now raising the RH to 0.8 (**Fig. 77c** and d), the hexagonal phase partially transforms into a cubic phase ($\text{Pm}3\text{n}$). This process is induced by the penetration of water into the thin film reducing the packing density and changing cylindrical micelles into spherical ones. The expansion of the network is directly deduced from the contraction of the reciprocal space (**Fig. 77b** and d). Interestingly, the cubic lattice coexists with the hexagonal phase for any RH. Varying the angle of incidence of the X-ray beam it is clearly shown that the cubic phase is located at the top of the thin film and the hexagonal phase at the bottom. The structure of the hexagonal phase has been studied in detail as function of the RH. After a few humidity cycles, the flexibility of the micelles hexagonal phase is reduced. From the GISAXS measurements at different RH, it is shown that the hexagonal network is pinned in the surface plane whereas in the perpendicular direction the network can expand freely as function of the intrusion or extrusion of water. The in-plane frozen state cannot be assigned to the condensation of the micelles network because there is no reason to distinguish in-plane and out-of-plane expansion properties. However it is probable that the coexistence of different grains of micelles networks in many different orientations prevents the grains from expanding in the surface plane. This effect is enhanced by the highly anisotropic shape of the micelles in the form of cylindrical rods.

The role of humidity is clearly proved in the above example and also by Tate and co-workers [296]. However, this is not the only parameter of control. Major changes in order and orientation are observed as function of the concentration of the silica and surfactant precursors solutions (silicate-to-ethylene oxide block molar ratio, Si/EO). At high Si/EO an ordered rhombohedral phase ($\text{R}3\text{m}$) is obtained (see **Fig. 78a**) whereas upon decreasing this ratio, a transition to a $\text{C}2\text{ mm}$ phase (distorted hexagonal phase) occurs. The breakdown of the orientational order is evidenced by a ring in GISAXS patterns (see **Fig. 78c–g**). This corresponds to a short range order of the micelles with no preferential orientation. From these measurements, it is possible to draw a phase diagram as function of RH and Si/EO. Therefore tuning the parameters of control it is possible to chose the phase under interest. The rhombohedral phase has been studied in details [296,297,154] by GISAXS, SAXS and Field Emission Scanning Electron Microscopy (FESEM). The films are highly oriented with (111) planes parallel with the substrate but with a rotational freedom. **Fig. 79** shows GISAXS images with overlays of simulated spots. The use of the DWBA allows reproducing all the characteristic spots whereas the BA does not. More importantly the BA predicts spots positions that are slightly shifted preventing potentially the identification of the crystallographic phases. No other cubic, rhombohedral or hexagonal space

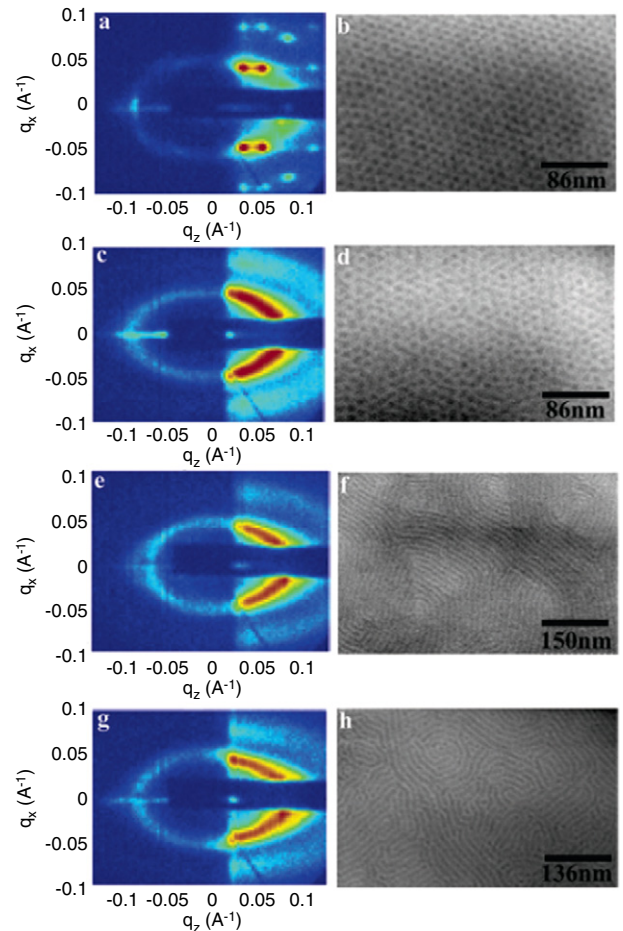


Fig. 78. GISAXS patterns and corresponding FESEM micrographs for different Si/EO ratio: (a–b) 4.24, (c–d) 3.29, (e–f) 2.81 and (g–h) 2.43. The RH is 40% except for (c–d) for which it is 60% (from Ref. [296]).

groups could reproduce quantitatively the experimental patterns. The (111) oriented primitive rhombohedral lattice has a lattice parameter $a = 11 \text{ nm}$ and an angle $\alpha = 86^\circ\text{--}87^\circ$.

More recently nanoporous silica films with the double-gyroid structure have been fabricated [298]. These structures offer interesting properties due to their high surface area (sensors) and because they provide a periodic and well-defined access to the substrate at the nanometer scale. The method of fabrication is also based on the Evaporation Induced Self-Assembly process controlling more particularly the curvature of the silica-surfactant interface. **Fig. 80** shows GISAXS patterns of such a thin film. The predicted spot positions are exactly at the position of the experimental spots. Moreover the silica double-gyroid thin film was grown on electrodes in order to electrodeposit metals (Pt) into the pores. By a subsequent etching of silica, an inverse double-gyroid structure was fabricated.

8.2.2. Low- k and ultralow- k nanoporous dielectric films

Among various candidates of low- k dielectrics materials to decrease power consumption of electronic devices and to reduce interconnect parasitic capacitance, porous SiOCH is the most ready for integration. Spin coating and PECVD techniques have been proposed to fabricate pores of nanometric size compatible with the Cu interconnections [299]. In all cases, the SiOCH matrix is mixed with a porogen (organic molecule) removed by a thermal treatment. The mechanical and dielectric properties are highly dependent on the deposition process and thermal annealing. The pore size, shape and spatial organization have been characterized

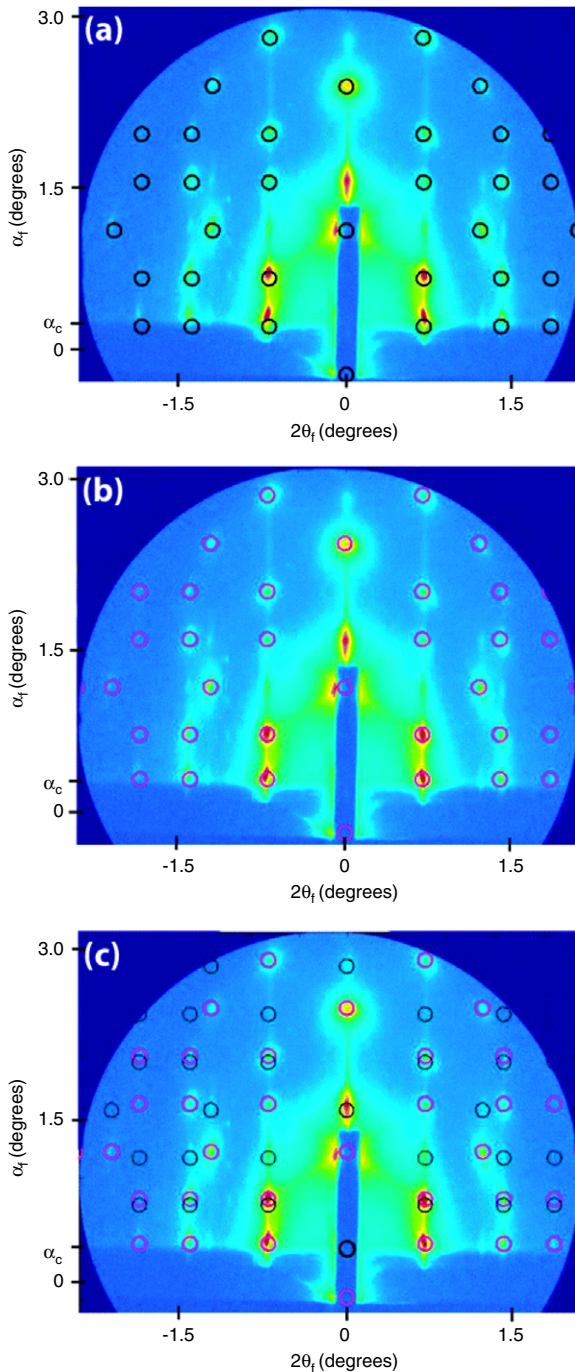


Fig. 79. GISAXS patterns of a rhombohedral nanoporous thin film. Overlays in (a) are calculated within the BA, (b) within the DWBA including refraction effects, (c) within the DWBA including reflection effects (from Ref. [154]).

by *ex situ* GISAXS at the ESRF (France) on the D2AM beamline. Fig. 81 shows seven GISAXS images obtained on different samples. The major observed differences can be described qualitatively. For the samples prepared by PECVD, the intensity scattered by the pores is much weaker than for spin-coated samples. This is probably due to the small size and the small density of pores. Moreover depending on the preparation conditions, a clear anisotropy is measured. For instance in Fig. 81e, correlation peaks are observed both in-plane and out-of-plane. The authors propose that the pores are ordered in a “pseudo-cubic” lattice which corresponds probably to a short-range order in the surface plane and a layering of the pores vertically. Unfortunately, no X-ray

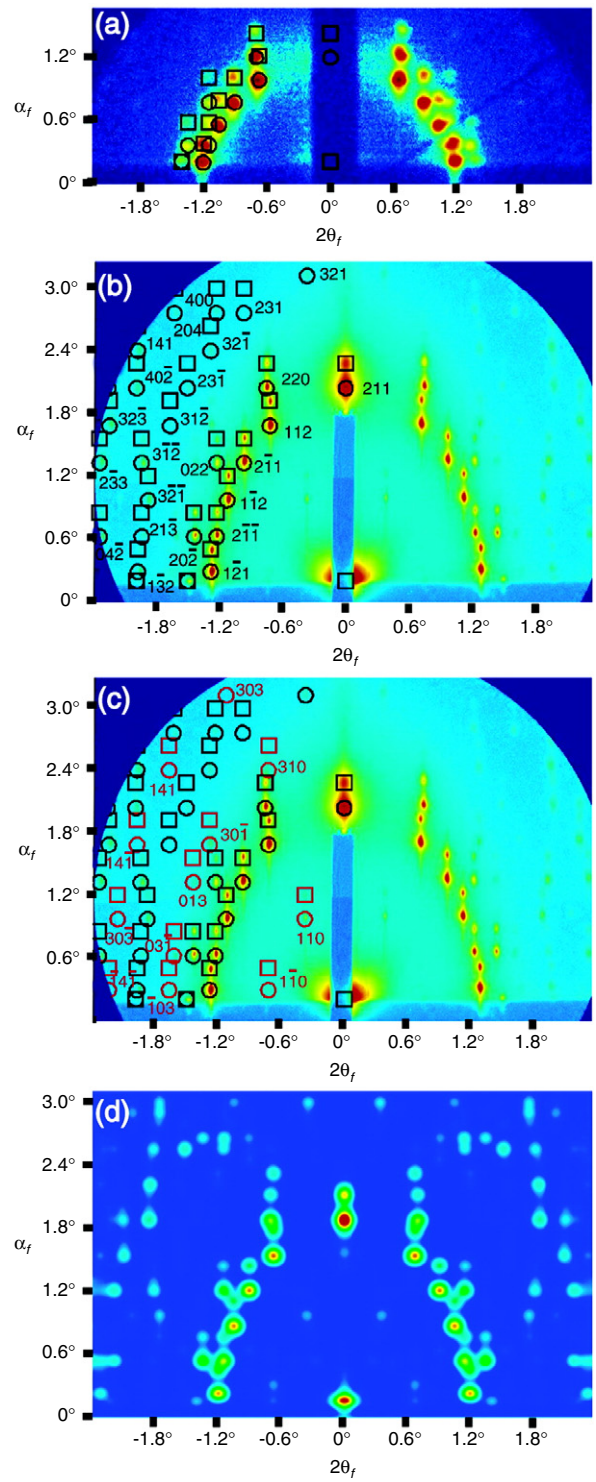


Fig. 80. Experimental GISAXS pattern of the thin film overlaid with predicted spot positions. The circles indicate diffraction spots from the incident beam (BA), whereas squares indicate diffraction spots from refracted and reflected beams (DWBA). (a) GISAXS pattern obtained with a CuK_α X-ray source. (b) GISAXS pattern measured with a synchrotron source. (c) same as (b) but with additional overlays considering broken glide plane symmetry elements. (d) Simulation of the GISAXS pattern calculated in the DWBA (from Ref. [298]).

Reflectivity measurements are shown to confirm this hypothesis. The interpretation of the GISAXS data is based on the analysis of the Porod (high q) and Guinier (low q) regimes. It appears that for the Porod's regime, the q^{-n} power law is smaller than 4 which can result from fractal like interfaces. The Guinier's

regime has been analyzed considering spherical pores and a log-normal distribution. The data are successfully compared with Ellipsometric Porosimetry. However the model is limited because the pore volume fraction as deduced from the fit is above the percolation threshold. Moreover the pore size is about 1 nm for the samples prepared by PECVD. Such a small size is not compatible with a conventional analysis of small angle scattering and a more detailed model of the pore morphology is probably necessary.

To improve the performance of integrated circuits in future microelectronics it has also been proposed to use different dielectrics other than silicon oxide or silicon nitride. Organic materials have attracted attention but due to their poor thermal and mechanical stabilities they cannot be used [300–302]. Dielectric organosilicate films are probably an interesting alternative. Lee et al. [303] have studied polysilsesquioxanes which exhibit good thermal stability (400°C) and minimal moisture uptake. However the dielectric constant k is still relatively high ($k = 2.7$) and it has been proposed to incorporate air ($k = 1.0$) into the dielectric to decrease the dielectric constant (see for instance Refs. [304–307]). The approach is to polymerize the polysilsesquioxanes precursors (polymethylsilsesquioxane) in presence of thermally labile organic porogens. The subsequent thermal decomposition of the porogens creates pores in the dielectrics. In this study, many different porogens have been tested to improve the miscibility properties with Polysilsesquioxanes precursors and to avoid any chemical reaction. It has been finally used globular 32- and 64- armed dendrimers capped with suitable agents (ethyl acrylate) to improve the compatibility with the precursor.

The nanoporous thin films spun onto silicon wafers were characterized by *ex situ* GISAXS at the BLC4C1 beamline of the Pohang Accelerator Laboratory (South Korea). Fig. 82 shows a GISAXS image of a nanoporous dielectric thin film. 1D GISAXS cuts have been analyzed considering embedded nanopores inside a thin film. All refraction and reflection effects at the surface of the thin film and at the film/substrate interface are taken into account using the Parratt formalism. However, a calculation of the intensity scattered by the nanopores is not obtained by the coherent sum of 4 scattering processes. The intensity of each scattering process is summed (*i.e.* the phase is lacking). From a general point of view this calculation is not rigorous in the framework of the DWBA. However the roughness can probably partially suppress the phase coherence between each scattering process. This point is however not discussed by the authors. The quantitative analysis of the GISAXS data is based on the description of the system by spheres and a lognormal size distribution. Excellent fits are obtained complemented with a power law analysis at high- q . The scattering profile is found to vary as q^{-4} showing that the nanopores/matrix interface is sharp.

8.2.3. Porosity in thin films prepared by chemical routes in solution

The controlled fabrication of thin films needs the development of appropriate growth methods. In that field, dip coating, spin coating or pyrosol processes are efficient and low cost techniques. However during thermal treatments, the solution containing precursors changes drastically by crystallization and degassing, potentially creating pores. These pores may alter the expected thin film properties.

Hammer et al. have investigated (see Ref. [308]) the structure of In-doped ZnO thin films grown by the pyrosol process. The fabrication of doped ZnO thin films has potential applications as gas sensors [309], transducers [310] or ultrasonic oscillators [311]. The characterization of the pores size has been performed by *ex situ* GISAXS at the LNLS in Campinas (Brazil). Fig. 83 shows 2 GISAXS patterns obtained for ZnO films deposited at 573 K and 723 K. Qualitatively, a clear anisotropy is visible for the sample prepared at 573 K whereas at 723 K the GISAXS intensity is isotropic. At the

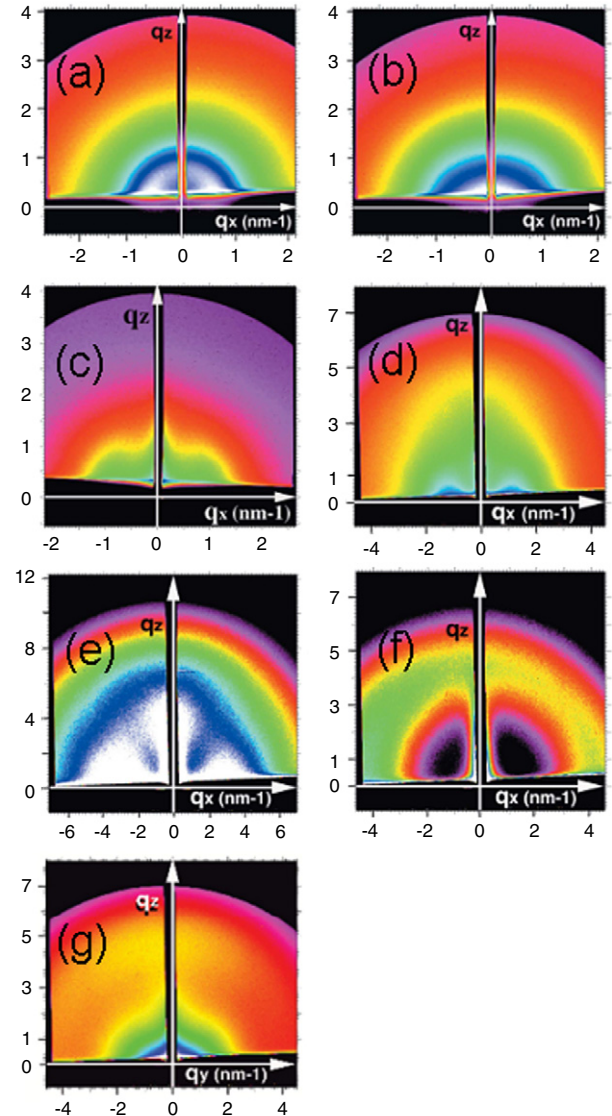


Fig. 81. GISAXS patterns of ultra low k samples made of SiOCH resulting from different processes: (a) spin coating with a sacrificial porogen, (b) self-assembling of polymers with a subsequent thermal treatment, (c) nanoclustering of Si precursors, (d) PECVD of an organosilicate precursor for the matrix and an additional porogen. The film is cured by an electron beam. (e–g) same as (d) but ultra-violet cured (from Ref. [299]).

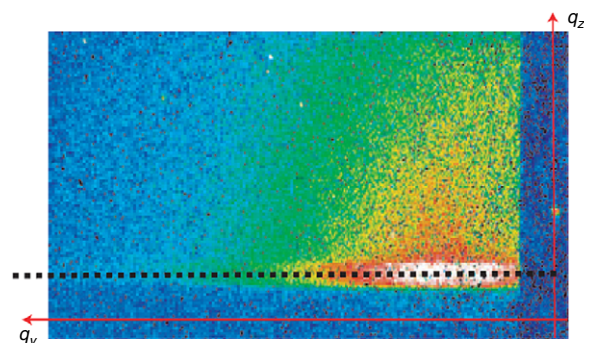


Fig. 82. GISAXS pattern of a 300 nm thick nanoporous film imprinted with 40 wt.% EA-PPI-64 porogen (from Ref. [303]).

lower temperature it is proposed that nanopores are present inside the ZnO thin film which are elongated perpendicular to the surface (growth direction). A detailed analysis is performed in the low q

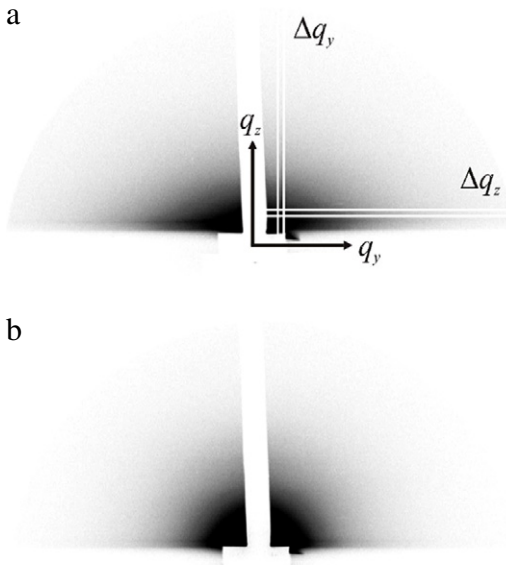


Fig. 83. GISAXS patterns of In-doped ZnO films (solutions with $In/Zn = 5\%$) deposited at (a) 573 K and (b) 723 K (from Ref. [308]).

regime (Guinier's regime). The radii of gyration are 2.7 nm and 1.8 nm respectively perpendicular to and parallel with the surface plane. On the contrary, at 723 K the pores are spherical with a radius of gyration varying between 2.3 nm and 2.6 nm. The pore size is a decreasing function of the In content. This reduction can be assigned to the increase of nucleation sites with In. Concerning the role of temperature, the pore density is a decreasing function of temperature. This result is supported by the crystallization of the ZnO thin film at high temperature reducing the number of defects and voids. This is confirmed by resistivity measurements showing a strong reduction of more than 5 orders of magnitude thanks to the densification of the film. Similar experiments have been performed on undoped and Sb-doped SnO₂ thin films prepared by dip-coating and subsequently fired [312]. The authors show that the density of the thin films is affected by the doping (lower density) and that even at 1173 K the sintering process is not complete (partial elimination of the smallest pores and spheroidisation of the larger ones).

8.3. Block copolymers thin films

8.3.1. Ordering of block copolymers thin films

Obtaining well defined patterned substrates at the nanometer scale is a challenge in view of the fabrication of long-range ordered nanostructures, e.g. for magnetic storage [313,314]. Many different routes have been followed, e.g. Evaporation Induced Self-Assembly, shear (roll casting) [315], electric field [316]. In Ref. [317], it is proposed to use the technique of directional casting, referred to as zone-casting. A PBA-*b*-PAN diblock copolymers solution in *N,N*-dimethylformamide (DMF) was deposited onto a moving substrate with a syringe equipped with a flat nozzle. The control of solution concentration, temperature (90 °C) and speed displacement (6 μm/s) made it possible to vary the film thickness from 1 μm to 100 nm. The surface morphology of the thin films of BA-*b*-PAN block copolymers has been studied by AFM and GISAXS (Fig. 84). Large scale ordered domains of diblock copolymers are observed by AFM. The striped morphology shows elongated domains of PAN (bright) and PBA (dark) phases. The periodicity is 37 nm from AFM and 36 nm from the position of the interference peak by GISAXS. The GISAXS pattern has been measured with the incident beam at 90° with respect to the casting direction. By rotating the sample in the surface plane it has been deduced that the

axis of preferential orientation fluctuates by about ±10°. The one-dimensional order is parallel with the flow of solution. This result suggests that the orientation is induced by the solvent evaporation front. The authors made a step further in the fabrication of patterned substrates by thermally treating the thin films to obtain a patterned carbon surface. The long-range order is preserved during the process even though a very substantial part of material was removed (sacrificial PBA phase). This stability is attributed to an interaction with the underlying Si substrate. Similarly it has been proposed by Müller-Buschbaum et al. [318] to fabricate shallow polymer nanochannels by wiping a highly diluted solution. The polymer is the Polydimethylsiloxane (PDMS) deposited onto a standard microscopy glass slide surface. The combination of wiping and evaporation of the solvent induces an anisotropic dewetting and the apparition of nanochannels (see Fig. 85). To determine the orientation of the nanochannels over a large area (inaccessible by AFM and optical microscopy), GISAXS has been performed with high resolution at the BW4 beamline (HASYLAB, Germany). The sample-detector distance is 13.0 m and the resolution about $2.75 \times 10^{-4} \text{ nm}^{-1}$. A precise orientational order at 6.4° with respect to the edges of the glass substrate has been determined. An other approach, in the fabrication of ordered copolymers, consists of adding small molecules. This method is widely used [319] in the fabrication process of bulk polymers. However such additives in block copolymers thin films processing have not been explored much until now. Du et al. [320] studied three different polymer systems with selected organic or inorganic additives. Diluted solutions are spin-coated onto Si wafers and the appropriate choice of the chemistry enables to remove one of the components. After processing, the thin film morphologies have been observed by AFM and GISAXS. In all cases AFM measurements show a hexagonal arrangement of pores and the GISAXS pattern (CHESS, D-line) shows clear in-plane correlations and out-of-plane intensity oscillations (Fig. 86). To extract quantitative information on the pore shape, simulations were performed with the IsGISAXS software [27] assuming cylinders or ellipsoid shapes. The GISAXS intensity is better reproduced considering cylinders, above all in the high q region. The typical deduced parameters are the pore-pore spacing (34.6 nm) and the film thickness (14 nm). Going a step further in the understanding of ordered systems, the Kosterlitz-Thouless-Halperin-Nelson-Young (KTNHY) description [321–323] of the behavior of a bidimensional phase has been addressed by Stein et al. [324]. The KTNHY behavior is characterized by a long-range orientational order but an algebraically decaying translational order with a correlation function $g(r) \sim r^{-\eta}$. In order to study the decay exponent η , GISAXS measurements have been performed on an array of 2D single crystals formed by the self-assembly of a monolayer of spherical block copolymers. The whole surface area is a few millimeters square providing reliable statistical information compared to near field microscopy or scanning electron microscopy. By standard lithography an array of hexagonal wells is fabricated (12 μm wide). Inside each cell, a single crystal of spherical block copolymers is confined exhibiting a hexagonal lattice of 29 nm lattice parameter. The diblock copolymer is the poly(styrene-*b*-2vinyl pyridine) (PS-PVP) with a minority of PVP forming spherical domains surrounded by a matrix of PS. The equilibrium is reached by a long thermal annealing (215 °C) just below the transition temperature from crystalline to hexatic (232 °C). Fig. 87 shows an in-plane map of the reciprocal space obtained by GISAXS and rotating the sample in the surface plane over an angular range of 80° by 0.25° increments. Clear diffraction peaks from the hexagonal lattice are measured: {10}, {11}, {20}, {21} and {30}. Both orientational and translational order have been analyzed theoretically taking into account the finite size of the network. The long-range orientational order is confirmed and the broadening of the reflection as a function of the modulus of the wavevector transfer is consistent with the KTNHY theory ($\eta \sim q^2$). The exponent η

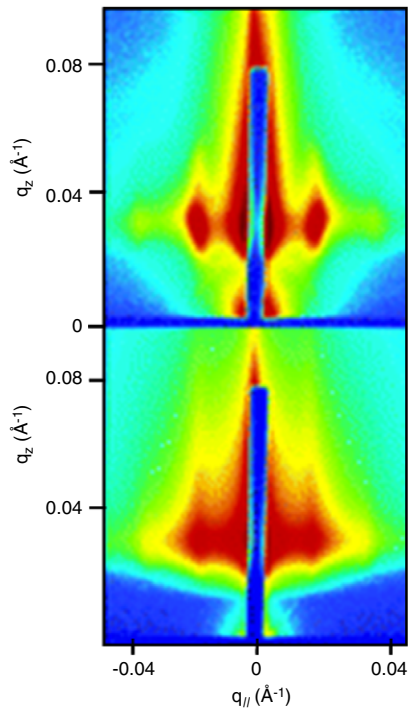


Fig. 84. GISAXS patterns measured at 90° with respect to the casting direction. Top: copolymer. Down: carbon (calcined). From Ref. [317].

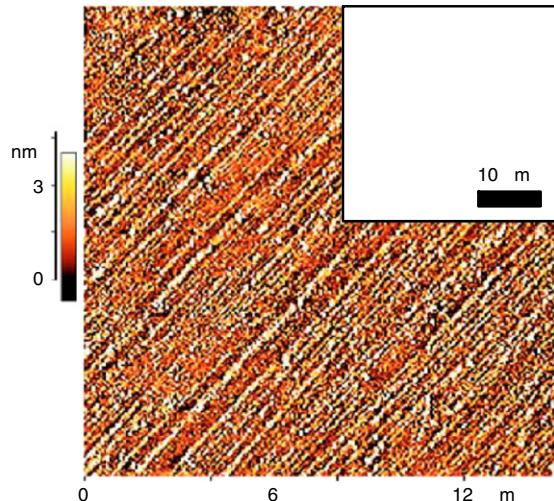


Fig. 85. AFM image and optical micrograph (inset) of polymer nanochannels (from Ref. [318]).

is strongly dependent on the elastic properties of the lattice and on the temperature. It is shown that the shear modulus μ of the lattice at 215 °C is 2×10^{-4} N/m. This study shows that the detailed GISAXS characterization of a 2D network by mapping the whole reciprocal space provides the opportunity to deeply understand the mechanical properties of the structure.

8.3.2. Phase transition of block copolymer thin films

The phase transitions of Polystyrene-*b*-Polyisoprene (PS-*b*-PI) diblock copolymers thin films have been investigated by Park et al. [325]. In bulk, PS-*b*-PI diblock copolymers upon annealing at 120 °C for 1 day [326] exhibit the Hexagonally Perforated Layer (HPL) structure. It changes into the Gyroid phase (G) upon annealing at 170 °C. To characterize the structure and ordering of the thin films, GISAXS measurements have been performed

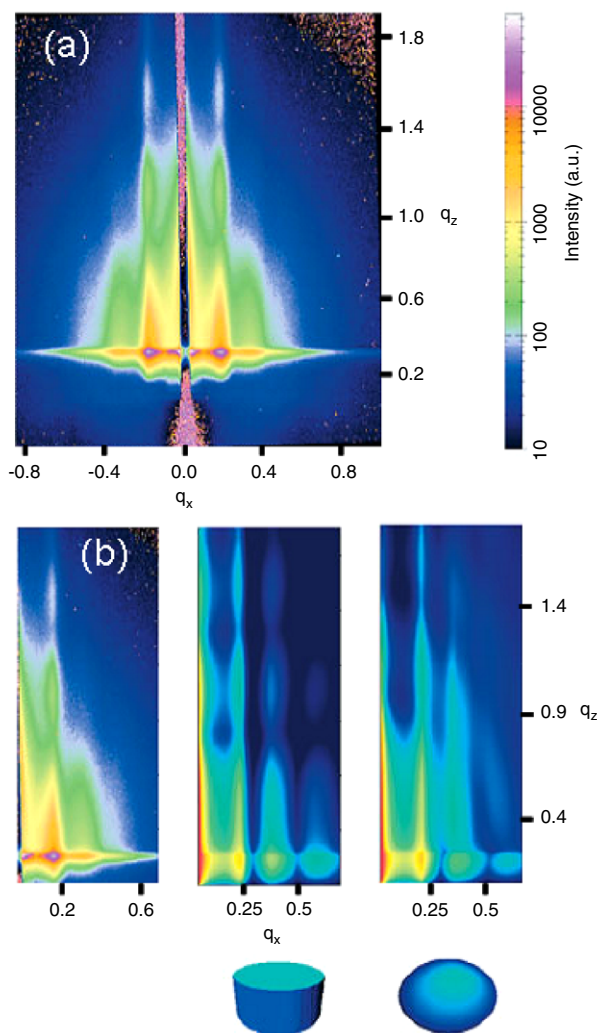


Fig. 86. (a) GISAXS pattern of a calcined thin film. (b) Comparison of experimental and simulated GISAXS patterns. Two types of scattering objects geometries were used for the simulations: cylinders and ellipsoids. The simulations are performed with the IsGISAXS software [27] (from Ref. [320]).

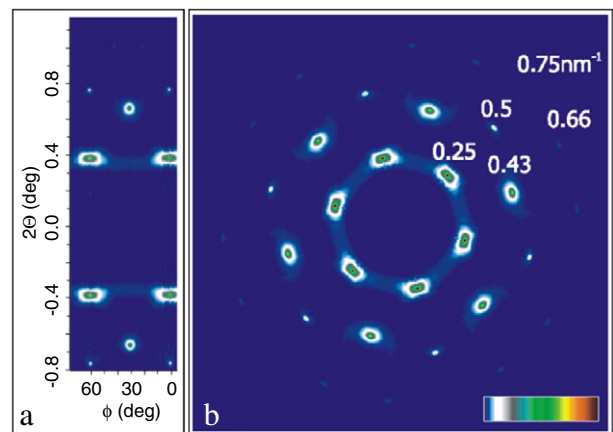


Fig. 87. (a) Intensity map as function of in plane diffraction angle (2Θ) and in plane rotation angle (ϕ). Corresponding polar map, i.e. map of the reciprocal space in the surface plane. Logarithmic color scale. From Ref. [324].

at the Pohang Accelerator Laboratory (Korea) on 4C1 and 4C2 beamlines. Fig. 88 shows a GISAXS pattern of a PS-*b*-PI thin film (~ 1250 nm) spin-coated on a silicon wafer and annealed at 120 °C

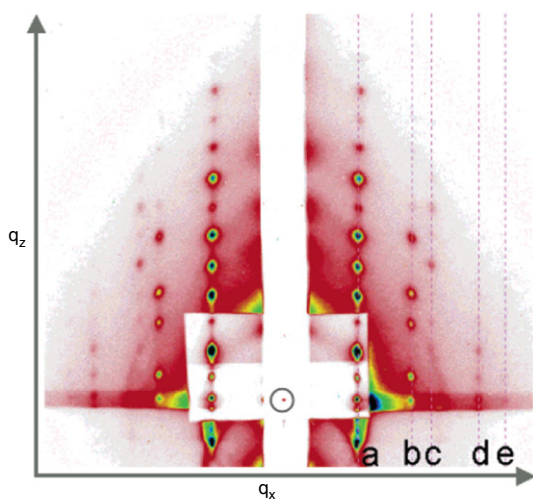


Fig. 88. GISAXS pattern of PS-*b*-PI thin film spin coated on silicon wafer (1.25 μm thick). From Ref. [325].

during 1 day. The incident angle is 0.22° . The relative in-plane positions of the peaks are $1:\sqrt{3}:\sqrt{4}:\sqrt{7}:\sqrt{9}$ (a–e), corresponding to the sequence of peaks of a hexagonal packing. This proves that the hexagonal arrangement forms microdomains randomly oriented in the surface plane. The out-of-plane interpretation of the peaks is more complicated due to the effects of reflection and refraction of the incident, reflected and transmitted beams at the different interfaces. In order to fully take into account these effects the simulations have been performed in the framework of the DWBA [204]. A good agreement between the calculation of the peak positions and the experimental ones is found considering a perfect ABC stacking sequence confirming that the block copolymer thin film has the HPL morphology. No AB stacking was detected. Increasing the temperature to 140°C and 160°C for 1 day, the GISAXS patterns (see Fig. 89) show different characteristic features. At 140°C , new peaks arise from the G phase and at 160°C the thin film has fully transformed. The HPL {003} plane is changed into the G {121} plane with a slightly larger in-plane spacing: 24.2 nm instead of 22.0 nm. Interestingly the authors found that the transition in a thin film occurs at a higher temperature than in the bulk. This can be assigned to the epitaxial relationship of the thin film with the substrate which freezes the lattice distortions in the surface plane.

8.3.3. Dewetting of polymer thin films

The dewetting of thin polymer films has attracted much interest in view of the controlled fabrication of surface coatings or bio-technologies. Müller-Buschbaum et al. [327] investigated the dewetting of thin polymer blend films of thickness smaller than the radius of gyration of the polymer chains. The studied blend is a mixture of deuterated polystyrene (dPS) and polyparamethylstyrene (PpMS). The dewetted film morphology and internal structure have been characterized by AFM, GISAXS (BW4 USAXS beamline, HASYLAB/DESY, Germany) and GISANS (D22 beamline, Institut Laue Langevin, France). From the density contrast point of view, X-rays and neutrons behave differently from X-rays the polymer blend film can be regarded as homogeneous ($\delta_{\text{dPS}}/\delta_{\text{PpMS}} = 0.9$) whereas for neutrons, the main scattering component is the deuterated polymer ($\delta_{\text{dPS}}/\delta_{\text{PpMS}} = 4.1$). The dewetting process is activated in presence of a toluene vapor. Incorporating toluene into the polymer blend, the viscosity is decreased, accelerating the kinetics and promoting the dewetting process. The samples were characterized at the end of the process. Fig. 90 shows (i) the power spectral density function of an AFM image, (ii) the in-plane X-ray scattering curve, and (iii) the in-plane neutron scattering curve for a 3.1 nm thick-film. In all cases a peak at $\zeta_A = 2\pi/q_A = 490 \pm 40$ nm is visible. It corresponds to the mean inter-droplet distance. However, except for neutron scattering a clear shoulder is observed at $\zeta_B = 2\pi/q_B = 150 \pm 20$ nm by GISAXS and AFM. This shoulder can be attributed to the mean diameter of the droplets. It is distinctly measured by X-rays due to the sharp interface of the droplets with the surrounding environment. By AFM the interface is broadened because of the finite resolution of the technique giving rise to a less pronounced shoulder in the power spectral density function. The absence of shoulder for neutron scattering provides additional information on the internal structure of the droplets. Because neutrons are mainly sensitive to the deuterated polymer, it reveals that inside the droplets, there is no ordering of the polymers. They are more or less randomly distributed and therefore the interface profile is not sharp for neutrons. The dewetting induced by toluene shows no phase separation. However changing the thin-film thickness a clear in-plane peak is observed at high q (period 72 nm) by GISANS corresponding to a chemical ordering of both polymers [328]. Similar experiments have been performed on the dewetting of polystyrene thin films on Si(100) [329] by combining X-ray reflectivity and GISAXS. In-plane scattered intensity (see Fig. 91) provides information on the local correlations in the surface plane. The authors put in evidence a new type of thin film instability exhibiting dimples of nanometer size surrounded by large droplets of micrometer size. This result is confirmed by AFM measurements of the surface morphology. In both examples AFM and

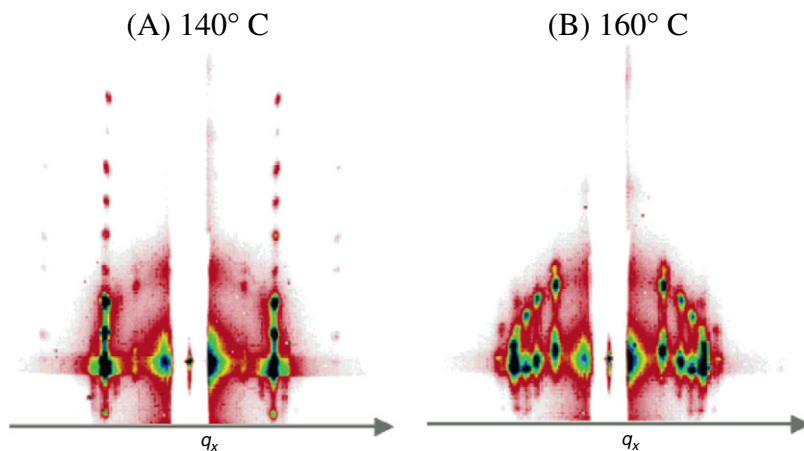


Fig. 89. GISAXS patterns of PS-*b*-PI thin film spin coated on a silicon wafer annealed at different temperatures (a) 140°C and (b) 160°C (from Ref. [325]).

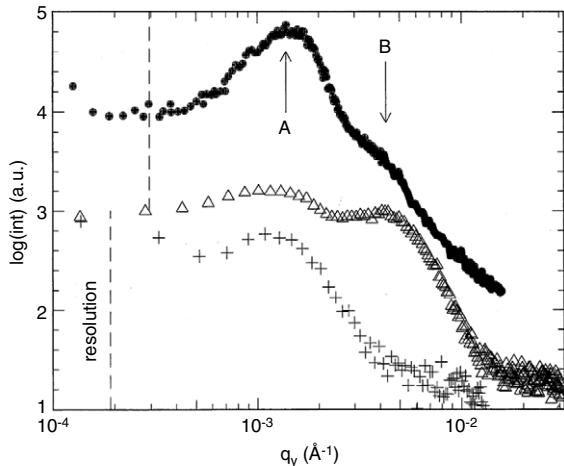


Fig. 90. Double logarithmic plot of horizontal slices from the 2D intensity distribution of the dewetted dPS:PpMS sample measured with AFM (filled circle), GISAXS (triangle) and GISANS (crosses). The position of characteristic peaks is marked with letters "A" and "B". The data are shifted for clarity (from Ref. [327]).

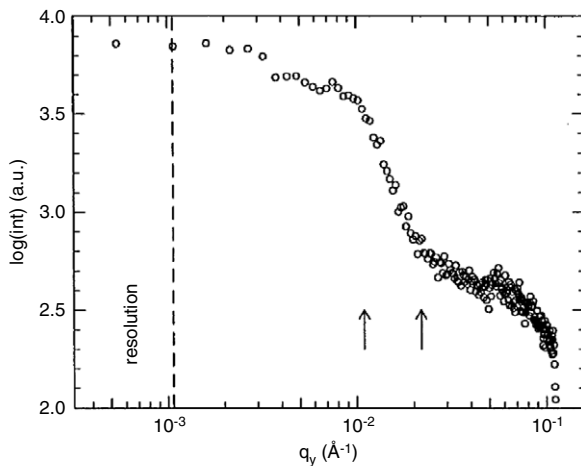


Fig. 91. Horizontal slice of the intensity scattered by a polystyrene thin film on Si(001) measured at $\alpha_f = 0.15$ (from Ref. [329]).

scattering techniques are very complementary tools. AFM provides a local morphological characterization which can be successfully compared with X-ray or neutron scattering techniques on a macroscopic area. Additionally, the internal structure of the polymer film can be extracted by small angle scattering techniques using neutrons or X-rays to enhance the contrast.

8.4. Thermal stability and reactivity of supported clusters

The control of the size and shape of metallic clusters is mandatory to make new catalysts or sensors [330]. However sintering of these nanoparticles during chemical reactions leads to their loss of selectivity and catalytic activity [331]. In order to study thermal effects on sintering as well as the role of gases, *in situ* GISAXS measurements (APS, BESSRC/12-ID beamline, USA) were performed in real time on supported Pt and Au clusters deposited on a naturally oxidized silicon surface [332,333] or on a thin alumina film [334]. The Al₂O₃/SiO₂/Si(100) films are obtained by the Atomic Layer Deposition (ALD) technique, with repeated cycles alternating exposures to trimethyl aluminum followed by deionized water in a viscous flow at 200 °C. The metal clusters are produced by vaporizing a source of Pt or Au with a YAG laser and He is used as the carrier gas. A narrow size distribution can

be produced (characterized by mass spectroscopy) adjusting the source temperature and the He pressure. The coverage rate of the surface is controlled by the number of shots of the laser applied on the metal target. The effect of temperature on the size distribution of Pt clusters deposited on silica has been first studied in Ref. [332]. A SiO₂/Si(111) surface was covered with Pt particles without mass selection, corresponding to 0.34 ML equivalent thickness, and then gradually heated until 400 °C. Fig. 92 shows slices of GISAXS patterns and the Guinier plot at increasing temperature. The radius of gyration at RT is $R_{gh} = 1.16$ nm for the horizontal slice and $R_{gv} = 1.11$ nm for the vertical one. It corresponds to roughly spherical nanoparticles with a diameter of 2.97 nm. During heating the vertical slices did not change whereas the horizontal slices changed at temperatures higher than 320 °C. The coalescence of the Pt clusters leads to the formation of oblate particles elongated in the surface plane (e.g. $R_{gh} = 1.45$ nm at 400 °C). To avoid the coalescence of Pt clusters, it has been proposed to change the substrate using a thin alumina film [334] (2-cycles Al₂O₃/SiO₂/Si(100)) grown by the ALD technique. The Pt clusters size distribution has been selected between 7 to 10 atoms and the surface coverage rate is about 0.02 ML to avoid aggregation of the clusters during the deposition process. The GISAXS signal arising from the nanoparticles is very weak at RT. Upon annealing the clusters size increases from 0.6 nm (mean radius of gyration) and reaches 0.8 nm at 400 °C in the vertical direction (1.05 nm in the horizontal direction). The particles shape changes from a sphere to an oblate ellipsoid. By increasing the thickness of the alumina film (6-cycles Al₂O₃/SiO₂/Si(100)) and making the same experiment the clusters size is kept constant after annealing at 400 °C. Moreover, the cluster size is extremely small (<0.3 nm) corresponding to aggregates of about 10 atoms. The comparison between these different results shows that surface diffusion is not activated on alumina at these temperatures. The different results obtained on the 2-cycle and 6-cycle alumina thin films can be assigned to the surface structure of both films. It seems that the 2-cycle alumina thin film still exposes large area of silica promoting the surface diffusion processes and therefore clusters aggregation. Similar experiments have been performed with Au [333]. The stability of Au clusters on oxide surfaces has been addressed as function of clusters size, level of coverage, temperature and presence of hydrogen or not. The real-time kinetics of clusters aggregation was monitored by GISAXS. As for Pt clusters, the aggregation of Au clusters can be avoided for level of surface coverage smaller than 0.05 ML. Moreover the role of the substrate is crucial. The alumina surface prevents clusters from aggregating whereas the silica surface does not (see Fig. 93). Concerning the role of gases on the aggregation processes, two identical samples were prepared by depositing 0.02 ML of size selected clusters (Au_{4–10}) on SiO₂/Si(111). Both were heated at 400 °C either in presence of hydrogen ($p_{H_2} = 30$ mTorr) or not. Without hydrogen, the increase of temperature leads to a slow increase of the lateral dimensions whereas the height is kept constant in agreement with a 2D agglomeration of clusters. Under hydrogen, the particle size increases in 3D (see Fig. 94). This result may be assigned to exothermic processes of reactions involving H₂, activating the mobility of the clusters at the surface. In these studies one of the main drawbacks of the characterization of such small clusters by GISAXS is the lack of a background subtraction method to separate the diffuse scattering arising from the clusters and from the surface roughness. For that sake, it has been proposed by B. Lee et al. [262] to use anomalous GISAXS. Changing the incident beam energy the electronic density contrast of the clusters is modified and assuming no interference between the waves scattered by the surface roughness and by the clusters, it is possible to extract only the clusters' contribution.

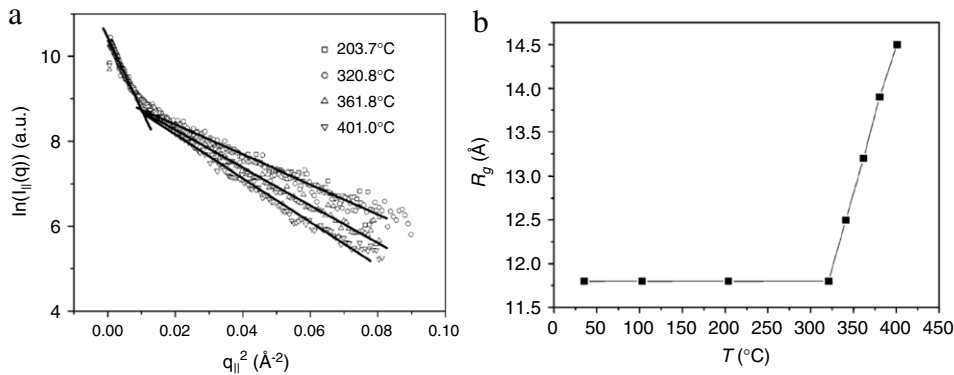


Fig. 92. (a) Horizontal slices of GISAXS patterns at different temperatures and fits obtained by Guinier analysis. The low q intensity results probably from the substrate roughness. (b) Change of radius of gyration as function of temperature (adapted from Ref. [332]).

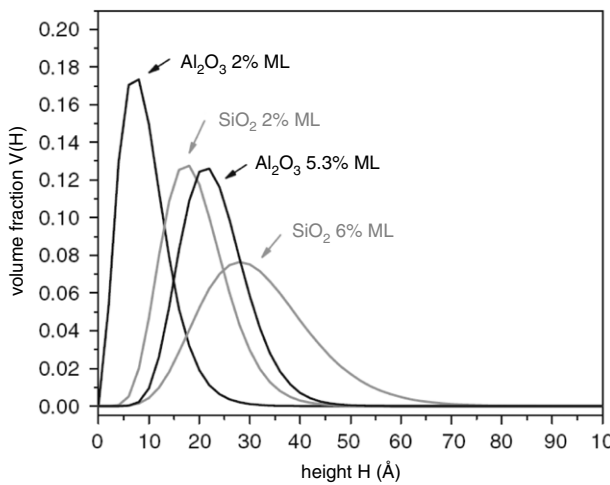


Fig. 93. Height distribution of supported clusters as function of the surface coverage of Au_{7-10} clusters. Two substrates are compared: $\text{SiO}_2/\text{Si}(111)$ and 1 ML of Al_2O_3 on $\text{SiO}_2/\text{Si}(111)$ (from Ref. [333]).

8.5. Ex situ GISAXS studies of semi-conductor nanostructures

8.5.1. Introduction

During the last decade, many efforts have been done to characterize low-dimensional semi-conductor structures such as quantum dots because of their potential applications in electronics and optoelectronics. Most of these nanostructures are naturally obtained by MBE through the standard Stranski-Krastanow growth in which, due to the lattice parameter mismatch between the overlayer and the substrate, the growth proceeds first layer-by-layer, then, above a critical thickness, through the formation of islands of different shapes, size, size distribution, composition and strain. Their physical properties depend very intimately on these structural parameters, which have thus been the object of intense research. Among the many structural tools available, such as AFM, STM, SEM, HRTEM ..., X-rays under grazing incidence have become unavoidable, both concerning the detailed average strain and composition, but also concerning their shape and organization. Indeed, of great interest were self-organized nanostructures, since self-organization leads to much narrower size distribution, which is much needed for application. For that sake, GISAXS started to be used by several German groups around 1998.

8.5.2. Self-assembled $\text{Si}_{1-x}\text{Ge}_x$ islands

The semi-conductor island system that has been the most studied by GISAXS is certainly the $\text{Si}_{1-x}\text{Ge}_x$ islands grown on $\text{Si}(001)$ substrates.

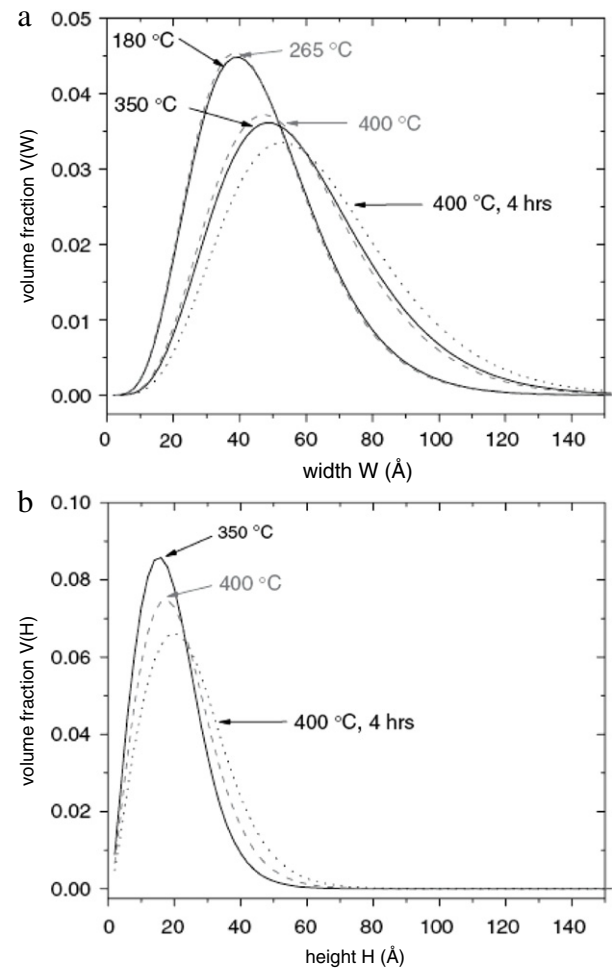


Fig. 94. Evolution of width and height distributions of Au clusters during heat treatment in presence of H_2 (from Ref. [333]).

As early as 1998, Metzger et al. [60,61] published review articles containing GISAXS data and analysis on two different GeSi quantum dot systems. The first one consisted of Ge (15 nm) deposited on boron terminated $\text{Si}(111)$. It was shown to have three-fold symmetry, in the form of triangular Ge pyramids with no orientational dispersion. Fig. 95 shows a sketch of the used setup, as well as in-plane GISAXS measurements taken for different azimuths ω . This study beautifully demonstrated that GISAXS is able to determine the complete symmetry of arbitrary shaped

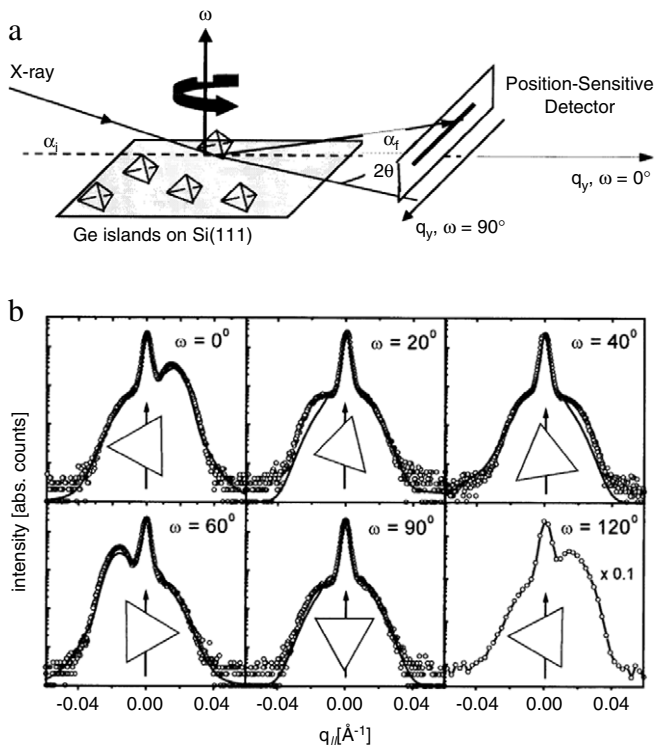


Fig. 95. (a) Geometry of GISAXS used to study the triangular Ge islands on Si(111). (b) Scattering patterns for different ω . The triangles indicate the orientation of the islands with respect to the incident beam (arrows). The solid lines are least-squares fits. From Ref. [60].

objects on a surface (see Section 6.2.7). Indeed, GISAXS clearly revealed the 3-fold symmetry of the islands, which would not be the case of conventional SAXS in transmission, since then the Friedel's law would induce a 6-fold symmetry of the scattering pattern. Further investigations of this system were published in 1999 and 2000 by Rauscher [37] and Paniago [335].

The second system consisted in coherent Ge islands embedded in a Si/Ge superlattice showing correlations both laterally and in the growth direction. On the surface, probed with small values of the incident angle α_i , the dots were organized in a short-range order square lattice, while buried dots, probed when increasing α_i , were found to be strongly correlated in the growth direction.

In 1998–99, Schmidbauer and co-workers [23,24] analyzed coherent $\text{Si}_{1-x}\text{Ge}_x$ islands grown by liquid-phase epitaxy (LPE) on Si(001) by a combined AFM/GISAXS analysis. Samples with different spatial island densities, *i.e.*, different mean island–island distances, were investigated. They found initial stages of developing ordering of the island array at very low island densities, which is manifested as island dimers oriented along the island base diagonal $\langle 100 \rangle$. At medium densities extended chains of islands along $\langle 100 \rangle$ appear; however, also increased ordering along $\langle 110 \rangle$ could be observed. At high island densities there is strong ordering along both $\langle 100 \rangle$ and $\langle 110 \rangle$ directions. There are interesting features revealed by in-plane GISAXS measurements taken with q_y along these two directions (Fig. 96). The close relationship between GISAXS and AFM power spectra is discussed. They concluded that these islands have the shape of {111} faceted truncated pyramids with a square base, exhibiting a unique shape and a narrow size distribution, with a strong ordering tendency along the $\langle 100 \rangle$ and $\langle 110 \rangle$ direction.

In this study, GISAXS was used to characterize the island ordering, rather than to determine the island shape, which was inferred from the AFM measurements. A detailed analysis of similar GISAXS data plus additional reciprocal space maps around

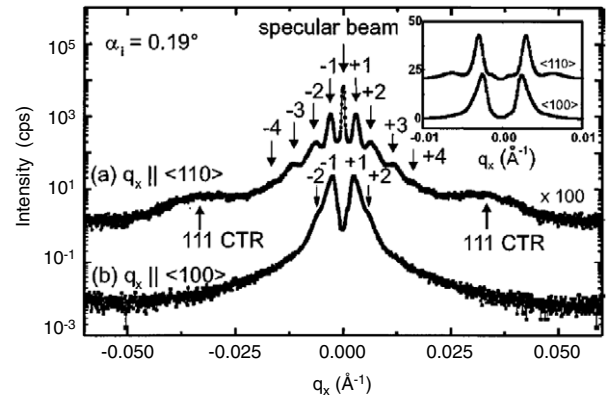


Fig. 96. $\text{Si}_{1-x}\text{Ge}_x$ dots grown by LPE; GISAXS intensity profiles (along q_y) of sample with a high island density for different azimuthal sample orientations with respect to the incoming beam. The specular beam has been displayed in curve (a) in order to illustrate the resolution achieved. In curve (b) the specular beam has been attenuated by a wire. The satellite peaks ($-4, -3, \dots, 3, 4$) are due to lateral ordering of the islands. The broad features appearing at about $q_y = \pm 0.033 \text{ \AA}$ are caused by the CTR originating from the {111} facets of the island. The inset clearly shows the different satellite line shapes observed along the two directions. From Ref. [23].

Bragg peaks was performed in 2005, on the basis of the 1D paracrystal model [336]. Note that the same group [337] developed further the DWBA to analyze the diffuse scattering from islands on a substrate both at small and wide angles, adding a fifth term with respect to the four introduced by Rauscher et al. [37] for scattering near Bragg reflections from the substrate. This fifth term arises from scattering by island-induced deformations in the substrate, below the islands. The theory was beautifully illustrated by simulating GISAXS and GIXD reciprocal space map measurements performed on such LPE-grown SiGe islands.

In 1999, Stangl [22] and co-workers used GISAXS to characterize the shape and size of carbon-induced self-assembled Ge quantum dots multilayers grown on Si(001) by MBE. The dot distribution was found isotropic (Fig. 97), and no correlation of the dot positions along the growth direction was found. The shape, mean radius, height and dot distance were determined by an original analysis using the Fourier transform of the experimental intensity (Fig. 98). Indeed, it can be shown that, for small \mathbf{r} -values, the Fourier transformation $I^{FT}(\mathbf{r})$ of the measured intensity is proportional to $S(\mathbf{r}) \otimes S(-\mathbf{r})$ where $S(\mathbf{r})$ is the shape function of the dot (unity inside and zero outside the dot volume). For large \mathbf{r} , $I^{FT}(\mathbf{r})$ shows a maximum for the average inter-dot distance $\langle L \rangle$. It turned out that the CGe quantum dots are of a symmetrical lens shape, about 12 nm wide and 1.7 nm high, with a mean distance of about 30 nm. These values agree reasonably well with AFM investigations of a single, uncapped CGe dot layer, and previous TEM investigations of the multilayer sample, having in mind that in the latter it is quite difficult to determine the exact dot dimensions due to the particularly large strain contrast in the CGe system. For the correlation properties, which are also difficult to obtain from TEM due to the small probed area, they found neither a vertically nor laterally ordered dot distribution.

GISAXS was further used by Stangl et al. [62,338] in 2000 to demonstrate the strain-induced ordering of SiGe quantum dots in a SiGe/Si multilayer. Step bunching of the vicinal Si substrate was used to reduce the fluctuations in lateral dot distances. Fig. 99 illustrates the resulting lateral ordering, revealed by the several orders of satellites parallel with the surface, when the incident beam is parallel with the steps, thus probing the island ordering perpendicular to the steps. They arise from constructive interferences between the waves scattered by the array of islands. When the beam is set perpendicular to the steps, some ordering remains, but much less pronounced.

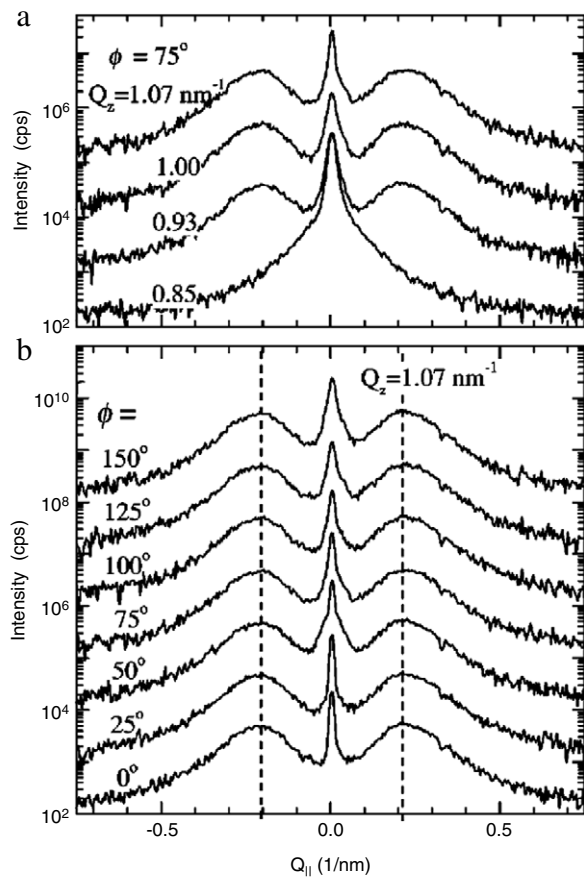


Fig. 97. GISAXS on carbon induced self-assembled Ge/Si(001) dots: q_y scans measured for various azimuth angles ω and constant $\alpha_{i,f}$, corresponding to $q_z = 1.07 \text{ nm}^{-1}$ (a). The position of the lateral maxima is independent of ω . In (b), the scans for constant ω and various q_z are shown. In both panels, the curves are shifted with respect to each other for clarity. From Ref. [22].

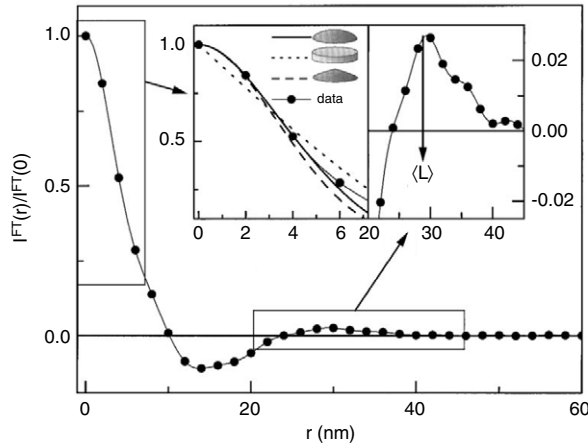


Fig. 98. Fourier transformation $I^{FT}(r)$ of the measured intensity. The insets show the best fit to the central peak for different dot shapes (left-hand side), and an enlargement of the peak around $r = 30$ nm, corresponding to the mean dot distance $\langle L \rangle$ (right-hand side). From Ref. [22].

This team presented a method to interpret reciprocal-space maps recorded in GISAXS geometry to obtain the shape and the lateral correlation properties of buried islands. From the maps, which have been recorded for various penetration depths, the autocorrelation function is calculated, from which the island parameters are obtained by comparison with simulations based on the distorted-wave Born approximation. As a demonstration of the

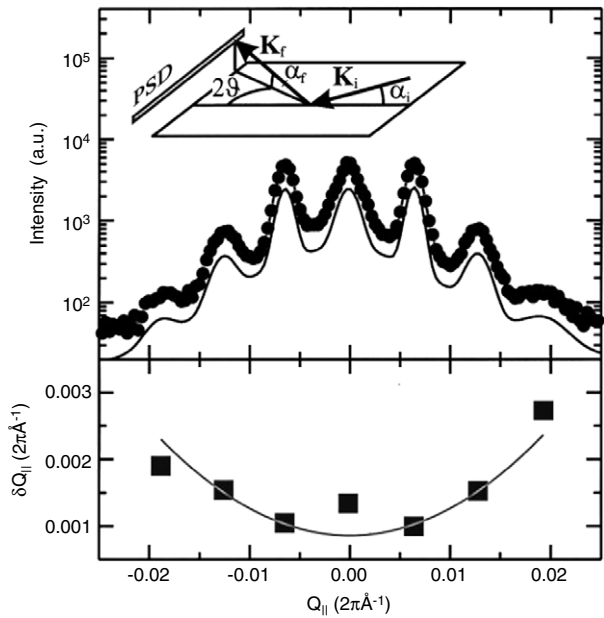


Fig. 99. GISAXS scan of the SiGe/Si dot multilayer (upper panel) in the azimuth q_y perpendicular to the step edges. The inset shows the measurement geometry. The lateral maxima have been fitted by Gaussian peaks to determine their width, which is displayed in the lower panel. From a quadratic fit to these values, the lateral correlation properties in the short-range order model have been obtained. From Ref. [62].

sensitivity of the method, measurements on self-organized SiGe islands in a Si/SiGe multilayer have been performed. It was possible to detect different shapes of the islands at the sample surface and those embedded in the multilayer.

The same group [64,21,339] investigated in 2001 self-organized SiGe quantum wires (and no longer dots as above) buried at the interfaces of a SiGe/Si multilayer, grown on a vicinal Si substrate with a rather large miscut angle. As shown in Fig. 100, a nearly periodic distribution of wires, induced again by step bunching of the vicinal Si(001) substrate, was found in the direction perpendicular to the steps (Fig. 100a), while no ordering was found parallel with them (Fig. 100b). The scattered intensity was analyzed using a model based on the distorted wave Born approximation. The lateral wire distribution was found to obey the short-range-order model based on the 1D paracrystal description, the mean distance of the buried wires equals that of the ripples at the sample surface. The shape of the wire cross section was determined from the relative heights of the intensity maxima as a function of q_z . From the heights of the lateral satellite maxima, the mean width of the wire was determined to be 35 nm i.e. less than the half of the wire distance, and the angle of its side facet to be 6°. Since this angle is larger than the crystallographic miscut, the self-organization process creating the wires cannot be explained by the bunching of monolayer steps alone.

8.5.3. Other self-assembled semi-conductor quantum dots

The planar ordering of dense self-organized arrays of InP/InGaP quantum dots was investigated in 2000 [340] using GISAXS, AFM and TEM. 2D in-plane GISAXS maps were recorded. They showed that the degree of in-plane ordering increased with increasing InP dot density. In 2001, Zhang et al. [63] investigated InAs quantum dots grown by MBE on GaAs(001) combining GISAXS and GIXRD. Pronounced diffuse scattering peaks were found in GISAXS (Fig. 101), with high diffraction orders along the $\langle 110 \rangle$ and $\langle 100 \rangle$ in-plane directions. Rods of scattering by facets were also observed, from which an octagonal-based shape was deduced, with $\{111\}$ and $\{101\}$ facet families. The ordering of the dots was found to be

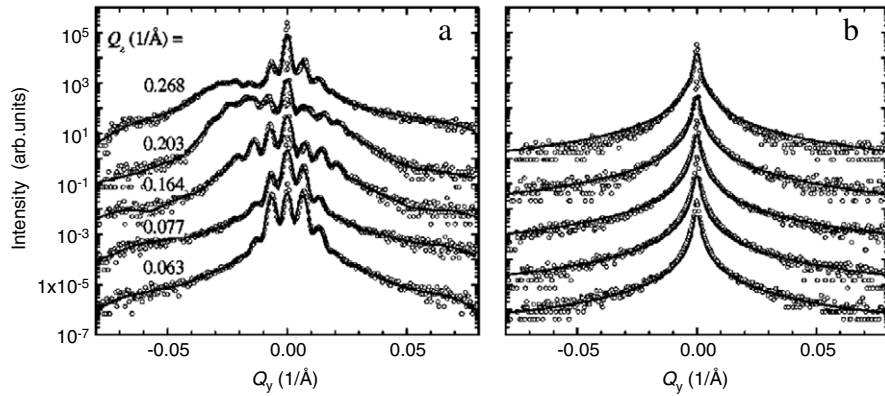


Fig. 100. GISAXS scans (circles) on SiGe quantum wires measured for different q_z with the incident beam parallel with (a) and perpendicular to (b) the step array, thus probing the order perpendicular to and parallel with them, respectively. Lines represent simulations. Curves are shifted vertically for clarity. From Ref. [64].

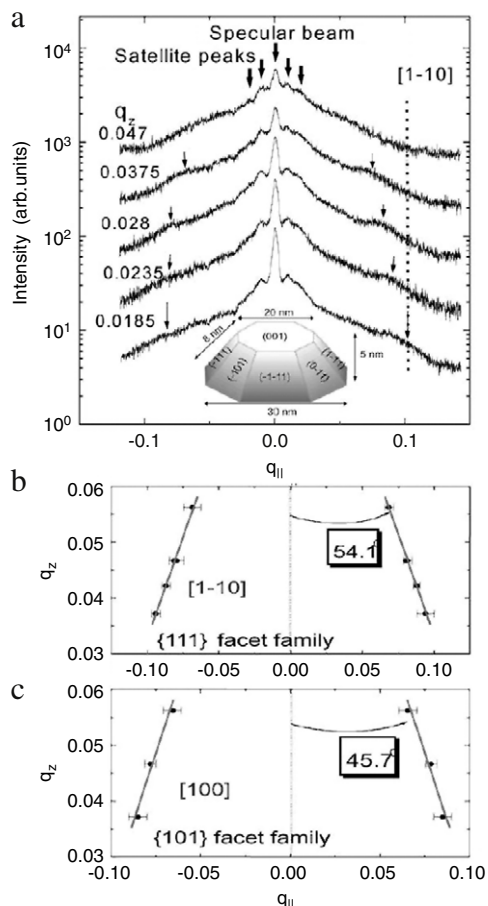


Fig. 101. GISAXS intensity from InAs/GaAs(001) dots at different q_z values are shown in (a) for q_y in the $[1\bar{1}0]$ direction; (b) and (c) show the CTR facet peak positions in (q_y, q_z) space for q_y in $[1\bar{1}0]$ and $[100]$ directions, respectively. From Ref. [63].

anisotropic, as deduced from analysis of the mean dot-dot distance and correlation length.

In 2001, V. Holy et al. [65,341] investigated the morphology of free-standing and buried triangular self-assembled PdSe quantum dots/PbEuTe superlattices with various thicknesses of PbEuTe spacer layers, grown by MBE. Fig. 102 shows AFM images of the PbSe dots on PbEuTe, illustrating the perfectness of the individual pyramids as well as their nice in-plane hexagonal arrangement. Fig. 103 shows in-plane two-dimensional intensity distributions for three samples. In sample 966, the dots are arranged vertically

and their lateral positions are random. In sample 950, the dot stacking is trigonal in three-dimensions, leading to well defined in-plane intensity satellites. In sample 906, the positions of the dots are random, which implies that no satellites are present in the reciprocal space maps, and the measured intensity corresponds to the scattering from a single dot. These data were fully simulated using the DWBA. Fig. 102 also shows the intensity along line scans extracted along the arrows of Fig. 103 for the most ordered sample, together with the best fits. It reveals several orders of satellite intensity peaks which confirm the excellent hexagonal ordering at short scale.

In 2002, Li and coworkers [342] analyzed the lateral composition modulation in $(InAs)_n/(AlAs)_n$ short-period superlattices by combining again GISAXS and GIXD. The GISAXS measurements were used to determine the interface profile of the vertical superlattice, which then served as the basis for the diffraction analysis of the lateral composition profile. The interfaces in the vertical superlattice were found to have an asymmetric profile with an average undulation wavelength of 28 nm, and an average amplitude of 0.1 nm. The lateral composition modulation was found to be predominantly caused by the morphological undulation of the individual short-period superlattice layers, rather than intermixing and decomposition.

In 2005, Krause and coworkers [343] presented GISAXS and GIXD measurements on free-standing, self-assembled InAs/GaAs quantum dots grown by MBE, with different arrangements of the dots: isolated, randomly distributed single dots, or dots assembled into a bimolecule, or into a quadmolecule (Fig. 104). As an example of their amazing results, Fig. 105 shows the GISAXS measurements obtained on the bimolecule, as a function of the azimuthal sample rotation. They clearly reveal the effect of the product of the dots' form factor by the structure factor of the bimolecule.

Another amazing GISAXS measurement is that of Sztucki et al., published in 2006 [344], in which nanoscopic InGaAs ring structures on GaAs(001) were formed by covering InAs quantum dots grown by Stranski-Krastanow self-assembly with a thin GaAs layer. The data (Fig. 106), revealing the circular symmetry of the shape, were nicely fitted by the squared Fourier transform of an empty ring, of which they could determine all dimensions, including side angle and width of size distribution.

8.5.4. GISAXS analysis of vertical stacking of semi-conductor quantum dots

In the following example, the vertical periodicity and stacking of quantum dots will be considered. Ordering in such systems can be enhanced by the growth on a template, or self-organized by surface anisotropy of the elastic constants and hence a mutual influence between the quantum dots and their positions relative

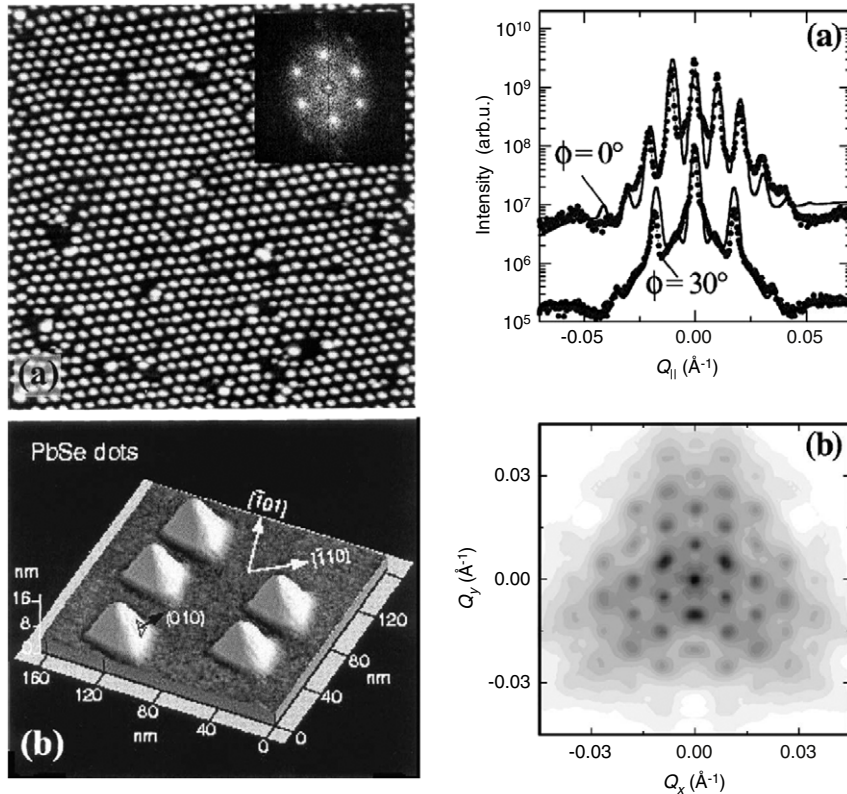


Fig. 102. Left: AFM images of PbSe dots on PbEuTe. (a) An overview showing the hexagonal in-plane arrangement of the islands, the inset shows a 2D power spectrum of the image. (b) High-resolution image showing the pyramidal island shape. Right: GISAXS spectra of the PbSe island sample for different azimuths of the incident beam (a), and combination of the individual spectra to the 2D intensity distribution, reflecting the in-plane arrangement of the PbSe islands (b). From Ref. [341].

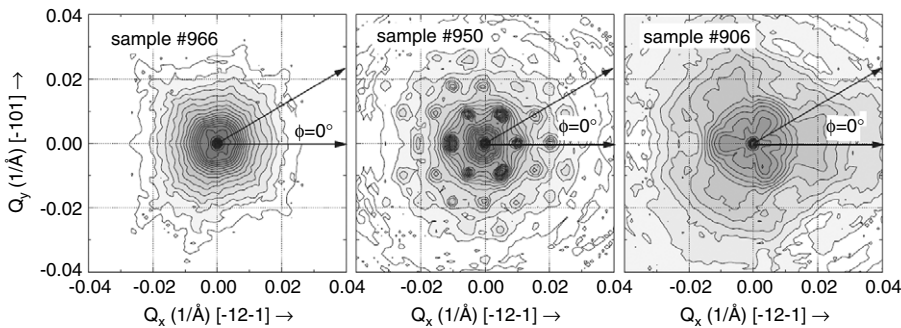


Fig. 103. Two-dimensional intensity distributions measured in the GISAXS geometry for the three samples. From Ref. [65].

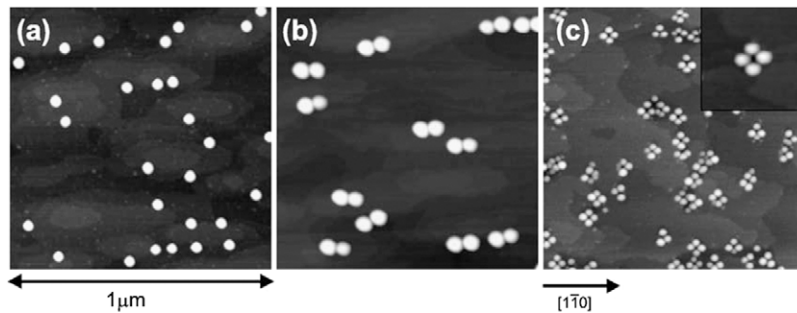


Fig. 104. AFM images of (a) conventional, single quantum InAs/GaAs dots, (b) bimolecules, and (c) quadmolecules. The inset in (c) shows an enlarged area of $0.1 \mu\text{m} \times 0.1 \mu\text{m}$. From Ref. [343].

to each other. In the case of quantum dot superlattices, vertical stacking can occur even without the presence of lateral order. This

stacking is strain-mediated by the distortion field around quantum dot in the spacer layers.

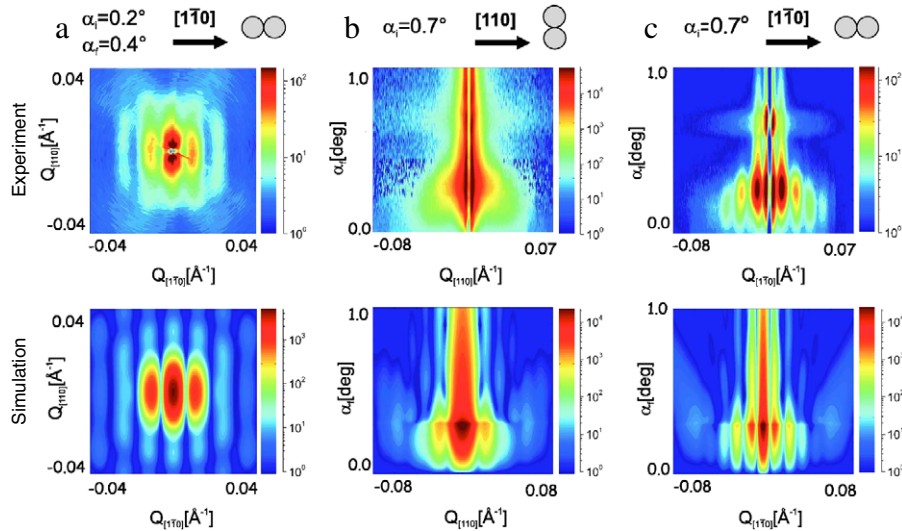


Fig. 105. GISAXS measurements of the quantum dot InAs/GaAs bimolecules and their simulations, shown in logarithmic intensity scale (arb. units, values below the range of the color scale are plotted in blue, values above in dark red). 2D intensity distribution at (a) constant incident angle α_i and exit angle α_f , (b) constant α_i and variable α_f with the in plane scattering vector perpendicular to the molecular axis, and (c) constant α_i and variable α_f with the in plane scattering vector parallel with the molecular axis. The scanning direction relative to the orientation of the bimolecule is indicated. From Ref. [343]. (For interpretation of the references to colour in this figure legend, the reader is referred to the web version of this article.)

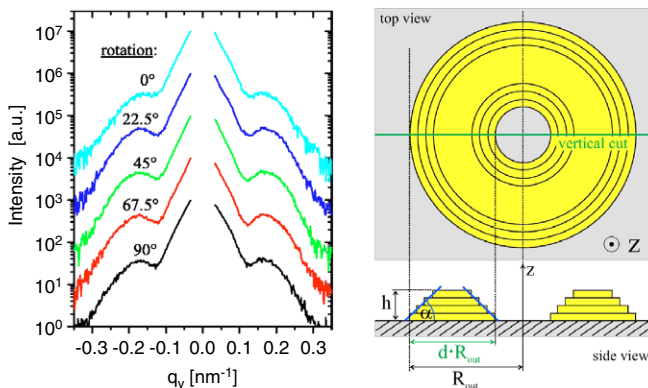


Fig. 106. Left: The figure shows the InAs/GaAs data measured with a linear position sensitive detector parallel with the sample surface (wavevector transfer q_y , $\alpha_i = 0.4^\circ$, and $\alpha_f = 0.32^\circ$) for different azimuthal positions as indicated. No azimuthal dependence on the sample rotation is observed, indicating that the lateral quantum ring shape is isotropic. The measured curves are shifted for clarity. Right: Schematic drawing of the model used for the simulation of the GISAXS measurements. The horizontal line in the top view marks the position of the vertical cross-section shown in the lower part of the figure. From Ref. [344].

A system widely studied for its applications in the field of wide bandgap semiconductors are GaN quantum dots embedded in an AlN multilayer matrix. For dots that are supposed to serve as light emitting media, a growth in multilayers means an increase in the number of dots but also can provide an improvement in size homogeneity, if self-ordering occurs in this process. Numerous studies have been published on the topic of the self-improvement of the order and the size homogeneity as a function of spacer layer thickness and the amount of deposited quantum dot layers. For such multilayered structures, the order can be studied best under GISAXS conditions since the typical distances and correlations are of the order of 10 to several 100 nm. In Fig. 107a, a typical GISAXS image from a GaN/AlN multilayer is shown. In the middle of the figure, a sketch presents the structure of the multilayered sample. During the deposition of 2.5 monolayers of GaN, a 2D-monolayer wetting layer grows before the QDs spontaneously form, thereby elastically relaxing the mismatch-induced elastic strain. Each of the n QD layers is covered by an AlN spacer layer. A steady state of the QD growth is reached after the deposition

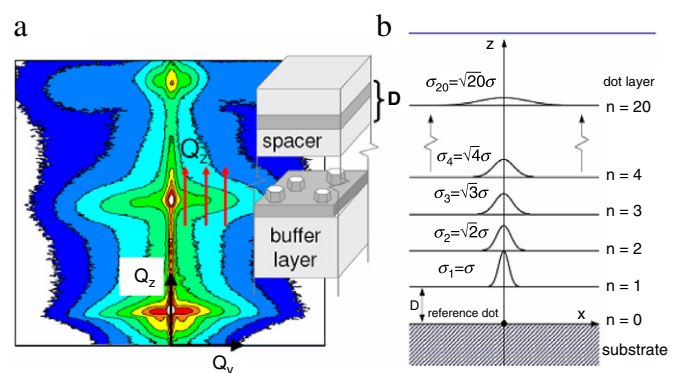


Fig. 107. Typical GISAXS pattern for a multilayered GaN/AlN sample of quantum dots separated by spacer layers. (b): sketch of the model used to describe the random walk like decay of the vertical order. From Ref. [345].

of 2–3 bilayers. The 2D GISAXS image shows periodic intensity maxima along q_z which are substantially extended in q_y . Their distance in q_z is directly related to the spacer bi-layer thickness of the multilayer. These so-called “Bragg sheet”, diffuse intensity of the multi-layered structure (see Section 5.4.3), can be used to analyze the strain driven vertical stacking order.

The strain propagation from the GaN dots through the AlN spacer layers creates a strain-modulated surface and thus preferential nucleation sites for the successive layer of GaN dots. An analytical model of strain driven stacking order and its effect on the scattered X-ray intensity has been developed by Kegel et al. [345]. It is based on the assumption that the strain is mediated only through one spacer layer, i.e. that every layer of quantum dots influences only one successive layer. Thus the probability that an island nucleates vertically aligned to the island underneath can be described in a random walk like manner. The random displacement from the aligned position depends on the correlation strength and is thus certainly dependent on the strain propagation and the capping layer thickness. For the n th layer, this random walk model results in a displacement $\sigma_n = \sqrt{n} \times \sigma$. As we have a vertically periodic layered structure, we expect intensity oscillations in q_z along the specular direction. Assuming a perfect vertical periodicity with a layer spacing D , it was shown [345] that

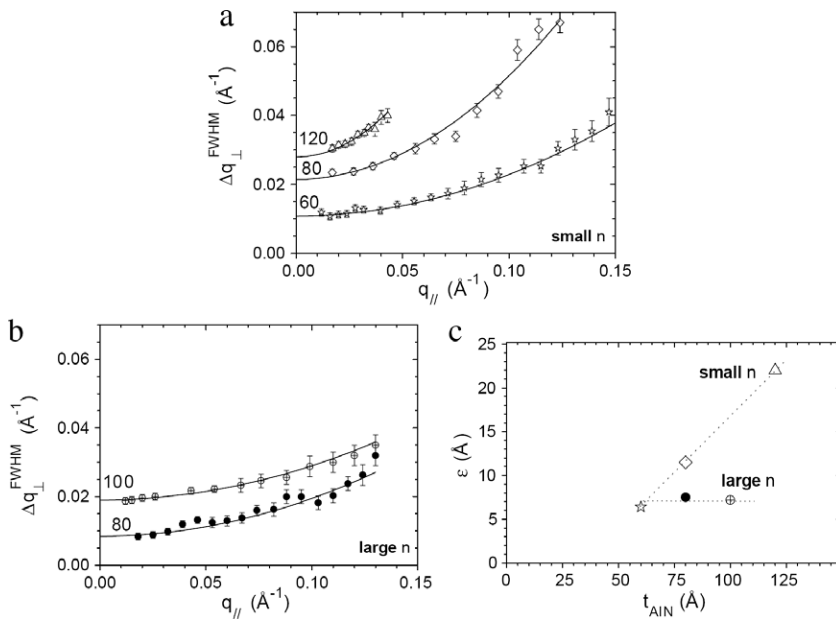


Fig. 108. (a): Full width Δq_z of the Bragg sheet in Fig. 107a as a function of q_y for three different samples with spacer thicknesses D from 60 to 120 Å and a low number of deposited bilayers as a function of spacer thickness D . (b): For $D = 80$ or 100 Å and a high number of deposited bilayers. (c): Mean displacement σ as a function of spacer thickness D . From Ref. [346].

the full width at half maximum of the intensity maxima along q_z (Δq_z) as a function of q_y can be approximated as: $\Delta q_z = 2\sigma^2/Dq_y^2 + 2\mu/D$. Δq_z is expected to increase as q_y^2 and the only open parameter describing the degree of order, σ , can be quantified from the experiment. The parameter μ describes the absorption correction that has an important contribution in the grazing incidence geometry. The most interesting parameters to be varied in a growth of a sample series are the spacer layer thickness D and the number of deposited bilayers n , as in the case of strain driven ordering, one expects an increase of order with a higher number of layers. Chamard et al. published studies [346, 347] showing that the order increases substantially for a high number n of bilayers, even for high values of the spacer thickness D . Fig. 108 shows the half width in q_z as a function of q_y along one Bragg sheet. With this parabolic dependency and the known parameters D and μ , the average lateral displacement σ can be extracted from the fits in Fig. 108. This average displacement between stacked quantum dots is plotted as a function of the spacer thickness D in Fig. 108. It is about 7 Å for a high number of bilayers, independent on the spacer layer thickness D . For a smaller number of periods n , this deviation still depends on the spacer layer thickness D . These results and in particular the parabolic relation between Δq_z and q_y served as an indirect proof of the strain driven nature of vertical stacking in these heterostructures. The ordering mechanism of stacked CdSe/ZnSSe quantum dots was studied in 2004/2005 by Schmidt et al. [348,349]. GISAXS was used to analyze the influence of the ZnSe spacer layer thickness (ranging from 2 to 8 nm), as well as the influence of the stacking number (3–10). Satellite spots (Fig. 109), indicative of quantum dot ordering, both laterally and vertically, have been observed for a spacer thickness of 4.5 nm, and for a stacking number of at least 5. This was explained by a self-organized ordering process driven by the lattice mismatch induced strain. The mean lateral quantum dot distance, ranging from 12 to 14.5 nm, was found to depend on the spacer thickness. In addition, an anisotropy with a two-fold symmetry has been observed, with the strongest correlation along $\langle 110 \rangle$. On the left-hand side of the figure, typical images obtained from the samples with 4.2 nm spacer thickness are shown. For the tenfold (a) and the fivefold (b) QD stack, satellite spots are clearly visible, the width along q_z of which is smaller (larger) for sample a

(b). This can be understood in terms of the finite thickness of the layer from which the correlation signal originates, i.e., in an ideal case the total thickness of the QD stack region. For the threefold stack sample (c), no satellite spots have been observed, not even for further enhanced image contrast. For sample (c) and for the reason mentioned above, the satellite spots are expected to be even wider along q_z , with a smaller integral intensity, since the correlation signal is generated in a smaller volume. However, this effect is not sufficient to explain the complete absence of satellite spots within the detection limit. Hence the ordering within the threefold QD stack (c) must be significantly weaker compared to samples (a) and (b). This can be interpreted in terms of a gradually increased ordering by self-organization, in which the bottom layers act as a seed for ordering in subsequently deposited layers, in agreement with theoretical predictions and experimental results obtained from other material systems. GISAXS images obtained from samples d–f are shown on the right-hand side. Assuming a comparable correlation for all three samples, the satellite spots are expected to be sharpest along q_z for sample (f) and therefore should be easily visible. However, satellite spots are clearly seen for sample (d) and (e), but not for sample (f). Hence it was concluded that there is virtually no QD correlation for sample (f), which has the largest spacer thickness. This further indicates that the strain fields originating from the mismatched QDs in lower layers is indeed the reason for the ordering of subsequently deposited layers. With increasing spacer thickness, these strain fields overlap progressively, smearing out the lateral strain modulation in the next layer, suppressing preferential nucleation sites.

8.5.5. Characterization of defects induced by implantation in semiconductors

The morphological characteristics of defects induced by the implantation of inert gases into silicon has attracted much attention [350]. For instance He implantation in crystalline Si leads to the formation of bubbles [351] (gas-filled cavities) that upon annealing coarsen and degas creating voids [352]. The size, shape and spatial organization of these internal structures are strongly dependent on the implantation parameters (energy, flux, temperature). The so-called {113} defects are probably the most

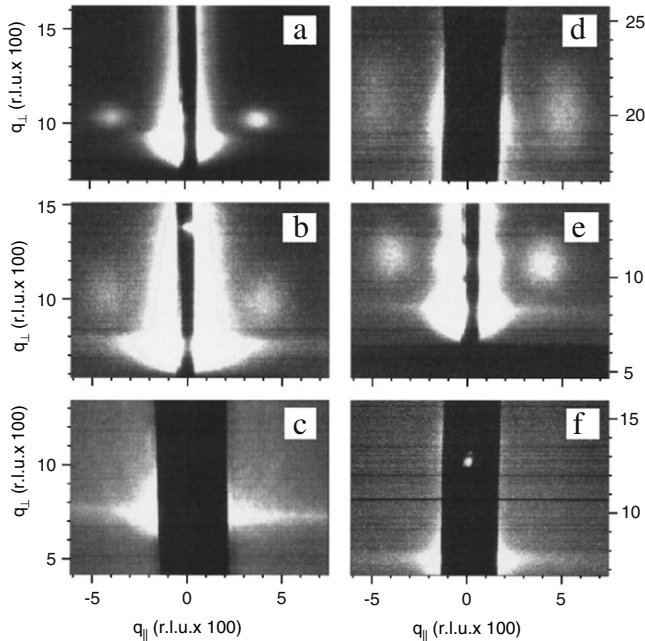


Fig. 109. Typical GISAXS images from stacked CdSe/ZnSSe quantum dots samples (a) with 10 stackings with spacing of 4.2 nm, (b) with 5 stackings, 4.2 nm, (c) 3 stackings, 4.2 nm, (d) 5 stackings, 2 nm, (e) 5 stacking with spacers of 4.5 nm, and (f) 5 stackings, 8 nm spacers, each taken at α_i values around 1° . From Ref. [348].

common extended defects into He-implanted Si. GISAXS studies of the early stages of bubble formation in helium-implanted [353], H-implanted [354] and deuterium-implanted [355] monocrystalline silicon where reported in 2003. For the He^+ implantation study [353], the early stages of bubble formation in Si(001) were investigated by implanting He^+ at 20 keV and treating the samples in the temperature range 100–450 °C. GISAXS combined with elastic recoil detection was used to measure the helium content and depth distribution, while the gas release was studied by thermal desorption spectrometry. To evidence the radiation damage evolution and the defect behavior, the results from Rutherford backscattering spectrometry in channeling conditions, cross-sectional transmission electron microscopy, and GISAXS were critically analyzed and compared. The study led to the identification of the steps followed by the defects during annealing and suggested that critical condition for the production of stable bubbles is the presence at low temperature of agglomerates composed of more than four vacancies decorated by helium. This kind of defect offers helium the room necessary to transform into gas phase and confer thermal stability to the bubble embryos. For the H^+ implantation study [354], the samples were implanted with H^+ ions at an energy of 31 keV and to the dose of 10^{16} ions/cm². Samples were annealed isochronally at different temperatures. Although the H depth distribution was expected to be smooth initially, nanosized features, like agglomerates of defects, have been detected. Annealing destroyed this feature due to the relaxation of defects, i.e. redistribution of vacancies and hydrogen. Above 300 °C a well defined film with highly correlated borders was found to form on the edge of the layer rich in defects, whose thickness was found to decrease slowly from 25 to 22 nm with increasing annealing temperature. Moreover, defects as well as hydrogen were found to migrate toward the surface with increasing annealing temperature, as indicated by the increase in surface roughness. In the deuterium implantation study [355], monocrystalline silicon samples were implanted with deuterium ions at an energy of 24 keV and at a dose of 2×10^{16} ions/cm². Samples were annealed isochronally at different temperatures in the range from 393 to 973 K. Due to the

relaxation of the defects structures, i.e. redistribution of vacancies and deuterium, strong particle like contribution was observed in addition to the rough surface scattering, already at 393 K annealing. During the annealing, these particles (agglomerations of vacancies) gradually dissolved until 623 K annealing temperature. Another agglomeration mechanism took over at about 773 K when a different type of particle growth was observed, and these dissolved again at about 973 K. The sizes of detected particles were in the 2–3 nm range. Also, the interference type of scattering from a film of about 30 nm thickness (the top layer, mostly unaffected by implantation) was observed. This film was gradually getting thinner with the increasing annealing temperature, due to the redistribution of the defects and the structure relaxation.

In the study of Refs. [356,357], He^+ and Ne^+ ions have been implanted into Si(001) at 873 K. The incident energy is 50 keV and the fluence is 5×10^{16} cm⁻². Another sample was implanted with 5×10^{16} cm⁻² He^+ at 473 K and then annealed at 873 K. For Si(001) wafers implanted with Ne^+ ions at 873 K or implanted with He^+ ions at 473 K post-annealed at 873 K, an isotropic diffuse scattering signal is measured by GISAXS which can be assigned to spherical cavities. On the contrary, in the case of He^+ implantation at 873 K, the GISAXS pattern is highly anisotropic (Fig. 110). Very narrow streaks are observed at 25.2° with respect to the surface normal. They correspond to voids exposing {113} facets. Enlarged streaks at 54.7° which can be assigned to {111} facets are also observed. The result is confirmed by rotating the sample in the surface plane. These characteristic streaks are observed only when the incident beam is aligned along the ⟨110⟩ direction (weak streaks are also observed in the ⟨310⟩ direction). The quantitative analysis of the GISAXS patterns are performed in the framework of the DWBA considering buried cavities [36]. A lognormal size distribution is used to fit the data assuming different kinds of shapes (sphere, faceted sphere, or disk). The authors attribute the streaks at 25.2° to faceted spheres exposing two {111} facets and the streaks at 54.7° to large disks exposing {113} planes. In the calculation all equiprobable orientation are considered, e.g. 4 orientations for the faceted spheres ({111} facets) and 12 orientations for the disks ({113} facets). It is found that the mean diameter of the faceted spheres is 20.1 nm and the FWHM is 26.7 nm. The disks are approximately 100 nm large with an average thickness of 2 nm. The simulations of the GISAXS patterns are in good agreement with the data. However one may wonder if the model of faceted spheres exposing only two {111} facets is relevant as faceted spheres should expose height {111} facets by symmetry. Similarly, the disk shape assumes no preferential crystallographic orientation in the radial direction whereas faceted edges (e.g. {111} planes) are probable. These points are not discussed. Nevertheless the GISAXS measurements unambiguously reveal that the vacancy-type defects induced by the He^+ implantation can agglomerate at high temperature into large faceted {113} voids. At lower temperature (<573 K) or in the case of implantation with Ne^+ , clustering of defects is not promoted, and small spherical voids are observed because the diffusion processes are not activated. Capello et al. investigated by quantitative GISAXS the hydrogen implantation induced cavities in silicon [359], with H^+ ions of energy (76 keV) and doses (1×10^{16} to 6×10^{16} cm⁻²) typical of the irradiation used for the Smart Cut™ technique. In this technology, ion implantation is used to stress and weaken a specific region of material below the surface, in which the fracture will be later induced, by thermal treatment for instance. During annealing, point defects and platelets transform to form cavities and microcracks, which finally enable the full wafer splitting. Two types of platelets, {111} and {001}, were shown to be present. They contain a large pressure of H_2 gas. Fig. 111 shows a typical GISAXS map with the incident beam along [110] for a sample implanted at 200 °C and annealed at 500 °C for 1 h. Strong intensity streaks are

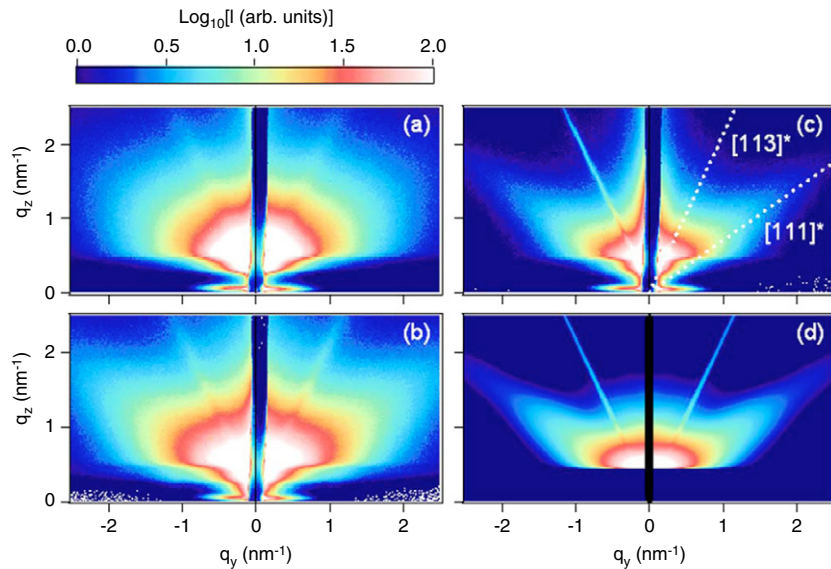


Fig. 110. (a) Two-dimensional experimental GISAXS pattern of Si(001) He-implanted at 873 K with the incident beam along the Si[110] direction. (b) Two-dimensional simulated GISAXS pattern assuming a log-normal distribution of {111} faceted cavities associated with elongated {113} defects. From Ref. [358].

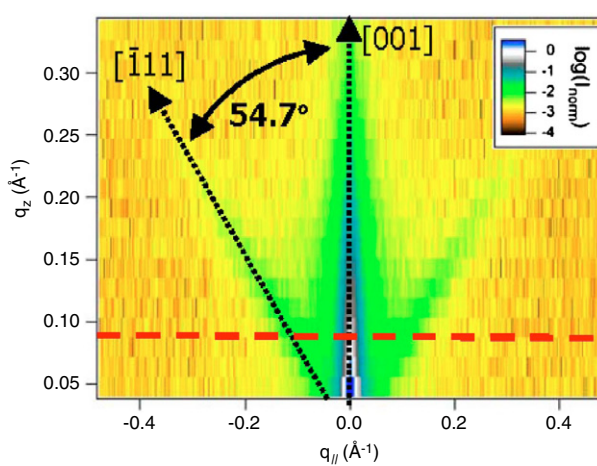


Fig. 111. GISAXS map in the (q_y , q_z) plane with the incoming beam along the [110] direction for (001) Si implanted with H $^+$ ions to 3×10^{16} cm $^{-2}$ at 200 °C and annealed at 350 °C for 1 h. The {111} streaks make an angle of 54.7° with the q_z direction. From Ref. [359].

found along {001} and {111} directions, these latter being absent when the beam is along the [100] direction. They arise because of the two types of platelets. Fig. 112 shows cuts of this image parallel to the surface. A full quantitative analysis allowed to deduce not only the length and the thickness of the cavities, but also their density.

In another study, GISAXS was also combined with vibrational spectroscopy to analyse the nanostructural properties of hydrogenated amorphous silicon and Si–C thin film alloys [360]. Amorphous hydrogenated silicon (a-Si:H) with high hydrogen content (10 to 40 at.%), and non-stoichiometric silicon–carbon thin film with a variation of the carbon to silicon ratio up to 0.3, were deposited by using a magnetron sputtering source. The Si $_{1-x}$ C $_x$ thin films were partially crystallized after deposition by thermal annealing up to 1050 °C. The GISAXS spectra of all of the prepared specimens indicate the presence of particles in the bulk of the films. For the a-Si:H samples, particles are most probably void agglomerates with a variation in size between 3 and 6 nm. The mean value of the size distribution of the particles increases while its width

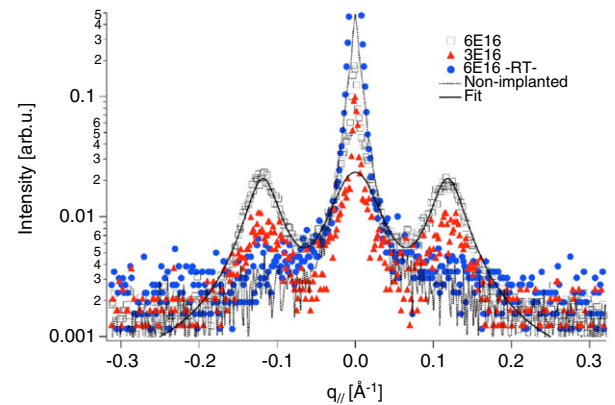


Fig. 112. GISAXS measurements at fixed $q_z = 0.096$ Å $^{-1}$, corresponding to the dashed line in Fig. 1. The symmetric intensity maxima at $q_y = 0.12$ Å $^{-1}$ correspond to sections of the {111}-oriented streaks. From Ref. [359].

slightly decreases with the hydrogen content in the film. This indicates a better structural ordering which is consistent with the results of Raman spectroscopy that show a decrease of the ratio between intensities of transversal acoustic (TA) and transversal optic (TO) phonon peaks, ITA/ITO, and a narrowing of the TO peak with increasing hydrogen content. These results are discussed as a consequence of the beneficial influence of hydrogen bombardment during the film growth. For Si $_{1-x}$ C $_x$ thin films, the particles are assumed to be SiC nanocrystals with a size between 2 and 14 nm and they are larger in films with a higher carbon concentration. Inside each of the films, the crystals are larger closer to surface and they grow faster in the direction parallel with the surface than in that which is perpendicular to it.

GISAXS was also used to analyze structural modifications in implantation-damaged Ge [361]. Samples were implanted by different doses of ^{74}Ge , at room- or liquid nitrogen-temperature. They found that the micro-structure in amorphous Ge was continuously and consistently evolving as a function of ion dose but differed according to the implantation temperature. In RT-samples small vacancy nanoclusters aggregated in the end-of-range region of implanted layer even before complete amorphisation. With higher doses nanoclusters increased and coalesced into nanovoids. For the highest dose, the onset of porosity was

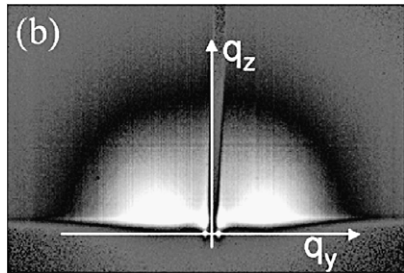


Fig. 113. GISAXS pattern of a nanoporous p-doped Si substrate. From Ref. [363].

confirmed. On the other hand, in LN-implanted samples, the clustering-related signal was much weaker and evolved more slowly.

8.5.6. Porous materials

Porous silicon obtained by electrochemical etching routes has been much studied in the past decades due to its luminescence properties [362]. However, the mechanisms of pore formation are unclear due to the difficulty of characterizing the shape, size and spatial organization of pores at the nanometer scale in thin layers. GISAXS is an ideal tool for characterization thanks to its sensitivity to the near surface region and the length scale probed (1–100 nm). *Ex situ* GISAXS measurements have been performed by Chamard and coworkers [363] at the ESRF on the ID1 beamline. Different anodization conditions have been used for the etching process of Si. Fig. 113 shows a typical GISAXS pattern obtained for a p-doped substrate. The main characteristic features are intense correlation peaks parallel with the surface plane. They can be assigned to a highly anisotropic spatial organization of pores oriented preferentially perpendicular to the surface. At high wave vector transfer, the intensity is roughly isotropic. The GISAXS intensity is fitted in the framework of the DWBA for buried nanostructures [36] and assuming a spherical shape (Gaussian distribution) of pores and an isotropic spatial distribution parallel with the surface plane. The average pore diameter is 6 nm (standard deviation 1.6 nm) and the first neighbor distance is about 8.6 nm. This is a very rough model because pores are interconnected due to the etching process and the in-plane organization of the pores is a clear indication of the presence of irregular channels oriented perpendicular to the mean surface plane. Moreover the porosity calculated from these parameters is 20% whereas it is 47% if one considers the angular position of the critical angle of total external reflection. A more sophisticated model of the morphology of porous Si is necessary. To complement GISAXS experiments, X-ray reflectivity measurements have been performed to characterize the surface morphology and the porous-Si/Si interface roughness generated by the pore front propagation. Simon et al. [299] compared GISAXS measurements on nanoporous low-k materials obtained by different routes. They showed that the pore morphology was drastically affected by the process used, ranging from well-defined pore sizes and shapes to ill-defined pores.

A combined XRR and GISAXS study of silicon oxynitride films [364] is worth mentioning here. A single chamber system for plasma enhanced chemical vapor deposition was employed to deposit different films of $\text{SiO}_x\text{N}_y\text{H}_z$ with $0.85 \leq x \leq 1.91$. All films were previously characterized by Rutherford back-scattering and infrared spectroscopy to determine the stoichiometry and the presence of various bonding configurations of constituent atoms. XRR was used to determine the electron density profile across the depth, and the top layer was found to be densified. GISAXS was used to study inhomogeneities (clustering) in the films, and it was shown that plate-like inhomogeneities exist in the top and sphere-like particles at the bottom part of the film. Their shape and size were shown to depend on the stoichiometry of the films.

The same group also investigated by GISAXS amorphous SiO/SiO_2 superlattices [365–367], which were prepared by high vacuum evaporation of 3 nm thin films of SiO and SiO_2 (10 layers each) on Si (100) substrate. Rotation of the Si substrate during evaporation ensured homogeneity of the films over the whole substrate. After evaporation samples were annealed at 1050 or 1100 °C for 1 h in vacuum. The analysis of the 2D GISAXS pattern has shown that Si nanocrystals are present in the annealed samples. From the 2D GISAXS pattern it is possible to determine the shape, size and inter-particle distance. Using a Guinier approximation, their inter-nanocrystal distance (5 nm) and radius of gyration (1.5 nm) have been obtained.

GISAXS was also used to investigate the influence of the substrate morphology on the growth of thin silicon films [368] with thicknesses between 100 and 300 nm, deposited by PECVD (Plasma Enhanced Chemical Vapor Deposition) in silane gas (SiH_4) highly diluted by hydrogen. The degree of dilution and the discharge power were varied in order to obtain different crystalline to amorphous fractions in the films. Two types of substrates were used. The first one was amorphous and relatively flat while the second one was polycrystalline with a roughness of a few tens of nanometers. The crystal fraction in the deposited samples, as estimated by Raman spectroscopy, varied between 0% and 40%, and the individual crystal size was between 2 and 8 nm. The larger individual crystals were usually present in those samples with the highest crystal fraction. The sample density, estimated upon the spectral distribution of the dielectric function in the infra red, was 15% to 25% less than the density of crystalline silicon. The GISAXS pattern of all of the examined samples indicated the presence of non-spherical-like particles in the bulk of the thin films, with an average particle size between 1.5 and 4 nm. These particles were most probably voids and their shape indicates columnar growth. By applying the GISAXS technique on samples deposited on different substrates, the borderline deposition conditions between transport limited growth and growth dominantly influenced by plasma surface reactions was estimated. In 2007, they reported on a study of amorphous nanocrystalline thin silicon films [369, 370]. The films with thicknesses between 100 and 400 nm, were deposited by radio frequency plasma enhanced chemical vapor deposition in silane gas (SiH_4) highly diluted by hydrogen. The growing conditions were varied to obtain different degrees of crystal fractions and a variety in individual crystal sizes. The crystalline to amorphous volume fraction, as estimated by Raman spectroscopy, varied from 5% to 45% while the individual crystal sizes varied from 2 to 8 nm. The average density of the samples was estimated by using near infrared spectroscopy and the effective medium approximation. All samples were porous and contained void volume fraction between 15% and 25%. The GISAXS patterns of all examined samples indicate the presence of particles in the bulk of the thin films with gyration radii in the range of 2 to 5 nm. The higher values were found for the samples with a higher crystalline fraction. The size and the size distribution of particles depend upon the deposition conditions. The samples which had been deposited with a higher discharge power and a lower silane fraction had larger particles and the roughness of their surface was higher.

8.5.7. GISAXS studies of semi-conductor nanocrystals

Semiconductor nanocrystals like CdS formed by ion beam synthesis and subsequent annealing in SiO_2 substrate were also characterized by GISAXS [371]. From the fits to the theoretical expressions, the average particle diameter, the shape, as well as the size distribution were determined. The obtained results were found to be in good agreement with TEM results performed on analogous samples. In 2004, the same group [372] studied the direct synthesis of nanoparticles formed by dual implantation

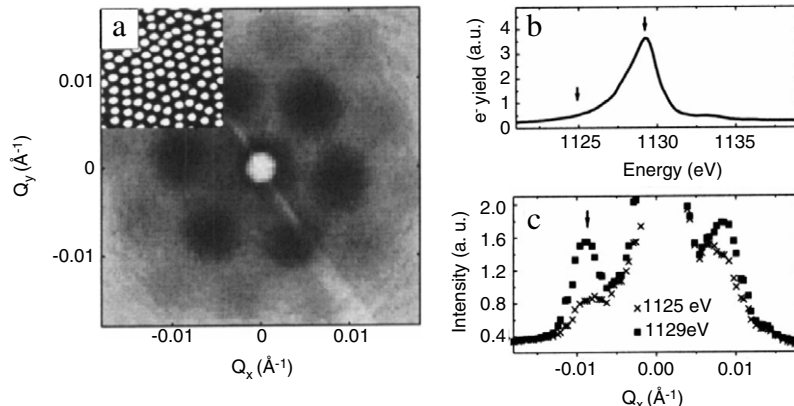


Fig. 114. (a) 2D GISAXS pattern recorded at 8 keV of a hexagonally ordered EuSe quantum dot layer as shown in the AFM image (inset). (b) X-ray absorption across the Eu MV edge at 1129 eV. (c) Anomalous small-angle X-ray scattering pattern at 1129 eV (squares) and 1125 eV (crosses). From Ref. [376].

of large and equal doses of Cd + S, Zn + Te, Cd + Te or Pb + Te ions into SiO₂ substrate. GISAXS, transmittance measurements and Raman spectroscopy were used to investigate implanted composites. The 2D GISAXS patterns suggest the synthesis of nanoparticles already during ion implantation, performed either at 300 or at 77 K, while annealing at higher T causes an increase of the fraction and the average size of synthesized nanoparticles. After high-T annealing both optical methods detected nanocrystals of compound semiconductors CdS, ZnTe or CdTe through the appearance of the respective first optical gaps, \$E_g\$, in transmittance measurements and characteristic LO peaks in Raman spectra. It was proposed that at high ion doses a fraction of implanted atoms already synthesize during implantation into amorphous aggregates of compound semiconductors, which transform into crystalline nanoparticles after annealing. In 2005, the influence of stoichiometry deviations on the properties of ion-beam synthesized CdSe quantum dots was investigated [373]. CdSe quantum dots (QDs) were synthesized by ion-implanting constituent atoms in SiO₂, thermally grown on Si wafer. The influence of implantation and post-implantation treatment parameters was studied. The effect of stoichiometry deviations was analyzed for various Cd/Se ratios in the range of 0.75 to 1.95. The best correlated ensemble of QDs in implanted layer was found for 1.33 and 1.1 Cd:Se ratios, and 30 s post-implant annealing at 700 °C. These findings were related with the amount of well-crystallized CdSe QDs, as found by Raman scattering.

The morphology of Ge nanocrystals formed by ion implantation in SiO₂ [374] was also characterized by GISAXS. Ge ion doses were up to \$10^{17}/\text{cm}^2\$, and subsequent annealing temperatures up to 1000 °C. Results suggest that ordered and correlated Ge QDs can be achieved by high-dose implantation followed by medium-T annealing.

8.5.8. Other GISAXS studies of semi-conductors

A few other GISAXS studies could not be classified under the above presentation. Stemmer et al. [375] combined GISAXS and HRTEM to investigate the phase separation in 4-nm-thick hafnium silicate films with 80 and 40 mol% HfO₂ after rapid thermal annealing between 700 and 1000 °C. Films of the two compositions showed distinctly different phase-separated microstructures, consistent with two limiting cases of microstructural evolution: nucleation/growth and spinodal decomposition. Films with 40 mol% HfO₂ phase separated in the amorphous by spinodal decomposition and exhibited a characteristic wavelength in the plane of the film. Decomposition with a wavelength of \$\approx\$3 nm could be detected at 800 °C. At 1000 °C the films rapidly unmixed with a wavelength of

5 nm. In contrast, films with 80 mol% HfO₂ phase separated by nucleation and growth of crystallites, and showed a more random microstructure. The factors determining specific film morphologies and phase separation kinetics are discussed.

Schülli et al. [376] used GISAXS to characterize EuSe nanoislands grown on a nanopatterned PbSe template. The islands were shown to form a regular hexagonal pattern, by performing 2D in plane GISAXS maps (Fig. 114). They combined it with soft X-ray magnetic scattering, which showed a coupling between the Eu spins at low temperature. Finally, the work of Vartanyants and co-workers [231] on the coherent X-ray imaging of individual islands in GISAXS geometry is worth pointing out. This is a theoretical work which shows that there are some favorable conditions with incident angle close to the critical angle when GISAXS diffraction patterns originating from the individual islands can be directly inverted using iterative phase retrieval techniques (see Section 6.2.9 for further explanation). Coherent X-ray scattering (see recent works Refs. [218–222] and all references therein) is a fast-growing field that allows a reconstruction of the shape of objects, and possibly their internal strain (with wide angle data), under favorable conditions, without resorting to any modeling, but only to some known real-space and reciprocal space constraints. Recently, the same team [377] achieved experimentally the model free reconstruction of square basis Ge/Si quantum dots using the GISAXS geometry which is free of strain effects [222] at variance to diffraction conditions but suffers from multiple scattering. They took benefit of the low polydispersity and low density of particles to enhance, by an incoherent sum, the coherent scattering from individual particles. They achieved a final resolution of 10–15 nm (see Fig. 115).

8.5.9. The use of \$q_x\$ and \$q_y\$ in plane directions to distinguish long-range and short-range order: The case of bonded Si wafers

The integration of quantum dots (QDs) into optoelectronic or microelectronics devices requires controlling both the size and density of semiconductor islands. The Stranski-Krastanow growth mode does not fulfill these requirements, and the use of patterned surfaces is a promising way to control lateral self-organization of QDs. For semiconductors, patterned surfaces can be achieved by subsurface arrays of dislocations [378,379]. As shown above, misfit dislocation networks may be used, but the periodicity of the networks is only controlled by the choice of the materials. This constraint may be overcome by using edge and screw dislocations obtained by molecular bonding with accurate control of the periodicity [380]. Using direct wafer bonding [381], a thin monocrystalline silicon layer of \$\approx\$200 nm is transferred to a bare silicon substrate. The in-plane rotation angle \$\psi\$ between the

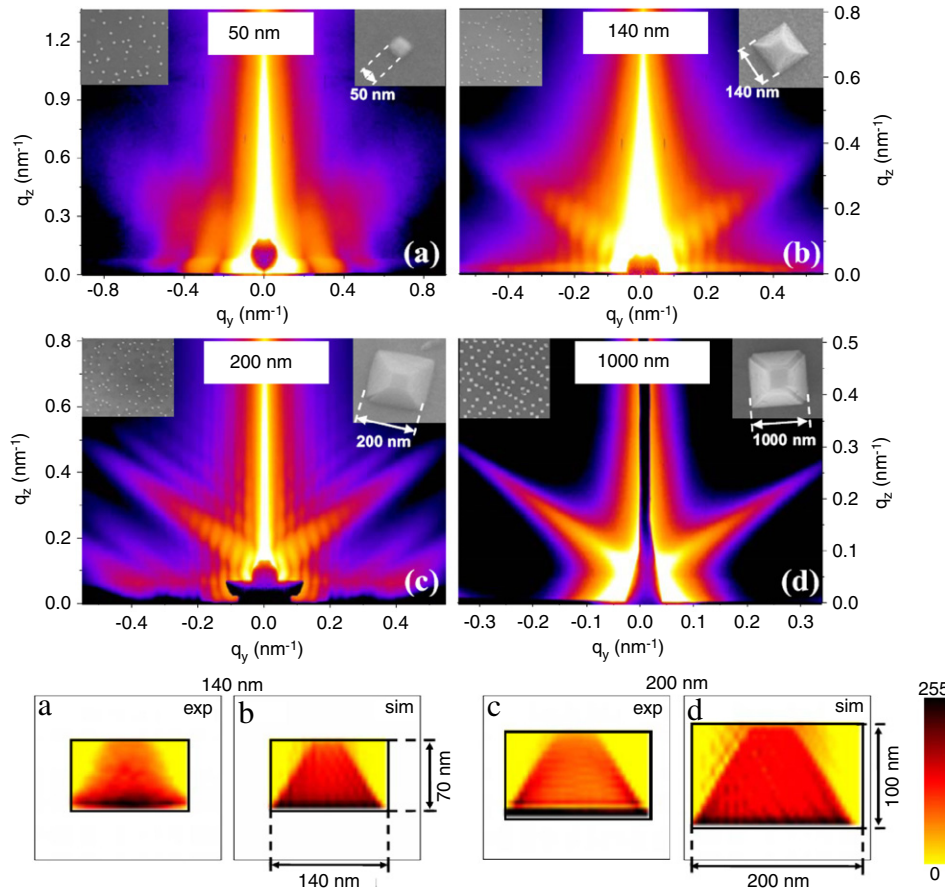


Fig. 115. (Top panel) GISAXS patterns from Ge/Si(001) quantum dots of various sizes ranging from 50, 140, 200 and 1000 nm. A SEM image with large and low resolution is also shown. The dynamic range in the image is about 10^5 to 10^6 . Note the CTR from side facets [216]. (Bottom panel) Reconstruction of the electron density projection for the 140 and 200 nm islands using iterative inversion algorithm from GISAXS pattern. The support used as a constraint is given by the black thin line. The obtained inversion from a simulated pattern is also shown. From Ref. [377].

bonded crystals defines a square network of screw dislocations, of periodicity $d = a/(2\sqrt{2}\sin(\psi/2))$, where a is the silicon lattice parameter. The flexion θ between the two crystals creates a network of average parallel lines, the periodicity of which is given by $l = a/2\sin(\theta)$. One average line is formed by consecutive alternated mixed-dislocation lines [382]. These networks induce a periodic strain field which propagates to the surface. To enhance the resulting deformations at the surface, the bonded silicon layer is thinned with sacrificial thermal oxidation down to a nominal value of 10 nm. STM investigations of the topology of such a surface after deoxidization show clearly smooth long-range undulations which look like one dimensional (1D) waves. These undulations are created by the flexion and rotation angles [383].

GISAXS experiments [384] were performed on the ID32 beamline. Knowing the sample-to-camera distance (1.25 m), each pixel can be related to a $(\alpha_f, 2\theta_f)$ couple, and therefore to a scattering vector $\mathbf{q} = (q_x, q_y, q_z)$. Note however that the orders of magnitude of the q_x and q_y scattering vectors are clearly different for the same number of pixels along the x or y direction. Let us calculate the ratio q_y/q_x , for a given, identical angular deviation β , for q_y within the sample plane (O, x, y), and for q_x within the specular plane (O, x, z). This means that q_y is defined by $(\alpha_f = 0, 2\theta = \beta)$, and q_x is defined by $(\alpha_f = \beta, 2\theta = 0)$. We derive the ratio $|q_y/q_x| = |\sin(\beta)/(\cos(\beta) - \cos(\alpha_i))|$. This ratio is larger than 100 for angles β between 0.1° and 1.2° , corresponding to our experimental conditions. Since the scattering vector is related to the real-space periodicity d by the relationship $d = 2\pi/|\mathbf{q}|$, this means that the characteristic length along the x direction is about two orders of magnitude larger than the characteristic length

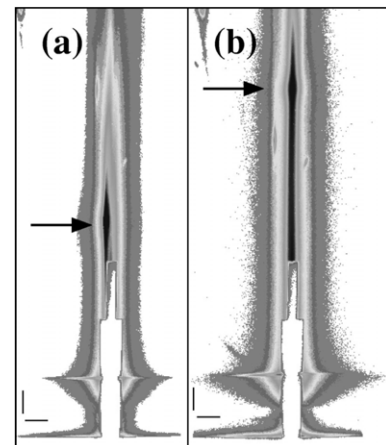


Fig. 116. GISAXS patterns from bonded silicon wafers for two different azimuths: (a) $\omega = -68.3^\circ$ and (b) $\omega = -20^\circ$. The vertical and horizontal scales are given by the bars down left of the pictures, each bar corresponds to an angular deviation of 0.128° . The scattering spot pointed by an arrow is two orders of magnitude more intense than any other part of the picture. From Ref. [384].

along the y direction. Fig. 116a and b show GISAXS patterns for two different azimuths. A striking feature can be observed, within the trail of specular scattering: a scattering spot (pointed by arrow) is present close to the specular plane, with a vertical position that depends on the azimuth. Since the spot is close to the specular plane, the angle 2θ is very small, and the horizontal deviation measured on the CCD camera is only a few pixels, which is within

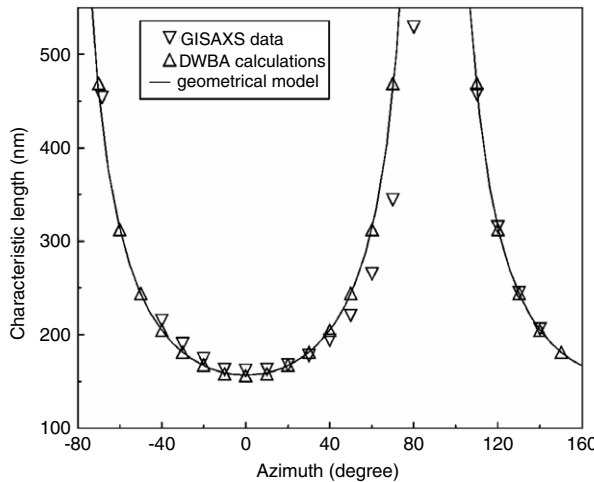


Fig. 117. Characteristic length d_x with respect to the azimuth angle ω . Down triangles are measurements extracted from GISAXS. Up triangles are calculated with DWBA from surface model, deduced from STM observations. The full curve is a fit using a basic geometrical model. From Ref. [384].

the error bar. This will only affect the q_y evaluation due to its sine dependence. This horizontal deviation can be observed on Fig. 116a, which is not symmetrical. On the contrary, the amplitude of the vertical movement of the spot is much larger and the relative error bar is smaller. In Fig. 117 is reported the plot of $d_x = 2\pi / |\mathbf{q}_x|$ with respect to the azimuth angle ω (down triangles). These data can be fitted considering that the scattering objects are parallel lines spaced by a length d . The length $d_x(\omega)$, which is the distance between two parallel lines measured along the X-ray direction, is simply related to d by $d_x(\omega) = d / \cos(\omega)$. A periodicity $d = 157 \pm 4$ nm is deduced by fitting (full line on Fig. 117). Within the framework of DWBA, the scattered intensity can be calculated as a function of q_x [35,174]. The height-height correlation function in these calculations was deduced from the STM observation of the surface. The plot of $d_x = 2\pi / |\mathbf{q}_x|$ with respect to the azimuth ω extracted from the bump positions is reported in Fig. 117 (up triangles). Calculations are in good agreement with data extracted from GISAXS, and with geometrical fit. It proves that the scattering spot observed on GISAXS patterns can be related directly to a q_x component of the scattering vector. Geometrical fit ($d = 157$ nm \pm 64 nm) is in a quite good agreement with the STM measurement (135 nm \pm 65 nm). These periods correspond respectively to flexion angles of $0.099^\circ \pm 0.003^\circ$, and $0.115^\circ \pm 0.005^\circ$, since GISAXS and STM invoke the inhomogeneities of the flexion angle to explain this discrepancy of 0.016° . These inhomogeneities can be induced by bowing and warping of the wafer before bonding.

In summary, this study has shown that GISAXS patterns could contain non-negligible signals related to the q_x scattering vector component for specific surface correlation length. This analysis of GISAXS differs from the classical interpretation in terms of $q_{||}$ and q_z (noted here, respectively as q_y and q_z) which forgets the curvature of the Ewald's sphere (see Section 2.2). To the first order, it is shown that a well-defined surface corrugation periodicity can be extracted from GISAXS with a simple geometrical model.

9. In situ GISAXS measurements in ultra-high vacuum, during growth

9.1. 3D-island growth: The metal/oxide interfaces case

9.1.1. Motivations

The oxides and their interplay with metals are of central importance in environmental and earth science as well as in technological applications [385,386]. The latter include catalysts, gas sensors,

as well as optical, electronic and magnetic devices [387]. Vapor-deposited metals grow generally on oxide surfaces in the form of three-dimensional (3D) nanometer-sized clusters rather than in a monolayer-by-monolayer mode [2,13]. A variety of related parameters is involved in the growth process (the surface free energies of the two materials, the interface energy, their respective electronic and crystalline structures, the lattice parameters, kinetic factors) which condition the shape and the size of the metallic nanoclusters. The cluster morphology and their statistical organization on the substrate determine in turn the physical and reactive properties of the overall system [388–390]. Many other questions have to be addressed to characterize the growth, among which, the type of nucleation, homogeneous or heterogeneous, the type of coalescence, static or dynamic, the adhesion energy between the metal and the oxide substrate, the diffusion energy of metal on the oxide surface, the equilibrium shape of the islands, the spread of the island size and shape, the possible existence of correlations between the sizes and separation of neighboring islands, most of these properties depending on growth temperature and thickness. In a mass non-conserved system *i.e.* upon arrival of new material on the surface, two main coalescence mechanisms are often invoked: [253, 8] static or dynamic. In static coalescence, neighboring growing islands merge when they touch, leading to a new island occupying the center of mass of the two primary islands. In all theoretical studies, the coalescence times and the reshaping time are supposed to be very small compared to the (inverse) flux of incoming atoms so that the islands are supposed to always keep the same shape. By contrast, dynamic coalescence involves the diffusion of islands (in the form of clusters of adatoms or small particles) on the surface. Deltour et al. [391] showed that island diffusion can be significant for non-epitaxial or non-coherent, small enough islands (typically less than 1000 atoms/island). Despite these numerous studies, very few experimental works are available regarding the type of nucleation, the diffusion energy, the coalescence mechanisms or the adhesion energy between metal and oxide surfaces. It is thus fundamental to characterize the morphology during the growth. For all these metal/oxide systems, many electron or tunneling-based tools available to characterize the morphology are hampered by the insulating character of the insulating substrate. *In situ* GISAXS is thus very useful to overcome these limitations. In addition, if many studies of the early stages of nucleation and growth exist, none or only few deal with the growth and coalescence regimes, which is the object of the GISAXS studies summarized below.

9.1.2. Investigated systems

In this section, we discuss the different growth of metals on oxide surfaces that were investigated *in situ* by GISAXS: Ag/MgO(001) [78], Pd/MgO(001) [29,79], Pt/MgO(001) [247], Fe/MgO(001) [57]; Co/NiO(111) [264]; Au/TiO₂(110) [81]; Ag/ZnO(0001) [150,151].

Metal/MgO(001). The very first *in situ* GISAXS study dealt with the growth of Fe on MgO(001) [57]. The Fe/MgO epitaxial system is also of technological interest, since Fe has been found to act as a seed layer for subsequent epitaxial deposition of other layers and multilayers [392]. Thin layers and multilayers of Fe also have interesting and potentially useful magnetic properties [393] which are related to their structure. Fe epitaxially oriented with MgO has been reported to possess higher magnetization and coercivity than bulk Fe.

The non-reactive Ag/, Pd/ and Pt/MgO(001) systems are test beds for the fundamental issues regarding the contact between dissimilar materials [394,395,389,13,2] because they offer favorable conditions for both experimental and theoretical investigations. Moreover, these systems have been thoroughly investigated as model catalysts [389,2]. The structural and epitaxial properties of these interfaces have been investigated in depth both experimentally (Ag/MgO [396–398], Pd/MgO [399], Pt/MgO [247] and Ni/MgO [400]) and theoretically [401–403], however, much remained to be done regarding the exact growth modes.

Ag/ZnO(0001). Zinc oxide exhibits physical (direct band gap in the UV region, high exciton binding energy, ...) and chemical (mixing of covalent-ionic characters, high solubility of group III donor impurities or transition metal atoms) properties [404] which give it considerable potential in many fields. Concerning metal-oxide interfaces, ZnO is already employed on industrial scale as a support of copper for methanol synthesis and water-gas shift reaction [405]. Another application of particular relevance is the use of ZnO as a support of silver for low-emissive and anti-solar coatings on glazing [406,407], the metal film acting as a mirror in the infrared wavelength range. A central concern in manufacturing the coatings is the way the silver film wets the oxide support. The peculiarity of the growth of noble and late transition metals on the basal planes of zinc oxide, namely the (0001) Zn-terminated and the (0001) O-terminated surfaces, is its enhanced two-dimensional character. The critical coverage, defined as the fraction of the surface covered by the metal at the onset of the formation of the second layer, has been estimated equal to 1 for platinum [408–410] and equal to 0.55 [389] (0.35 [411]) for copper on O (Zn) face. Copper has been shown to form flat-top clusters [389,412] and a pseudo layer-by-layer growth is inferred, tentatively explained considering either electronic transfer from metal to surface states [413] or purely kinetic mechanisms [389].

Au/TiO₂(110). Recently, catalysts made of gold nanoparticles [414] have attracted the interest of numerous scientists because of their potential applications to many reactions of industrial and environmental importance. Gold catalysts are extraordinarily active for the oxidation of CO at room temperature and by far more active than other noble metals below 400 K. The titania support is the warhorse of numerous fundamental studies aimed at understanding the catalytic mechanisms and at elucidating the origin of this surprising reactivity as neither titania nor bulk gold alone are active. Because the cluster morphology seems a key parameter in the understanding of the catalytic activity of gold [415], many studies were performed by using vacuum techniques on planar TiO₂(110) substrate (see reviews Ref. [416,417]). The growth of gold on titania was characterized by microscopy techniques (STM [388,418–427], HRSEM and HRTEM [428,429]) and Low Energy Ion Scattering [430,411,390]. At low coverage (0.1 ML), the gold clusters grow as quasi-2D particles of one or two atomic layers high, with diameters between 1–2 nm, which appear to be the most catalytically active [388]. For higher coverages (>0.2 ML), they are rapidly mixed with hemispherical 3D particles with a diameter in the range 2.5–4 nm. The biggest particles (diameter larger than 4 nm) have a higher contact angle ($\theta_c \simeq 122^\circ$).

Co/NiO(111). The Co/NiO(111) interface was investigated [264] because it involves a ferromagnetic medium on an antiferromagnetic one. It is then involved in the fabrication of spin valves sensors, used as magnetic read heads in computer hard drives, position sensors, and magnetic random access memory elements. The interfacial magnetic characteristics and behaviors are often explained by speculations on the interface properties such as roughness, diffusion, etc. A detailed *in situ* study of the structure and morphology evolution during growth was then thought to be mandatory.

9.1.3. Preparation of samples

Very important for these studies is the sample preparation, since in general, surfaces as ideal as possible are needed to avoid heterogeneous nucleation due to roughness or contamination. For the Fe/MgO(001) study [57], the MgO substrates were simply organically cleaned, and next annealed at 360 °C in the UHV chamber. As a result, the surface was rough, which implies direct 3D growth with heterogeneous nucleation on the many steps

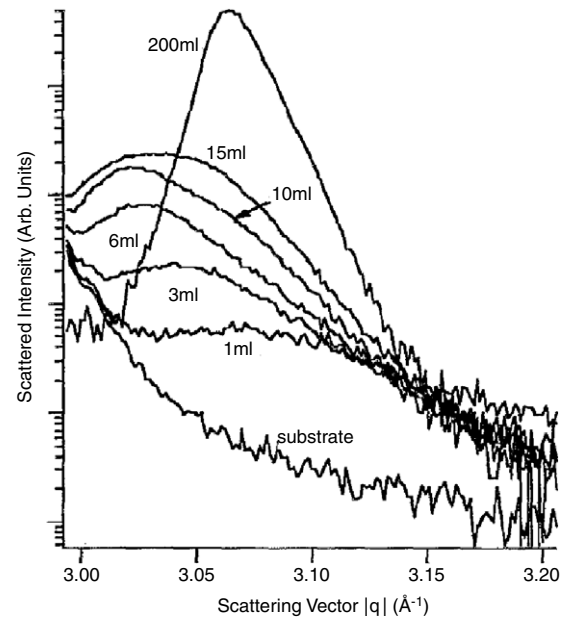


Fig. 118. 1. In-plane X-ray scattering from various average coverages of Fe(001) on MgO(001) versus the scattering vector magnitude along the MgO[100] direction. From Ref. [57].

edges. Fe was deposited monolayer after monolayer at a high sputtering rate of 0.25 Å/s thanks to planar magnetron sputter guns. For the growths of Ag, Pd and Pt on MgO(001), the MgO(001) substrates provided oriented and polished by Earth Chemical (Japan) were first annealed in air at 1500 °C for 24 h, which yielded crystals of very high quality with micron-size large (001) terraces. The contaminants segregated at the surface were next removed in a remote UHV chamber by Ar⁺ ion bombardment at 1500 °C, thus yielding clean flat terraces while keeping the high crystallinity, and finally annealed at 900 °C for 20 min and cooled down under 10⁻⁴ mbar of O₂ in order to restore a perfect surface stoichiometry [431]. This procedure used to prepare the MgO(001) substrate results in extremely flat surfaces with a rms surface roughness of typically 0.24 nm. These surfaces were protected by an approximately 100 nm thick Ag film before being transferred in the X-ray chamber, where the Ag film was desorbed by annealing at approximately 700 °C. For the NiO(111) surfaces, a special procedure was also developed. The NiO boule was first annealed at 1850 K for 24 h in air, then cut, polished, and reannealed at 1300 K for 3 h, which yields a flat, shiny surface. A mosaicity of 0.054° and a typical mean terrace size of 1800 Å were obtained. The TiO₂(110) and ZnO(0001)-O₂Zn surfaces were prepared in a standard way by cycles of ion bombardment followed by annealing, with a last annealing and cooling under O₂ partial pressure. The deposition procedures are described in corresponding papers, using either effusion cells (e.g. for Ag or Au) or Omicron EFM4 e-beam bombardment deposition cells equipped typically with 2 mm diameter, high purity (99.99%) rods for Pd, Pt or Co. Typical evaporation rates were $\simeq 1$ Å/min except for Pt, for which it was 10 times smaller. The fluxes were calibrated *in situ* by a quartz microbalance and X-ray reflectivity.

9.1.4. General trends during growth and coalescence of islands

Fe/MgO(001). The very first *in situ* study [57] was done during the growth of Fe/MgO(001), by performing a (0D) detector scan parallel with the surface, while integrating (over 1°) perpendicular to it. Fig. 118 shows the GISAXS measurements for various average thicknesses, where the background intensity for zero coverage has been subtracted from the scans. Some residual intensity near

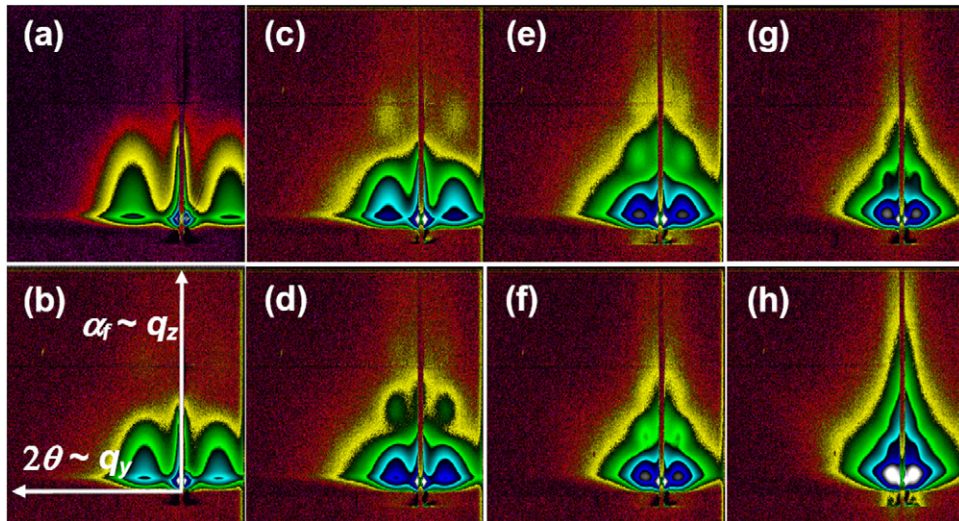


Fig. 119. Evolution of the 2D GISAXS patterns during the *in situ* growth of Ag on a MgO(001) surface at 300 K (ID32 setup), with the incident beam along the MgO[100] direction, for different equivalent deposited thicknesses: (a) 1 nm, (b) 1.8 nm, (c) 2.2 nm, (d) 3.6 nm, (e) 4.4 nm, (f) 6.2 nm, (g) 7 nm, and (h) 10 nm. The intensity is represented on a logarithmic scale. Each black contour between two colors corresponds to an order of magnitude change in intensity. The q_y (respectively q_z) axis ranges from 0 to 2.5 nm^{-1} (respectively 2.6 nm^{-1}). From Ref. [79].

$q_y = 0$ remains after the background subtraction. An offset has been applied to each of the curves shown for clarity in the figure. A clear peak at 2.1 \AA^{-1} in the scattered intensity appears at a coverage of 1 monolayer (ML), which moves to lower angle with increasing thickness. This peak was related to a nearest-neighbor island distance either by assuming Bragg law or by locating peaks in the radial distribution function for cylindrical symmetry, since in this case the diffuse in-plane scattering yields the height-height correlation function of the surface. These two different approaches yielded indistinguishable inter island spacings. The inter island distance was found to increase continuously with coverage. The total volume of scattering material was inferred from the integrated scattering intensity. It was found to increase up to a coverage of 20 ML, and subsequently decrease. The transition was attributed to the onset of continuous films growth, *i.e.* of parallel distances too large to be probed by GISAXS.

Other metal/oxide studies. Similar measurements were performed, also in the 90th, during the growth of Ag/MgO(001) by Guenard et al. [397] and Robach et al. [398] in Renaud's group. We do not present these results obtained by scanning slits along one direction while integrating over the other, since they are by far less informative than 2D GISAXS measurements performed later. Detailed 2D GISAXS studies were performed during the *in situ* growth of Co on NiO(111) surfaces [264], but were not fully exploited. Only the evolution of the average dimensions D , d and h with deposited thickness were analyzed. They were mostly used to evaluate the coverage, and thus the sticking coefficient, as a function of deposited thickness. We concentrate in the following on complete 2D GISAXS measurements.

2D GISAXS studies during growth. For most metal/oxide systems studied, and whatever the growth temperature, the 2D GISAXS patterns and their evolution during growth look qualitatively similar: they are characteristic of the Volmer-Weber three dimensional growth mode expected from the poorly adhesive noble metal-oxide systems [389]. We thus illustrate the *in situ* GISAXS measurements during growth on only two systems: Ag/MgO(001) for two deposition temperatures (Fig. 119): 300 K and 540 K, and Au/TiO₂(110) at 300 K (Fig. 121). Measurements were always performed with the incident X-ray beam oriented along at least the [100] and [110] directions of the MgO(001) substrate and several in plane directions of the TiO₂(110). In all

cases, qualitatively, the experimental GISAXS patterns present two intensity maxima visible along the parallel direction, separated by the specular rod, partly hidden by the beamstop, as exemplified in Figs. 119 and 120. They arise because the islands are not completely distributed at random, but are separated by a preferential nearest neighbor (center-to-center) distance D . As a consequence, for a given value of q_y , there are constructive interferences between the waves scattered by neighboring island. The absence of intensity minima parallel with the surface reveals a wide distribution of lateral sizes. When growth proceeds, the two scattering maxima along the parallel direction move toward the origin and become more intense as the metal deposit increases. This reveals an increase of the average inter-island distance D , which can only be explained by the coalescence of neighboring islands. In addition, the overall diffuse scattering becomes more and more concentrated toward the origin of the reciprocal space. As the extension of the scattering is inversely proportional to the size of the islands, this means that the islands become larger. The observed evolution is thus characteristic of a growth and coalescence mechanism.

Ag/MgO(001). In the Ag/MgO(001) case (Figs. 119 and 120), for large enough thicknesses, a second and even a third order maxima along the perpendicular direction are observed (*e.g.* at Ag thicknesses of 2.2 nm and 3.6 nm for the 300 K growth), meaning that the height of the islands is well defined, with a small distribution. Note that the second order maxima are at a smaller q_z coordinate than the specular one. As a matter of fact, the separation in q_z of the off specular peaks is inversely proportional to the average height of the islands, while that of the specular peaks is inversely proportional to the average film thickness. Hence, this q_z coordinate difference is linked to the metal morphology. Finally, in the case of Ag, this third and then second order maxima along the perpendicular direction disappear and the GISAXS pattern looks like an apex (at a Ag thickness of 10 nm), meaning that the islands become flatter. This corresponds to the percolation regime, in which neighboring islands become connected and evolve toward very large, flat islands, exposing a top (001) surface and side {111} facets [432].

In the Ag/ZnO cases (not shown), on the O terminated face, the second-order lobes observed along the surface normal direction for Ag thicknesses higher than 0.4 nm, suggest the formation

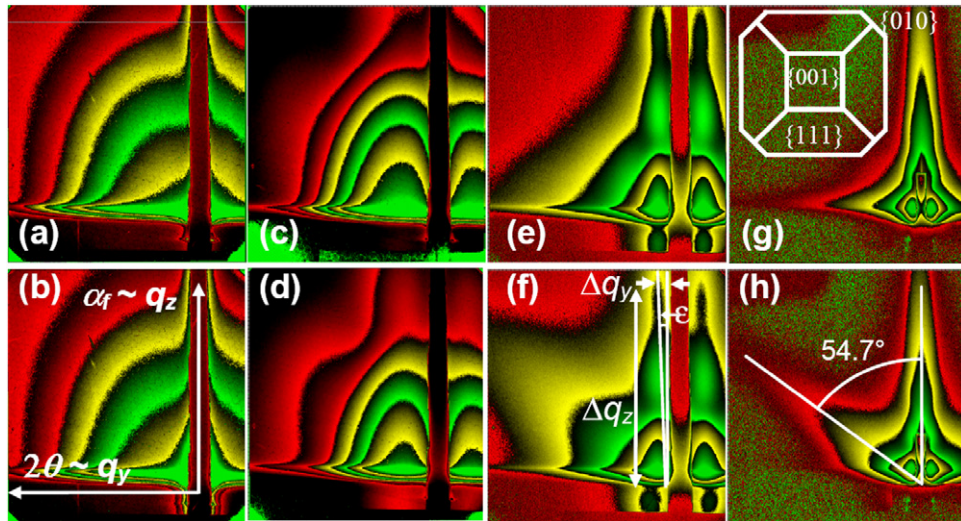


Fig. 120. Evolution of GISAXS patterns during the *in situ* growth of Ag on a MgO(001) surface at 540 K with the incident beam along the [100] direction of the MgO(001) substrate for (a), (c), (e), (g) and with the incident beam along the [110] direction for (b), (d), (f), (h). Several equivalent thicknesses are reported: (a) and (b) 0.1 nm, (c) and (d) 0.3 nm, (e) and (f) 2 nm, (g) and (h) 7 nm. The intensity is represented on a logarithmic scale. Each black contour between two colors corresponds to an order of magnitude change in intensity. The q_y (respectively q_z) axis ranges from 0 to 2.7 nm⁻¹ (respectively 3 nm⁻¹). Inset: top view of the truncated cubo-octahedron island shape with the {001}, {111}, and {010} facets. From Ref. [79].

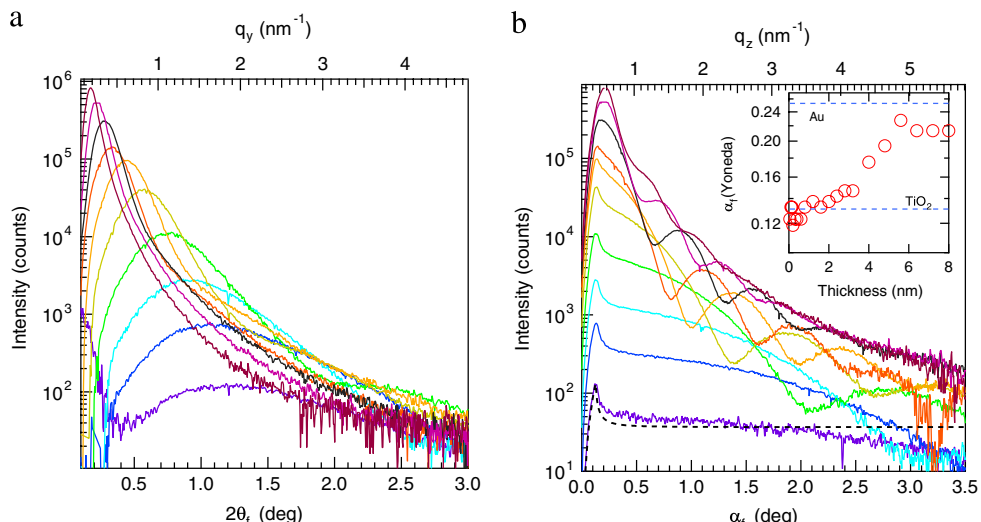


Fig. 121. Intensity cross sections of the GISAXS patterns measured during the growth of Au on TiO₂(110). The cuts are made (a) along the $2\theta_f$ direction at the location of the Yoneda's peak and (b) along α_f at the location of the correlation peak. The intensities have been rescaled accordingly to the counting time. The equivalent thicknesses are (from bottom to top) 0.05, 0.15, 0.3, 0.6, 1.2, 2.0, 2.8, 4.0, 5.6 and 8.0 nm. The inset shows a plot of the Yoneda's peak location as function of deposited thickness while the dotted curve in Fig. b corresponds to the transmission function of TiO₂. From Ref. [81].

of clusters with a high diameter/height aspect-ratio and a well-defined top-facet. The second-order lobes correspond indeed to interferences between the waves scattered by the island/support interface and the waves scattered by the top facets. Because of the epitaxial relationship, this top facet is of (111) orientation.

Au/TiO₂(110). For RT growth of Au/TiO₂, the analysis method will be further discussed as a last example. In this case [81], upon increasing coverage (Fig. 121), (i) interference fringes appear in the perpendicular direction (0.6 nm) up to show three bounces and (ii) the Yoneda's peak becomes round and shifts from the critical angle α_c of TiO₂ (0.1311°) to a value close to α_c of gold (0.2528°) (inset of Fig. 121). Shifts and rounding cannot be accounted for by the standard DWBA which refraction effect only comes from the substrate [155]. In the parallel direction, the in-plane correlation peaks are clearly separated from the specular rod. As previously suggested [29], the analysis of such a profile is not tractable within the Decoupling Approximation [73,217,40,42,255] as neglecting all

correlations leads to a too intense incoherent diffuse scattering for size distributed island collections. The Local Monodisperse Approximation (LMA) [433,234,259,233] would better fit the result, but it assumes scattering by independent monodisperse domains, an unphysical hypothesis in the present context. In an attempt to overcome these difficulties, the analysis of the data has been performed through two new approximations developed by Lazzari et al. [155], the DWBA on the graded interface and the SSCA model (see Section 6.4.3). Note that, contrary to Ag and MgO(001), in the case of the RT growth of Au/TiO₂(110), GISAXS patterns were nearly independent from azimuthal rotation [81]. Thus, the analysis was limited to data collected with the X-ray beam aligned along the $[1\bar{1}0]_{\text{TiO}_2}$ direction.

As explained in Section 6.3.3 and in Ref. [29], the sensitivity to the particle shape is found in the high- q wave vector transfer range. The Porod's plot of the 8 nm film (Fig. 122) demonstrates a power law behavior in the high- q range $I(q_\parallel) \sim q_\parallel^n$ and $I(q_\perp) \sim$

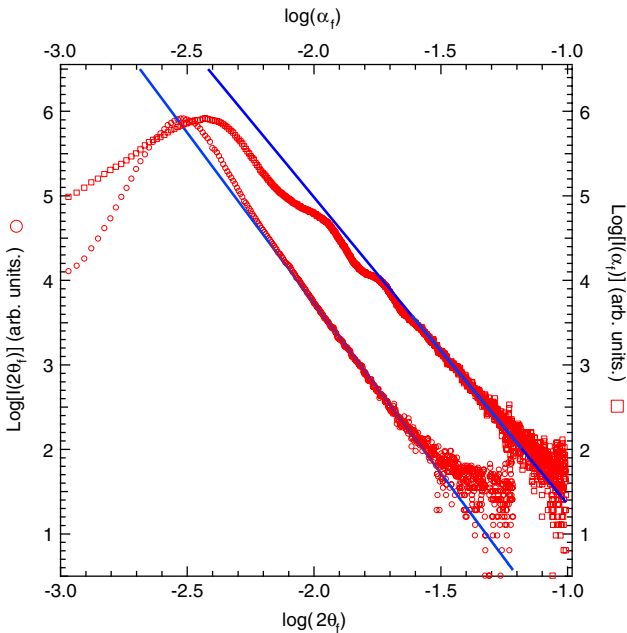


Fig. 122. Growth of Au/TiO₂(110): Log-Log plot of the cross sections for the 8 nm deposit with a power law fit of the high q -range. From Ref. [81].

q_{\perp}^m . If considering only shapes with z-revolution axis, the found exponents $n = 4.02$ and $m = 3.63$ are consistent with a truncated sphere profile ($n = 4$, $m = 2$ for a hemisphere; $n = 4$, $m = 4$ for a sphere; $n = 3$, $m = 2$ for a cylinder [29]). Analyses were consistently performed with truncated spheres over the entire study. The radius R and height H distribution has been taken as a joint-normal law with a correlation coefficient ρ between R and H . The data have been fitted with the IsGISAXS software [27,28] using a χ^2 criterion, with error bars proportional to the square-root of the intensity, as checked from the fluctuations of data points along each cross-section. At each coverage, two cross sections (averaged over a window of five pixels to keep the resolution on the Yoneda's peak) were fitted, (i) along $\alpha_f \sim q_z$ at the correlation peak and (ii) along $2\theta_f \sim q_y$ at an exit angle α_f equal to three times that of the Yoneda's peak ($\alpha_f = 3\alpha_c$). To avoid distortions in fitting the sharp Yoneda's peak, the fit was only performed on data points $\alpha_f > 3\alpha_c$. The total χ^2 and the total reliance factor R_B [27] laid always below 4 and 0.12, respectively, at any coverage. The shape of the correlation peak, the decrease in intensity near the specular rod and the high- q_{\parallel} range were well reproduced. The agreement was also good in the perpendicular direction (Fig. 123b), except perhaps fringes at the highest coverage. A likely explanation is the oversimplified description of the particle shape and size distribution. If fitted, the incident angle α_i was found close to that determined from sample-beam alignment. The good modeling of the Yoneda's peak (even though not explicitly included in the fitting process !) gives confidence in the theoretical treatment of DWBA on the graded interface.

9.1.5. Evolution of morphological parameters with thickness: Nucleation, growth and coalescence

Ag/MgO(001) case: Comparison between the very fast and the extensive GISAXS data analyses. In the Ag/MgO(001) case, the very fast and quantitative GISAXS data analyses have been compared [29]. The inter-island distance, the lateral size and the height of the islands obtained from both analyses are plotted in Fig. 124 as a function of the Ag deposit for three temperatures: 300, 540 and 640 K. The three sizes D , d and H increase steadily with the deposited thickness at the three studied temperatures.

The inter-island distance determined by the rapid data analysis is similar to that determined by the extensive data analysis. The relative difference between both D determinations is less than 15%. On the contrary, the relative difference between both H (resp. d) determinations is much larger and can reach 30% (resp. 35%). This discrepancy originates in the difference between both island models used. In one case, the island is modeled by an arbitrary shape without any size distribution. In the other case, the island is modeled by the real shape with a size distribution.

One may thus conclude that a quick analysis can be used if only the average morphological parameters are needed within an accuracy of $\pm 15\%$ on the distance and 30%–40% on the size, knowing they probably will be over estimated. In addition, the average distance and diameter obtained from TEM for the 2-nm thick Ag deposit at 540 K ($D = 15.7$ nm and $d = 10.5$ nm) are in very good agreement with the results obtained from the complete GISAXS analysis for this sample.

Pt/MgO case. In the case of Pt/MgO(001), the evolution with deposited thickness of the obtained morphological parameters (diameter, height and inter island distance) are presented in Fig. 125, for three growth temperatures (600 K, 800 K and 1000 K). A comparison between the mean film thickness calculated from these latter and the expected one shows that the sticking coefficient of Pt/MgO(001) is between 0.35 and 0.55 at the studied temperatures. At the smallest coverage of 0.3 nm, the inter island distance is around 2.5 nm at 600 and 800 K, which is characteristic of nucleation on defects because the corresponding density of particles is very high ($\rho \sim 1/D^2 = 1.6 \times 10^{13} \text{ cm}^{-2}$) and does not depend on temperature. However, for the same coverage at 1000 K, $D = 6$ nm is twice higher probably because of a temperature-enhanced detrapping of atoms from defect sites and an increase of the critical nucleus size needed to avoid dissolution.

Pd/MgO(001) case. In the Pd/MgO(001) case, the validity of the GISAXS analysis was tested by comparing the dimensional parameters deduced from GISAXS and from TEM for 0.9 nm thick Pd at 550 K and 3.0 nm thick Pd at 740 K [29]. For the latter case, the agreement is excellent for all parameters, unambiguously demonstrating the adequacy of the GISAXS measurements and quantitative analysis. For the former case, the agreement is good as concerns the width of the size distribution. However, the inter-island distance and radius deduced from GISAXS are approximately 20% smaller than those deduced from TEM. Note that the TEM and GISAXS statistics are very different. TEM probes only a very small portion of the surface, as opposed to GISAXS. Hence, the observed difference in the TEM and GISAXS results might arise from inhomogeneity of the island distribution on the surface. Moreover, this difference is most likely related to the very diverse and not always compact shapes of the particles for this low temperature deposit. Obviously, in this case, representing these diverse shapes by a simple spherical shape is a crude approximation. At the very beginning of growth, in the nucleation regime, the 0.1 nm thick Pd/MgO(001) deposit has small vertical and lateral size distributions, which are similar. Then, for a Pd deposit from a few 0.1 to several nm, a striking result is that the height distribution is smaller than the lateral size distribution whatever the temperature is from 550 to 740 K. This behavior, which seems to be independent of temperature and film thickness, is believed to originate from growth mechanisms. First, the denser (111) faces grow faster than the (001) facets. Second, while the (111) side facets grow from both vapor phase and atom diffusion, the (001) top facets grow mostly from the vapor phase as if they were isolated, because of the high energy barrier an atom has to overcome to jump from a (111) to a (001) facet [434,435].

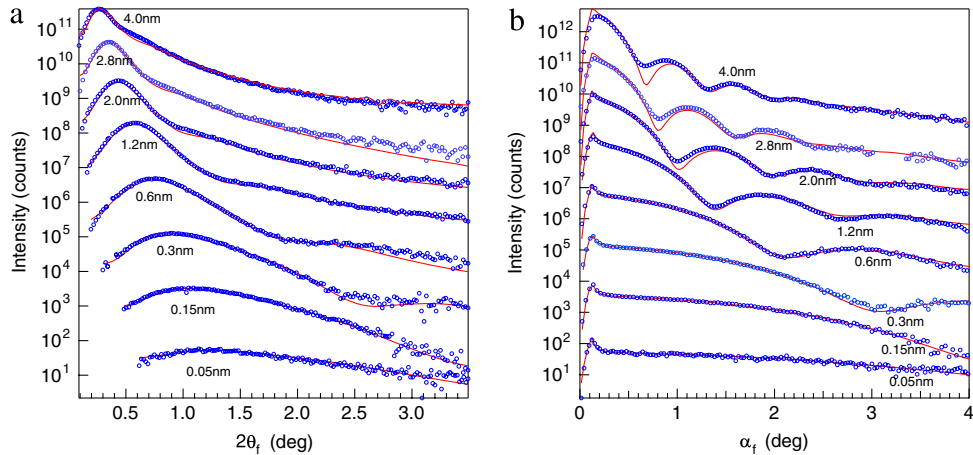


Fig. 123. Au/TiO₂(110): Fits (continuous line) of the GISAXS intensity cross-sections (circles) all along the growth. The equivalent deposited thicknesses are given on the figure. Data have been modeled by scattering from size distributed truncated spheres within the SSCA and the DWBA on the graded interface. The curves have been shifted for clarity. From Ref. [81].

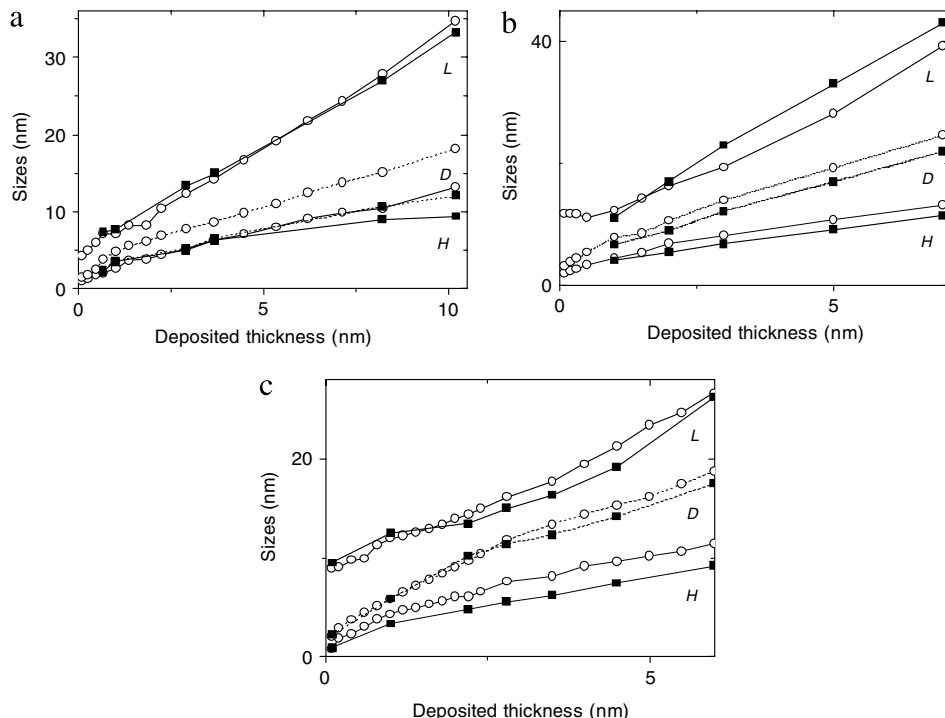


Fig. 124. Evolution of morphological parameters obtained from the GISAXS measurements for Ag on MgO(001). Bold line, D ; dashed line, d ; thin line, H . Open circles, rapid data analysis; filled squares, extensive data analysis. (a) 300 K; (b) 540 K; (c) 640 K. From Ref. [79].

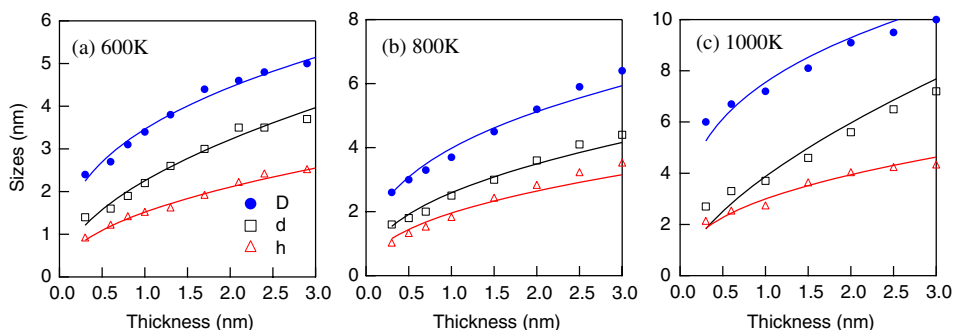


Fig. 125. Results deduced from a full GISAXS analysis of the data for Pt deposits on MgO(001) made at (a) 600 K, (b) 800 K and (c) 1000 K. The evolution of island spacing D (solid circles), mean lateral size d (open squares) and mean height H (open triangles) with increasing Pt thickness are shown with the power law fit (continuous line). From Ref. [247].

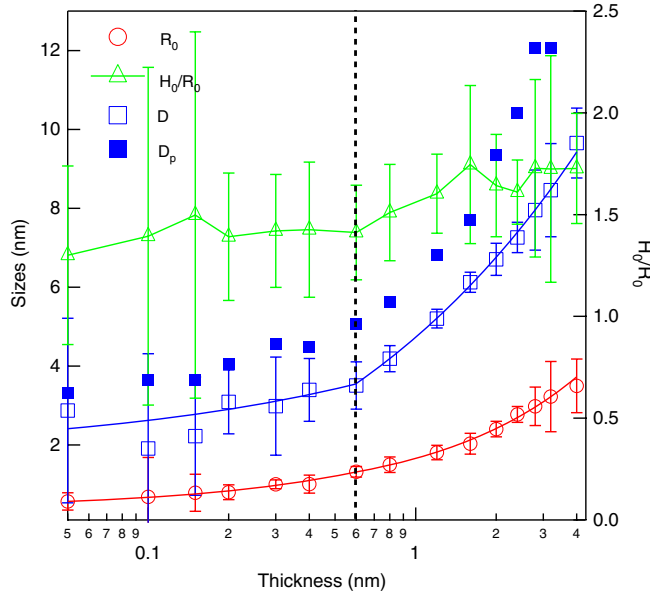


Fig. 126. Evolution of the Au/TiO₂(110) morphological parameters as function of the deposited thickness (a) Central radius $\langle R \rangle$ (red open circles), (b) Central height over radius $H_0/\langle R \rangle$ (green open triangles), (c) Average spacing between islands D (blue open square) and the value D_p (blue filled squares) as deduced from the location of the correlation peak $D_p = 2\pi/q_f^0$. The island shape was taken as a truncated sphere and the (R,H) size distribution has been chosen as joint-normal. The separation (vertical dotted line) between growth and coalescence is characterized by the power law fits of $\langle R \rangle \propto t^{0.31 \pm 0.1}$, $t^{0.54 \pm 0.07}$ and $D \propto t^{0.15 \pm 0.2}$, $t^{0.51 \pm 0.05}$ (continuous lines). In passing, note that this corresponds to the onset of decrease of catalytic activity toward the oxidation of CO of Au clusters on TiO₂(110) [388]. From Ref. [81]. (For interpretation of the references to colour in this figure legend, the reader is referred to the web version of this article.)

Au/TiO₂(110). For the Au/TiO₂(110) system, the central radius $\langle R \rangle$, central height $\langle h \rangle$ and distance between islands D are shown in Fig. 126. In the following, we discuss how the evolution of the morphological parameters with deposited thickness can be used to examine the type of nucleation, the growth modes, the characteristics of the coalescence, as well as the equilibrium shape, the interfacial energy and the adhesion energy.

9.1.6. Information on growth modes

Further insight on the growth mode can be gained by studying the evolution of the inter-island distance and of the lateral size versus the deposition time. Since the growth process is interrupted during GISAXS acquisitions, before comparing with theoretical models, it should be determined whether the film might evolve during the measurements upon coarsening. Such coarsening can fortunately be discarded for Au on TiO₂(110) at 300 K [390], as well as for Ag/MgO(001) and Pt/MgO(001) at all studied temperatures. As shown below, for these three cases, the growth exponents lead to very similar conclusions.

Pt/MgO(001). For Pt/MgO(001), the continuous increase of inter island distance D (Fig. 125) evidences that coalescence occurs all along the deposition and that the nucleation-growth step happens before the start of the GISAXS measurements, i.e. before 0.25 nm thickness. Data points at all temperatures can be represented by power laws with evaporation time, i.e. $d \sim t^{0.5}$ and $D \sim t^{0.3}$, respectively (Fig. 125). The coalescence mechanism may involve the static meeting of particle growing at fixed position or a dynamic diffusion of clusters. If the reshaping of particles is faster than the time scale of impinging atoms, analytical models, scaling descriptions and numerical simulations [436–438] of static coalescence agree on a $d \sim t^1$ power law behavior. Power laws relative to the spacing between clusters are more scattered: $D \sim t^1$

(Refs. [436,437]), $D \sim t^{0.135}$ (Refs. [439,275]) for homogeneous nucleation and $D \sim t^{0.5}$ (Ref. [275]) for heterogeneous nucleation. The discrepancy with the actual measurement on the diameter d rules out the static mechanism. Instead, the actual $d \sim t^{0.5}$ and $D \sim t^{0.3}$ laws are close to that derived for dynamic coalescence in breath figures [440] in a case in which the diffusion of droplets leads to a bimodal size distribution where the biggest particles follow $d \sim t^{0.48}$ and $D \sim t^{0.25}$.

Au/TiO₂(110). For Au/TiO₂(110), during the first stage of growth at constant particle density, i.e. during the nucleation and growth regimes, the power law $\langle R \rangle \propto t^{0.31 \pm 0.1}$ corresponds to that expected ($\langle R \rangle \propto t^{1/3}$) for particles growing by a diffusion limited mechanism (and not an attachment limited one) with a negligible direct impingement on the particle and a nearly full condensation [441,436]. A similar result comes from the analytical solution of the growth of a droplet by attachment of diffusing monomers with a constant flux at infinity [440]. The found exponent is closer to that expected from the rate equations of growth [75] for a nucleation on defects ($\langle R \rangle \propto t^{1/3}$) than a homogeneous nucleation behavior ($\langle R \rangle \propto t^{2/9}$) in the case of complete condensation. Indeed, on one hand the sticking coefficient is found close to one and on the other hand, strong re-evaporation would lead to $\langle R \rangle \propto t$ whatever the defect concentration is. The corresponding density of particles $1/D^2 \propto 10^{13} \text{ cm}^{-2}$ is a typical concentration of defects (vacancies and step edges) on TiO₂(110) surface obtained by ion bombardment and annealing procedure [416]. The regime observed at higher coverage most likely corresponds again to dynamic coalescence. Theoretical works on dynamic coalescence of 3D particles on a 2D substrate are scarce [253]. For a mass conserved system, a logarithmic correction was found for the exponents of the power laws $\langle R \rangle \propto [t/\ln(t)]^{1/3(1-\gamma)}$ and $D \propto [t/\ln(t)]^{1/2(1-\gamma)}$ within simulations in which the Brownian particle diffusion coefficient scales with the volume of the particles $D_F \propto R^{3\gamma}$ (Ref. [438]). Fitting the data leads to $\gamma_R = 0.63 \pm 0.18$ for the radius and $\gamma_D = 0.20 \pm 0.14$ for the distance, thus to an enhanced diffusion of the biggest particles.

Ag/MgO(001). In a similar way for the Ag/MgO(001) system, the hypothesis that the deposited thickness is proportional to an equivalent “deposition time” of a hypothetical growth without interruption is validated by the fact that, for all deposits and all temperatures, the GISAXS data were found steady during annealing. This arises because the diffusion energy of Ag on MgO(001) (0.05 eV, see below) and of Ag on Ag (less than 0.1 eV) [442] are very small. As a result, the islands and their distribution on the substrate reach their equilibrium state just after the deposit is made, in a time much shorter than the measurement time. In Fig. 127, two regimes can be distinguished, as a clear slope break appears on the inter-island distance for a deposited thickness of 2–3 nm. Below this value, at least at 300 and 540 K, the inter-island distance is nearly constant and the lateral size increases according to a power law $d \propto t^m$, with $m \simeq 0.32$ –0.35. This regime can be assigned to the nucleation and growth of islands at nearly constant density with an increase of surface coverage (Fig. 128). Again, the $m \simeq 1/3$ exponent on the lateral size power law corresponds to the growth of islands by capture of diffusing species in their surface of influence with a negligible direct impingement on the islands [436]. Above a 2–3 nm thickness, the inter-island distance increases according to a power law $D \propto t^n$, n varying from 0.70 to 0.85 in the temperature range 300–640 K. The lateral size also increases according to a power law $d \propto t^m$, with $m \simeq 0.62$ –0.64. This regime can be assigned to coalescence with a nearly constant surface coverage (30%–40% according to the temperature) (Fig. 127) below the jamming limit of 55% for the percolation and formation of interconnected structures [253,443]. A static coalescence process would yield a power law $d \propto t^1$ for

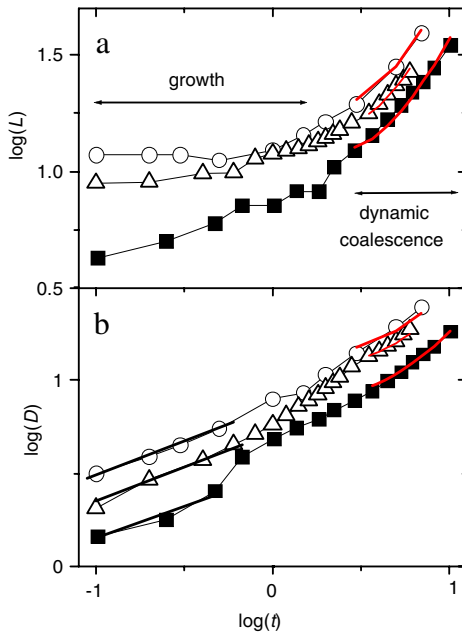


Fig. 127. Growth of Ag/MgO(001) analyzed by GISAXS. Double-logarithmic representation of (a) the inter-island distance D and of (b) the lateral size d obtained by GISAXS as a function of time, for different deposition temperatures. The parameter t is the Ag deposited thickness. Filled squares, $T = 300$ K; open circles, $T = 540$ K; up triangles, $T = 640$ K. The thick black lines correspond to the approximated slopes used to determine n and m in $D \propto t^n$ and $d \propto t^m$. The thick red lines correspond to the fit with $\gamma = 0.8$ in the laws $D \propto [t/\ln(t)]^{1/2(1-\gamma)}$ and $d \propto [t/\ln(t)]^{1/3(1-\gamma)}$. From Ref. [79]. (For interpretation of the references to colour in this figure legend, the reader is referred to the web version of this article.)

the island lateral size, and can thus be ruled out as the dominant process [436–438]. The smaller m value corresponds rather to dynamic coalescence. The logarithmic correction for the power law of the droplet diameter and distance given above in the Au/TiO₂ case are verified with $\gamma \simeq 0.8$. This positive value leads to a behavior of enhanced diffusion of the largest islands contrary to what is expected from standard models [444] of diffusion of the center of mass of the particle through periphery atom mobility. As a matter of fact, in this dynamic coalescence regime, the Ag islands are no longer in coherent registry on MgO(001), and display interfacial dislocations [398]. As a result, they may diffuse much more easily than coherent islands as shown by molecular dynamics simulations [391]. This behavior has been already observed for Au islands on amorphous Al₂O₃ combining TEM and Kinetic Monte Carlo Simulation, [445], as well as for small Pd islands on MgO(001) [446]. In summary, the three above examples show how the growth modes can be inferred from GISAXS measurements. Similar analyses, not discussed here, were performed in the other metal/oxide growth studies.

9.1.7. Equilibrium shape, Wulff-Kaischew construction and adhesion energy

GISAXS yields unique information on the island shape, *in situ*, not destructively, which is especially interesting on a theoretical point of view. In most of the studied systems, there are regimes in which the islands reach their equilibrium shape, allowing to deduce the adhesion energy by application of the Wulff-Kaischew construction [447,448] or of the Young-Dupré equation. Indeed, when the metal diffusion on the surface is fast enough, the islands reach their equilibrium shape on a time scale much shorter than that of the measurements, i.e. a sub-second time-scale. This procedure has been applied in the different growth cases presented above for Pd/MgO(001) [25,29], Pt/MgO(001) [247], Au/TiO₂(110) [81] and Ag/MgO(001) [79].

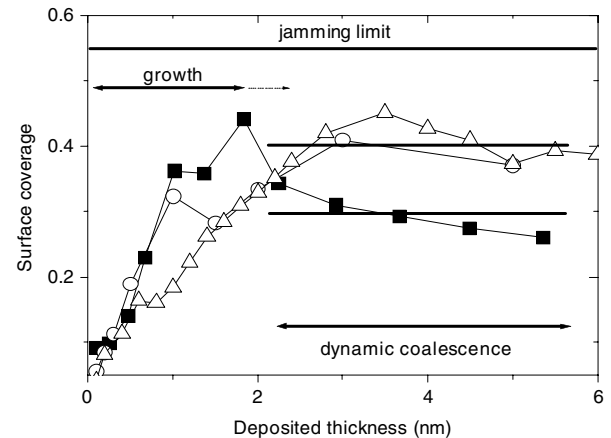


Fig. 128. Growth of Ag/MgO(001) analyzed by GISAXS. Surface coverage obtained by GISAXS as a function of the deposited thickness. Filled squares, $T = 300$ K; open circles, $T = 540$ K; up triangles, $T = 640$ K. From Ref. [79].

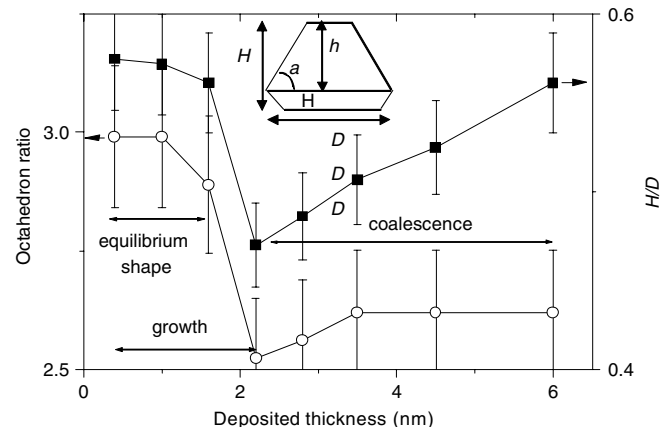


Fig. 129. Growth of Ag/MgO(001): Evolution of the island shape as a function of the deposited thickness at 640 K. Filled circles, octahedron aspect ratio *i.e.* $h/(H-h)$ with Y-axis on the left hand side; filled squares, H/d with Y-axis on the right-hand side. Inset: side view of a truncated octahedron. From Ref. [79].

Ag/MgO(001). In this last case, for instance, at 640 K, the island shape is a truncated octahedron whose aspect ratios, height over width H/d , and $r_H = h/(H-h)$ between the top and bottom height, are constant below 1.6 nm deposited (Fig. 129). The adhesion energy is related to the aspect ratio as:

$$\beta = \sigma_{001}(1 - 1/r_H), \quad (196)$$

where $\sigma_{001} = 1.20 \text{ J m}^{-2}$ (Ref. [449]) is the surface free energy of the (001) facet of Ag. $r_H \simeq 3.0$ yields $\beta \simeq 0.80 \pm 0.1 \text{ J m}^{-2}$, which compares well with the most recent determination. In the deposition thickness range of 1.6–2.2 nm, the ratio H/d decreases, meaning that the islands become flatter. This is expected as during the nucleation and growth regime, the island growth occurs by capture of diffusing species in its surface of influence with a negligible direct impingement on the island. Indeed, while the (111) side facets grow from both vapor phase and atom diffusion, the (001) top facets grow mostly from the vapor phase as if they were isolated, because of the high energy barrier an atom has to overcome to jump from a (111) to a (001) facet [434,435]. Then, above a deposited thickness of 2.2 nm, the ratio H/d increases. During the coalescence regime, it has been pointed out that the facets play an important role. Due to the facets, the diffusion is not the limiting process, but the limiting step of the relaxation following the coalescence is the nucleation of a germ of the size of the smallest facet on a larger facet [450,451]. In the considered

cubo-octahedron, the larger facets are the {001} and {111} facets of the upper island part, and the smaller facets are the {111} and {011} facets of the bottom part. Due to experimental uncertainties, one cannot distinguish which facet among {001} or {111} is the largest. The increase of the H/d ratio would indicate that the island growth occurs preferentially on the {001} facet, which would be the largest facet of the cubo-octahedron.

$\text{Au}/\text{TiO}_2(110)$. In the $\text{Au}/\text{TiO}_2(001)$ case, during the coalescence stage, the aspect ratio $\langle H \rangle / \langle R \rangle$ is nearly constant while the correlation coefficient ρ between the particle height and radius is close to one, indicating that clusters are close to equilibrium. The truncated sphere shape and the full size distribution allow to calculate a mean contact angle θ_c and an adhesion energy from the Young-Dupré formula $E_{adh} = \gamma_{\text{Au}}(1 + \cos \theta_c)$, where $\gamma_{\text{Au}} = 1.131 \text{ J/m}^2$ is the surface energy of gold [389], as a function of the coverage. The value of $\theta_c = 130^\circ \pm 5^\circ$ for the contact angle of large particles is again in good agreement with the most precise determinations [417]. The finding of a change in contact angle (adhesion) around a mean size of $\langle R \rangle \sim 1.3 \text{ nm}$ (~ 500 atoms/cluster, average thickness of 0.6 nm) at the onset of the particle coalescence is compatible with the transition from “flat” 3D shape to spherical 3D shape around a coverage of 0.4–0.6 nm [418,417]. The GISAXS measurements are less sensitive to the 2D or quasi-2D particles seen by low energy ion scattering [430] or scanning tunneling microscopy [418]. These quasi-2D particles are dispersed on terraces and appear at the early beginning of the growth (below 0.2 nm); their height is between 1 and 3 monolayers. But they are in fact mixed with “flat” 3D clusters that mainly grow along the step edges [418,423], a fact that may explain the slight GISAXS anisotropy observed at the beginning of the growth on the mean spacing between particles in the $[110]_{\text{TiO}_2}$ and $[001]_{\text{TiO}_2}$ directions. The morphological transition from 2D or quasi-2D to “flat” 3D particles was interpreted by a stabilization of “flat” 3D particles thanks to an accumulation of vacancies on the substrate below the particles [423].

9.2. Looking by GISAXS at nanoparticles during a catalytic reaction

9.2.1. Scientific background: Bridging the pressure gap in surface science

One major issue in heterogeneous catalysis by supported metallic particles is to relate microscopic properties such as atomic composition, morphology and electronic structure to macroscopic quantities such as catalytic activity and selectivity. Unfortunately, the complexity of actual catalysts precludes a detailed knowledge of their microscopic properties. Surface science studies bypass the complexity gap by looking at flat extended metallic surfaces or supported metallic particles on oxide substrates or thin films. However, a pressure gap of more than ten orders of magnitude does exist between ultra-high vacuum studies and real world catalysts. New physics and chemistry is expected simply by raising the pressure due the huge increase of chemical potential of gas phase reactants; not only the thermodynamic equilibrium of the surface is modified but also the kinetics of phenomena because of the high impinging rate of molecules on the surface. To bridge this pressure gap, a current trend of surface science is to develop characterization techniques beyond the molecular regime in pressure conditions close to realistic ones but starting with the knowhow of UHV to prepare and characterize extended surfaces. There is a wealth of new techniques (or a renewal) to tackle such issues: environmental transmission electron microscopy [452], high pressure STM [453–456], ambient pressure photo emission spectroscopy (Ref. [457] and references therein), high pressure surface X-ray diffraction [458–461,33] etc.... Contrary to electron probes for which specially designed

cells or differential pumping set-ups are needed, the X-ray techniques are intrinsically compatible with any kind of pressure range by simply backfilling the chamber with reactive gases, the only constraints being the inertness of the gas/surface system under beam. The first X-ray set-up was developed at ESRF on the ID03 beamline [458]. Among others, it was used to show that $\text{Ni}(110)$ experiences a massive restructuring at high CO pressure and above room temperature [459], and that the reaction of oxidation of CO at atmospheric pressure does not happen on metallic $\text{Pt}(110)$ but on metastable oxides. Recently, a batch reactor [33,34] (see Section 3.4) inspired from a classical chamber for surface X-ray diffraction was designed to combine scattering studies (SXRD, GIXD and GISAXS) and reactivity measurements. Promising results are expected with such a tool, in particular for supported particles as size and shape effects on the nanometer scale are thought to play an important role. Among others, gold catalyst is a good example. Inert in its bulk form, it becomes highly reactive for the reaction of oxidation of CO (even at RT contrary to Pt) when the particle diameter is reduced to a few nanometers [462]. The explanation of the mechanism of the reaction and the nature of the active sites are highly debated [3]. “Gold-only” explanations involve either the promotion of absorption/dissociation of O_2/CO on highly uncoordinated metal sites or a quantum size effect with an opening of a band gap for two layer high flat particles [388]. Other arguments involve anionic or cationic gold species (depending upon the defectiveness of the support or the preparation method) or reaction/activation at the perimeter between the particle and the support [463]. A clear consensus exists on the strong dependence of the activity on the particle size below 3 nm. However, measuring concomitantly the particle diameter *in situ* and its reactivity is difficult. Work has started in this direction with GISAXS [33,34].

9.2.2. *In operando* study of gold nanoparticles on $\text{TiO}_2(110)$

Experiment conditions. The morphological and crystallographic modifications of $\text{TiO}_2(110)$ supported gold nanoparticles were studied during the CO oxidation reaction at millibar pressure by GISAXS and GIXD [34]. The used setup [33,34] was briefly described in Section 3.4. The gold particles were grown by vapor deposition from an effusion cell in the additional UHV chamber on a clean $\text{TiO}_2(110)$ surface that was Ar^+ sputtered and annealed at 1100 K under 10^{-5} mbar of O_2 . The deposition rate of 0.1 nm/min was calibrated by a quartz microbalance. After transfer in the reactor, the deposit was submitted to various gas and annealing treatments while recording GIXD and GISAXS from the nanoparticles and while monitoring the gas composition by mass spectrometry. The partial pressures were determined after ionisation and fragmentation cross section corrections and by introducing a small amount of Ar as calibration. It was checked by blanking the beam that X-rays do not modify the chemical activity. The measurements steps of roughly two hours long were:

- as deposited in UHV at RT;
- during exposure to 20 mbar of O_2 at RT;
- after adding 0.1 mbar of CO;
- after pumping down to UHV;
- after annealing up to 470 K under UHV;
- during exposure to 20 mbar of O_2 at 470 K;
- after adding 0.1 mbar of CO at 470 K;
- after pumping down to UHV at 470 K.

Following previous work of the literature, a strong excess of O_2 and thermal activation were used to get high enough conversion rates.

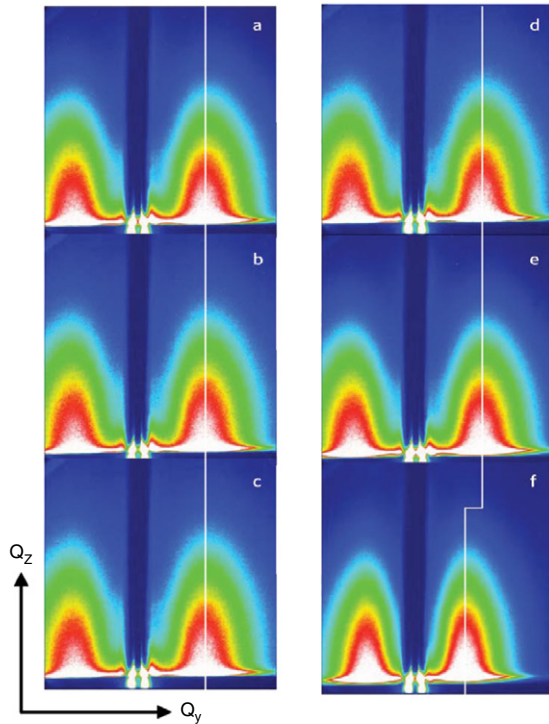


Fig. 130. GISAXS patterns acquired on a 0.1 nm thick gold film grown on $\text{TiO}_2(110)$ under the following conditions: (a) UHV at room temperature (RT); (b) under 20 mbar of O_2 at RT; (c) under the reactive mixture 20 mbar of $\text{O}_2+0.1$ mbar of CO at RT; (d) under UHV at 470 K; (e) under 20 mbar of O_2 at 470 K; (f) under 20 mbar of $\text{O}_2+0.1$ mbar of CO at 470 K. The vertical line pinpoints the correlation peak evolution. $\alpha_i = \alpha_c$; beam along the $[1\bar{1}0]$ direction. From Ref. [34].

Sintering of the nanoparticles and catalytic activity. Following Refs. [155,81], cuts of intensities on the GISAXS patterns were fitted using LMA or SSCA and DWBA on the graded interface assuming a truncated sphere shape. Similar results as those of Lazzari and coworkers [81] (see Fig. 126) were found for the overall morphology in the thickness range of 0.1–0.7 nm i.e. for particles pinned on defects. The aspect ratio h/d was close to 0.6 and thus larger than the expected three layer high clusters that were described as the more reactive [388]. The fits are clearly worse if the particle height is fixed at such a value while the GISAXS measurement are less sensitive to the exact shape (cylinder

or sphere). Fig. 130 evidences that the particles do not undergo any morphological changes at room temperature whatever are the gas partial pressures (a large range was explored). At variance, at higher temperature $T = 470$ K, the particles sinter only during the reaction, not under gas nor upon annealing in vacuum. For 0.1 nm of equivalent thickness (Fig. 130), their diameter increases from 2.4 to 2.8 ± 0.7 nm while their spacing increases simultaneously from 4 to 5.1 ± 0.5 nm, keeping the same aspect ratio. Simultaneously, the reaction product is detected. This sintering affects mainly the most reactive particles of size lower than ≤ 3 nm that are pinned on defects. For a coverage higher than 0.23 nm, neither morphological changes nor reactivity were detected. Indeed, the bigger particles have already undergone coalescence as shown by the UHV study of the growth mode [81]. Sintering under reactive mixture was already observed by others authors [419] but also, at variance to the present work, under pure oxygen [464,420]. These discrepancies may be due to the substrate preparation and density of defects. The evolution of the partial pressures of CO and CO_2 (Fig. 131a) is deduced from the evolution of mass 28 and 44 after various corrections. The reaction rate is obtained by the slope at the beginning of the exposure. It is given by the number of CO molecules converted per second per gold atom and is plotted in Fig. 131b against the equivalent film thickness and particle diameter estimated from GISAXS. Unfortunately, the measurements could not be performed for all thicknesses during the available beam time. Therefore, the experimental conditions were carefully reproduced at the laboratory. A clear result is that the rate of reaction increases continuously while reducing the particle size without any maximum in the range 2.4–5.2 nm. Such a finding differs from previous STM results [388] where a maximum was found. GISAXS experiments have been undertaken recently to confirm accurately those results with the actual particle size accounting for the observed reaction induced sintering. This opens the possibility of the determination of the relationship between the size and the reactivity of gold catalysts really during the chemical reaction itself with a sampling of a vast collection of nanoparticles.

9.3. Stranski-Krastanow growth in the Ge/Si(001) system

The physical properties of semiconductor nanoparticles depend entirely on their size, shape, internal structure, strain and composition, which thus have to be fully controlled and understood. Semiconductor nanostructures are classically grown by the

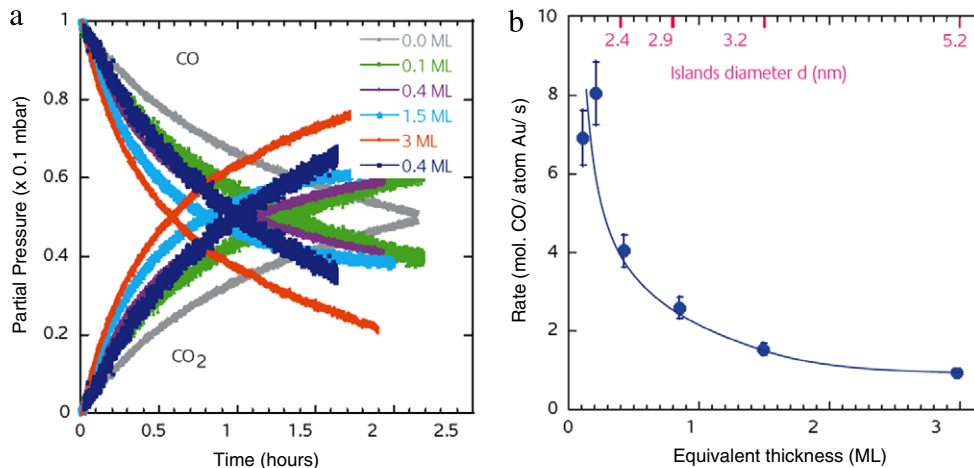


Fig. 131. Activity of gold nanoparticles supported on $\text{TiO}_2(110)$ measured in a batch reactor for 10 mbar $\text{O}_2+0.1$ mbar CO partial pressures. 1 ML corresponds to one compact $\text{Au}(111)$ plane. (a) Evolution of the decrease of CO pressure and uptake of the CO_2 pressure as deduced from the mass 28 and 44 after ionization factor and fragmentation corrections. The gray curve corresponds to the background reactivity while the blue one corresponds to 0.4 ML measured during X-ray experiments. (b) Atomic rate of CO conversion into CO_2 as function of the film thickness after background subtraction. The diameter d measured by GISAXS has been reported on the top axis. From Ref. [34].

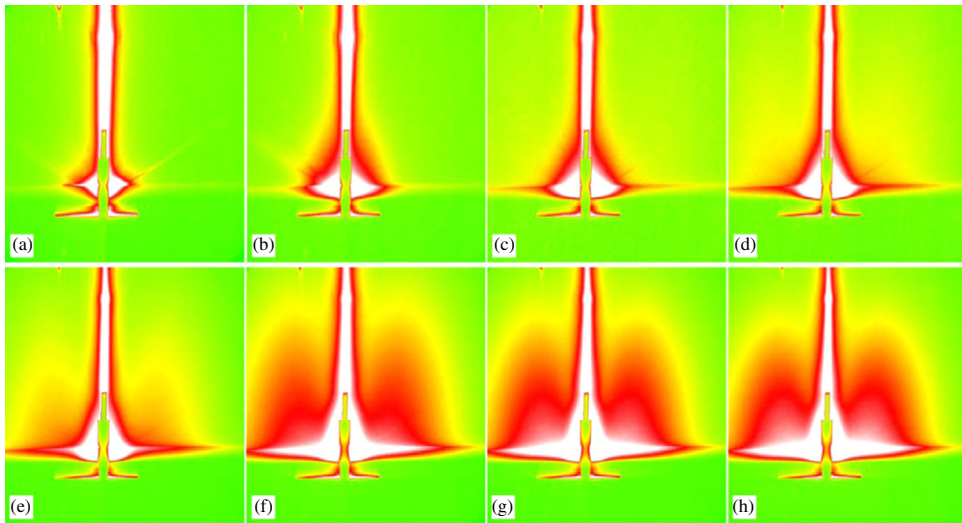


Fig. 132. GISAXS patterns collected during the *in situ* growth of Ge/Si(001) at 700 K (incidence angle $\alpha_i = 0.2^\circ$ and beam energy of 10 keV). (a) Bare substrate GISAXS signal. From (b) to (h), patterns have been recorded for an equivalent thickness ranging from 2 to 8 Å. Observation of the diffusion halo indicates that the Stranski–Krastanow transition occurs between 5 and 6 Å of Ge. The GISAXS images do not depend on the direction of observation thus implying an isotropic shape for the islands. From Ref. [475].

Stranski–Krastanow (SK) mechanism for which, beyond a critical thickness, islands are formed on a two-dimensional wetting layer. The mechanism of the SK growth of Ge layers on Si(001) substrates has been investigated extensively. By increasing the Ge coverage the shape of the islands changes from square pyramids having {105} facets to dome-shaped islands with {105}, {113}, {15 3 23} facets, and the top (001) facet [465,466]. Finally, the dome islands may evolve into coherent islands, called ‘barns’ with additional {111} and {20 4 23} facets [467,468] before the appearance of large, dislocated islands named ‘superdomes’ [469]. Recently, it has been shown that the shape transition from pyramids to domes is thermodynamically driven, *i.e.*, during the growth the islands with sub-critical sizes (pyramids) shrink and the over-critically sized islands (domes) grow [470]. However, the kinetics of the island growth and of the shape transitions is still not completely understood. In particular, the evolution with temperature [471] and deposited thickness of the islands size and shape are not fully determined, neither the state, equilibrium or transient, of the dome-shaped islands during growth. This calls for *in situ* investigations as a function of temperature. The morphology of islands during their growth has been investigated by many *in situ* methods, such as electron or synchrotron diffraction [472], scanning tunneling or low-energy electron microscopy [473,474]. With *in situ* GISAXS, contrary to other *in situ* techniques, not only the average diameter and height of the islands but also the average size of each facet can be directly estimated during the growth. We report here on several *in situ* GISAXS studies during the growth of Ge on Si(001).

First experiments on ID32

The first experiments [475] were performed using the ID32 setup. Ge was deposited on Si(001) by amounts of 1 Å, at a substrate temperature of 700 K, up to an equivalent thickness of 10 Å. GISAXS pictures were recorded for each deposited Å of Ge, keeping the sample at constant temperature. Fig. 132 shows a typical set of GISAXS pictures. From these observations, the Stranski–Krastanow transition takes place between 5 and 6 Å. Indeed, up to 4 Å (Fig. 132a–c), the GISAXS signal is consistent with a weakly rough surface: only a very small scattering out of the specular beam is observed. At 5 Å (Fig. 132d), the scattered intensity starts to increase on each side of the specular beam, which is related to an increase of the roughness. Nevertheless, there are not yet well-defined features that could indicate the presence of 3D islands. The 3D islands appear only above 6 Å,

as revealed by the symmetrical rounded shapes of the scattered intensity. GISAXS patterns do not depend on the direction of observation, which means that the island distributions at the surface and their shape are isotropic. The sizes and separations of these islands was deduced by a fast analysis [475]. After the growth of 10 Å of Ge at 700 K, a progressive annealing of the sample was performed to investigate the morphological evolution of the islands as a function of the temperature. No significant change was observed until 900 K, where a 15 min anneal induced a dramatic change in morphology. The corresponding GISAXS data (Fig. 133) revealed clear scattering double streaks, corresponding to {311} and {111} facets. The streaks were found to be double. For $\alpha_i = 0.1^\circ$, they point at the refracted beam, while for $\alpha_i = 0.4^\circ$ they point at the transmitted beam. In the case of $\alpha_i = 0.2^\circ$, when there is a doubling of the truncation rods, the upper (in terms of q_z) set of streaks points at the refracted beam whereas the lower set points at the transmitted beam. These observations are perfectly consistent with the DWBA treatment of GISAXS. Within this framework, the IsGISAXS software was used to simulate the scattering by facets. Ge islands shape was taken as a square basis truncated pyramid with {311} facets. The mean lateral size of Ge islands was 50 nm, with a Gaussian distribution of sizes, of width $\sigma_R/R = 0.2$. The height to lateral size ratio of the islands is 0.3. Fig. 134 shows such a simulation for a grazing angle $\alpha_i = 0.2^\circ$. The calculated scattered intensity as a function of the exit angles α_f and $2\theta_f$ shows the splitting of the truncation rods when the incident angle is near the critical angle. The inset part of Fig. 134 shows a cross-section of the amplitudes associated with each term of the DWBA. This cross-section is performed as a function of α_f , at fixed $2\theta_f = 0.5^\circ$. This discrimination between the different terms of the DWBA shows that, apart from the first component corresponding to the Born approximation, only the second component is non-negligible in the observed pattern. This indicates that the main scattering process to explain the second truncation rod is a reflection of the incoming beam by the surface prior to a scattering by the islands. Simulations performed at incident angles of 0.1° and 0.4° (not shown here) reproduce the main experimental observed features. These simulations also show that the third and fourth terms of the DWBA are of little importance as soon as $\alpha_i > \alpha_c$. To conclude, GISAXS measurements during the thermally activated faceting of Ge/Si(001) yielded a direct experimental evidence of grazing incidence scattering effects. In particular, the origin of the doubling of the facets truncation rod was well reproduced within the DWBA.

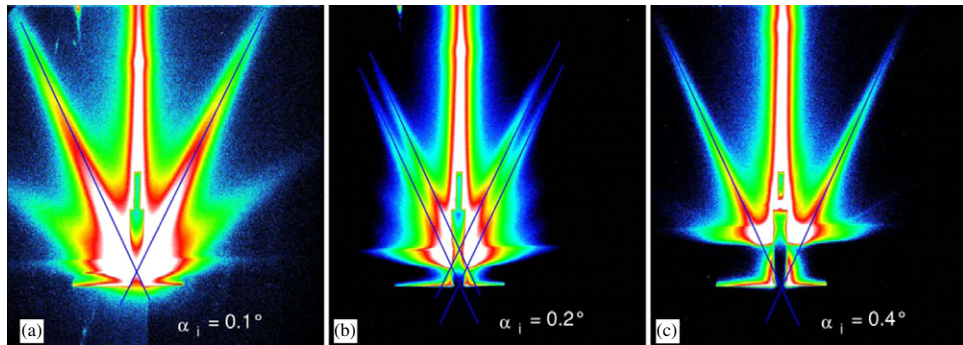


Fig. 133. GISAXS study of scattering by Ge facets, as a function of the grazing angle, after 15 min of annealing at 900 K. (a): $\alpha_i = 0.1^\circ$, (b): $\alpha_i = 0.2^\circ$, (c): $\alpha_i = 0.4^\circ$. The incident beam is along the $\langle 110 \rangle$ direction. From Ref. [475].

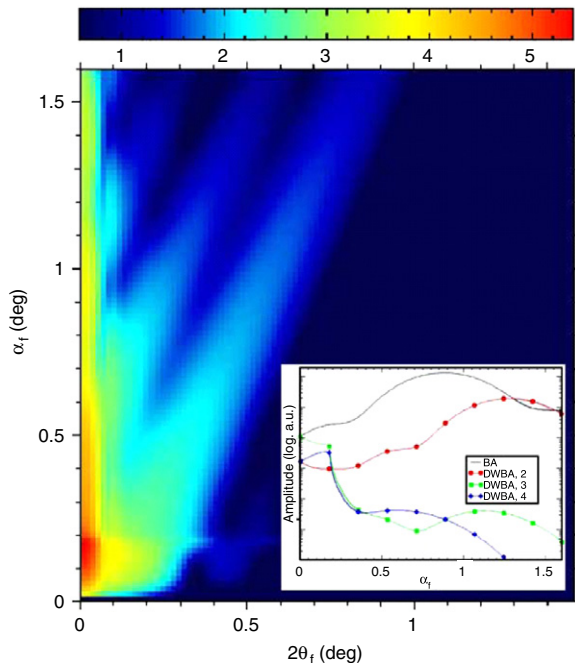


Fig. 134. GISAXS simulation of $\{311\}$ faceted Ge islands on Si(001) within the DWBA framework, for a grazing angle $\alpha_i = 0.2^\circ$. The intensity map is calculated as a function of the exit angles α_f and $2\theta_f$. The intensity scale is in arbitrary logarithmic units (top color band). One can notice the splitting of the truncation rods associated to the facets. Inset: cross-sections of the scattered amplitudes, for each term of DWBA, as a function of α_f , at fixed $2\theta_f = 0.5^\circ$. From Ref. [475].

Ge island nucleation and wetting layer

Further studies, performed using the BM32 setup, were aimed at fully characterizing the shape, size, strain and composition of Ge islands on Si(001), *in situ*, during their growth, by combining GIXD, XRR, GISAXS and GI-MAD. This last technique, Grazing Incidence Multiple Anomalous Diffraction, consist of performing GIXS measurements (GIXD or GISAXS or XRR) at several energies (typically 12) around an absorption edge of the element whose composition has to be determined. This strongly varies the scattering factor of this element, thus rendering X-ray scattering composition sensitive. It thus allows determining the composition of zones that are selected by their strain value. Fig. 135 sketches the different probed regions in reciprocal space of such a sample.

All Si(001) surfaces were deoxidized at 900 °C under ultrahigh vacuum conditions in the BM32 UHV chamber, and characterized for their surface quality with GIXD and RHEED. The surfaces showed a 2×1 reconstruction whose average domain size was $\approx 1 \mu\text{m}$. For each deposited Ge monolayer, GISAXS patterns were

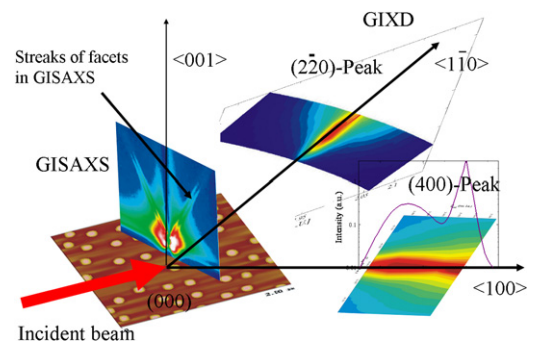


Fig. 135. Sketch of the *in situ* X-ray scattering setup for the study of the growth of Ge on Si(001). Under grazing incidence conditions, the evolution of the sample morphology can be followed in the small angle regime; the formation of facets is indicated in the GISAXS pattern. The lattice relaxation is monitored by the appearance of Bragg peaks in GIXD. Intensity maps around the (220) and (400) Si and Ge Bragg peaks, integrated perpendicular to the surface, are also shown. From Ref. [476].

collected in the $\langle 110 \rangle$, $\langle 100 \rangle$, and $\langle 15\bar{3}\bar{0} \rangle$ azimuthal orientations. For a growth temperature of 500 °C, a series of radial scans (not shown) across the (400) reflection were performed. No lattice relaxation was visible up to 4 ML coverage. For 5 and 6 ML deposit, two shoulders developed, indicating a bimodal growth in this temperature regime. The shoulder closest to the Si peak corresponds to highly strained islands that form in very early stages of the nucleation. For depositions higher than 6 ML, only more relaxed islands continued to grow. After the growth, domes of variable size and hut clusters were observed by AFM. In order to further characterize this morphological transition, the recorded GISAXS patterns have to be considered. For the bare Si(001) surface, a typical GISAXS pattern is shown in Fig. 136a. It is dominated in its central part by stray radiation from the direct beam (hidden by a beam stop) and by diffuse scattering from the surface. To record the appearance of islands and, in particular, of facets, different low-index azimuthal orientations were regarded. Fig. 136b shows a GISAXS image in the $\langle 100 \rangle$ azimuth for early nucleation stages at 500 °C. Broad and diffuse streaks in the $\langle 105 \rangle$ direction (highlighted by arrows) indicate the formation of $\{105\}$ faceted hut clusters and/or pyramids. Due to the flat facet orientation (11°) with respect to the (001) surface, these islands are highly strained. For the $\langle 110 \rangle$ azimuth, no evolution can be observed for low deposits (see Fig. 136c) up to 5 ML. For 6 ML deposition (Fig. 136d), streaks in the $\langle 113 \rangle$ direction appear. The splitting of the streaks occurs as a consequence of the fourfold scattering process found by the DWBA when working close to the critical angle. The same behavior is observed for $\langle 15\bar{3}\bar{0} \rangle$ azimuth, where $\langle 15\bar{3}\bar{2}\bar{3} \rangle$ facets appear at 6 ML (not shown here). The previously described $\{105\}$ facets remain almost unchanged at this

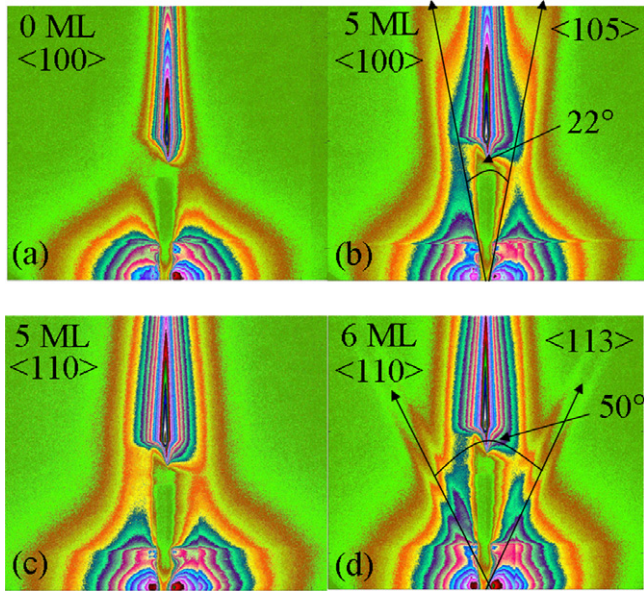


Fig. 136. Growth of Ge on Si(001). GISAXS images for different deposition stages and azimuthal orientations for a deposition temperature of $T = 500$ °C. (a) From a flat surface in the $\langle 100 \rangle$ sample azimuth; the central beam is blocked by a beam stop. (b) $\{105\}$ facets attributed to pyramids at 5 ML deposited. The bare substrate GISAXS from (a) was subtracted. The indicated angle of $2 \times 11^\circ$ corresponds to twice the angle between the facet normal $\langle 105 \rangle$ and the surface normal $\langle 100 \rangle$. (c) The $\langle 110 \rangle$ azimuth for a deposition of 5 ML. (d) At 6 ML the sharp pyramid to dome transition is reached and $\{113\}$ facets appear. From Ref. [476].

point. These latter three orientations describe the multifaceted dome shape as reported in earlier works.

Growth laws of Ge superdomes on Si(001), as studied by GISAXS

The experiments described above were again performed in the BM32 UHV chamber with a very slow Ge deposition rate (170 s for one Ge monolayer (ML)). Ge was deposited monolayer after monolayer at four growth temperatures (773 K, 823 K, 873 K and 923 K). To avoid any evolution of the islands between successive deposits, the samples were immediately cooled down to 723 K after each added monolayer, as a reference temperature at which the X-ray measurements were performed, so that significant morphological evolution or Si-Ge intermixing between successive deposits can be safely neglected [476,477,474]. Consequently, the successive deposits are almost equivalent to a continuous deposit with constant rate, as a function of time: the deposited amount θ is proportional to an equivalent deposition time t . Fig. 137 shows the measured GISAXS data for the growth temperature of 923 K as functions of the q_y and q_z coordinates of the scattering vector, i.e., for the $[110]$ azimuthal directions of the primary beam. Very similar results were gained for the X-ray beam along the $[15\ 3\ 0]$ direction.

The intensity maps exhibit nearly no changes for the nominal Ge coverages θ between 0 and 4–5 MLs for a growth temperature of 923 K along the $[110]$ and $[15\ 3\ 0]$ azimuths. Above this thickness, diffuse intensity streaks are visible along the $\langle 113 \rangle$ and $\langle 15\ 3\ 23 \rangle$ directions. At 8–9 MLs, additional streaks along $\langle 111 \rangle$ appear in the $[110]$ azimuth. No changes are observable (images not shown here) between 0 and 4 MLs along the $[110]$ and $[15\ 3\ 0]$ azimuths for the growth temperature of 873 K and between 0 and 5 MLs at 823 K and 773 K.

For the analysis of the measured data the DWBA for islands [37] (Section 6.2) was adapted to deduce directly the average height of the facets [478]. Let $F(\mathbf{q})$ be the Fourier transform of the shape function $S(\mathbf{r})$ of a single island. In the case of islands with flat facets, it is suitable to convert the volume integral calculating $F(\mathbf{q})$ into

an integral over the island surface $A = \cup_j A^{(j)}$ using the Stokes formula, which yields

$$\mathcal{Q}^{\text{FT}}(\mathbf{q}) = \frac{I}{q^2} \sum_j q_{\perp}^{(j)} e^{-iq_{\perp}^{(j)} r_{\perp}^{(j)}} F_j(\mathbf{q}_{\parallel}^{(j)}). \quad (197)$$

In this equation, $\mathbf{n}^{(j)}$ denotes the unit vector of the outer normal of the facet j with the area $S^{(j)}$, then $r_{\perp}^{(j)} = \mathbf{r} \cdot \mathbf{n}^{(j)}$ is the distance of this facet from the origin (the origin is at the center of the bottom of the islands), $q_{\perp}^{(j)} = \mathbf{q} \cdot \mathbf{n}^{(j)}$ is the component of \mathbf{q} perpendicular to the facet and $\mathbf{q}_{\parallel}^{(j)} = \mathbf{n}^{(j)} \times (\mathbf{q} \times \mathbf{n}^{(j)})$ is the component of \mathbf{q} parallel to the facet. The Fourier transformation of the shape function of the facet j is equal to $F_j(\mathbf{q}_{\parallel}^{(j)}) = \int_{S^{(j)}} d^2 \mathbf{r}_{\parallel}^{(j)} e^{-i\mathbf{q}_{\parallel}^{(j)} \cdot \mathbf{r}_{\parallel}^{(j)}}$.

The above equation makes it possible to analyze the contribution of individual facets to the intensity $I(\mathbf{q})$. Assuming that the island positions are completely random, the intensity of the scattered radiation is an incoherent superposition of intensities scattered by individual islands. The expression for the scattered intensity can be simplified as follows

$$I(\mathbf{q}) \simeq \text{const.} \sum_j \sum_{n=1}^4 |A_n|^2 \left(\frac{q_{\perp}^{(j)}}{q_n^2} \right)^2 \left\langle |F_j(\mathbf{q}_{\parallel n}^{(j)})|^2 \right\rangle, \quad (198)$$

where the sums run over the scattering processes, A_n and \mathbf{q}_n are the amplitude and scattering vector of process n . The direct (kinematical) process $n = 1$ is the scattering of the incident wave, the indirect processes $n = 2, 3, 4$ comprise the scattering of the wave specularly reflected from the flat surface between the islands ($n = 2$), specular reflection of the wave scattered from the island ($n = 3$), and specular reflection of both the primary and the scattered waves ($n = 4$) (see [37] and Section 6.2 for details). Within this approximation, the intensity is a sum of the contributions of individual facets. Each facet gives rise to a narrow streak in reciprocal space parallel with $\mathbf{n}^{(j)}$. The width of the streak is inversely proportional to the facet width L . Along the streak, the intensity drops as $(q_{\perp}^{(j)})^{-2}$. In the case of a non-faceted island with a rounded surface, the scattered intensity decreases as q^{-4} (the Debye–Porod law [73,217]), so that from the asymptotic intensity decrease it is possible to identify individual facets. The intensity distribution across the streaks is determined by $\langle |F_j(\mathbf{q}_{\parallel})|^2 \rangle$, where the average is taken over the distribution of facet sizes. Numerical estimates have revealed that this intensity distribution obeys the asymptotic formula $\langle |F_j(\mathbf{q}_{\parallel})|^2 \rangle \propto |\mathbf{q}_{\parallel}^{(j)}|^{-3}$ for large $|\mathbf{q}_{\parallel}^{(j)}|$ for any facet shape and any statistical distribution of the facet sizes. The full-width at half maximum (FWHM) δq_{\parallel} of the streak is inversely proportional to the mean facet size $L_0 \equiv \langle L \rangle$, however, the proportionality factor decreases with increasing root mean square (rms) deviation σ_L of L . For $\sigma_L \rightarrow 0$, $L_0 \rightarrow 2\pi/\delta q_{\parallel}$ holds. The indirect scattering processes ($n = 2, 3, 4$) give rise to an additional streak for each facet, if its wave vector transfer $q_{nz} > 0$. The intensity streaks stem from two scattering processes, namely for $n = 1, 2$ (if $\alpha_f > \alpha_c$) or $n = 1, 3$ ($\alpha_f < \alpha_c$). Due to the reflection from the free surface, the additional streak is shifted vertically by $2k \sin \alpha_i$, and its intensity depends on the incidence or exit angles due to the reflectivity coefficients $r_{i,f}$. The distance between the peaks stemming from various scattering processes is $\Delta q_{\parallel} = 2k \sin \alpha_{i,f} \sin \beta$, where β is the angle of the facet with (001). This effect has to be taken into account in the determination of the facet size from the streak width.

Fig. 138 shows an example of a fit of a line scan extracted from the GISAXS measurement in the $[110]$ azimuth for $\theta = 10$ MLs for the growth temperature of 873 K. This line scan is fitted by the sum of three modified Lorentzian functions, one corresponds to the streak of the top facet (on the right side of the figure), the other two stem from $\{113\}$. The study was not performed for the $\{105\}$ facets appearing in the $[100]$ azimuth because the flat facet orientation

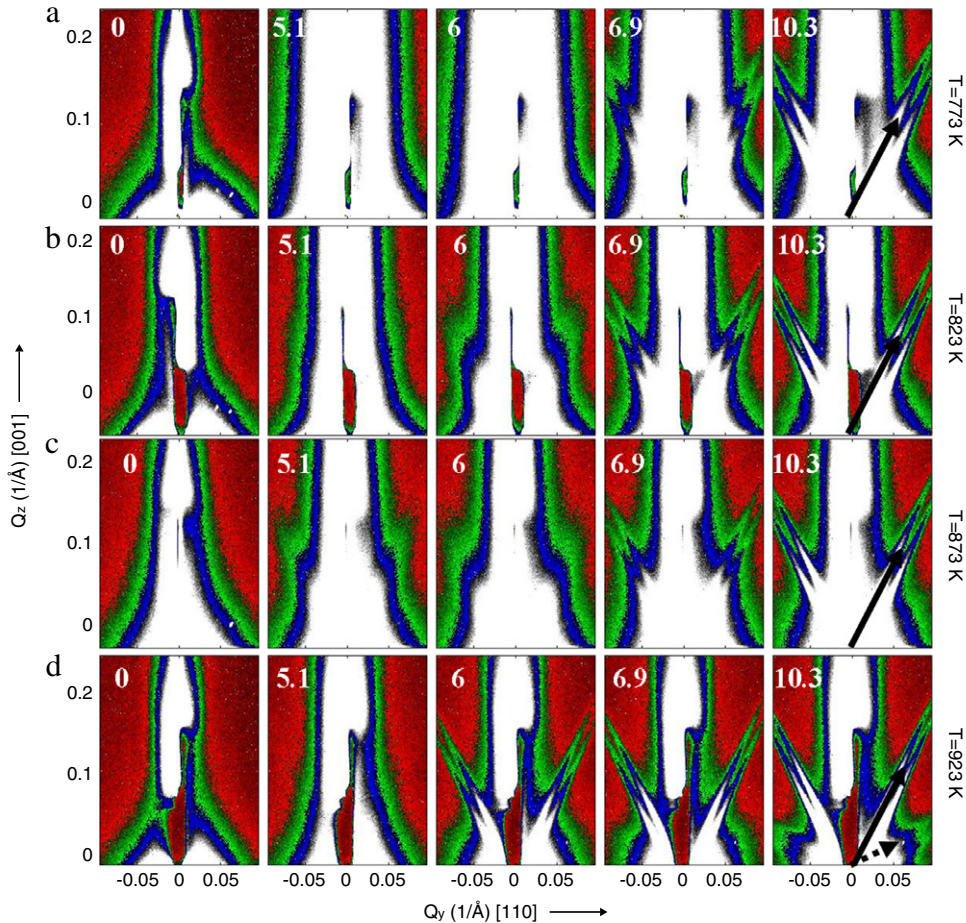


Fig. 137. GISAXS intensity maps along the [110] azimuth obtained at growth temperatures of 773 K (a), 823 K (b), 873 K (c) and 923 K (d); the numbers denote the nominal Ge thickness in ML, the arrows are along (113) (full arrows) and (111) (dashed arrow). From Ref. [478].

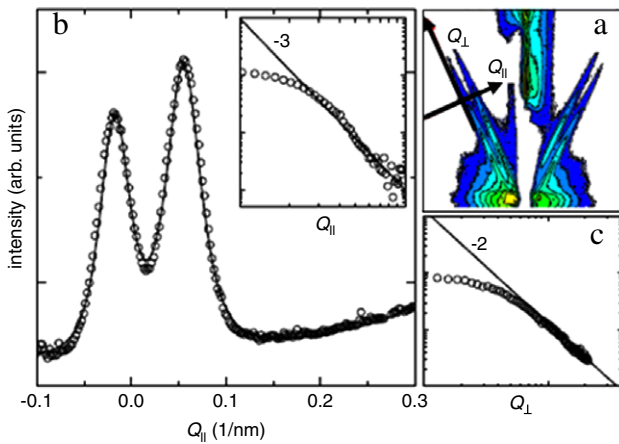


Fig. 138. Figure (a) shows a GISAXS image (azimuth [110], $\theta = 10$ ML), from which the line scans in panels (b), (c) are extracted along the Q_{\parallel} and Q_z axes. (b) The linear scan extracted from the GISAXS intensity map across the {113} facet streak (points) and its fit by a sum of three $f(q_{\parallel})$ functions (see text); the inset shows the tail of this line scan in a loglog representation. (c) The line scan along the facet streak. From figures (b) and (c), the q_z^{-2} and q_{\parallel}^{-3} slopes are clearly visible. From Ref. [478].

(11° with respect to the (001) axis) and the small facet size induce a broadening of the {105} diffuse streaks which makes difficult the analysis. Therefore, only the {113} and {15 3 23} facet sizes were characterized. The insets in Fig. 138 show the linear scans extracted from the intensity map in the [110] azimuth for $\theta = 10$ MLs at a growth temperature of 873 K along and across the intensity

streaks. The above predicted q_z^{-2} and q_{\parallel}^{-3} asymptotic dependencies are clearly visible. The values of the mean sizes L_0 for the last deposits deduced from these fits are consistent with those deduced from the *ex situ* AFM measurements performed after growth. In Fig. 139 is plotted the dependence of the mean sizes L_0 of the {113} and {15 3 23} facets, for the growth temperatures of 773 K, 823 K, 873 K and 923 K as a function of the deposited thickness θ . The evolution shown in Fig. 139 was found to be fitted well by a power-law of the type: $L_0 = B(\theta - \theta_c)^{1/3}$, where θ_c and B are constant. This 1/3 power evolution of the different facet sizes implies that the island volume V is proportional to the deposited thickness θ , neglecting the small volume variation possibly induced by a different size variation of the {105} facets.

From the fit of the experimental data to the $\theta^{1/3}$ dependence, the critical thickness for the dome-to-superdome transition was determined as being $\theta_c = (6 \pm 0.3)$ MLs for 773 K, $\theta_c = (5.97 \pm 0.25)$ MLs for 823 K, $\theta_c = (5.1 \pm 0.2)$ MLs for 873 K and to $\theta_c = (4.8 \pm 0.25)$ MLs for 923 K. The critical thickness was found to decrease with increasing temperature, which is consistent with the results of Cimalla [479]. The average sizes of the {113} and {15 3 23} facets are found to increase with temperature, as expected. These results confirm that the pyramid-to-dome transition is thermally activated.

In summary, the evolution of the size of crystallographic facets during a slow growth of Ge (super-)domes on Si(001) has been studied using *in situ* GISAXS. From the evolution of the widths of intensity streaks in reciprocal space, the kinetics of the growth of the {113} and {15 3 23} facets was deduced. Up to 823 K, the facet sizes are found to obey a $\theta^{1/3}$ -dependence. This implies that, above

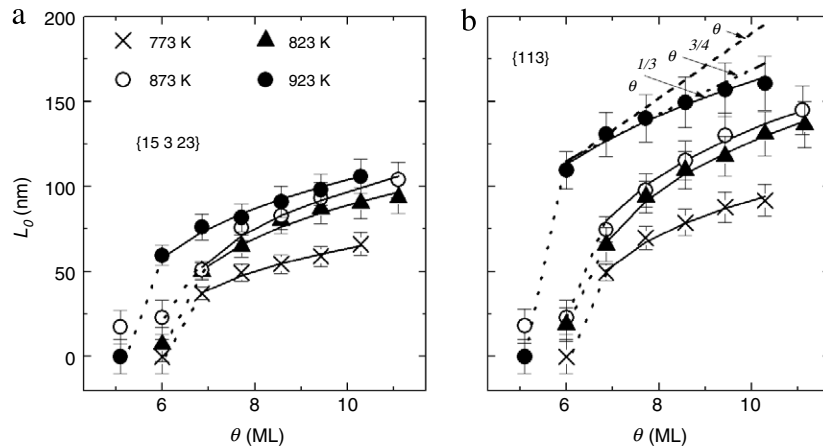


Fig. 139. The dependence of the mean facet sizes L_0 of Ge superdomes on Si(001) on the nominal coverage θ of the deposited Ge layer. Above 6 ML at 923 K and 6.9 ML at the three other temperatures, the data for the $\{15\ 3\ 23\}$ (a) and $\{113\}$ (b) facets were fitted to a $B(\theta - \theta_c)^{1/3}$ function (full lines). From Ref. [478].

a certain critical thickness, the domes do not change their shape and that they grow self-similarity, reaching their equilibrium shape.

An *ex situ* study from the group of Dubček deserved to be mentioned here. In 2006, they reported on a 2D GISAXS *ex situ* study combined with AFM of Ge islands grown on Si(001) substrates [480]. The samples were prepared by magnetron sputtering of a 5 nm thick Ge layer in a very high vacuum on Si(100) substrate held at different temperatures. The vertical cut (perpendicular to the surface) of the experimental 2D GISAXS pattern has been fitted using a Guinier approximation. The optimum temperature for the islands formation was 650 °C. At this temperature, islands grow in conical shape with very similar dimensions; however, inter-island distances varied significantly.

9.4. Self-organized growth of nanostructures

The miniaturization of devices makes their production lengthy and expensive when using conventional techniques like lithography. The self-organized growth of atoms in the first stage of an overlayer growth is seen as a smart solution to overcome the expensive and heavy demanding procedures necessary for shaping materials at the nanoscale. To become a reliable alternative, the self-assembling process has to demonstrate the capability of giving rise to collections of nanoparticles with a narrow size distribution and an ordered spatial arrangement: the so-called self-organized growth. The major challenge in order to achieve this goal is to avoid random growth by taking advantage of regular surface nanopatterning to control the nucleation process. Several routes have been explored: vicinal surfaces [481] (exhibiting a regular step array), surfaces strained by buried nanostructures [482], ordered phases of adsorbates [483], surface reconstructions [30,484,485], thin films of a few monolayers having coincidence lattice sites with the substrate [486,442] or buried dislocation networks [487,488]. These experiments have demonstrated the potential of the self-organized growth process, producing well ordered collections of nanoparticles of a given size and shape. However fabricating a regular pattern is not enough, it is necessary to avoid homogeneous nucleation in order to grow only one nanostructure per unit cell [442]. The parameters of control for the growth are the temperature and the flux of atoms deposited on the surface. To find the optimal experimental conditions, the use of *ex situ* characterization tools may be very time consuming. At variance *in situ* and more suitable real time X-ray techniques offer the opportunity of a feed back control of the growth processes to orient toward self-organization. They provide the crystallographic structure (GIXD) as well as the shape, size and spatial organization

(GISAXS) of a macroscopic number of nanostructures. In the following, we will focus on recent GISAXS studies of ordered growth of Co or Ni nanostructures on different kinds of surface:

- the Au(111) surface reconstruction as a model system [32];
- a kinked vicinal surface of Au(111) [215,489];
- a thin film of Ag strained by a misfit dislocation network buried at the interface with a MgO(001) substrate [488];
- a cobalt-oxide thin film induced patterned by a buried misfit dislocation network [490].

9.4.1. The ordered growth of Co on Au(111)

The growth of Co nanostructures on Au(111) is certainly one of the most popular example of ordered growth of nanostructures on metal surfaces [30,5]. The main advantages of this system are (i) its robustness in temperature since the growth is ordered in a wide range of temperature [491] (120 K to 400 K); and (ii) the large size of its unit cell. The Au(111) surface exhibits a reconstruction ($22 \times \sqrt{3}$) that has been characterized by GIXD [492], STM [493], and Helium Atom diffraction [494]. Top layer atoms are successively in fcc and hcp stacking and both domains are separated by stacking-faults. As the Au(111) surface has a threefold symmetry, three different variants of the reconstruction co-exist on the surface. A superstructure involving two variants of the reconstruction, rotated at 120° and separated by a kink, is called herringbone reconstruction. For length scales of about 100 nm, different domains of the herringbone reconstruction rotated at ±120° are observed in agreement with the symmetry of the surface. Consequently the Au(111) surface is spontaneously ordered over areas of 100×100 nm² and more importantly it is a template for the ordered growth of Co nanostructures. The nucleation of Co on Au(111) is heterogeneous and occurs at the kinks of the herringbone reconstruction (see Fig. 140a–c) thanks to an insertion mechanism [495]. Different questions have been addressed by GISAXS: in the submonolayer regime, the size and content of the unit cell of Co nanostructures have been studied as a function of deposit. At the coalescence of the Co nanostructures and beyond, the structure of the Co thin film has been investigated by Anomalous GISAXS and GIXD. At last, in order to increase the blocking temperature of the Co nanostructures, nanopillars have been grown by sequential deposition of Co and Au.

Qualitative interpretation of the scattering rods by the Conanostructure network. The network of Co dots is characterized by a unit cell (**A**, **B**) of rectangular shape of about $7.7 \times 15 - 50$ nm² (Ref. [497]) filled with two nanostructures of approximately two monolayers high (see Fig. 140c). The main crystallographic axis of the Co dots

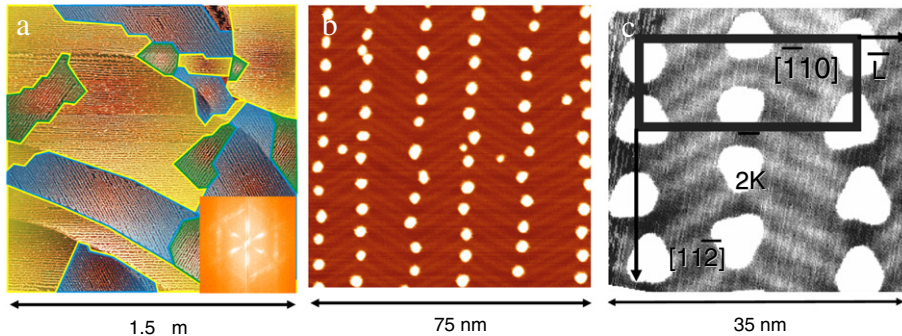


Fig. 140. (a) STM images of the self-organized growth of Co nanostructures on the Au(111) herringbone reconstruction. (a) Large scale image ($1.5 \times 1.5 \mu\text{m}^2$) and its Fourier Transform (Inset). The three different domains of the Co nanostructures network are highlighted by different colors. (b) Image of one domain for 0.05 ML of Co. (c) Small scale image. A sketch of the unit cell is shown (from Refs. [32,496]).

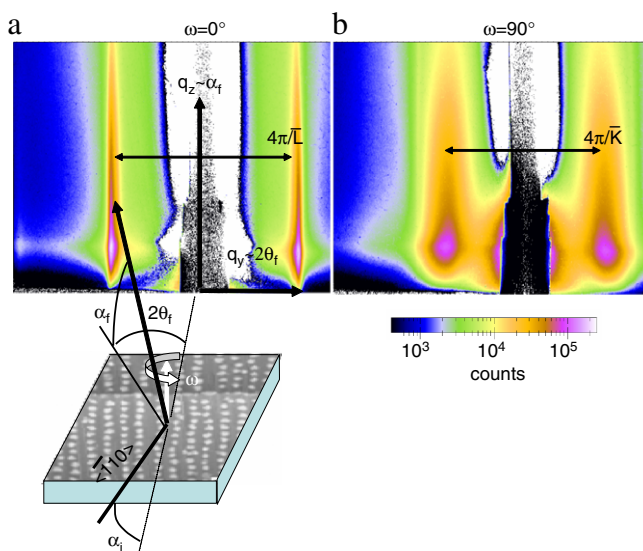


Fig. 141. (a) Sketch of the principle of a GISAXS measurement and experimental image for an incident X-ray beam aligned along the $\langle 1\bar{1}0 \rangle$ direction. The distance separating the scattering rods is inversely proportional to the intra-row distance (L). (b) Experimental GISAXS image obtained for the beam aligned along the $\langle 1\bar{1}2 \rangle$ direction. The inter-row distance (K) is probed (from Ref. [32]).

network are aligned along the $\langle 1\bar{1}2 \rangle$ and $\langle \bar{1}\bar{1}0 \rangle$ directions referring to the fcc lattice of Au. We call intra-row spacing the distance between the nanostructures in the $\langle 1\bar{1}2 \rangle$ direction, i.e. governed by the size of the $22 \times \sqrt{3}$ reconstruction. The inter-row spacing is the distance between the nanostructures in the $\langle \bar{1}\bar{1}0 \rangle$ direction (kink periodicity). Fig. 141a and b show respectively two GISAXS images measured for an incident beam aligned along the main crystallographic orientations $\langle 1\bar{1}0 \rangle$ and $\langle 1\bar{1}2 \rangle$. They are both characterized by correlation peaks in the surface plane showing the presence of a bidimensional order. The normalized FWHM of the scattering rods of the intra-row spacing ($\Delta q_{||}/q_{||} = 3\%$) is very small (see Fig. 141a). This reveals a long range order arising from the underlying $N \times \sqrt{3}$ reconstruction for which the periodicity is very well defined ($N = 22 \pm 1$). About the inter-row spacing (see Fig. 141b), the scattering rods are much broader revealing a short range order. A one-dimensional analysis gives a mean distance of 8.5 nm and a standard deviation of 2.1 nm. The quality of the order in this direction can be assigned to the fluctuations of the spacing between two kinks of the reconstruction. Fluctuations are large because the energetic equilibrium of the surface structure is mainly controlled by the $22 \times \sqrt{3}$ reconstruction and the kink spacing is a second order effect. In the direction perpendicular to the surface the scattering rods are very extended due to the very small height (2 ML) of the nanostructures as put in evidence earlier by STM [30].

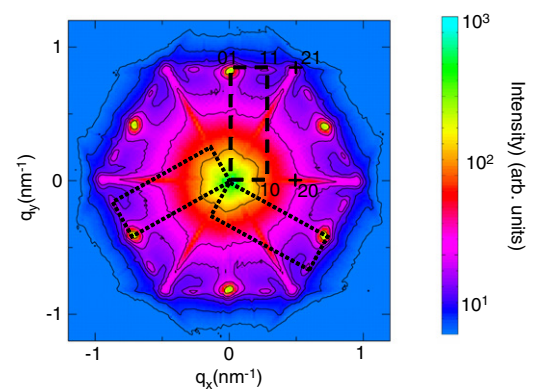


Fig. 142. Map of the reciprocal space of the Co dots network in the surface plane. It has been measured for 0.9 ML of Co. The three variants of the herringbone reconstruction are observed at $\pm 120^\circ$ and one can define the rectangular elementary unit cell of the reciprocal space. The narrow intra-row peak (01) and the broad inter-row peak (20) are clearly evidenced, as well as the (11) et (21) crossed peaks. From Ref. [32].

3D characterization of reciprocal space of Co/Au(111) by GISAXS. In order to fully characterize the super-crystal of Co nanostructures, a mapping of the reciprocal space has been performed at the nanometer scale. In Fig. 142 a map of the reciprocal space in the surface plane is shown for a deposit of 0.9 ML of Co, i.e. for half-coverage of the surface. This map results from 85 GISAXS images measured at different azimuths, rotating the sample by step of 1° . The intensity at $q_z \approx 0$ (i.e. at the Yoneda peak) has been extracted for each GISAXS images. The sixfold symmetry is in agreement with the threefold symmetry of the surface combined with the Friedel law $I(\mathbf{q}) = I(-\mathbf{q})$ (see Section 6.2.7) which applies for $q_z = 0$ [37]. Let us consider the contribution of only one variant of the surface reconstruction. From the schematic drawing of the unit cell depicted on Fig. 143c the position of the different peaks can be assigned. The main peak arises from the intra-row spacing (01), narrow and intense (Fig. 142). The second one is given by the inter-row spacing and is much broader. It is called (20) in agreement with the pattern of the unit cell which is statistically centered along the $\langle 1\bar{1}0 \rangle$ direction. The (10) and (30) peaks are forbidden in agreement with the previous remark. From these simple arguments the mean position of the Co nanostructure inside the unit cell reads (\bar{K}, y) where \bar{K} is the mean inter-row spacing and y has to be determined (see Fig. 143c). This preliminary analysis gives some insight into the structure of the unit cell of Co nanostructures, however due to disorder much caution is necessary and a quantitative analysis is mandatory to go further on.

Modeling and quantitative analysis of the growth of Co/Au(111). In order to calculate the intensity scattered by the network of Co

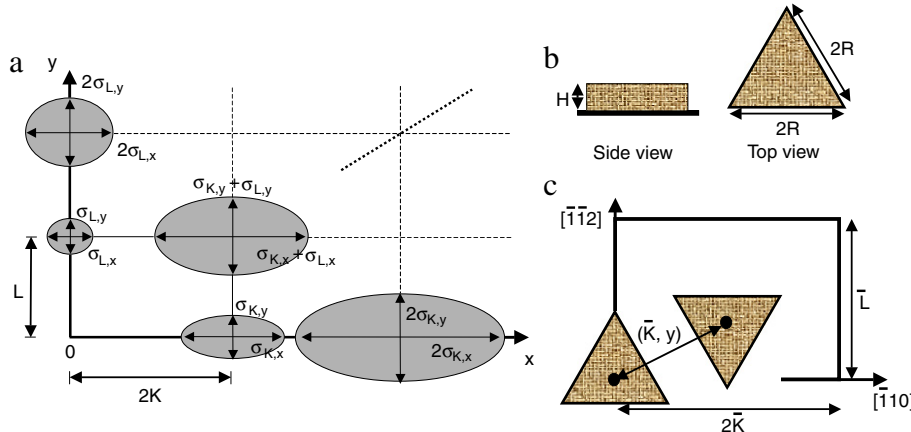


Fig. 143. (a) Sketch of the probability density of the first neighbor's distance in the 2D paracrystal model. The gray areas bound the most probable areas of the probability distribution. $2\bar{K}$ and \bar{L} are the mean distances between the nodes. $\sigma_{K,x}$, $\sigma_{K,y}$, $\sigma_{L,x}$ and $\sigma_{L,y}$ are the standard deviation of the nearest neighbor distance distributions. In the paracrystal framework, the disorder propagates in a cumulative way from nodes to nodes. (b) Shape and size of the Co nanostructures. (c) Rectangular unit cell of the Co nanostructures network. From Ref. [32].

nanostructures a model is built relying on the above analysis of the growth of Co on Au(111) and previous STM images (e.g. Fig. 140).

- The spatial organization is modeled by two perpendicular paracrystals [42] (see Section 6.3.4) which describe the intra-row and inter-row spacings (Fig. 143a). In the framework of this model, both directions are independent (ideal paracrystal). The probability laws of the distances between first neighbors are bidimensional with a Gaussian shape and characterized by the mean distances (\bar{L} and $2\bar{K}$) and the standard deviation ($\sigma_{K,x}$, $\sigma_{K,y}$, $\sigma_{L,x}$ and $\sigma_{L,y}$).
- The unit cell is built by two nanostructures of triangular shape (see Fig. 143b). One is located at the node of the lattice and the other one, rotated by 180° , is close to the center of the unit cell (\bar{K}, y) (Fig. 143c). The fluctuations of positions inside the unit cell are modeled by a Debye–Waller type disorder.

To fit the parameters of the model, cross sections of the GISAXS images have been extracted. Then the parameters are fitted minimizing the total χ^2 . As an example, let us consider the cases of 0.2 and 1 ML of Co deposited at RT (see Fig. 144a–f and g–l). Two GISAXS patterns have been measured for both deposits with the X-ray beam impinging in the main azimuthal directions $\langle 1\bar{1}0 \rangle$ and $\langle 11\bar{2} \rangle$. The extracted cross-sections are shown with dotted lines. The parameters are fitted simultaneously and finally a GISAXS image is simulated and compared to the experimental one (see for instance Fig. 145).

The morphological parameters of the Co network are shown in Table 1. First the relative uncertainty on the parameters of the 2D-paracrystal is much smaller (a few %) than the uncertainty on the Co dots size and position in the unit cell (20%). The mean inter-row and intra-row distances are: $2\bar{K} = 16.9$ nm and $\bar{L} = 7.7$ nm and the standard deviations are approximately constant. Therefore we confirm that the spatial organization is controlled by the surface reconstruction of Au(111) which induces preferential nucleation sites. The size and position of the Co dots are in agreement with previous STM studies until half-coalescence. The small y value shows that the inner Co dot is close to the edge of the unit cell (typical STM image Fig. 140c).

Beyond 1 ML of deposit, the fit of the parameters does not give reliable values revealing that the same modeling is not suitable to describe the observed GISAXS pattern beyond coalescence.

Beyond coalescence of Co nanostructures. Experimentally an increase of the total intensity of the scattering rods is observed until 2 ML and a persistent signal even for a continuous thin film of Co (coverage >8 ML) [497]. Moreover the FWHM of the scattering rods parallel with the surface plane does not broaden indicating that the order quality is preserved at the coalescence of the nanostructures (see Fig. 146). Using a simple model, and considering 2 ML high dots, the total intensity should decrease from 1 ML of deposit and give zero intensity at the coalescence stage (2 ML) when the film is continuous. To understand this experimental result, a topographic analysis of STM data has been performed by O. Fruchart et al. [497,32]. It is shown that a residual roughness still exists on the surface after coalescence of the Co dots with the same periodicity as the surface reconstruction of Au(111). The calculation of the GISAXS pattern allows one to conclude that some intensity should be measured until 4 ML of Co deposit. However, as a significant signal is measured for a much thicker film, the origin of the signal cannot be assigned only to the topography. The intensity may arise from the underlying Au substrate. This latter may be strained periodically by the Co dots and since Au has a much larger electronic density than Co it may give a significant contribution to the scattering. Other effects such as interdiffusion are also possible since Au adatoms are very mobile at RT and the surface energy of Au is much smaller than the Co one. To check these hypotheses, anomalous GISAXS measurements have been performed in order to discriminate the contributions of Co and Au in the scattering rods.

• Experimental method of Anomalous GISAXS [32]

The principle of anomalous GISAXS is to measure the intensity scattered at different energies around an absorption edge of a chemical element of the sample. This modifies its scattering factor giving the opportunity to extract the structure factor and phase shift of each compounds assuming that preliminary absorption calibrations have been performed. GISAXS images have been collected at 9 energies around the Co-K edge (7.709 keV). In the framework of the DWBA and assuming that Co nanostructures have a small height and the depth of the electronic density variations of Au are small enough (<1 nm), the total intensity reads approximately (see Section 6.2.8):

$$\frac{d\sigma}{d\Omega}(\mathbf{q}_1, E) \simeq |t_{01}(\alpha_i)t_{01}(\alpha_f)|^2 \\ |F_{Co}^0(\mathbf{q}_1) + F'_{Co}(\mathbf{q}_1, E) + iF''_{Co}(\mathbf{q}_1, E) + F_{Au}^0(\mathbf{q}_1)e^{i\varphi}|^2 \quad (199)$$

where $F_{Co}^0(\mathbf{q}_1)$ and $F_{Au}^0(\mathbf{q}_1)$ are the Thompson scattering form factors of the Co nanostructures and the Au substrate

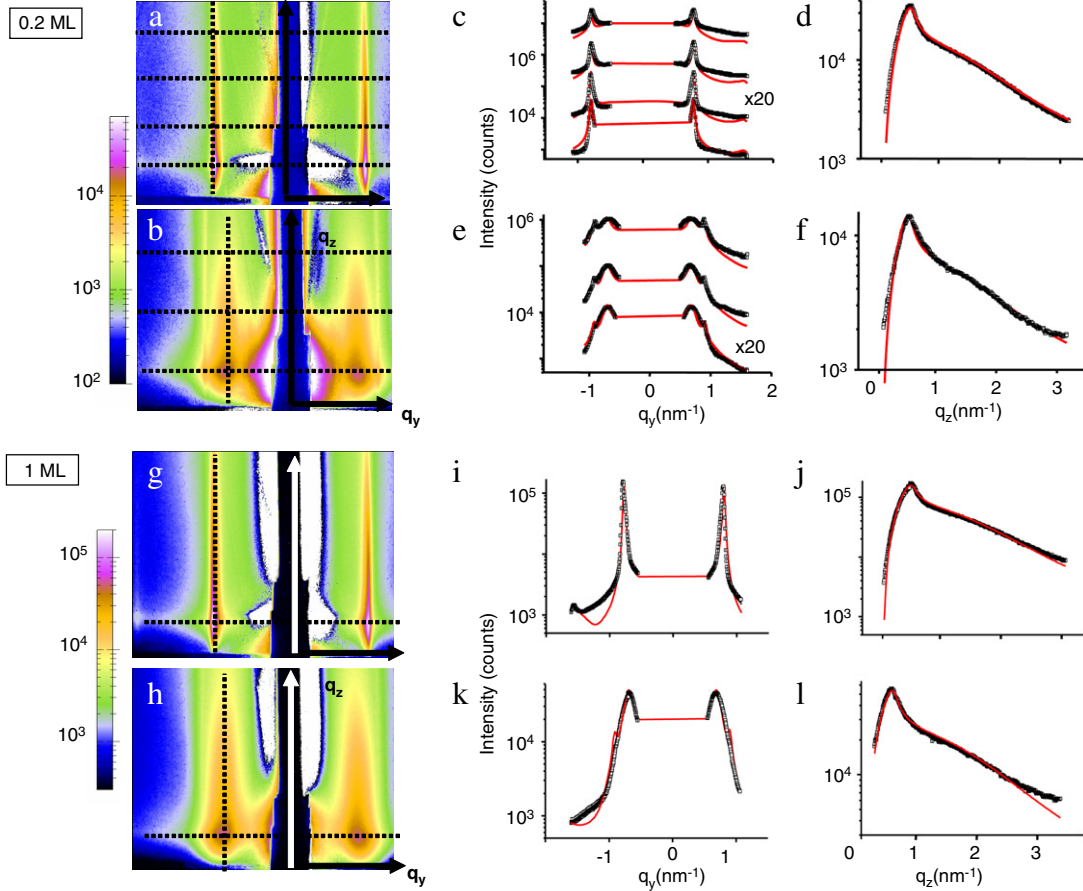


Fig. 144. GISAXS patterns and cut of intensities for a deposit of 0.2 ML of Co on Au(111) for an incident beam along $\langle 1\bar{1}0 \rangle$ (a,c,d) and $\langle 11\bar{2} \rangle$ (b,e,f) azimuths. The dotted lines show the positions of the cross sections extracted for the fit displayed on the right of the image (q_{\parallel} , c,e) and q_{\perp} (d,f) cuts. The full line corresponds to the fit while the squares are the data points. From (g) to (j), same as from (a) to (f) but for 1 ML of Co on Au(111). Adapted from Ref. [32].

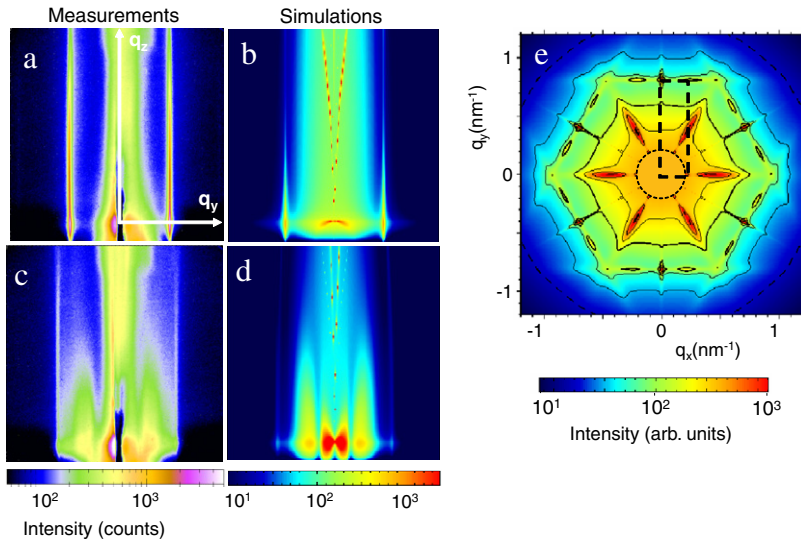


Fig. 145. For 0.3 ML of Co: (a) and (b) GISAXS patterns and their simulations for the beam along the $\langle 1\bar{1}0 \rangle$ direction. (c) and (d) Same as (a,b) but with the beam along the $\langle 11\bar{2} \rangle$ direction. (e) Corresponding simulation of a map of the reciprocal space in the surface plane ($q_z = 0$), the agreement with Fig. 142 is remarkable. From Ref. [32].

respectively. $t_{01}(\alpha_i)t_{01}(\alpha_f)$ are the transmission functions in incidence and in emergence while $\mathbf{q}_1 = \mathbf{k}_{f,1} - \mathbf{k}_{i,1}$ is the wave vector transfer inside the substrate. $F'_{\text{Co}}(\mathbf{q}_1, E)$ and $F''_{\text{Co}}(\mathbf{q}_1, E)$ are the anomalous contributions of the Co nanostructures. φ is the phase shift between Co and Au arising from the different positions of the scatterers (see Fig. 147a).

- Experimental results and analysis

The experimental measurements have been performed for a deposit of 2 ML. At this stage, the Co dots have just coalesced in the intra-row direction [497,498] and therefore the scattering rod's intensity should be small whereas it is a maximum suggesting a possible role of Au. The scattering

Table 1

Results of the quantitative analysis of the GISAXS images. The parameters of the spatial organization are first presented (paracrystal) and then the parameters of the unit cell.

Co amount (ML)	Paracrystal parameters					
	$2\bar{K}$ (nm)	\bar{L} (nm)	$\sigma_{K,x}$ (nm)	$\sigma_{K,y}$ (nm)	$\sigma_{L,x}$ (nm)	$\sigma_{L,y}$ (nm)
0.2	16.82 ± 0.20	7.68 ± 0.01	2.34 ± 0.13	0.99 ± 0.05	0.83 ± 0.05	0.66 ± 0.02
0.3	16.89 ± 0.11	7.66 ± 0.01	2.34	1	0.70 ± 0.04	0.63 ± 0.02
1	16.90 ± 0.06	7.69 ± 0.01	2.37 ± 0.03	1.01 ± 0.01	0.86 ± 0.02	0.66 ± 0.01

Co amount (ML)	Unit cell parameters					
	R (nm)	σ_R/R	H (nm)	y (nm)	Δ (nm)	Thickness (ML)
0.2	1.96 ± 0.37	0.46 ± 0.15	0.41	0.12 ± 0.08	0.13 ± 0.03	0.25 ± 0.1
0.3	2.84 ± 0.40	0.43 ± 0.16	0.42	0.10 ± 0.03	0.05 ± 0.02	0.4 ± 0.15
1	3.01 ± 0.14	0.1	0.39	0.098 ± 0.016	0.065 ± 0.005	0.5 ± 0.05

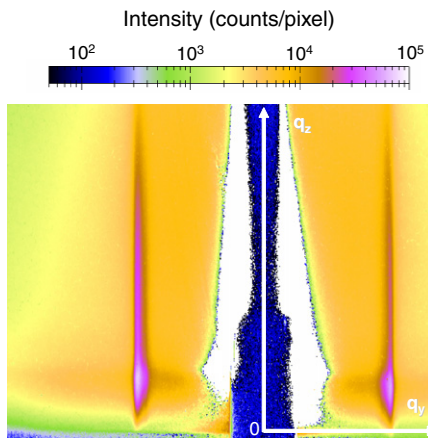


Fig. 146. GISAXS image measured for 6 ML of Co on Au(111). The incident beam is along the $(\overline{1}\overline{1}0)$ direction. Very narrow and intense scattering streaks are still visible with the initial periodicity of the Co dots network. However, there is a large background scattering compared to images measured for less than 1 ML of Co (from Ref. [32]).

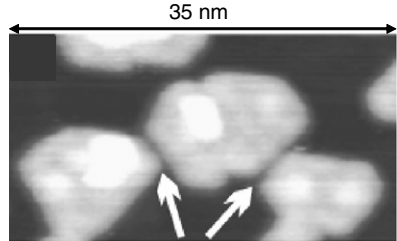


Fig. 148. STM image of 1.1 ML of Co on Au(111). The arrows show trenches between the Co nanostructures. They correspond to further grain boundaries (From Ref. [497]).

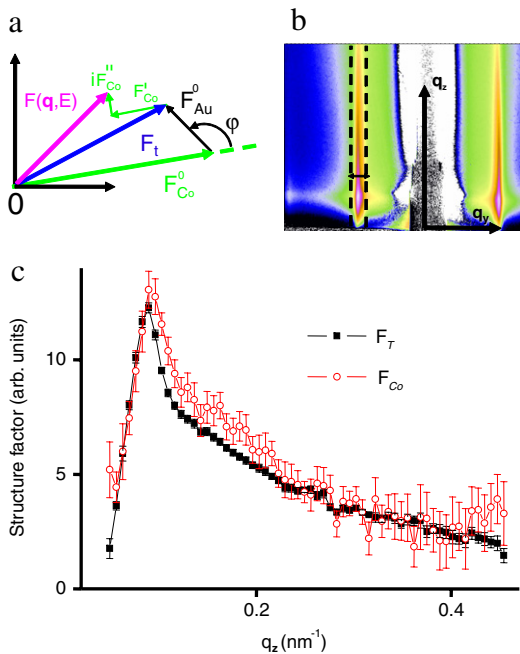


Fig. 147. (a) Principle of anomalous scattering. $F(\mathbf{q}, E)$ and $F_t(\mathbf{q})$ are respectively the total scattering factor, and the Thompson scattering factor, i.e. without the anomalous contribution. (b) The intensity is extracted from the scattering rod of the intra-row periodicity at the coalescence stage. (c) The total structure factor (F_t) of the scattering rod of the intra-row distance is shown as well as the contribution of Co as deduced from the fit (F_{Co}). The Co term is clearly predominant. From Ref. [32].

rods have been analyzed in the direction perpendicular to the surface integrating the signal parallel with the surface plane to increase the signal/noise ratio (see Fig. 147b). The results show that most intensity comes from Co (see Fig. 147c). The Au contribution is small, within the error bar, and cannot explain such a large intensity at the coalescence. The hypothesis of a periodic interdiffusion of Au or strain field inside the substrate can be ruled out. But as the contribution of Co cannot be only topographic, the most likely hypothesis is the contribution of grain boundaries resulting from the partial coalescence of the Co nanostructures. The grain boundaries keep the initial periodicity of the Co dots network and give rise to narrow scattering rods as observed experimentally. This is supported by high resolution STM measurements [30,497] revealing the presence of defects at the coalescence due to the non-commensurability of the Co and Au crystallographic lattices (see Fig. 148). This result is also supported by GIXD measurements [32].

Growth of Co nanopillars [496,497]. The ordered growth of Co dots on Au(111) has been stimulated by new phenomena arising from the reduction of the dimensions as well as the growth mechanisms in ordered systems. However such nanostructures cannot be used in magnetic devices because they are too small and thus exhibit superparamagnetic properties at low temperatures. To increase the size of the Co nanostructures it has been proposed to make Co pillars by sequential deposition. The basic idea has been first reported by Xie et al. [499] for semiconductors. They have observed that dots from successive layers tend to stack vertically, due to strain modulation. The in-plane organization evolves toward a 3D organization. This method has been applied to the growth of Co pillars on Au(111) by O. Fruchart et al. (see Ref. [496]). The principle is to alternate many times the growth of a fraction of 1 ML of Co and to complete the layer with Au to have a smooth surface. The growth of Co pillars has been characterized by indirect methods, i.e. height analysis by STM and pillars volume estimation by magnetic measurements. To give a more direct proof of the growth and the ordering of Co pillars, *in situ* GISAXS measurements have been performed. The different steps are: (i) growth of ordered Co dots

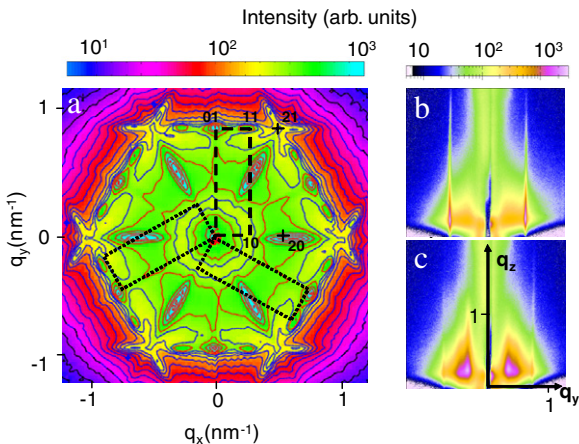


Fig. 149. (a) Map of the reciprocal space of pillars at $q_z = 0$ (from Ref. [32]). (b) and (c) GISAXS images for an incident beam aligned respectively in the $\langle 1\bar{1}0 \rangle$ and in the $\langle 1\bar{1}\bar{2} \rangle$ directions.

on Au(111) dots at RT (0.4 ML); (ii) subsequent growth of Au (3.6 ML) at 425 K to have a smooth surface of 2 ML; (iii) sequential growth of Co (0.4 ML) and Au(0.6 ML) at 500 K (15 times). As the number of sequences increases the scattering rods from the intra row and inter row distances are more intense. This reveals that the volume of matter of the pillars continuously increases. Moreover the scattering rods are very narrow thus the order is preserved during the process. In Fig. 149 are shown two GISAXS images of the pillars network and a map of the reciprocal space in the surface plane ($q_z = 0$) for 15 ML of Co and Au. The in-plane peaks shows that the order has not been destroyed and the map can be successfully compared to the previous one obtained for 0.9 ML of Co/Au(111) (see Fig. 142). The same peaks can be measured at the same positions.

Conclusion. GISAXS has been applied to the study of the model system Co/Au(111). In the submonolayer regime the unit cell and the spatial ordering of the Co nanostructures have been characterized. At the coalescence and beyond anomalous GISAXS have shown (with complementary GIXD and STM) that a 2D network of grain boundaries persists for a 8ML-thick film of Co. At last a direct proof of the growth of Co nanopillars by sequential deposition of Co and Au is put in evidence. This Co/Au(111) example highlights the capability of the GISAXS technique to probe buried density fluctuations.

9.4.2. The ordered growth of Co on a kinked vicinal surface of Au(111)

The growth of Co on Au(111) is well ordered over areas of $100 \times 100 \text{ nm}^2$. However at larger scales, the three-fold symmetry of the surface implies that other variants of the herringbone reconstruction exist on the surface thus limiting the long-range order (see Fig. 140a). Moreover defects, mainly steps, affect the coherence of the network. The use of vicinal surfaces allows one to solve both drawbacks of the Au(111) surface. Breaking the symmetry, only one variant of the reconstruction is favored and steps which were the main defects are now ordered and participate to the patterning of the surface. The first studies of the growth of Co on vicinal surfaces of Au have been performed in the group of Sylvie Rousset [495,500]. They have put in evidence the crucial role of temperature [501] in the long range order quality of the Co dots network. A campaign of GISAXS experiments has been performed on the SUV instrument of the BM32 beam line (ESRF) to study the growth of Co on a slightly kinked vicinal surface of Au(111). The complementarity between GISAXS and STM was clearly put in evidence.

The kinked Au(677) surface – A combined STM and GISAXS study. The kinked vicinal surface of Au(111) (see Fig. 150a) is made of a regular staircase of monoatomic steps (0.235 nm). Contrary to the nominal Au(111) surface only one variant of the reconstruction is observed due to an energetic raised degeneracy thanks to symmetry breaking. The reconstruction is put in evidence by STM showing a surface corrugation with double lines in the $\langle \bar{2}11 \rangle$ direction. They are clearly visible subtracting the vicinal staircase on the STM images. They probably reveal the presence of stacking faults between domains of fcc and hcp crystallographic structures as already seen in the case of the Au(788) surface [495]. The surface under study is close to a Au(677) surface but the step edges are slightly misoriented with respect to the $\langle 0\bar{1}1 \rangle$ direction. This is revealed by the occurrence of kinks at the step edges as seen by STM (Fig. 150a). A more precise analysis shows that they are not monoatomic kinks, but they pack periodically and make tilted and diffuse areas. Subtracting numerically the vicinal staircase on the STM images to highlight fine details of the surface morphology, it seems that the kinks are trapped in between the stacking fault lines, inside fcc stacking areas. This behavior has already been observed on the Au(111) surface by Repain et al. [502]: the stacking fault lines cross only the $\{111\}$ step edges and never the $\{100\}$. The kinks are therefore excluded from the hcp areas and pack together in the fcc areas.

To obtain statistical information on the surface morphology, the kinked Au(677) surface was studied by GISAXS. A map of the reciprocal space has been measured in the small-angle regime. GISAXS patterns have been collected at different azimuth rotating the sample by steps of 1° over a large angular range (140°). It results in a tomographic measurement of the reciprocal space close to the origin. On Fig. 151, a projection of the GISAXS intensity in the surface plane is shown. The scattering rods from the step network (10) and (20) are visible, as well as those arising from the kink long-range order, (01) and (02), turned of $\pi/2 - \varepsilon$; where the angular shift ε arises from the rotation of the mean step edge orientation induced by the kinks. Higher order scattering rods coming from both periodicities (11) and (12) have also been measured. This last point is interesting because it tells us that the surface cannot be described as the simple superposition of two 1D networks (steps and kinks). The presence of cross terms implies developing a global model for the calculation of the diffuse scattering. However one may wonder if the GISAXS intensity comes from the surface topography and/or the surface reconstruction which modifies also the electronic density contrast. GISAXS measurements performed on the Au(111) surface did not reveal any signal from the reconstruction. Assuming that the dilatation effects induced by the reconstruction on Au(111) and Au(677) are similar, the kinks are probably responsible for the diffuse scattering observed at the periodicity of the reconstruction. Thus the intensity scattered by the kinked Au(677) surface can be evaluated only by a topographic model.

The paracrystal model: A tool to describe kinked vicinal surfaces [235, 215,489]. The calculation of the intensity scattered by surface morphologies is a classical problem in surface science. In the case of a perfectly ordered surface, only the calculation of the structure factor of the unit cell which repeats on the surface is necessary. In the non-ideal case, a statistical description of the surface is necessary. Since the pioneer work of Lent and Cohen [503] and Pukite et al. [504], many analytical results have been obtained [505, 506]. However until now these calculations were based on a 1D description of the surface topography and focused on Spot Profile Analysis Low Energy Electron Diffraction (SPA-LEED) [507,508], Helium Atom Scattering (HAS) [136,509,510] or Reflection High Energy Electron Diffraction (RHEED) [511] techniques. A method based on the paracrystal model allows one to extend older works in the framework of X-ray scattering considering a 3D description

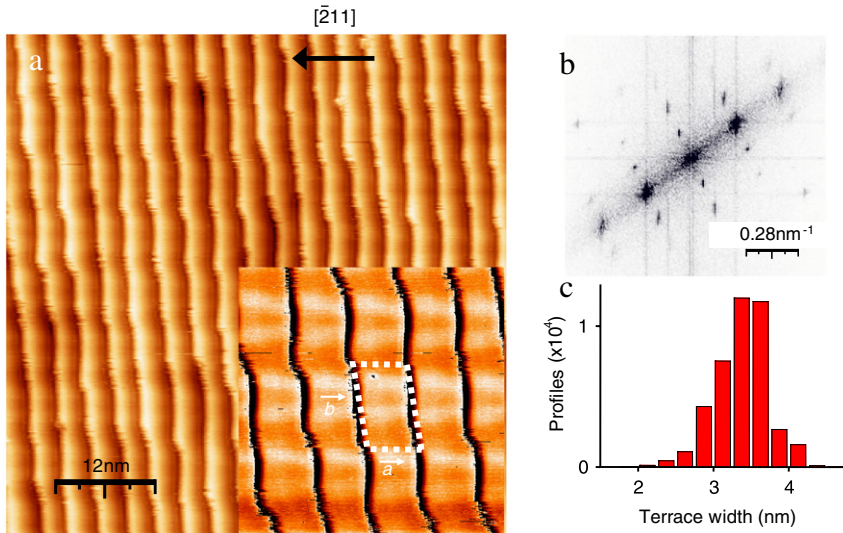


Fig. 150. (a) STM image of the kinked Au(677) surface. Inset: Zoom on the surface where the vicinal staircase has been subtracted numerically to highlight the double stacking fault lines of the reconstruction. **a** and **b** are the base vectors of the unit cell. The kinks are visible as diffuse and tilted areas. The angular offset ε between the average step direction and the [011] direction is $5^\circ \pm 1^\circ$. (b) Fourier transform of an image. The periods of the step network and the reconstruction/kinks are visible. (c) Histogram of the terrace width performed over 20 000 profiles. From Ref. [489].

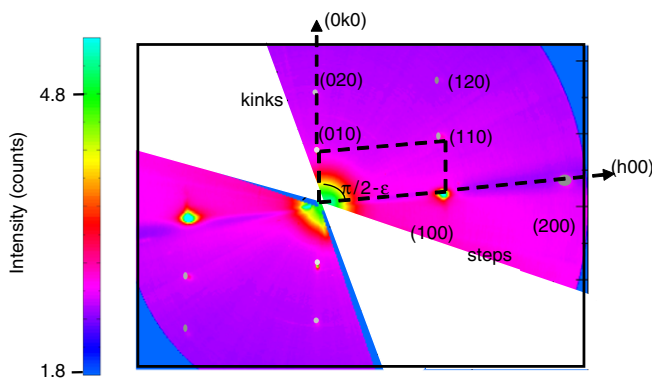


Fig. 151. Experimental map of the reciprocal space in the surface plane of the kinked vicinal surface of Au(111). The angular offset ε deduced from this map is $\varepsilon = 4.95^\circ$ (from Ref. [489]).

of the surface morphology [235,215,489]. Details of this approach are given in the following for the kinked vicinal surface. To model the surface morphology, a fixed step height h and a fixed kink size a are first assumed in order to simplify the calculation. We define an elementary building block which is a parallelepiped of height h and lateral size a . In the y direction it is semi-infinitely extended (Fig. 152). The calculation of the form factor of this elementary object reads:

$$F_{\text{kinked vicinal}}(\mathbf{q}) = \int_{-h/2}^{h/2} e^{iq_z z} dz \int_{-k/2}^{k/2} e^{iq_x x} dx \int_{-\infty}^0 e^{iq_y y + \mu y} dy \\ = \frac{-4i}{q_x q_y q_z} \sin(q_z h/2) \sin(q_x k/2). \quad (200)$$

To build a whole crystal and its surface, this elementary object is ordered in two main directions: along the mean step edge and perpendicular to the steps to take into account possible correlations between kinks of neighboring steps. This can be done in the framework of the ideal 2D paracrystal model considering a probability law of the distance between nearest neighbor kinks in the two main directions. This hypothesis is questionable because kinks interact via long-range interactions (e.g. elastic interaction). This problem exists also for steps for which there

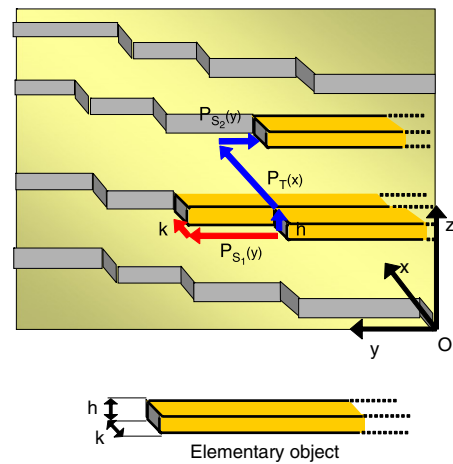


Fig. 152. Sketch of the principle of the construction of a kinked vicinal surface (fixed kink and step dimensions). Elementary object: a parallelepiped of height h , width k and semi-infinitely extended in the y direction. The surface is built similarly to the vicinal surface adding step by step elementary objects along two directions: along the step edges and perpendicular to the steps. A probability law $P_{S_1}(y)$ provides the distance distribution between the kinks at the step edges and two probability laws give the terrace width $P_T(x)$ and the relative displacement in the y direction of two neighboring kinks at adjacent step edges, $P_{S_2}(y)$. From Ref. [489].

are correlations with far steps arising from elastic interactions. However, this makes the analysis much more complex and our purpose is to calculate the intensity scattered by a kinked vicinal surface assuming size distributions for the terrace width and the kink–kink distance. In summary, we are in the simple case where an elementary object is ordered along two directions which are modeled by the ideal 2D paracrystal model. In the direction parallel with the mean step edge, the interference function reads:

$$S_{||}(q_x, q_y) = \text{Re} \left\{ \frac{1 + e^{iq_x k} \tilde{P}_{S_1}(q_y)}{1 - e^{iq_x k} \tilde{P}_{S_1}(q_y)} \right\}, \quad (201)$$

where $\tilde{P}_{S_1}(q_y)$ is the characteristic function of the kink–kink distance along the step edge. For the direction perpendicular to the

step edges:

$$S_{\perp}(q_x, q_y, q_z) = \operatorname{Re} \left\{ \frac{1 + e^{iq_z h} \tilde{P}_T(q_x) \tilde{P}_{S_2}(q_y)}{1 - e^{iq_z h} \tilde{P}_T(q_x) \tilde{P}_{S_2}(q_y)} \right\}, \quad (202)$$

where $\tilde{P}_T(q_x)$ and $\tilde{P}_{S_2}(q_y)$ are respectively the characteristic functions of the terrace width distribution and the characteristic function of the distribution of distances of the first neighbor kinks along a step edge (Fig. 152).

The kinked vicinal surface of Au(677) under study is a bit more complex as monoatomic kinks are packed together. They are modeled as a large kink and a size distribution $P_K(x)$. The previous result can be generalized for any kink size distribution (fixed step height):

$$I(q_x, q_y, q_z) = \left[\frac{2}{q_x q_y q_z} \right]^2 \operatorname{Re} \left\{ \frac{(1 - \tilde{P}_{S_1})(1 - \tilde{P}_K(q_x))}{1 - \tilde{P}_{S_1} \tilde{P}_K(q_x)} \right\} \\ \times \operatorname{Re} \left\{ \frac{(1 - e^{iq_z h})(1 - \tilde{P}_T(q_x) \tilde{P}_{S_2}(q_y))}{1 - e^{iq_z h} \tilde{P}_T(q_x) \tilde{P}_{S_2}(q_y)} \right\}. \quad (203)$$

The total number of size distributions is four. To give explicit expressions they are modeled by Gaussian laws characterized by their first two moments (mean size and standard deviation). From this model it is possible to extract from the GISAXS data, the kink size distribution $P_K(x)$, the kink–kink distance along the step edges $P_{S_1}(y)$, the terrace width distribution $P_T(x)$ and the distribution of the displacement of the kink position along (Oy) on a neighbor step edge, $P_{S_2}(y)$.

Measurements and simulations. The principle of the analysis is to fit the experimental data with the previous model (see Eq. (203)). As the model is able to reproduce all the features of the reciprocal space, *i.e.* the scattering rods from the steps, the kinks and the cross terms, all the parameters have been fitted simultaneously using all the data set. GISAXS patterns have been collected at many azimuths, giving a 3D picture of the reciprocal space and more than 30 cross sections have been extracted and fitted at the same time (Fig. 153). Such a huge amount of data constrains the parameters of the model. For clarity, some results for each scattering rod are given (see Fig. 154). The relative amplitude of the scattering rods is well reproduced by the model, more particularly the two orders of magnitude between the intensity of the scattering rod of the steps (10L) and the scattering rod (11L) (cross term).

Analysis of the parameters and comparison of STM and GISAXS results. From the above analysis (see Table 2), the angular disorientation of the step edge with respect to the $(\bar{1}10)$ direction is precisely 4.95° . It is comparable to the angle measured by STM ($5 \pm 1^\circ$) but with a higher precision for two main reasons: (i) any length measured by STM needs a previous calibration (*e.g.* the lattice parameter of the surface of graphite), and the thermal drift of the piezo-electric makes difficult such measurement. (ii) The disorientation angle is precisely defined on a macroscopic scale and not on a local scale. The mean terrace size, is 3.42 nm, in good agreement with the one obtained by STM. The standard deviation of the terrace width distribution is twice as small as the one deduced from the STM data. This discrepancy arises mainly from the definitions of the terrace width distributions which are different in both cases. For the STM analysis, the terrace width distribution includes the fluctuations of the step–step distance (assuming straight lines), the fluctuations of the kink positions as well as those arising from their sizes. A quantitative analysis of the GISAXS data allows one to distinguish between all these contributions, so the terrace width distribution, *i.e.* the step–step distance assuming they are straight is much narrower for the GISAXS analysis than in the case of the STM analysis.

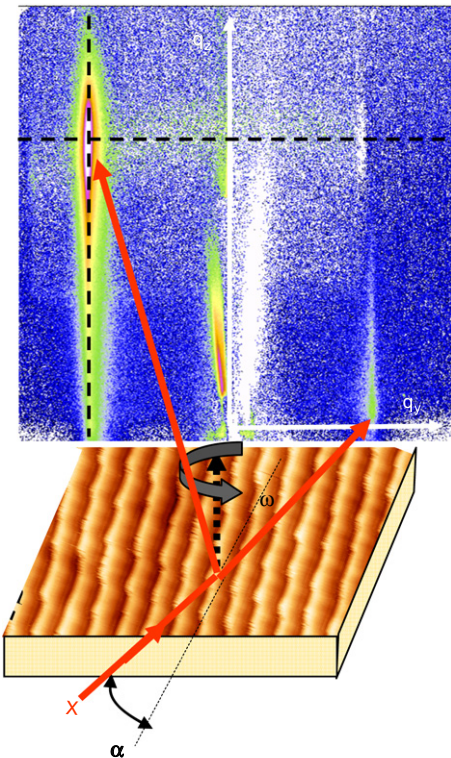


Fig. 153. Example of a GISAXS pattern. α is the incident angle perpendicular to the surface, ω is the in-plane orientation (azimuth angle) of the incident X-ray beam with respect to the average step edge direction. Here the X-ray beam is offset by $\omega = 6^\circ$ with respect to the mean step edge direction. The scattering rod arising from the step network crosses the Ewald sphere at wide out-of-plane angles. Two cross sections (dotted lines) of intensity are extracted from this 2D map to fit the parameters of the model (from Ref. [489]).

The specific parameters that we can deduce from the GISAXS analysis are the following: the kink size is about 3 ± 1 monoatomic kinks which are packed together. They are well ordered along two directions: (i) perpendicular to the step edge, they are at a distance of 3.42 nm (mean terrace size), with a standard deviation of a monoatomic distance *i.e.* 0.23 nm. The displacement along neighbor step edges is centered around zero and the fluctuations are very small (0.3 nm). This result illustrates the crucial role of the reconstruction which induces the long-range ordering of the kinks from step to step. (ii) In the direction parallel with the step edges, the kinks are ordered according to the period of the reconstruction, 8.04 nm, and the standard deviation is 0.62 nm. The period of the reconstruction is larger than the one observed on Au(111) vicinal surfaces with smaller miscut angles [500]: 6.3 nm, 7 nm, 7.2 nm, 8.0 nm respectively for the Au(111), (11, 12, 12), (788) and (677) surfaces. This reveals that steps, and at some points kinks, give additional possibilities to the surface to relieve the surface stress [512,513] and therefore the periodicity increases.

Growth of Co on the kinked Au(677) surface studied by GISAXS. The GISAXS study of the Co growth has been performed in real-time. A qualitative understanding of the evolution of the intensity as a function of time gives some insight into the growth process. Initially the intensity decreases on the (10L) scattering rod (step network) and increases on the (01L) scattering rod (kink network). Only interference effects between the waves scattered by the surface and the Co nanostructures can explain these effects: the waves scattered by the Co nanostructures interfere destructively with that scattered by the steps and constructively with that scattered by the kinks. Therefore the Co nanostructures grow at the step edges and in between two kinks which is in agreement with STM images of the growth of Co on Au(788) [514]. To extract

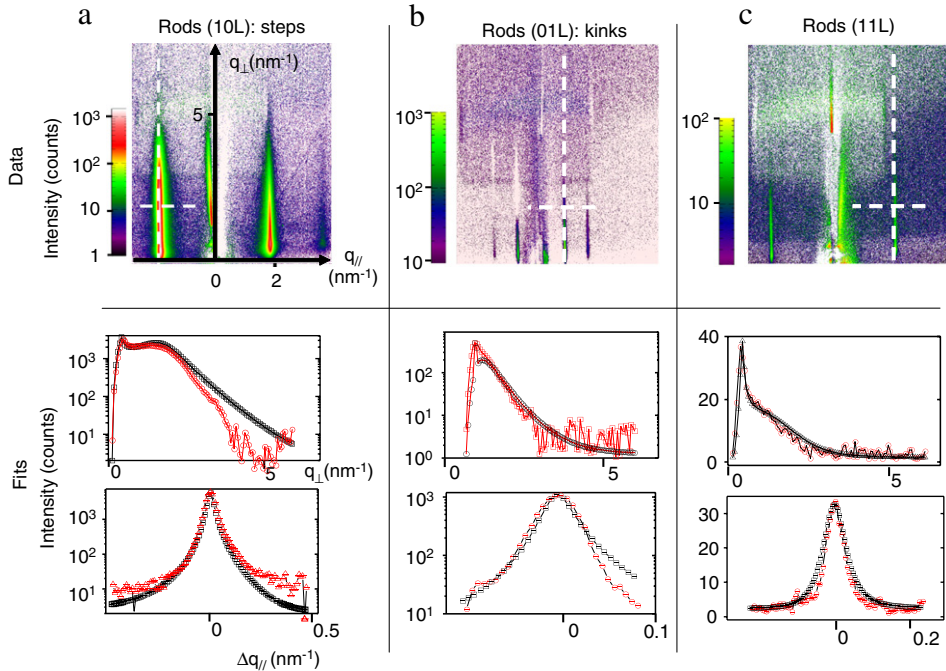


Fig. 154. Top: experimental GISAXS images of the step network (a), kink network (b) and cross term (c). Bottom: fits (black) and data (red) of the cross sections parallel with and perpendicular to the surface plane. The corresponding cross-sections are shown on the GISAXS images (dotted lines). Adapted from Ref. [489]. (For interpretation of the references to colour in this figure legend, the reader is referred to the web version of this article.)

Table 2

Topographic parameters of the kinked Au(677) surface deduced from the quantitative analysis of GISAXS data. The step height is fixed at 0.235 nm.

Kink size	Kink-kink distances							
	Step P_{S_1}		Terrace P_T		Kink P_{S_2}			
Width (nm)	Distribution (nm)	Height (nm)	S_1 (nm)	σ_{S_1} (nm)	T (nm)	σ_T (nm)	S_2 (nm)	σ_{S_2} (nm)
0.7	0.35	0.235	8.04	0.62	3.42	0.23	0	0.3

more information on the Co growth, the interference effects have to be interpreted more precisely. A statistical model of the surface topography and the Co dots has been developed to simulate the GISAXS patterns. However, the previous model developed for the bare surface, cannot be applied for supported Co nanostructures in a straightforward way. The basic idea is to use an other elementary object. One can use a semi-infinite parallelepiped with a Co dot on top at a given position but considering no size distribution (fixed kink size, fixed step height and fixed Co nanostructure shape and size). That way the surface is entirely built considering this elementary object and two main directions for the periodicity. The intensity reads:

$$I(q_x, q_y, q_z) = \left| \frac{-4i}{q_x q_y q_z} \sin(q_z h/2) \sin(q_x k/2) + F_{Co}(q_x, q_y, q_z) e^{i(q_x V - q_y U)} \right|^2 \\ \times \text{Re} \left\{ \frac{(1 + e^{iq_x k} \tilde{P}_{S_1}(q_y))}{(1 - e^{iq_x k} \tilde{P}_{S_1}(q_y))} \right\} \\ \times \text{Re} \left\{ \frac{1 + e^{iq_z h} \tilde{P}_T(q_x) \tilde{P}_{S_2}(q_y)}{1 - e^{iq_z h} \tilde{P}_T(q_x) \tilde{P}_{S_2}(q_y)} \right\} \quad (204)$$

where F_{Co} is the shape factor of the Co dots and U and V are their relative positions from the kink site respectively along the (Oy) and (Ox) directions (Fig. 155). The Co dots are modeled as cylinders with an elliptic base and a fixed height (two monolayers) (Fig. 155).

Table 3

Morphological parameters of the Co nanostructures deduced from the fit. H has been fixed at 0.4 nm (2 ML height) and U at 4.02 nm (i.e. the Co nanostructures are in between the kinks).

Deposit (ML)	D (nm)	L (nm)	H (nm)	U (nm)	V (nm)
0.2	1.2	1.2	0.4	4.02	0.25
0.4	1.4	2	0.4	4.02	0.35
0.6	1.6	2.7	0.4	4.02	0.4
0.8	1.7	3.3	0.4	4.02	0.45

The shape factor of the Co dots is:

$$F_{Co}(q_x, q_y, q_z) = 2\pi DLH \frac{J_1 \left(\sqrt{(q_x D/2)^2 + (q_y L/2)^2} \right)}{\sqrt{(q_x D/2)^2 + (q_y L/2)^2}} \\ \times \frac{\sin(q_z H/2)}{q_z H/2}, \quad (205)$$

where J_1 is the Bessel function of first order.

The results of the fits show a good agreement between the simulated GISAXS patterns and the experimental ones (Fig. 156). The morphological parameters of the Co dots can be estimated as well as their position with respect to the kink sites (Table 3).

The results are also in agreement with the STM data obtained on Co/Au(788) [500]. They show that the Co nanostructures grow first at the step edges and come into the upper terrace. They are all the more anisotropic than the amount of Co deposited on the surface is large [515].

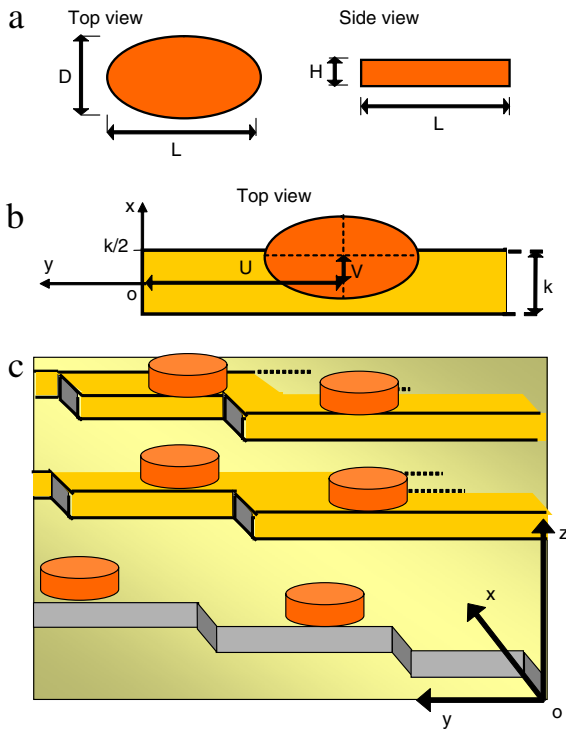


Fig. 155. (a) Co nanostructures are modeled with cylinders with an elliptic base to take into account their shape anisotropy. Their height is fixed at 2 ML. (b) The elementary object is built as the superposition of a semi-infinite parallelepiped and a Co dot on top which position can be adjusted. (c) The spatial organization is modeled by an ideal 2D paracrystal. The main directions are the step edge and perpendicular to the steps (from Ref. [489]).

Conclusion. To be able to characterize by GISAXS the self-organized growth of Co dots on the kinked vicinal Au(677) surface, it is first mandatory to describe precisely the bare surface in order to take into account the interference between the waves scattered by the surface topography and by the Co dots. For that

sake, a 3D model of the surface topography has been developed and a tomographic measurement of the intensity in the reciprocal space has been performed. The parameters deduced from the quantitative analysis of the GISAXS images are in agreement with the STM data. The long-range order of the kinks is revealed and assigned to their interaction with the surface reconstruction. They are trapped inside the fcc stacking areas of the surface, *i.e.* in between the stacking fault lines.

9.4.3. Self-organized growth of Co on a misfit dislocation network Ag/MgO(001)

This last example [488] focuses on the self-organized growth of nanostructures on a dislocation network. This approach is based on two principles: (i) dislocation networks are well ordered: the dislocation density is fixed by the energetic gain of the plastic relaxation and the cost of their creation and interaction. As the interaction is repulsive and long-range a preferential distance separating the dislocations minimizes the interaction energy. (ii) The strain field induced by the dislocations modifies the local environment of the surface atoms [442] and favors a nucleation on specific sites. In the literature dislocation networks have been used successfully for different systems such as the growth of Co, Ni or Fe nanostructures as well as the growth of Co pillars on Au(111) for which the surface reconstruction can be seen as a surface dislocation network [484,30]. Fe (resp. Ag) nanostructures have also been grown on a dislocation network made of a bilayer of Cu (resp. a monolayer of Ag) on Pt(111) [487]. However these approaches need the use of expensive single crystals of Au(111) or Pt(111) and only nanostructures of a few atomic layers high have been obtained [30].

An other approach has been proposed based on a buried dislocation network [516] but only very few experiments have demonstrated that the strain field created by buried interfacial dislocations can propagate into a film of several nanometer of thickness resulting in a surface with a nanostructuration suitable for the successive growth of ordered self-assembled nanoparticles [488]. This approach has been applied in the case of the self-organized growth of Co dots on a thin film of Ag [488]. This

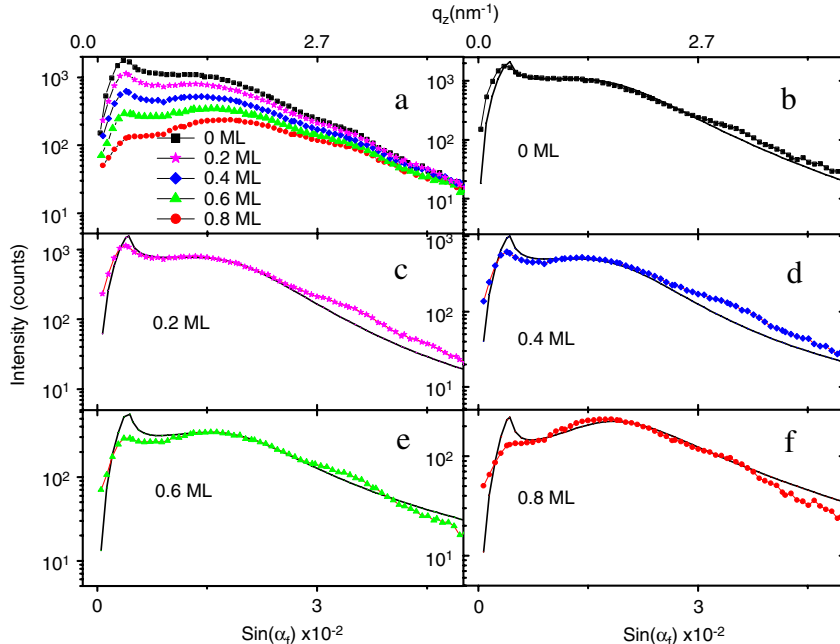


Fig. 156. Experimental data and fit of the (10ℓ) scattering rods from the steps array during the growth of Co ($\omega = 0^\circ$). The incident beam is aligned parallel with the mean step edge direction. (a) Time evolution of the scattering rods intensity integrated parallel to the surface plane. (b) to (f) Experimental data (\circ) and fit (solid line) for different amounts of Co. From Ref. [489].

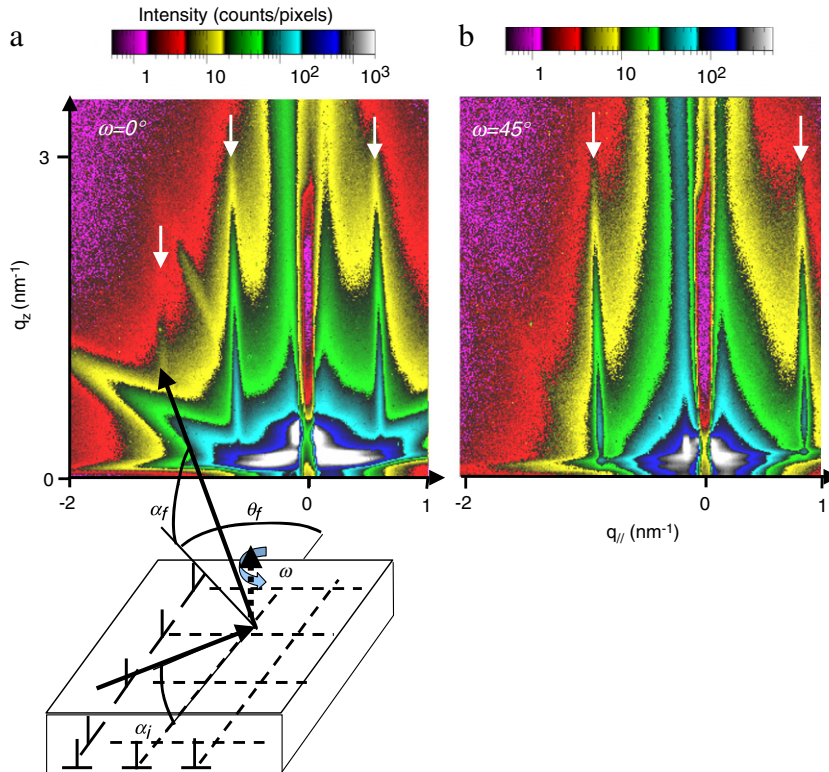


Fig. 157. (a) Sketch of the experiment and GISAXS images obtained for an incident X-ray beam oriented parallel with the $\langle 110 \rangle$ direction, i.e. at $\omega = 0^\circ$ (logarithmic intensity scale). q_{\parallel} coordinate (resp. q_z) ranges from -1 to 2 nm^{-1} (resp. 0 to 3.26 nm^{-1}). Scattering rods of the dislocation network are indicated by arrows (1st and 2nd orders). Ag(111) facets give rise to a broad scattering rod at 54° with respect to the normal to the surface. (b) same as (a) with an incident beam parallel with the $\langle 100 \rangle$ direction of MgO(001), i.e. at $\omega = 45^\circ$. Adapted from Ref. [489].

couple of materials has been chosen because the growth of Co on Ag is three-dimensional and no alloying is expected at RT [517]. To modulate the surface strain field the thin film of Ag is grown in cube-on-cube epitaxy on a MgO(001) single crystal [518,397]. As the lattice parameter mismatch is 3% between both materials the interface exhibits a coincidence site lattice of about 10 nm period that relaxes in a dislocation network [397,13]. To succeed in the self-organized growth of nanostructures, the thickness of the film must be small enough, i.e. smaller than the period of the dislocation network as theoretically predicted by isotropic and linear elasticity [516]. However the thinner the film, the larger is the stored elastic energy and the dislocation network may collapse. Therefore the thickness must be intermediate between the period of the dislocation network and the critical thickness for plastic relaxation [519].

For this system we have used the GISAXS technique to study the growth of Co nanostructures as well as buried dislocation network at the Ag/MgO interface thanks to the electronic density contrast induced by the dislocations [40,520].

The misfit dislocation network of the Ag/MgO(001) interface. Fig. 157a and b show two GISAXS images measured on a thin film of Ag on MgO(001) with an incident X-ray beam respectively parallel with the crystallographic directions $\langle 110 \rangle$ and $\langle 100 \rangle$ of MgO(001). Narrow scattering rods in the q_{\parallel} direction reveal a periodic nanopatterning in the surface plane. The extension of the intensity perpendicular to the surface (q_z) is a signature of the in-depth profile of the strain field perpendicular to the surface. The large terrace size deduced from the GIXD measurements at anti-Bragg conditions proves that the signal does not arise from surface roughness but from buried layers. The position of the scattering rods gives a period L of 10.95 nm . The fourfold symmetry, the orientation as well as the lattice parameter of the super-lattice is in agreement with that of a square dislocation

network oriented along the $\langle 110 \rangle$ directions and with a Burger vector $\mathbf{b} = \frac{1}{2}[110]$ [13]. Therefore the Ag atoms are in coincidence with those of Mg (or O) every $A = 37$ atoms. The lattice parameter of Ag deduced from the position of the Bragg peaks shows that 90% of the interfacial stress is relieved by the dislocations, which highlights the stability of the Ag film at such a small thickness. The remaining 10% stress is relaxed by a homogeneous strain field. The linear increase of the FWHM of the scattering rods in q_{\parallel} can be assigned to a cumulative disorder effect of the distance separating the dislocations. From the 1D-paracrystal model [42], the standard deviation σ , of the distance between two neighbor dislocations can be evaluated from the FWHM of the first order scattering rods: $\sigma = L \Delta q_{\parallel} / q_{\parallel} = 0.6 \text{ nm}$. A quantitative study of the dislocation network was achieved by the analysis of its scattering rods. Due to the order quality of the network, the scattering rods are the Fourier components (modulus square) in the surface plane of the dilatation field. The first and the second order scattering rods have been measured, i.e. $(\frac{1}{A}, \frac{1}{A}L)$ and $(\frac{2}{A}, 0L)$. To fit their intensity modulation, the dilatation field of the dislocation network has to be modeled. The linear and isotropic theory of elasticity applied to a perfectly ordered dislocation network predicts that the dilatation field $\theta(\mathbf{r})$ decomposes into Fourier series in each material (layer and substrate):

$$\theta_{l,s}(\mathbf{r}) = \frac{1}{4\pi^2} \sum_{\mathbf{q}_{\parallel}} \tilde{\theta}_{l,s}(\mathbf{q}_{\parallel}, z) e^{-i\mathbf{q}_{\parallel} \cdot \mathbf{r}_{\parallel}} \quad (206)$$

for which each \mathbf{q}_{\parallel} -component is damped exponentially from the interface toward the thin film $\tilde{\theta}_l(\mathbf{q}_{\parallel})$ and towards the substrate $\tilde{\theta}_s(\mathbf{q}_{\parallel})$ [521]:

$$\tilde{\theta}_l(\mathbf{q}_{\parallel}, z) = \gamma_l \exp[-z/\lambda(\mathbf{q}_{\parallel})] \quad \text{and} \quad \tilde{\theta}_s(\mathbf{q}_{\parallel}) = \gamma_s \exp[z/\lambda(\mathbf{q}_{\parallel})]. \quad (207)$$

$z = 0$ is the interface position and $\lambda(\mathbf{q}_{\parallel})$ is the attenuation length which may vary as a function of the Fourier component under consideration. The elastic constants of each materials are taken into account by the Fourier coefficients γ_l and γ_s which are fixed in the model. Rigorously, it should be also considered the strain field which is reflected by the surface (not the interface) [521]. It decreases exponentially from the surface inside the thin film. It has been dropped out because theoretically its amplitude is negligible for a 5 nm thick film.

The GISAXS calculation of the intensity scattered by a dislocation network must take into account the grazing incidence and emergence angles. In the framework of DWBA, the most adequate choice for the unperturbed system is an homogeneous thin film over the substrate without dislocation network. The wavefield inside this latter is readily obtained from the Helmholtz equation (Eq. (138)). The dielectric contrast due to the dislocation dilatation field $\theta(\mathbf{r})$ is treated as a small perturbation of the wave propagation inside the film:

$$\delta n^2(\mathbf{r}) = (1 - n_l^2)\theta_l(\mathbf{r}) + (1 - n_s^2)\theta_s(\mathbf{r}). \quad (208)$$

n_l^2 and n_s^2 being the dielectric constant of the bulk material (film and substrate). The validity of such an approach relies on the smallness of the variations of dielectric constant induced by the strain field ($\leq 10\%$). The perturbation acts both inside the film of thickness t and inside the substrate. Following the same reasoning of Sections 6.2.3 and 6.2.4 about buried dielectric contrasts, the scattering cross section in DWBA reads:

$$\frac{d\sigma}{d\Omega}(\mathbf{q}_{\parallel}, k_{iz,0}, k_{fz,0}) = \left| \sum_{\mathbf{q}_{\parallel}} (1 - n_l^2) \mathcal{F}_l(\mathbf{q}_{\parallel}, k_{iz,0}, k_{fz,0}) + (1 - n_s^2) \mathcal{F}_s(\mathbf{q}_{\parallel}, k_{iz,0}, k_{fz,0}) \right|^2, \quad (209)$$

where the DWBA form factors of the mode \mathbf{q}_{\parallel} are given by:

$$\begin{aligned} \mathcal{F}_l(\mathbf{q}_{\parallel}, k_{iz,0}, k_{fz,0}) &= \tilde{A}_1^-(k_{iz,1}) \tilde{A}_1^-(k_{fz,1}) \tilde{\theta}_l(\mathbf{q}_{\parallel}, k_{fz,1} - k_{iz,1}) e^{i(k_{fz,1} - k_{iz,1})t} \\ &+ \tilde{A}_1^+(\mathbf{q}_{\parallel}, k_{iz,1}) \tilde{A}_1^-(k_{fz,1}) \tilde{\theta}_l(\mathbf{q}_{\parallel}, k_{fz,1} + k_{iz,1}) e^{i(k_{fz,1} + k_{iz,1})t} \\ &+ \tilde{A}_1^-(k_{iz,1}) \tilde{A}_1^+(\mathbf{q}_{\parallel}, k_{fz,1}) \tilde{\theta}_l(\mathbf{q}_{\parallel}, -k_{fz,1} - k_{iz,1}) e^{i(-k_{fz,1} - k_{iz,1})t} \\ &+ \tilde{A}_1^+(\mathbf{q}_{\parallel}, k_{iz,1}) \tilde{A}_1^+(\mathbf{q}_{\parallel}, k_{fz,1}) \tilde{\theta}_l(\mathbf{q}_{\parallel}, -k_{fz,1} + k_{iz,1}) e^{-i(k_{fz,1} + k_{iz,1})t} \\ \mathcal{F}_s(\mathbf{q}_{\parallel}, k_{iz,0}, k_{fz,0}) &= \tilde{A}_2^+(k_{iz,2}) \tilde{A}_2^+(k_{fz,2}) \tilde{\theta}_s(\mathbf{q}_{\parallel}, k_{fz,2} - k_{iz,2}) e^{i(k_{fz,2} - k_{iz,2})t}. \end{aligned} \quad (210)$$

The amplitude scattered by the dislocation network is the coherent sum of five terms (Fig. 158) where four arises from the film and one arises from the substrate. From Eqs. (209)–(210), the intensity scattered by the dislocation network is explicitly known. The only free parameter is the penetration depth $\lambda(\mathbf{q}_{\parallel})$ of each mode of the dilatation field (except the scale factor). To extract $\lambda(\mathbf{q}_{\parallel})$, the intensity of the measured scattering rods ($\frac{1}{\Lambda} \frac{1}{\Lambda} L$) and ($\frac{2}{\Lambda} 0L$) have been fitted. The best fit (Fig. 159) has been obtained for $\lambda = 1.05$ nm for each scattering rods. This value has to be compared to the expected one from the linear isotropic elasticity theory: $\lambda_{(\frac{1}{\Lambda} \frac{1}{\Lambda} L)} = 1.74$ nm and $\lambda_{(\frac{2}{\Lambda} 0L)} = 1.23$ nm [521]. A more rigorous analysis should be done in the framework of the anisotropic elasticity theory. It would probably give a better agreement.

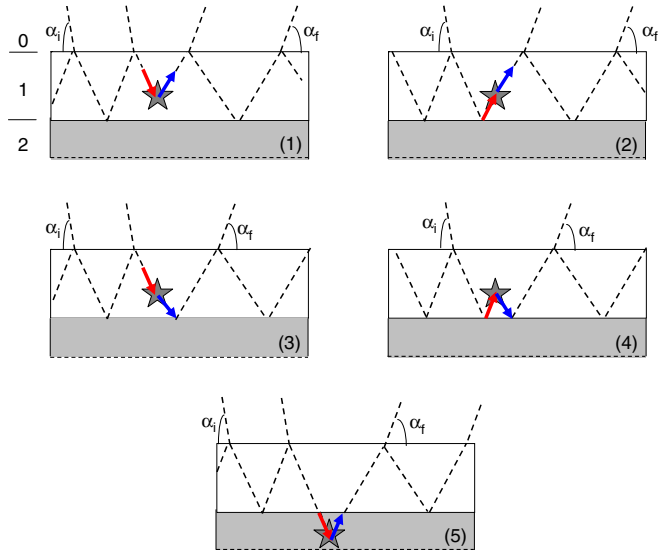


Fig. 158. Sketch of the different pathways taken into account in the calculation of the intensity scattered by the dislocations. The number associated to each process corresponds to its position in Eq. (210).

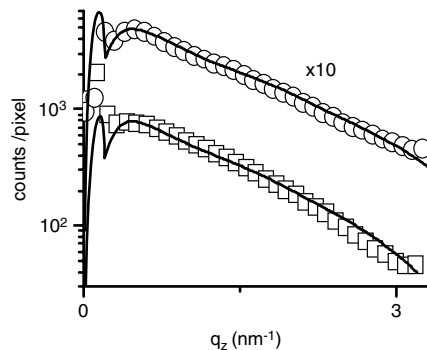


Fig. 159. Cross-section in q_z of the scattering rods of the dislocation network. (□) Experimental data for the $(\frac{1}{\Lambda} \frac{1}{\Lambda} L)$ scattering rod. (○) Experimental data for the $(\frac{2}{\Lambda} 0L)$ scattering rod, ($\times 10$). Fit (full lines). From Ref. [489].

The self-organized growth of Co nanostructures on Ag/MgO(001). The growth of Co on the Ag thin film has been studied in real-time with the X-ray beam parallel with the $\langle 110 \rangle$ crystallographic direction. From the very beginning of the growth process (0.2 ML), the subtraction of the intensity measured after and before the deposition of Co shows oscillations along the scattering rods of the dislocation network (Fig. 160). The amplitude of the oscillations increases with time, reaches a maximum for 0.95 ML of Co and decreases (Fig. 161). The period of the oscillations gives a height of 5 nm, in agreement with the thickness of the thin film measured by X-ray Reflectivity. The main result is that these oscillations prove that the growth of the Co nanostructures is well ordered. Indeed interference effects can only occur if the phase shift between the waves scattered by the nanostructures and those scattered by the dislocations is well defined i.e. if the position of the Co nanostructures is correlated to the dislocations. The measured intensity is thus the sum of three terms: one comes from the dislocation network, one comes from the Co nanostructures and one comes from the interference term between both waves:

$$I = |\mathcal{F}_{DN}|^2 + |\mathcal{F}_{Co}|^2 + 2\mathcal{F}_{DN}\mathcal{F}_{Co} \cos(\mathbf{q}_{\parallel} \mathbf{d}_{\parallel} + q_z d_z), \quad (211)$$

where \mathcal{F}_{DN} (resp. \mathcal{F}_{Co}) is the form factor of the dislocations (resp. Co nanostructures); \mathbf{d}_{\parallel} are d_z are the parallel and perpendicular coordinates of the Co nanostructures with respect to the crossing point of the dislocations. As the Co nanostructures are small

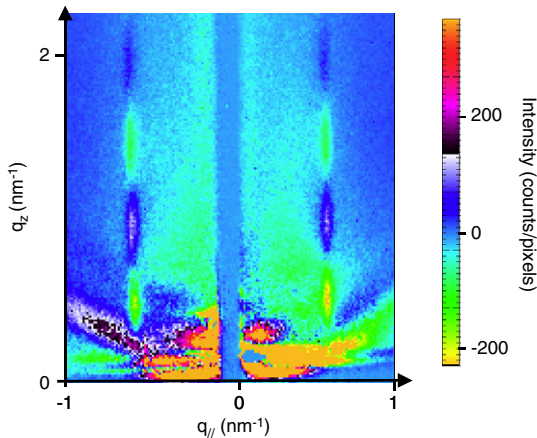


Fig. 160. Experimental image of the interference term (subtracting two GISAXS images: after (0.8 ML) and before Co deposit). The incident beam is parallel with the (110) direction. The intensity scale is linear. The q_{\parallel} (resp. q_z) coordinate ranges from -1 to 1 nm^{-1} (resp. 0 to 2.24 nm^{-1}). Adapted from Ref. [489].

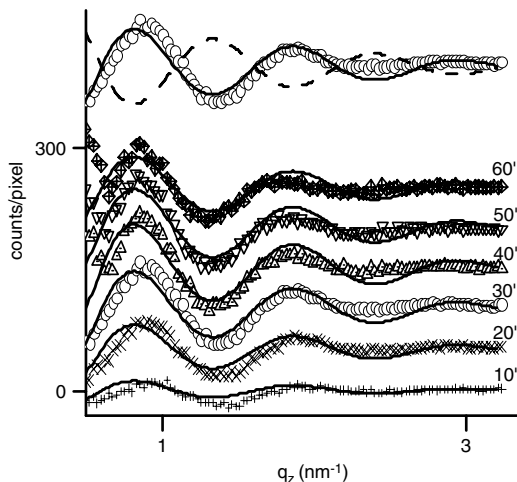


Fig. 161. Intensity of the interference term as a function of q_z for different amounts of Co deposited on the surface. The best fits have been obtained considering that the Co dots are upon the dislocation cores. A vertical translation proportional to the time has been introduced for clarity. Last curve (top) for 0.8 ML of Co. It has been added to the experimental data (○) the best fit (full line), and a simulation in case the Co dot is in between the cores of the dislocations (dotted line). The interference is in phase opposition (from Ref. [489]).

($|\mathcal{F}_{Co}| \ll |\mathcal{F}_{DN}|$), the $|\mathcal{F}_{Co}|^2$ term is negligible in Eq. (211). The interference term which contains the information on the position of the nanostructures is obtained by subtracting the GISAXS data after and before Co deposition. Two high symmetry sites are possible for the localization of the Co dots: above the crossing point of the dislocation lines or at the center of the square formed by four dislocation lines. By symmetry any other possibility gives more than one nanostructure per unit cell. This is not expected because there is one nucleation site per unit cell and the diffusion length of Co atoms is large at the chosen temperature to avoid any homogeneous nucleation.

To obtain the position of the Co nanostructures, it is necessary to precisely describe the interference effect along the ($\frac{1}{A}\frac{1}{A}L$) scattering rod. Since the form factor of the dislocation network has been previously determined only the form factor of the Co nanostructures and the position in the unit cell is lacking. The quantitative analysis of the interference effect has been performed in the framework of the DWBA taking into account the Ag thin film which modifies the reflection properties of the surface. Following Eqs. (91) and (138), the form factor of the Co nanostructures is the

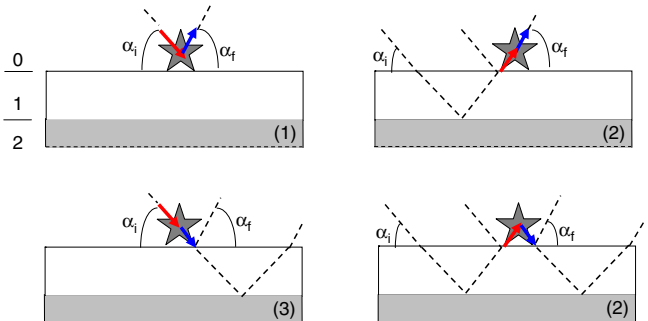


Fig. 162. Sketch of the different pathways involved in the calculation of the intensity (DWBA) scattered by the Co dots on top of the thin film of Ag. The number associated to each process corresponds to its position in Eq. (212).

coherent sum of four scattering processes (Fig. 162):

$$\begin{aligned} \mathcal{F}_{Co}(\mathbf{q}_{\parallel}, k_{iz,0}, k_{fz,0}) = & A_0^+(k_{iz,0})A_0^+(k_{fz,0})F_{Co}(\mathbf{q}_{\parallel}, -k_{fz,0} + k_{iz,0}) \\ & + A_0^-(k_{iz,0})A_0^+(k_{fz,0})F_{Co}(\mathbf{q}_{\parallel}, -k_{fz,0} - k_{iz,0}) \\ & + A_0^+(k_{iz,0})A_0^-(k_{fz,0})F_{Co}(\mathbf{q}_{\parallel}, k_{fz,0} + k_{iz,0}) \\ & + A_0^-(k_{iz,0})A_0^-(k_{fz,0})F_{Co}(\mathbf{q}_{\parallel}, k_{fz,0} - k_{iz,0}) \end{aligned} \quad (212)$$

where F_{Co} is the Fourier transform of the nanostructures shape. To calculate the interference between the waves scattered by the nanostructures and the dislocations (Eq. (211)) nine terms have to be calculated (respectively four and five for the nanostructures and the dislocations). To give an explicit expression of the calculation, the Co dots are modeled with a cylindrical shape with an integer number of atomic planes in the height. The best fit has been obtained for Co dots localized above the dislocation crossing lines, ($\mathbf{d}_{\parallel} = \mathbf{0}$), i.e. in compressive sites and for 2 ML-high nanostructures (see Fig. 161).

Conclusion. In conclusion, the self-organized growth of Co nanostructures above a square misfit dislocation network of Ag/MgO (001) is put in evidence, by *in situ* GISAXS. Contrary to the most common idea, small angle scattering techniques such as GISAXS are sensitive to strain as it is put in evidence in the case of a buried dislocation network. A comparison between the linear and isotropic theory of elasticity and the experimental data confirms that the strain field is exponentially damped from the interface into the film and the substrate.

9.4.4. Self-organized growth of Ni clusters on a cobalt-oxide thin film induced by a buried misfit dislocation network

Achieving self-organized growth of metallic nanoparticles on oxide surfaces is especially important in view of their potential magnetic or catalytic properties, which strongly depend on their exact size and shape. The possibility of obtaining an ordered collection of metallic clusters on an oxide film of 5 nanometer of thickness has been demonstrated [490] by a combination of *in situ* GIXD and GISAXS. Due to the 3.25% lattice mismatch between the CoO overlayer and the Ag(001) substrate, a square network of dislocations forms at the CoO/Ag(001) interface. The interfacial dislocation network creates a periodic atomic displacement field that extends up to the surface, thus influencing the growth of a Ni overlayer, which develops a spatially ordered distribution of clusters.

Grazing Incidence X-ray Diffraction (GIXD) and Small Angle X-ray Scattering (GISAXS) experiments were performed using the BM32 setup. The substrate used was an Ag(001) single crystal cleaned by repeated cycles of Ar^+ bombardment and annealing at 700 K. CoO(001) films were prepared *in situ* by evaporating Co on the clean Ag surface in 1×10^{-7} mbar of oxygen pressure, at a substrate temperature of 460 K. Ni was next evaporated at room

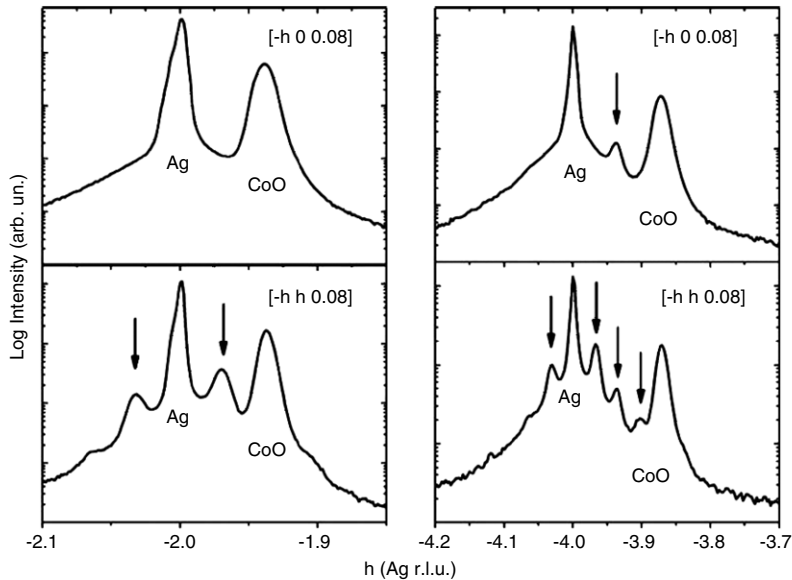


Fig. 163. Scans along the $\langle \bar{h}, 0, 0.08 \rangle$ direction around the Ag $(\bar{2}00)$ and $(\bar{4}00)$ Bragg peaks, and along the $\langle \bar{h}, h, 0.08 \rangle$ direction around the Ag and CoO $(\bar{2}20)$ and $(\bar{4}40)$ Bragg peaks. From Ref. [490].

temperature on the CoO(001) surface from a Knudsen cell with a very low evaporation rate of 0.005 nm/min. The structure of the CoO film deposited on the Ag(001) surface was first investigated by GIXRD. Fig. 163 shows radial scans around the Ag (220) , (200) , (400) and (440) Bragg peaks along the $\langle h, h, 0.08 \rangle$ and $\langle h, 0, 0.08 \rangle$ directions for a CoO film of 23 ML of thickness.

Along the $\langle h, h, 0.08 \rangle$ direction, the Bragg peak of CoO is located at $h = 1.936$ (Ag relative lattice units) which corresponds to a lattice parameter of 0.2979 ± 0.0005 nm. The value of the CoO parameter, very close to that (0.302 nm) of a bulk CoO single crystal, indicates that the strain induced by the mismatch with the Ag substrate is almost completely released at this thickness. Besides the Bragg peaks of Ag and CoO, satellite peaks (marked by arrows in Fig. 163) are found on a periodic network of spacing 0.0325 reciprocal lattice unit. This observation is in good agreement with the Coincidence Lattice Model (CSL) for coherent interfaces, defined as the smallest lattice in common between the substrate and the overlayer [13]. For the CoO/Ag(001) interface, it has a period $\Lambda = 0.2979/0.0325 = 9.2$ nm. At variance with previous studies [488,13] of the MgO(001)/Ag(001) interface, the double periodicities of the satellites along the $\langle h, h, 0.08 \rangle$ direction indicate that the dislocations are pure edge dislocations forming a square network with $1/2[110]$ Burger's vectors and with lines along $\langle 110 \rangle$ directions.

The influence of a dislocation network in the CoO film on the successive growth of a nickel overlayer has been investigated by GISAXS and STM. STM showed that the surface had large flat areas uniformly covered by small round Ni clusters. *In situ* GISAXS reveals the organization of the Ni clusters, and allows in addition determining the relationships between the locations of the interfacial dislocations and the Ni cluster nucleation centers [488]. Fig. 164a shows a GISAXS intensity map measured with the incident X-ray beam parallel with the $\langle 110 \rangle$ crystalline axis before the Ni deposit. Two scattering rods, marked in the figure by arrows, indicate the presence of a regularly spaced dislocation network in the CoO film [488]. The distance between the two scattering rods and the specular rod is inversely proportional to the separation between the dislocations, yielding again 9.2 nm. Fig. 164b shows the same GISAXS image after the deposition of about 0.18 nm of Ni, and Fig. 164c shows the difference between the two above images. The intensity of the two scattering rods in the

perpendicular direction clearly shows periodic oscillations. This effect arises from the interference between the waves scattered by the dislocation network and the Ni overlayer with increasing perpendicular wavevector transfer [488]. The existence of these interference demonstrates that there is a constant separation between the core of the dislocations and the positions of the Ni clusters, and thus that the cluster ordering is induced by the dislocation network. Moreover, the period of the sinusoidal variation as a function of the out-of plane wavevector transfer (Fig. 164d) is inversely proportional to the out-of plane separation between the dislocation cores (located at the interface), and the Ni clusters [488]. A value of 5.6 nm is obtained, which is in fair agreement with the nominal thickness of the CoO film of 25 ML. These measurements thus demonstrate that the ordering of the Ni clusters is driven by the presence of the buried dislocation network at the CoO/Ag(001) interface. These findings are of a great relevance because the formation of interfacial dislocations is a common strain relief mechanism in oxide/metal interfaces [522–524]; it could thus become a useful route to realize the organized growth of metallic nanoparticles on oxide thin films.

In conclusion this study has shown that a square interfacial misfit dislocation network can be formed at the interface between a CoO film and a Ag(001) surface. The periodic displacement field of this network extends up to the CoO(001) surface, providing a network of sites for preferential nucleation and growth of metallic nanoparticles. This self-organized growth is achieved at room temperature instead of the more common low temperatures, which shows that the dislocation-induced nucleation sites are strongly energetically favorable. This however needs a very low deposition rate for which the diffusion length of the Ni atoms on the oxide surface is of the order of the nanostructuration period. The resulting ordered Ni nanoparticles have a narrow size distribution, which is essential to keep well defined properties over an assembly of nanoparticles. The achievement of the control of the self-assembling process of metal clusters on the surface of a 5 nm thick oxide film represents a step forward in the production of real devices by self-organized growth. Moreover this experiment reveals the great potentiality of the GISAXS technique in the study of the self assembled structures being able to probe, in a non-destructive way, the surface and the buried part of a thin film.

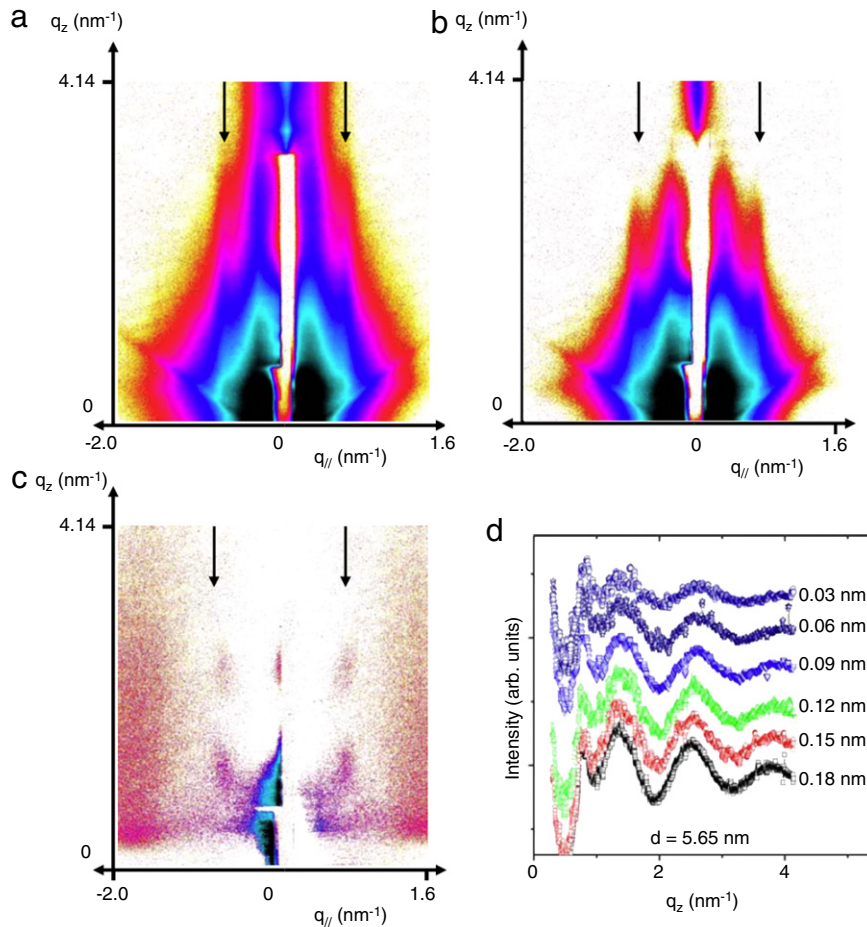


Fig. 164. GISAXS image of 25 ML CoO/Ag(001) recorded with the incident beam parallel with the [110] direction. (b) Same image of panel (a) after the deposition of 0.18 nm of Ni. (c) Difference between panel (a) and (b). (d) Sections of panel (c) along the arrows for different Ni coverages. From Ref. [490].

Table 4

Morphological parameters deduced from the analysis of GISAXS images measured for 1.1 ML of Pt on W(111) annealed at 715 K.

Sample	Morphological parameters						
	Δd (nm)	ΔH (nm)	D (nm)	d (nm)	σ_d/d	H (nm)	σ_H/H
1.1 ML of Pt on W(111) annealed at 715 K	0.27	0.10	5.75 ± 0.6	5.15 ± 1.0	0.21 ± 0.06	0.52 ± 0.1	0.11 ± 0.03

9.5. Surface nanofacetting: The case of Pt on W(111)

The importance of bimetallic catalysts has been increasing in recent decades [525]. In particular refractory metals (W, Mo, Re, etc ...) with Pt-group metals are active catalysts for hydrogenation and hydrogenolysis reactions [526–529]. The large majority of the studies devoted to these systems have focused on the interaction of ultrathin metal films with atomically smooth, close packed substrates, e.g. fcc(111), fcc(100), bcc(110), bcc(100) etc It has been observed structural rearrangement in the overlayer and little or no change in the substrate. By contrast, recent studies have addressed the interaction of ultrathin metal films on unstable atomically rough substrates [530–532]. For instance, a bcc metal like W exposing a (111) surface covered with 1 ML of another metals (Pt, Pd, Rh, Ir, Au). In this case, the surface undergoes a massive reconstruction (Fig. 165) to form three-sided pyramids of nanometer scale dimensions exposing {211} facets [533,534]. The process is activated at temperatures larger than 700 K and is reversible: after evaporation of Pt, a flat W(111) surface is recovered. The faceting transition has been attributed to the surface energy anisotropy [535,533,536] and it is kinetically

limited by surface diffusion. The fundamental questions of surface morphology instability in a bimetallic system like Pt/W(111) against faceting have initiated a wealth of experiments using different techniques (STM [533,534], LEED, AES, LEEM [537,538], XPS [539]). However, none of them allow to follow *in situ*, in real time, the faceting transition combining a crystallographic and a morphological (nanometer scale) characterization. In addition nanostructured surfaces can be used as templates to grow ordered dots exhibiting for instance magnetic properties. For that sake, a detailed study of the faceting of Pt/W(111) has been performed by GISAXS [248] as a function of time and temperature to determine the appropriate conditions for the ordering of small nanoparamids. Then this template has been used to grow Co nanostructures.

9.5.1. Nucleation and growth of 3-fold symmetry nanoparamids

First onset of nanofaceting of 1 ML of Pt on W(111) has been observed by GISAXS at 715 K. As shown in Fig. 166a two well defined scattering lobes along q_{\perp} are visible. They correspond to a preferential distance between first neighbor pyramids, indicating that they are short range ordered. Interestingly, the lobe located at $q_{\parallel} > 0$ extends farther along the q_{\perp} direction than the lobe at $q_{\parallel} <$

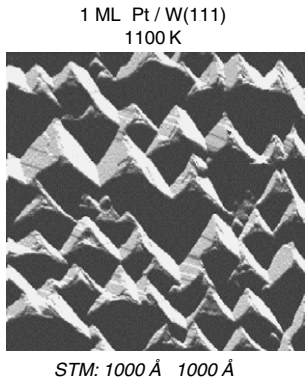


Fig. 165. STM image of Pt/W(111) which has undergone faceting after thermal treatment at 1100 K. Notice the three side {211} nanoparamids. Courtesy of T.E. Maday.

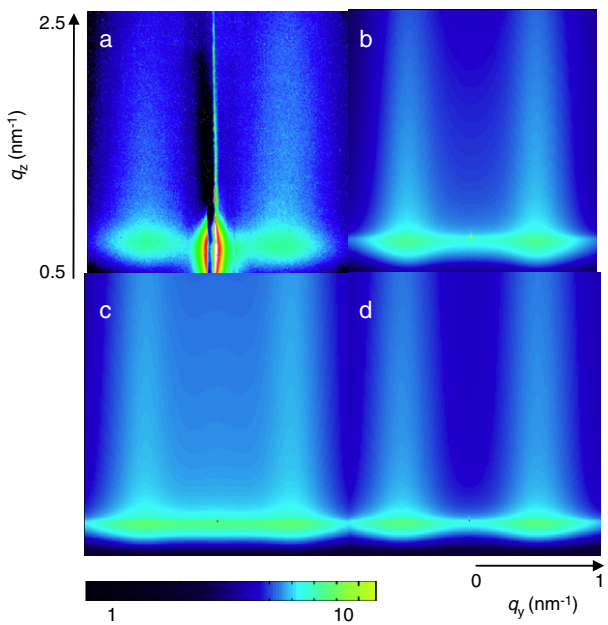


Fig. 166. GISAXS images for 1.1 ML of Pt on W(111) annealed at 715 K: (a) experimental data, (b) LMA simulation, (c) DA simulation and (d) SSCA simulation. From Ref. [248].

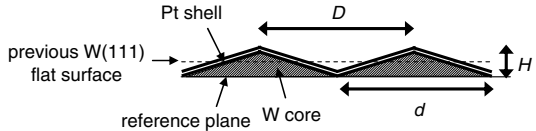


Fig. 167. Sketch of the morphology of the faceted Pt/W{211} surface.

0. This asymmetry arises because there is no 2-fold symmetry (the nanoparamids have a 3-fold symmetry) and because the Friedel law does not apply for GISAXS images as shown by Rauscher et al. [37]. The measurement of the tilt angle of the facets with respect to the surface plane is difficult because of the broadness of the scattering rods and because the interference function tends to re-orientate the scattering rods perpendicular to the surface plane and not perpendicular to the facets. The exact orientation of the facets has been obtained by examining the facet truncation rods by GIXD (see Ref. [248]). At wide scattering angles, the information concerning the short range order between pyramids is lost and thus the truncation rods are perpendicular to the facets. The measurement of their orientations reveals unambiguously the presence of {211} facets at 19.5° from the (111) plane. After

this first interpretation of the surface morphology (symmetry, pyramid shape, facet orientation), a quantitative GISAXS analysis of the images has been undertaken to obtain the lateral size d , the height H and the distance D between the pyramids (see Fig. 167). Previous analysis by STM [538] has shown that the faceted surface is made of pyramids and pits (inverted pyramids) to keep the amount of matter constant. In order to simplify the GISAXS analysis, it was assumed that the surface is covered by pyramids using a reference plane located at the bottom of the average pit. Assuming that pyramids and tips have the same size, the pyramid size deduced from our model is two times too large. The theoretical model for the calculation is based on the DWBA for supported pyramids on a flat W surface. The three-sided pyramids are modeled with a W-core and a 1 ML Pt-shell ($\Delta d = 0.27 \text{ nm}$ and $\Delta H = 0.10 \text{ nm}$). Distributions of lateral sizes and heights are taken into account using Gaussian probability laws. Concerning the spatial organization of the pyramids different models have been considered. For the classical approximations, LMA [234] and DA [255], a 1D paracrystal function was chosen for the interference function [42,242] because no in-plane anisotropy of the inter-pyramid distance could be detected. A more sophisticated model (SSCA [155,81], Section 6.4) has also been applied considering that the size and the spacing between neighboring pyramids are correlated (see STM images in Ref. [540]). Intensity cross-sections (at least two) extracted from 2D GISAXS images are fitted simultaneously using the dedicated IsgISAXS software based on a χ^2 minimization [27]. Finally a complete 2D GISAXS image is simulated and compared to the experimental one. An overall agreement validates the obtained parameters (see Table 4). The LMA and SSCA simulations (see Fig. 166b and (d)) give a good agreement with experimental data whereas the DA simulation (see Fig. 166c) has too large intensity close to $q_{\parallel} = 0$. It is a classical drawback of this approximation which neglects local correlations between the size and the spacing of scatterers (see Section 6.4). This gives rise to large fluctuations of electronic density and therefore to a large background scattering close to the origin [73]. This is the aim of the SSCA to include such local correlations in the calculation of the intensity. Assuming that the distance between neighboring pyramids increases with their size, the diffuse scattering close to the origin decreases in agreement with the experimental data. The LMA gives the same parameters as the SSCA (see Table 4). However it is not physically relevant because it makes the hypothesis that the pyramids are all identical on the coherence length of the X-ray beam (a few μm) which is far from the actual morphology as seen by STM [540]. However the LMA is a usual approximation and is far simpler to use than the SSCA. The following analyses are therefore performed in the framework of the LMA (see for instance in Fig. 168 the analysis of a faceted Pt/W{211} surface annealed at 800 K by GISAXS).

The evolution of the faceting has been studied by increasing the temperature from 715 to 1340 K by steps of 10 min. As the temperature increases the intensity scattered by the pyramids concentrates close to the origin of the reciprocal space in agreement with the increase of the size of the pyramids and the distances. No correlation peak of the interference function is visible at temperatures higher than 1040 K due to the finite divergence of the incident beam and the beamstop size. Therefore the scattering rods by the facets are no longer affected by the interference function and get intense and narrow as the facets size increases (see Fig. 169). The angle of the facets is now clearly defined (19.5°) and corresponds to {211} planes. The GISAXS images have been fully analyzed (see Fig. 170). The average morphological parameters increase slowly between 715 and 800 K and then faster above 800 K. The ratio of the distance between pyramids and their lateral size (D/d) is approximately constant (1.1–1.2) which shows that the pyramids are connected at all temperatures and the

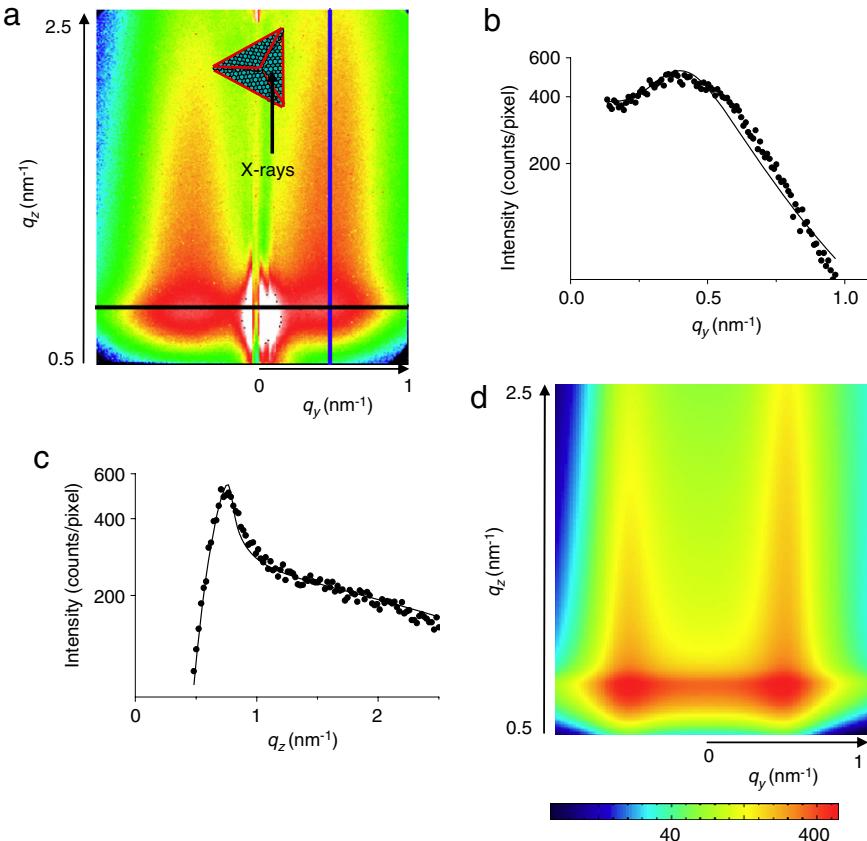


Fig. 168. (a) GISAXS image (and scattering geometry in inset) for 1.1 ML of Pt on W(111) annealed at 800 K. (b) Cross section of the experimental image parallel with the surface plane (thick black line) and best fit. (c) Cross section of the experimental image perpendicular to the surface plane (thick black line) and best fit. d) GISAXS image simulated with the parameters obtained from the fit of both cross-sections. Note that the specular beam is not simulated. From Ref. [248].

surface is fully faceted. This is confirmed by the absence of CTR's from the W(111) surface (see Ref. [248]). The nucleation density of pyramids ($3 \cdot 10^{12} \text{ cm}^{-2}$) has been estimated from the mean inter-pyramid distance at the onset of nanofaceting. Interestingly the minimum lateral size of the nanopyramids measured by GISAXS is estimated to be 5.16 nm. This minimum size for the nucleation arises from the competition between the surface energy gain and the energy cost of the facet edge to buckle and make a 3-sided pyramid. From geometric arguments the energy per unit length of the facet edges has been obtained ($\eta = 2.5 \text{ eV/nm}$ at 715 K).

9.5.2. Validity of the DWBA: GISAXS as function of the incident angle

In order to study the effects of grazing angles of incidence and exit and the validity of the first order DWBA to calculate the intensity, GISAXS patterns have been recorded at different incident angles on a faceted Pt/W{211} sample annealed at 1340 K (see Fig. 171). For $\alpha_i \ll \alpha_c$ ($\alpha_i = 0.1^\circ$ in Fig. 171a), the GISAXS pattern exhibits one scattering rod arising from the {211} facets (label 1). For $\alpha_c/2 \ll \alpha_i \ll \alpha_c$, the previous scattering rod splits into 2 parallel scattering rods (see Fig. 171b, c, label 1-2). The rod with the smallest emergent angle can be assigned to a single scattering process. It is taken into account in the framework of the Born Approximation or in the first term of the DWBA for supported objects (see Eq. (134)). It is called a BA scattering rod in the following. The wavevector transfer perpendicular to the surface reads $q_z = k^f z - k^i z$. The rod with the largest emergent angle comes from the second scattering process in Eq. (134). It takes into account first the reflection of the incident beam on the surface and then the scattering of the reflected wave by the pyramids. The angle separating these two scattering rods is $\Delta\alpha = 2\alpha_i$. Cross-sections perpendicular to both scattering rods

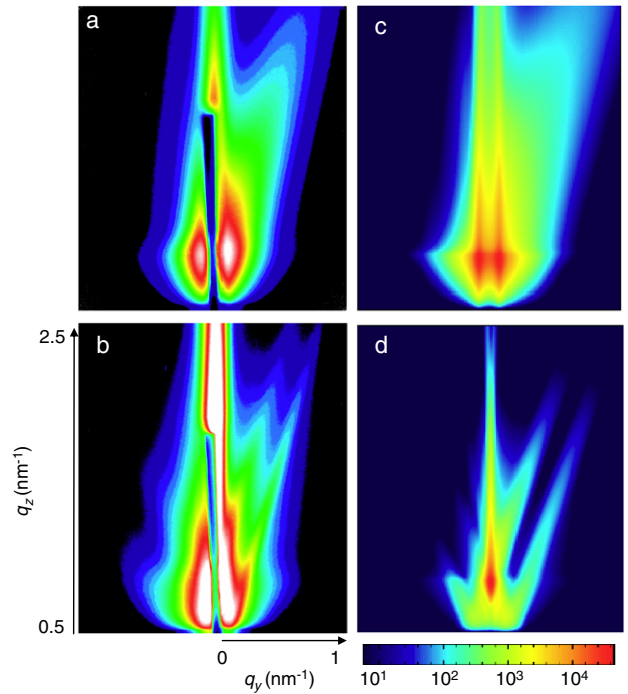


Fig. 169. GISAXS images of 1.1 ML of Pt on W(111) annealed at (a) 1040 K and (b) 1340 K. (c) and (d) Corresponding simulated images. From Ref. [248].

clearly show that the FWHM of the upper scattering rod is much larger than the FWHM of the BA scattering rod. The first order

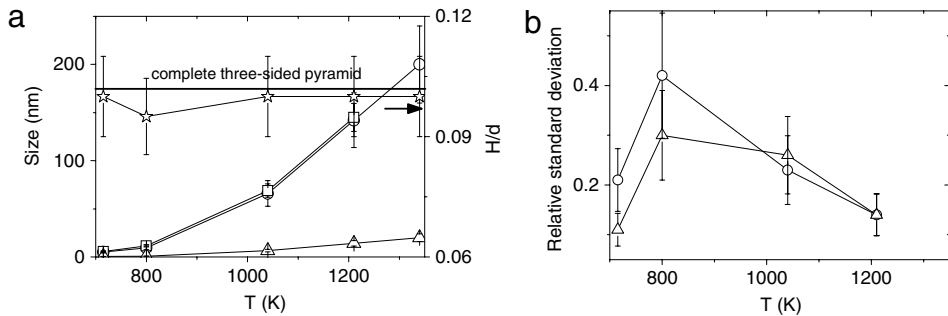


Fig. 170. (a) Evolution of the morphological parameters as function of temperature of annealing. (b) Evolution of the normalized standard deviation of the size of the pyramids as function of temperature. From Ref. [248].

DWBA cannot account for this difference. The calculation of the upper scattering rod intensity takes into account the reflection on the substrate (i) by the Fresnel coefficient of reflection at the incident angle and (ii) by an angular shift of $2\alpha_i$. However no broadening is expected. This is because the surface is supposed to be perfectly homogeneous at least in the surface plane. To obtain this broadening effect it is necessary to use a reference state for the surface with in-plane inhomogeneities (however the exact calculation of the electromagnetic field may be difficult) or to use a higher order DWBA [102]. When $\alpha_i > \alpha_c$, the upper scattering rod vanishes (see Fig. 171d) because the Fresnel coefficient of reflection decreases very fast as function of the incident angle above α_c . However in Fig. 171d, a new characteristic feature appears: a broad scattering rod (label 3 of Fig. 171d) points toward decreasing exit angles (α_f) and after an elbow changes into a narrow scattering rod pointing toward increasing emergent angles. The first part originates from the third process in Eq. (134). It results from the scattering of the incident wave by the pyramids followed by a reflection of the scattered wave by the average surface plane. The wavevector transfer perpendicular to the surface reads: $p_z = -k_{fz} - k_{iz} = 2\pi/\lambda[-\sin(\alpha_f) + \sin(\alpha_i)]$. As α_f decreases p_z increases, thus the scattering rod points toward decreasing angles as expected. At $\alpha_f < 0$, the scattering rod is hidden by the surface plane. It crosses the BA scattering rod at $\alpha_f = 0$ making an elbow. For the same reason as before, the FWHM of the scattering rod arising from the third process in Eq. (134) is much larger than for the BA scattering rod. This highlights the breakdown of the first order DWBA to reproduce correctly broadening effects. Concerning the fourth term in Eq. (134), it has not been isolated properly because it gives a significant contribution only for $\alpha_i \ll \alpha_c$ and $\alpha_f \ll \alpha_c$. As a conclusion the main features of the GISAXS images can be simulated in the framework of the first order DWBA. However to make a detailed study of supported nanostructures, they must be small enough, i.e. $q_z\sigma < 1$ and $p_z\sigma < 1$, where σ is the roughness of the surface [35].

9.5.3. The growth of Co on a faceted Pt/W{211} surface

The nanofaceted Pt/W{211} surface with the smallest three-sided pyramids, obtained by a 10 min annealing at 715 K (see Fig. 172a), has been used as a nanotemplate for the growth Co nanostructures. Although Co and Pt form ordered alloys [541], and Pt has a strong tendency to segregate [542], we expect a preferential nucleation of Co nanostructures induced by the surface morphology, i.e. at the apex of the pyramids or at the bottom of the pits. The surface was covered at RT by 4 ML of Co. The corresponding GISAXS image (see Fig. 172b) is more intense in agreement with the increase of matter. Moreover the asymmetry of the image is preserved (3-fold symmetry) suggesting that Co does not alter the initial morphology of the surface. The increase of intensity may be interpreted as arising from 3D

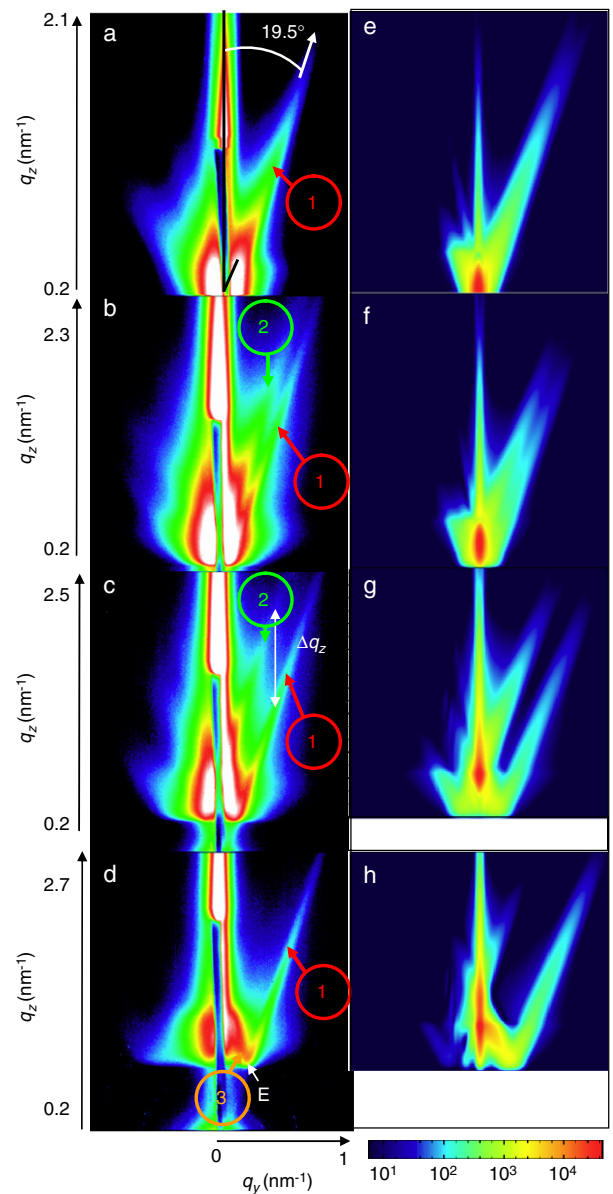


Fig. 171. (a)–(d) GISAXS images at increasing incident angles (0.1° , 0.22° , 0.42° and 0.68°) for a faceted Pt/W{211} surface. The labeled rods refer to the first, second and third term in the first order DWBA expression. The letter E stands for the elbow (see text). (e)–(h) Corresponding GISAXS simulations. The intensity scale is logarithmic. From Ref. [248].

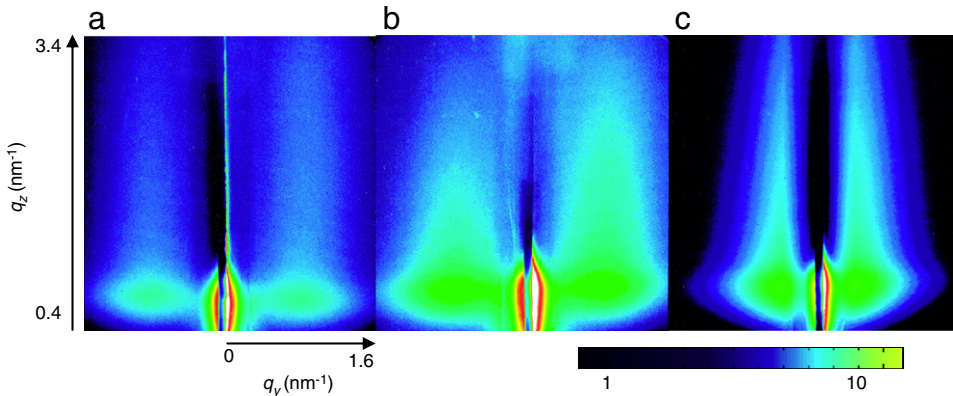


Fig. 172. Experimental GISAXS images (a) for 1.1 ML of Pt on W(111) annealed at 715 K, (b) for 4 ML of Co on 1.1 ML Pt/W(111) at RT, (c) for 4 ML of Co on 1.1 ML Pt/W(111) annealed from 700 to 770 K during 3 min. From Ref. [248].

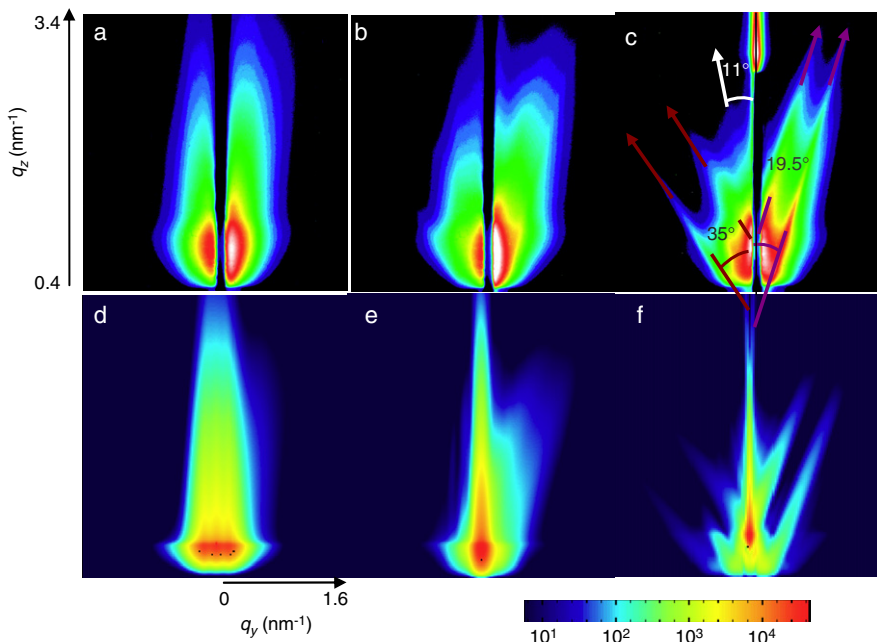


Fig. 173. (a)–(c) Experimental GISAXS images for 4 ML of Co on 1.1 ML Pt/W(111) after annealing during 3 min at (a) 920–1000 K, (b) 1020–1100 K, (c) 1140–1210 K. (d)–(f) Corresponding simulations. From Ref. [248].

nanostructures of Co correlated with the Pt/W nanopyramids. The evolution of the system upon annealing is rather complex. After a short annealing (3 min) from 700 to 770 K, the asymmetry between the two correlation peaks is less pronounced suggesting the disappearance of the facets or at least a roughening of the morphology (see Fig. 172c). From the possible segregation of Pt, we expect that the Co adlayer is in contact with the W surface. As Co on W(111) is known to be stable [543], the {211} nanopyramids are thus probably unfavored. However as the annealing proceeds, at 920 K, the GISAXS images become again more asymmetric (see Fig. 173a–b) and at 1200 K scattering rods at 19.5° with respect to the direction perpendicular to the surface proves the presence of large {211} facets (see Fig. 173c). Rods at 35.3° are also found suggesting the presence of {110} facets. These facets may arise from 6-sided pyramids or from 2 types of 3-sided pyramids exposing respectively {211} and {110} facets. Moreover, the rise up at 1200 K of a specular peak is an indication of the beginning of the defaceting of the surface due to the evaporation of the adlayer of Co and Pt. This complex process has also been studied by GIXD showing the formation of alloys during annealing [248]. The alloys are probably responsible for the defaceting/faceting of the surface morphology decreasing/increasing the surface energy anisotropy.

9.6. Semi-conductor surfaces nanostructures induced by sputtering

One of the possibilities to form surface patterning at the nanometer scale is the spontaneous pattern formation during low-energy ion beam sputtering. This technique has proved to be a very flexible self-organization method for the production of ordered, uniform structures with sizes down to 10 nm, on the surface of metals, semiconductors, and insulators. In particular, hexagonal arrays of nanodots are produced at normal incident ion irradiation or under off-normal incidence with simultaneous sample rotation, whereas at off-normal incidence and static sample very regular ripple patterns are formed.

The first *in situ* GISAXS study of surface nanostructuring during ion sputtering, as a function of time and for different temperatures, has been performed in 2002 by Ludwig et al. [544]. They investigated the evolution of the Si(001) surface morphology under normal-incidence Ar^+ sputtering as a function of ion energy, in the range 100–500 eV. Below 300 eV, they found two structures with distinct individual length-scales and behaviors. A smaller scale (20–50 nm) morphology grows in intensity and coarsens with time, while a larger scale (\simeq 100 nm) morphology grows

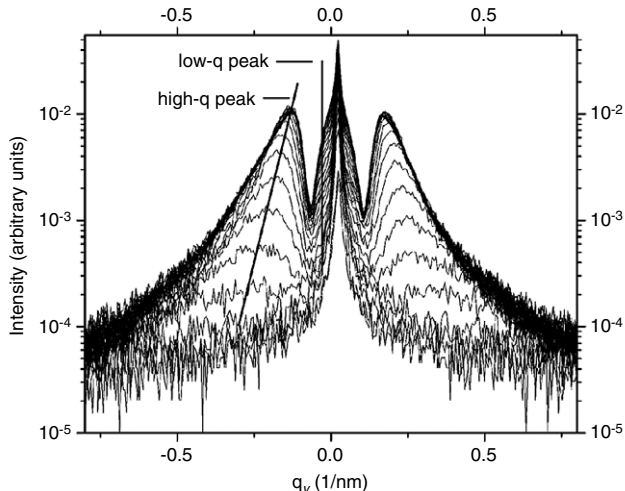


Fig. 174. GISAXS scans of a Si sample bombarded at 1000 eV in the presence of Mo seeding. The low- q and high- q peaks indicate the growth of long length-scale corrugations and self-organized dots, respectively. From Ref. [545].

in scattering intensity, but does not coarsen. At higher energies, sputtering causes the Si(001) surface to become smoother on length scales smaller than 200 nm.

In 2005, the same group [545–547] reported a real-time GISAXS study of Mo-seeded Si nanodot formation during ion bombardment. *In situ* GISAXS was used to follow the surface morphology during 1000 eV energy Ar⁺ ion bombardment at room temperature. Without Mo seeds, the surface was found to roughen according to expected power-law behaviors. When the sample was mounted with Mo clips, the ion bombardment of these clips induces the spread of Mo atoms in small quantity on the surface. These were found to act as seeds to the formation and development of highly correlated, self-organized surfaces nanoscale structures (dots) that are typically 3 nm high with a spatial correlation of ≈ 30 nm (Fig. 174). The presence of only a small surface atom fraction of Mo atoms is sufficient to facilitate the dot formation. These saturate with time, and further surface roughening is dominated by the growth of long-wavelength corrugations. Note that, as an alternative to GISAXS, *ex situ* GIXD has been used successfully to characterize the nanodot formation induced by ion sputtering of Si(001) and Si(111) surfaces [548,549].

In 2007, Plantevin and coworkers published an *in situ* GISAXS study of the formation of self-organized nanodots by ion beam sputtering of GaSb(001) surfaces [550]. The temporal evolution of the pattern was monitored at different ion energies (300–1200 eV). The pattern forms after a few minutes of bombardment, and then rapidly coarsens in the characteristic wavelength until reaching a saturation value that scales with ion energy. The pattern evolves slower toward saturation for the lower ion energy while attaining a higher correlation length, normalized to the wavelength. The pattern time dependence is correlated with the influence of the sputtering rate on the pattern formation.

Ozaydin et al. [551] also performed a real time *in situ* study of the temperature dependence of the Si(001) surface morphology during 1000 eV Ar⁺ ion bombardment at normal incidence. They found that the surface becomes amorphous at room temperature but remains smooth. Surface roughening occurs above 400 °C, with a transition region from amorphous to crystalline surface. Above 500 °C, the surface remains crystalline and the growing corrugations exhibit a power-law scaling in amplitude with a characteristic length-scale, which is typical of surface diffusion driven instabilities.

9.7. *In situ* studies of GaN surfaces

In 2006, Coraux and coworkers [552] coupled *in situ* anomalous GISAXS and anomalous GIXD to study the vertical correlation and capping effects during GaN/AlN quantum dot growth. Clear vertical correlations were revealed by GISAXS.

In 2006, Öscan et al. [553] employed real-time GISAXS to study the adsorption and desorption of Ga on c-sapphire and Ga terminated polar GaN surfaces. Formation of self-organized liquid Ga nanodroplets on sapphire was detected. Subsequent nitridation of the nanodroplets converted them into GaN nanodots. At a lower Ga flux, the adsorption and desorption of Ga have been studied in the predroplet regime. For identical processing conditions, significantly different Ga adsorption/desorption rates were observed on sapphire and GaN surfaces. They used the Fourier transform of the measured in-plane GISAXS data to determine the average droplet size and average distance between them. The same group [554] analyzed the formation of GaN nanodot by droplet epitaxy on sapphire. A thin GaN continuous layer of around three monolayers thick was observed on the sample grown at a substrate temperature of 620 °C, but no such layer was observed for the substrate temperature of 710 °C. This suggests that there is little mobility of Ga atoms in contact with the sapphire substrate at the lower temperature so that they cannot easily diffuse to nearby droplets and instead form a thin layer covering the surface.

10. Conclusion

The aim of this report was to review the state-of-the-art of the Grazing Incidence Small-Angle X-Ray Scattering (GISAXS) technique, both from the experimental and theoretical points of view. This technique is now mature and well established to characterize the morphology of all kinds of nanoscopic or mesoscopic materials, providing detailed information on the nanoparticle shapes, sizes, distributions of sizes, faceting, spatial correlations, in a statistical way, averaged over millions of particles. The probed length-scales vary between 1 nm and several μm . In addition, GISAXS is intrinsically extremely sensitive to the ordering of the nanoparticles at short-range, long-range or in between. When used *in situ* during growth, it can thus be helpful to adjust the growth conditions and find the optimal parameters for self-organization. GISAXS starts to be a widespread technique in soft-condensed and hard-condensed matter studies, to analyze nanoparticles on surfaces or buried below a surface, as well as multilayers of particles, whether they are ordered or not. This possibility to investigate buried nanoparticles in a non-destructive way makes GISAXS an unique tool. One of the main drawback of the technique is that it most often requires synchrotron radiation, which means that a limited amount of time is devoted to a particular study, so that all pertinent parameters (such as for instance substrate temperature or defect density) cannot be systematically varied.

The understanding of the information contained in GISAXS patterns is now quite complete and analysis software is available. However the underlying theories are complex, not only because of the refraction effects, but also because of the difficulty to described the particle-particle correlations, especially when they depend on the particle types or sizes. In most cases, a correct quantitative analysis needs very accurate data, extending far in reciprocal space, which requires a background as low as possible, minimum distortion, and a very precise knowledge of the angles, especially the incident and emergent angles (to within better than 0.01°). Hence, although a GISAXS experiment is in principle extremely simple, great care must be taken in practice to perfectly define the incoming beam, which should have a small size perpendicular to the sample (typically a few tens of μm), and a small and

well-defined divergence (typically smaller than 0.01°), to perfectly orientate the sample, and, most importantly, to cut any source of background, such as those induced by slits or windows in the beam path.

To assert the accuracy of the technique, many studies compared the morphological characteristics deduced by accurate GISAXS analysis to those obtained by other techniques such as AFM, STM or TEM, with in general a good agreement, thus demonstrating the high accuracy of a complete quantitative GISAXS analysis, which has the advantages of probing a large sample area, in a non-destructive way. If only the average morphological parameters are required, with a limited accuracy, then much simpler and faster analysis of the GISAXS data can be performed, using for instance the asymptotic behaviors (classically known as Porod and Guinier analysis). If the size distribution is not too large, a rough modeling can provide the average size and separation to within $\pm 20\%$, as well as other average parameters, such as e.g. the facet's size, by analyzing the width of the corresponding scattering streaks. However, accurate analysis of GISAXS patterns can become tedious when facing problems of accounting cross-correlations between parameters and statistical description of the morphology. This difficulty is intrinsic to the description of diffuse scattering. In the future, it could be overcome by Reverse Monte Carlo or Maximum Entropy fitting algorithms for finding configurations which are the most compatible with the information brought by a given pattern. However, to our knowledge, these procedures have been applied only to radial distribution function obtained from scattering by amorphous materials [555] and not yet to small angle scattering from particle systems.

Although this report dealt only with the GISAXS technique, which probes the scattering only at small angles (or small momentum transfer), and thus nanometer-size objects, the technique can very easily be combined with X-ray reflectivity to characterize the order perpendicular to the surface, and with Grazing Incidence X-Ray Scattering to probe the atomic structure (lattice parameter, strain, composition ...) of the nanostructures. This is an ongoing trend during synchrotron experiments. The results of the GISAXS analysis (size, shape, size distribution, particle-particle correlation, ordering ...), can be useful to unfold several contributions such as strain or crystalline defects which arise at wide angles. In addition, all three techniques can gain a lot, by using anomalous scattering (when possible) to have a chemical sensitivity in a multi-component system. This could be used for instance to discriminate between the GISAXS signal arising from the matrix (or substrate) and that arising from nanostructures, as shown in the Co/Au(111) case, or to unravel the internal morphology of multicomponent nanostructures such as e.g. core-shell clusters. Anomalous scattering may also be used to normalize the intensity or to subtract the substrate roughness contribution from the scattering of the sample. Hence, one important development of the technique is believed to be this coupling between GISAXS and anomalous scattering.

Note in passing that performing GISAXS on an absolute scale, i.e. deducing the exact amount of matter giving rise to GISAXS, is possible if the incident beam is made small enough so that all the beam hits the sample, and if the incoming flux is quantitatively measured. The GISAXS intensity can then be expressed in electron units (i.e. in multiple of the scattering cross-section of one electron).

One of the most interesting strengths of the technique (like most X-ray based techniques) is its ability to perform *in situ* experiments, with many possible sample environments (UHV chamber, liquid throats, high pressure cells, catalytic reactors, electrochemical cells, straining systems ...), thus allowing one to characterize *in situ*, and sometimes in real time the effects of controlled parameters (temperature, deposition rate, pressure,

applied stress, exposure to different gases, application of an electric field, magnetic field ...) on the morphology of the sample. In addition, it is possible to simultaneously measure other physical properties by other techniques, mainly involving light (Raman, UV-visible reflectivity, second-harmonic generation ...). This advantage will be certainly used in the near future to design new instruments not only optimized for GISAXS measurements, but also for complementary tools.

Two drawbacks of the approaches described in this report ought to be discussed and lead to future perspectives for the application of novel X-ray techniques that can only be exploited at current 3rd generation synchrotrons and/or future free electron based X-ray sources. One drawback is that in all examples described above, real space model assumptions for the nanoparticles are needed to fit the pattern; this is due to the well known “phase problem” inherent to all X-ray scattering measurements, which does not allow for a direct reconstruction of the morphology from the measured intensity distribution in reciprocal space. The other drawback is that the information obtained is based on measurements on large nanoparticle ensembles, thus measuring their mean morphology rather than the variation of individual morphological properties. The knowledge on the variation of properties is especially important for nanoparticles grown by self-organization, where differences from one island to another are expected. Recently, two major technical improvement of third generation synchrotrons have allowed new kinds of GISAXS measurements, by offering beams with partial coherence and by focusing X-rays to submicron dimensions. The focusing of hard X-rays reached beam sizes in the 100 nm range and below. The use of (incoherent) micro-beams, allows for instance to scan an inhomogeneous sample, yielding GISAXS images characteristic of (sub)micron-size areas of the sample. The use of a small coherent X-ray beam set to image one particle yields an image from which the complete sample shape and size can in principle be deduced without assumption, thus solving the “phase problem”.

The future developments of the GISAXS technique will almost certainly be driven by the increase of brilliance of the next generation synchrotron sources, and by the advent of the free electron lasers. This will provide more intense beam, more coherent, with a smaller size and a smaller divergence, allowing for the development of coherent GISAXS, as well as dynamic studies at a much smaller timescale than presently possible. The combination of both will allow also to follow the evolution of speckles with time [556,557] (X-ray Coherent Spectroscopy), thus yielding important information on the different characteristic times in a system under evolution. Last but not least, new two-dimensional detectors, for instance based on the hybrid pixel technology, are being available, with a much smaller background, much larger dynamics and faster response. This should allow, among others, to measure both the specular and diffuse scattering at once.

Acknowledgements

We would like to thank C. Revenant, T.U. Schülli, A. Létoublon, E.A. Soares, M.-I. Richard, M. Ducruet, O. Ulrich, M.C. Saint-Lager, S. Garaudé, P. Dolle, O. Robach, M. Mantilla, J. Jupille, J. Olander, N. Chaâbane for their help during measurements and/or analysis and F. Finocchi for discussion about scattering theory.

Appendix. The analytical Fourier transforms of simple shapes

The particle shape are described in Fig. 175 as well as the relevant parameters. Note that the z-axis is upward and the x-axis is aligned along a particle edge if any. V , S , R_g are respectively the volume, the area of the surface seen from top and the radius obtained upon the rotation along the z-axis. $\sin_c(x) = \sin(x)/x$ is the cardinal sine, $J_1(x)$ the Bessel function of first order [165].

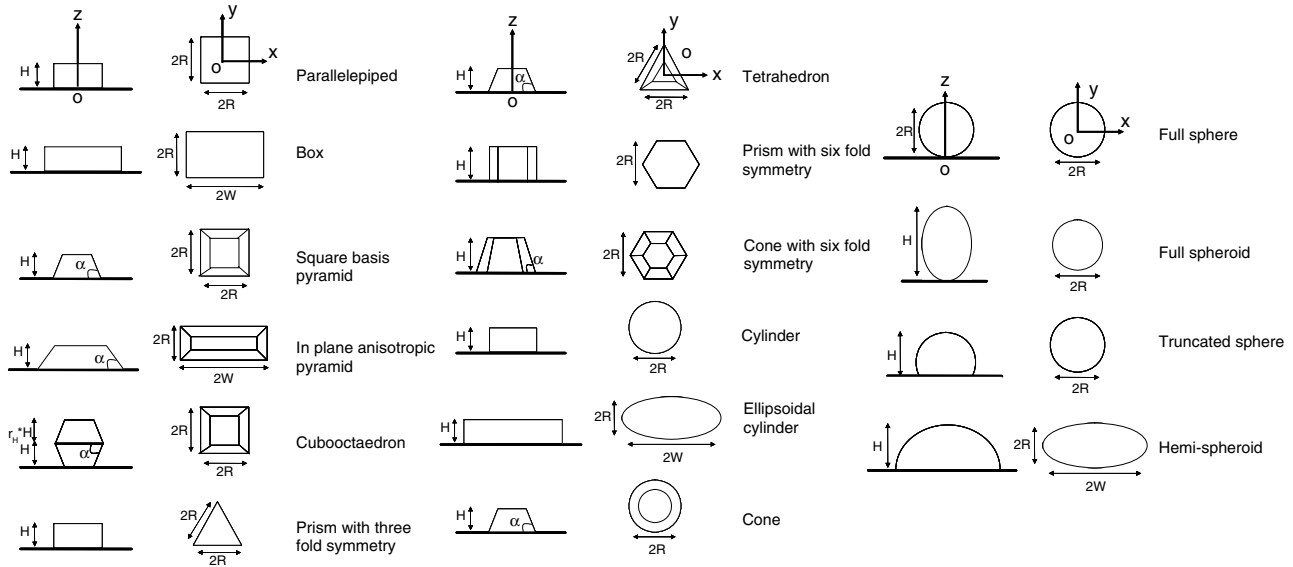


Fig. 175. Particle shapes which form factors are given in equations in Appendix A. Left panel: side view, right panel: top view.

- **Parallelepiped:**

$$\begin{aligned} F_{pa}(\mathbf{q}, R, H) &= 4R^2H \sin_c(q_xR) \sin_c(q_yR) \sin_c(q_zH/2) e^{iq_zH/2} \\ V_{pa} &= 4R^2H, \quad S_{pa} = 4R^2, \quad R_{pa} = \sqrt{2}R. \end{aligned} \quad (213)$$

- **Box:**

$$\begin{aligned} F_{\text{box}}(\mathbf{q}, R, W, H) &= 4RWH \sin_c(q_xR) \sin_c(q_yW) \sin_c(q_zH/2) e^{iq_zH/2} \\ V_{\text{box}} &= 4RWH, \quad S_{\text{box}} = 4RW, \quad R_{\text{box}} = \sqrt{R^2 + W^2}. \end{aligned} \quad (214)$$

- **Square basis pyramid:**

$$\begin{aligned} F_{py}(\mathbf{q}, R, H, \alpha) &= \int_0^H 4R_z^2 \sin_c(q_xR_z) \sin_c(q_yR_z) e^{iq_zz} dz \\ R_z &= R - z/\tan(\alpha) \\ H/R &< \tan(\alpha) \\ V_{py} &= \frac{4}{3} \tan(\alpha) \left[R^3 - \left(R - \frac{H}{\tan(\alpha)} \right)^3 \right], \\ S_{py} &= 4R^2, \quad R_{py} = \sqrt{2}R; \\ F_{py}(\mathbf{q}, R, H, \alpha) &= \frac{H}{q_x q_y} \{ \cos[(q_x - q_y)R] K_1 + \sin[(q_x - q_y)R] K_2 \} \\ &\quad - \cos[(q_x + q_y)R] K_3 - \sin[(q_x + q_y)R] K_4 \} \end{aligned}$$

$$\begin{aligned} K_1 &= \sin_c(q_1H) e^{iq_1H} + \sin_c(q_2H) e^{-iq_2H} \\ K_2 &= -i \sin_c(q_1H) e^{iq_1H} + i \sin_c(q_2H) e^{-iq_2H} \\ K_3 &= \sin_c(q_3H) e^{iq_3H} + \sin_c(q_4H) e^{-iq_4H} \\ K_4 &= -i \sin_c(q_3H) e^{iq_3H} + i \sin_c(q_4H) e^{-iq_4H} \\ q_1 &= \frac{1}{2} \left[\frac{q_x - q_y}{\tan(\alpha)} + q_z \right], \quad q_2 = \frac{1}{2} \left[\frac{q_x - q_y}{\tan(\alpha)} - q_z \right] \\ q_3 &= \frac{1}{2} \left[\frac{q_x + q_y}{\tan(\alpha)} + q_z \right], \quad q_4 = \frac{1}{2} \left[\frac{q_x + q_y}{\tan(\alpha)} - q_z \right]. \end{aligned} \quad (215)$$

- **In plane anisotropic pyramid:**

$$\begin{aligned} F_{anpy}(\mathbf{q}, R, W, H, \alpha) &= \int_0^H 4R_z W_z \sin_c(q_xR_z) \sin_c(q_yW_z) e^{iq_zz} dz \\ R_z &= R - z/\tan(\alpha) \\ W_z &= W - z/\tan(\alpha) \end{aligned}$$

$$H/R < \tan(\alpha) \quad \text{and} \quad W/R < \tan(\alpha) \quad (216)$$

$$V_{anpy} = 4 \left[WRH - \frac{H^2(R+W)}{2\tan(\alpha)} + \frac{H^3}{3\tan^2(\alpha)} \right],$$

$$S_{anpy} = 4RW, \quad R_{anpy} = \sqrt{R^2 + W^2};$$

$$\begin{aligned} F_{anpy}(\mathbf{q}, R, W, H, \alpha) &= \frac{H}{q_x q_y} \{ \cos[q_xR - q_yW] K_1 + \sin[q_xR - q_yW] K_2 \\ &\quad - \cos[q_xR + q_yW] K_3 - \sin[q_xR + q_yW] K_4 \} \end{aligned}$$

$$\begin{aligned} K_1 &= \sin_c(q_1H) e^{iq_1H} + \sin_c(q_2H) e^{-iq_2H} \\ K_2 &= -i \sin_c(q_1H) e^{iq_1H} + i \sin_c(q_2H) e^{-iq_2H} \\ K_3 &= \sin_c(q_3H) e^{iq_3H} + \sin_c(q_4H) e^{-iq_4H} \\ K_4 &= -i \sin_c(q_3H) e^{iq_3H} + i \sin_c(q_4H) e^{-iq_4H} \\ q_1 &= \frac{1}{2} \left[\frac{q_x - q_y}{\tan(\alpha)} + q_z \right], \quad q_2 = \frac{1}{2} \left[\frac{q_x - q_y}{\tan(\alpha)} - q_z \right] \\ q_3 &= \frac{1}{2} \left[\frac{q_x + q_y}{\tan(\alpha)} + q_z \right], \quad q_4 = \frac{1}{2} \left[\frac{q_x + q_y}{\tan(\alpha)} - q_z \right]. \end{aligned} \quad (217)$$

- **Cubooctahedron:**

$$\begin{aligned} F_{cu}(\mathbf{q}, R, H_1, H_2, \alpha) &= e^{iq_zH} [F_{py}(q_x, -q_y, -q_z, R, H, \alpha) \\ &\quad + F_{py}(q_x, q_y, q_z, R, r_H H, \alpha)] \end{aligned}$$

$$H/R < \tan(\alpha), \quad r_H H/R < \tan(\alpha) \quad (218)$$

$$V_{cu} = \frac{4}{3} \tan(\alpha) \left[2R^3 - \left(R - \frac{H}{\tan(\alpha)} \right)^3 - \left(R - \frac{Hr_H}{\tan(\alpha)} \right)^3 \right],$$

$$S_{cu} = 4R^2, \quad R_{cu} = \sqrt{2}R.$$

- **Prism with three fold symmetry:**

$$\begin{aligned} F_{pr3}(\mathbf{q}, R, H) &= \frac{2\sqrt{3}e^{-iq_yR/\sqrt{3}}}{q_x(q_x^2 - 3q_y^2)} \left[q_x e^{iq_yR\sqrt{3}} - q_x \cos(q_xR) \right. \\ &\quad \left. - i\sqrt{3}q_y \sin(q_xR) \right] \sin_c(q_zH/2) e^{iq_zH/2} \end{aligned}$$

$$V_{pr3} = \sqrt{3}R^2H, \quad S_{pr3} = \sqrt{3}R^2, \quad R_{pr3} = \frac{2}{\sqrt{3}}R. \quad (219)$$

• *Tetrahedron*

$$\begin{aligned}
 F_{te}(\mathbf{q}, R, H, \alpha) &= \frac{2\sqrt{3}}{q_x(q_x^2 - 3q_y^2)} \int_0^H e^{-iq_y R_z/\sqrt{3}} \\
 &\times \left[q_x e^{iq_y R_z \sqrt{3}} - q_x \cos(q_x R_z) - i\sqrt{3}q_y \sin(q_x R_z) \right] e^{iq_z z} dz \\
 R_z &= R - \sqrt{3}/\tan(\alpha)z \\
 H/R &< \tan(\alpha)/\sqrt{3} \\
 V_{te} &= \frac{1}{3} \tan(\alpha) \left[R^3 - \left(R - \frac{\sqrt{3}H}{\tan(\alpha)} \right)^3 \right], \\
 S_{te} &= \sqrt{3}R^2, \quad R_{te} = \frac{2}{\sqrt{3}}R; \\
 F_{te}(\mathbf{q}, R, H, \alpha) &= \frac{H}{\sqrt{3}q_x(q_x^2 - 3q_y^2)} e^{iq_z R \tan(\alpha)/\sqrt{3}} \\
 &\times \left\{ -(q_x + \sqrt{3}q_y) \sin_c(q_1 H) e^{iq_1 L} \right. \\
 &\left. + (-q_x + \sqrt{3}q_y) \sin_c(q_2 H) e^{-iq_2 L} + 2q_x \sin_c(q_3 H) e^{iq_3 L} \right\} \\
 q_1 &= \frac{1}{2} \left[\frac{\sqrt{3}q_x - q_y}{\tan(\alpha)} - q_z \right], \quad q_2 = \frac{1}{2} \left[\frac{\sqrt{3}q_x + q_y}{\tan(\alpha)} + q_z \right], \\
 q_3 &= \frac{1}{2} \left[\frac{2q_y}{\tan(\alpha)} - q_z \right] \\
 L &= \frac{2 \tan(\alpha)R}{\sqrt{3}} - H. \tag{220}
 \end{aligned}$$

• *Prism with six fold symmetry*

$$\begin{aligned}
 F_{pr6}(\mathbf{q}, R, H) &= \frac{4\sqrt{3}}{3q_y^2 - q_x^2} \left[q_y^2 R^2 \sin_c(q_x R/\sqrt{3}) \sin_c(q_y R) \right. \\
 &\left. + \cos(2q_x R/\sqrt{3}) - \cos(q_y R) \cos(q_x R/\sqrt{3}) \right] \\
 &\times \sin_c(q_z H/2) e^{iq_z H/2} \\
 V_{pr6} &= 2\sqrt{3}R^2 H, \quad S_{pr6} = 2\sqrt{3}R^2, \quad R_{pr6} = \frac{2}{\sqrt{3}}R. \tag{221}
 \end{aligned}$$

• *Cone with six fold symmetry*

$$\begin{aligned}
 F_{co6}(\mathbf{q}, R, H) &= \frac{4\sqrt{3}}{3q_y^2 - q_x^2} \int_0^H \left[q_y^2 R_z^2 \sin_c(q_x R_z/\sqrt{3}) \sin_c(q_y R_z) \right. \\
 &\left. + \cos(2q_x R_z/\sqrt{3}) - \cos(q_y R_z) \cos(q_x R_z/\sqrt{3}) \right] e^{iq_z z} dz \\
 R_z &= R - z/\tan(\alpha) \\
 H/R &< \tan(\alpha) \tag{222}
 \end{aligned}$$

• *Cylinder*

$$\begin{aligned}
 F_{cy}(\mathbf{q}, R, H) &= 2\pi R^2 H \frac{J_1(q_\parallel R)}{q_\parallel R} \sin_c(q_z H/2) e^{iq_z H/2} \\
 q_\parallel &= \sqrt{q_x^2 + q_y^2} \\
 V_{cy} &= \pi R^2 H, \quad S_{cy} = \pi R^2, \quad R_{cy} = R. \tag{223}
 \end{aligned}$$

• *Ellipsoidal cylinder*

$$F_{ell}(\mathbf{q}, R, W, H, \alpha) = 2\pi RWH \frac{J_1(\gamma)}{\gamma} \sin_c(q_z H/2) e^{iq_z H/2}$$

$$\gamma = \sqrt{(q_x R)^2 + (q_y W)^2}$$

$$V_{ell} = \pi RWH, \quad S_{anpy} = \pi RW, \quad R_{anpy} = \sqrt{R^2 + W^2}. \tag{224}$$

• *Cone*

$$\begin{aligned}
 F_{co}(\mathbf{q}, R, H, \alpha) &= \int_0^H 2\pi R_z^2 \frac{J_1(q_\parallel R_z)}{q_\parallel R_z} e^{iq_z z} dz \\
 q_\parallel &= \sqrt{q_x^2 + q_y^2}, \quad R_z = R - z/\tan(\alpha) \\
 H/R &< \tan(\alpha) \\
 V_{co} &= \frac{\pi}{3} \tan(\alpha) \left[R^3 - \left(R - \frac{H}{\tan(\alpha)} \right)^3 \right], \\
 S_{co} &= \pi R^2, \quad R_{co} = R. \tag{225}
 \end{aligned}$$

• *Full sphere*

$$\begin{aligned}
 F_{fsp}(\mathbf{q}, R) &= 4\pi R^3 \frac{\sin(qR) - qR \cos(qR)}{(qR)^3} e^{iq_z R} \\
 V_{fsp} &= \frac{4}{3}\pi R^3, \quad S_{fsp} = \pi R^2, \quad R_{fsp} = R. \tag{226}
 \end{aligned}$$

• *Full spheroid*

$$\begin{aligned}
 F_{fsph}(\mathbf{q}, R, H) &= e^{iq_z H/2} \int_0^{H/2} 4\pi R_z^2 \frac{J_1(q_\parallel R_z)}{q_\parallel R_z} \cos(q_z z) dz \\
 q_\parallel &= \sqrt{q_x^2 + q_y^2}, \quad R_z = R \sqrt{1 - 4\frac{z^2}{H^2}} \\
 V_{fsph} &= \frac{4}{3}\pi R^2 H, \quad S_{fsph} = \pi R^2, \quad R_{fsph} = R. \tag{227}
 \end{aligned}$$

• *Truncated sphere*

$$\begin{aligned}
 F_{sp}(\mathbf{q}, R, H) &= e^{iq_z(H-R)} \int_{R-H}^H 2\pi R_z^2 \frac{J_1(q_\parallel R_z)}{q_\parallel R_z} e^{iq_z z} dz \\
 q_\parallel &= \sqrt{q_x^2 + q_y^2}, \quad R_z = \sqrt{R^2 - z^2} \\
 0 &< H/R < 2 \\
 V_{sp} &= \pi R^3 \left[\frac{2}{3} + \frac{H-R}{R} - \frac{1}{3} \left(\frac{H-R}{R} \right)^3 \right], \\
 S_{sp} &= \begin{cases} \pi R^2 & \text{if } H > R \\ \pi(2RH - H^2) & \text{if } H < R, \end{cases} \\
 R_{sp} &= \begin{cases} R & \text{if } H > R \\ \sqrt{2RH - H^2} & \text{if } H < R. \end{cases}
 \end{aligned} \tag{228}$$

• *Hemi-spheroid:*

$$\begin{aligned}
 F_{hsphe}(\mathbf{q}, R, W, H) &= 2\pi \int_0^H R_z W_z \frac{J_1(\gamma)}{\gamma} e^{iq_z z} dz \\
 R_z &= R \sqrt{1 - \left(\frac{z}{H} \right)^2}, \quad W_z = W \sqrt{1 - \left(\frac{z}{H} \right)^2} \\
 \gamma &= \sqrt{(q_x R_z)^2 + (q_y W_z)^2} \\
 V_{hsphe} &= \frac{2}{3}\pi RWH, \quad S_{hsphe} = \pi RW, \\
 R_{hsphe} &= \sqrt{R^2 + W^2}. \tag{229}
 \end{aligned}$$

References

- [1] C. Teichert, Self-organization of nanostructures in semiconductor heteroepitaxy, *Surf. Sci. Rep.* 365 (2002) 335–342.

- [2] C. Henry, Surface studies of supported model catalysts, *Surf. Sci. Rep.* 31 (1998) 231–325.
- [3] R. Meyer, C. Lemire, S.K. Shaikhutdinov, H.J. Freund, Surface chemistry of catalysis by gold, *Gold Bull.* 37 (2004) 72–124.
- [4] S.H. Sun, C.B. Murray, D. Weller, L. Folks, A. Moser, Monodisperse fept nanoparticles and ferromagnetic fept nanocrystal superlattices, *Science* 287 (2000) 1989–1992.
- [5] J. Bansmann, S.H. Baker, C. Binns, J.A. Blackman, J.-P. Bucher, J. Dorantes-Davila, V. Dupuis, L. Favre, D. Kechrakos, A. Kleibert, K.-H. Meiwes-Broer, G.M. Pastor, A. Perez, O. Toulemonde, K.N. Trohidou, J. Tuailon, Y. Xie, Magnetic and structural properties of isolated and assembled clusters, *Surf. Sci. Rep.* 56 (2005) 189–275.
- [6] C. Lamberti, Characterization of Semiconductor Heterostructures and Nanostructures, Elsevier, 2008.
- [7] E. Borovitskaya, M. Shur, Quantum Dots, World Scientific, New Jersey, London, Singapore, Hong Kong, 2002.
- [8] M. Zinke-Allmang, L.C. Feldman, M.H. Grabow, Clustering on surfaces, *Surf. Sci. Rep.* 16 (1992) 377–463.
- [9] W.C. Marra, P. Eisenberger, A.Y. Cho, X-ray total-external-reflection-bragg diffraction: A structural study of the ga-as-al interface, *J. Appl. Phys.* 50 (1979) 6927.
- [10] P. Eisenberger, W.C. Marra, X-ray diffraction study of the ge(001) reconstructed surface, *Phys. Rev. Lett.* 46 (1981) 1081.
- [11] R. Feidenhans'l, Surface structure determination by X-ray diffraction, *Surf. Sci. Rep.* 10 (1989) 105–188.
- [12] I.K. Robinson, D.J. Tweet, *Rep. Prog. Phys.* 55 (1992) 599.
- [13] G. Renaud, Oxide surfaces and metal/oxide interfaces studied by grazing incidence X-ray scattering, *Surf. Sci. Rep.* 32 (1998) 1–90.
- [14] J. Daillant, A. Gibaud, X-ray and Neutron Reflectivity: Principle and Applications, in: Lectures Notes in Physics, Springer, 1999.
- [15] V. Holý, U. Pietsch, T. Baumbach, High-resolution X-ray scattering from thin films and multilayers, in: Springer Tracts in Modern Physics, vol. 149, Springer, 1998.
- [16] J.R. Levine, J.B. Cohen, Y.W. Chung, P. Georgopoulos, Grazing incidence small angle X-ray scattering: A new tool for studying thin film growth, *J. Appl. Crystallogr.* 22 (1989) 528–532.
- [17] J.R. Levine, J.B. Cohen, Y.W. Chung, Thin film island growth kinetics: A grazing incidence small angle X-ray scattering study of gold on glass, *Surf. Sci.* 248 (1991) 215–224.
- [18] A. Naudon, D. Thiaudiére, Grazing incidence small angle scattering: Morphology of deposited clusters and nanostructure of thin films, *J. Appl. Crystallogr.* 30 (1997) 822–827.
- [19] D. Thiaudiére, O. Proux, J.-S. Micha, C. Revenant, J.-R. Regnard, S. Lequien, Structural and morphological studies of Co/SiO₂ discontinuous multilayers, *Physica B* 283 (2000) 114–118.
- [20] F. Gonella, E. Cattaruzza, G. Battaglin, F. D'acapito, C. Sada, P. Mazzoldi, C. Maurizio, G. Mattei, A. Martorana, A. Longo, F. Zontone, *J. Non-Cryst. Solids* 280.
- [21] T. Rochand, V. Holý, A. Daniel, E. Höflinger, M. Meduna, T.H. Metzger, G. Bauer, J. Zhu, K. Brunner, G. Abstreiter, *J. Phys. D: Appl. Phys.* 34.
- [22] J. Stangl, V. Holý, P. Mikulik, G. Bauer, I. Kegel, T.H. Metzger, O.G. Schmidt, C. Lange, K. Eberl, Self-assembled carbon-induced germanium quantum dots studied by grazing-incidence small-angle scattering, *Appl. Phys. Lett.* 74 (25) (1999) 3785–3787.
- [23] M. Schmidbauer, T. Wiebach, H. Raidt, M. Hanke, R. Köhler, H. Wawra, Ordering of self-assembled Si_{1-x}Ge_x islands studied by grazing incidence small-angle X-ray scattering and atomic force microscopy, *Phys. Rev. B* 58 (1998) 10523.
- [24] M. Schmidbauer, T. Wiebach, H. Raidt, M. Hanke, R. Köhler, H. Wawra, *J. Phys. D: Appl. Phys.* 32.
- [25] G. Renaud, R. Lazzari, C. Revenant, A. Barbier, M. Noblet, O. Ulrich, F. Leroy, J. Jupille, Y. Borensztein, C.R. Henry, J.-P. Deville, F. Scheurer, J. Mane-Mane, O. Fruchart, Real-time monitoring of growing nanoparticles, *Science* 300 (2003) 1416.
- [26] G. Renaud, M. Ducret, O. Ulrich, R. Lazzari, Apparatus for real time in situ quantitative studies of growing nanoparticles by grazing incidence small angle X-ray scattering and surface differential reflectance spectroscopy, *Nucl. Inst. Meth. B* 222 (3–4) (2004) 667–680.
- [27] R. Lazzari, IsGISAXS: A program for grazing-incidence small-angle X-ray scattering analysis of supported islands, *J. Appl. Crystallogr.* 35 (2002) 406–421.
- [28] R. Lazzari, IsGISAXS web site: <http://www.insp.jussieu.fr/axe2/Oxydes/IsGISAXS/isisaxs.htm>, 2002.
- [29] C. Revenant, F. Leroy, R. Lazzari, G. Renaud, C.R. Henry, Quantitative analysis of grazing incidence small angle X-ray scattering: pd/MgO(001)growth, *Phys. Rev. B* 69 (2004) 035411–1.
- [30] B. Voigtländer, G. Meyer, N.M. Amer, Epitaxial growth of thin magnetic cobalt films on Au(111) studied by scanning tunneling microscopy, *Phys. Rev. B* 44 (18) (1991) 10354–10357.
- [31] O. Fruchart, G. Renaud, J.-P. Deville, A. Barbier, F. Scheurer, M. Klaua, J. Barthel, M. Noblet, O. Ulrich, J. Mane-Mane, J. Kirschner, *J. Cryst. Growth.* 237–239 (2002) 2035.
- [32] F. Leroy, G. Renaud, A. Létoublon, R. Lazzari, Growth of Co on Au(111) studied by multiwavelength anomalous grazing incidence small angle X-ray scattering: From ordered nanostructures to percolated thin films and nanopillars, *Phys. Rev. B* 77 (2008) 235429.
- [33] M.C. Saint-Lager, A. Bailly, P. Dolle, R. Baudoin-Savois, P. Taunier, S. Garaudée, S. Cuccaro, S. Douillet, O. Geaymond, G. Perroux, O. Tissot, J.-S. Micha, O. Ulrich, F. Rieutord, New reactor dedicated to in operando studies of model catalysts by means of surface X-ray diffraction and grazing incidence small angle X-ray scattering, *Rev. Sci. Inst.* 78 (2007) 083902.
- [34] M.C. Saint-Lager, A. Bailly, M. Mantilla, S. Garaudée, R. Lazzari, P. Dolle, O. Robach, J. Jupille, I. Laoufi, P. Taunier, Looking by grazing incidence small angle X-ray scattering at gold nanoparticles supported on rutile TiO₂(110) during co oxidation, *Gold. Bull.* 42 (2008) 159.
- [35] S.K. Sinha, E.B. Sirota, S. Garoff, H.B. Stanley, X-ray and neutron scattering from rough surfaces, *Phys. Rev. B* 38 (4) (1988) 2297–2311.
- [36] M. Rauscher, T. Salditt, H. Spohn, Small-angle X-ray scattering under grazing incidence: The cross section in the distorted-wave Born approximation, *Phys. Rev. B* 52 (23) (1995) 16855–16863.
- [37] M. Rauscher, R. Paniago, T.H. Metzger, Z. Kovats, J. Domke, H.D. Pfannes, J. Schulze, I. Eisele, Grazing incidence small angle X-ray scattering from free-standing nanostructures, *J. Appl. Phys.* 86 (12) (1999) 6763–6769.
- [38] J. Als-Nielsen, D. McMorrow, Elements of modern X-ray physics, John Wiley & Sons, New York, 2001.
- [39] Y. Yoneda, Anomalous surface reflection of X-rays, *Phys. Rev.* 131 (1963) 2010–2013.
- [40] A. Guinier, X-ray Diffraction in Crystals Imperfect Crystals and Amorphous Bodies, Dover Publications, Inc, New York, 1963.
- [41] B.E. Warren, X-ray Diffraction, Dover Publication Inc, New York, 1969.
- [42] R. Hosemann, S.N. Bagchi, Direct Analysis of Diffraction by Matter, North-Holland Publishing Company, Amsterdam, 1962.
- [43] H. Dosch, Critical Phenomena at Surfaces and Interfaces: Evanescent X-ray and Neutron Scattering, Springer-Verlag, Berlin, 1992.
- [44] S. Dietrich, A. Haase, Scattering of X-rays and neutrons at interfaces, *Phys. Rep.* 260 (1995) 1–138.
- [45] E. Vlieg, Integrated intensities using a six-circle surface X-ray diffractometer, *J. Appl. Crystallogr.* 30 (1997) 532.
- [46] O. Robach, Y. Garreau, K. Aid, M. Véron-Jolliot, Corrections for surface X-ray diffraction measurements using the z-axis geometry: Finite size effects in direct and reciprocal space, *J. Appl. Crystallogr.* 33 (2000) 1006–1018.
- [47] E. Chason, T.M. Mayer, Thin film and surface characterization by specular X-ray reflectivity, *Critical Reviews in Solid State and Materials Sciences* 22 (1997) 1–67.
- [48] A. Gibaud, S. Hazra, X-ray reflectivity and diffuse scattering, *Current Science* 78 (2000) 1467–1477.
- [49] H. Kiessig, *Ann. der Physik* 10 (1931) 715.
- [50] T. Salditt, D. Lott, T.H. Metzger, J. Peisl, G. Vignaud, P. Høghøj, O. Schärf, P. Hinze, R. Lauer, Interfacial roughness and related growth mechanism in sputtered w/si multilayers, *Phys. Rev. B* 54 (1996) 5860–5872.
- [51] J.R. Levine, P. Georgopoulos, Y.W. Chung, J.B. Cohen, Gisaxs: Glancing incidence small angle X-ray scattering, *J. Phys. IV C8* (3) (1993) 411–417.
- [52] A. Naudon, T. Slimani, P. Goudeau, *J. Appl. Crystallogr.* 24 (1991) 501–508.
- [53] A. Naudon, D. Babonneau, D. Thiaudiére, S. Lequien, Grazing-incidence small-angle X-ray scattering applied to the characterization of aggregates in surface regions, *Physica B* 283 (2000) 69–74.
- [54] D. Thiaudiére, A. Naudon, Grazing-incidence X-ray scattering – analysis of aggregate morphology, *J. Phys. IV* 6 (1996) 553–560.
- [55] D. Babonneau, F. Petroff, J.L. Maurice, F. Fettar, A. Vaurès, A. Naudon, Evidence of self-organized growth in granular Co/Al₂O₃ multilayers, *Appl. Phys. Lett.* 76 (20) (2000) 2892–2894.
- [56] D. Babonneau, I.R. Videnočić, M.G. Garnier, P. Oelhafen, Morphology and size distribution of gold nanoclusters in a-C:H film studied by grazing incidence small-angle X-ray scattering, *Phys. Rev. B* 63 (2001) 195401–1.
- [57] B.M. Lairson, A.P. Payne, S. Brennan, N.M. Rensing, B.J. Daniels, B.M. Clemens, *In situ* X-ray measurements of the initial epitaxy of Fe(0001) films on Mg(001), *J. Appl. Phys.* 78 (7) (1995) 4449–4455.
- [58] V. Holý, J. Kubuena, I. Ohlídal, K. Lischka, W. Plotz, X-ray reflection from rough layered systems, *Phys. Rev. B* 47 (23) (1993) 15896–15903.
- [59] V. Holý, T. Baumbach, Non specular X-ray reflection from rough multilayers, *Phys. Rev. B* 49 (15) (1994) 10668–10676.
- [60] T.H. Metzger, I. Kegel, R. Paniago, J. Peisl, Grazing incidence X-ray scattering: Shape, size strain and correlations in quantum dot systems studied by grazing incidence X-ray scattering methods, *Thin Solid Films* 336 (8) (1998) 1–8.
- [61] T.H. Metzger, I. Kegel, R. Paniago, J. Peisl, Grazing incidence X-ray scattering: An ideal tool to study the structure of quantum dots, *J. Phys. D: Appl. Phys.* 32 (1999) A202–A207.
- [62] J. Stangl, V. Holý, T. Roch, A. Daniel, G. Bauer, J. Zhu, K. Brunner, G. Abstreiter, Grazing incidence small angle X-ray scattering study of buried and free-standing SiGe islands in a SiGe/Si superlattice, *Phys. Rev. B* 62 (11) (2000) 7229–7236.
- [63] K. Zhang, C. Heyn, W. Hansen, T. Schmidt, J. Falta, Grazing incidence structural characterization of InAs quantum dots on GaAs(001), *Appl. Surf. Sci.* 175–176 (2001) 606–612.
- [64] V. Holý, T. Roch, J. Stangl, A. Daniel, G. Bauer, T.H. Metzger, Y.H. Zhu, K. Brunner, G. Abstreiter, Grazing incidence small-angle X-ray scattering study of self-organized size wires, *Phys. Rev. B* 63 (2001) 205318.
- [65] V. Holý, J. Stangl, G. Springholz, M. Pincelots, G. Bauer, High resolution X-ray diffraction from self-organized PbSe/PbEuTe quantum dots superlattices, *J. Phys. D: Appl. Phys.* 34 (2001) A1–A5.
- [66] BM32 web site: http://www.esrf.fr/exp_facilities/BM32/index.htm, 2004.

- [67] J.M. Bloch, Angle and index calculations for a z-axis X-ray diffractometer, *J. Appl. Crystallogr.* 18 (1985) 33.
- [68] R. Baudouin-Savois, M.De. Santis, M.C. Saint-Lager, P. Dolle, O. Geaymond, P. Taunier, P. Jeantet, J.P. Roux, G. Renaud, A. Barbier, et al A new uhv diffractometer for surface structure and real time molecular beam deposition studies with synchrotron radiations at esrf, *Nucl. Instr. Meth. Phys. Res. B* 149 (1999) 213–227.
- [69] O. Balmes, R. Van rijn, D. Wermelle, A. Resta, L. Petit, H. Isern, T. Dufrane, R. Felici, The id03 surface diffraction beamline for in-situ and real-time X-ray investigations of catalytic reactions at surfaces, *Catal. Today* 145 (2009) 220–226.
- [70] A. Naudon, *Modern Aspects of Small Angle Scattering*, Kluwer Academic Netherlands, 1995.
- [71] R.W. James, *The optical principles of the diffraction of X-rays*, Cornell University Press, New York, 1965.
- [72] O. Robach, Etude in situ de la croissance de Ag sur MgO(100) et de Ni/Ag(001) et de la nituration du GaAs par diffusion de rayons x en incidence rasante, Ph.D. Thesis, Université Joseph Fourier Grenoble I, France, 1997.
- [73] A. Guinier, G. Fournet, *Small-angle scattering of X-rays*, John Wiley & Sons, New York, 1955.
- [74] P.W. Zhu, J.W. White, Small angle X-ray scattering of an ordering aggregation, *J. Chem. Phys.* 22 (8) (1996) 9169–9173.
- [75] J.A. Venables, Rate equations approaches to thin film nucleation kinetics, *Phil. Mag.* 27 (3) (1973) 697–738.
- [76] M. Baus, J.L. Colot, Thermodynamics and structure of a fluid of hard rods disks, spheres or hyperspheres from rescaled virial expansion, *Phys. Rev. A* 36 (8) (1987) 3912–3925.
- [77] R. Balescu, *Equilibrium and Nonequilibrium Statistical Mechanics*, John Wiley & Sons, New York London Sidney Toronto, 1975.
- [78] C. Revenant, G. Renaud, R. Lazzari, Growth of Ag on MgO(001) studied in situ by grazing incidence small angle X-ray scattering, *Nucl. Inst. Meth. B* 246 (2006) 112.
- [79] C. Revenant, G. Renaud, R. Lazzari, J. Jupille, Defect-pinned nucleation growth and dynamic coalescence of Ag islands on MgO(001): An in situ grazing-incidence small-angle X-ray scattering study, *Phys. Rev. B* 79 (2009) 1.
- [80] R. Lazzari, G. Renaud, C. Revenant, J. Jupille, Y. Borensztein, Adhesion of growing nanoparticles at a glance: Surface differential reflectivity spectroscopy and grazing incidence small angle X-ray scattering, *Phys. Rev. B* 79 (2009) 125428.
- [81] R. Lazzari, F. Leroy, G. Renaud, J. Jupille, Self-similarity during growth of the Au/TiO₂(110) model catalyst as seen by grazing incidence X-ray scattering techniques, *Phys. Rev. B* 76 (2007) 125412.
- [82] J.S. Pedersen, Analysis of small-angle scattering data from colloids and polymer solutions: Modeling and least-squares fitting, *Advances in Colloid and Interface Science* 70 (1997) 171–210.
- [83] J. Als-Nielsen, D. Jacquemain, K. Kjaer, F. Leveiller, M. Lahav, Principles and applications of grazing incidence X-ray and neutron scattering from ordered molecular monolayers at the air-water interface, *Phys. Rep.* 246 (1994) 251–313.
- [84] X.L. Zhou, S.H. Chen, Theoretical foundation of X-ray and neutron reflectometry, *Phys. Rep.* 257 (1995) 223–348.
- [85] J.K. Basu, M.K. Sanyal, Ordering and growth of langmuir-blodgett films: X-ray scattering studies, *Phys. Rep.* 363 (2002) 1–84.
- [86] L. Landau, E. Lifchitz, *Electrodynamics of Continuous Media*, Mir, Moscow, 1967.
- [87] J.D. Jackson, *Classical Electrodynamics*, Wiley & Sons, New York, 1975.
- [88] D.R. Lee, S.K. Sinha, D. Haskel, Y. Choi, J.C. Lang, S.A. Stepanov, G. Srayer, X-ray resonant magnetic scattering from structurally and magnetically rough interfaces in multilayered systems: I. specular reflectivity, *Phys. Rev. B* 68 (2003) 224409.
- [89] D.R. Lee, S.K. Sinha, C.S. Nelson, J.C. Lang, C.T. Venkataraman, G. Srayer, R.M. Osgood, X-ray resonant magnetic scattering from structurally and magnetically rough interfaces in multilayered systems: II. diffuse scattering, *Phys. Rev. B* 68 (2003) 224410.
- [90] LBN. Laboratory, Center for X-ray optics, <http://www-cxro.lbl.gov/>.
- [91] I. Schiff, *Quantum Mechanics*, MacGraw-Hill, New-York, 1968.
- [92] A. Messiah, *Quantum Mechanics*, vols. 1–2, Dunod, Paris, 1964.
- [93] S. Dietrich, H. Wagner, Critical surface scattering of X-rays at grazing angles, *Z. Phys. B* 56 (1984) 207.
- [94] J. Lekner, *Theory of Reflection*, Martinus Nijhoff, Dordrecht, The Netherlands, 1987.
- [95] M. Born, E. Wolf, *Principles of Optics*, 7th ed., Cambridge University Press, 1999.
- [96] F. Abelès, *Ann. de Physique* 5 (1950) 596.
- [97] L.G. Parratt, Surface studies of solids by total reflection of X-rays, *Phys. Rev.* 95 (1954) 359–369.
- [98] B. Vidal, P. Vincent, Metallic multilayers for x rays using classical thin-film theory, *Appl. Opt.* 23 (1984) 1794–1801.
- [99] P. Beckmann, A. Spizzichino, *The scattering of electromagnetic waves from rough surfaces*, Pergamon, New York, 1963.
- [100] P. Croce, L. Nérot, Etude des couches minces et des surfaces par réflexion rasante, spéculaire ou diffuse, de rayons x, *Rev. Phys. Appl.* 11 (1976) 113.
- [101] L. Nérot, P. Croce, Caractérisation des surfaces par réflexion rasante des rayons x, application à l'étude du polissage de quelques verres silicates, *Rev. Phys. Appl.* 15 (1980) 761–779.
- [102] D.K.G. de Boer, Influence of the roughness profile on the specular reflectivity of X-rays and neutrons, *Phys. Rev. B* 49 (9) (1994) 5817–5820.
- [103] J. Rayleigh, *The Theory of Sound*, MacMillan, London, 1895.
- [104] J.C. Kimball, D. Bittel, Surface roughness and the scattering of glancing-angle X-rays: Application to X-rays lenses, *J. Appl. Phys.* 74 (1993) 877–883.
- [105] D.G. Stearns, The scattering of X-rays from nonideal multilayer structures, *J. Appl. Phys.* 65 (1989) 491–506.
- [106] R. Pynn, Neutron scattering by rough surfaces at grazing incidence, *Phys. Rev. B* 45 (1992) 602–612.
- [107] V.F. Sears, Generalized distorted-wave born approximation for neutron reflection, *Phys. Rev. B* 48 (1993) 17477–17485.
- [108] D.K.G. de Boer, X-ray reflection and transmission by rough surfaces, *Phys. Rev. B* 51 (1995) 5297–5305.
- [109] D.K.G. de Boer, X-ray scattering and X-ray fluorescence from materials with rough interfaces, *Phys. Rev. B* 53 (1996) 6048–6064.
- [110] D.K.G. de Boer, A.J.G. Leenaers, Probing interface roughness by X-ray scattering, *Physica B* 221 (1996) 18–26.
- [111] A. Caticha, Reflection and transmission of X-rays by graded interfaces, *Phys. Rev. B* 52 (1995) 9214–9223.
- [112] I.D. Feranchuk, A.A. Minkevich, A.P. Ulyanenkov, About non-gaussian behaviour of the debye-waller factor at large scattering vectors, *Eur. Phys. J. Appl. Phys.* 24 (2003) 21–26.
- [113] M.K. Sanyal, S.K. Sinha, A. Gibaud, K.G. Huang, B.L. Carvalho, M. Rafailovich, J. Sokolov, X. Zhao, W. Zhao, Fourier reconstruction of density profiles of thin films using anomalous X-ray reflectivity, *Eur. Phys. Lett.* 21 (1993) 691–696.
- [114] K.M. Zimmermann, M. Tolan, R. Weber, J. Stettner, A.K. Doerr, W. Press, Phase determination of X-ray reflection coefficients, *Phys. Rev. B* 62 (2000) 10377–10382.
- [115] J.K. Blasie, S. Zheng, J. Strzalka, Solution of the phase problem for specular X-ray or neutron reflectivity from thin films on liquid surfaces, *Phys. Rev. B* 67 (2003) 224201.
- [116] J. Lekner, Reflection theory and the analysis of neutron reflection data, *Physica B* 173 (1991) 99–111.
- [117] X.L. Zhou, Quantitative analysis of the nonlinear relationship between neutron or X-ray reflectance and the scattering-length-density profile, *Phys. Rev. E* 52 (1995) 1938–1952.
- [118] T.L. Crowley, A uniform kinematic approximation for specular reflectivity, *Physica A* 195 (1993) 354–374.
- [119] X.L. Zhou, S.H. Chen, G.P. Felcher, New analytical formula for neutron reflection from surface films, *J. Phys. Chem.* 95 (1991) 9025–9029.
- [120] X.L. Zhou, S.H. Chen, G.P. Felcher, Improved analytical formulas for X-ray and neutron reflection from surface films, *Phys. Rev. A* 46 (1992) 1839–1843.
- [121] X.L. Zhou, L. He, Weighted-superposition approximation for X-ray and neutron reflectance, *Phys. Rev. E* 49 (1994) 5345–5353.
- [122] I.D. Feranchuk, S.I. Feranchuk, L.I. Komarov, S. Sytova, A. Ulyanenkov, Analytical ansatz for self-consistent calculations of X-ray transmission and reflection coefficients at graded interfaces, *Phys. Rev. B* 67 (2003) 235417–1.
- [123] I.D. Feranchuk, S.I. Feranchuk, A.P. Ulyanenkov, Self-consistent approach to X-ray reflection from rough surfaces, *Phys. Rev. B* 75 (2007) 085414–1.
- [124] P.S. Epstein, *Proc. Natl. Acad. Sci. U.S.A.* 16 (1930) 627.
- [125] A.V. Andreev, A.G. Michette, A. Renwick, Reflectivity and roughness of X-ray multilayer mirrors: Specular reflection and angular spectrum of scattered radiation, *J. Mod. Opt.* 35 (1988) 1667–1687.
- [126] A. Steyerl, S.S. Malik, L.R. Iyengar, Specular and diffuse reflection and refraction at surfaces, *Physica B* 173 (1991) 47–64.
- [127] W.A. Hamilton, R. Pynn, The effect of surface roughness on the phase of neutrons specularly reflected at grazing incidence, *Physica B* 173 (1991) 71–73.
- [128] J. Ogilvy, *Theory of Wave Scattering from Random Rough Surfaces*, IOP Pub, Bristol, 1991.
- [129] A. Voronovich, *Wave Scattering from Rough Surfaces*, Springer Verlag, Berlin, 1994.
- [130] A. Maradudin, *Light Scattering and Nanoscale Surface Roughness*, Springer Verlag, Berlin, 2007.
- [131] B. Lippman, J. Schwinger, *Phys. Rev.* 79 (1949) 469.
- [132] M. Gell-Mann, M.L. Goldberger, The formal theory of scattering, *Phys. Rev.* 91 (1953) 398–408.
- [133] D.L. Mills, The scattering of low energy electrons by electric field fluctuations near crystal surfaces, *Surf. Sci.* 48 (1975) 59–79.
- [134] H. Ichab, D.L. Mills, *Electron Energy Loss Spectroscopy and Surface Vibrations*, Academic Press, New York, 1982.
- [135] P. Mazur, D.L. Mills, Inelastic scattering of neutrons by surface spin waves on ferromagnets, *Phys. Rev. B* 26 (1982) 5175–5186.
- [136] D. Farias, K.-H. Rieder, Atomic beam diffraction from solid surfaces, *Rep. Prog. Phys.* 61 (1998) 1575–1664.
- [137] A.A. Maradudin, D.L. Mills, Scattering and absorption of electromagnetic radiation by semi-infinite medium in the presence of surface roughness, *Phys. Rev. B* 11 (1975) 1392–1415.
- [138] J.C. Charmet, P.G. de Gennes, Ellipsometric formulas for an inhomogeneous layer with arbitrary refractive-index profile, *J. Opt. Soc. Am.* 73 (1983) 1777–1784.
- [139] G.H. Vineyard, Grazing-incidence diffraction and the distorted-wave approximation for the study of surfaces, *Phys. Rev. B* 26 (1982) 4146–4159.
- [140] U. Mohanty, S.A. Rice, X-ray total external reflectance-diffraction as a probe of the structure of the liquid-vapor interface, *J. Chem. Phys.* 79 (1983) 2482–2486.

- [141] S. Dietrich, H. Wagner, Critical surface scattering of X-rays and neutron at grazing angles, *Phys. Rev. Lett.* 51 (1983) 1469–1471.
- [142] A. Messiah, *Quantum Mechanics*, North-Holland Publishing Company, 1961.
- [143] O.J. Guentert, Study of anomalous surface reflection of x rays, *Phys. Rev.* 36 (1965) 1361–1366.
- [144] A.N. Nigam, Origin of anomalous surface reflection of X-rays, *Phys. Rev.* 138 (1965) A1189–A1191.
- [145] W. Weber, B. Lengeler, Diffuse scattering of hard x rays from rough surfaces, *Phys. Rev. B* 46 (1992) 7953–7956.
- [146] W. Wu, Off-specular reflection from flat interfaces with density or compositional fluctuations, *J. Chem. Phys.* 98 (1993) 1687–1694.
- [147] D.K.G. de Boer, Glancing-incidence fluorescence of layered materials, *Phys. Rev. B* 44 (1991) 498–511.
- [148] J. Daillant, O. Bélorgey, Surface scattering of X-rays in thin films. Part i. Theoretical treatment, *J. Chem. Phys.* 97 (1992) 5824–5836.
- [149] J. Daillant, Bélorgey, Surface scattering of x rays in thin films. Part ii. Experiments on thin, *J. Chem. Phys.* 97 (1992) 5837–5843.
- [150] N. Jedrecy, G. Renaud, R. Lazzari, et al., Flat-top silver nanocrystals on the two polar faces of ZnO: An all angle X-ray scattering investigation, *Phys. Rev. B* 72 (2005) 45430.
- [151] N. Jedrecy, G. Renaud, R. Lazzari, et al., Unstrained islands with interface coincidence sites versus strained islands: X-ray measurements on Ag/ZnO, *Phys. Rev. B* 72 (2005) 195404.
- [152] K. Omote, Y. Ito, S. Kawamura, Small angle X-ray scattering for measuring pore-size distributions in porous low- κ films, *Appl. Phys. Lett.* 82 (2003) 544–546.
- [153] B. Lee, J. Yoon, W. Oh, Y. Hwang, K. Heo, K.S. Jin, J. Kim, K.W. Kim, M. Ree, In-situ grazing incidence small-angle X-ray scattering studies on nanopore evolution in low- k organosilicate dielectric thin films, *Macromolecules* 38 (2005) 3395–3405.
- [154] M. Tate, V.N. Urade, J.D. Kowalski, T. Wei, B.D. Hamilton, B.W. Eggiman, H.W. Hillhouse, Simulation and interpretation of 2d diffraction patterns from self-assembled nanostructured films at arbitrary angles of incidence: From grazing incidence (above the critical angle) to transmission perpendicular to the substrate, *J. Phys. Chem. B* 110 (2006) 9882–9892.
- [155] R. Lazzari, F. Leroy, G. Renaud, Grazing incidence small angle X-ray scattering from dense packing of islands on surfaces: Development of dwba and correlation between particle sizes and spacing, *Phys. Rev. B* 76 (2007) 125411.
- [156] R. Pottou, Reciprocity in optics, *Rep. Prog. Phys.* 67 (2004) 717–754.
- [157] A. Caticha, Asymptotic form of the reciprocity theorem with applications in X-ray scattering, *Phys. Rev. B* 62 (2000) 3639–3647.
- [158] J.E. Slipe, New green-function formalism for surface optics, *J. Opt. Soc. Am. B* 4 (1987) 481–489.
- [159] S.K. Sinha, M. Tolan, A. Gibaud, Effects of partial coherence on the scattering of X-rays by matter, *Phys. Rev. B* 57 (1998) 2740–2758.
- [160] M. Tolan, S.K. Sinha, X-ray scattering with partial coherent radiation: The exact relationship between “resolution” and “coherence”, *Physica B* 248 (1998) 399–404.
- [161] I.A. Vartanyants, I.K. Robinson, Partial coherence effects on the imaging of small crystals using coherent X-ray diffraction, *J. Phys.: Condens. Matter* 13 (2001) 10593–10611.
- [162] I.A. Vartanyants, I.K. Robinson, Origins of decoherence in coherent X-ray diffraction experiments, *Opt. Commun.* 222 (2003) 29–50.
- [163] A.P. Payne, B.M. Clemens, Influence of roughness distribution and correlation on X-ray diffraction from superlattices, *Phys. Rev. B* 47 (1993) 2289–2300.
- [164] A. Sentenac, G. Toso, M. Saillard, Study of coherent scattering from one-dimensional rough surfaces with a mean-field theory, *J. Opt. Soc. Am. A* 15 (1998) 924–931.
- [165] P.M. Morse, H. Feshbach, *Methods of Theoretical Physics*, Vol. Part 1 and 2, New-York, 1953.
- [166] P.Z. Wong, A.J. Bray, Scattering by rough surfaces, *Phys. Rev. B* 37 (1988) 7751–7758.
- [167] D.G. Stearns, X-ray scattering from interfacial roughness in multilayer structures, *J. Appl. Phys.* 71 (1992) 4286–4298.
- [168] S.K. Sinha, X-ray diffuse scattering as a probe for thin film and interface structure, *J. Phys. III France* 4 (1994) 1543–1557.
- [169] T. Salditt, T.H. Metzger, C. Brandt, U. Klemradt, J. Peisl, Determination of the static scaling exponent of self-affine interfaces by nonspecular X-ray scattering, *Phys. Rev. B* 51 (1995) 5617–5627.
- [170] T. Salditt, T.H. Metzger, J. Peisl, B. Reinker, M. Moske, K. Samwer, Determination of the height-height correlation function of rough surfaces from diffuse X-ray scattering, *Europhys. Lett.* 32 (1995) 331–336.
- [171] Y. Waseda, *The structure of non-crystalline materials*, Mc. Graw-Hill, New-York, 1980.
- [172] A. Braslav, P.S. Pershan, G. Swislow, B.M. Ocko, J. Als-Nielsen, Capillary waves on the surface of simple liquids measured by X-ray reflectivity, *Phys. Rev. B* 38 (1988) 2457–2470.
- [173] G. Palasantzas, Roughness spectrum and surface width of self-affine fractal surfaces via the k -correlation model, *Phys. Rev. B* 48 (1993) 14472–14478.
- [174] G. Palasantzas, J. Krim, Effect of the form of the height-height correlation function on diffuse X-ray scattering from self-affine surface, *Phys. Rev. B* 48 (1993) 2873–2877.
- [175] T. Salditt, T.H. Metzger, J. Peisl, G. Goerigk, Non-specular X-ray scattering from thin films and multilayers with small-angle scattering equipment, *J. Phys. D.: Appl. Phys.* 28 (1995) A236–A240.
- [176] C. Thompson, G. Palasantzas, Y. Feng, S.K. Sinha, J. Krim, X-ray reflectivity study of the growth kinetics of vapor-deposited silverfilms, *Phys. Rev. B* 49 (1994) 4902–4907.
- [177] R. Chiarello, V. Panella, J. Krim, C. Thompson, X-ray reflectivity and adsorption isotherm study of fractal scaling in vapor-deposited films, *Phys. Rev. Lett.* 67 (1991) 3408–3411.
- [178] H. You, R.P. Chiarello, H.K. Kim, K.G. Vandervoort, X-ray reflectivity and scanning tunneling microscope study of kinetic roughening of sputter-deposited gold films during growth, *Phys. Rev. Lett.* 70 (1993) 2900–2903.
- [179] A. Barabási, H. Stanley, *Fractal Concepts in Surface Growth*, Cambridge University Presss, 1995.
- [180] D.E. Savage, J. Kleiner, N. Schimke, Y.H. Phang, T. Jankowski, J. Jacobs, Determination of roughness correlations in multilayer films for X-ray mirrors, *J. Appl. Phys.* 69 (1991) 1411–1424.
- [181] D.E. Savage, N. Schimke, Y.H. Phang, M.G. Lagally, Interfacial roughness correlation in multilayer films: Influence of total film and individual layer thicknesses, *J. Appl. Phys.* 71 (1992) 3283–3293.
- [182] J.M. Eastman, in: G. Hass, Francombe, M.H. (Eds.), *Physics of Thin Films, Advances in Research and Development*, vol. 10, Academic Press, New York, 1978, p. 167.
- [183] E. Spiller, D. Stearns, M. Krumrey, Multilayer X-ray mirrors: Interfacial roughness, scattering and image quality, *J. Appl. Phys.* 74 (1993) 107–118.
- [184] M. Kopecky, Diffuse scattering of x rays from nonideal layered structures, *J. Appl. Phys.* 77 (1995) 2380–2387.
- [185] D. Bahr, W. Press, R. Jebasinski, S. Mantl, X-ray reflectivity and diffuse scattering study of CoSi₂ layers in Si produced by ion-beam synthesis, *Phys. Rev. B* 47 (1993) 4385–4393.
- [186] D.K.G. de Boer, Comments on ‘X-ray scattering from a randomly rough surface’, *Waves Random Media* 9 (1999) 459–460.
- [187] P. Mikulí, T. Baumbach, X-ray reflection by rough multilayer gratings: Dynamical and kinematical scattering, *Phys. Rev. B* 59 (1999) 7632–7643.
- [188] G.T. Baumbach, S. Tixier, U. Pietsch, V. Holý, Grazing-incidence diffraction from multilayers, *Phys. Rev. B* 51 (1995) 16848–16859.
- [189] S.A. Stepanov, E.A. Kondrashkina, M. Schmidbauer, R. Köller, J.-U. Pfeiffer, T. Jach, A.Y. Sourovov, Diffuse scattering from interface roughness in grazing-incidence X-ray diffraction, *Phys. Rev. B* 54 (1996) 8150–8162.
- [190] Y.H. Phang, R. Kariotis, D.E. Savage, M.G. Lagally, Diffraction from multilayer films with partially correlated interfacial roughness, *J. Appl. Phys.* 72 (1992) 4627–4633.
- [191] Z.H. Ming, A. Krol, Y.L. Soo, Y.H. Kao, J.S. Park, K.L. Wang, Microscopic structure of interfaces in Si_{1-x}Ge_x/Si heterostructures and superlattices studied by X-ray scattering and fluorescence yield, *Phys. Rev. B* 47 (1993) 16373.
- [192] J. Stettner, L. Schwalowsky, O.H. Seeck, M. Tolan, W. Press, C. Schwarz, H.V. Känel, Interface structure of mbe-grown CoSi₂/Si/CoSi₂ layers on Si(111): Partially correlated roughness and diffuse X-ray scattering, *Phys. Rev. B* 53 (1996) 1398–1412.
- [193] V. Holý, C. Giannini, L. Tapfer, T. Marschner, W. Stoltz, Diffuse X-ray reflection from multilayers with stepped interfaces, *Phys. Rev. B* 55 (1997) 9960–9968.
- [194] V. Holý, A.A. Darhuber, J. Stangl, G. Bauer, J. Nützel, G. Abstreiter, Oblique roughness replication in strained sige/si multilayers, *Phys. Rev. B* 57 (1998) 12435–12442.
- [195] V.M. Kaganer, S.A. Stepanov, R. Köhler, Bragg diffraction peaks in X-ray diffuse scattering from multilayers with rough interfaces, *Phys. Rev. B* 52 (1995) 16369–16372.
- [196] J.B. Korthright, Non specular X-ray scattering from multilayer structures, *J. Appl. Phys.* 70 (1991) 3620–3625.
- [197] T. Salditt, T.H. Metzger, J. Peisl, Kinetic roughness of amorphous multilayers studied by diffuse X-ray scattering, *Phys. Rev. Lett.* 73 (1994) 2228–2231.
- [198] D.R. Lee, K. Shin, O.H. Seeck, K. Hyunjun, Y.S. Seo, M. Tolan, M.H. Rafailovich, J. Sokolov, S.K. Sinha, X-ray scattering from free stranding polymer films with geometrically curved surfaces, *Phys. Rev. Lett.* 90 (2003) 185503–1.
- [199] T. Salditt, D. Lott, T.H. Metzger, J. Peisl, G. Vignaud, J. Legrand, G. Grübel, P. Höghöi, O. Schärpf, Characterization of interface roughness in w/si multilayers by high resolution diffuse X-ray scattering, *Physica B* 221 (1996) 13–17.
- [200] J.P. Schlomka, M. Tolan, L. Schwalowsky, O.H. Seeck, J. Stettner, W. Press, X-ray diffraction from Si/Ge layers: Diffuse scattering in the region of total external reflection, *Phys. Rev. B* 51 (1995) 2311–2321.
- [201] O.H. Seeck, P. Müller-Buschbaum, M. Tolan, W. Press, Diffuse X-ray scattering in specular direction: Analysis of a wetting film, *Europhys. Lett.* 29 (1995) 699–704.
- [202] W. Press, M. Tolan, J. Stettner, O.H. Seeck, J.P. Schlomka, V. Nitz, L. Schwalowsky, P. Müller-Buschbaum, D. Bahr, Roughness of surfaces and interfaces, *Physica B* 221 (1996) 1–9.
- [203] S. Stepanov, X ray server: <http://sergey.gmca.aps.anl.gov>, 1997.
- [204] B. Lee, I. Park, J. Yoon, S. Park, J. Kim, C.T. Kim, K.-W. Ree, Structural analysis of block copolymer thin films with grazing incidence small-angle X-ray scattering, *Macromolecules* 38 (2005) 4311–4323.
- [205] C. Vettier, Resonant X-ray scattering from magnetic materials, *J. Magn. and Mag. Mat.* 129 (1994) 59–65.
- [206] C. Vettier, Magnetic scattering experiments, *J. Magn. and Mag. Mat.* 226–230 (2001) 1053–1057.
- [207] C. Vettier, Resonant X-ray scattering in transition metal and rare-earth materials, *J. Elec. Spec. Rel. Phen.* 117–118 (2001) 113–128.
- [208] S.K. Stepanov, S.A. Sinha, X-ray resonant reflection from magnetic multilayers: Recursion matrix algorithm, *Phys. Rev. B* 61 (2000) 15302–15311.

- [209] M. Tolan, W. Press, F. Brinkop, J.P. Kotthaus, X-ray diffraction from laterally structured surfaces: Total external reflection, *Phys. Rev. B* 51 (1995) 2239–2251.
- [210] M. Wormington, I. Pape, T.P.A. Hase, B.K. Tanner, D.K. Bowen, Evidence of grading at polished surfaces from grazing-incidence X-ray scattering, *Phil. Mag. Lett.* 74 (1996) 211–216.
- [211] S.S. Fanchenko, A.A. Nefedov, Variational approach to X-ray diffuse scattering, *Phys. Stat. Sol. B* 212 (1999) R3.
- [212] A. Sentenac, J.-J. Greffet, Mean-field theory of light scattering by one-dimensional rough surface, *J. Opt. Com. Am. A* 15 (1998) 528–532.
- [213] B. Lee, C.T. Lo, P. Thiagarajan, D.R. Lee, Z. Niu, Q. Wang, Structural characterization using the multiple scattering effects in grazing-incidence small-angle X-ray scattering, *J. Appl. Crystallogr.* 41 (2008) 134–142.
- [214] M. Von laue, *Ann. Phys. (Leipzig)* 26 (1936) 55–85.
- [215] F. Leroy, R. Lazzari, G. Renaud, X-ray scattering from stepped and kinked surfaces: An approach with the para crystal model, *Surf. Sci.* 601 (2007) 1915–1929.
- [216] I.A. Vartanyants, A.V. Zozulya, K. Mundboth, O. Yefanov, M.I. Richard, E. Wintersberger, J. Stangl, A. Diaz, C. Mocuta, T.H. Metzger, G. Bauer, T. Boeck, M. Schmidbauer, Crystal truncation planes revealed by three-dimensional reconstruction of reciprocal space, *Phys. Rev. B* 77 (2008) 115317.
- [217] G. Glatter, O. Kratky, *Small angle X-ray scattering*, Academic Press, 1982.
- [218] J. Miao, P. Charalambous, J. Kirz, D. Sayre, Extending the methodology of X-ray crystallography to allow imaging of micrometre-sized non-crystalline specimens, *Nature* 400 (1999) 342–344.
- [219] I.K. Robinson, I.A. Vartanyants, G.J. Willimans, M.A. Pfeifer, J.A. Pitney, Reconstruction of the shape of gold nanocrystals using coherent X-ray diffraction, *Phys. Rev. Lett.* 87 (2001) 195505–1.
- [220] J. Miao, T. Ishikawa, B. Johnson, E.H. Anderson, B. Lai, K.O. Hodgson, High resolution 3d X-ray diffraction microscopy, *Phys. Rev. Lett.* 89 (2002) 088303–1.
- [221] G.J. Williams, M.A. Pfeifer, I.A. Vartanyants, I.K. Robinson, Three-dimensional imaging of microstructures in Au nanocrystals, *Phys. Rev. Lett.* 90 (2003) 175501–1.
- [222] M.A. Pfeifer, G.J. Williams, I.A. Vartanyants, R. Harder, I.K. Robinson, Three-dimensional mapping of a deformation field inside a nanocrystal, *Nature* 442 (2006) 63–66.
- [223] D.K. Saldin, V.L. Shneerson, Direct method for surface crystallography, *J. Phys.: Condens. Matter*, 20 (2008) 304208.
- [224] I.K. Robinson, R. Pindak, R.M. Fleming, S.B. Dierker, K. Ploog, G. Grübel, D.L. Abernathy, J. Als-Nielsen, Observation and explanation of one-dimensional X-ray speckle patterns from synthetic multilayers, *Phys. Rev. B* 52 (1995) 9917–9924.
- [225] J.L. Libbert, R. Pindak, S.B. Dierker, I.K. Robinson, Speckle in coherent X-ray reflectivity from Si(111) wafers, *Phys. Rev. B* 56 (1997) 6454–6457.
- [226] I.K. Robinson, J.A. Pitney, J.L. Libbert, I.A. Vartanyants, Surface morphology by reflectivity of coherent X-rays, *Physica B* 248 (1998) 387–394.
- [227] I.K. Robinson, J.L. Libbert, I.A. Vartanyants, J.A. Pitney, D.M. Smilgies, D.L. Abernathy, G. Grübel, Coherent X-ray diffraction imaging of silicon oxide growth, *Phys. Rev. B* 60 (1999) 9965–9972.
- [228] I.A. Vartanyants, J.A. Pitney, J.L. Libbert, I.K. Robinson, Reconstruction of surface morphology from coherent X-ray reflectivity, *Phys. Rev. B* 55 (1997) 13193–13202.
- [229] I.A. Vartanyants, I.K. Robinson, J.D. Onken, M.A. Pfeifer, G.J. Williams, F. Pfeiffer, H. Metzger, Z. Zhong, G. Bauer, Coherent X-ray diffraction from quantum dots, *Phys. Rev. B* 71 (2005) 245302.
- [230] F. Pfeiffer, W. Zhang, I.K. Robinson, Coherent grazing exit X-ray scattering geometry for probing the structure of thin films, *Appl. Phys. Lett.* 84 (2004) 1847–1849.
- [231] I.A. Vartanyants, D. Grigoriev, A.V. Zozulya, *Thin Solid Films* 515 (2007) 5546.
- [232] T.E. Faber, J.M. Ziman, A theory of the electrical properties of liquid metals. The resistivity of binary alloys, *Phil. Mag.* 11 (1965) 153–173.
- [233] D. Gazzillo, A. Giacometti, R. Guido della valle, E. Venutti, F. Carsughi, A scaling approximation for structure factors in the integral equation theory of polydisperse nonionic colloidal fluids, *J. Chem. Phys.* 111 (1999) 7636–7645.
- [234] J.S. Pedersen, Determination of size distributions from small-angle scattering data for systems with effective hard-sphere interactions, *J. Appl. Crystallogr.* 27 (1994) 595–608.
- [235] F. Leroy, R. Lazzari, G. Renaud, Effects of near-neighbor correlations on the diffuse scattering from a one-dimensional paracrystal, *Acta. Cryst. A* 60 (2004) 565–581.
- [236] T.R. Welberry, G.H. Miller, C.E. Carroll, Paracrystal and growth disorder models, *Acta. Cryst. A* 36 (1980) 921–929.
- [237] R. Hosemann, Die parakristallin feinstruktur natürlicher und synthetischer eiweise.visuellesnährungsverfahren zur bestimmung der schwankungsstensoren vongitterzellen, *Acta. Cryst. A* 4 (1951) 520–530.
- [238] R. Hosemann, A. Hindle, J. Macromol. Sci. Phys. B 34 (1995) 327–356.
- [239] H. Matsuoka, H. Tanaka, T. Hashimoto, N. Ise, Elastic scattering from cubic lattice systems with paracrystalline distortion, *Phys. Rev. B* 36 (3) (1987) 1754–1765.
- [240] H. Matsuoka, H. Tanaka, T. Hashimoto, N. Ise, Elastic scattering from cubic lattice systems with paracrystalline distortion ii, *Phys. Rev. B* 41 (6) (1990) 3854–3856.
- [241] X.-Q. Mu, X-ray diffraction by one-dimensional paracrystal of limited size, *Acta. Cryst. A* 54 (1998) 606–616.
- [242] R.P. Millane, J.L. Eads, Diffraction by one-dimensional paracrystals and perturbed lattices, *Acta. Cryst. A* 56 (2000) 497–506.
- [243] W. Wilke, General lattice factor of the ideal paracrystal, *Acta. Cryst. A* 39 (1983) 864–867.
- [244] J.L. Eads, R.P. Millane, Diffraction by the ideal paracrystal, *Acta. Cryst. A* 57 (2001) 507–517.
- [245] B. Busson, J. Doucet, Distribution and interference functions for two-dimensional hexagonal paracrystals, *Acta. Cryst. A* 56 (2000) 68–72.
- [246] A. Gibaud, A. Baptiste, D.A. Doshi, C.J. Brinker, L. Yang, B. Ocko, Wall thickness and core radius determination in surfactant templated silica thin films using SAXS and X-ray reflectivity, *Europhys. Lett.* 63 (2003) 833–839.
- [247] J. Olander, R. Lazzari, B. Mangili, J. Goniakowski, G. Renaud, J. Jupille, Size- and temperature-dependent epitaxy for a strong film-substrate mismatch: The case of Pt/MgO(001), *Phys. Rev. B* 76 (2007) 075409.
- [248] C. Revenant, F. Leroy, G. Renaud, R. Lazzari, A. Létoeblon, T.E. Maday, Structural and morphological evolution of co on faceted Pt/W(1 1 1) surface upon thermal annealing, *Surf. Sci.* 601 (2007) 3431–3449.
- [249] A. Vrij, *J. Chem. Phys.* 69 (1978) 1742.
- [250] A. Vrij, Mixtures of hard spheres in the Percus-Yevick approximations. Light scattering at finite angles, *J. Chem. Phys.* 71 (1979) 3267–3270.
- [251] P. Van beurten, A. Vrij, Polydispersity effects in the small-angle scattering of concentrated solutions of colloidal spheres, *J. Chem. Phys.* 74 (1981) 2744–2748.
- [252] J.S. Rowlinson, *Liquid, Liquid and Liquid Mixtures*, Butterworth, London, 1969.
- [253] M. Zinke-Allmang, Phase separation on solid surfaces: Nucleation, coarsening and coalescence kinetics, *Thin Solid Films* 346 (1999) 1–68.
- [254] J. Venables, *Introduction to Surface and Thin Film Processes*, Cambridge University Press, Cambridge, United Kingdom, 2000.
- [255] M. Kotlarchyk, S.-H. Chen, Analysis of small angle neutron scattering spectra from polydisperse interacting colloids, *J. Chem. Phys.* 79 (1983) 2461–2469.
- [256] J.S. Pedersen, P. Vyskocil, B. Schönfeld, G. Kostorz, Small-angle neutron scattering of precipitates in Ni-rich Ni-Ti alloys. II. Methods for analysing anisotropic scattering data, *J. Appl. Crystallogr.* 30 (1997) 975–985.
- [257] W.K. Bertram, Response to Pedersen's (1998) comment on correlation effects in small-angle neutron scattering from closely packed spheres, *J. Appl. Crystallogr.* 31 (1998) 489.
- [258] J.S. Pedersen, Comments on correlations effects in small-angle neutron scattering from closely packed spheres by Bertram (1996), *J. Appl. Crystallogr.* 31 (1998) 488–489.
- [259] W.K. Bertram, Correlation effects in small-angle neutron scattering from closely packed spheres, *J. Appl. Crystallogr.* 29 (1996) 682–685.
- [260] P. Fratzl, J.L. Lebowitz, O. Penrose, J. Amar, Scaling functions self-similarity and the morphology of phase-separating systems, *Phys. Rev. B* 44 (1991) 4794–4811.
- [261] D. Gazzillo, A. Giacometti, F. Carsughi, Corresponding-states approach to small-angle scattering from polydisperse ionic colloidal fluids, *Phys. Rev. E* 60 (1999) 6722–6733.
- [262] B. Lee, S. Seifert, S.J. Riley, G. Tikhonov, N.A. Tomczyk, S. Vajda, R.E. Winans, Anomalous grazing incidence small-angle X-ray scattering studies of platinum nanoparticles formed by cluster deposition, *J. Chem. Phys.* 123 (2005) 074701–1.
- [263] W.H. Press, S.A. Teukolsky, W.T. Vetterling, B.P. Flannery, *Numerical Recipes in Fortran*, Cambridge University Press, 1992.
- [264] C. Mocuta, A. Barbier, G. Renaud, P. Panabière, Bayle-Guillemaud, Structure and growth of metal on nio(111) single crystal interfaces, *J. Appl. Phys.* 95 (2004) 2151.
- [265] C.R. Henry, C. Chapon, C. Duriez, S. Giorgio, *Surf. Sci.* 253 (1991) 177.
- [266] W.P. Halperin, Quantum size effects in metal particles, *Rev. Modern Phys.* 58 (3) (1986) 533–606.
- [267] A. Naudon, D. Babonneau, F. Petroff, A. Vaurès, Morphological study of cobalt aggregates in magnetic multilayers by grazing-incidence small angle X-ray scattering, *Thin Solid Films* 319 (1998) 81–83.
- [268] L. Favre, V. Dupuis, E. Bernstein, P. Melinon, A. Perez, S. Stanescu, T. Epicier, J.-P. Simon, D. Babonneau, J.-M. Tonnerre, J.-L. Hodeau, Structural and magnetic properties of copolymerized clusters, *Phys. Rev. B* 74 (2006) 014439.
- [269] A. Gibaud, S. Hazra, C. Sella, P. Laffez, A. Désert, A. Naudon, G. Van tendeloo, Particle layering in the ceramic-metal thin film Pt – Al₂O₃, *Phys. Rev. B* 63 (19) (2001) 193407.
- [270] D. Babonneau, T. Cabioch, A. Naudon, J.C. Girard, M.F. Denanot, Silver nanoparticles encapsulated in carbon cages obtained by co-sputtering of the metal and graphite, *Surf. Sci.* 409 (1998) 358–371.
- [271] D. Babonneau, A. Naudon, D. Thiaudière, S. Lequien, Morphological characterization of ion-sputtered C-Ag/C-C-Ag and Ag/C films by GISAXS, *J. Appl. Crystallogr.* 32 (2) (1999) 226–233.
- [272] C.L. Chien, Nanostructure-induced properties in granular metallic solids, *Nanostruct. Mater.* 1 (1992) 179–184.
- [273] L.F. Schelp, A. Fert, F. Fettar, P. Holody, S.F. Lee, J.L. Maurice, F. Petroff, A. Vaurès, Spin-dependent tunneling with Coulomb blockade, *Phys. Rev. B* 56 (10) (1997) R5747–R5750.
- [274] J.M. Dubuisson, J.M. Dauvergne, C. Depautex, P. Vachette, C.E. Williams, Asaxs spectrometer, *Nucl. Instrum. Meth. A* 246 (1986) 636–640.
- [275] F. Family, P. Meakin, Kinetics of droplet growth processes: Simulations, theory and experiments, *Phys. Rev. A* 40 (1989) 3836–3854.
- [276] D. Beysens, C.M. Knobler, H. Schaffar, Scaling in the growth of aggregates on a surface, *Phys. Rev. B* 41 (14) (1990) 9814–9818.
- [277] G.M. Pastor, J. Dorantes-Dávila, S. Pick, H. Dreyssé, Magnetic anisotropy of 3d transition-metal clusters, *Phys. Rev. Lett.* 75 (2) (1995) 326–329.

- [278] H.W. Kroto, J.R. Heath, S.C. O'brien, R.F. Curl, R.E. Smalley, *Nature* 318 (1985) 162.
- [279] D. Babonneau, T. Cabioch, M.C. Denanot, A. Naudon, Microstructural study of a C-Fe alloy synthesized by ion-beam sputtering co-deposition, *Phys. Lett.* 74 (6) (1999) 800–802.
- [280] D. Babonneau, A. Naudon, T. Cabioch, O. Lyon, Morphology of encapsulated iron nanoparticles obtained by co-sputtering and implantation: A GISAXS study, *J. Appl. Crystallogr.* 33 (3 Part 1) (2000) 437–441.
- [281] G. Franz, A. Schroeder, R. Hauer, Surface analysis and bioreactions of Ti- and V-containing a-c; H, *Surf. Interface Anal.* 28 (1999) 3–7.
- [282] N.W. Ashcroft, J. Lekner, Structure and resistivity of liquid metals, *Phys. Rev.* 145 (1) (1966) 83–90.
- [283] D. Babonneau, F. Pailloux, J.-P. Eymery, M.-F. Denanot, P. Guerin, E. Fonda, O. Lyon, Spontaneous organization of columnar nanoparticles in Fe-Bn nanocomposite films, *Phys. Rev. B* 71 (3) (2005) 035430.
- [284] D. Babonneau, J. Touret, S. Camilio, F. Pailloux, T. Cabioch, T. Girardeau, Encapsulation of metallic nanoclusters in carbon and boron nitride thin films prepared by ion-beam sputtering, *Surf. Coat. Technol.* 200 (22–23) (2006) 6251–6257.
- [285] E. Cattaruzza, F. D'acapito, F. Gonella, A. Longo, A. Martorana, G. Mattei, C. Maurizio, D. Thiaudiére, GISAXS study of Cu-Ni alloy clusters obtained by double ion implantation in silicate glasses, *J. Appl. Crystallogr.* 33 (3 Part 1) (2000) 740–743.
- [286] F. D'acapito, C. Maurizio, F. Gonella, E. Cattaruzza, G. Mattei, C. Mondelli, A. Longo, A. Martorana, On the use of grazing-incidence small-angle X-ray scattering (GISAXS) in the morphological study of ion-implanted materials, *J. Sync. Rad.* 11 (3) (2004) 272–277.
- [287] K. Domansky, J. Liu, L.-Q. Wang, M.H. Engelhard, S. Baskaran, Chemical sensors based on dielectric response of functionalized mesoporous silica films, *J. Mater. Res.* 16 (2001) 2810–2816.
- [288] P. Yang, G. Wirsberger, H.C. Huang, S.R. Cordero, M.D. Mcgehee, B. Scott, T. Deng, G.M. Whitesides, B.F. Chmelka, S.K. Buratto, G.D. Stucky, Mirrorless lasing from mesostructured waveguides patterned by soft lithography, *Science* 287 (5452) (2000) 465–467.
- [289] H. Fan, Y. Lu, A. Stump, S.T. Reed, T. Baer, R. Schunk, V. Perez-Luna, G.P. Lopez, C.J. Brinker, Rapid prototyping of patterned functional nanostructures, *Nature* 405 (2000) 56–60.
- [290] D. Gross, A.R. Balkenende, P.A. Albouy, A. Ayral, H. Amenitsch, F. Babonneau, Two-dimensional hexagonal mesoporous silica thin films prepared from block copolymers: Detailed characterization and formation mechanism, *Chem. Mater.* 13 (5) (2001) 1848–1856.
- [291] D. Gross, F. Babonneau, P.-A. Albouy, H. Amenitsch, A.R. Balkenende, A. Brunet-Bruneau, J. Rivory, An in situ study of mesostructured ctab-silica film formation during dip coating using time-resolved sas and interferometry measurements, *Chem. Mater.* 14 (2) (2002) 931–939.
- [292] F. Cagnol, D. Gross, J.d.A. Galo soler-Illia, E.L. Crepaldi, F. Babonneau, H. Amenitsch, C. Sanchez, Humidity-controlled mesostructuration in ctab-templated silica thin film processing. The existence of a modifiable steady state, *J. Mater. Chem.* 13 (2003) 61–66.
- [293] C.J. Brinker, Y. Lu, A. Sellinger, H. Fan, Evaporation-induced self-assembly: Nanostructures made easy, *Adv. Mater.* 11 (1999) 579–585.
- [294] D.A. Doshi, A. Gibaud, V. Goletto, M. Lu, H. Gerung, B. Ocko, S. Han, C.J. Brinker, Peering into the self-assembly of surfactant templated thin-film silica mesophases, *J. Am. Chem. Soc.* 125 (38) (2003) 11646–11655.
- [295] A. Gibaud, S. Dourdain, O. Gang, B.M. Ocko, In situ grazing incidence small-angle X-ray scattering real-time monitoring of the role of humidity during the structural formation of templated silica thin films, *Phys. Rev. B* 70 (2004) 161403.
- [296] M.P. Tate, B.W. Eggiman, J.D. Kowalski, H.W. Hillhouse, Order and orientation control of mesoporous silica films on conducting gold substrates formed by dip-coating and self-assembly: A grazing angle of incidence small-angle X-ray scattering and field emmission scanning electron microscopy study, *Langmuir* (2005) 10112–10118.
- [297] B.W. Eggiman, M.P. Tate, H.W. Hillhouse, Rhombohedral structure of highly ordered and oriented self-assembled nanoporous silica thin films, *Chem. Mater.* 18 (3) (2006) 723–730.
- [298] V.N. Urade, T.C. Wei, M.P. Tate, J.D. Kowalski, H.W. Hillhouse, Nanofabrication of double-gyroid thin films, *Chem. Mater.* 19 (4) (2007) 768–777.
- [299] J.-P. Simon, V. Joussemaume, G. Rolland, *J. Appl. Crystallogr.* 40 (2007) s363.
- [300] M. Morgen, E.T. Ryan, J.-H. Zhao, C. Hu, T. Cho, P.S. Ho, Low dielectric constant materials for ulsi interconnects, *Ann. Rev. Mat. Sci.* 30 (1) (2000) 645–680.
- [301] G. Maier, Low dielectric constant polymers for microelectronics, *Prog. Polym. Sci.* 26 (2001) 3–65.
- [302] K. Maex, M.R. Baklanov, D. Shamiryan, F. Lacopi, S.H. Brongersma, Z.S. Yanovitskaya, Low dielectric constant materials for microelectronics, *J. Appl. Phys.* 93 (11) (2003) 8793–8841.
- [303] B. Lee, Y.-H. Park, Y.-T. Hwang, W. Oh, J. Yoon, M. Ree, Ultralow-k nanoporous organosilicate dielectric films imprinted with dendritic spheres, *Nature Materials* 4 (2005) 147–150.
- [304] J.L. Hedrick, R.D. Miller, C.J. Hawker, K.R. Carter, W. Volksen, D.Y. Yoon, M. Trollsås, Templating nanoporosity in thin-film dielectric insulators, *Adv. Mater.* 10 (1998) 1049–1053.
- [305] H.-J. Lee, E.K. Lin, H. Wang, W. Wu, W. Chen, E.S. Moyer, Structural comparison of hydrogen silsesquioxane based porous low-k thin films prepared with varying process conditions, *Chem. Mater.* 14 (4) (2002) 1845–1852.
- [306] S. Yang, P. Mirau, C.-S. Pai, O. Nalamasu, E. Reichmanis, E.K. Lin, H.-J. Lee, D. Gidley, J. Sun, Molecular templating of nanoporous ultralow dielectric constant organosilicates by tailoring the microphase separation of triblock copolymers, *Chem. Mater.* 13 (9) (2001) 2762–2764.
- [307] E. Huang, M.F. Toney, W. Volksen, D. Mecerreyes, P. Brock, H.-C. Kim, C.J. Hawker, J.L. Hedrick, V.Y. Lee, T. Magbitang, R.D. Miller, L.B. Lurio, Pore size distributions in nanoporous methyl silsesquioxane films as determined by small angle X-ray scattering, *Appl. Phys. Lett.* 81 (12) (2002) 2232–2234.
- [308] P. Hammer, M.S. Tokumoto, C.V. Santilli, S.H. Pulcinelli, A.F. Craievich, A. Smith, Nanostructure and properties of ZnO films produced by the pyrosol process, *J. Appl. Crystallogr.* 36 (3 Part 1) (2003) 435–438.
- [309] J. Nishino, T. Kawarada, S. Ohshio, H. Saitoh, K. Mayurama, K. Kamatadoi, Conductive indium-doped zinc oxide films prepared by atmospheric-pressure chemical vapour deposition, *J. Mater. Sci. Lett.* 16 (1997) 629–631.
- [310] B.M. Ataev, A.M. Bagamadova, A.M. Djabrailov, V.V. Mamedov, R.A. Rabadanov, Highly conductive and transparent Ga-doped epitaxial ZnO films on sapphire by cvd, *Thin Solid Films* 260 (1995) 19–20.
- [311] R. Wang, L.L.H. King, A.W. Sleight, Highly conducting transparent thin films based on zinc oxide, *J. Mater. Res.* 11 (1996) 1659–1664.
- [312] A.P. Rizzato, C.V. Santilli, S.H. Pulcinelli, A.F. Craievich, Structural characterization of undoped and Sb-doped SnO₂ thin films fired at different temperatures, *J. Appl. Crystallogr.* 36 (3 Part 1) (2003) 736–739.
- [313] M. Park, C. Harrison, P.M. Chaikin, R.A. Register, D.H. Adamson, Block Copolymer Lithography: Periodic Arrays of $\sim 10^{11}$ Holes in 1 Square Centimeter, *Science* 276 (1997) 1401–1404.
- [314] C. Ross, Patterned magnetic recording media, *Annu. Rev. Mater. Res.* 31 (1) (2001) 203–235.
- [315] R.J. Albalak, E.L. Thomas, Roll-casting of block copolymers and of block copolymer-homopolymer blends, *J. Poly. Sci. B: Polym. Phys.* 32 (1994) 341–350.
- [316] T.L. Morkved, M. Lu, A.M. Urbas, E.E. Ehrichs, H.M. Jaeger, P. Mansky, T.P. Russell, Local control of microdomain orientation in diblock copolymer thin films with electric fields, *Science* 273 (5277) (1996) 931–933.
- [317] C. Tang, A. Tracz, M. Kruk, R. Zhang, D.-M. Smilgies, K. Matyjaszewski, T. Kowalewski, Long-range ordered thin films of block copolymers prepared by zone-casting and their thermal conversion into ordered nanostructured carbon, *J. Am. Chem. Soc.* 127 (19) (2005) 6918–6919.
- [318] P. Müller-Buschbaum, E. Bauer, E. Maurer, K. Schlogl, S.V. Roth, R. Gehrke, Route to create large-area ordered polymeric nanochannel arrays, *Appl. Phys. Lett.* 88 (2006) 083114.
- [319] K. Yurekli, R. Krishnamoorti, M.F. Tse, K.O. Mcelrath, A.H. Tsou, H.-C. Wang, Structure and dynamics of carbon black-filled elastomers, *J. Polym. Sci. B: Polym. Phys.* 39 (2001) 256–275.
- [320] P. Du, M. Li, K. Douki, X. Li, C.B.W. Garcia, A. Jain, D.-M. Smilgies, L.J. Fetter, S.M. Gruner, U. Wiesner, C.K. Ober, Additive-driven phase-selective chemistry in block copolymer thin films: The convergence of top-down and bottom-up approaches, *Adv. Mater.* 16 (12) (2004) 953–957.
- [321] B.I. Halperin, D.R. Nelson, Theory of two-dimensional melting, *Phys. Rev. Lett.* 41 (2) (1978) 121–124.
- [322] D.R. Nelson, B.I. Halperin, Dislocation-mediated melting in two dimensions, *Phys. Rev. B* 19 (5) (1979) 2457–2484.
- [323] J.M. Kosterlitz, D.J. Thouless, Ordering metastability and phase transitions in two-dimensional systems, *J. Phys. C: Solid State Phys.* 6 (1973) 1181–1203.
- [324] G.E. Stein, E.J. Kramer, X. Li, J. Wang, Single-crystal diffraction from two-dimensional block copolymer arrays, *Phys. Rev. Lett.* 98 (8) (2007) 086101.
- [325] I. Park, B. Lee, J. Ryu, K. Im, J. Yoon, M. Ree, T. Chang, Epitaxial phase transition of polystyrene-*b*-polysisoprene from hexagonally perforated layer to gyroid phase in thin film, *Macromolecules* 38 (25) (2005) 10532–10536.
- [326] S. Park, K. Kwon, D. Cho, B. Lee, M. Ree, T. Chang, Phase diagram constructed from the hplc fractions of a polystyrene-*b*-polysisoprene prepared by anionic polymerization, *Macromolecules* 36 (12) (2003) 4662–4666.
- [327] P. Müller-Buschbaum, J.S. Gutmann, M. Stamm, R. Cubitt, S. Cunis, G. Von krosigk, R. Gehrke, W. Petry, Dewetting of thin polymer-blend films examined with gisas, *Physica B* 283 (1–3) (2000) 53–59.
- [328] P. Müller-Buschbaum, M. Wolkenhauer, O. Wunnickie, M. Stamm, R. Cubitt, W. Petry, Structure formation in two-dimensionally confined diblock copolymer films, *Langmuir* 17 (18) (2001) 5567–5575.
- [329] P. Müller-Buschbaum, M. Stamm, Dewetting of thin polymer films: An X-ray scattering study, *Physica B* 248 (1–4) (1998) 229–237.
- [330] M. Haruta, Size- and support-dependency in the catalysis of gold, *Catalysis Today* 36 (1) (1997) 153–166.
- [331] B.K. Min, A.K. Santra, D.W. Goodman, Understanding silica-supported metal catalysts: Pd/silica as a case study, *Catalysis Today* 85 (2–4) (2003) 113–124.
- [332] R.E. Winans, S. Vajda, B. Lee, S.J. Riley, S. Seifert, G.Y. Tikhonov, N.A. Tomczyk, Thermal stability of supported platinum clusters studied by *in situ* gisas, *J. Phys. Chem. B* 108 (47) (2004) 18105–18107.
- [333] S. Vajda, R.E. Winans, J. Elam, B. Lee, M. Pellin, S. Seifert, G.Y. Tikhonov, N.A. Tomczyk, Supported gold clusters and cluster-based nanomaterials: Characterization stability and growth studies by *in situ* gisas under vacuum conditions and in the presence of hydrogen, *Topics Catalysis* 39 (3–4) (2006) 161–166.
- [334] R.E. Winans, S. Vajda, G. Ballentine, J. Elam, B. Lee, M. Pellin, S. Seifert, G.Y. Tikhonov, N.A. Tomczyk, Reactivity of supported platinum nanoclusters studied by *in situ* gisas: Clusters stability under hydrogen, *Topics Catalysis* 39 (3–4) (2006) 145–149.
- [335] R. Paniago, T.H. Metzger, M. Rauscher, Z. Kovats, J. Peisl, J. Schulze, I. Eisele, S. Ferrer, *J. Appl. Crystallogr.* 33 (2000) 433.

- [336] M. Schmidbauer, M. Hanke, R. Köhler, Phys. Rev. B 71 (2005) 115323.
- [337] M. Schmidbauer, D. Grigoriev, M. Hanke, P. Schäfer, T. Wiebach, R. Köhler, Phys. Rev. B 71 (2005) 115324.
- [338] J. Stangl, T. Roch, V. Holý, M. Pinczolits, G. Springholz, G. Bauer, I. Kegel, T.H. Metzger, J. Zhu, K. Brunner, G. Abstreiter, Grazing incidence small angle X-ray scattering study of buried and free-standing SiGe islands in a SiGe/Si superlattice, *J. Vac. Sci. Technol. B* 18 (11) (2000) 2187.
- [339] T. Roch, V. Holý, J. Stangl, E. Höflinger, A. Daniel, G. Bauer, I. Kegel, T.H. Metzger, J. Zhu, K. Brunner, G. Abstreiter, *Phys. Stat. Sol. (b)* 224 (2001) 241.
- [340] F. Hatami, U. Müller, H. Kissel, K. Braune, R.-P. Blum, S. Rogaschewski, H. Niehus, H. Kirmse, W. Neumann, M. Schmidbauer, R. Köhler, W.T. Masselink, *J. Cryst. Growth* 213 (2000) 26.
- [341] J. Stangl, V. Holý, G. Springholz, G. Bauer, I. Kegel, T.H. Metzger, *Mater. Sci. Eng. C* 19 (2002) 349.
- [342] J.H. Li, V. Holý, M. Meduna, S.C. Moss, A.G. Norman, A. Mascarenhas, J.L. Reno, Lateral composition modulation in $(\text{InAs})_n/\text{AlAs}_m$ short-period superlattices investigated by high-resolution X-ray scattering, *Phys. Rev. B* 66 (2002) 115312–1.
- [343] B. Krause, T.H. Metzger, A. Rastelli, R. Songmuang, S. Kiravittaya, O.G. Schmidt, *Phys. Rev. B* 72 (2005) 085339.
- [344] M. Sztucki, T.H. Metzger, V. Chamard, A. Hesse, V. Holý, *J. Appl. Phys.* 99 (2006) 033519.
- [345] I. Kegel, T.H. Metzger, J. Peisl, Lateral ordering of coherent Ge islands on Si(001) studied by triple-crystal grazing incidence diffraction, *Appl. Phys. Lett.* 74 (20) (1999) 2978–2980.
- [346] V. Chamard, T.H. Metzger, C. Ferrero, E. Bellet-Amalric, B. Daudin, H. Mariette, G. Mula, *Physica E* 13 (2002) 1115.
- [347] V. Chamard, T.H. Metzger, M. Sztucki, V. Holý, M. Tolan, E. Bellet-Amalric, C. Adelmann, B. Daudin, H. Mariette, *Europhys. Lett.* 63 (2003) 268.
- [348] T. Schmidt, T. Clausen, J. Falta, G. Alexe, T. Passow, D. Hommel, S. Bernstorff, *Appl. Phys. Lett.* 84 (2004) 4367.
- [349] T. Schmidt, E. Roventa, T. Clausen, J.I. Flege, G. Alexe, S. Bernstorff, C. Kübel, A. Rosenauer, D. Hommel, J. Falta, *Phys. Rev. B* 72 (2005) 195334.
- [350] D.M. Follstaedt, S.M. Myers, G.A. Petersen, J.W. Medernach, Cavity formation and impurity gettering in He-implanted Si, *J. Electron. Mater.* 25 (1996) 157–164.
- [351] C.C. Griffioen, J.H. Evans, P.C. De Jong, A. Van Veen, Helium desorption/permeation from bubbles in silicon: A novel method of void production, *Nucl. Instrum. Meth. B* 27 (1987) 417–420.
- [352] M.L. David, M.F. Beaufort, J.F. Barbot, Effect of implant temperature on defects created using high fluence of helium in silicon, *J. Appl. Phys.* 93 (3) (2003) 1438–1442.
- [353] B. Pivac, O. Milat, P. Dubček, S. Bernstorff, F. Corni, C. Nobili, R. Tonini, *Phys. Stat. Sol. (a)* 198 (2003) 29.
- [354] B. Pivac, P. Dubček, S. Bernstorff, F. Corni, R. Tonini, *J. Alloys Compd.* 382 (2004) 75.
- [355] P. Dubček, B. Pivac, S. Bernstorff, F. Corni, R. Tonini, G. Ottaviani, *J. Appl. Crystallogr.* 36 (2003) 447.
- [356] D. Babonneau, M.-F. Beaufort, A. Declémery, J.-F. Barbot, J.-P. Simon, Grazing incidence small-angle X-ray scattering from defects induced by helium implantation in silicon, *J. Appl. Phys.* 99 (11) (2006) 113507.
- [357] D. Babonneau, S. Peripolli, M.-F. Beaufort, J.-F. Barbot, J.-P. Simon, Gisaxs study of cavities and 113 defects induced by neon and helium implantation in silicon, *J. Appl. Crystallogr.* 40 (s1) (2007) s350–s354.
- [358] D. Babonneau, S. Peripolli, M.-F. Beaufort, J.-F. Bardot, J.-P. Simon, J. Appl. Crystallogr. 40 (2007) s350.
- [359] L. Capello, F. Rieutord, A. Tauzin, F. Mazen, *J. Appl. Phys.* 102 (2007) 026106.
- [360] D. Gracin, K. Juraic, P. Dubček, A. Gajovic, S. Bernstorff, *Appl. Surf. Sci.* 252 (2006) 5598.
- [361] I.D. Desnica-Frankovic, P. Dubček, U.V. Desnica, S. Bernstorff, M.C. Ridgway, C.J. Glover, *Nucl. Instrum. Meth. B* 249 (2006) 114.
- [362] A.G. Cullis, L.T. Canham, P.D.J. Calcott, The structural and luminescence properties of porous silicon, *J. Appl. Phys.* 82 (3) (1997) 909–965.
- [363] V. Chamard, P. Bastie, D.L. Bolloch, G. Dolino, E. Elkaïm, C. Ferrero, J.-P. Lauriat, F. Rieutord, D. Thiaudiére, *Phys. Rev. B* 64 (2001) 245416.
- [364] S. Bernstorff, P. Dubček, B. Pivac, I. Kovacevic, A. Sassella, A. Borghesi, *Appl. Surf. Sci.* 253 (2006) 33.
- [365] B. Pivac, I. Kovacevic, P. Dubček, N. Radic, S. Bernstorff, *Thin Solid Films* 515 (2006) 756.
- [366] I. Kovacevic, B. Pivac, P. Dubček, N. Radic, S. Bernstorff, A. Slaoui, *Thin Solid Films* 511–512 (2006) 463.
- [367] S. Bernstorff, P. Dubček, I. Kovacevic, N. Radic, B. Pivac, *Thin Solid Films* 515 (2007) 5637.
- [368] D. Gracin, S. Bernstorff, P. Dubček, A. Gajovic, K. Juraic, *Thin Solid Films* 515 (2007) 5615.
- [369] D. Gracin, S. Bernstorff, P. Dubček, A. Gajovic, K. Juraic, *J. Appl. Crystallogr.* 40 (2007) s373.
- [370] D. Grozdanic, B. Rakvin, B. Pivac, P. Dubček, N. Radic, S. Bernstorff, *Thin Solid Films* 515 (2007) 5620.
- [371] M. Buljan, K. Salamon, P. Dubček, S. Bernstorff, I. Desnica-Frankovic, O. Milat, U. Desnica, *Vacuum* 71 (2003) 65.
- [372] U.V. Desnica, M. Buljan, I.D. Desnica-Frankovic, P. Dubček, S. Bernstorff, M. Ivanda, H. Zorc, *Nucl. Instrum. Meth. B* 216 (2004) 407.
- [373] I.D. Desnica-Frankovic, P. Dubček, M. Buljan, K. Furic, U.V. Desnica, S. Bernstorff, H. Karl, I. Großhans, B. Stritzker, *Nucl. Instrum. Meth. B* 238 (2005) 302.
- [374] U.V. Desnica, P. Dubček, K. Salamon, I.D. Desnica-Frankovic, M. Buljan, S. Bernstorff, U. Serincan, R. Turan, *Nucl. Instrum. Meth. B* 238 (2005) 272.
- [375] S. Stemmer, Y. Li, B. Foran, P.-S. Lysaght, S.-K. Striffer, P. Fuoss, S. Seifert, *Appl. Phys. Lett.* 83 (2003) 3141.
- [376] T.U. Schülli, R.T. Lechner, J. Stangl, G. Springholz, G. Bauer, S. Dhesi, P. Bencok, *Appl. Phys. Lett.* 84 (2004) 2661.
- [377] A.V. Zozulya, O.M. Yefanov, I.A. Vartanyants, K. Mundboth, C. Mocuta, T.H. Metzger, J. Stangl, G. Bauer, T. Boeck, M. Schmidbauer, Imaging of nanoislands in coherent grazing-incidence small-angle X-ray scattering experiments, *Phys. Rev. B* 78 (2008) 121304.
- [378] M. Bruel, World Patent Publication Number WO9905711A1.
- [379] A.E. Romanov, P.M. Petroff, J.S. Speck, *Appl. Phys. Lett.* 74 (1999) 2280.
- [380] F. Fournel, K. Rousseau, H. Moriceau, J. Eymery, J.L. Rouviere, N. Magnea, B. Aspar, *Appl. Phys. Lett.* 80 (2002) 793.
- [381] F. Fournel, H. Moriceau, N. Magnea, J. Eymery, D. Buttard, J.L. Rouviere, K. Rousseau, B. Aspar, *Thin Solid Films* 380 (2000) 10.
- [382] J. Eymery, D. Buttard, F. Fournel, H. Moriceau, G.T. Baumbach, D. Lubbert, *Phys. Rev. B* 65 (2002) 165337.
- [383] F. Leroy, J. Eymery, P. Gentile, F. Fournel, *Appl. Phys. Lett.* 80 (2002) 3078.
- [384] F. Leroy, J. Eymery, D. Buttard, G. Renaud, R. Lazzari, F. Fournel, Grazing incidence X-ray scattering investigation of si surface patterned with buried dislocation networks, *Appl. Phys. Lett.* 82 (2003) 2598–2600.
- [385] H.J. Freund, Clusters and islands on oxides: From catalysis via electronics and magnetism to optics, *Surf. Sci.* 500 (2002) 271–299.
- [386] J. Jupille, A few issues regarding oxide surfaces, *Surf. Rev. Lett.* 8 (2001) 69.
- [387] J.L. Menéndez, P. Caro, A. Cebollada, *J. Cryst. Growth* 192 (1998) 164.
- [388] M. Valden, X. Lai, D.W. Goodman, Onset of catalytic activity of gold clusters on titania with the appearance on nonmetallic properties, *Science* 281 (1998) 1647–1650.
- [389] C.T. Campbell, *Surf. Sci. Rep.* 27 (1997) 1.
- [390] C.T. Campbell, S.C. Parker, D.E. Starr, The effect of size-dependent nanoparticle energetics on catalyst sintering, *Science* 298 (2002) 811.
- [391] P. Deltour, J.L. Barrat, P. Jensen, Fast diffusion of a lennard-jones cluster on a crystalline surface, *Phys. Rev. Lett.* 78 (1997) 4597–4600.
- [392] P. Etienne, J. Massies, S. Lequien, R. Cabanel, F. Petroff, *J. Cryst. Growth* 111 (1991) 1003.
- [393] J.M. Fiorzak, E.D. Dahjberg, *Phys. Rev. B* 44 (1991) 9338.
- [394] C. Noguera, Physics and Chemistry at Oxide Surfaces, Cambridge University Press, Cambridge, 1995.
- [395] A. Miyamoto, T. Hattori, T. Inui, *Appl. Surf. Sci.* 60–61 (1992) 660.
- [396] A.M. Flank, R. Delaunay, P. Lagarde, M. Pompa, J. Jupille, *Phys. Rev.B* 53 (1996) R1737.
- [397] P. Guénard, G. Renaud, B. Villette, Structure translational state and morphology of the Ag/MgO(001) interface during its formation, *Physica B* 221 (1996) 205.
- [398] O. Robach, G. Renaud, A. Barbier, Structure and morphology of the Ag/MgO(001) interface during insitugrowth at room temperature, *Phys. Rev. B* 60 (1999) 5858–5871.
- [399] G. Renaud, A. Barbier, O. Robach, *Phys. Rev. B* 60 (1999) 5872.
- [400] A. Barbier, G. Renaud, A. Stierle, The NiO(111)-(1 × 1) surface, *Surf. Sci.* 402–404 (1998) 757–760.
- [401] A.M. Ferrari, G. Pachioni, *J. Phys. Chem.* 100 (1996) 9032.
- [402] I. Yudanov, G. Pachioni, K. Neyman, N. Rösh, *J. Phys. Chem. B* 101 (1997) 2786.
- [403] J. Goniakowski, *Phys. Rev. B* 57 (1998) 1935.
- [404] W. Hirschwald, Zinc Oxide: Properties and Behaviour of the Bulk the Solid/Vacuumand Solid/Gas Interface, in: Material Science, vol. 7, E. Kaldis North Holland Publishing, 1981.
- [405] R. Zhang, A. Ludviksson, C.T. Campbell, The chemisorption of h₂O and o₂ on cu films on ZnO(0001)-o, *Surf. Sci.* 289 (1993) 1–9.
- [406] E. Valkonen, B. Karlsson, C.G. Rissing, *Solar Energy* 32 (1984) 2121.
- [407] http://www.cenerg.ensmp.fr/ease/advanced_glassing.
- [408] S. Roberts, R.J. Gorte, A comparison of Pt overlayers on α -Al₂O₃(0001) ZnO(0001)-Zn and ZnO(0001)-O, *J. Chem. Phys.* 93 (7) (1990) 5337–5344.
- [409] W.T. Petrie, J.M. Vohs, Interaction of platinum films with the (001) and (0001) surfaces of ZnO, *J. Chem. Phys.* 101 (9) (1994) 8098–8107.
- [410] P.V. Radulovic, C.S. Feigerle, S.H. Overbury, Structure of Pt overlayers on ZnO(0001) and ZnO(0001̄) surfaces, *J. Phys. Chem.* 104 (2000) 3028–3034.
- [411] Y. Yoshihara, S.C. Parker, C.T. Campbell, Island growth kinetics during vapor deposition of Cu onto the Zn-terminated ZnO(0001) surface, *Surf. Sci.* 439 (1999) 153–162.
- [412] N. Jedrecy, S. Gallini, M. Sauvage-Simkin, R. Pinchaux, Copper growth on the o-terminated ZnO(000) surface: Structure and morphology, *Phys. Rev. B* 64 (2001) 085424.
- [413] B. Meyer, D. Marx, Density-functional study of cu atoms, monolayers, films, and coadsorbates on polar ZnO surfaces, *Phys. Rev. B* 69 (2004) 235420.
- [414] M. Haruta, M. Daté, Advances in the catalysis of au nanoparticles, *Appl. Catal. A* 222 (2001) 427.
- [415] T.V. Choudhary, D.W. Goodman, Catalytically active gold: The role of cluster morphology, *Appl. Catal. A* 291 (2005) 32–36.
- [416] U. Diebold, The surface science of titanium dioxide, *Surf. Sci. Rep.* 48 (2003) 53.
- [417] F. Cosandey, T.E. Maday, Growth, morphology and interfacial effects and catalytic properties of au on TiO₂, *Surf. Rev. Lett.* 8 (1–2) (2001) 73–93.
- [418] X. Lai, T.P. St. Clair, M. Valden, D.W. Goodman, Scanning tunneling microscopies studies of metal clusters supported on TiO₂(110): Morphology and electronic structure, *Prog. Surf. Sci.* 59 (1998) 25–52.

- [419] X. Lai, D.W. Goodman, Structure-reactivity correlations for oxide-supported metal catalysts: New perspectives from stm, *J. Mol. Cat. A: Chem.* 162 (2000) 33–50.
- [420] A. Kolmakov, D.W. Goodman, Scanning tunneling microscopy of gold clusters on $TiO_2(110)$: Co oxidation at elevated pressures, *Surf. Sci.* 490 (2001) L597–L601.
- [421] N. Spiridis, J. Haber, J. Korecki, Stm studies of au nano-clusters on $TiO_2(110)$, *Vacuum* 63 (2001) 99–105.
- [422] C.E.J. Mitchell, A. Howard, M. Carney, R.G. Edgell, Direct observation of behaviour of au nanoclusters on $TiO_2(110)$ at elevated temperatures, *Surf. Sci.* 490 (2001) 196–210.
- [423] E. Wahlström, N. Lopez, R. Schaub, P. Thostrup, A. Rønnau, C. Africh, E. Lægggaard, J.K. Nørskov, R. Besenbacher, Bonding of gold nanoclusters to oxygen vacancies on rutile $TiO_2(110)$, *Phys. Rev. Lett.* 90 (2003) 026101–1.
- [424] A.K. Santra, F. Yang, D.W. Goodman, The growth of Ag–Au bimetallic nanoparticles on $TiO_2(110)$, *Surf. Sci.* 548 (2004) 324–332.
- [425] Y. Maeda, T. Fujitani, S. Tsubota, M. Haruta, Size and density of Au particles deposited on $TiO_2(110)$ –(1 × 1) and cross-linked (1 × 2) surfaces, *Surf. Sci.* 562 (2004) 1–6.
- [426] T. Minato, T. Susaki, S. Shiraki, H.S. Kato, M. Kawai, K. Aika, Investigation of the electronic interaction between $TiO_2(110)$ surfaces and au clusters by pes and stm, *Surf. Sci.* 566–568 (2004) 1012–1017.
- [427] W.T. Wallace, B.K. Min, D.W. Goodman, The stabilization of supported gold clusters by surface defects, *J. Mol. Cat. A: Chem.* 228 (2005) 3–10.
- [428] L. Zhang, F. Cosandey, R. Persaud, T.E. Madey, Initial growth and morphology of thin Au films on $TiO_2(110)$, *Surf. Sci.* 439 (1999) 73–85.
- [429] F. Cosandey, L. Zhang, T.E. Madey, Effect of substrate temperature on the epitaxial growth of au on $TiO_2(110)$, *Surf. Sci.* 474 (2001) 1–13.
- [430] L. Zhang, R. Persaud, T. Madey, Ultrathin metal films on a metal oxide surface: Growth of au on $TiO_2(110)$, *Phys. Rev. B* 73 (1999) 73.
- [431] O. Robach, G. Renaud, A. Barbier, Very-high-quality MgO(001) surfaces: Roughness, rumpling and relaxation, *Surf. Sci.* 401 (1998) 227–235.
- [432] A. Trampert, F. Ernst, C.P. Flynn, H.F. Fischmeister, M. Ruhle, High resolution transmission electron microscopy studies of the Ag/MgO interface, *Acta Met. Mat.* 40 (1992) S227–S236.
- [433] C.G. Vonk, On two methods of determination of particle size distribution functions by means of small-angle X-ray scattering, *J. Appl. Crystallogr.* 9 (1976) 433–440.
- [434] F. Ehrlich, F.G. Hudda, *J. Chem. Phys.* 44 (1966) 1030.
- [435] R.L. Schwoebel, E.J. Shipsey, *J. Appl. Phys.* 37 (1966) 3682.
- [436] J.L. Viovy, D. Beyens, C.M. Knobler, Scaling description for the growth of condensation patterns on surfaces, *Phys. Rev. A* 37 (1988) 4965–4970.
- [437] B.J. Briscoe, K.P. Galvin, Growth with coalescence during condensation, *Phys. Rev. A* 43 (1991) 1906–1917.
- [438] P. Meakin, Droplet deposition growth coalescence *Rep. Prog. Phys.* 55 (1992) 157–240.
- [439] F. Family, P. Meakin, Scaling of droplet-size distribution in vapor deposited thin films, *Phys. Rev. Lett.* 61 (1988) 428–431.
- [440] A. Steyer, P. Guenoun, D. Beyens, Growth of droplets on a substrate by diffusion and coalescence, *Phys. Rev. A* 44 (12) (1991) 8271–8277.
- [441] B.K. Chakraverty, Grain size distribution in thin films-2: Non-conservative systems, *J. Phys. Chem. Sol* 28 (1967) 2413–24121.
- [442] H. Brune, Microscopic view of epitaxial metal growth: Nucleation and aggregation, *Surf. Sci. Rep.* 31 (1998) 121–229.
- [443] N.C. Bartelt, T.L. Einstein, E.D. Williams, Nucleation and growth of square islands during deposition: Sizes, coalescence, separations and correlations, *Surf. Sci.* 298 (1993) 421.
- [444] S.V. Khare, T.L. Einstein, Brownian motion and shape fluctuations of a single-layer adatom and vacancy clusters on surfaces: Theory and simulations, *Phys. Rev. B* 54 (1996) 11752–11761.
- [445] J. Carrey, J.L. Maurice, F. Petroff, Vaurès, Growth of Au clusters on amorphous Al_2O_3 : Evidence of cluster mobility above a critical size, *Phys. Rev. Lett.* 86 (2001) 4600–4603.
- [446] G. Barcaro, A. Fortunelli, F. Nita, R. Ferrando, Diffusion of palladium clusters on magnesium oxide, *Phys. Rev. Lett.* 95 (2005) 246103.
- [447] G. Wulff, Z. Kristallogr. 34 (1901) 449.
- [448] Kaischew, *Bull. Acad. Sci. Ser. Phys.* 2 (1951) 191.
- [449] L. Vitos, A. Ruban, H. Skriver, J. Kollár, The surface energy of metals *Surf. Sci.* 411 (1998) 186.
- [450] P. Jensen, N. Combe, *Comput. Mater. Sci.* 24 (2002) 78.
- [451] N. Combe, P. Jensen, A. Pimpinelli, *Phys. Rev. Lett.* 85 (2000) 110.
- [452] P.L. Hansen, J.B. Wagner, S. Helveg, J.R. Rostrup-Nielsen, B.S. Clausen, H. Topsøe, Atom-resolved imaging of dynamic shape changes in supported nanocrystals, *Science* 295 (2002) 2053.
- [453] P.B. Rasmussen, B.L.M. Hendriksen, H. Zeijlemaker, H.G. Ficke, J.W.M. Frenken, The "reactor stm": A scanning tunneling microscope for investigation of catalytic surfaces at semi-industrial reaction conditions, *Rev. Sci. Inst.* 69 (1998) 3879–3884.
- [454] A. Kolmakov, D.W. Goodman, *In situ* scanning tunneling microscopy of individual supported metal clusters at reactive gas pressures from 10^{-8} to 10^4 pa, *Rev. Sci. Inst.* 74 (2003) 2444–2450.
- [455] B.L.M. Hendriksen, J.W.M. Frenken, Co oxidation on pt(110): Scanning tunneling microscopy inside a high pressure flow reactor, *Phys. Rev. Lett.* 89 (2002) 046101–1.
- [456] B.L.M. Hendriksen, S.C. Bobaru, J.W.M. Frenken, Looking at heterogeneous catalysis at atmospheric pressure using tunnel vision, *Top. Catal.* 36 (2005) 43–54.
- [457] M. Salmeron, R. Schlögl, Ambient pressure photoemission spectroscopy: A new tool for surface science and nanotechnology, *Surf. Sci. Rep.* 63 (2008) 169–199.
- [458] P. Bernard, K. Peters, J. Alvarez, S. Ferrer, Ultrahigh vacuum/high pressure chamber for surface X-ray diffraction experiments, *Rev. Sci. Inst.* 70 (1999) 1478–1480.
- [459] K.F. Peters, C.J. Walker, P. Steadman, O. Robach, H. Isern, S. Ferrer, Adsorption of carbon monoxide on Ni(110) above atmospheric pressure investigated with surface X-ray diffraction, *Phys. Rev. Lett.* 86 (2001) 5325–5328.
- [460] M.D. Ackermann, T.M. Pedersen, B.L.M. Hendriksen, O. Robach, S.C. Bobaru, S.C. Popa, C. Quiros, H. Kim, B. Hammer, S. Ferrer, J.W.M. Frenken, Structure and reactivity of surface oxides on pt(110) during catalytic co oxidation, *Phys. Rev. Lett.* 95 (2005) 255505.
- [461] M.C. Saint-Lager, Y. Jugnet, P. Dolle, L. Piccolo, R. Baudoing-Savois, J. Bertolini, A. Bailly, O. Robach, C. Walker, S. Ferrer, Pd_8Ni_2 surface structure from surface X-ray diffraction. Surface evolution under hydrogen and butadiene reactants at elevated pressure, *Surf. Sci.* 587 (2005) 229–235.
- [462] M. Haruta, Gold as a novel catalyst in the 21st century: Preparation, working mechanism and applications, *Gold. Bull.* 37 (2004) 27–36.
- [463] M. Haruta, *Cattech* 6 (2002) 102.
- [464] A. Kolmakov, D.W. Goodman, Imaging gold clusters on $TiO_2(110)$ at elevated pressures and temperatures, *Catal. Lett.* 70 (2000) 93–97.
- [465] G. Medeiros-Ribeiro, A.-M. Bratkowski, T.I. Kamins, D.-A.A. Ohlberg, R.-S. Williams, *Science* 279 (1998) 353.
- [466] D.J. Smith, D. Chandrasekhar, S. Chaparro, P.A. Crozier, J. Drucker, M. Floyd, M.R. Mccartney, Y. Zhang, *J. Cryst. Growth* 259 (2003) 232.
- [467] E. Sutter, P. Sutter, J.E. Bernard, *Appl. Phys. Lett.* 84 (2004) 2100.
- [468] M. Stoffel, A. Rastelli, J. Tersoff, T. Merdhanova, O.G. Schmidt, *Phys. Rev. B* 74 (2006) 155326.
- [469] A. Rastelli, H.V. Känel, *Surf. Sci. Lett.* 515 (2002) L493.
- [470] A. Rastelli, M. Stoffel, J. Tersoff, G.S. Kar, O.G. Schmidt, *Phys. Rev. Lett.* 95 (2005) 026103.
- [471] D.J. Eaglesham, R. Hull, *Mater. Sci. Eng. B* 30 (1995) 197.
- [472] M. Takahasi, T. Kaizu, J. Mizuki, *Appl. Phys. Lett.* 88 (2006) 101917.
- [473] O. Kirfel, E. Müller, D. Grützmacher, K. Kern, A. Hesse, J. Stangl, V. Holý, G. Bauer, *Appl. Surf. Sci.* 224 (2004) 139.
- [474] F.M. Ross, R.M. Tromp, M.C. Reuter, *Science* 286 (1999) 3.
- [475] F. Leroy, J. Eymery, D. Buttard, G. Renaud, R. Lazzari, Growth of Ge on Si(001) studied in situ by grazing incidence small angle X-ray scattering, *J. Cryst. Growth* 275 (2005) e2195–e2200.
- [476] T.U. Schülli, M.I. Richard, G. Renaud, V. Favre-Nicolin, E. Wintersberger, G. Bauer, In situ investigation of the island nucleation of Ge on Si(001) using X-ray scattering methods, *Appl. Phys. Lett.* 89 (2006) 143114.
- [477] G. Medeiros-Ribeiro, T.I. Kamins, D.A.A. Ohlberg, R.S. Williams, *Phys. Rev. B* 58 (1998) 7.
- [478] M.I. Richard, T.-U. Schülli, G. Renaud, E. Wintersberger, G. Bauer, V. Holý, textit{in situ} X-ray scattering study on the evolution of ge island morphology and relaxation for low growth rate: Advanced transition to superdomes, *Phys. Rev. B* 79 (2009) 1.
- [479] V. Cimalla, K. Zekentes, *Appl. Phys. Lett.* 77 (2000) 10.
- [480] N. Radic, B. Pivac, P. Dubček, I. Kovacevic, S. Bernstorff, *Thin Solid Films* 515 (2006) 752.
- [481] P. Gambardella, A. Dallmeyer, K. Maiti, M.C. Malagoli, W. Eberhardt, K. Kern, C. Carbone, Ferromagnetism on one-dimensional monatomic metal chains, *Nature* 416 (2001) 301.
- [482] G. Springholz, V. Holý, M. Pinczelits, G. Bauer, Self-organized growth of three dimensional quantum-dot crystals with fcc-like stacking and a tunable lattice constant, *Science* 282 (1998) 734.
- [483] H. Ellmer, V. Repain, M. Sotto, S. Rousset, Pre-structured metallic template for the growth of ordered square-based nanodots, *Surf. Sci.* 511 (2002) 183.
- [484] D.D. Chambliss, R.J. Wilson, S. Chiang, Nucleation of ordered Ni island arrays on Au(111) by surface-lattice dislocations, *Phys. Rev. Lett.* 66 (13) (1991) 1721–1724.
- [485] P. Gambardella, M. Blanc, H. Brune, K. Kuhnke, K. Kern, *Phys. Rev. B* 61 (2000) 2254–2262.
- [486] A. Ohtake, N. Koguchi, *Appl. Phys. Lett.* 89 (2006) 083108.
- [487] H. Brune, M. Giovannini, K. Bromann, K. Kern, Self-organized growth of nanostructured arrays on strain-relief patterns, *Nature* 394 (1998) 451.
- [488] F. Leroy, G. Renaud, A. Létoeblon, R. Lazzari, C. Motte, J. Goniakowski, Self-organized growth of nanoparticles on a surface patterned by a buried dislocation network, *Phys. Rev. Lett.* 95 (18) (2005) 185501.
- [489] F. Leroy, G. Renaud, A. Létoeblon, S. Rohart, Y. Girard, V. Repain, S. Rousset, A. Coati, Y. Garreau, Kink ordering and organized growth of co clusters on a stepped Au(111) surface: A combined grazing-incidence X-ray scattering and stm study, *Phys. Rev. B* 77 (2008) 045430–045443.
- [490] P. Torelli, E.A. Soares, G. Renaud, L. Gragnaniello, S. Valeri, X.X. Guo, P. Luches, *Phys. Rev. B* 77 (2008) 081409(R).
- [491] S. Padovani, Ph.D. Thesis of Louis Pasteur University, Strasbourg, France, 1999.
- [492] A.R. Sandy, S.G.J. Mochrie, D.M. Zehner, K.G. Huang, D. Gibbs, Structure and phases of the Au(111) surface: X-ray-scattering measurements, *Phys. Rev. B* 43 (6) (1991) 4667–4687.
- [493] J.V. Barth, H. Brune, G. Ertl, R.J. Behm, Scanning tunneling microscopy observations on the reconstructed Au(111) surface: Atomic structure long-range superstructure, rotational domains, and surface defects, *Phys. Rev. B* 43 (15) (1990) 9307–9318.

- [494] U. Harten, A.M. Lahee, J.P. Toennies, C. Wöll, Observation of a soliton reconstruction of Au(111) by high-resolution helium-atom diffraction, *Phys. Rev. Lett.* 54 (24) (1985) 2619–2622.
- [495] V. Repain, G. Baudot, H. Ellmer, S. Rousset, Two-dimensional long-range-ordered growth of uniform cobalt nanostructures on a Au(111) vicinal template, *Europhys. Lett.* 58 (2002) 730.
- [496] O. Fruchart, M. Klaua, J. Barthel, J. Kirschner, Self-organized growth of nanosized vertical magnetic Co pillars on Au(111), *Phys. Rev. Lett.* 83 (1999) 2769–2772.
- [497] O. Fruchart, G. Renaud, A. Barbier, M. Noblet, O. Ulrich, J.-P. Deville, F. Scheurer, J. Mane-Mane, V. Repain, G. Baudot, S. Rousset, X-ray super-cell crystallography of self-organized Co/Au(111) deposits, *Europhys. Lett.* 63 (2) (2003) 275–281.
- [498] S. Padovani, I. Chado, F. Scheurer, J.-P. Bucher, Transition from zero-dimensional superparamagnetism to two-dimensional ferromagnetism of co clusters on Au(111), *Phys. Rev. B* 59 (1999) 11887–11891.
- [499] Q. Xie, A. Madhukar, P. Chen, N.P. Kobayashi, Vertically self-organized inas quantum box islands on gaas(100), *Phys. Rev. Lett.* 75 (1995) 2542.
- [500] S. Rousset, V. Repain, G. Baudot, Y. Garreau, J. Lecoeur, Self-ordering of Au(111) vicinal surfaces and application to nanostructure organized growth, *J. Phys.: Condens. Mater.* 15 (2003) S3363–S3392.
- [501] S. Rohart, G. Baudot, V. Repain, Y. Girard, S. Rousset, H. Bulou, C. Goyhenex, L. Proville, Atomistic mechanisms for the ordered growth of Co nanodots on Au(788): A comparison between vt-stm experiments and multi-scaled calculations, *Surf. Sci.* 559 (2004) 47–62.
- [502] V. Repain, J.M. Berroir, S. Rousset, J. Lecoeur, Interaction between steps and reconstruction on Au(111), *Europhys. Lett.* 47 (1999) 435.
- [503] C.S. Lent, P.I. Cohen, Diffraction from stepped surfaces: I. Reversible surfaces, *Surf. Sci.* 139 (1984) 121–154.
- [504] P.R. Pukite, C.S. Lent, P.I. Cohen, Diffraction from stepped surfaces: II. Arbitrary terrace distributions, *Surf. Sci.* 161 (1985) 39–68.
- [505] B. Croset, C. de Beauvais, Diffraction by a surface with terraces distribution: The phase matrix method, *Surf. Sci.* 409 (1998) 403–412.
- [506] G. Uimin, P.-A. Lindgård, Analytical theory of diffuse scattering from distributions of non-overlapping structures, *Acta Crystallogr. A* 53 (1) (1997) 15–27.
- [507] J. Tegenkamp, J. Wollschläger, H. Pfntür, F.-J. Meyer zu Heringdorf, M. Horn-von Hoegen, Step and kink correlations on vicinal Ge(100) surfaces investigated by electron diffraction, *Phys. Rev. B* 65 (2002) 235316.
- [508] M. Sotto, B. Croset, Self-organisation of adsorbed nitrogen on (100) and (410) copper faces: A SPA-LEED study, *Surf. Sci.* 461 (2000) 78–86.
- [509] A. Crottini, D. Cvetko, L. Floreano, R. Gotter, A. Morgante, F. Tommasini, Step height oscillations during layer-by-layer growth of Pb on Ge(001), *Phys. Rev. Lett.* 79 (8) (1997) 1527–1530.
- [510] H.-J. Ernst, F. Fabre, J. Lapujoulade, Nucleation and diffusion of Cu adatoms on Cu(100): A Helium-atom-beam scattering study, *Phys. Rev. B* 46 (3) (1992) 1929–1932.
- [511] F. Dulot, B. Kierren, D. Malterre, Lineshape analysis of RHEED pattern: Scaling behavior and linewidth oscillations, *Thin Solid Films* 428 (2003) 72–75.
- [512] B. Salanon, P. Hecquet, Stress on vicinal surfaces, *Surf. Sci.* 412–413 (1998) 639–644.
- [513] P. Müller, A. Saül, Elastic effects on surface physics, *Surf. Sci. Rep.* 54 (2004) 157–258.
- [514] V. Repain, G. Baudot, H. Ellmer, S. Rousset, Ordered growth of cobalt nanostructures on a Au(111) vicinal surface: Nucleation mechanisms and temperature behavior, *Mater. Sci. Eng. B* 96 (2002) 178–187.
- [515] N. Witkowski, Y. Borensztein, G. Baudot, V. Repain, Y. Girard, S. Rousset, Combined scanning tunneling microscopy and reflectance anisotropy spectroscopy study of self-organized anisotropic cobalt nanodots on a vicinal Au(111) surface, *Phys. Rev. B* 70 (8) (2004) 85408.
- [516] A. Bourret, How to control the self-organization of nanoparticles by bonded thin layers, *Surf. Sci.* 432 (1999) 37–53.
- [517] B. Degroote, J. Dekoster, G. Langouche, Step decoration and surface alloying: Growth of cobalt on Ag(100) as a function of deposition temperature, *Surf. Sci.* 452 (2000) 172–178.
- [518] P.W. Palmberg, T.N. Rhodin, C.J. Todd, *Appl. Phys. Lett.* 11 (1967) 33.
- [519] A. Rockett, C.J. Kiely, Energetics of misfit- and threading-dislocation arrays in heteroepitaxial films, *Phys. Rev. B* 44 (3) (1991) 1154–1162.
- [520] A.K. Seeger, Small angle scattering from dislocations in deformed single crystals, *J. Appl. Phys.* 30 (5) (1959) 629–637.
- [521] R. Bonnet, J.-L. Verger-Gaugry, Thin epitaxial film on semiinfinite substrate – role of intrinsic dislocation and thickness in elastic-deformation, *Phil. Mag. A* 66 (5) (1992) 849.
- [522] J. Wollschläger, D. Erdos, H. Goldbach, R. Hopken, K.M. Schroder, *Thin Solid Films* 400 (2001) 1–8.
- [523] M. Dynna, J.L. Vassent, A. Marty, B. Gilles, *J. Appl. Phys.* 80 (1996) 2650.
- [524] S. Benedetti, H. Benia, N. Nilius, S. Valeri, H. Freund, *Chem. Phys. Lett.* 430 (2006) 330.
- [525] J. Sinfelt, *Bimetallic Catalysts*, Wiley, New-York, 1983.
- [526] B.N. Kuznetsov, Y.I. Yermakov, M. Boudart, J.P. Collman, The conversion of neopentane on supported catalysts Pt + W/SiO₂ and Pt + Mo/SiO₂ obtained through organometallic compounds of Pt, W and Mo, *J. Mol. Catal.* 4 (1) (1978) 49.
- [527] Y.I. Yermakov, B.N. Kuznetsov, Y.A. Ryndin, Hydrogenolysis of ethane on supported (Mo + Pt)/SiO₂ catalysts, *J. Catal.* 42 (1) (1976) 73.
- [528] G. Leclercq, I. Romero, S. Pietrzyk, J. Grimalt, L. Leclercq, Properties of platinum-molybdenum bimetallic catalysts deposited on silica, *J. Mol. Catal.* 25 (1–3) (1984) 67.
- [529] A. Trunschke, H. Ewald, D. Gutschick, H. Miessner, M. Skupin, B. Walther, H.-C. Bottcher, New bimetallic rh-mo and rh-w clusters as precursors for selective heterogeneous co hydrogenation, *J. Mol. Catal.* 56 (1–3) (1989) 95.
- [530] T.E. Madey, J. Guan, C.-H. Nien, C.-Z. Dong, H.-S. Tao, R.A. Campbell, *Surf. Rev. Lett.* 3 (1996) 1315.
- [531] T.E. Madey, C.-H. Nien, K. Pelhos, J.-J. Kolodziej, I.M. Abdelrehim, H.-S. Tao, Faceting induced by ultrathin metal films: Structure, electronic properties and reactivity, *Surf. Sci.* 438 (1999) 191–206.
- [532] T.E. Madey, K. Pelhos, Q. Wu, R. Barnes, I. Ermanoski, W. Chen, J.-J. Kolodziej, J.E. Rowe, *PNAS* 99 (2002) 6503.
- [533] K.-J. Song, R.A. Demmin, C. Dong, E. Garfunkel, T.E. Madey, Faceting induced by an ultrathin metal film: Pt on w(111), *Surf. Sci.* 227 (1990) L79–L85.
- [534] T.E. Madey, K.-J. Song, C.-Z. Dong, R.A. Demmin, The stability of ultrathin metal films on w(110) and w(111), *Surf. Sci.* 247 (2–3) (1991) 175–187.
- [535] C. Herring, *Phys. Rev.* 82 (1951) 87.
- [536] J.G. Che, C.T. Chan, C.H. Kuo, T.C. Leung, Faceting induced by ultrathin metal films: A first principles study, *Phys. Rev. Lett.* 79 (21) (1997) 4230–4233.
- [537] K. Pelhos, J.B. Hannon, G.L. Kellogg, T.E. Madey, Leem investigation of the faceting of the pt covered w(111) surface, *Surf. Sci.* 432 (1999) 115–124.
- [538] K. Pelhos, T.E. Madey, J.B. Hannon, G.L. Kellogg, *Surf. Rev. Lett.* 5 (1999) 767.
- [539] J.J. Kolodziej, T.E. Madey, J.W. Keister, J.E. Rowe, Photoelectron spectroscopy studies of growth, thermal stability, and alloying for transition metal-tungsten (111) bimetallic systems, *Phys. Rev. B* 65 (7) (2002) 075413.
- [540] C.-H. Nien, T.E. Madey, Y.W. Tai, T.C. Leung, J.G. Che, C.T. Chan, Coexistence of 011 facets with 112 facets on w(111) induced by ultrathin films of Pd, *Phys. Rev. B* 59 (15) (1999) 10335–10340.
- [541] M. De Santis, R. Baudoing-Savois, P. Dolle, M.C. Saint-Lager, Chemical ordering in the first stages of Co-Pt film growth on pt(111), *Phys. Rev. B* 66 (8) (2002) 085412.
- [542] A.V. Ruban, H.L. Skriver, J.K. Nørskov, Surface segregation energies in transition-metal alloys, *Phys. Rev. B* 59 (24) (1999) 15990–16000.
- [543] J. Guan, R.A. Campbell, T.E. Madey, Ultrathin metal films on W(111): Morphology and faceting reconstruction, *Surf. Sci.* 341 (1995) 311.
- [544] J.F. Ludwig, J.C.R. Eddy, O. Malis, R.L. Headrick, *Appl. Phys. Lett.* 81 (2002) 2770.
- [545] G. Ozaydin, A.S. Özcan, Y. Wand, K. Ludwig, H. Zhou, R.L. Headrick, D.P. Siddons, *Appl. Phys. Lett.* 87 (2005) 163104.
- [546] G. Ozaydin, Y. Wang, K.F. Ludwig, H. Zhou, R.L. Headrick, *Nucl. Instrum. Meth. Phys. Res. B* 264 (2007) 47.
- [547] G. Ozaydin, K.F. Ludwig, H. Zhou, R.L. Headrick, *J. Vac. Sci. Technol. B* 26 (2008) 551.
- [548] R. Gago, L. Vázquez, O. Plantévin, T.H. Metzger, J. Muñoz-García, R. Cuerno, M. Castro, *Appl. Phys. Lett.* 89 (2006) 233101.
- [549] R. Gago, L. Vázquez, O. Plantévin, J.A. Sánchez-García, M. Varela, M.C. Ballesteros, J.M. Albelia, T.H. Metzger, *Phys. Rev. B* 73 (2006) 155414.
- [550] O. Plantévin, R. Gago, L. Vázquez, A. Biermanns, T.-H. Metzger, *Appl. Phys. Lett.* 91 (2007) 113105.
- [551] G. Ozaydin, K.F. Ludwig, H. Zhou, L. Zhou, R.L. Headrick, *J. Appl. Phys.* 103 (2008) 033512.
- [552] J. Coraux, H. Renevier, V. Favre-Nicolin, G. Renaud, B. Daudin, *Appl. Phys. Lett.* 88 (2006) 153125.
- [553] A.S. Özcan, Y. Wang, G. Ozaydin, K.F. Ludwig, A. Bhattacharyya, T.D. Moustakas, D.P. Siddons, *J. Appl. Phys.* 100 (2006) 084307.
- [554] Y. Wang, A.S. Özcan, C. Sanborn, K.F. Ludwig, A. Bhattacharyya, R. Chandrasekaran, T.D. Moustakas, L. Zhou, D.J. Smith, *J. Appl. Phys.* 102 (2007) 073522.
- [555] R.L. McGreevy, Reverse monte carlo modelling, *J. Phys. Condens. Mater.* 13 (2001) R877–R913.
- [556] S. Narayanan, D.R. Lee, A. Hagman, X. Li, J. Wang, Particle dynamics in polymer-metal nanocomposite thin films on nanometer-length scales, *Phys. Rev. Lett.* 98 (2007) 185506.
- [557] S. Streit, C. Guut, V. Chamard, A. Robert, M. Sprung, H. Sternemann, M. Tolan, Two-dimensional dynamics of metal nanoparticles on the surface of thin polymer films studied with coherent X-rays, *Phys. Rev. Lett.* 98 (2007) 047801.